

Drug metabolism and transport: The frontier of personalized medicine

Edited by

Junmin Zhang, Rong Wang and Sofia Azeredo Pereira

Published in

Frontiers in Pharmacology



FRONTIERS EBOOK COPYRIGHT STATEMENT

The copyright in the text of individual articles in this ebook is the property of their respective authors or their respective institutions or funders. The copyright in graphics and images within each article may be subject to copyright of other parties. In both cases this is subject to a license granted to Frontiers.

The compilation of articles constituting this ebook is the property of Frontiers.

Each article within this ebook, and the ebook itself, are published under the most recent version of the Creative Commons CC-BY licence. The version current at the date of publication of this ebook is CC-BY 4.0. If the CC-BY licence is updated, the licence granted by Frontiers is automatically updated to the new version.

When exercising any right under the CC-BY licence, Frontiers must be attributed as the original publisher of the article or ebook, as applicable.

Authors have the responsibility of ensuring that any graphics or other materials which are the property of others may be included in the CC-BY licence, but this should be checked before relying on the CC-BY licence to reproduce those materials. Any copyright notices relating to those materials must be complied with.

Copyright and source acknowledgement notices may not be removed and must be displayed in any copy, derivative work or partial copy which includes the elements in question.

All copyright, and all rights therein, are protected by national and international copyright laws. The above represents a summary only. For further information please read Frontiers' Conditions for Website Use and Copyright Statement, and the applicable CC-BY licence.

ISSN 1664-8714
ISBN 978-2-8325-3067-2
DOI 10.3389/978-2-8325-3067-2

About Frontiers

Frontiers is more than just an open access publisher of scholarly articles: it is a pioneering approach to the world of academia, radically improving the way scholarly research is managed. The grand vision of Frontiers is a world where all people have an equal opportunity to seek, share and generate knowledge. Frontiers provides immediate and permanent online open access to all its publications, but this alone is not enough to realize our grand goals.

Frontiers journal series

The Frontiers journal series is a multi-tier and interdisciplinary set of open-access, online journals, promising a paradigm shift from the current review, selection and dissemination processes in academic publishing. All Frontiers journals are driven by researchers for researchers; therefore, they constitute a service to the scholarly community. At the same time, the *Frontiers journal series* operates on a revolutionary invention, the tiered publishing system, initially addressing specific communities of scholars, and gradually climbing up to broader public understanding, thus serving the interests of the lay society, too.

Dedication to quality

Each Frontiers article is a landmark of the highest quality, thanks to genuinely collaborative interactions between authors and review editors, who include some of the world's best academicians. Research must be certified by peers before entering a stream of knowledge that may eventually reach the public - and shape society; therefore, Frontiers only applies the most rigorous and unbiased reviews. Frontiers revolutionizes research publishing by freely delivering the most outstanding research, evaluated with no bias from both the academic and social point of view. By applying the most advanced information technologies, Frontiers is catapulting scholarly publishing into a new generation.

What are Frontiers Research Topics?

Frontiers Research Topics are very popular trademarks of the *Frontiers journals series*: they are collections of at least ten articles, all centered on a particular subject. With their unique mix of varied contributions from Original Research to Review Articles, Frontiers Research Topics unify the most influential researchers, the latest key findings and historical advances in a hot research area.

Find out more on how to host your own Frontiers Research Topic or contribute to one as an author by contacting the Frontiers editorial office: frontiersin.org/about/contact

Drug metabolism and transport: The frontier of personalized medicine

Topic editors

Junmin Zhang — Lanzhou University, China

Rong Wang — People's Liberation Army Joint Logistics Support Force 940th
Hospital, China

Sofia Azeredo Pereira — Universidade Nova de Lisboa, Portugal

Citation

Zhang, J., Wang, R., Pereira, S. A., eds. (2023). *Drug metabolism and transport: The frontier of personalized medicine*. Lausanne: Frontiers Media SA.
doi: 10.3389/978-2-8325-3067-2

Table of contents

- 06 **Editorial: Drug metabolism and transport: the Frontier of personalized medicine**
Junmin Zhang, Rong Wang and Sofia Azeredo Pereira
- 09 **Plasma metabolomic profiling reveals factors associated with dose-adjusted trough concentration of tacrolimus in liver transplant recipients**
Huaijun Zhu, Min Wang, Xiaofu Xiong, Yao Du, Danying Li, Zhou Wang, Weihong Ge and Yizhun Zhu
- 23 **Combined metabolomics and network pharmacology to elucidate the mechanisms of Dracorhodin Perchlorate in treating diabetic foot ulcer rats**
Pin Deng, Huan Liang, Shulong Wang, Ruinan Hao, Jinglu Han, Xiaojie Sun, Xuyue Pan, Dongxiao Li, Yinwen Wu, Zhichao Huang, Jiajia Xue and Zhaojun Chen
- 46 **Population pharmacokinetics and dosing optimization of unbound teicoplanin in Chinese adult patients**
Wen-Qian Fu, Ting-Ting Tian, Min-Xin Zhang, Hong-Tao Song and Li-Li Zhang
- 57 **Pharmacogenetics-based population pharmacokinetic analysis and dose optimization of valproic acid in Chinese southern children with epilepsy: Effect of *ABCB1* gene polymorphism**
Xianhuan Shen, Xinyi Chen, Jieluan Lu, Qing Chen, Wenzhou Li, Jiahao Zhu, Yaodong He, Huijuan Guo, Chenshu Xu and Xiaomei Fan
- 71 **Testis- specific Y-encoded- like protein 1 and cholesterol metabolism: Regulation of *CYP1B1* expression through Wnt signaling**
Xiujuan Zhu, Huanyao Gao, Sisi Qin, Duan Liu, Junmei Cairns, Yayun Gu, Jia Yu, Richard M. Weinshilboum and Liewei Wang
- 83 **Understanding inter-individual variability in pharmacokinetics/pharmacodynamics of aripiprazole in children with tic disorders: Individualized administration based on physiological development and CYP2D6 genotypes**
Yingying Xin, Liuliu Gao, Yali Tuo, Gang Nie, Yan Mei, Chen Chen, Jun Wang, Sichan Li, Dan Sun, Qiaoqiao Qian, Yongli Fu, Yang Wang and Zhisheng Liu
- 102 **Transporter and metabolizer gene polymorphisms affect fluoroquinolone pharmacokinetic parameters**
Nurul Annisa, Melisa I. Barliana, Prayudi Santoso and Rovina Ruslami
- 112 **The therapeutic prospects of N-acetylgalactosamine-siRNA conjugates**
Lei Zhang, Yayu Liang, Guohui Liang, Zhili Tian, Yue Zhang, Zhihui Liu and Xinying Ji

- 125 **Pharmacokinetics, distribution, metabolism, and excretion of body-protective compound 157, a potential drug for treating various wounds, in rats and dogs**
Lei He, Donglin Feng, Hui Guo, Yueyuan Zhou, Zhaozhao Li, Kuo Zhang, Wangqian Zhang, Shuning Wang, Zhaowei Wang, Qiang Hao, Cun Zhang, Yuan Gao, Jintao Gu, Yingqi Zhang, Weina Li and Meng Li
- 141 **Myriocin enhances the antifungal activity of fluconazole by blocking the membrane localization of the efflux pump Cdr1**
Hongkang Wang, Zhe Ji, Yanru Feng, Tianhua Yan, Yongbing Cao, Hui Lu and Yuanying Jiang
- 153 **A single high-dose irradiation changes accumulation of methotrexate and gene expression levels of SLC and ABC transporters in cancer cells**
Kakeru Sato, Tatsuya Seki, Asuka Mizutani, Yuka Muranaka, Shiho Hirota, Kodai Nishi, Kana Yamazaki, Ryuichi Nishii, Takeo Nakanishi, Ikumi Tamai, Keiichi Kawai and Masato Kobayashi
- 159 **Mechanism of crocin I on ANIT-induced intrahepatic cholestasis by combined metabolomics and transcriptomics**
Dandan Song, Pei Zhu, Yankai Dong, Mengchao Wang, Anna Zhao, Hongdong Xia, Yunting Chen, Qingguang Zhou, Lun Xiang, Junyi Zhang, Guangming Luo and Yangjing Luo
- 174 **Characterization of the metabolism of eupalinolide A and B by carboxylesterase and cytochrome P450 in human liver microsomes**
Yingzi Li, Xiaoyan Liu, Ludi Li, Tao Zhang, Yadong Gao, Kewu Zeng and Qi Wang
- 186 **Integrating strategies of metabolomics, network pharmacology, and experiment validation to investigate the processing mechanism of Epimedium fried with suet oil to warm kidney and enhance yang**
E. Sun, Ran Huang, Ke Ding, Ling Wang, Jian Hou, Xiaobin Tan, Yingjie Wei, Liang Feng and Xiaobin Jia
- 204 **Integrating metabolomics, bionics, and culturomics to study probiotics-driven drug metabolism**
Bohai Li, Lai-Yu Kwok, Dandan Wang, Lu Li, Shuai Guo and Yongfu Chen
- 216 **Bioaccumulation and biotransformation of simvastatin in probiotic bacteria: A step towards better understanding of drug-bile acids-microbiome interactions**
Maja Đanić, Nebojša Pavlović, Slavica Lazarević, Bojan Stanimirov, Saša Vukmirović, Hani Al-Salami, Armin Mooranian and Momir Mikov
- 228 **Inhibitory effect of *Selaginella doederleinii* hieron on human cytochrome P450**
Fei Lin, Xinhua Lin, Xuewen Wang, Guanghui Mei, Bing Chen, Hong Yao and Lingyi Huang

- 241 **Effect of polymorphisms in drug metabolism and transportation on plasma concentration of atorvastatin and its metabolites in patients with chronic kidney disease**
Zebin Jiang, Zemin Wu, Ruixue Liu, Qin Du, Xian Fu, Min Li, Yongjun Kuang, Shen Lin, Jiaxuan Wu, Weiji Xie, Ganggang Shi, Yanqiang Peng and Fuchun Zheng
- 256 **Pharmacokinetics and tissue distribution of bleomycin-induced idiopathic pulmonary fibrosis rats treated with cryptotanshinone**
Xiangjun He, Zhi Zhong, Quan Wang, Zhenmao Jia, Jing Lu, Jianwen Chen and Peiqing Liu
- 268 **Hypolipidemic and insulin sensitizing effects of salsalate beyond suppressing inflammation in a prediabetic rat model**
Martina Hüttel, Irena Markova, Denisa Miklánková, Iveta Zapletalova, Petr Kujal, Jan Šilhavý, Michal Pravenec and Hana Malinska
- 279 **Evaluation and clinical implications of interactions between compound Danshen dropping pill and warfarin associated with the epoxide hydrolase gene**
Xixi Chen, Xurui Zuo, Yingqiang Zhao, Yuhong Huang and Chunxiao Lv



OPEN ACCESS

EDITED AND REVIEWED BY
Jaime Kapitulnik,
Hebrew University of Jerusalem, Israel

*CORRESPONDENCE

Junmin Zhang,
✉ zhangjunmin@lzu.edu.cn
Rong Wang,
✉ wangrong-69@163.com
Sofia Azeredo Pereira,
✉ sofia.pereira@nms.unl.pt

RECEIVED 24 June 2023

ACCEPTED 30 June 2023

PUBLISHED 10 July 2023

CITATION

Zhang J, Wang R and Pereira SA (2023),
Editorial: Drug metabolism and transport:
the Frontier of personalized medicine.
Front. Pharmacol. 14:1246827.
doi: 10.3389/fphar.2023.1246827

COPYRIGHT

© 2023 Zhang, Wang and Pereira. This is
an open-access article distributed under
the terms of the [Creative Commons
Attribution License \(CC BY\)](#). The use,
distribution or reproduction in other
forums is permitted, provided the original
author(s) and the copyright owner(s) are
credited and that the original publication
in this journal is cited, in accordance with
accepted academic practice. No use,
distribution or reproduction is permitted
which does not comply with these terms.

Editorial: Drug metabolism and transport: the Frontier of personalized medicine

Junmin Zhang^{1*}, Rong Wang^{1,2*} and Sofia Azeredo Pereira^{3*}

¹School of Pharmacy and State Key Laboratory of Applied Organic Chemistry, Lanzhou University, Lanzhou, China, ²Department of Pharmacy, The 940th Hospital of Joint Logistic Support Force of PLA, Lanzhou, China, ³Medical School, Universidade Nova de Lisboa, Lisboa, Portugal

KEYWORDS

drug metabolism, drug transport, pharmacokinetics, drug-drug interactions, metabolic enzymes, drug transporters, external factors, gut microbiota

Editorial on the Research Topic

Drug metabolism and transport: the Frontier of personalized medicine

Current personalized drug therapy presents many unique challenges (Pristner and Warth, 2020; van Groen et al., 2022). Pharmacokinetic (PK) and pharmacodynamic (PD) investigations of drugs contribute to ensuring the safety and efficacy of clinical use. In particular, understanding PK properties is essential for drug development and precision drug use. Research on drug metabolizing enzymes and transporter proteins in PK assays is advancing rapidly and accurately provides a new understanding of the transcriptional and post-transcriptional regulatory mechanisms that lead to inter-individual variability in drug therapy (Li et al., 2019). Clinical research on drug-drug interactions (DDI) of drug metabolism or transport is also attracting attention (Tornio et al., 2019). In addition, recent advances such as changes in metabolic enzymes and transporter proteins, and gut bacteria with disease progression help standardize personalized drugs and promote rational clinical use (Zhang et al., 2018; Zhang and Wang, 2022).

This Research Topic includes manuscripts covering the studies focusing on PK, excretion, metabolism, and distribution characteristics of drugs, the elucidation of *in vivo* targets of action, metabolites, metabolic enzymes, and pathways of active molecules of herbal medicines based on metabolomics, network pharmacology, and transcriptomics, the influence of transporters, cytochrome P450, metabolite gene polymorphisms on drug metabolism kinetics, the studies of the complex interactions between the gut microbiota and bile acids, all that have a significant impact on the rational drug use.

First, multiple reports focus on the pharmacokinetics, excretion, metabolism, and distribution characteristics of drugs to contribute to clinical translation or rational drug use. He et al. reported the pharmacokinetics, excretion, metabolism, and distribution characteristics of a body-protective compound 157 (BPC157) in rats and dogs. The results revealed that the main excretion pathways of compound BPC157 involved urine and bile. These results contribute to the clinical translation of the target compound. A study by Shen et al., in which 376 steady-state trough concentrations of valproic acid (VPA) were collected from 103 children with epilepsy, aimed to establish a population pharmacokinetic (PPK) model of VPA in children with epilepsy in southern China to provide guidance for individualized dosing of VPA therapy. Fu et al. identified the pharmacokinetics of unbound teicoplanin in Chinese adult patients and proposed an adjusted dosing regimen depending

on glomerular filtration rate (eGFR) and serum albumin concentration to serve as a rationale for unconjugated drug-guided dosing. Liu et al. presented the pharmacokinetics and tissue distribution of cryptotanshinone in the treatment of bleomycin-induced idiopathic pulmonary fibrosis in rats. The findings suggest that the pathological changes of pulmonary fibrosis favor the pulmonary exposure of cryptotanshinone and serve as a therapeutic target organ for cryptotanshinone. These results offer new references for pharmacokinetic and pharmacodynamic research on experimental drugs.

Secondly, several works illustrate the *in vivo* targets, metabolites, metabolic enzymes and pathways for the active molecules of herbal medicines using metabolomics, network pharmacology and transcriptomics. Song et al. demonstrated a therapeutic effect of crocin I (CR) on intrahepatic cholestasis (IC) by combined metabolomic and transcriptomic analysis. This therapeutic effect is attributed to the regulation of bile acid and bilirubin biosynthesis in the bile secretion pathway and the expression of 3-hydroxy-3-methylglutaryl-coenzyme A reductase, sulfotransferase 2A1, and ATP-binding cassette transporter G5. Deng et al. elucidated the mechanism of dracorhodin perchlorate topically applied to diabetic foot ulcer (DFU) rats using a combination of metabolomics and network pharmacology. The findings suggest that dracorhodin perchlorate improves wound healing in DFU through multiple targets and pathways and is potentially useful for the treatment of DFU. A study performed by Sun et al. reports the establishment of an “active compound-target-metabolic pathway” network based on an integrated GC-TOF/MS metabolomics and network pharmacology analysis strategy. This approach identified the active compounds, targets and metabolic pathways involved in the Epimedium fried with suet oil to warm kidney and enhance yang. The authors finally revealed that the mechanism of action of Epimedium fried with suet oil to warm kidney and enhance yang is primarily involved in oxidative stress and amino acid metabolism. By analyzing the plasma metabolomics of liver transplant recipients, Zhu et al. identified microbiota-derived uremic retention solutes, bile acids, steroid hormones, and medium- and long-chain acylcarnitines as the major metabolites associated with dose-adjusted trough concentrations of tacrolimus in liver transplant recipients. This work provides a rationale for predicting the optimal dose of tacrolimus to be administered to liver transplant recipients.

Additionally, several research and reviews focused on the effect of transporters, cytochrome P450, and metabolite gene polymorphisms on the pharmacokinetics of drugs. Annisa et al. reviewed the effect of transporter and metabolite gene polymorphisms on the kinetic parameters of fluoroquinolone, suggesting that the presence of gene polymorphisms can affect the pharmacokinetic parameters of fluoroquinolone such as area under the curve (AUC), creatinine clearance (C_{Cr}), maximum plasma concentration (C_{max}), half-life ($t_{1/2}$), and time to peak (t_{max}). Zhu et al. revealed a novel mechanism by which testis-specific Y-coding-like protein 1 (TSPYL1) regulates the expression of cholesterol metabolizing cytochrome P450s (CYPs), especially CYP1B1, through Wnt/ β -catenin signaling. Their results increase the possibility that TSPYL 1 might be a molecular target affecting cholesterol homeostasis. Xin et al. established a combined population pharmacokinetic (PPK) model of aripiprazole (ARI) and its main active metabolite dehydroaripiprazole (DARI) in

pediatric patients with tic disorders (TD) and investigated inter-individual variability in ARI pharmacokinetics/pharmacodynamics caused by physiological and genetic factors to optimize dosing regimens in pediatric patients. The findings showed that the pharmacokinetics of ARI and DARI in pediatric patients with TD were significantly influenced by body weight and CYP2D6 genotype. The authors recommend an individualized dosing regimen for pediatric patients with TD to ensure clinical efficacy. Sato et al. examined the relationship between methotrexate (MTX) accumulation and gene expression levels of solute carrier (SLC) and ATP-binding cassette (ABC) transporters in cancer cells after single and high doses of X-ray irradiation. Their results indicate that single high-dose irradiation alters the accumulation of MTX and the gene expression levels of SLC and ABC transporters in cancer cells. Li et al. investigated the metabolic stability and enzymatic kinetics of carboxylesterase-mediated hydrolysis and cytochrome P450 (CYP)-mediated oxidation of Eupalinolide A (EA; Z-configuration) and Eupalinoide B (EB; E-configuration) in human liver microsomes. The results revealed that EA and EB were promptly eliminated compared to CYP-mediated oxidation, largely through carboxylesterase-mediated hydrolysis. EA and EB were metabolized by multiple CYPs, with CYP3A4 playing a particularly important role. The findings from Wang et al. revealed that Myriocin enhances the antifungal activity of fluconazole by blocking the membrane localization of the efflux pump Cdr1. Another study by Jiang et al. identified two functional polymorphisms in the ABCC4 gene that may affect transcriptional activity and thus directly or indirectly affect the release of atorvastatin and its metabolites from hepatocytes into the circulation. These results provide a strong rationale for the clinical use of drugs.

There are also two more interesting studies on the combined use of herbal ingredients and Chinese compound prescription. A study by Chen et al. reported on the evaluation and clinical significance of the interaction of compound Danshen dropping pill (CDDP) with epoxide hydrolase gene-related warfarin. The findings indicated that a reasonable combination of CDDP and warfarin is safe without risk of bleeding, but also requires therapeutic management. In another study, Lin et al. reported the effect of ethyl acetate extract (SDEA extract) from *Selaginella doederleinii* hieron on human cytochrome P450 enzymes (CYP450). The results revealed that amentolavone may be one of the main reasons for the inhibition of CYPs by SDEA. When SDEA or amentolavone is used in combination with other clinical drugs, potential herbal interactions should be considered.

In addition, the findings from Malinska et al. that the hypolipidemic effect of salsalate was implicated in the differential expression of genes regulating lipid metabolism in the liver, indicating that the administration of salsalate in prediabetic patients with symptoms of non-alcoholic fatty liver disease (NAFLD) may be beneficial. Zhang et al. reviewed the therapeutic prospects of N-acetylgalactosamine-siRNA couples, highlighting the efficiency and stability of GalNAc-siRNA couples. Their results imply that new approaches to developing oligonucleotide drugs hold promise for gene therapy.

Even though pharmacokinetics, pharmacogenetics and pharmacogenomics have been at the forefront of research aimed at finding new personalized therapies, the focus of recent research has been extended to the potential of the gut microbiota to affect

drug efficacy. The complex interactions of the gut microbiota with bile acids may have a significant impact on the pharmacokinetics of drugs. Đanić et al.'s findings suggest that bioaccumulation and biotransformation of simvastatin through gut bacteria may be a potential mechanism for its altered bioavailability and therapeutic efficacy. Li et al. utilized an integrated metabolomics, culturomics and bionomics framework to discover that multiple drugs are metabolized by selected probiotic bacteria, providing practical guidance for probiotic drug combinations and new insights into precision probiotics.

Altogether, the focused release of these results provides sufficient reference data to standardize personalized drugs and promote rational clinical use. We hope you enjoy them.

Author contributions

JZ and RW develop the concept and write the front paper. JZ and RW, and SP revise the manuscript. All authors contributed to the article and approved the submitted version.

References

- Li, Y., Meng, Q., Yang, M., Liu, D., Hou, X., Tang, L., et al. (2019). Current trends in drug metabolism and pharmacokinetics. *Acta Pharm. Sin. B* 9 (6), 1113–1144. doi:10.1016/j.apsb.2019.10.001
- Pristner, M., and Warth, B. (2020). Drug–exposome interactions: The next frontier in precision medicine. *Trends Pharmacol. Sci.* 41 (12), 994–1005. doi:10.1016/j.tips.2020.09.012
- Tornio, A., Filppula, A. M., Niemi, M., and Backman, J. T. (2019). Clinical studies on drug–drug interactions involving metabolism and transport: Methodology, pitfalls, and interpretation. *Clin. Pharmacol. Ther.* 105 (6), 1345–1361. doi:10.1002/cpt.1435
- van Groen, B. D., Allegaert, K., Tibboel, D., and de Wildt, S. N. (2022). Innovative approaches and recent advances in the study of ontogeny of drug metabolism and transport. *Br. J. Clin. Pharmacol.* 88 (10), 4285–4296. doi:10.1111/bcp.14534
- Zhang, J., and Wang, R. (2022). Changes in CYP3A4 enzyme expression and biochemical markers under acute hypoxia affect the pharmacokinetics of sildenafil. *Front. Physiol.* 13, 755769. doi:10.3389/fphys.2022.755769
- Zhang, J., Zhang, J., and Wang, R. (2018). Gut microbiota modulates drug pharmacokinetics. *Drug Metab. Rev.* 50 (3), 357–368. doi:10.1080/03602532.2018.1497647

Acknowledgments

We appreciate the financial support from the National Natural Science Foundation of China (82003779) are acknowledged.

Conflict of interest

The authors declare that the research was conducted in the absence of any commercial or financial relationships that could be construed as a potential conflict of interest.

Publisher's note

All claims expressed in this article are solely those of the authors and do not necessarily represent those of their affiliated organizations, or those of the publisher, the editors and the reviewers. Any product that may be evaluated in this article, or claim that may be made by its manufacturer, is not guaranteed or endorsed by the publisher.



OPEN ACCESS

EDITED BY

Junmin Zhang,
Lanzhou University, China

REVIEWED BY

Xuan Qin,
Baylor College of Medicine,
United States
Evelyn Jacqz-Aigrain,
Institut National de la Santé et de la
Recherche Médicale (INSERM), France

*CORRESPONDENCE

Yizhun Zhu,
yzzhu@must.edu.mo
Weihong Ge,
geweihong.nju@gmail.com

[†]These authors have contributed equally
to this work and share first authorship

SPECIALTY SECTION

This article was submitted to Drug
Metabolism and Transport,
a section of the journal
Frontiers in Pharmacology

RECEIVED 16 September 2022

ACCEPTED 13 October 2022

PUBLISHED 31 October 2022

CITATION

Zhu H, Wang M, Xiong X, Du Y, Li D,
Wang Z, Ge W and Zhu Y (2022), Plasma
metabolomic profiling reveals factors
associated with dose-adjusted trough
concentration of tacrolimus in liver
transplant recipients.
Front. Pharmacol. 13:1045843.
doi: 10.3389/fphar.2022.1045843

COPYRIGHT

© 2022 Zhu, Wang, Xiong, Du, Li, Wang,
Ge and Zhu. This is an open-access
article distributed under the terms of the
[Creative Commons Attribution License](https://creativecommons.org/licenses/by/4.0/)
(CC BY). The use, distribution or
reproduction in other forums is
permitted, provided the original
author(s) and the copyright owner(s) are
credited and that the original
publication in this journal is cited, in
accordance with accepted academic
practice. No use, distribution or
reproduction is permitted which does
not comply with these terms.

Plasma metabolomic profiling reveals factors associated with dose-adjusted trough concentration of tacrolimus in liver transplant recipients

Huaijun Zhu^{1,2,3†}, Min Wang^{2,3†}, Xiaofu Xiong^{2,4}, Yao Du^{2,3},
Danying Li^{2,3}, Zhou Wang⁵, Weihong Ge^{2,3*} and Yizhun Zhu^{1,5*}

¹Department of Pharmacology, School of Pharmacy, Fudan University, Shanghai, China, ²Department of Pharmacy, the Affiliated Drum Tower Hospital of Nanjing University Medical School, Nanjing, China, ³Nanjing Medical Center for Clinical Pharmacy, Nanjing, China, ⁴Department of Pharmacy, The First Affiliated Hospital of Zhengzhou University, Zhengzhou, China, ⁵State Key Laboratory of Quality Research in Chinese Medicine and School of Pharmacy, Macau University of Science and Technology, Macau, China

Inter- and inpatient variability of tacrolimus exposure is a vital prognostic risk factor for the clinical outcome of liver transplantation. New factors or biomarkers characterizing tacrolimus disposition is essential for optimal dose prediction in recipients of liver transplant. The aim of the study was to identify potential plasma metabolites associated with the dose-adjusted trough concentration of tacrolimus in liver transplant recipients by using a global metabolomic approach. A total of 693 plasma samples were collected from 137 liver transplant recipients receiving tacrolimus and regular therapeutic drug monitoring. Untargeted metabolomic analysis was performed by ultraperformance liquid chromatography-quadrupole time-of-flight mass spectrometry. Univariate and multivariate analyses with a mixed linear model were conducted, and the results showed that the dose-adjusted tacrolimus trough concentration was associated with 31 endogenous metabolites, including medium- and long-chain acylcarnitines such as stearyl carnitine ($\beta = 0.222$, $p = 0.001$), microbiota-derived uremic retention solutes such as indolelactic acid ($\beta = 0.194$, $p = 0.007$), bile acids such as taurohyodeoxycholic acid ($\beta = -0.056$, $p = 0.002$), and steroid hormones such as testosterone ($\beta = 0.099$, $p = 0.001$). A multiple linear mixed model including 11 metabolites and clinical information was established with a suitable predictive performance (correlation coefficient based on fixed effects = 0.64 and correlation coefficient based on fixed and random effects = 0.78). These data demonstrated that microbiota-derived uremic retention solutes, bile acids, steroid hormones, and medium- and long-chain acylcarnitines were the main metabolites associated with the dose-adjusted trough concentration of tacrolimus in liver transplant recipients.

KEYWORDS

liver transplantation, tacrolimus, metabolomics, therapeutic drug monitoring, trough concentration

1 Introduction

Tacrolimus is considered the primary immunosuppressant in solid organ transplantation and has been used in liver transplant recipients for approximately two decades (Muduma et al., 2016). Pharmacokinetics-guided dosing is recommended to individualize tacrolimus treatment due to the narrow therapeutic window and wide interindividual pharmacokinetic variability (Brunet et al., 2019). Although the dose-interval area under the curve (AUC) of tacrolimus would be best associated with clinical effects, a multiple sampling strategy is not feasible in clinical practice. A limited sampling strategy with trough concentration (C₀) is regularly adopted in most center for therapeutic drug monitoring (TDM) (Brunet et al., 2019; Birdwell et al., 2015). Pharmacogenomics is also essential in pharmacokinetics of tacrolimus, with CYP3A5 genotypes used to guide initial tacrolimus dosing (Brunet et al., 2019). Nevertheless, limitations and challenges for tacrolimus use exist. In liver transplantation, guidelines for CYP3A5 genotype and tacrolimus dosing are recommended only when the donor and recipient genotypes are identical (Birdwell et al., 2015). Furthermore, genotypes provide less information and low predictive value for inpatient variability (IPV) (Shuker et al., 2015), whereas a recent study identified IPV of tacrolimus exposure as a crucial prognostic risk factor for the clinical outcome in solid organ transplantation, including liver transplantation (Del Bello et al., 2018). Although the most important clinical cause influencing such IPV is medication nonadherence, which is modifiable by clinical interventions, other factors, including drug-drug interactions, food intake, herbal or nutritional constituents and gastrointestinal disorders, also have shown significant roles (Gonzales et al., 2020). Pathophysiological changes such as graft function recovery, inflammation, and altered plasma protein concentrations may affect the tacrolimus disposition of recipients after liver transplantation (Ganesh et al., 2017). Thus, the identification of novel factors or biomarkers characterizing tacrolimus disposition is essential for predicting the optimal dose in liver transplant recipients.

Cytochrome P450 3A isoenzymes (CYP3A), mainly CYP3A4 and CYP3A5, are involved in tacrolimus metabolism. Several human studies have been conducted to identify endogenous biomarkers of CYP3A activity. With the advent of serendipity and hypothesis-driven processes, urinary and plasma metabolites were evaluated as endogenous metrics through the main phenotyping validation criteria (Magliocco et al., 2019). The ability to provide insights into phenotypic metabolite changes with wide coverage and high throughput allows metabolomics to be a promising method for biomarker

discovery (Tolstikov et al., 2020). Mass spectrum (MS)-based metabolomic methods involving targeted or untargeted approaches have also been used to detect novel CYP3A biomarkers. Urinary cortisol/6 β -hydroxycortisol, cortisone/6 β -hydroxycortisone, dehydroepiandrosterone (DHEA)/(7 β -OH-DHEA plus 16 α -OH-DHEA), and plasma cholesterol/4 β -hydroxycholesterol are reliable predictive markers of hepatic CYP3A activity (Shin et al., 2013). Phapale et al. conducted a pharmacometabolomic study on the urine of healthy volunteers to identify a predictive metabolic phenotype of individualized tacrolimus pharmacokinetics and identified four metabolites, namely, cortisol, methylguanosine, acetyl-arginine, and phosphoethanolamine, representing steroid-related, nucleotide/purine, amino acid-related, and glycerophospholipid metabolism, respectively, to predict the pharmacokinetic parameters of tacrolimus (Phapale et al., 2010).

With respect to liver transplant recipients, many clinical factors and drugs could alter the metabolomic profile (Oweira et al., 2018). Thus, the biomarkers for tacrolimus disposition identified in healthy controls should be applied in clinical practice with caution, and a study performed in liver transplant recipients may provide more insight views for metabolomics-guided dosing. Additionally, dose-adjusted tacrolimus trough concentration (C₀/D) was commonly used as a surrogate marker for dose response or an index of clearance in most of the studies conducted in patient (Riva et al., 2019). Thus, the present study attempted to identify potential plasma endogenous metabolites associated with tacrolimus C₀/D in liver transplant recipients by using a global metabolomic approach.

2 Materials and method

2.1 Subjects

The present retrospective study was conducted at the Hepatobiliary Center, the Affiliated Drum Tower Hospital of Nanjing University Medical School. Adult patients receiving liver transplantation between January 2018 and July 2019 were included. All the recipients received tacrolimus-based regimens and TDM. Subjects with incomplete electronic medical records, and patients undergoing multivisceral transplantation or other additional organ transplantation were excluded. Plasma samples for metabolomics study were available residual biosamples for TDM assay from the biobank of our laboratory. Samples with a C₀ of tacrolimus lower than the quantitation limit or with a volume not enough for such analysis were excluded. The enrolled subjects were randomly

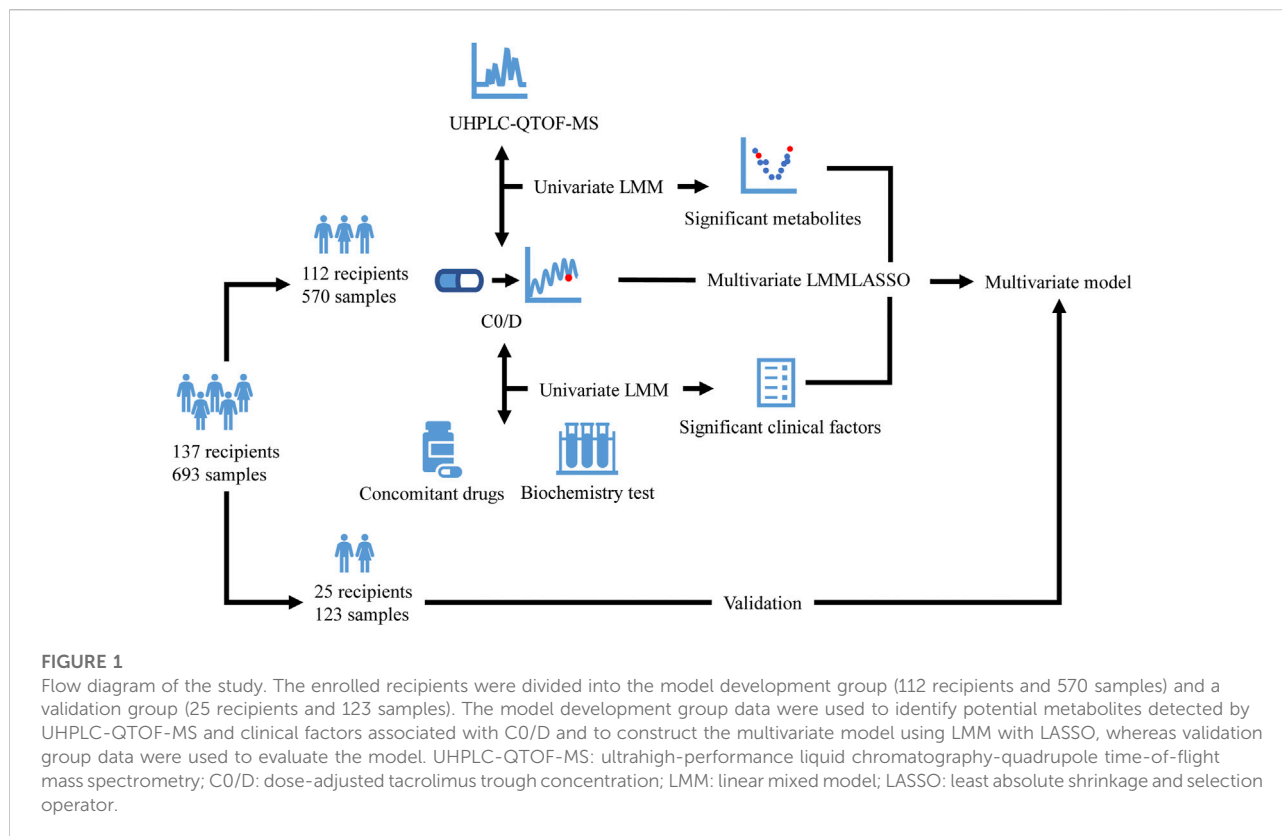


FIGURE 1

Flow diagram of the study. The enrolled recipients were divided into the model development group (112 recipients and 570 samples) and a validation group (25 recipients and 123 samples). The model development group data were used to identify potential metabolites detected by UHPLC-QTOF-MS and clinical factors associated with C0/D and to construct the multivariate model using LMM with LASSO, whereas validation group data were used to evaluate the model. UHPLC-QTOF-MS: ultrahigh-performance liquid chromatography-quadrupole time-of-flight mass spectrometry; C0/D: dose-adjusted tacrolimus trough concentration; LMM: linear mixed model; LASSO: least absolute shrinkage and selection operator.

divided into the model development group and a validation group. The model development group data were used to identify potential metabolites associated with C0/D and to construct the multivariate model, whereas validation group data were used to evaluate the results (Figure 1). The study was carried out in accordance with the principles of the Helsinki Declaration and approved by the Institutional Review Board at Nanjing Drum Tower Hospital (No. 2020-053-01). Informed consent was waived due to the deidentified data provided to researchers and residual biosamples used.

2.2 Treatment and TDM

Recipients received a tacrolimus-based immunosuppressive regimen including mycophenolate mofetil and corticosteroids. The initial dose of tacrolimus (Prograf®, Astellas, Killorglin, Ireland; or Saifukai®, Huadong Medicine, Hangzhou, China) was generally 2–3 mg orally twice daily, whereas the posttransplantation C0 target levels were 8–12 ng/ml in the first month, 7–10 ng/ml during the next months, and 5–7 ng/ml after the first year. TDM was performed for patients receiving tacrolimus at a fixed dose for about 3 days, and whole blood samples for C0 detection were taken within 1 hour before the morning dose. The concentration of tacrolimus was determined

by the enzyme multiplied immunoassay technique (EMIT) using a drug testing system (Viva-E, Siemens Healthcare Diagnostics Inc, Erlangen, Germany) and EMIT® 2000 tacrolimus assay kit (Siemens Healthcare Diagnostics Inc, Erlangen, Germany). The procedures were conducted according to the manufacturer's instructions. The calibration range of the assay was 2.0–30 ng/ml, and samples with a C0 level lower than 2.0 ng/ml were excluded from the study. The performance of the tacrolimus assay in our laboratory was verified in an external quality assessment organized by the National Center for Clinical Laboratories. The internal quality assessment during the study was regularly performed, while the average bias was 6.47%, −1.67% and 1.35%, and the average coefficient of variation was 13.44%, 7.69% and 6.30% for low-, medium- and high-quality controls, respectively. An aliquot of 500 µL of whole blood was also centrifuged at 2,500 g for 10 min at 4°C once the sample was received in the clinical laboratory. The plasma and blood cells were stored at −80°C for further analysis.

2.3 Data collection

Patient data around C0 sampling were collected retrospectively from the hospital information system (HIS) and included daily doses of tacrolimus, weight, concomitant

TABLE 1 Demographic and medical information of liver allograft recipients^a.

Characteristics	Total subjects	Model development group	Validation group	<i>p</i> Value
Number of subjects (n)	137	112	25	
Age (years)	49 (43–57)	49 (42–56)	50 (43–58)	0.781
Sex (n)				
Female	35 (25.55%)	28 (25.00%)	7 (28.00%)	
Male	102 (74.45%)	84 (75.00%)	18 (72.00%)	0.753
Weight (kg)	65 (56–73.5)	63.75 (56–72.5)	68 (55–75)	0.628
Height (cm)	169 (163–173)	169 (163–173)	169 (161–171)	0.414
BMI (kg/m ²)	23.31 (20.64–25.25)	23.03 (20.69–25.01)	24.08 (20.40–25.95)	0.444
History of smoking (n)	15 (10.95%)	11 (9.82%)	4 (16.00%)	0.371
History of alcohol consumption (n)	15 (10.95%)	11 (9.82%)	4 (16.00%)	0.371
Hypertension (n)	21 (15.33%)	17 (15.18%)	3 (12.00%)	0.684
Diabetes (n)	16 (11.68%)	15 (13.51%)	1 (4.00%)	0.182
Graft type (n)				
Deceased	131 (95.62%)	106 (94.64%)	25 (100.00%)	
Living	6 (4.38%)	6 (5.36%)	0 (0.00%)	0.237
Primary diagnosis (n)				
End-stage liver cirrhosis	78 (56.93%)	62 (55.36%)	16 (64.00%)	
Malignancies	27 (19.71%)	22 (19.64%)	5 (20.00%)	
Acute liver failure	19 (13.87%)	17 (15.18%)	2 (8.00%)	
Cholestatic liver disease	11 (8.03%)	9 (8.04%)	2 (8.00%)	
Metabolic liver disease	2 (1.46%)	2 (1.79%)	0 (0.00%)	0.905
Concomitant medication (n)				
Voriconazole	8 (5.84%)	6 (5.36%)	2 (8.00%)	0.572
Fluconazole	17 (12.41%)	15 (13.39%)	2 (8.00%)	0.460
Wuzhi capsule	85 (62.04)	66 (58.93%)	19 (76%)	0.112
Omeprazole/Esomeprazole	43 (31.39%)	35 (31.25%)	8 (32.00%)	0.942
Caspofungin	41 (29.93%)	32 (28.57%)	9 (36.00%)	0.463
DHP CBB	24 (17.52%)	22 (19.64)	2 (8.00%)	0.166
Warfarin	10 (7.30%)	10 (8.93%)	0 (0.00%)	0.208
Mycophenolic acid/Mycophenolate mofetil	129 (94.16%)	104 (92.86%)	25 (100%)	0.350
Magnesium isoglycyrrhizinate	99 (72.26%)	79 (70.54%)	20 (80%)	0.339
Clinical biochemistry parameters				
ALT (IU/L)	47.02 (22.55–91.03)	44.95 (22.35–89.03)	50.67 (26.28–121.08)	0.493
AST (IU/L)	34.53 (24.04–57.70)	32.85 (23.04–54.97)	41.34 (31.69–76.72)	0.077
GGT (IU/L)	61.80 (42.13–105.60)	63.87 (41.27–105.60)	60.84 (50.25–96.90)	0.787
Total bilirubin (μmol/L)	22.57 (12.92–37.43)	22.53 (12.65–37.50)	28.45 (15.87–35.05)	0.607
Direct bilirubin (μmol/L)	10.57 (5.23–23.77)	10.30 (4.93–24.70)	13.42 (7.03–23.36)	0.486
Albumin (g/L)	40.70 (38.83–42.97)	40.73 (38.87–42.97)	40.59 (38.67–42.97)	0.902
Glucose (mmol/L)	6.08 (5.34–7.64)	6.08 (5.28–7.64)	6.16 (5.55–7.06)	0.483
Creatinine (μmol/L)	67.82 (58.22–94.17)	67.00 (58.22–90.33)	71.50 (58.20–101.33)	0.444
Cholesterol (mmol/L)	3.18 (2.70–3.70)	3.19 (2.70–0.68)	3.15 (2.55–3.77)	0.670
Hematocrit (%)	34.40 (30.35–38.17)	34.40 (30.36–37.68)	33.74 (29.25–40.58)	0.834
Tacrolimus				
Total number of samples (N)	693	570	123	
Number of samples per patients	4 (3–6)	4 (3–6)	3 (3–5)	0.528
C0 (ng/ml)	7.50 (6.35–9.53)	7.42 (6.41–9.56)	8.03 (6.32–9.25)	0.732
Sampling time point (day after surgery)	89 (51.67–150.4)	92.81 (52.33–153.67)	78.25 (48.67–118.00)	0.311
Daily dose (mg)	3.16 (2.50–3.73)	3.15 (2.50–3.79)	3.25 (2.67–3.67)	0.776

(Continued on following page)

TABLE 1 (Continued) Demographic and medical information of liver allograft recipients^a.

Characteristics	Total subjects	Model development group	Validation group	p Value
Daily dose normalized (mg/kg)	0.048 (0.036–0.060)	0.048 (0.036–0.060)	0.045 (0.039–0.060)	0.843
C0/D [(ng/ml)/(mg/kg)]	178.08 (129.85–244.58)	180.48 (128.04–244.46)	170.33 (140.83–251.21)	0.585
log ₂ (C0/D) {log ₂ [(ng/ml)/(mg/kg)]}	7.33 (6.90–7.86)	7.31 (6.90–7.86)	7.34 (6.92–7.82)	0.734

^aContinuous variables are presented as median (25th–75th percentiles), whereas categorical variables are expressed as frequency and percentage. The Mann-Whitney *U* test and chi-square test (or Fisher's exact test as appropriate) were used to compare the continuous and categorical data, respectively between the model development and validate groups. BMI: Body Mass Index; AST: aspartate aminotransferase; ALT: alanine aminotransferase; GGT: gamma-glutamyl transpeptidase; C0: trough concentration; C0/D: trough concentration normalized by daily dose (normalized by weight); DHP CCB: dihydropyridine calcium channel blockers.

drugs (voriconazole, fluconazole, Wuzhi capsule, omeprazole or esomeprazole, caspofungin, and dihydropyridine calcium channel blockers [DHP CCB]), and blood biochemistry parameters. Wuzhi capsule is a Chinese patent medicine, and its abundant active ingredients include deoxyschizandrin, schisantherin A, schisandrol B and schisandrin (Qin et al., 2014). This is a common drug used to increase the exposure to tacrolimus in most transplantation centers in China.

2.4 Untargeted metabolomics

Plasma samples were thawed on ice, and a 40-μL aliquot was mixed with 160 μL of cold acetonitrile by vortexing for 5 min. After centrifugation at 20,000 g for 15 min at 4°C, the supernatant was collected and centrifuged again. The new supernatant was prepared for injection and separation using ultrahigh-performance liquid chromatography (UHPLC) (ExionLC AD UHPLC, ABSciex, Framingham, MA, United States) with a Kinetex C18 (2.6 μm, 100 mm × 2.1 mm, Phenomenex, CA, United States) column at 40°C. All samples were analyzed using a TripleTOF 5,600 + system (ABSciex, Framingham, MA, United States) in positive and negative electrospray ionization modes. Untargeted metabolomics methods and metabolomics data analysis are shown in the [Supplementary Material](#).

2.5 Statistical analyses

The C0/D of tacrolimus was calculated by dividing the trough by the daily dose (D) normalized to actual body weight, whereas the log-transformed C0/D (log₂C0/D) was investigated as the dependent variable in the subsequent univariate and multivariate analyses. The enrolled subjects were randomly divided into the model development group and a validation group using the function of “createDataPartition” in “caret” package in R software, and unsupervised principal component analysis (PCA) was adopted to evaluate the assay quality and the homogeneity of the metabolic data by using the SIMCA 14.1 (Umetrics, Uppsala, Sweden) software package. Considering the log₂C0/D variation at

two levels (between subjects and within subjects due to the repeated measures), metabolites associated with log₂C0/D were identified using a linear mixed model, with each feature as the fixed effect and subject as the random effect on log₂C0/D. *p* values of the fixed effect were adjusted by the false discovery rate (FDR) (“qvalue” package in R software) for multiple comparisons, and power was estimated by a simulation-based method (“simr” package in R software). Mummichog algorithm prediction (Li et al., 2013) was performed to identify enriched pathways.

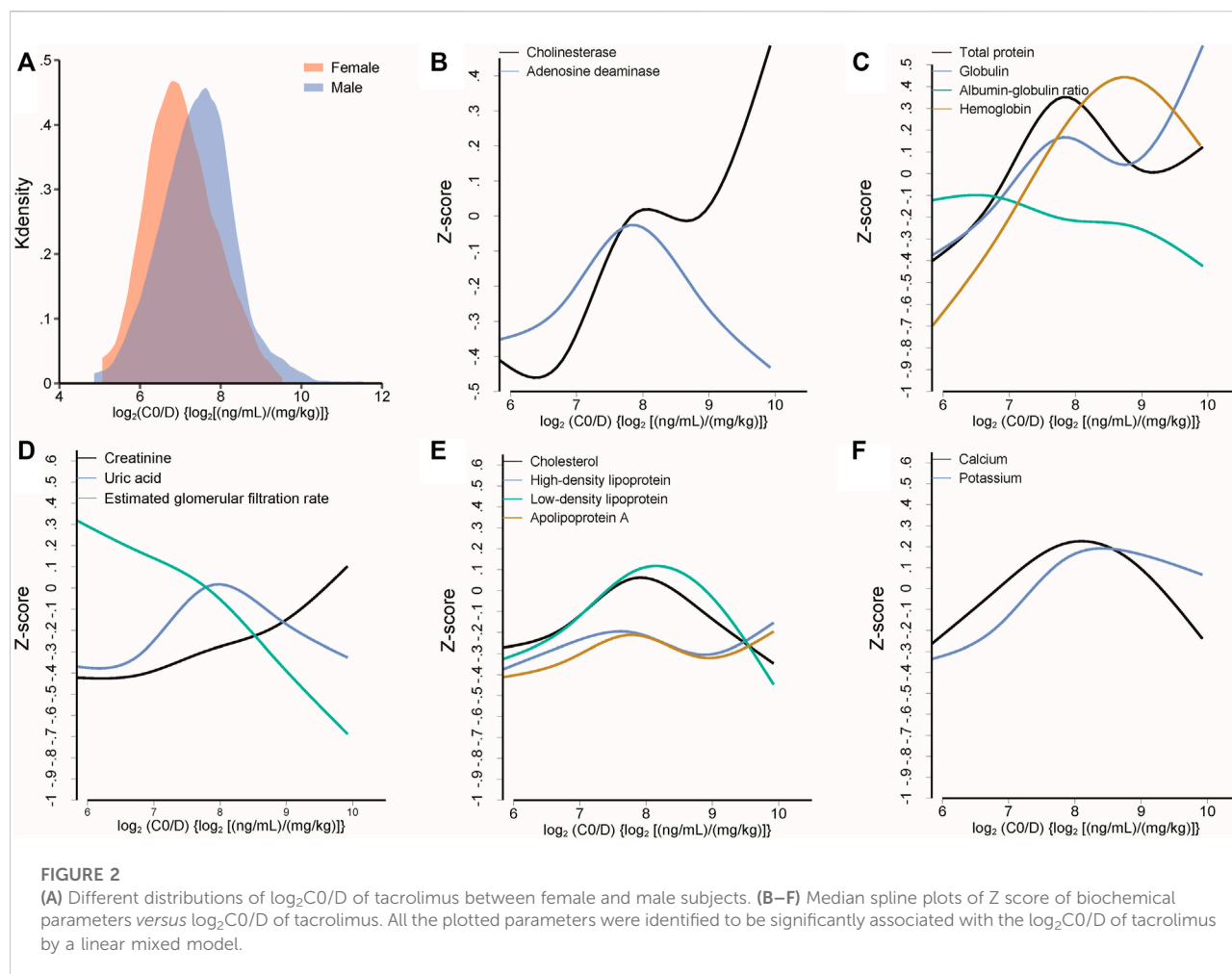
To build a multivariate model in the model development group, all the metabolites and other factors including demographic information, biochemistry parameters and concomitant drug use with statistically significance in univariate analysis were included, and variable selection and penalization were performed by minimizing Akaike information criteria (AIC) using the method of least absolute shrinkage and selection operator (LASSO) augmented with 10-fold cross-validation. The predictive accuracy of the final model was assessed numerically in the model development and validation group through calculation of the correlation coefficient (*R*) by the fixed effects and full model, the mean error (ME), the mean absolute error (MAE), the mean relative error (MRE), and the relative root mean squared error (RMSE).

All statistical analyses were performed using STATA MP 16.0 (StataCorp, TX, United States), RStudio 1.3.959 (R Foundation for Statistical Computing, Vienna, Austria), and R-3.6.3 (R Foundation for Statistical Computing, Vienna, Austria). *p* values were two-sided, and values <0.05 were considered statistically significant.

3 Results

3.1 Subjects

A total of 137 liver transplant recipients and 693 samples were finally include in the study ([Supplementary Figure S1](#)). The median age of the patients was 49 years [interquartile range (IQR): 43–57 years], with a body mass index (BMI) of 23.31 (20.64–25.25) kg/m². Most of the recipients were primarily diagnosed with end-stage liver cirrhosis (56.9%) and malignancies (19.7%) and underwent transplantation from a



deceased donor (95.6%). Data regarding the concomitant medications were retrieved from HIS. Voriconazole was observed in 22 samples from eight patients, fluconazole in 65 samples from 17 patients, omeprazole or esomeprazole in 68 samples from 43 patients, and DHP CCB in 50 samples from 24 patients. Additionally, Wuzhi capsule was concomitantly administered in 198 samples from 85 subjects. The differences in the demographic information, clinical biochemistry parameters, and tacrolimus dose and concentration between the two groups were statistically nonsignificant (Table 1).

3.2 Associations of demographic information and biochemistry parameters with $\log_2 C_0/D$ in model development group

The linear mixed model exhibited that $\log_2 C_0/D$ increased with postoperative days [$\beta = 0.002$, standard error (SE) = 0.0003, $p < 0.001$] and height ($\beta = 0.026$, SE = 0.009, $p = 0.005$). Male subjects

exhibited a higher $\log_2 C_0/D$ than females ($\beta = 0.432$, SE = 0.138, $p = 0.002$) (Figure 2, A). Cholinesterase, adenosine deaminase, total protein, globulin, and hemoglobin were positively associated with $\log_2 C_0/D$. Tacrolimus pharmacokinetics were negatively associated with renal function and positively associated with parameters related to lipids (Figures 2B–F).

3.3 Metabolites identification by untargeted metabolomics analysis

The features were subjected to PCA after data normalization, and the results are illustrated in Supplementary Figures S2A,B. Quality control samples were clustered well in both ion modes, indicating platform stability and metabolomics data reliability. The illustration of grouping homogeneity suggested no evident separation trends between the model development and validation groups in either mode. Pearson's correlation analysis exhibited good agreement of creatinine, urea, and uric acid levels between the levels

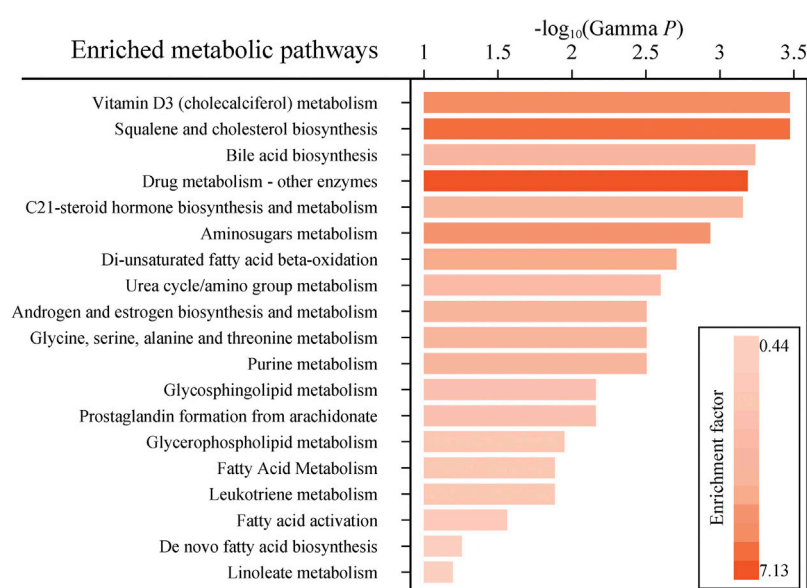


FIGURE 3

Enriched metabolic pathways predicted by the mummichog algorithm with a p value ≤ 0.05 . Colors with gradients of the bars represent relatively high to low values of the enrichment factor.

obtained in the clinical laboratory and intensity in the metabolomics data (creatinine: $R = 0.95$, $p < 0.001$; urea: $R = 0.94$, $p < 0.001$; uric acid: $R = 0.90$, $p < 0.001$; Supplementary Figure S2C). Obvious differences were also observed for voriconazole, fluconazole, and omeprazole at the metabolomics level between samples with and without drug use, indicating high reliability of the metabolomics data (Supplementary Figure S2D).

Considering the inherent limitation of chemical identification in metabolomics, only features with MS2 information were included in the subsequent analysis. The linear mixed model with the subjects as the random effect was performed in the model development group to evaluate the fixed effect of each feature. The Mummichog algorithm using the m/z and p value indicated that the metabolic pathways were significantly enriched in Vitamin D3 (cholecalciferol) metabolism, squalene and cholesterol biosynthesis, bile acid biosynthesis, C21-steroid hormone biosynthesis and metabolism, aminosugars metabolism and so on (Figure 3). The results from the linear mixed model are illustrated as a volcano plot in Figure 4, exhibiting 633 features with significance, of which 112 were identified by accurate m/z and MS2 spectra matching. The power for each identified significant metabolite was evaluated, and the metabolite with a value of power ≥ 0.80 was retained. Finally, 31 endogenous metabolites were revealed as potential markers of tacrolimus pharmacokinetics (Table 2).

3.4 Association between concomitant drug use and $\log_2\text{C}_0/\text{D}$ and metabolites

The mixed model analysis exhibited higher $\log_2\text{C}_0/\text{D}$ in the samples taken after voriconazole or Wuzhi capsule use than the samples not related to drug use (voriconazole: $\beta = 1.878$, $\text{SE} = 0.203$, $p < 0.001$; Wuzhi capsule: $\beta = 0.485$, $\text{SE} = 0.085$, $p < 0.001$) (Figure 5A), confirming significant pharmacokinetic interactions of voriconazole and Wuzhi capsule with tacrolimus. Conversely, DHP CCB and caspofungin exhibited an inhibitory effect on $\log_2\text{C}_0/\text{D}$ (DHP CCB: $\beta = -0.611$, $\text{SE} = 0.130$, $p < 0.001$; caspofungin: $\beta = -0.309$, $\text{SE} = 0.130$, $p = 0.017$). The 31 endogenous metabolites with significance were compared between the samples with and without the four drug uses. The Venn diagram demonstrated two overlapping metabolites, namely, carnitine and testosterone, among all the comparisons and five metabolites, phenylalanine, uric acid, 17 α -hydroxyprogesterone, monoolein, and taurohyodeoxycholic acid, among the comparisons of Wuzhi capsule, DHP CCB, and caspofungin (Figures 5B,C).

3.5 Multiple regression model analysis

The multivariate model included 11 endogenous metabolites and 12 clinical characteristics as fixed effects (Table 3). A visual inspection of the residual distribution exhibited no obvious deviation from homoscedasticity or normality (Supplementary

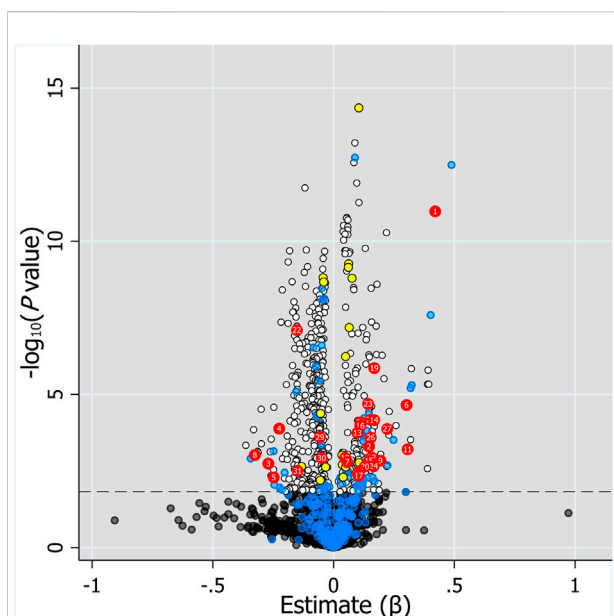


FIGURE 4

Volcano plot of the association of 2,110 features with MS2 information and $\log_2 C_0/D$ evaluated by linear mixed model with the fixed effect of each feature and the subjects as the random effect. Horizontal dotted line represents $-\log_{10}(p \text{ value})$ of 1.823 controlling FDR at 0.05. Black and white dots represent unidentified metabolites with $q \text{ value} > 0.05$ and ≤ 0.05 , respectively. Blue dots below the horizontal dotted line represent identified metabolites with $q \text{ value} > 0.05$, whereas blue dots above the dotted line represent identified metabolites with $q \text{ value} \leq 0.05$ but power < 0.8 . Red and yellow dots represent endogenous metabolites and drugs or drug metabolites with $q \text{ value} \leq 0.05$ and power ≥ 0.8 , respectively. Labels on dots represent the number of metabolites in Table 2.

Figures S3A,B). Figure 6 illustrates the correlations between $\log_2 C_0/D$ and predictions based on the estimated fixed and fixed plus random effects in the model-developed group ($R_{\text{fixed}} = 0.64$ and $R_{\text{total}} = 0.78$) and predictions based on the estimated fixed effects in the validation group ($R_{\text{fixed}} = 0.57$). The predictive performance of the multiple regression model in the model development and validation groups is presented in Table 4. No significant difference of prediction error (%) between the two groups was found ($\beta = 0.871$, $SE = 1.894$, $p = 0.645$) (Supplementary Figure S4).

4 Discussion

The present study applied the method of plasma metabolomics in biomarker finding of tacrolimus pharmacokinetics in liver transplantation recipients. Results of metabolomics identified steady state C_0/D of tacrolimus was associated with several endogenous metabolites mainly including medium long chain acylcarnitines, microbiota-derived uremic

retention solutes, bile acids, and steroid hormones. Furthermore, levels of several metabolites were obviously altered according to inhibitor or inducer use. A multiple linear mixed model was established and factors including 11 metabolites and clinical information presented a suitable predictive performance for $\log_2 C_0/D$.

Our study suggested that biochemistry parameters and metabolites related to renal function, such as creatinine, uric acid, pseudouridine, and eGFR, were associated with tacrolimus $\log_2 C_0/D$. Studies have reported creatinine as a factor influencing tacrolimus pharmacokinetics. Fukudo et al. treated serum creatinine as a categorical covariate in adult liver transplant recipients, and tacrolimus clearance was decreased by 19% in subjects with creatinine greater than 1 mg/dl (Fukudo et al., 2003). A linear relation described the serum creatinine effect on clearance, with a coefficient of 0.0801 in adult and pediatric liver transplant recipients (Sam et al., 2006). Pseudouridine and uric acid were also in the list of biomarkers for chronic kidney disease progression using a metabolomic approach (Ye and Mao, 2016; Niewczas et al., 2017).

The observed association between tacrolimus disposition and renal function remains to be explained because tacrolimus undergoes almost no renal elimination (Yu et al., 2018). Studies have demonstrated a twofold higher peak tacrolimus concentration after intraintestinal administration in rats with experimental renal dysfunction than in normal controls (Okabe et al., 2000). The absorption rate of tacrolimus in the intestine might be elevated due to the enhanced nonspecific permeability during renal failure. P-glycoprotein (Pgp) function was suppressed in the liver as opposed to that in the kidney in rats with glycerol-induced acute renal failure, resulting in an increase in tacrolimus bioavailability (Okabe et al., 2002; Huang et al., 2000). Interactions of microbiota-derived uremic retention solutes with drug metabolizing enzymes and transporters were considered to account for that (Prokopienko and Nolin, 2018). Endogenous metabolites associated with tacrolimus $\log_2 C_0/D$ in the present study also comprised microbiota-derived uremic retention solutes such as hippuric acid, 3-indoxylsulfate, indolelactic acid, and substances involved in the metabolism of such solutes, including indole-3-carboxaldehyde, tryptophan, and phenylalanine. These results confirmed the significance of tryptophan metabolism by intestinal microorganisms into indole and its derivatives, some of which are ligands of the aryl hydrocarbon receptor (AhR) regulating the expression of genes encoding drug metabolizing enzymes and transporters involved in tacrolimus pharmacokinetics (Agus et al., 2018). Although indoxylsulfate is also considered a ligand to AhR, an inhibitory effect on CYP3A was reported in studies by Hubbard et al. and Prokopienko et al. (Hubbard et al., 2015; Prokopienko and Nolin, 2018). These findings are partially concurrent with the findings of the present study. Additionally, indole-3-carbinol, a dietary indole from cruciferous vegetables, has

TABLE 2 Identified endogenous metabolites with significance using generalized linear mixed model^a.

Metabolites		RT (min)	Mass (m/z)	Database	Estimate (β)	SE	q value	SLC
1	Creatinine ^b	0.57	114.0660	HMDB0000562	0.421	0.060	2.482×10^{-9}	1
2	Indole-3-carbinol ^c	2.06	130.0637	HMDB0005785	0.147	0.042	0.003	1
3	Indole-3-carboxaldehyde ^d	1.2	146.0589	HMDB0029737	−0.270	0.086	0.009	1
4	Carnitine ^d	0.56	162.1126	HMDB0000062	−0.225	0.058	0.001	1
5	Phenylalanine ^d	0.64	166.0855	HMDB0000159	−0.248	0.088	0.021	1
6	Uric acid ^b	0.6	169.0360	HMDB0000289	0.302	0.071	<0.001	1
7	Hippuric acid ^c	1.66	180.0654	HMDB0000714	0.057	0.018	0.008	1
8	Tryptophan ^c	1.2	205.0969	HMDB0000929	−0.326	0.098	0.005	1
9	Indolelactic acid ^d	2.07	206.0798	HMDB0000671	0.194	0.061	0.007	1
10	3-Indoxylsulfate ^b	1.74	212.0029	HMDB0000682	0.048	0.015	0.006	2
11	Pseudouridine ^d	0.6	243.0611	HMDB0000767	0.307	0.089	0.004	1
12	Car 8:0 ^d	2.57	288.2178	HMDB0000791	0.106	0.036	0.014	2
13	Testosterone ^b	5.13	289.2155	HMDB0000234	0.099	0.026	0.001	2
14	Car 9:1 ^d	2.59	300.2173	CID138309474	0.168	0.042	0.001	2
15	Car 9:0 ^d	3.18	302.2317	HMDB0013288	0.146	0.046	0.007	2
16	Car 10:2 ^d	2.95	312.2166	CID138251486	0.111	0.028	0.001	2
17	Car 10:1 ^d	3.29	314.2335	HMDB0240585	0.104	0.037	0.019	2
18	Car 10:0 ^c	3.94	316.248	HMDB0000651	0.099	0.034	0.016	2
19	17 α -hydroxyprogesterone ^c	2.43	331.2255	HMDB0000374	0.168	0.035	1.822×10^{-5}	2
20	Car 12:2 ^d	4.23	340.2463	CID138257751	0.130	0.042	0.010	2
21	Car 12:1 ^d	4.67	342.2631	CID138234473	0.111	0.028	0.001	2
22	Monoolein ^c	14.5	357.2992	HMDB0011567	−0.152	0.028	1.700×10^{-6}	2
23	Car 14:2 ^d	5.53	368.28	CID138240173	0.143	0.033	<0.001	2
24	Car 14:0 ^d	7.29	372.3104	HMDB0005066	0.166	0.054	0.010	2
25	Car 16:2 ^d	6.92	396.3098	CID138145981	0.152	0.038	0.001	2
26	Car 18:3 ^d	7.53	422.3235	CID138158433	0.154	0.042	0.002	2
27	Car 18:0 ^d	10.42	428.3743	HMDB0000848	0.222	0.058	0.001	2
28	Car 20:1 ^d	10.72	454.3878	CID138158433	0.158	0.048	0.006	2
29	Taurohyodeoxycholic acid ^c	3.55	464.2837	CID119046	−0.056	0.015	0.002	1
30	Glycocholic acid ^c	4.05	466.3155	HMDB0000138	−0.049	0.015	0.006	1
31	LPC 16:1 ^d	8.08	538.3124	HMDB0010383	−0.149	0.050	0.014	2

^aEstimates (β) and standard error (SE) were obtained by linear mixed effects model with each feature as the fixed effect and subject as the random effect on log₂C0/D.

^bMetabolites with expected effect on dose-adjusted tacrolimus trough concentration (C0/D) supported by clinical study.

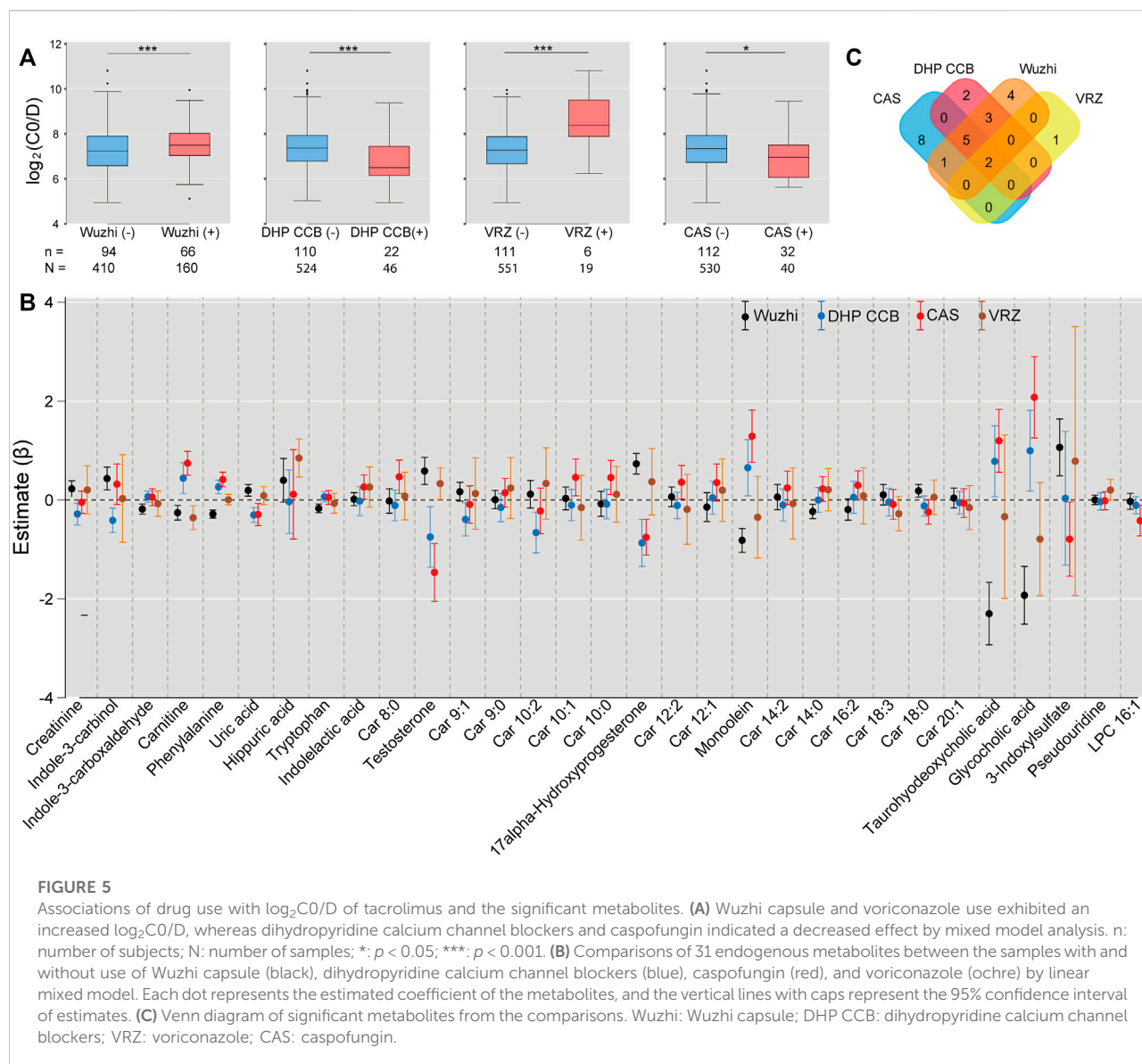
^cMetabolites with effects on or as the substrates of cytochrome P450 (CYP450) enzymes or transporters involving in tacrolimus pharmacokinetics, supported by animal or cell experiments.

^dMetabolites not yet explained. *q* value was calculated by adjusting *p* value using the Benjamini–Hochberg procedure for multiple comparisons. Car, acylcarnitine; LPC, lysophosphatidylcholine; RT, retention time; SLC, Schymanski level of confidence.

been reported to reverse multidrug resistance to vinblastine and doxorubicin mediated by Pgp (Arora and Shukla, 2003). The inhibitory effect of indole-3-carbinol on Pgp may account for the positive association between indole-3-carbinol and tacrolimus C0/D in the present study.

Glycocholic acid and taurohyodeoxycholic acid are the primary and secondary conjugated bile acids, respectively. Zhang et al. proposed taurohyodeoxycholic acid as a tertiary bile acid because it is derived from redox modification by the host on the steroid skeleton of secondary bile acid, which is produced by microbial enzymes (Zhang et al., 2019). CYP3A4 is the predominant enzyme involved in the transformation (Chen

et al., 2014). However, the apparent *K_m* for hydroxylation by human liver microsomes was high, resulting in limited levels of taurohyodeoxycholic acid. These levels increased when bile acids accumulated in cholestatic liver disease. Thus, taurohyodeoxycholic acid may be an indicator of CYP3A4 activity and biomarker of tacrolimus pharmacokinetics in liver transplant recipients, as the incidence of biliary complications after liver transplantation was up to 50% (Watt and McCashland, 2008). Collectively, the complex relationships among microbiota-derived uremic retention solutes, metabolites involved in tryptophan metabolism, bile acid metabolism influencing the effects of



gut bacteria, and tacrolimus $\log_2 C_0/D$ indicate the significance of the microbiome on the liver and interorgan communication through the gut-liver-kidney axis proposed in other studies (Patel and Shawcross, 2018; Nigam and Bush, 2019).

Univariate analysis also revealed a positive association between several medium- and long chain acylcarnitines and tacrolimus C_0/D . Kim et al. identified five ω - or (ω -1)-hydroxylated medium-chain acylcarnitines as novel urinary biomarkers for CYP3A activity in healthy subjects (Kim et al., 2018). The previous study demonstrated that hydroxylated medium-chain acylcarnitine levels in urine correlated positively with tacrolimus clearance. However, a negative correlation was observed in our study. Recently, negative effects of a high-fat diet on intestinal permeability were

summarized, and such effects were related to modulation of the expression and distribution of tight junctions, stimulations of a shift to barrier-disrupting hydrophobic bile acids, and induction of oxidative stress and apoptosis in intestinal epithelial cells (Rohr et al., 2020). Tomita et al. evaluated the effects of acylcarnitines on the transporting system in Caco-2 cell monolayers and observed that lauroylcarnitine (acylcarnitine 12:0, Car 12:0) and palmitoylcarnitine (acylcarnitine 16:0, Car 16:0) increased influx and decreased efflux in a manner dependent on their concentration and acyl chain lengths (Tomita et al., 2010). The association of the acylcarnitine profile with tacrolimus C_0/D may be attributed to the hydroxylation of medium-chain acylcarnitines by CYP3A4, detergent effects on membranes disrupting membrane barriers, and increasing membrane

TABLE 3 Parameter estimates of the multiple regression model using LASSO^a.

Parameters	Estimate	SE	z	p Value	95% CI
Endogenous metabolites (a.u.)					
Creatinine	0.328	0.146	2.238	0.025	0.042–0.614
Indole-3-carbinol	−0.108	0.076	−1.422	0.155	−0.257–0.041
Uric acid	0.061	0.126	0.480	0.631	−0.186–0.308
17alpha-Hydroxyprogesterone	−0.080	0.067	−1.198	0.231	−0.211–0.051
Car 12:1	−0.001	0.107	−0.005	0.996	−0.211–0.209
Monoolein	−0.060	0.048	−1.248	0.212	−0.154–0.034
Car 14:2	−0.316	0.179	−1.765	0.078	−0.667–0.035
Car 16:2	0.445	0.190	2.339	0.019	0.073–0.817
Car 18:3	0.123	0.084	1.462	0.144	−0.042–0.288
Car 18:0	−0.058	0.115	−0.506	0.613	−0.283–0.167
Taurohyodeoxycholic acid	0.019	0.028	0.692	0.489	−0.036–0.074
Clinical and basic information					
Days after transplantation (days)	0.001	0.001	1.597	0.110	−0.001–0.003
Cholinesterase (KU/L)	−0.015	0.050	−0.300	0.764	−0.113–0.083
Total protein (g/L)	−0.014	0.010	−1.393	0.164	−0.034–0.006
Globulin (g/L)	0.038	0.016	2.399	0.016	0.007–0.069
Potassium (mM/L)	0.184	0.102	1.792	0.073	−0.016–0.384
Cholesterol (mM/L)	−0.042	0.085	−0.490	0.624	−0.209–0.125
High-density lipoprotein (mM/L)	−0.339	0.206	−1.642	0.101	−0.743–0.065
eGFR (MDRD)	0.0002	0.002	−0.096	0.924	−0.004–0.004
Hemoglobin	0.009	0.003	2.570	0.010	0.003–0.015
Wuzhi capsule use	0.288	0.150	1.918	0.055	−0.006–0.582
Voriconazole use	1.669	0.314	5.323	<0.001	1.054–2.284
DHP CCB use	−0.548	0.203	−2.697	0.007	−0.946–0.15
Intercept	5.959	0.064	92.649	<0.001	5.834–6.084

^aEstimates and standard error (SE) were obtained by multiple linear mixed effects model with subject as the random effect on log₂C0/D using the method of least absolute shrinkage and selection operator (LASSO) augmented with 10-fold cross-validation. Wuzhi capsule, voriconazole, and DHP CCB, use: 0: no use, 1: use. Car, acylcarnitine; DHP CCB: dihydropyridine calcium channel blockers; eGFR: estimated glomerular filtration rate (MDRD).

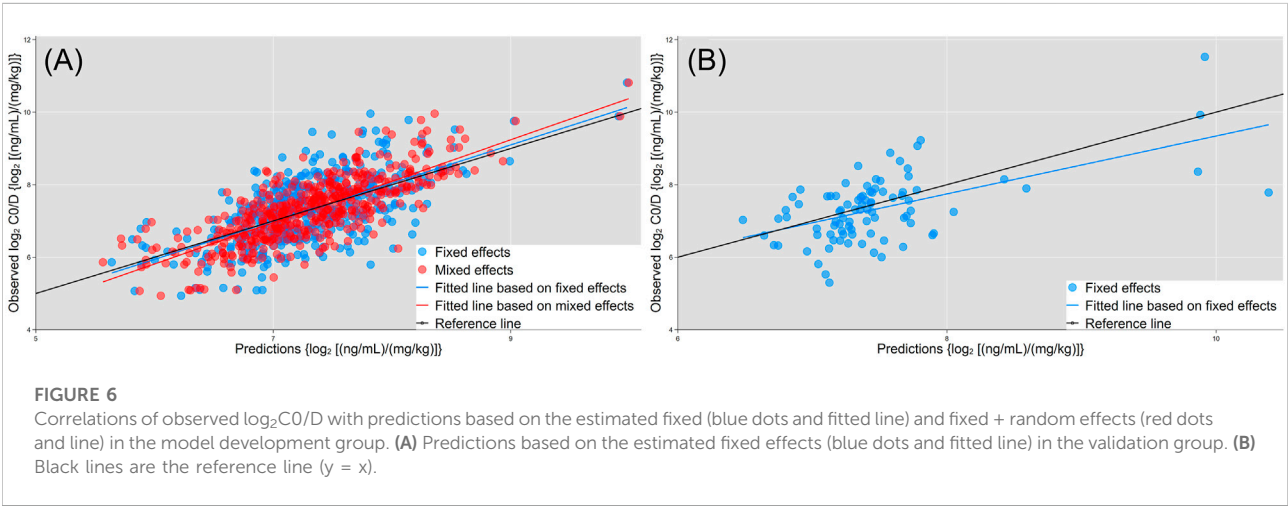


TABLE 4 Predictive performance of the multiple regression model in model development group and validation group.

log ₂ C0/D	Model development group		Validation group
	Fixed effects	Fixed + random effects	Fixed effects
ME	−0.010	<0.001	0.148
MAE	0.563	0.450	0.611
MRE	0.077	0.062	0.081
RMSE	0.704	0.575	0.788

ME: mean error; MAE: mean absolute error; MRE: mean relative error; RMSE: root-mean-square error.

solubility of long chain acylcarnitines. The exact mechanism of these actions must be further investigated.

Significantly, our results indicated that tacrolimus C0/D increased with days after transplantation in univariate and multivariate regression analysis. Tacrolimus is largely bound to erythrocytes (Woillard et al., 2018), and the increased tacrolimus C0/D with postoperative days in our study may be related to the increase of hematocrit over time after liver transplantation. Additionally, increased bioavailability and the variation of drug-drug interaction could also attribute to that (Riva et al., 2019). In fact, the frequency of comedication with Wuzhi capsule was increased when the graft function was stable in our study.

Multiple regression model established in the study included 11 factors of metabolites, nine factors of clinical biochemistry, and three comedications. There is no significant difference of prediction error (%) between the model development and validation group, indicating a successful application of the model to validation dataset. Inter- and intra-individual variability of tacrolimus pharmacokinetics are relatively large, and most published models performed inadequately in adult liver transplant recipients (Cai et al., 2020). The prediction performance for C0/D (or trough) of the multiple regression model in validation group are relative superior among the published models (Cai et al., 2020). Our findings will also provide an insight into candidate covariates for further model development.

The present study has certain limitations. Firstly, some metabolites exhibiting significance in metabolomics data were not confirmed using authentic standards, which limited the confidence levels of the identification. The identification confidence level is at least two according to the method proposed by Schymanski et al. (Schymanski et al., 2014). The high correlations of typical metabolites between levels obtained in the clinical laboratory and intensity in metabolomics data have confirmed the acceptable identification confidence of these approaches. Secondly, we did not incorporate the genotypic information in recipients and donors, which was suggested to play important roles in

tacrolimus pharmacokinetics. The primary objective of the present study is to identify potential plasma metabolomic factors, and metabolomics reflects the comprehensive effects of genetic, environmental, and physiological impacts (Pang et al., 2019). Further studies taking genotypes into account may provide more insights about the interactions between gene and metabolites. Thirdly, the present study is repeated cross-sectional designed, and the limitations inherent to this type of descriptive study do not allow it to establish a causal relationship between metabolic factors and tacrolimus C0/D. Therefore, the ability of the metabolites level prior to the drug administration for predicting of tacrolimus C0/D and guiding tacrolimus dosing should be verified in a cohort study with longitudinal design.

5 Conclusion

Thus, the present study focused on metabolomics in liver transplant recipients to identify potential factors associated with tacrolimus dose-adjusted concentration. Microbiota-derived uremic retention solutes, bile acids, steroid hormones, and medium- and long-chain acylcarnitines were the main metabolites identified with significance. Although a multiple regression model incorporating such metabolites was established, further investigation in a larger, more balanced panel is required with additional information on both donor and recipient genotypes and the integration of innovative strategies such as machine learning. Our findings provide valuable insight into metabolomics on individual dosing and guide research on transporters and metabolizing enzymes.

Data availability statement

The original contributions presented in the study are included in the article/Supplementary Material, further inquiries can be directed to the corresponding authors.

Ethics statement

The studies involving human participants were reviewed and approved by Institutional Review Board at Nanjing Drum Tower Hospital. Written informed consent for participation was not required for this study in accordance with the national legislation and the institutional requirements.

Author contributions

All authors participated in the interpretation of the study results and in the drafting, critical revision, and approval of the final version of the manuscript. HZ, WG and YZ were involved in the study design, writing-original draft and writing-review and editing. HZ, MW and ZW were involved in the data curation and data analyses. XX, YD and DL were involved in sample and data collection. HZ, MW and XX were responsible for sample processing and methodology.

Funding

This work was supported by the grants from the Jiangsu Provincial Medical Youth Talent Project (No. QNRC2016013), National Natural Science Foundation of China (No.

NSFC81803634 and No. NSFC81302849) and Nanjing Medical Science and Technique Development Foundation (No. YKK17075).

Conflict of interest

The authors declare that the research was conducted in the absence of any commercial or financial relationships that could be construed as a potential conflict of interest.

Publisher's note

All claims expressed in this article are solely those of the authors and do not necessarily represent those of their affiliated organizations, or those of the publisher, the editors and the reviewers. Any product that may be evaluated in this article, or claim that may be made by its manufacturer, is not guaranteed or endorsed by the publisher.

Supplementary material

The Supplementary Material for this article can be found online at: <https://www.frontiersin.org/articles/10.3389/fphar.2022.1045843/full#supplementary-material>

References

- Agus, A., Planchais, J., and Sokol, H. (2018). Gut microbiota regulation of tryptophan metabolism in health and disease. *Cell Host Microbe* 23, 716–724. doi:10.1016/j.chom.2018.05.003
- Arora, A., and Shukla, Y. (2003). Modulation of vinca-alkaloid induced P-glycoprotein expression by indole-3-carbinol. *Cancer Lett.* 189, 167–173. doi:10.1016/S0304-3835(02)00550-5
- Birdwell, K. A., Decker, B., Barbarino, J. M., Peterson, J. F., Stein, C. M., Sadee, W., et al. (2015). Clinical Pharmacogenetics Implementation Consortium (CPIC) guidelines for CYP3A5 genotype and tacrolimus dosing. *Clin. Pharmacol. Ther.* 98, 19–24. doi:10.1002/cpt.113
- Brunet, M., Van Gelder, T., Åsberg, A., Haufroid, V., Hesselink, D. A., Langman, L., et al. (2019). Therapeutic drug monitoring of tacrolimus-personalized therapy: Second consensus report. *Ther. Drug Monit.* 41, 261–307. doi:10.1097/FTD.0000000000000640
- Cai, X., Li, R., Sheng, C., Tao, Y., Zhang, Q., Zhang, X., et al. (2020). Systematic external evaluation of published population pharmacokinetic models for tacrolimus in adult liver transplant recipients. *Eur. J. Pharm. Sci.* 145, 105237. doi:10.1016/j.ejps.2020.105237
- Chen, J., Zhao, K. N., and Chen, C. (2014). The role of CYP3A4 in the biotransformation of bile acids and therapeutic implication for cholestasis. *Ann. Transl. Med.* 2, 7. doi:10.3978/j.issn.2305-5839.2013.03.02
- Del Bello, A., Congy-Jolivet, N., Danjoux, M., Muscari, F., Lavayssière, L., Esposito, L., et al. (2018). High tacrolimus intra-patient variability is associated with graft rejection, and de novo donor-specific antibodies occurrence after liver transplantation. *World J. Gastroenterol.* 24, 1795–1802. doi:10.3748/wjg.v24.i16.1795
- Fukudo, M., Yano, I., Fukatsu, S., Saito, H., Uemoto, S., Kiuchi, T., et al. (2003). Forecasting of blood tacrolimus concentrations based on the bayesian method in adult patients receiving living-donor liver transplantation. *Clin. Pharmacokinet.* 42, 1161–1178. doi:10.2165/00003088-200342130-00006
- Ganesh, S., Almazroo, O. A., Tevar, A., Humar, A., and Venkataramanan, R. (2017). Drug metabolism, drug interactions, and drug-induced liver injury in living donor liver transplant patients. *Clin. Liver Dis.* 21, 181–196. doi:10.1016/j.cld.2016.08.011
- Gonzales, H. M., Chandler, J. L., McGillicuddy, J. W., Rohan, V., Nadig, S. N., Dubay, D. A., et al. (2020). A comprehensive review of the impact of tacrolimus intrapatient variability on clinical outcomes in kidney transplantation. *Am. J. Transpl.* 20, 1969–1983. doi:10.1111/ajt.16002
- Huang, Z. H., Murakami, T., Okochi, A., Yumoto, R., Nagai, J., and Takano, M. (2000). Expression and function of P-glycoprotein in rats with glycerol-induced acute renal failure. *Eur. J. Pharmacol.* 406, 453–460. doi:10.1016/S0014-2999(00)00699-3
- Hubbard, T. D., Murray, I. A., and Perdew, G. H. (2015). Indole and tryptophan metabolism: Endogenous and dietary routes to ah receptor activation. *Drug Metab. Dispos.* 43, 1522–1535. doi:10.1124/dmd.115.064246
- Kim, B., Lee, J., Shin, K. H., Lee, S. H., Yu, K. S., Jang, I. J., et al. (2018). Identification of ω - or (ω -1)-hydroxylated medium-chain acylcarnitines as novel urinary biomarkers for CYP3A activity. *Clin. Pharmacol. Ther.* 103, 879–887. doi:10.1002/cpt.856
- Li, S., Park, Y., Duraisingham, S., Strobel, F. H., Khan, N., Soltow, Q. A., et al. (2013). Predicting network activity from high throughput metabolomics. *PLoS Comput. Biol.* 9, e1003123. doi:10.1371/journal.pcbi.1003123
- Magliocco, G., Thomas, A., Desmeules, J., and Daali, Y. (2019). Phenotyping of human CYP450 enzymes by endobiotics: Current knowledge and methodological approaches. *Clin. Pharmacokinet.* 58, 1373–1391. doi:10.1007/s40262-019-00783-z
- Muduma, G., Saunders, R., Odeyemi, I., and Pollock, R. F. (2016). Systematic review and meta-analysis of tacrolimus versus ciclosporin as primary immunosuppression after liver transplant. *PLoS One* 11, e0160421. doi:10.1371/journal.pone.0160421
- Niewczas, M. A., Mathew, A. V., Croall, S., Byun, J., Major, M., Sabiseti, V. S., et al. (2017). Circulating modified metabolites and a risk of ESRD in patients with type 1 diabetes and chronic kidney disease. *Diabetes Care* 40, 383–390. doi:10.2337/dc16-0173

- Nigam, S. K., and Bush, K. T. (2019). Uraemic syndrome of chronic kidney disease: Altered remote sensing and signalling. *Nat. Rev. Nephrol.* 15, 301–316. doi:10.1038/s41581-019-0111-1
- Okabe, H., Hashimoto, Y., and Inui, K. I. (2000). Pharmacokinetics and bioavailability of tacrolimus in rats with experimental renal dysfunction. *J. Pharm. Pharmacol.* 52, 1467–1472. doi:10.1211/0022357001777676
- Okabe, H., Yano, I., Hashimoto, Y., Saito, H., and Inui, K. (2002). Evaluation of increased bioavailability of tacrolimus in rats with experimental renal dysfunction. *J. Pharm. Pharmacol.* 54, 65–70. doi:10.1211/0022357021771931
- Oweira, H., Lahdou, I., Opelz, G., Daniel, V., Terness, P., Schmidt, J., et al. (2018). Association of pre- and early post-transplant serum amino acids and metabolites of amino acids and liver transplant outcome. *Transpl. Immunol.* 46, 42–48. doi:10.1016/j.trim.2017.12.003
- Pang, H., Jia, W., and Hu, Z. (2019). Emerging applications of metabolomics in clinical Pharmacology. *Clin. Pharmacol. Ther.* 106, 544–556. doi:10.1002/cpt.1538
- Patel, C. A. W. V. C., Shawcross, A. S. D. L., SingAnAyAgAm, A., and Shawcross, D. L. (2018). Review article : The gut microbiome as a therapeutic target in the pathogenesis and treatment of chronic liver disease. *Aliment. Pharmacol. Ther.* 47, 192–202. doi:10.1111/apt.14397
- Papale, P. B., Kim, S. D., Lee, H. W., Lim, M., Kale, D. D., Kim, Y. L., et al. (2010). An integrative approach for identifying a metabolic phenotype predictive of individualized pharmacokinetics of tacrolimus. *Clin. Pharmacol. Ther.* 87, 426–436. doi:10.1038/clpt.2009.296
- Prokopenko, A. J., and Nolin, T. D. (2018). Microbiota-derived uremic retention solutes: Perpetrators of altered nonrenal drug clearance in kidney disease. *Expert Rev. Clin. Pharmacol.* 11, 71–82. doi:10.1080/17512433.2018.1378095
- Qin, X. L., Chen, X., Wang, Y., Xue, X. P., Wang, Y., Li, J. L., et al. (2014). *In vitro* effects of six bioactive lignans of wuzhi tablet (schisandra sphenanthera extract) on the CYP3A/pglycoprotein-mediated absorption and metabolism of tacrolimus. *Drug Metab. Dispos.* 42, 193–199. doi:10.1124/dmd.113.053892
- Riva, N., Woillard, J. B., Distefano, M., Moragas, M., Dip, M., Halac, E., et al. (2019). Identification of factors affecting tacrolimus trough levels in Latin American pediatric liver transplant patients. *Liver Transpl.* 25, 1397–1407. doi:10.1002/lt.25495
- Rohr, M. W., Narasimhulu, C. A., Rudeski-Rohr, T. A., and Parthasarathy, S. (2020). Negative effects of a high-fat diet on intestinal permeability: A review. *Adv. Nutr.* 11, 77–91. doi:10.1093/advances/nmz061
- Sam, W. J., Lai, S. T., Holmes, M. J., Aw, M., Seng, H. Q., Kang, H. L., et al. (2006). Population pharmacokinetics of tacrolimus in whole blood and plasma in Asian liver transplant patients. *Clin. Pharmacokinet.* 45, 59–75. doi:10.2165/00003088-200645010-00004
- Schymanski, E. L., Jeon, J., Gulde, R., Fenner, K., Ruff, M., Singer, H. P., et al. (2014). Identifying small molecules via high resolution mass spectrometry: Communicating confidence. *Environ. Sci. Technol.* 48, 2097–2098. doi:10.1021/es5002105
- Shin, K. H., Choi, M. H., Lim, K. S., Yu, K. S., Jang, I. J., and Cho, J. Y. (2013). Evaluation of endogenous metabolic markers of hepatic CYP3A activity using metabolic profiling and midazolam clearance. *Clin. Pharmacol. Ther.* 94, 601–609. doi:10.1038/clpt.2013.128
- Shuker, N., Van Gelder, T., and Hesselink, D. A. (2015). Intra-patient variability in tacrolimus exposure: Causes, consequences for clinical management. *Transpl. Rev.* 29, 78–84. doi:10.1016/j.trre.2015.01.002
- Tolstikov, V., James Moser, A., Sarangarajan, R., Narain, N. R., and Kiebish, M. A. (2020). Current status of metabolomic biomarker discovery: Impact of study design and demographic characteristics. *Metabolites* 10, 224. doi:10.3390/metabo10060224
- Tomita, M., Doi, N., and Hayashi, M. (2010). Effects of acylcarnitines on efflux transporting system in Caco-2 cell monolayers. *Eur. J. Drug Metab. Pharmacokinet.* 35, 1–7. doi:10.1007/s13318-010-0001-1
- Watt, K. D. S., and McCashland, T. M. (2008). “Cholestasis post liver transplantation,” in *Cholestatic liver disease*. Editors K. D. Lindor and J. A. Talwalkar (Totowa, NJ: Humana Press), 171–181. doi:10.1007/978-1-59745-118-5_10
- Woillard, J. B., Saint-Marcoux, F., Debord, J., and Åsberg, A. (2018). Pharmacokinetic models to assist the prescriber in choosing the best tacrolimus dose. *Pharmacol. Res.* 130, 316–321. doi:10.1016/j.phrs.2018.02.016
- Ye, L., and Mao, W. (2016). Metabonomic biomarkers for risk factors of chronic kidney disease. *Int. Urol. Nephrol.* 48, 547–552. doi:10.1007/s11255-016-1239-6
- Yu, M., Liu, M., Zhang, W., and Ming, Y. (2018). Pharmacokinetics, pharmacodynamics and pharmacogenetics of tacrolimus in kidney transplantation. *Curr. Drug Metab.* 19, 513–522. doi:10.2174/1389200219666180129151948
- Zhang, J., Gao, L. Z., Chen, Y. J., Zhu, P. P., Yin, S. S., Su, M. M., et al. (2019). Continuum of host-gut microbial co-metabolism: Host cyp3a4/3a7 are responsible for tertiary oxidations of deoxycholate species. *Drug Metab. Dispos.* 47, 283–294. doi:10.1124/dmd.118.085670



OPEN ACCESS

EDITED BY

Junmin Zhang,
Lanzhou University, China

REVIEWED BY

Qiang Fu,
Chengdu University, China
Yan Kai Dong,
Northwest University, China
Sumarno Adi Subrata,
Muhammadiyah University of Magelang,
Indonesia
Bo Li,
Sun Yat-sen Memorial Hospital, China

*CORRESPONDENCE

Zhaojun Chen,
zhaojunchen66@126.com
Jiajia Xue,
jjiajiaxue@mail.buct.edu.cn

[†]These authors have contributed equally
to this work

SPECIALTY SECTION

This article was submitted to Drug
Metabolism and Transport,
a section of the journal
Frontiers in Pharmacology

RECEIVED 07 September 2022

ACCEPTED 31 October 2022

PUBLISHED 18 November 2022

CITATION

Deng P, Liang H, Wang S, Hao R, Han J,
Sun X, Pan X, Li D, Wu Y, Huang Z, Xue J
and Chen Z (2022), Combined
metabolomics and network
pharmacology to elucidate the
mechanisms of Dracorhodin
Perchlorate in treating diabetic foot
ulcer rats.
Front. Pharmacol. 13:1038656.
doi: 10.3389/fphar.2022.1038656

COPYRIGHT

© 2022 Deng, Liang, Wang, Hao, Han,
Sun, Pan, Li, Wu, Huang, Xue and Chen.
This is an open-access article
distributed under the terms of the
Creative Commons Attribution License
(CC BY). The use, distribution or
reproduction in other forums is
permitted, provided the original
author(s) and the copyright owner(s) are
credited and that the original
publication in this journal is cited, in
accordance with accepted academic
practice. No use, distribution or
reproduction is permitted which does
not comply with these terms.

Combined metabolomics and network pharmacology to elucidate the mechanisms of Dracorhodin Perchlorate in treating diabetic foot ulcer rats

Pin Deng^{1,2†}, Huan Liang^{3†}, Shulong Wang^{1,2†}, Ruinan Hao^{4,5†},
Jinglu Han^{1,2}, Xiaojie Sun^{1,2}, Xuyue Pan², Dongxiao Li^{1,2},
Yinwen Wu¹, Zhichao Huang^{1,2}, Jiajia Xue^{4,5*} and
Zhaojun Chen^{2*}

¹School of Graduates, Beijing University of Chinese Medicine, Beijing, China, ²Department of Hand and Foot Surgery, Beijing University of Chinese Medicine Third Affiliated Hospital, Beijing, China, ³Department of Orthopedics, Beijing Longfu Hospital, Beijing, China, ⁴State Key Laboratory of Organic-Inorganic Composites, Beijing University of Chemical Technology, Beijing, China, ⁵Beijing Laboratory of Biomedical Materials, Beijing University of Chemical Technology, Beijing, China

Background: Diabetic foot ulcer (DFU) is a severe chronic complication of diabetes, that can result in disability or death. Dracorhodin Perchlorate (DP) is effective for treating DFU, but the potential mechanisms need to be investigated. We aimed to explore the mechanisms underlying the acceleration of wound healing in DFU by the topical application of DP through the combination of metabolomics and network pharmacology.

Methods: A DFU rat model was established, and the rate of ulcer wound healing was assessed. Different metabolites were found in the skin tissues of each group, and MetaboAnalyst was performed to analyse metabolic pathways. The candidate targets of DP in the treatment of DFU were screened using network pharmacology. Cytoscape was applied to construct an integrated network of metabolomics and network pharmacology. Moreover, the obtained hub targets were validated using molecular docking. After the topical application of DP, blood glucose, the rate of wound healing and pro-inflammatory cytokine levels were assessed.

Results: The levels of IL-1, hs-CRP and TNF- α of the Adm group were significantly downregulated. A total of 114 metabolites were identified. These could be important to the therapeutic effects of DP in the treatment of DFU. Based on the network pharmacology, seven hub genes were found, which were partially consistent with the metabolomics results. We focused on four hub targets by further integrated analysis, namely, PAH, GSTM1, DHFR and CAT, and the crucial metabolites and pathways. Molecular docking results demonstrated that DP was well combined with the hub targets.

Conclusion: Our research based on metabolomics and network pharmacology demonstrated that DP improves wound healing in DFU through multiple targets and pathways, and it can potentially be used for DFU treatment.

KEYWORDS

diabetic foot ulcer, Dracorhodin Perchlorate, metabolomics, network pharmacology, mechanisms

1 Introduction

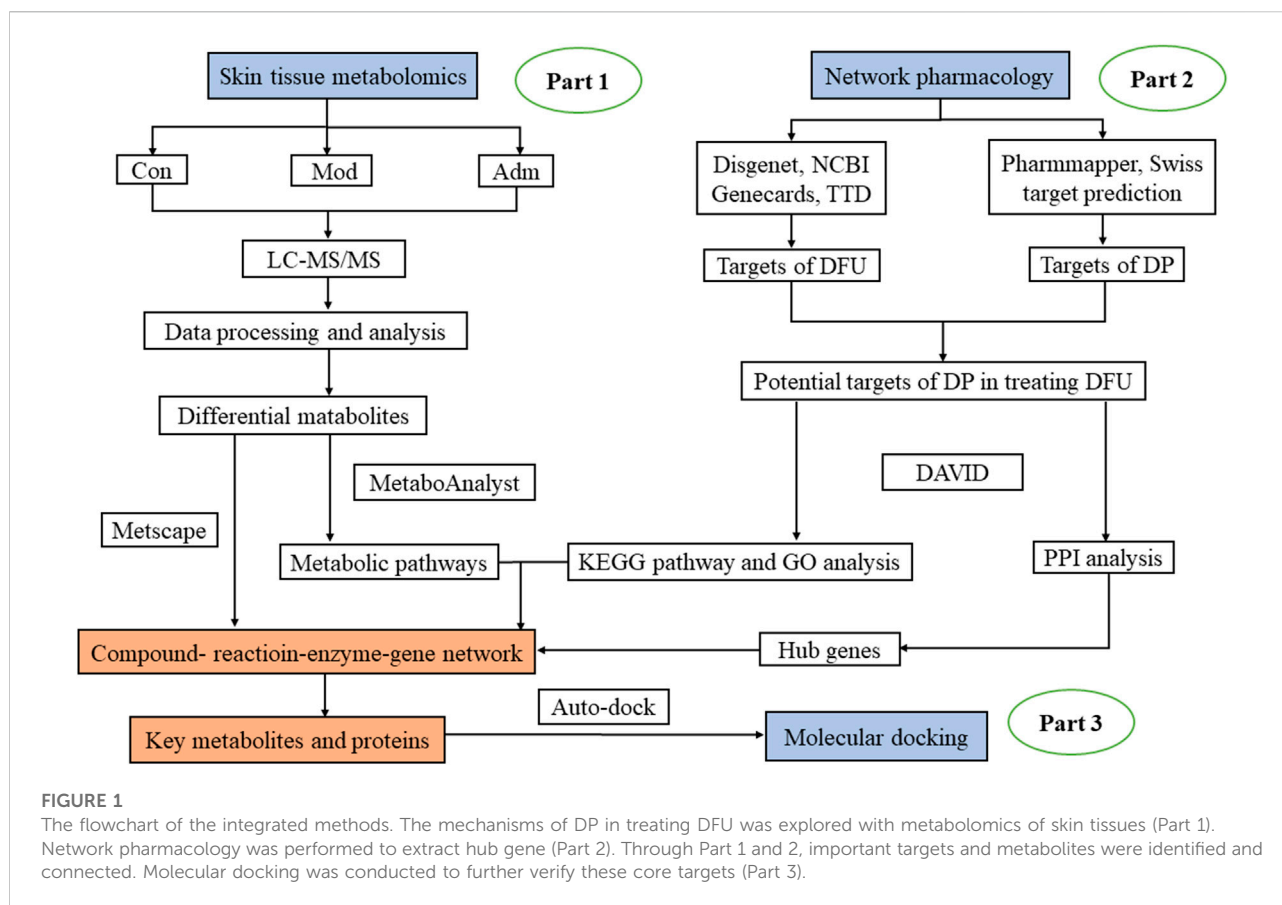
Diabetic foot ulcer (DFU), which can cause disability or death in severe cases, is a common chronic complication of diabetes mellitus (DM) (Deng et al., 2022). Reportedly, 19%–34% of people would be afflicted with DFU in a lifetime (Bonnet JB, 2021). DFU is the cause of 50%–70% of limb amputations. One leg is amputated due to DFU every 30 s in the world (Alven et al., 2022). Most wound dressing scaffolds currently in use are ineffective for treating DFU. Amputations are common when ulcer wounds are not adequately treated. The International Working Group on the Diabetic Foot (IWGDF) indicated that the severity of the diabetic foot is largely related to differences in the standard care of the foot (Bus et al., 2020). The guidelines suggest that the best dressing selection should be based primarily on secretion control, comfort and cost to promote wound healing based on the usual optimal care in individuals with DFUs (Rayman et al., 2020). *Dracaena Draconis* (DD) has been used topically to treat foot ulcers. DD is also known as “*Kirin Draconis*”, which tastes sweet and salty. It has a flat nature, enters the liver and heart meridians, and has the following effects: promotes blood circulation and removes blood stasis, haemostasis, analgesia, astringent sores and regenerating muscles. It is extensively applied in traditional Chinese Medicine surgery to repair the wound. The Compendium of Materia Medica calls it “the holy medicine for activating blood circulation”. Its effectiveness has been highly praised by doctors in all dynasties and is an essential medicine for muscle regeneration. According to the summary of predecessors, *Dracaena Draconis* is the most frequently used drug in Shengji prescriptions recorded in ancient books of traditional Chinese medicine (Yanliang Yan, 2002). Dracorhodin perchlorate (DP, C₁₇H₁₅ClO₇, 366.75 g/mol, Supplementary Figure S1) is the main extract of dracorhodin and currently used as substitute of *Draconis* in scientific research; it is widely used by researchers. Research pointed out that draconisin perchlorate preferentially activates EGFR on the surface of fibroblasts and then activates the phosphorylation of downstream pathways ERK and PI3K, resulting in the activation of a series of cell proliferation-related pathways. Thus, the regulation of cell proliferation is realised, promoting ulcer wound healing (Lin). This finding gives a theoretical foundation for the use of *Dracaena Draconis* to treat wound repair. The mechanisms and targets of DP in the treatment of DFU remain obscure. Similar to DP, potential treatments for DFU exist, such as paeoniflorin, mangiferin, and luteolin. Paeoniflorin effectively inhibits NLRP3 and NF- κ B-mediated inflammation in DFU by inhibiting CXCR2 (Sun et al., 2021). Topical application of mangostin inhibits

the prolongation of the inflammatory phase of diabetic wounds by suppressing inflammation and oxidative stress (Lwin et al., 2021). Luteolin promotes wound repair in DFU rats by inactivating NF- κ B and upregulating Nrf2 to improve inflammation and oxidative stress (Chen et al., 2021).

DFU is associated with the variations of complicated metabolic physiologies. Meanwhile, as a helpful method, metabolomics can track the dynamic changes of pathological metabolites (Li et al., 2021). Nevertheless, traditional metabolomics is used to reflect the ultimate changes in disease and treatment (Fu C, 2019). Endogenous mechanisms underlying the changes of metabolites are unknown; these involve the producing process of these metabolites, their related proteins and pathways and which proteins DP acts on. As a result, metabolomics alone may limit DP’s application.

The concept of “network pharmacology” was first proposed by Hopkins. It is a method to analyse the potential therapeutic targets of drug intervention and disease (Deng et al., 2021). However, it is constrained by a single calculation method that relies on a publicly accessible database. Based on network pharmacology, it only predicts the possibilities of pathway analysis and compound-target combination (Zhong et al., 2018). Whether DP binds to target cells *in vivo* and whether DP has an inhibitory, activating, or ineffective combination effect on target cells are unknown. Metabolomics is a promising histological method for understanding biological mechanisms. Based on untargeted or targeted metabolomics analysis, metabolites in biological samples (tissues, cells, and others) were identified by comparing controls with altered groups, receiving different treatments, undergoing different levels of stress, dietary modifications or disease or condition-specific promotions using sophisticated analytical techniques, advanced data processing and statistical analysis (Canuto et al., 2017). Network pharmacology and metabolomics are bioinformatic approaches that enrich the analysis of pathways.

Hence, we used a method based on combination of network pharmacology and metabolomics. The untargeted metabolomics was undertaken to explore DP’s effects on DFU and confirm the key metabolites. After that, with network pharmacology, we investigated the targets on which DP acted in the treatment of DFU and the targets and reactions that regulated the metabolites. The advantage of this strategy is as follows. On the one hand, short of validation with experiment of network pharmacology can be compensated; on the other hand, it addresses the shortness of targets’ binding to drug and molecular mechanisms in



metabolomics. This method could help researchers better understand the therapeutic principles of natural compounds used to treat DFU. In this research, we applied for the first time a combined metabolomics and network pharmacology approach to explore the core targets and mechanisms of DP for DFU treatment. It sheds new light on the mechanistic study of DP in treating DFU. Figure 1 depicts the research flowchart.

2 Material and methods

2.1 Chemicals and kits

DP was purchased from Shanghai Yuanye (China). No: B21414-20 mg.

Jishuitan Hospital kindly donated L929 mouse fibroblasts cells. Hyclone provided Cell Counting Kit-8 (CCK-8), tryptone, Dulbecco's modified eagle medium (DMEM), foetal bovine serum (FBS) and phosphate buffer saline (PBS, PH = 7.4) (United States). Methacrylate Gelatin (GelMA) was obtained from Suzhou Yongqinquan Intelligent Equipment Co., Ltd. Sigma-Aldrich (United States) provided streptozotocin (STZ), and citric acid/sodium citrate buffer was provided by Beijing Chengxin Kangrun Medical Equipment Co., Ltd. Ethacridine

lactate solution (ELS) was from Hebei Wuluo Pharmaceutical Co., Ltd., Hebei, China. TNF- α , hs-CRP and IL-1 kits were from Quanzhou Ruixin Biotechnology Co., Ltd., Quanzhou, China. All chemicals in the experiment were analytical grade.

2.2 Cell proliferation experiment

The viability of L929 cells on a hydrogel/nanofiber dressing loaded with DP at various concentrations was assessed using the CCK-8 assay. The dressing was fixed in a 24-well plate, and 100 μ L of L929 cells suspension (20000 cells/well) and 300 μ L of cell culture medium were plated onto the sample and incubated at 37°C. The CCK-8 assay for testing cells viability on the dressing at each time interval (days 1, 3 and 5).

2.3 Experimental animals

Beijing University of Chinese Medicine Laboratory Animal Centre (Beijing, China) provided 7-week-old -specific-pathogen-free Sprague Dawley male rats weighing 200–250 g each (the production license number of animals was SCXK (jing) 2021-0006). All male rats were housed in a well-ventilated room with a

temperature of 25°C and a 12-h dark-light cycle. They were given free access to water and food for free. The Animal care was carried out in accordance with the Beijing University of Chinese Medicine Laboratory Animal Centre Animal Care and Use Guidelines. Beijing University of Chinese Medicine approved the protocol of the Medical Ethics Committee under approval number 4-2021120302-4121.

2.4 Experimental animal design

2.4.1 DM experimental model

After 40 SD rats were acclimatised to the basal diet for 1 week. Ten of them were randomly selected and fed with a normal diet to serve as the control group (Con). The remaining 30 rats were fed with high-fat and high-sugar diets for 1 month. Then all rats fasted for 12h, a diabetic rat model was prepared by the intraperitoneal injection of 40 mg/kg streptozotocin (STZ, STZ injection dose formula: body weight \times STZ preset dosage)/1,000 = stz dosage (mg) solution. STZ is prepared into a solution with 1% concentration with citric acid/sodium citrate buffer before use, PH4.2 (Bonner-Weir S et al., 1983). Rats in the Con group were injected intraperitoneally with an equal volume of 0.1 mol/L citric acid/sodium citrate buffer without STZ. The diabetic rat was evaluated by drawing blood from the tail vein and measuring fasting blood glucose (FBG) 3 days after the injection of STZ with an Accu-Chek glucometer (Roche, Germany). The rats were observed to have polydipsia and polyuria, dirty back hair, wet padding and others. Having an FBG value of greater than 16.7 mmol/L was considered a sign of diabetes.

2.4.2 DFU experimental model

Rats in the Con group and the diabetes model group were anaesthetized by intraperitoneal injection of 1% concentration of pentobarbital (40mg/kg) at a dose of 0.4ml/100g. The long hairs on the spine of the rats were removed with an electric razor. The modelling area was marked in the depilation area with a circular seal. Under sterile conditions, the skin in the modelling area was cut off to reach the fascia. A circular wound with a diameter of 1.5 cm was formed, and the animals were fed in a single cage. The wound was coated with glacial acetic acid once a day. A 5 cm \times 7 cm \times 4-layer gauze block was used for binding and fixing. The diabetic skin ulcers were formed 1 week later. The success of the skin ulcer model was evaluated by the absence of granulation tissue growth around the wound, the appearance of swelling and abscesses in the skin and the absence of oozing blood with a large-headed needle prick (Jia et al., 2018).

FBG measurements were taken on days 0, 3, 7, 10, 14, 21, and 28 following the start of topical DP treatment on the wound. Wound area and wound healing rate were recorded on days 0, 3,

7, 10, 14, 21, and 28. The size of the wound area was measured using ImageJ, which is a java-based public image processing tool designed by the National Institutes of Health. Wound healing rate (%) was determined as follows (wound area before administration-unhealed wound area)/the wound area before administration \times 100%.

2.4.3 Preparation of DP dressing (bilayer hydrogel/nanofiber dressing)

To prepare a homogeneous GelMA (20 w/v %) solution, 0.2 g GelMA was added to a PBS solution containing a photoinitiator and heated for 30 min at 60°C. Then, DP (3 μ g) was added to the GelMA solution (1 ml) to form a homogeneous loaded-DP precursor solution. The electrospun mats were put in moulds to create the bilayer hydrogel/nanofiber dressing, and 400 μ l of the loaded-DP hydrogel precursor solution (before UV crosslinking) was added to each mould. After that, UV crosslinking was done for 60 s. Eventually, DP dressing was made (Each DP dressing contains 1.2 μ g DP).

2.4.4 Grouping of experimental animals and methods of intervention

All male rats were assigned to four groups at random: Normal wound group (Con); Model group (Mod); Western medicine group (Wmg), in which the wound surface was externally applied with Ethacridine lactate solution (ELS) (Jia et al., 2018), wrapped and fixed with medical paper tape, once a day; and DP group, also known as Adm group. The topical application of DP dressing was performed in the Adm group. There was no need to change the DP dressing during the treatment. No intervention was applied to rats in the Con and Mod groups.

2.5 Blood sample and skin tissue collection

Blood samples were extracted from the abdominal aorta of the rat, placed in a 4°C refrigerator refrigerated for 30 min and centrifuged at 3,000 rpm for about 15 min for obtaining serum. The serum levels of TNF- α , IL-1 and hs-CRP were determined by using Enzyme-linked immunosorbent assay (ELISA). After the male rats were sacrificed, the wound skin tissue was removed and rapidly frozen in liquid nitrogen, transferred to a -80°C refrigerator, and subsequently used for the assays.

2.6 Pathological analysis

The dermal tissues around the wound of DFU rats on the 28th day were collected for pathological analysis to observe the microscopic changes during wound healing. The re-epithelialisation of damaged skin was estimated by

hematoxylin-eosin (H&E) staining. To assess collagen formation and deposition, Masson staining was used.

Skin tissue fixed in 4% paraformaldehyde was subsequently cut into 1 cm diameter coin-sized tissue sections, which were then embedded in paraffin wax and transformed into pathological sections. Sections were dewaxed.

H&E staining: the dewaxed tissue sections were stained in hematoxylin staining solution for 3–5 min, washed in tap water, fractionated in fractionation solution, washed in tap water, returned to blue in return blue solution and rinsed in running water. Slices were dehydrated in 85% and 95% gradient alcohol for 5 min each and stained in eosin staining solution for 5 min. Slices are placed in anhydrous ethanol I for 5 min, anhydrous ethanol II for 5 min, anhydrous ethanol III for 5 min, dimethyl I for 5 min and xylene II for 5 min for transparency and sealed with neutral gum.

Masson staining: dewaxed tissue sections were soaked in potassium dichromate overnight and washed in tap water. Ferric hematoxylin A solution was mixed with B solution in equal proportions to form ferric hematoxylin staining solution. Slices were placed into ferric hematoxylin for 3 min, washed with tap water, differentiated with differentiation solution, washed with tap water, returned to blue with blue return solution and rinsed with running water. Slices were stained in Ponceau acid fuchsin staining buffer for 5–10 min and then rinsed with tap water. Phosphomolybdic acid in aqueous solution for 1–3 min After phosphomolybdic acid, without washing, directly into aniline blue staining solution for 3–6 min. The slices were divided with 1% glacial acetic acid and dehydrated in two tanks of anhydrous ethanol. The sections were placed in a third tank of anhydrous ethanol for 5 min, xylene for 5 min for transparency and neutral gum to seal the sections.

The H&E and Masson sections were then magnified and photographed using a light microscope (ZEISS ZEN3.4, Germany). Wound healing, collagen deposition and inflammation were examined using Image-Pro Plus 6.0 (Media Cybernetics, Inc, Rockville, MD, United States).

2.7 Cytokine assays

The TNF- α , hs-CRP and IL-1 were detected through ELISA. The experiments were carried out according to the manufacturer's instructions. A microplate reader (Thermo Scientific Microplate Reader, United States) was used to measure the absorbance at 450 nm.

2.8 Skin tissue metabonomic analysis

2.8.1 Metabolite extraction

Metabolite extraction (Dunn et al., 2011) was performed to control the quality of sample preparation. Tissue (25 mg) was weighed. The extraction reagent at 800 μ l was added after

precooling (methanol: acetonitrile: water (2:2:1, v/v/v) along with internal standard mixture 1 (IS1: L-Leucine-d3, L-PHENYLALANINE) and 2 (IS2: L-Tryptophan-d5, Progesterone-2,3,4-13C3). Then, metabolites were extracted. After homogenising the samples for 5 min with a TissueLyser (JXFSTPRP, China), they were sonicated for 10 min and incubated for 1 h at -20°C . After centrifuging the samples at 25,000 rpm and 4°C for 15 min, the transferred supernatant was subjected to vacuum freeze drying. We resuspended the metabolites in 200 μ l of 10% methanol and then sonicated for 10 min at 4°C before centrifugation for 15 min at 25,000 rpm. The supernatants were transferred to autosampler vials for LC-MS analysis. For evaluating the reproducibility of the entire Liquid Chromatography-Mass Spectrometry (LC-MS) analysis, quality control (QC) was prepared by pooling the same volume of all samples.

2.8.2 LC-MS/MS analysis

Using a Waters 2D UPLC (Waters, United States) tandem Q Exactive high resolution mass spectrometer (Thermo Fisher Scientific, United States), metabolite was separated and detected. A Waters 2D UPLC (Waters, United States) coupled to a Thermo Fisher Scientific Q-Exactive mass spectrometer with a heated electrospray ionisation (HESI) source and controlled by the Xcalibur 2.3 software program (Thermo Fisher Scientific, Waltham, MA, United States) was used for sample analysis. Waters ACQUITY UPLC BEH C₁₈ column (1.7 μ m, 2.1 mm \times 100 mm, Waters, United States) was used to perform chromatographic separation. We set the temperature of a column to 45°C . There were 0.1% formic acid (A) and acetonitrile (B) in the mobile phase in the positive mode and 10 mM ammonium formate (A) and acetonitrile (B) in the negative mode. The gradient conditions are shown in [Supplementary Table S1](#). The flow rate was 0.35 ml/min, and the injection volume was 5 μ l. We injected one QC sample for every 10 samples.

2.8.3 Data processing and analysis

Using Compound Discoverer 3.1 (Thermo Fisher Scientific, United States), the LC-MS/MS raw data (raw file) was processed, including retention time correction, peak extraction, additive ion pooling, background peak labelling, missing value filling and metabolite identification, before information on retention time, molecular weight and peak area was exported. The identification of metabolites was the result of a combination of mzCloud, Human Metabolome Database (HMDB), Kyoto Encyclopedia of Genes and Genomes (KEGG) and LipidMaps. Fragment Mass Tolerance lower than 10 ppm, Precursor Mass Tolerance lower than ppm and Tolerance for RT lower than 0.2 min are the main parameters of metabolite identification.

We imported result data into metaX for preprocessing to do the following: 1. To obtain relative peak area, normalise the data using Probabilistic Quotient Normalization [PQN (Di

Guida et al., 2016)]; 2. To use QC-RLSC (quality control-based robust LOESS signal correction) to correct the batch effect; and 3. To determine the relative peak area's CV (Coefficient of Variation) in each QC sample, and remove compounds with a CV of more than 30%.

After standardisation, we screened different metabolites based on $VIP > 1$ and $p < 0.05$ with principal component analysis (PCA), partial least-squares discrimination analysis (PLS-DA), and T-test. Using the HMDB database, the names of each metabolite were standardised. Using the PeakView software, potential endogenous metabolites were identified. It was possible to predict the metabolic pathways connected to DFU by using MetaboAnalyst 5.0 (<https://www.metaboanalyst.ca/>).

2.9 The construction of network pharmacology

With cytoscape 3.8.2, the network was constructed to visualise the the relationship of metabolite-protein-pathway and to elaborate the hub metabolites and related proteins. The steps were as follows (Figure 1). 1) The targets of DFU were obtained *via* searching the keywords “diabetic foot ulcer” in the gene maps of Disgenet (<https://www.disgenet.org/>), NCBI (<https://www.ncbi.nlm.nih.gov/>), Therapeutic Target Database (TTD, <http://db.idrblab.net/ttd/>) and genecards (<https://www.gene-cards.org/>). 2) The molecular targets of DP were filtered by searching Phrammapper ([lilab-ecust.cn/Phrammapper/index.chromatographic separation.html](http://lilab-ecust.cn/Phrammapper/index.chromatographic%20separation.html)) and SwissTargetPrediction (<http://www.swisstargetprediction.ch/>) for the keywords “Dracorhodin Perchlorate”. To screen the related proteins in *Rattus norvegicus*, the structure of DP was imported into SwissTargetPrediction and Phrammapper, respectively. 3) The intersection of 1) and 2) was thought to be a potential target of DP in the treatment of DFU. With UniProtKB (<http://www.uniprot.org/>), the names of targets were standardised. 4) Targets were imported into STRING 11.0 (<https://string-db.org/>) and protein-protein interaction (PPI) network was constructed using Cytoscape 3.8.2. 5) Through the DAVID (<https://david.ncifcrf.gov/>) database, the pathway and Gene Ontology (GO) enrichments of potential targets were analysed. We set the $p < 0.05$ for the standard of the KEGG pathway. 6) To achieve the compound-reaction-enzyme-gene network, we imported the identified differential metabolites in metabolomics and the intersection targets of DP in treating DFU into MetScape of Cytoscape. Then, the crucial metabolites and proteins were recognised.

2.10 Molecular docking

PubChem (<https://www.ncbi.nlm.nih.gov/pccompound/?term>) was used to obtain the 3D structure of DP (PubChem

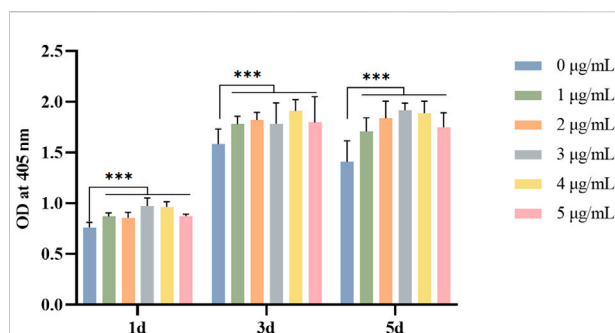


FIGURE 2
Effect of DP with different concentration on fibroblast viability in different days. * $p < 0.05$, ** $p < 0.01$ and *** $p < 0.001$.

CID: 6443665). With RCSB Protein Data Bank (<https://www.rcsb.org/>), we downloaded the structures of targets. Seven targets were investigated: Glutathione S-Transferase Mu 1 (GSTM1, PDB ID:1YJ6), Thymidylate Synthetase (TYMS, PDB ID:1RTS) (Rogerio R. Sotelo-Mundo, 1999), and Phenylalanine Hydroxylase (PAH, PDB ID: 3PAH) (Heidi Erlandsen, 1998), and Dopa Decarboxylase (DDC, PDB ID: 3RCH) (Giardina et al., 2011), Dihydrofolate Reductase (DHFR, PDB ID:4M6J) (Bhabha et al., 2013), Catalase (CAT, PDB ID:1dgb) and Phosphoglucomutase 1 (PGM1, PDB ID: 6uiq) (Stiers and Beamer, 2018). AutoDockTools 1.5.6 was used to convert DP (mol2 format) and targets (pdb format) to pdbqt format (Deng et al., 2021). Molecular docking was then conducted with Autodock Vina. Supplementary Table S2 lists coordinates of active pockets in targets. Discovery Studio 2019 was used to visualise the docking results.

2.11 Statistical analysis

Presented data as mean \pm standard deviation (mean \pm SD). With one-way ANOVA, statistical analysis was performed. GraphPad Prism (Inc, La Jolla, CA, United States) 9.1 was used for Dunnett's multiple comparisons. $p < 0.05$ was defined as the significance. T-tests were conducted on skin metabolome data.

3 Results

3.1 Results of cell proliferation experiment

The L929 cells showed a trend of increment on GelMA hydrogels loaded with Draconis perchlorate. The results of the cell proliferation experiment revealed that DP could promote the proliferation and vitality of fibroblasts and had the potential to promote DFU wound healing. We found the optimal dose of DP to be 3 μ g (as shown in Figure 2).

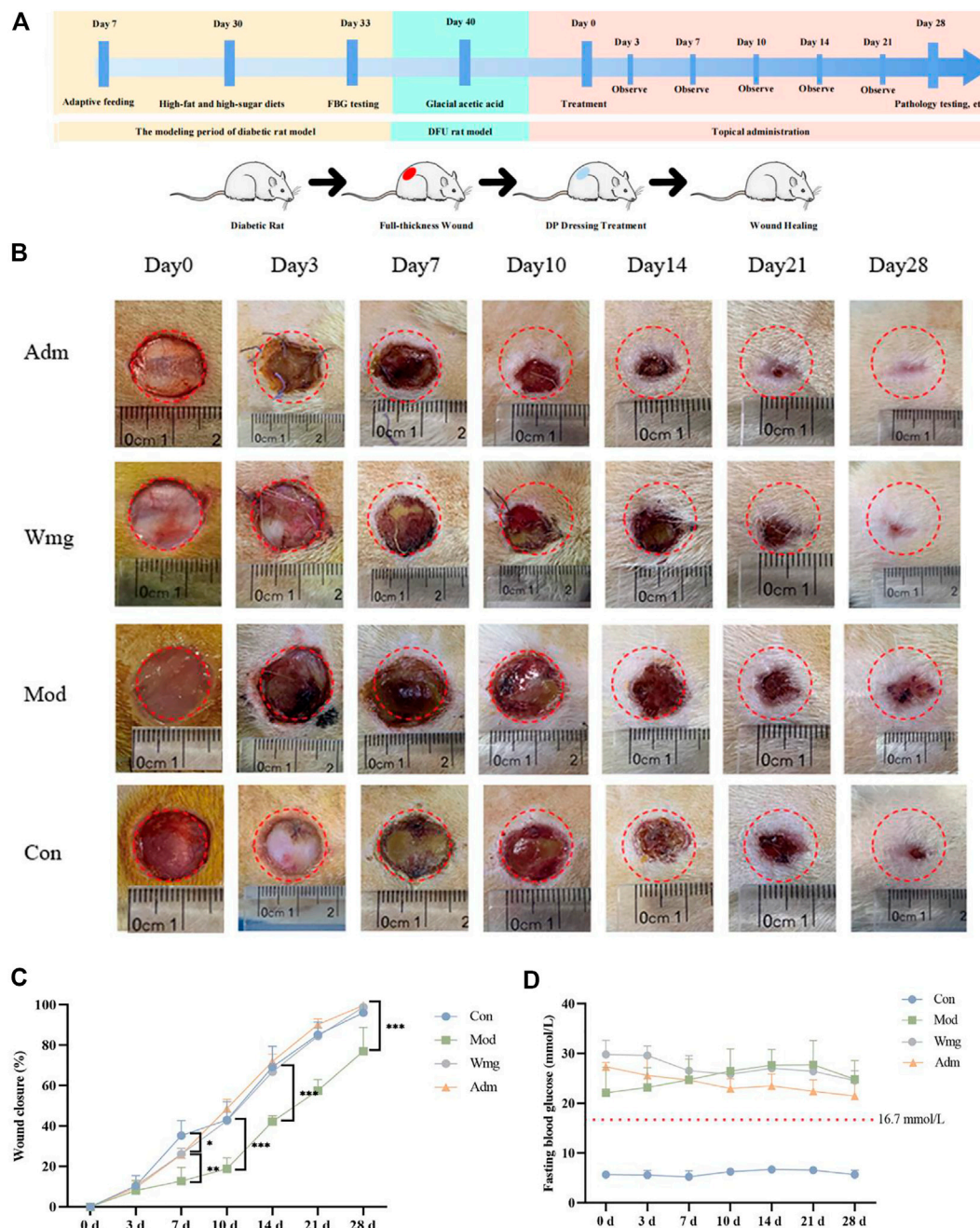


FIGURE 3

DP improves the wounds of DFU rats. (A) The time diagram of the experiment. (B) Representative figures of different time points of healing area of DFU rats. (C) Wound closure (%) of different groups at days 0, 3, 7, 14, 21 and 28. * $p < 0.05$ represent significance. (D) Images present the levels of FBG on 0th, 3th, 7th, 10th, 14th, 21st and 28th day.

3.2 Animal experiment results

3.2.1 General conditions of rats

Thirty rats on a high-fat and high-sugar diet were injected with 40 mg/kg streptozotocin (STZ) solution intraperitoneally, and the blood glucose was continuously

measured for 3 days. Finally, 18 diabetes rats with blood glucose >16.7 mmol/L were included for the modelling of the DFU model. In the Con group, six rats were made normal wound models. During the modelling period, rats that failed or died were excluded. Finally, 24 rats were included, six each in the Con, Mod, Wmg and Adm groups.

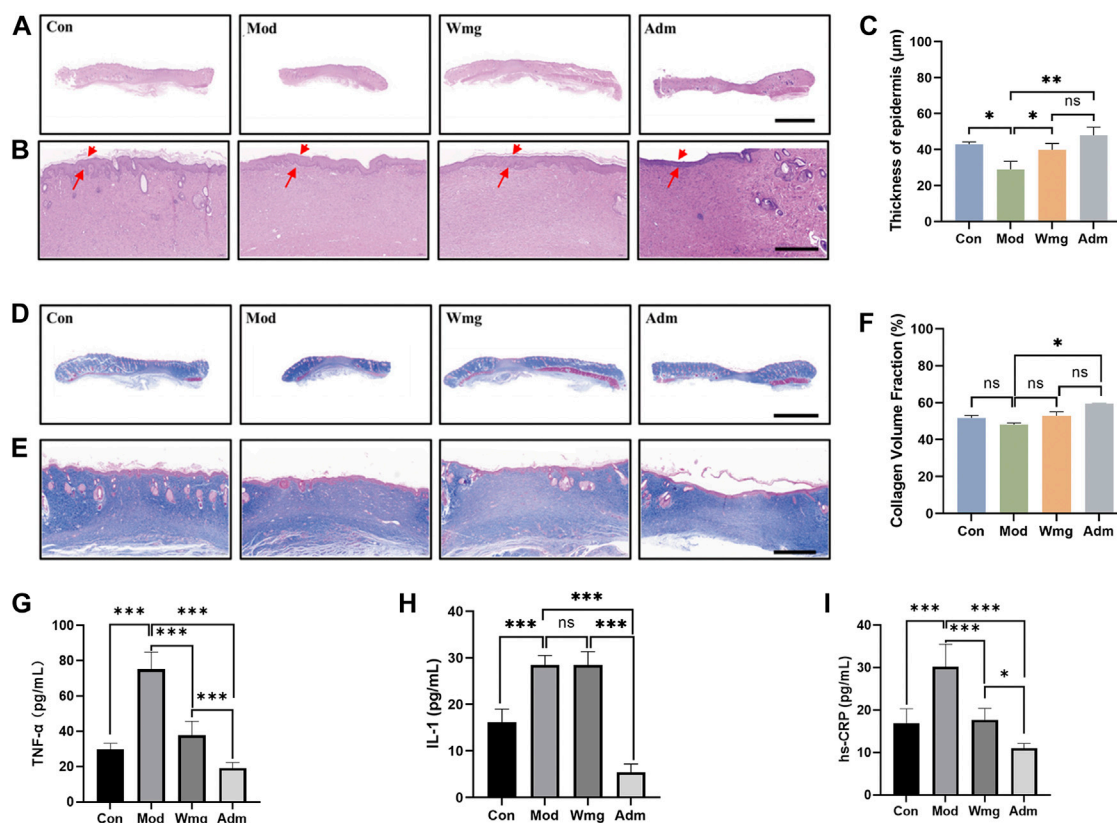


FIGURE 4

H&E staining, Masson staining and cytokine assay of different groups of wound tissues. (A–B) Representative images of wound sections with H&E staining on day 28 (scale bar = 5 mm, scale bar = 500 μm). Red arrow indicates regenerating epidermis. (C) Thickness of epidermis (* $p < 0.05$, ** $p < 0.01$ and *** $p < 0.001$). (D–E) Representative images of wound sections with Masson's trichrome staining on day 28 (Masson's trichrome: scale bar = 5 mm, scale bar = 1,000 μm). The blue colored ones are collagen fibres and collagen bundles, and the red ones are muscle fibres. (F) Fraction of collagen volume in wound tissue (* $p < 0.05$, ** $p < 0.01$ and *** $p < 0.001$). (G) The level of TNF-α of in each group. (H) The level of IL-1 of in each group. (I) The level of hs-CRP of in each group.

Compared with the Con, all diabetes rats showed poor mental state, withered and yellow hair, obvious depilation, significantly reduced activity and other symptoms. At the same time, they could drink more, eat more, urinate more and lose weight obviously. The longer the time was, the more obvious the symptoms were.

3.2.2 Topical application of DP on FBG levels in DFU rats

The level of FBG remained stable in all experimental groups throughout the treatment period, i.e., on days 0, 7, 14, 21, and 28, respectively (Figure 3D). This finding showed that the DFU rat model in this study was successful. The blood glucose concentration of the Adm group was lower than that of the Mod group, suggesting that topical application of DP had a certain hypoglycaemic effect.

3.2.3 Macroscopic effect of DP treating wound

Figure 3A depicts the timing diagram of the experiment, divided into three periods, the diabetic rat modeling phase, the DFU rat modeling phase, and the DP dressing administration phase. Figure 3B depicted the closure area of wound after the topical application of DP from days 0–28. The DP group showed more enhanced and faster wound closure than the Wmg and Mod groups. In terms of wound healing rates, on the seventh day, the wound healing rates were higher in the Adm group than those in the Mod and Wmg groups, as shown in Figure 3C. However, the wound healing rates of the Con group were great on the seventh day. Possibly, the metabolic disorder and inflammatory state in DFU rats influenced the wound closure. On the 14th day, a lower rate of wound healing was found in the Wmg group compared with the Adm group. On the 28th day, 99.6% of the Adm group's wounds were closed. The rates of wound closure

were 98.8% and 77% in the Wmg and Mod groups. Macroscopic analysis showed that the DP accelerated healing more quickly than the Wmg treatment.

Compared with the Con group, the Mod had poorer wound healing by day 28, and this finding was associated with high blood glucose and inflammation in the Mod. These inhibited the wound healing rate. When compared with the Mod group, the Adm group wound healed better. Compared with the Wmg group, the Adm group showed better results. The study's findings revealed that the wound healing rate of the Adm group was greater than that in the Wmg group and greater than that in the Mod group.

3.2.4 H&E and masson staining

Chronic wound healing is a complex process that includes wound contraction, granulation formation, re-epithelialisation and collagen deposition. As a result, histological analysis was performed to assess the quality of regenerated epidermis in the defect. The re-epithelialisation of damaged skin was estimated by H&E staining. H&E staining revealed that a new epidermis formed in the damaged area, and the dermis was repaired by large amounts of connective tissue. Compared with the Mod group, the Adm group had a complete epidermis covering the wounds and more apparent granulation tissue on the 28th day after the application of DP. The tissue was closer to the structure of normal skin (Figures 4A,B). At the same time, the quantitative statistics of the thickness of regenerated epidermis showed that the thickness of the new epidermis in the Adm group was 47.5 μm , which was obviously greater than that in other groups (Figure 4C). The Adm group would show an effectively enhanced re-epithelialisation process compared with other groups.

The abundant deposition of collagen fibres in the dermis can strengthen newly formed skin tissue and constitute a suitable microenvironment for wound closure. To assess collagen formation and deposition, Masson staining was used. In the Adm group, the dermis had large deposits of collagen fibres and good collagen bundles, whereas, in the Mod group, the wounds had only small deposits of collagen fibres and poorly developed collagen bundles (Figures 4D,E). Quantitative analysis also revealed that the proportions of collagen volume in the dermis were 51.7%, 48.1%, 52.8%, and 59.5% in Con, Mod, Wmg and Adm, respectively (Figure 4F). Therefore, the Adm group healed the fastest wounds and promoted collagen deposition, thereby accelerating wound healing.

3.2.5 Elisa analysis

This study found that the Adm group's TNF- α level was lower than that in the Mod group, and the Adm group's TNF- α content was only 0.255 times that of the Mod group and 0.5 times that of the Wmg group, which was similar to that of the Con group (Figure 4G). The IL-1 content of the Adm group was lower than that in Mod and Wmg groups in

Figure 4H. Similarly, as shown in Figure 4I, the hs-CRP content of the Adm group was lower than those in Mod and Wmg groups. DP could effectively alleviate the inflammatory response of DFU rat wounds, regulate macrophage transformation from pro-inflammatory M1 to repair M2, accelerate the transformation from inflammation to proliferation and maintain stable wound remodelling.

3.3 Metabolomics profiling

Following data preprocessing, a total of 1983 features in skin tissue were determined (Supplementary Material S1). By using Quality Control (QC) samples, the stability and repeatability of metabolomics were assessed. Supplementary Figure S2 depicts that the QC samples were within the range of $\pm 2\text{std}$, regardless of the positive and negative ion modes, suggesting that the equipment was stable and reliable, and the method was reproducible. There were large peak capacities and good peak shapes in the sample, as can be seen from the base peak chromatogram (BPC) char (Supplementary Figure S3).

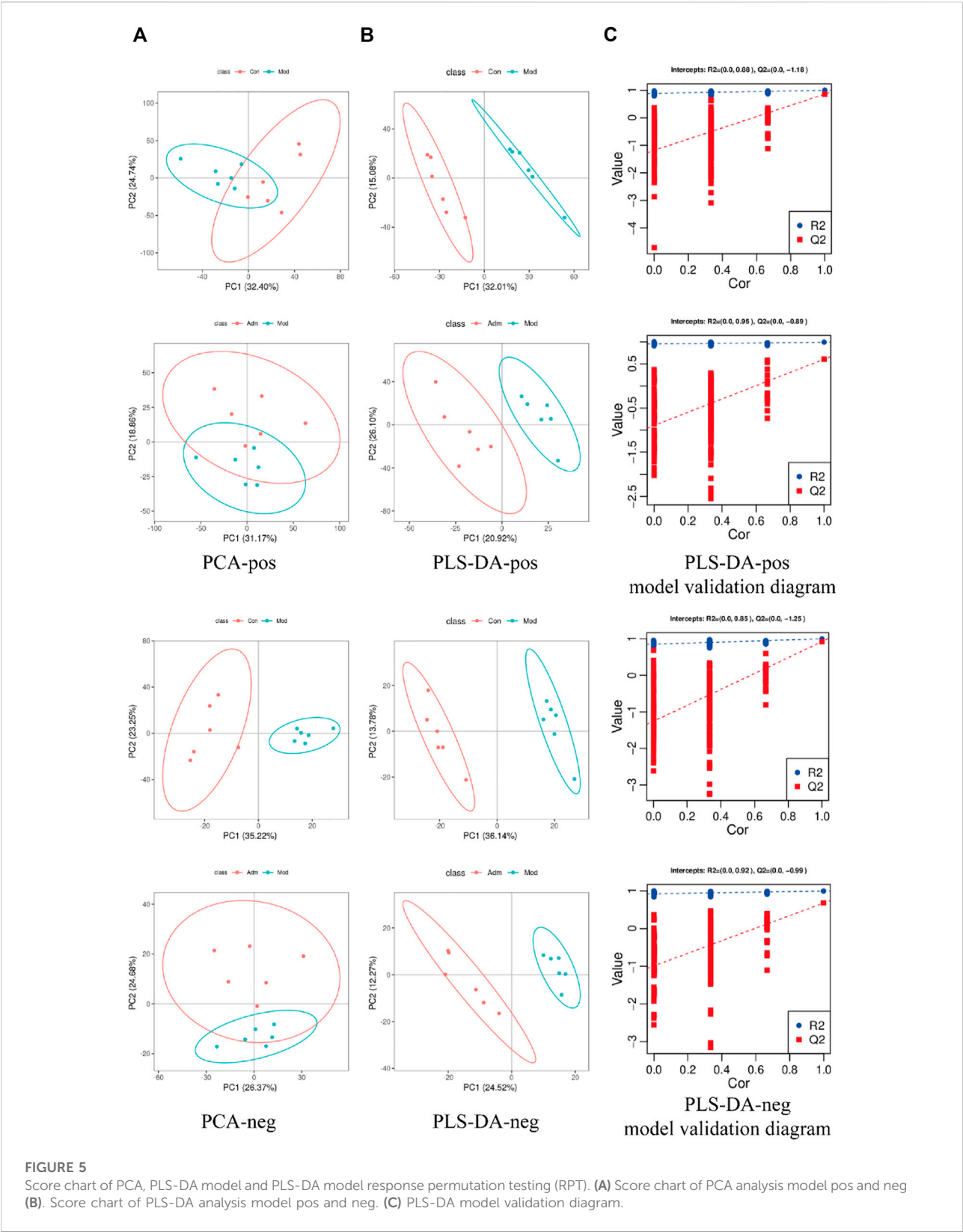
We used the PCA and PLS-DA to examine the separation among the Adm, Mod and Con groups. From the PCA of positive (pos) and negative (neg) models, the samples of different groups have been separated (Figure 5A). PLS-DA disclosed that the same group clustered together, whereas different groups distinguished well (Figure 5B). The PLS-DA parameters of skin tissue samples were $R^2 > 0$, $Q^2 < 0$ (Validation parameters) (Supplementary Table S3), which indicated that the model is not over-fitted and is relatively stable.

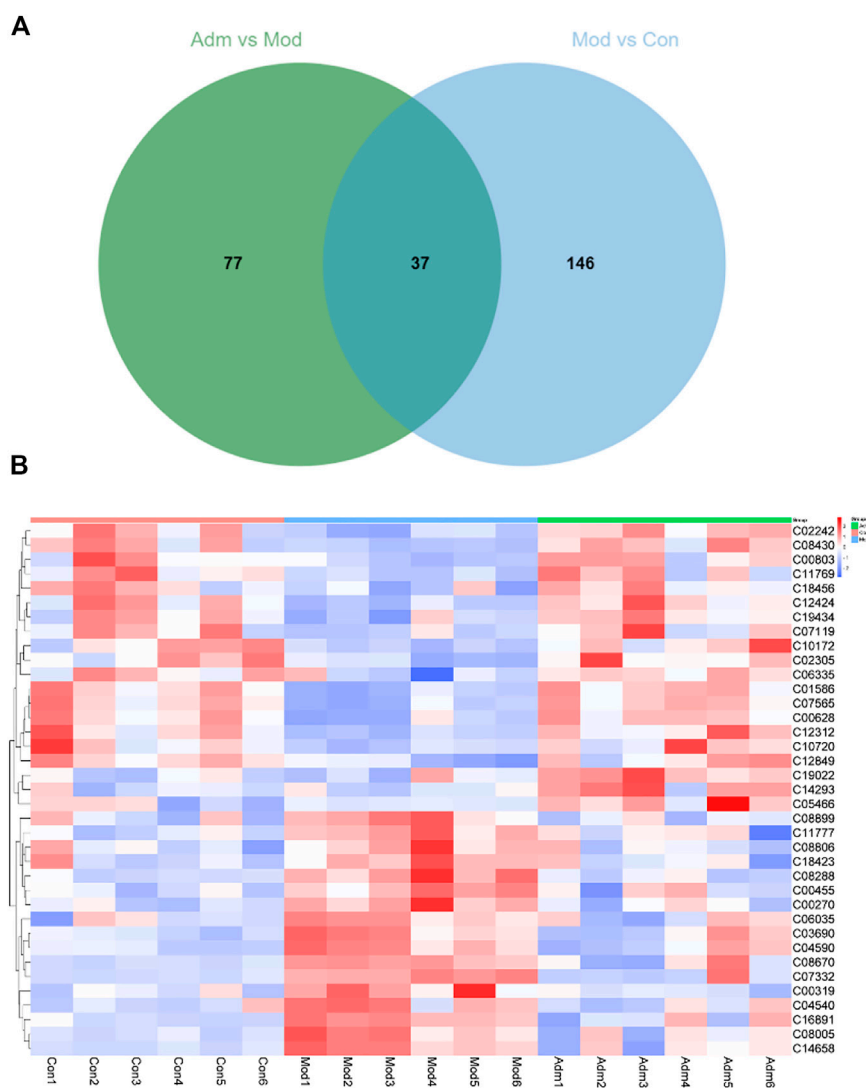
3.4 Metabolites identification and pathway analysis

PLS-DA was performed to identify the differently expressed metabolites. There was good separation in each PLS-DA model, suggesting that sample classification information had a good explanatory ability. Additionally, permutation test demonstrated that the models were trustworthy and non-overfitting (Figure 5C), which consistent with the result of Supplementary Table S3.

According to $p < 0.05$ and $\text{VIP} > 1$, 183 differentially expressed metabolites were identified between the Con and Mod groups (Supplementary Material S2). There were 114 metabolites that differed in expression between the Adm and Mod groups (Supplementary Material S3). The two groups were intersected (<http://jvenn.toulouse.inra.fr/app/example.html>), and then, 37 differential metabolites of the effect of DP on DFU are presented (Figure 6A).

We established heat maps to depict the distinctions in metabolites between the three groups. According to



**FIGURE 6**

The differential metabolites in DFU rats treated with DP. **(A)** Venn diagrams of the common metabolites related to DFU and DP treatment. **(B)** The heat map of potential metabolites.

Figure 6B, all candidate metabolites were altered in the Mod group, and the majority were reversed in the Adm group, reflecting that DP treatment could improve metabolic disorder.

We imported 114 different metabolites into MetaboAnalyst 5.0 to investigate the metabolic pathways of DP in the treatment of DFU rats. As shown in Figure 7A, six pathways were screened based on pathway impact > 0.1, including the following: Glycine, serine and threonine metabolism; Tyrosine metabolism; One carbon pool by folate; Pyrimidine metabolism; Glyoxylate and dicarboxylate metabolism; Amino sugar and nucleotide sugar metabolism. The metabolites related to these pathways were as follows: Glycine; Dopamine;

2,5-Dihydroxybenzoate; 5,10-Methenyltetrahydrofolate; Uridine; Cytidine 5'-monophosphate (CMP); Thymidine; Thymine; N-Acetylneuraminate; N-Acetyl-alpha-D-glucosamine 1-phosphate; and D-Glucosamine 6-phosphate. Tyrosine metabolism is most relevant to the effects on skin tissues. As shown in Figure 7B, three pathways had an impact of >0.1, including the following: ascorbate and aldarate metabolism; citrate cycle (TCA cycle); and alanine, aspartate and glutamate metabolism.

Furthermore, we made a correlation heatmap by “corrplot” package in R language to explore the correlation of different metabolites. As shown in Figure 8A, Pearson correlation analysis demonstrated that the C03690 and C04590,

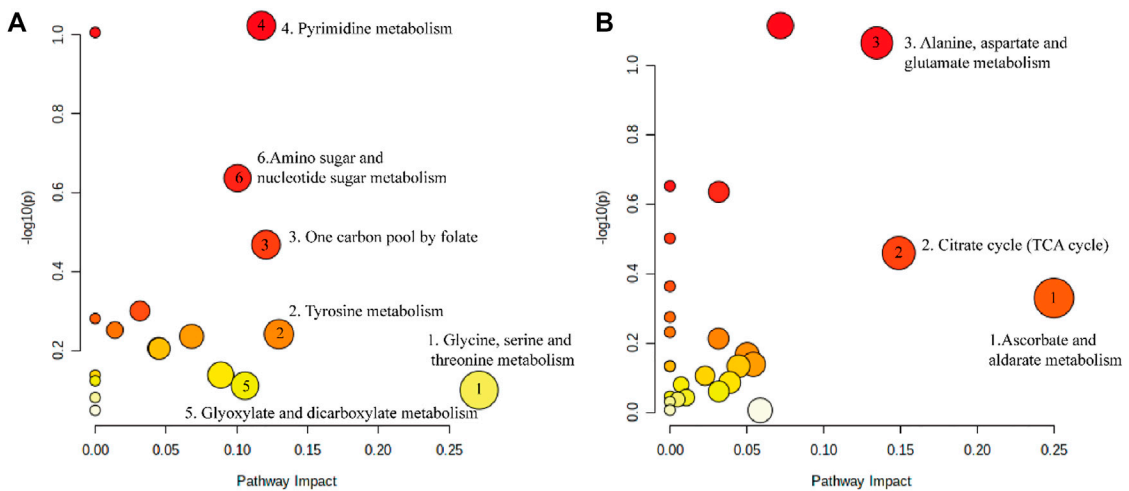


FIGURE 7
The metabolic pathways enriched by significant metabolite. (A) Metabolic pathway of DP in the treatment of DFU. (B) Metabolic pathway disorder caused by DFU.

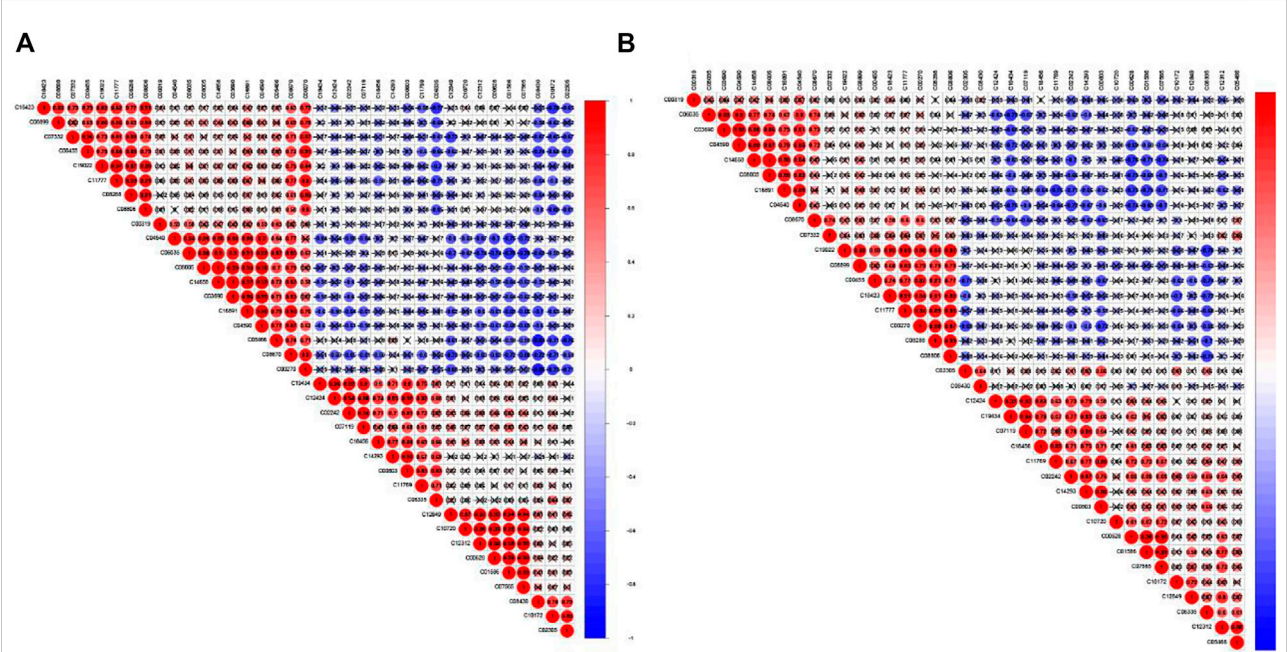


FIGURE 8
Correlation matrix of interaction in 37 differential metabolites. Coefficients of negative correlation (blue) and positive correlation (red) were plotted. The closer that the correlation coefficient was to 1, the redder the colour was, and the greater the positive correlation was. The closer that the correlation coefficient was to -1, the bluer the colour and the greater the negative correlation were. (A) The correlation heatmap of Adm and Mod groups. (B) The correlation heatmap of Mod and Con groups.

C00628 and C01586 and C07565, C01586 and C07565 were strongly correlated, and their correlation coefficients were 0.98, 0.96, 0.98, and 0.99, respectively. Figure 8B shows that the highest correlation was observed for C08005 and C1465 with a

correlation coefficient of 1. C08005 and C03690 and C16891 and C04590 were also strongly correlated, and their correlation coefficients were 0.99. The names of 37 metabolites are presented in Table 1 and Supplementary Material S4.

TABLE 1 The differential metabolites in DP-treated DFU rats.

Rank	Metabolites	Formula	Molecular weight	RT (min)	MS/MS	Keggid	Adm vs. mod		Mod vs. con	
							VIP	p-value	VIP	p-value
1	8-hydroxyquinoline	C9 H7 N O	145.053	2.358	0.0003; 1.8363	C19434	2.3506	0.0084	1.386	0.0478
2	Binapacryl	C15 H18 N2 O6	322.1165	3.374	0;-0.006	C19022	2.1745	0.0147	1.8152	0.003
3	Cyproconazole	C15 H18 Cl N3 O	291.1141	5.322	0.0002; 0.7606	C18456	1.6722	0.0261	1.5941	0.0227
4	Thiodicarb	C10 H18 N4 O4 S3	354.0498	0.62	0.0008; 2.1597	C18423	1.3454	0.024	1.0393	0.0181
5	Callystatin a	C29 H44 O4	456.3221	9.366	-0.0019; -4.1474	C16891	1.7808	0.0207	3.4022	0
6	2062850	C23 H34 O3	358.2508	7.277	0;-0.0539	C14658	2.3474	0.0208	3.1382	0
7	Furaspor	C6 H7 N O4	157.0378	4.361	0.0003; 1.9149	C14293	1.7549	0.018	1.5618	0.007
8	Aklavinone	C22 H20 O8	412.1164	2.754	0.0006; 1.5147	C12424	2.8943	0.0014	1.6729	0.0096
9	2-oxindole	C8 H7 N O	133.053	4.945	0.0002; 1.7935	C12312	2.0915	0.0027	1.5062	0.006
10	Iproniazid	C9 H13 N3 O	179.1062	3.528	0.0003; 1.9039	C11777	1.9009	0.044	1.3339	0.0018
11	R-soterenol	C12 H20 N2 O4 S	288.1144	4	0;-0.0067	C11769	1.3351	0.0316	1.733	0.0071
12	Stachydrine	C7 H13 N O2	143.0947	0.698	0.0001; 0.6792	C10172	2.0737	0.0096	1.1946	0.0082
13	Gitogenin	C27 H44 O4	432.324	9.74	0.0001; 0.1832	C08899	1.7512	0.0046	1.2122	0.035
14	(+)-cassaine	C24 H39 N O4	405.288	6.327	0.0001; 0.1614	C08670	1.4728	0.0453	3.5603	0
15	Indospicine	C7 H15 N3 O2	173.1168	2.965	0.0004; 2.1138	C08288	3.0717	0.0007	2.6712	0.0003
16	Alfentanil	C21 H32 N6 O3	416.2541	7.273	0.0005; 1.1703	C08005	2.3074	0.0204	2.7639	0.0003
17	Benzyl succinate	C18 H18 O4	298.1218	4.975	0.0013; 4.4335	C07332	3.9133	0.0107	3.6341	0
18	4-methylene-2-oxoglutarate	C6 H6 O5	158.0218	4.403	0.0003; 1.7232	C06035	1.1701	0.0467	2.0472	0.0089
19	Glycochenodeoxycholate	C26 H43 N O5	449.3143	7.697	0.0001; 0.3032	C05466	2.2593	0.0175	1.0836	0.028
20	Bis(2-ethylhexyl) phthalate	C24 H38 O4	390.2771	7.834	0.0001; 0.3222	C03690	1.5677	0.0487	3.3478	0
21	Phosphocreatine	C4 H10 N3 O5 P	211.0361	0.741	0.0003; 1.2875	C02305	2.1276	0.0059	1.1389	0.0159
22	Epiguanine	C6 H7 N5 O	165.0654	1.028	0.0003; 1.8545	C02242	2.163	0.0001	1.0414	0.0178
23	Hippurate	C9 H9 N O3	179.0586	3.845	0.0003; 1.7581	C01586	2.6146	0.0003	2.0338	0.0005
24	B-nicotinamide mononucleotide	C11 H15 N2 O8 P	334.0566	1.221	0; 0.0514	C00455	1.5921	0.0426	1.5837	0.0008
25	D-sphingosine	C18 H37 N O2	299.2824	8.271	-0.0001;-0.2512	C00319	1.4659	0.0068	1.064	0.0127
26	4-phenolsulfonic acid	C6 H6 O4 S	173.9986	2.93	0;-0.2785	C12849	1.6561	0.0196	1.8013	0.0007
27	90,049	C14 H18 O7	298.1048	4.532	-0.0004;-1.3638	C10720	1.6011	0.0198	1.1469	0.0209
28	Cucurbitacin s	C30 H42 O6	498.3005	9.827	0.0024; 4.7174	C08806	1.4406	0.0256	1.4663	0.0261
29	Convicine	C10 H15 N3 O8	305.0854	2.787	-0.0005;-1.5802	C08430	2.1701	0.0011	1.1435	0.0231

(Continued on following page)

TABLE 1 (Continued) The differential metabolites in DP-treated DFU rats.

Rank	Metabolites	Formula	Molecular weight	RT (min)	MS/MS	Keggid	Adm vs. mod		Mod vs. con	
							VIP	p-value	VIP	p-value
30	Acetanilide	C8 H9 N O	135.0684	2.955	0; 0.148	C07565	2.4849	0.0004	1.8611	0.0007
31	Medroxyprogesterone	C22 H32 O3	344.2347	8.933	-0.0004;-1.2028	C07119	1.2394	0.0448	1.3328	0.0188
32	Sulfanilic acid	C6 H7 N O3 S	173.0146	4.528	0;-0.0987	C06335	1.5748	0.0436	1.3003	0.041
33	Sn-3-o-(geranylgeranyl)glycerol 1-phosphate	C23 H41 O6 P	444.2638	7.595	-0.0002;-0.5344	C04590	1.4605	0.0266	3.3553	0
34	N4-(beta-n-acetyl-d-glucosaminy)-l-asparagine	C12 H21 N3 O8	335.1324	0.695	-0.0004;-1.2919	C04540	1.1283	0.016	1.1051	0.0034
35	Valeric acid	C5 H10 O2	102.0681	3.456	0; 0.0327	C00803	1.6896	0.0078	1.2316	0.0283
36	Gentisic acid	C7 H6 O4	154.0266	3.552	0;-0.1854	C00628	2.2384	0.0024	1.9753	0.0015
37	N-acetylneuraminate	C11 H19 N O9	309.1055	0.696	-0.0005;-1.5163	C00270	1.0222	0.0063	1.6635	0.0001

3.5 Result of network pharmacology

For further investigating the mechanisms of DP in treating DFU, we conducted network pharmacology. First, the targets of DFU through Disgenet, NCBI, TTD and Genecards and targets of DP from PharmMapper and SwissTargetPrediction were gathered. After the intersection of DP and DFU-related targets, we identified 108 potential targets for DP-treating DFU (Supplementary Figure S4). With the UniProt database, we normalised common targets to the official symbols.

Subsequently, DAVID was used for gene ontology and pathway analysis. The findings revealed that the biological process (BP) of DP in the treatment of DFU evolved primarily in response to drugs, cellular response to growth factor stimulus, hypoxia and positive regulation of cell proliferation. The cellular component (CC) was primarily involved in the cytoplasm, macromolecular complex, cytosol and perinuclear region of the cytoplasm. The molecular function (MF) was principally engaged in enzyme, protein and macromolecular complex binding. The KEGG enrichment analysis revealed that the HIF-1 signaling, TGF-beta signaling and metabolic pathways were the pathways most significantly impacted (Figure 9).

We constituted a PPI network through Cytoscape to pinpoint key genes of DP in the treatment of DFU. An overview of the relationships between 108 targets was presented in Supplementary Figure S5. The top seven genes were chosen as hub genes (TGFBR1, FN1FNG, Src, FN1, Hsp90aa1, Cat and Notch1).

3.6 Integration of network pharmacology and metabolomics

We built a network based on the integration of network pharmacology and metabolomics to gain a deeper understanding

of the mechanisms of DP in treating DFU (Figure 10). By importing 114 different metabolites and 108 targets into Cytoscape's MetScape plug-in, networks of compound-reaction-enzyme-gene were built. Seven critical targets, namely, GSTM1, TYMS, PAH, DDC, DHFR, PGM1 and ABAT, were found by matching the genes in MetScape analysis with the potential targets found in the network pharmacology (Table 2). The key metabolites were Glycine; Thymine; Thymidine; Cytidine 5'-monophosphate (CMP); Uridine; 4-(2-Aminoethyl)-2-benzenediol; D-Glucosamine 6-phosphate; N-Acetyneuraminate; and Imidazole-4-acetate. These were nine significant metabolites. The affected pathways were as follows: Leukotriene and Pyrimidine metabolism; Vitamin B9 (folate) metabolism; Urea cycle and metabolism of arginine, proline, glutamate and asparagine; Tyrosine metabolism, Amino sugar metabolism; and Histidine metabolism. They might be key players in how DP treated DFU therapeutically. Combined with network pharmacology and metabolomics, PAH, DHFR, GSTM1 and CAT were found to be the key genes.

3.7 Molecular docking analysis

Molecular docking was used to explore interaction between key targets and DP. With molecular docking, the binding energies of DP with PAH, DHFR, TYMS, DDC, GSTM1, CAT and PGM1 were -8.7 (RMSD:1.105), -7.9 (RMSD: 1.952), -7.3 (RMSD: 1.345), -5.3 (RMSD: 0.886), -5.2 (RMSD: 1.753), -9.6 (RMSD:1.710) and -6.5 (RMSD: 1.311) kcal/mol, respectively. The docking results revealed that DP had a high affinity for the key targets, particularly PAH, DHFR, GSTM1 and CAT. Van der Waals and Pi-Alkyl were the primary forces between the ligand and the receptors (Figure 11).

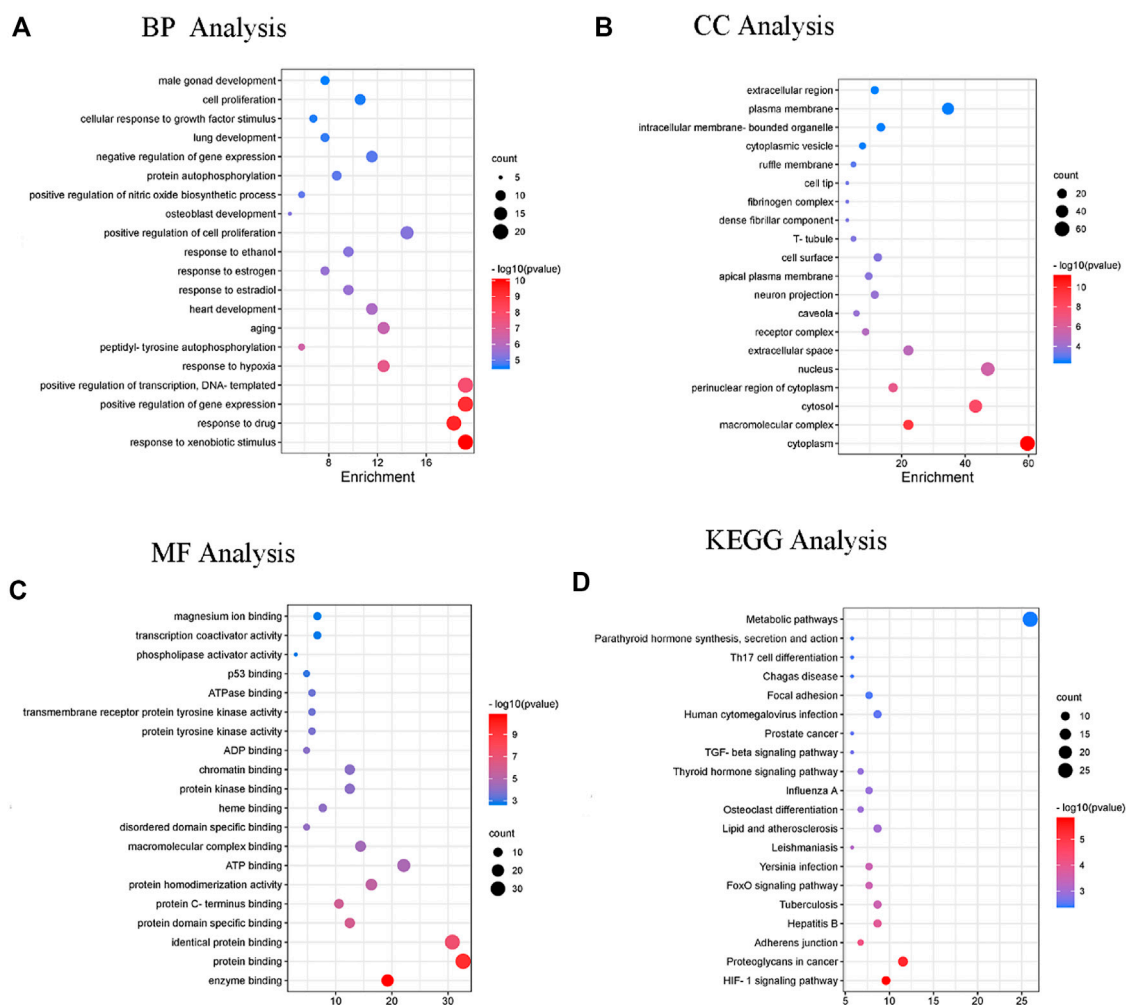


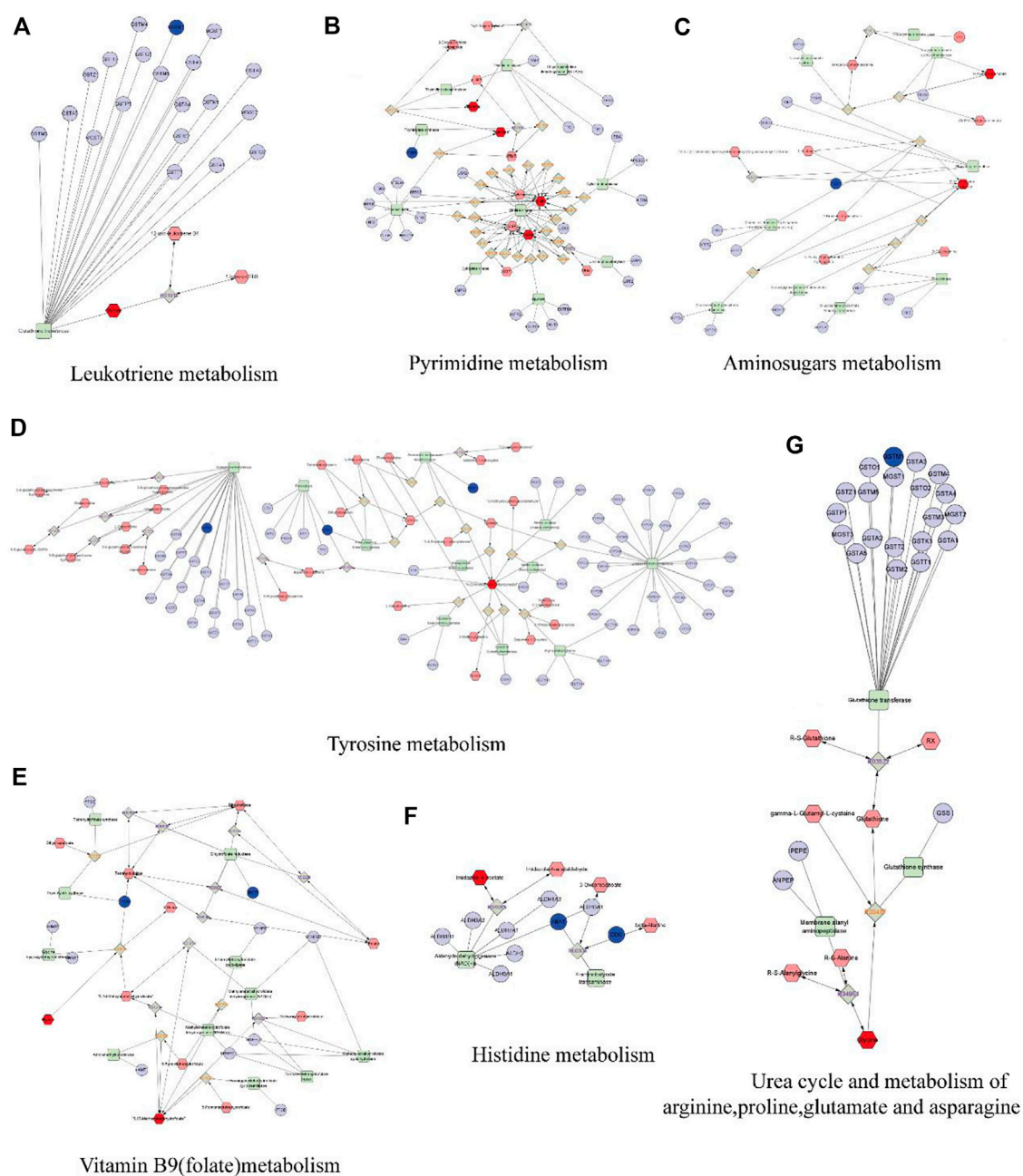
FIGURE 9

The enrichment analysis of GO and KEGG pathway of DP for the treatment of DFU. Enriched GO terms are for (A) BP analysis (B) CC analysis (C) MF analysis; and (D) KEGG pathway analysis.

4 Discussion

The wound healing of DFU is challenging. The healing process of a DFU is divided into three main periods, namely, the inflammatory, granulation tissue formation and remodelling stages. Traditional Chinese medicine, Dragon's blood, can hasten the healing of wounds of DFU rats. It produces anti-inflammatory and antioxidant benefits for the wound (C. Desmarchelier, 1997; Lopes et al., 2004; Gupta et al., 2008). Moreover, it might accelerate epithelial cell differentiation and fibroblast proliferation (A. J. Vaisberg, 1989; Porras-Reyes et al., 1993). In the present research, whether DP, a key component of Dragon's blood, improves wound healing was explored. Our findings showed that the DP could hasten the wound closure of DFU rats, especially during the inflammatory and granulation tissue formation stages. It inhibits the inflammatory response in

the DFU during the inflammatory stage and stimulates collagen deposition to promote wound healing in the granulation tissue formation stage. Furthermore, this is the first-time study to investigate the mechanisms of DP promoting wound healing in DFU rats through the integration of metabolomics and network pharmacology. DP dressing (multi-layered hydrogel/nanofiber dressing loaded with DP) is a novel dressing for the treatment of chronic skin ulcers. The multilayer grade hydrogel/nanofiber dressing is a cured laminate of electrostatic spinning technology and methacrylate-based gelatin, which has the advantages of high porosity, mutual macropore network connectivity, large specific surface area, strong ability to absorb tissue exudate and suitable biodegradability (Hao et al., 2021). DP dressing has unique advantages in the treatment of DFU, because it eliminates the need for repeated routine dressing changes after application, reduces wound irritation and facilitates wound healing. In

**FIGURE 10**

The compound-reaction-enzyme-gene networks of the crucial targets and metabolites. The red hexagons represent the active compounds. The grey diamonds represent the reaction. The green round rectangle represent enzyme. The light purple circles present general genes, and the blue circles represent key genes. (A) Leukotriene metabolism. (B) Pyrimidine metabolism. (C) Amino sugars metabolism. (D) Tyrosine metabolism. (E) Vitamin B9 (folate) metabolism. (F) Histidine metabolism. (G) Urea cycle and metabolism of arginine, proline, glutamate and asparagine.

addition, gelatine provides the arginine-glycine-aspartate (RGD) peptide sequence; this gives the hydrogel made from this polymer good cell adhesion and higher haemostatic capacity (Hao et al., 2021). These are the innovations of our study. We found that Leukotriene metabolism and Pyrimidine metabolism, Urea cycle

and metabolism of arginine and proline were important for DP's DFU treatment. The PAH, DHFR, GSTM1 and CAT are the key genes of DP for the treatment of DFU.

The inflammatory microenvironment plays an essential role in DFU wound repair. In chronic wounds, the inflammation

TABLE 2 The information of key targets, metabolites and pathways.

Related pathway	Key target	Key metabolite
Leukotriene metabolism	GSTM1	Glycine
Pyrimidine metabolism	TYMS	Thymine, Thymidine, CMP, Uridine
Tyrosine metabolism	GSTM1, PAH, DDC	4-(2-Aminoethyl)-1,2-benzenediol
Urea cycle and metabolism of arginine, proline, glutamate and asparagine	GSTM1	Glycine
VitaminB9 (folate)metabolism	DHFR, TYMS	Glycine; 5,10-Methenyltetrahydrofolate
Amino sugars metabolism	PGM1	D-Glucosamine 6-phosphate; N-Acetyneuraminate
Histidine metabolism	ABAT; DDC	Imidazole-4-acetate

phase is significantly prolonged or even prevented from transitioning into the proliferation phase. As a result, macrophages primarily have a pro-inflammatory M1 phenotype, releasing inflammatory cytokines that cause tissue destruction and organ dysfunction. To further evaluate the internal causes of the wound healing process, the contents of TNF- α , IL-1 and hs-CRP were detected in the wound by ELISA assays. Hs-CRP, the acute phase reactant protein, is used to study the association between inflammation and various chronic diseases, such as metabolic and heart diseases (Doumatey et al., 2014). DFU is a chronic wound, and the sustained high level of hs-CRP is among the factors of wound ischemia; this is not conducive to wound healing. As a well-known pro-inflammatory cytokine, TNF- α is produced by macrophages and monocytes, which are involved in the inflammatory response and immune response. It is a type of polypeptide cytokine secreted by monocyte-macrophages with a variety of biological activities related to the acute phase response, collective immune response and inflammation (Vandekerckhove, 1991).

IL-1 is involved in various inflammatory phenomena, metabolism and cell repair. In addition, as an internal release hormone, it can stimulate the systemic inflammatory response, make the body show a stress state, regulate the cells in the immune system and is closely related to wound repair (Wang, 1997). Several studies showed the proliferation and differentiation of fibroblasts could be influenced by the discharge and secretion of inflammatory cytokines, including IL-1 and TNF- α (P. Qian, 2003). According to Figures 4G–I, the levels of TNF- α , IL-1 and hs-CRP decreased in the Adm group compared with the Wmg and Mod groups. This research demonstrates that DP could enhance wound closer by suppressing inflammation. Topical administration of DP treatment to DFU wounds sustained low inflammation levels, which could effectively stop the inflammatory stage in hyperglycaemic wound tissue from being prolonged. This is consistent with the study of Jiang et al. (2017). Some researchers discovered that Dragon's blood, as a traditional Chinese medicine, has a noticeable effect on wounds, ulcers, inflammation, diarrhoea and cancer (Z.-P. Chen, 1994; L. Pieters and Berghe, 1995).

However, the effect of DP on wound closure has received little attention.

The field of metabolomics is becoming increasingly popular among researchers as a tool for investigating illness processes and potential treatment options. We discovered nine important metabolites and associated pathways of DP in the treatment of DFU. Nevertheless, teamwork is necessary for data analysis and interpretation in the field of metabolomics because of its complexity and heterogeneity (Eicher et al., 2020). Network pharmacology optimised the screening of metabolites of DP in treating DFU and revealed its mechanisms of action. Using a methodology that considers both metabolomics and network pharmacology, we found eight key targets (GSTM1, TYMS, PAH, DDC, DHFR, PGM1, ABAT and CAT), nine key metabolites (Glycine; Thymine; Thymidine; CMP; Uridine; 4-(2-Aminoethyl)-2-benzenediol; D-Glucosamine 6-phosphate; N-Acetyneuraminate; and Imidazole-4-acetate) and seven related pathways (Leukotriene metabolism; Vitamin B9 (folate) metabolism; Pyrimidine metabolism; Amino sugars metabolism; Tyrosine metabolism; Urea cycle and metabolism of arginine, proline, glutamate and asparagine; and Histidine metabolism). This strategy provides an appropriate method for validating the results of the two approaches. Screening for metabolites and targets in other natural compounds is also feasible.

DP is a man-made synthetic analogue of dracorhodin. It is a popular choice for use as a high-performance liquid chromatography (HPLC) standard and for researching the biological functions of dracorhodin. It possesses wound healing action on rats, *in vitro* angiogenic activity on HUVEC cells and *in vivo* angiogenic activity on zebrafish embryos (Jiang et al., 2017; Krishnaraj et al., 2019). Previous studies have investigated the possible pathways that could be involved when using DP to treat DFU. According to the findings of some research, DP sped up the process of skin wound healing in DFU rats by regulating the expression of pro-inflammatory cytokines that were triggered by the TLR4 pathway (Li et al., 2016). Additionally, experts elaborated that DP accelerates wound healing by increasing late wound NO levels and eNOS protein expression. Furthermore, according to Jiang X report, DP

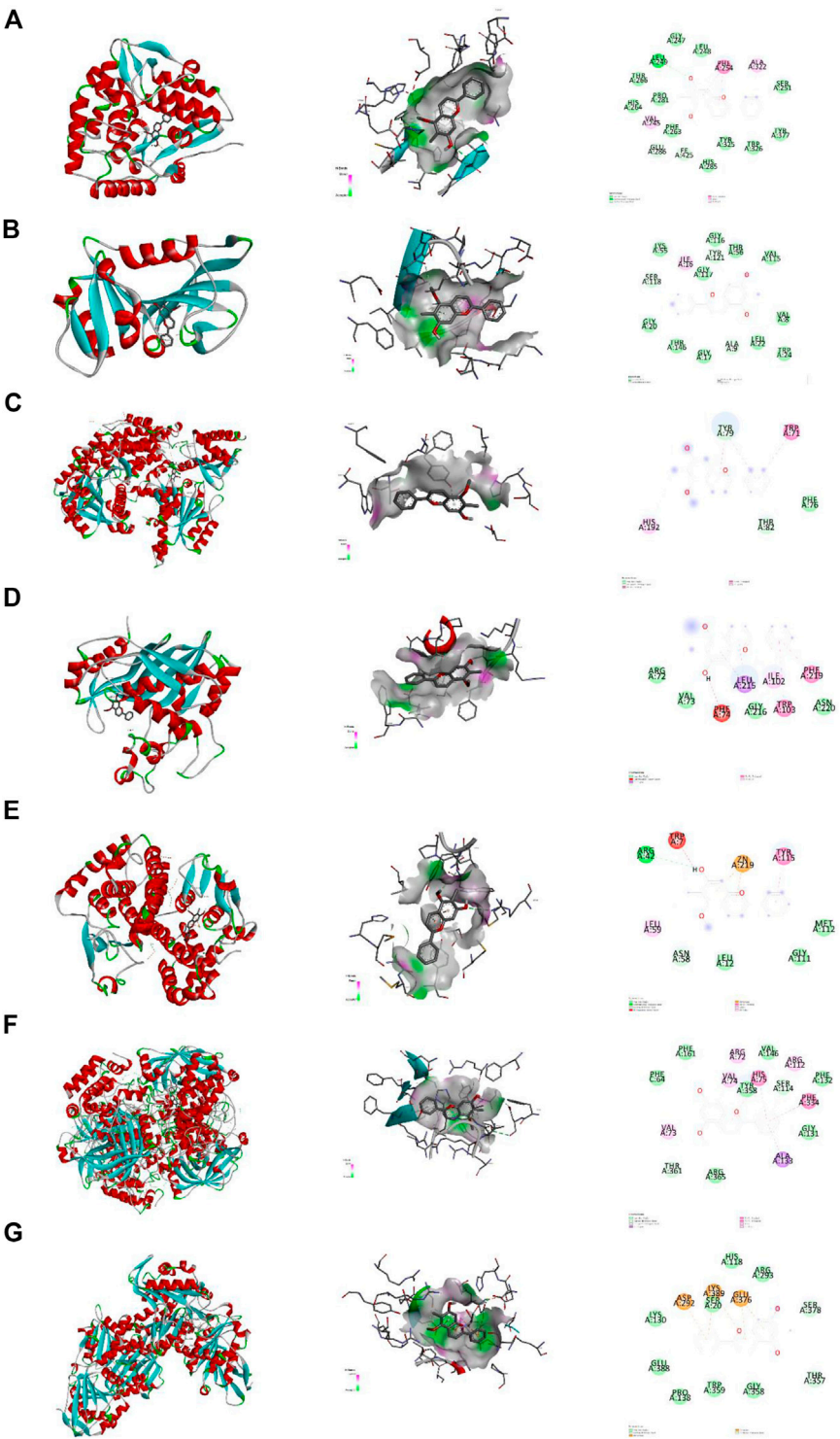


FIGURE 11
Molecular docking. Note. Binding mode of proteins and ligands. (A) Binding mode of GSTM1 with DP. (B) Binding mode of TYMS with DP. (C) Binding mode of PAH with DP. (D) Binding mode of DDC with DP. (E) Binding mode of DHFR with DP. (F) Binding mode of CAT with DP. (G) Binding mode of PGM1 with DP.

regulates fibroblast proliferation to expedite rat wound healing (Jiang et al., 2018), which is consistent with this research. Zhang et al. (2014). Found that DP significantly inhibited cell proliferation. It also caused cell cycle arrest and apoptosis in fibroblasts, at least in part by modulating caspase-3 expression and activity, indicating that DP is a feasible choice for hypertrophic scar treatment. DP has been shown by Jiang et al. (2017) to inhibit TNF- α and IL-1 β secretions, thereby reducing inflammation. It stimulates TGF and VEGF protein expression, collagen deposition and microvessel formation and then promotes wound closure. He (2011) reported that the therapeutic effect of dragon's blood on diabetes ulcers was better than that of the insulin in the insulin control group, and the down-regulation of Smad3 and Smad4 expression was the mechanism involved in the promotion of wound healing. In this study, we researched the metabolic changes in the skin tissue of DFU rats. The higher significant number of metabolites and pathways affected by DFU in the skin tissue and the more complex network of interactions are evidence of a more severe metabolic disturbance in DFU rats.

Metabolomics research is limited to metabolites and pathways; no deeper investigation in their interactions has been conducted. Network pharmacology is a method based on bioinformatics and systems pharmacology (Zhong et al., 2018), which assess drug polypharmacological effects at the molecular level to investigate the interaction between natural products and targets and confirm major mechanisms (Sheng et al., 2014). Network pharmacology can help investigate reaction networks and key targets and metabolites (Yu et al., 2012). This integrated strategy discovers the crucial targets and important mechanisms of DP treating DFU rat by integrating network pharmacology and metabolomics.

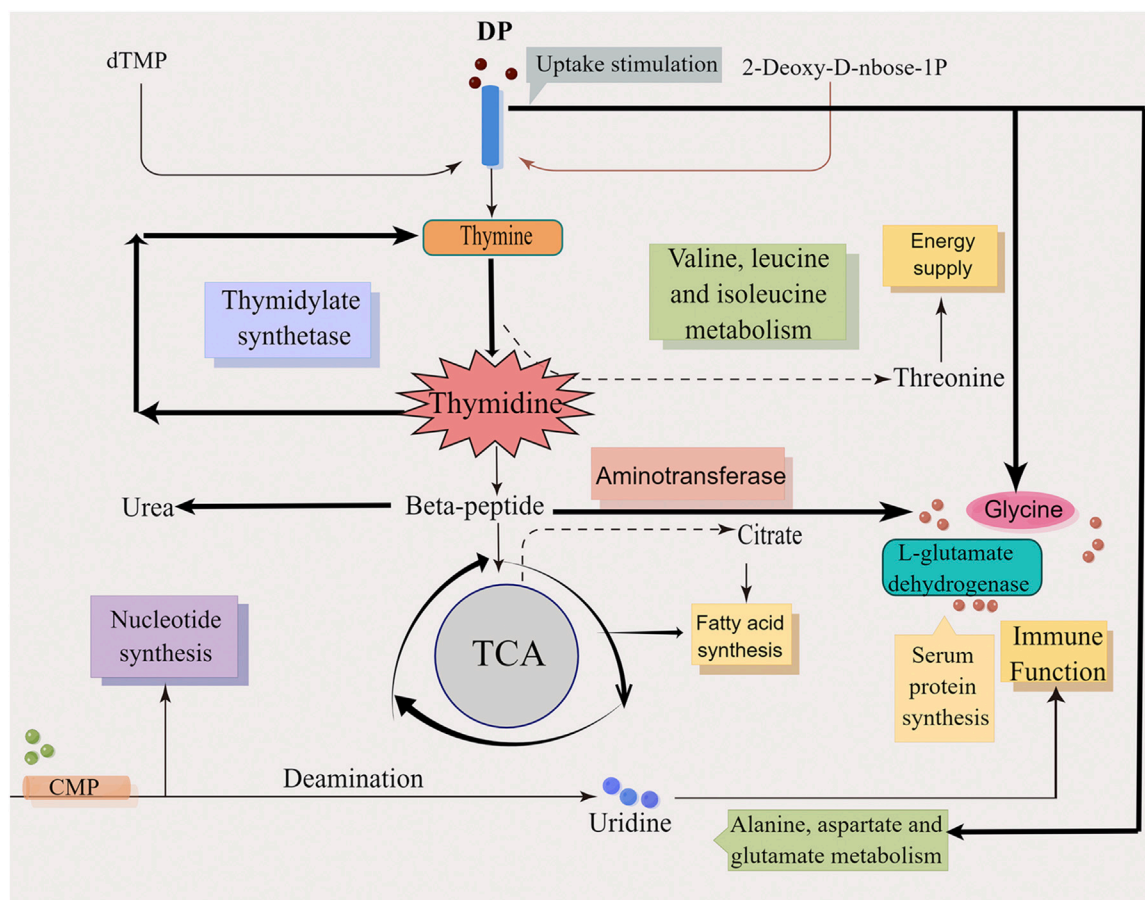
Arginine is important in cellular physiology. Like other amino acids, it plays a role in the production of proteins. The conversion of arginine to nitric oxide and other polyamines has a role in cell signalling and cell proliferation. Arginine is an essential substrate for wound healing processes due to its multiple functions. In numerous studies, supplying arginine alleviates or improves healing (Witte, 2003). A previous study suggested that arginine metabolite-nitric oxide played a key role in wound healing. As a semi-essential amino acid, arginine is metabolised by arginase and nitric oxide synthase. Wound-healing emphasises the important role of strict reciprocal control among these enzymes (Stechmiller, 2008).

Arginase signalling plays a vital role in chronic wound pathophysiology and healing. As an evolutionarily conserved enzyme, arginase (ARG) can be expressed in a variety of cells. In the last stage of the urea cycle, arginine protects excess ammonia under homeostatic conditions by producing L-ornithine and urea. L-ornithine is located at the intersection of Arg dependent pathway and urea cycle, contributing to collagen production, cell proliferation and detoxification (Szondi et al., 2021). Collagen is an important component of connective tissue;

thus, healing requires collagen formation and deposition (B. Behm, 2012). L-proline is an important collagen building block (Shih et al., 2010). Raised synthesis of proline, a component of collagen, leads to post-traumatic increases in wound tensile strength, and wound hydroxyproline levels are increased by parenteral L-arginine injection in both normal and diabetic Lewis rats (Witte, 2003; Caldwell et al., 2018). According to this study, the density of collagen content in Adm group was higher than of Wmg and Mod groups, indicating that DP promoted proline secretion during wound healing. We speculate that DP promotes the production of more arginine and proline in skin tissue to improve the wound and then promotes collagen synthesis and deposition.

Oxidative stress is a major resource of the inflammatory response, and the markers of oxidative stress, such as catalase (CAT) and plasma total antioxidants, play a significant role in non-healing of DFUs. Vairamon et al. discovered factors that influence foot ulcer healing in type 2 diabetics. This research focused on oxidative stress, which is the cause of inflammation. Researchers examined oxidative stress markers in blood samples, such as lipid peroxidation, CAT and others. Catalase levels were higher in subjects with neuroischemic noninfectious ulcers than those with neuroischemic infectious ulcers ($p < 0.001$). The total antioxidant status in plasma gradually decreased in subjects from uninfected ulcer to ischemic infection ($p < 0.0001$). We concluded that level of lipid peroxidation in plasma was high. The decrease of total antioxidant status and the deficiency of antioxidant enzymes are the main reasons for the prolonged inflammatory reaction and chronic ulcer. In type 2 diabetes patients, oxidative stress may be one of the factors leading to the nonhealing of diabetes foot ulcers (Viswanathan, 2010). Based on our study, DP treatment reduced the inflammatory response compared with the control group. This result implied that DP shields organisms from oxidative stress. According to the network pharmacology analysis, the mechanism may involve CAT, which activates metabolic pathways. The topical application of DP increased the activity of antioxidant enzymes such as CAT, which promotes wound healing. Molecular docking also showed that DP and CAT are well combined. In DFU, where tissue inflammation and oxidative stress were elevated primarily due to an increase in reactive oxygen species (ROS) (Busik et al., 2008), the topical administration of DP alleviates the ROS insults, thus protecting the wound skin tissue from oxidative injuries.

The enzyme dihydrofolate reductase (DHFR) is a validated target for several antimicrobials. Meanwhile, it is necessary for the *de novo* biosynthesis of folate species. Gustavo P. ribodi et al. investigated the structural and biochemical properties of *Mycoplasma ulcerum* DHFR, and explored its interaction with P218. This research revealed the P218 could be further developed as a therapeutic strategy for Buruli ulcer (Riboldi et al., 2021). Shailesh K et al. discovered *Klebsiella pneumoniae* containing DHFR in eight out of (18.18%) of 44 different DFU patients. Based on case



The nucleophilic assault of reduced glutathione (GSH) on electrophiles or other compounds that are attracted to electrons is facilitated by glutathione s-transferases (GSTs). GSTs occupy important positions in two ways, as follows: the binding of glutathione and endogenous products of lipid peroxidation; and protecting cells from harmful oxidative stress. GSTM1 and GSTT1, two isoforms of GST with functional polymorphisms, have been investigated in many chronic diseases. Romério Alencar de Oliveira

The liver produces phenylalanine hydroxylase (PAH), an amino acid metabolic enzyme that catalyses the reaction of phenylalanine to tyrosine, thus participating in the gluconeogenesis process. In diabetes, the activity of this enzyme is obviously increased, gluconeogenesis is accelerated, and blood sugar is increased (Liang, 1996). In this study, we discovered that compared with the Mod group, blood glucose of Adm group decreased significantly after DP treatment. Further molecular docking analysis (the binding

energy of DP and PAH is -8.7 kcal/mol) indicated that the mechanisms of DP's promotion of wound closure in DFU rats may be through the inhibition of the activity of PAH, thereby exerting a hypoglycaemic effect.

Tyrosine metabolism is also implicated in DFU. The concentration of L-tyrosine is significantly elevated in DFU patients. This is fatal in the chronic state and can lead to amputation in severe cases (Roy, 2020). The Mod group had more L-tyrosine than that of the Con group, which may have a negative impact on wound healing. Bonner-Weir S, 1983, Liang, 1996, Lin, 2018.

Collectively, the main action mechanisms for treating DFU by DP was attributed to the regulation of pyrimidine metabolism and alanine, aspartate and glutamate metabolism and other pathways and metabolites, as well as the regulation of protein synthesis, energy supply, immune function and other biological processes that promote wound healing (Figure 12).

However, this study has some limitations. We still need to verify the precise mechanisms *via* systematic molecular biology experiments. For example, this study will be more perfect if WB and Q-PCR were added to detect the expression of important targets in different groups and proteomics and transcriptomics are used to further explore the mechanism of DP treatment of DFU at different levels.

5 Conclusion

In this study, we used a combined metabolomics and network pharmacology approach for the first time to elucidate the mechanisms of DP in treating DFU rats. The topical application of DP promotes wound healing in the DFU rats *via* various mechanisms that result in the maintenance of tissue growth and proliferation at the wound site. By inhibiting inflammation response and oxidative stress, DP may suppress the prolonged inflammatory phase in DFU wounds and stimulate collagen deposition to promote wound healing. The results obtained in this study indicated the core targets and mechanisms of DP in treating DFU rats. In DFU rats, DP could regulate the metabolic response of skin tissue and accelerate wound healing. The integration revealed four core targets with associated metabolites and pathways. Molecular docking was performed to further validate the interaction between targets and DP. Our study provides theoretical and data support for a more in-depth study of the mechanisms of DP in the treatment of DFU and provides an experimental basis for the development of a new type of dressing to promote the wound healing of DFU.

Data availability statement

The datasets presented in this study can be found in online repositories. The names of the repository/repositories and

accession number(s) can be found in the article/Supplementary Material.

Ethics statement

The animal study was reviewed and approved by Beijing University of Chinese Medicine approved the protocol of the Medical Ethics Committee under approval number 4-2021120302-4121.

Author contributions

PD, HL, SW, and RH contributed equally to this work. SW, JH, XS, XP, DL, YW, and ZH: assisted to do animal experiments. RH does cell proliferation experiments and preparation of DP dressing. ZC and JX: performed the supervision. PD and SW: data analysis of metabolomics and network pharmacology. PD and HL reviewed and edited the manuscript.

Funding

This work was supported by horizontal topic name: Real-world observational study on the treatment of acute ankle sprains with Qizheng xiaotong plaster.

Conflict of interest

The authors declare that the research was conducted in the absence of any commercial or financial relationships that could be construed as a potential conflict of interest.

Publisher's note

All claims expressed in this article are solely those of the authors and do not necessarily represent those of their affiliated organizations, or those of the publisher, the editors and the reviewers. Any product that may be evaluated in this article, or claim that may be made by its manufacturer, is not guaranteed or endorsed by the publisher.

Supplementary material

The Supplementary Material for this article can be found online at: <https://www.frontiersin.org/articles/10.3389/fphar.2022.1038656/full#supplementary-material>

References

- Alven, S., Peter, S., Mbese, Z., and Aderibigbe, B. A. (2022). Polymer-based wound dressing materials loaded with bioactive agents: Potential materials for the treatment of diabetic wounds. *Polym. (Basel)* 14 (4), 724. doi:10.3390/polym14040724
- Asha, M. K., Debraj, D., Prashanth, D., Edwin, J. R., Srikanth, H. S., Muruganatham, N., et al. (2013). *In vitro* anti-Helicobacter pylori activity of a flavonoid rich extract of Glycyrrhiza glabra and its probable mechanisms of action. *J. Ethnopharmacol.* 145 (2), 581–586. doi:10.1016/j.jep.2012.11.033
- Behm, B., Landthaler, M., and Schreml, S. (2012). Cytokines, chemokines and growth factors in wound healing. *J. Eur. Acad. Dermatol. Venereol.* 26 (7), 812–820. doi:10.1111/j.1468-3083.2011.04415.x
- Bhabha, G., Ekiert, D. C., Jennewein, M., Zmasek, C. M., Tuttle, L. M., Kroon, G., et al. (2013). Divergent evolution of protein conformational dynamics in dihydrofolate reductase. *Nat. Struct. Mol. Biol.* 20 (11), 1243–1249. doi:10.1038/nsmb.2676
- Bonner-Weir S, T. D., and Trent, D. F. (1983). Partial pancreatectomy in the rat and subsequent defect in glucose-induced insulin release. *J. Clin. Invest.* 71 (71), 1544–1553. doi:10.1172/jci110910
- Bonnet Jb, S. A., and Sultan, A. (2021). Narrative review of the relationship between CKD and diabetic foot ulcer. *Kidney Int. Rep.* 7 (3), 381–388. doi:10.1016/j.ekir.2021.12.018
- Bus, S. A., Van Netten, J. J., Hinchliffe, R. J., Apelqvist, J., Lipsky, B. A., Schaper, N. C., et al. (2020). Standards for the development and methodology of the 2019 international working group on the diabetic foot guidelines. *Diabetes. Metab. Res. Rev.* 36 (1), e3267. doi:10.1002/dmrr.3267
- Busik, J. V., Mohr, S., and Grant, M. B. (2008). Hyperglycemia-induced reactive oxygen species toxicity to endothelial cells is dependent on paracrine mediators. *Diabetes* 57 (7), 1952–1965. doi:10.2337/db07-1520
- Caldwell, R. W., Rodriguez, P. C., Toque, H. A., Narayanan, S. P., and Caldwell, R. B. (2018). Arginase: A multifaceted enzyme important in health and disease. *Physiol. Rev.* 98 (2), 641–665. doi:10.1152/physrev.00037.2016
- Canuto, G., Costa, J. L., Cruz, P., Souza, A., Faccio, A., Klassen, A., et al. (2017). Metabolômica: Definições, estado-da-arte E Aplicações representativas. *Quim. Nova.* doi:10.21577/0100-4042.20170134
- Chen, L. Y., Cheng, H. L., Kuan, Y. H., Liang, T. J., Chao, Y. Y., and Lin, H. C. (2021). Therapeutic potential of luteolin on impaired wound healing in streptozotocin-induced rats. *Biomedicines* 9 (7), 761. doi:10.3390/biomedicines9070761
- Chen, Z. P., and Phillipson, J. D. (1994). Studies on the anti-tumour, anti-bacterial, and wound-healing properties of Dragon's blood. *Planta Med.* 60 (6), 541–545. doi:10.1055/s-2006-959567
- de Oliveira Filho, R. A., Silva, G. J., de Farias Domingos, I., Hatzlhofer, B. L., da Silva Araujo, A., de Lima Filho, J. L., et al. (2013). Association between the genetic polymorphisms of glutathione S-transferase (GSTM1 and GSTT1) and the clinical manifestations in sickle cell anemia. *Blood Cells Mol. Dis.* 51 (2), 76–79. doi:10.1016/j.bcmd.2013.03.003
- Deng, P., Liang, H., Xie, K., Han, J., Huang, F., Liu, H., et al. (2021). Study on the molecular mechanism of Guizhi Jia Shao Yao decoction for the treatment of knee osteoarthritis by utilizing network pharmacology and molecular docking technology. *Allergol. Immunopathol.* 49 (6), 16–30. doi:10.15586/aei.v49i6.484
- Deng, P., Shi, H., Pan, X., Liang, H., Wang, S., Wu, J., et al. (2022). Worldwide research trends on diabetic foot ulcers (2004–2020): Suggestions for researchers. *J. Diabetes Res.* 2022, 7991031. doi:10.1155/2022/7991031
- Desmarchelier, C. F., Coussio, J., and Cicca, G. (1997). Effects of Sangre de Drago from Croton lechleri Muell.-Arg. on the production of active oxygen radicals. *J. Ethnopharmacol.* 58, 103–108. doi:10.1016/s0378-8741(97)00087-1
- Di Guida, R., Engel, J., Allwood, J. W., Weber, R. J., Jones, M. R., Sommer, U., et al. (2016). Non-targeted UHPLC-MS metabolomic data processing methods: A comparative investigation of normalisation, missing value imputation, transformation and scaling. *Metabolomics* 12, 93. doi:10.1007/s11306-016-1030-9
- Doumatey, A. P., Zhou, J., Adeyemo, A., and Rotimi, C. (2014). High sensitivity C-reactive protein (Hs-CRP) remains highly stable in long-term archived human serum. *Clin. Biochem.* 47 (4–5), 315–318. doi:10.1016/j.clinbiochem.2013.12.014
- Dunn, W. B., Broadhurst, D., Begley, P., Zelena, E., Francis-McIntyre, S., Anderson, N., et al. (2011). Procedures for large-scale metabolic profiling of serum and plasma using gas chromatography and liquid chromatography coupled to mass spectrometry. *Nat. Protoc.* 6 (7), 1060–1083. doi:10.1038/nprot.2011.335
- Eicher, T., Kinnebrew, G., Patt, A., Spencer, K., Ying, K., Ma, Q., et al. (2020). Metabolomics and multi-omics integration: A survey of computational methods and resources. *Metabolites* 10 (5), E202. doi:10.3390/metabo10050202
- Fu C, W. Q., Zhang, Z., Xia, Z., Ji, H., Lu, H., et al. (2019). UPLC-ESI-IT-TOF-MS metabolomic study of the therapeutic effect of Xuefu Zhuyu decoction on rats with traumatic brain injury. *J. Ethnopharmacol.* 245 (0), 112149. doi:10.1016/j.jep.2019.112149
- Giardina, G., Montioli, R., Gianni, S., Cellini, B., Paiardini, A., Voltattorni, C. B., et al. (2011). Open conformation of human DOPA decarboxylase reveals the mechanism of PLP addition to Group II decarboxylases. *Proc. Natl. Acad. Sci. U. S. A.* 108 (51), 20514–20519. doi:10.1073/pnas.1111456108
- Gupta, D., Bleakley, B., and Gupta, R. K. (2008). Dragon's blood: Botany, chemistry and therapeutic uses. *J. Ethnopharmacol.* 115 (3), 361–380. doi:10.1016/j.jep.2007.10.018
- Hao, R., Cui, Z., Zhang, X., Tian, M., Zhang, L., Rao, F., et al. (2021). Rational design and preparation of functional hydrogels for skin wound healing. *Front. Chem.* 9, 839055. doi:10.3389/fchem.2021.839055
- He, X. (2011). Experimental study on Dragon's blood dragon promoting the healing of diabetes skin ulcer. *New Chin. Med.* 43 (8), 144. doi:10.13457/j.cnki.jncm.2011.08.072
- Heidi Erlandsen, T. F., Raymond, C., Stevens, R. C., and Hough, E. (1998). Crystallographic analysis of the human phenylalanine hydroxylase catalytic domain with bound catechol inhibitors at 2.0 Å resolution. *Biochemistry* 37 (0), 15638–15646. doi:10.1021/bi9815290
- Jia, H., Yang, B., Li, Y., Liang, C., Lu, H., Lin, D., et al. (2018). Chinese medicine ulcer oil promotes the healing of diabetic foot ulcers. *J. Int. Med. Res.* 46 (7), 2679–2686. doi:10.1177/0300060518769529
- Jiang, X., Liu, L., Qiao, L., Zhang, B., Wang, X., Han, Y., et al. (2018). Dracorhodin perchlorate regulates fibroblast proliferation to promote rat's wound healing. *J. Pharmacol. Sci.* 136 (2), 66–72. doi:10.1016/j.jpps.2017.12.003
- Jiang, X. W., Qiao, L., Liu, L., Zhang, B. Q., Wang, X. W., Han, Y. W., et al. (2017). Dracorhodin perchlorate accelerates cutaneous wound healing in wistar rats. *Evid. Based. Complement. Altern. Med.* 2017, 8950516. doi:10.1155/2017/8950516
- Krishnaraj, P., Chang, Y., Ho, T. J., Lu, N. C., Lin, M. D., and Chen, H. P. (2019). *In vivo* pro-angiogenic effects of dracorhodin perchlorate in zebrafish embryos: A novel bioactivity evaluation platform for commercial dragon blood samples. *J. Food Drug Anal.* 27 (1), 259–265. doi:10.1016/j.jfda.2018.08.005
- Li, F., Jiang, T., Liu, W., Hu, Q., and Yin, H. (2016). The angiogenic effect of dracorhodin perchlorate on human umbilical vein endothelial cells and its potential mechanism of action. *Mol. Med. Rep.* 14 (2), 1667–1672. doi:10.3892/mmr.2016.5442
- Li, T., Zhang, W., Hu, E., Sun, Z., Li, P., Yu, Z., et al. (2021). Integrated metabolomics and network pharmacology to reveal the mechanisms of hydroxysafflower yellow A against acute traumatic brain injury. *Comput. Struct. Biotechnol. J.* 19, 1002–1013. doi:10.1016/j.csbj.2021.01.033
- Liang, Y. W. (1996). Determination and preliminary evaluation of phenylalanine hydroxylase. *J. South China Univ. Technol. Nat. Sci.* 24 (0), 117–119. doi:10.1038/gim.2013.157
- Lin, L. Regulation of dracorhodin perchlorate on fibroblast proliferation and its mechanism[D]. Beijing: Beijing University of traditional Chinese Medicine.2018,, 1–51. doi: doi:10.1016/j.jvs.2013.08.003
- Lopes, M. I., Saffi, J., Echeverrigaray, S., Henriques, J. A., and Salvador, M. (2004). Mutagenic and antioxidant activities of Croton lechleri sap in biological systems. *J. Ethnopharmacol.* 95 (2–3), 437–445. doi:10.1016/j.jep.2004.08.025
- Lwin, O. M., Giribabu, N., Kilari, E. K., and Salleh, N. (2021). Topical administration of mangiferin promotes healing of the wound of streptozotocin-nicotinamide-induced type-2 diabetic male rats. *J. Dermatol. Treat.* 32 (8), 1039–1048. doi:10.1080/09546634.2020.1721419
- Pieters, L., Poel, B. V., Vingerhoets, R., Totte, J., Berghe, D. V., et al. (1995). *In vivo* wound healing activity of Dragon's Blood (Croton spp.), a traditional South American drug, and its constituents. *Phytomedicine* 2(1), 17–22. doi:10.1016/S0944-7113(11)80043-7
- Porras-Reyes, B. H., Lewis, W. H., Roman, J., Simchowicz, L., and Mustoe, T. A. (1993). Enhancement of wound healing by the alkaloid taspine defining mechanism of action. *Proc. Soc. Exp. Biol. Med.* 203 (1), 18–25. doi:10.3181/00379727-203-43567
- Qian, P., and Xiao, Z. (2003). The function of platelet endothelial cell adhesion and proinflammatory mechanism of TNF- α And IL-1. *Mod. Rehabil.* 12 (04), 521–524.
- Rayman, G., Vas, P., Dhataria, K., Driver, V., Hartemann, A., Londahl, M., et al. (2020). Guidelines on use of interventions to enhance healing of chronic foot ulcers in diabetes (IWGDF 2019 update). *Diabetes. Metab. Res. Rev.* 36 (1), e3283. doi:10.1002/dmrr.3283

- Riboldi, G. P., Zigweid, R., Myler, P. J., Mayclin, S. J., Counago, R. M., and Staker, B. L. (2021). Identification of P218 as a potent inhibitor of *Mycobacterium ulcerans* DHFR. *RSC Med. Chem.* 12 (1), 103–109. doi:10.1039/d0md00303d
- Rogério, R., Sotelo-Mundo, J. C., Dzik, Jolanta M., Rode, W., Maley, F., Maley, G. F., et al. (1999). Crystal structures of rat thymidylate synthase inhibited by tomudex, a potent anticancer drug. *Biochemistry* 38 (0), 1087–1094. doi:10.1021/bi981881d
- Roy, S. N., Nagabooshanam, S., Krishna, K., Wadhwa, S., Chauhan, N., Jain, U., et al. (2020). Electroanalytical sensor for diabetic foot ulcer monitoring with integrated electronics for connected health application. *ELECTROANALYSIS* 32 (9), 2082–2089. doi:10.1002/elan.201900665
- Shahi, S. K., Singh, V. K., Kumar, A., Gupta, S. K., and Singh, S. K. (2013). Interaction of dihydrofolate reductase and aminoglycoside adenylyltransferase enzyme from *Klebsiella pneumoniae* multidrug resistant strain DF12SA with clindamycin: A molecular modelling and docking study. *J. Mol. Model.* 19 (3), 973–983. doi:10.1007/s00894-012-1635-5
- Sheng, S., Wang, J., Wang, L., Liu, H., Li, P., Liu, M., et al. (2014). Network pharmacology analyses of the antithrombotic pharmacological mechanism of Fufang Xueshuanong Capsule with experimental support using disseminated intravascular coagulation rats. *J. Ethnopharmacol.* 154 (3), 735–744. doi:10.1016/j.jep.2014.04.048
- Shih, B., Garside, E., McGrouther, D. A., and Bayat, A. (2010). Molecular dissection of abnormal wound healing processes resulting in keloid disease. *Wound Repair Regen.* 18 (2), 139–153. doi:10.1111/j.1524-475X.2009.00553.x
- Stechmiller, B. C. J. K., Stechmiller, J. K., and Schultz, G. S. (2008). Arginine metabolites in wound fluids from pressure ulcers: A pilot study. *Biol. Res. Nurs.* 10 (12), 87–92. doi:10.1177/1099800408322215
- Stiers, K. M., and Beamer, L. J. (2018). A hotspot for disease-associated variants of human PGM1 is associated with impaired ligand binding and loop dynamics. *Structure* 26 (10), 1337–1345. e1333. doi:10.1016/j.str.2018.07.005
- Sun, X., Wang, X., Zhao, Z., Chen, J., Li, C., and Zhao, G. (2021). Paeoniflorin inhibited nod-like receptor protein-3 inflammasome and NF- κ B-mediated inflammatory reactions in diabetic foot ulcer by inhibiting the chemokine receptor CXCR2. *Drug Dev. Res.* 82 (3), 404–411. doi:10.1002/ddr.21763
- Szondi, D. C., Wong, J. K., Vardy, L. A., and Cruickshank, S. M. (2021). Arginase signalling as a key player in chronic wound pathophysiology and healing. *Front. Mol. Biosci.* 8, 773866. doi:10.3389/fmolb.2021.773866
- Vaisberg, A. J., Planas, M. C., Cordova, J. L., de Agusti, E. R., Ferrer, R., et al. (1989). Taspine is the cicatriz ant principle in sangre de Grado extracted from *croton lechleri*. *Planta Med.* 55 (2), 140–143. doi:10.1055/s-2006-961907
- Vandekerckhove, A. B., and Billi, A. (1991). Cytokines and their interactions with other inflammatory mediators in the pathogenesis of sepsis and septic shock. *Eur. J. Clin. Invest.* 21 (6), 559–573. doi:10.1111/j.1365-2362.1991.tb01410.x
- Viswanathan, V. (2010). Epidemiology of diabetic foot and management of foot problems in India. *Int. J. Low. Extrem. Wounds* 9 (3), 122–126. doi:10.1177/1534734610380026
- Wang, X. F. D. (1997). Beijing, 151–153. doi:10.1111/jfbc.14072 Basis of wound repair *People's Mil. Med. Publ. House* 0
- Witte, M. B., and Barbul, A. (2003). Arginine physiology and its implication for wound healing. *Wound Repair Regen.* 11 (0), 419–423. doi:10.1046/j.1524-475x.2003.11605.x
- Yanliang Yan, Z. H. (2002). A brief analysis of the external use of ancient remedies named after the efficacy of muscle growth in ancient texts. *J. Guangzhou Univ. Chin. Med.* 19 (3), 234–235.
- Yu, H., Chen, J., Xu, X., Li, Y., Zhao, H., Fang, Y., et al. (2012). A systematic prediction of multiple drug-target interactions from chemical, genomic, and pharmacological data. *PLoS One* 7 (5), e37608. doi:10.1371/journal.pone.0037608
- Zhang, P., Li, J., Tang, X., Zhang, J., Liang, J., and Zeng, G. (2014). Dracorhodin perchlorate induces apoptosis in primary fibroblasts from human skin hypertrophic scars via participation of caspase-3. *Eur. J. Pharmacol.* 728, 82–92. doi:10.1016/j.ejphar.2014.01.068
- Zhong, Y., Luo, J., Tang, T., Li, P., Liu, T., Cui, H., et al. (2018). Exploring pharmacological mechanisms of xuefu zhuyu decoction in the treatment of traumatic brain injury via a network pharmacology approach. *Evid. Based. Complement. Altern. Med.* 2018, 8916938. doi:10.1155/2018/8916938



OPEN ACCESS

EDITED BY

Rong Wang,
People's Liberation Army Joint Logistics
Support Force 940th Hospital, China

REVIEWED BY

Muhammad Usman,
University of Veterinary and Animal
Sciences, Pakistan
Jiangeng Huang,
Huazhong University of Science and
Technology, China

*CORRESPONDENCE

Li-Li Zhang,
zhangll325@163.com

SPECIALTY SECTION

This article was submitted to Drug
Metabolism and Transport,
a section of the journal
Frontiers in Pharmacology

RECEIVED 16 September 2022

ACCEPTED 07 November 2022

PUBLISHED 23 November 2022

CITATION

Fu W-Q, Tian T-T, Zhang M-X, Song H-T
and Zhang L-L (2022), Population
pharmacokinetics and dosing
optimization of unbound teicoplanin in
Chinese adult patients.
Front. Pharmacol. 13:1045895.
doi: 10.3389/fphar.2022.1045895

COPYRIGHT

© 2022 Fu, Tian, Zhang, Song and
Zhang. This is an open-access article
distributed under the terms of the
[Creative Commons Attribution License](#)
(CC BY). The use, distribution or
reproduction in other forums is
permitted, provided the original
author(s) and the copyright owner(s) are
credited and that the original
publication in this journal is cited, in
accordance with accepted academic
practice. No use, distribution or
reproduction is permitted which does
not comply with these terms.

Population pharmacokinetics and dosing optimization of unbound teicoplanin in Chinese adult patients

Wen-Qian Fu¹, Ting-Ting Tian¹, Min-Xin Zhang¹,
Hong-Tao Song¹ and Li-Li Zhang^{1,2*}

¹Department of Pharmacy, 900th Hospital of Joint Logistics Support Force, Fuzhou, China,

²Department of Purchasing Management, 900th Hospital of Joint Logistics Support Force, Fuzhou, China

Objectives: To develop a population pharmacokinetic (PopPK) model describing unbound teicoplanin concentrations in Chinese adult patients and perform Monte Carlo simulations to optimize the dosing regimens.

Methods: The raw data for PopPK analysis in this study were collected from Chinese adult patients. A PopPK model of unbound teicoplanin was developed and Monte Carlo simulations were used to optimize the dosing regimens. The trough concentrations of unbound teicoplanin were targeted at 0.75 mg/L and 1.13 mg/L for most infection induced by Gram-positive bacteria and endocarditis or severe infections, respectively.

Results: A total of 103 teicoplanin unbound concentrations were collected from 72 Chinese adult patients. A one-compartment pharmacokinetic model with first-order elimination was established. The typical values of clearance and the volume of distribution were 11.7 L/h and 811 L, respectively. The clearance and volume of distribution of unbound teicoplanin were positively correlated with estimated glomerular filtration rate (eGFR) and serum albumin concentrations, respectively. Dosing simulation results showed that standard dosing regimens were unable to meet the treatment needs of all patients, and the dosing regimen need optimize based on eGFR and serum albumin concentrations. The high eGFR and serum albumin concentration were associated with reduced probability of achieving target unbound trough concentrations.

Conclusion: We successfully characterized the pharmacokinetics of unbound teicoplanin in Chinese adult patients. Importantly, we further highlight the importance of guiding dosing through unbound drugs. To achieve safe and effective treatment, the dosing regimens need to be adjusted according to eGFR and serum albumin concentrations.

KEYWORDS

unbound teicoplanin, Chinese adult patients, population pharmacokinetics, dosing optimization, Monte Carlo simulation

Introduction

Teicoplanin is a glycopeptide antibiotic and is widely used in the treatment of serious infections caused by drug-resistant Gram-positive bacteria, such as methicillin-resistant *Staphylococcus aureus* (MRSA), methicillin-resistant coagulase-negative *Staphylococci* and penicillin-resistant *Streptococcus pneumonia* (Lu and Song 2014). A review and meta-analysis that included 24 randomized controlled trials concluded that teicoplanin is not inferior to vancomycin with regard to efficacy and is associated with lower adverse events rate than vancomycin (Svetitsky et al., 2009).

Teicoplanin has time-dependent antibacterial activity with evident post-antibiotic effects and has a long half-life of elimination (30–180 h) (Li and Wang, 2016; Gao et al., 2020). Teicoplanin clinical efficacy is closely associated with trough concentration (C_{trough}). For most infection induced by Gram-positive bacteria, the suggested therapeutic total C_{trough} is no less than 10 mg/L (detected by HPLC method); For endocarditis and severe infection, the suggested therapeutic total C_{trough} is no less than 15 mg/L (detected by HPLC method). Previous studies have shown that adverse events increased significantly when C_{trough} exceeds suggested range. Thrombocytopenia was more common at total $C_{trough} > 60$ mg/L (Pauluzzi et al., 1987), so the therapeutic total C_{trough} is suggested to not exceed 60 mg/L (Tobin et al., 2010). At present, total C_{trough} is used to guide dosing, however, the standard dosing regimens (three loading doses of 400 mg q12h followed by maintenance doses of 400 mg/200 mg qd) may not consistently achieve the therapeutic concentrations.

Importantly, teicoplanin is highly bound to serum albumin (90%–95%) (Gao et al., 2020) and the majority of drug is excreted unchanged in the urine by glomerular filtration (Rowland, 1990; Tobin et al., 2010). Only the unbound (free) teicoplanin is able to distribute into body tissues and exert pharmacological (antibacterial) activity. Previous studies demonstrated the level of serum albumin was an important determinant of teicoplanin pharmacokinetic (PK) variability. Hypoproteinemia (serum albumin < 25 g/L) could result in higher unbound fractions and large variability of protein binding ratio (Yano et al., 2007; Roberts et al., 2014; Byrne et al., 2017a). Theoretically, one can expect higher active concentrations in patients with hypoproteinemia. However, increased unbound fractions may result in increased distribution and clearance (because glomeruli only filtrate the unbound drug), which could reduce total concentrations (Ulldemolins et al., 2011). Therefore, it might be not comprehensive to evaluate the efficacy and safety of teicoplanin only by total concentrations (Aulin et al., 2021). Meanwhile, for the antibacterial drugs whose efficacy are evaluated by trough concentrations, the correlation between unbound concentrations and efficacy is greater than that of total concentrations (Brink et al., 2015). Consequently, in the clinical, while monitoring the total concentrations, it is also

necessary to focus on the unbound concentrations of the patients.

According to the estimation method in previous study (Byrne et al., 2018), the therapeutic unbound teicoplanin C_{trough} was calculated based on the suggested therapeutic total C_{trough} described above and the protein binding ratio (90%–95%). In this study, the protein binding ratio was calculated as the average value of 92.5%. For the most infection induced by Gram-positive bacteria, the suggested therapeutic unbound C_{trough} was no less than 0.75 mg/L. For endocarditis and severe infection, the suggested therapeutic unbound C_{trough} was no less than 1.13 mg/L. And the unbound C_{trough} was suggested to not exceed 4.5 mg/L.

Recently, Therapeutic drug monitoring (TDM) combined with population pharmacokinetics (PopPK) are commonly used to achieve individual dosing (Su et al., 2015). Since the 1990s, there have been several teicoplanin PopPK studies (Ramos-Martín et al., 2014; Byrne et al., 2017b; Kasai et al., 2018), but most studies to date were based on foreign population, and focused on total teicoplanin concentrations rather than unbound concentrations. Considering the ethnic differences, it might not be appropriate to directly extrapolate the PopPK model to the Chinese population. To ensure the safety and efficacy of teicoplanin in Chinese adult patients, this study collected unbound teicoplanin concentrations and other clinical data of Chinese adult patients, developed a PopPK model describing unbound teicoplanin and performed Monte Carlo simulations to propose optimal dosing regimens likely to achieve suggested therapeutic unbound concentrations in Chinese adult patients.

Materials and methods

Study population and data collection

This was a prospective study, the raw data of teicoplanin used for the PopPK analysis were collected from patients treated with teicoplanin at 900th Hospital of Joint Logistics Support Force between January 2019 and December 2019. Patients aged 18 years or older treated with teicoplanin intravenously were included. The pregnant female patients, hemodialysis patients, disseminated intravascular coagulation patients, and continuous renal replacement therapy patients were excluded.

Data used for PopPK analysis in this study included, but were not limited to, demographics (gender, age, and weight [WT]), physiological and biochemical parameters (serum creatinine [Scr], blood urea nitrogen [BUN], cystatin C [Cys C], white blood cell [WBC] and serum albumin), dosing information (trade name, dose, infusion time, administration rate, administration interval), and PK sampling information (sampling time, unbound concentrations), etc. Estimated glomerular filtration rate (eGFR) was estimated by CKD-EPI equations (Center for Drug Evaluation, 2021):

$$eGFR = 144 \times \left(\frac{Scr}{0.7}\right)^{-0.329} \times 0.993^{Age}, \text{ if female and } Scr \leq 0.7 \quad (1)$$

$$eGFR = 144 \times \left(\frac{Scr}{0.7}\right)^{-1.209} \times 0.993^{Age}, \text{ if female and } Scr > 0.7 \quad (2)$$

$$eGFR = 141 \times \left(\frac{Scr}{0.9}\right)^{-0.411} \times 0.993^{Age}, \text{ if male and } Scr \leq 0.9 \quad (3)$$

$$eGFR = 141 \times \left(\frac{Scr}{0.9}\right)^{-1.209} \times 0.993^{Age}, \text{ if male and } Scr > 0.9 \quad (4)$$

Note: Age: years, Scr: mg·dL⁻¹, 1 mg dL⁻¹ = 88.4 μmol L⁻¹

This study has been approved by the Ethics Committee of 900th Hospital of Joint Logistics Support Force, and all subjects signed informed consent form.

Teicoplanin dosing, blood sampling, and measurement

Teicoplanin was administered intravenously by infusion for 40 min. According to the relevant guidelines (Li and Wang, 2016), the standard dosing regimens of teicoplanin was 400 mg every 12 h for three doses followed by 400 mg/200 mg once daily. However, prescribed dosing regimens were at the discretion of treating physicians based on the severity of the patient's disease and the standard dosing regimen was not always followed. The daily dose range of patients included in this study was 50–1,600 mg.

Blood samples were typically collected within 30 min to 1 h preceding the 4th dose and the 6th dose, and depending on the actual clinical situation, blood samples might be taken at other time for TDM during the treatment. The Plasma samples were placed in a Centrifree[®] ultrafiltration device and placed in a 37°C water bath for 30 min, followed by centrifugation at 37°C, 1,500 × g for 30 min, and the ultrafiltrate was directly used for the determination of unbound concentration by ultra-performance liquid chromatography-tandem mass spectrometry (UPLC-MS/MS) method. The calibration curve of unbound teicoplanin in plasma was linear over the range of 0.10–8.00 μg/ml ($r = 0.999$). The intra-assay precision and the inter-assay precision of samples did not exceed 7.00%. The average relative recovery ratio was 97.9%, and the matrix effect factor was 0.97. Details of blood handling, storage and measurement have been described previously (Fu et al., 2020).

Population pharmacokinetic analysis

The PopPK modeling was performed using NONMEM (non-linear mixed effects modeling, v7.2, Globomax Corp, United States), and Wings for NONMEM (v6.1, Nick Holford, University of Auckland, New Zealand) was used as an auxiliary

software for NONMEM execution. R (v3.6.1, Saik Urien, U.R.C. Paris Centre, Hopital Tarnier, France) was used for exploratory data analysis, data assembly, and graphical presentation of modeling and simulation results.

One-compartment (ADVAN1 TRANS2) and two-compartment (ADVAN3 TRANS4) PK models with first-order elimination were used to fit the PK observations of unbound teicoplanin. The parameter estimation method for PopPK model was FOCEI (first order conditional estimation with η - ϵ interaction option). The inter-individual variability (IIV) of the parameters were estimated using exponential random effects.

$$\theta_i = \theta \cdot e^{\eta_i} \quad (5)$$

Where θ_i is the estimated parameter value of the individual i , θ represents the typical population parameter, and η_i (IIV) is assumed to follow the normal distribution with mean of 0 and variance of ω^2 and was estimated during model fitting.

The additive, proportional, and mixed residual error models were compared separately, and finally the mixed residual error model was selected for data fitting.

$$Y = F \times (1 + \epsilon_1) + \epsilon_2 \quad (6)$$

where Y represents the observed unbound teicoplanin concentrations, F is the individual prediction, and ϵ_1 and ϵ_2 are the proportional error and additive error, respectively, which followed the normal distributions with mean of 0 and variance of σ_1^2 and σ_2^2 , respectively.

Covariate analysis

Covariate modeling analysis was used to explore the source of variability. Age, gender, WT, Scr, BUN, Cys C, serum albumin, eGFR, WBC and the teicoplanin type (teicoplanin produced by Sanofi-Aventis S. p.A or HISUN) received during teicoplanin therapy were investigated as potential variables on PK parameters.

The stepwise covariate modeling approach was used to establish the covariate model in this analysis. During the forward selection step, all covariates were added to the PK parameters in the base model one by one. Covariates were screened based on the changes in objective function values (OFV) and graphical evaluation. The covariate with a significant effect ($p < 0.05$, e.g., $df = 1$, $\Delta OFV \geq 3.84$) would be added to the basic model to build a full model. Based on the full model, the existing covariates were deleted one by one as the backward elimination step. For each deleted covariate, the increase in OFV should be ≥ 10.83 ($p < 0.001$, $df = 1$), otherwise, this covariate should be excluded from the final model.

Continuous covariates (e.g., WT) were added to the model according to the following equation.

$$\theta_i = \theta_{TV} \times \left(\frac{\text{cov}_i}{\text{cov}_{\text{median}}} \right)^{\theta_x} \quad (7)$$

Where θ_i is the parameter value of the i th individual; θ_{TV} is the population typical value of PK parameters; cov_i is the covariate value of the i th individual; $\text{cov}_{\text{median}}$ is the median value of this covariate; θ_x is the influence coefficient of the covariate on the parameters.

Categorical covariates (e.g., gender) were added to the model according to the following equations:

$$\theta_i = \theta_{TV} + \theta_{x,\text{cov}=x_i} \quad \text{if Cov} = X_i \quad (8)$$

$$\theta_i = \theta_{TV} \quad \text{if Cov} = X_0 \quad (9)$$

Where $\theta_{x,\text{cov}=x_i}$ is the change in a parameter when covariate X is at level i compared with the reference level (0).

Model evaluation

To evaluate the accuracy, appropriateness and stability of the final model, goodness-of-fit plots, non-parametric bootstrap, normalized prediction distribution errors (NPDE) were performed.

Goodness-of-fit plots were used to assess the appropriateness of the model. It included the plots of observed values against individual or population predictions and conditional weighted residuals (CWRESs) against time or population predictions.

The performance and stability of the final model were estimated using non-parametric bootstrap. 1,000 datasets generated by random sampling were evaluated. The 95% confidence interval and median of the final parameters were calculated and compared to the final parameters estimated by NONMEM program.

The descriptive performance of the model was evaluated by calculation of the NPDE. 1,000 times simulations were performed based on the final model. The results were used for plotting, including quantile-quantile plot, the NPDE histogram, NPDE versus time and PRED plots.

Simulation and dosing optimization

Monte Carlo simulations were performed for adult patients ($n = 1,000$) based on the final PopPK model. Six levels of eGFR (20, 30, 45, 60, 90, and 130 ml/min) and six levels of serum albumin concentrations (15, 20, 25, 30, 35, and 40 g/L) were evaluated. Three loading doses (q12h) followed by maintenance doses (qd) were simulated. The probability of target attainment (PTA) for achieving a target unbound C_{through} of 0.75 mg/L (most infection induced by Gram-positive bacteria) or 1.13 mg/L (endocarditis and severe infection) at 48 h and 96 h was calculated. The PTA (risk)

of achieving the unbound C_{through} of 4.5 mg/L at 96 h ($C_{\text{through}} \geq 4.5$ mg/L means more adverse events) was also calculated. The optimal dosing regimens were finally selected based on above PTA calculations.

Results

Study population

Data for the PopPK analysis were obtained from 72 subjects, including 26 female patients and 46 male patients. A total of 103 PK observations were obtained. Demographic information and physiological or biochemical parameters for this analysis are presented in Table 1.

Population pharmacokinetics modeling

In this analysis, one-compartment and two-compartment models were used as structural models to fit the PK observations. The results showed that one-compartment model could successfully minimize and the parameters were estimated reasonably (OFV = -24.4, condition number = 18.8). Compared with one-compartment model, the two-compartment model showed no significant change in OFV value ($\Delta\text{OFV} = -0.24$), and the condition number was large (condition number = $1.16e + 007$), at the same time, the IIV of the clearance between peripheral and central compartments and the volume of distribution in peripheral compartment could not be accurately estimated. Based on above analyses, the one-compartment PopPK model with first-order elimination was selected as the basic structural model describing the PK characteristics of unbound teicoplanin.

The results of covariate analysis showed that eGFR was a significant covariate of the clearance (CL) of the unbound teicoplanin, serum albumin concentrations significantly affected the volume of distribution (V) of the unbound teicoplanin, and the model OFV values decreased by 11.037 and 13.442, respectively. Type of teicoplanin, gender, age, WT, Scr, BUN, WBC and Cys C were not significant covariates of the PK parameters of the unbound teicoplanin. The final model could be described using following equations:

$$\text{CL (L/h)} = 11.7 \times \left(\frac{\text{eGFR}}{84} \right)^{0.476} \times e^{\eta_{\text{CL}}} \quad (10)$$

$$\text{V (L)} = 811 \times \left(\frac{\text{ALB}}{32} \right)^{1.6} \times e^{\eta_{\text{V}}} \quad (11)$$

where CL is clearance, eGFR is estimated glomerular filtration rate, ALB is serum albumin concentrations, V is the volume of distribution. The final model parameter estimates are shown in Table 2.

TABLE 1 Characteristics of patients included in the study.

Parameters (unit)	Value ^a
Number of patients (male/female)	72 (46/26)
Number of PK observations	103
Age (years)	69 ± 20 (18–99)
WT (kg)	61.0 ± 9.8 (40–85)
Type of teicoplanin/(teicoplanin produced by Sanofi-Aventis or HISUN)	44/28
Daily dose (mg)	50–1,600
Unbound teicoplanin concentrations (µg/ml)	1.5 ± 0.9 (0.4–4.4)
Scr (µmol/L)	86.2 ± 48.3 (32.1–263.0)
BUN (mmol/L)	9.5 ± 7.4 (1.6–36.8)
Cys C (mg/L)	1.4 ± 0.8 (0.6–3.7)
eGFR (ml/min)	80.8 ± 27.1 (17.4–134.0)
Albumin (g/L)	31.0 ± 5.1 (18.3–46.0)
WBC (10 ⁹ /L)	10.6 ± 5.3 (2.1–32.5)
The infection type (%)	
Pulmonary infection	58 (80.6)
Bacteremia	3 (4.2)
Pyemia	4 (5.6)
Abdominal infection	2 (2.8)
Skin infection	6 (8.3)
Hepatapostema	1 (1.4)
Biliary tract infection	2 (2.8)

Note: BUN, blood urea nitrogen; Cys C, cystatin C; eGFR, estimated glomerular filtration rate; PK, pharmacokinetic; Scr, serum creatinine; WBC, white blood cell; WT, weight.

^avalues are expressed as mean ± SD (range) or as n.

TABLE 2 PK parameter estimates and results of bootstrap analysis for the final model.

Parameter	NONMEM			Bootstrap		Bias (%)
	Estimates	RSE (%)	Shrinkage (%)	Median	95% CI	
θ_{CL} (L/h)	11.7	7.4	—	11.38	9.06–13.4	−2.72
θ_V (L)	811	11.1	—	822	616–1,025	1.42
θ_{ALB} (g/L)	1.60	27.4	—	1.55	0.690–2.55	−3.11
θ_{eGFR} (ml/min)	0.476	50	—	0.501	0.229–1.40	5.21
η_{CL} (%)	38.6	16.5	35	36.2	17.9–49	−6.17
η_V (%)	53.7	13.2	31	51.9	23.6–71.0	−3.34
ϵ_1 (%)	18.3	14.5	36	17.8	9.04–25.0	−3.03
ϵ_2 (µg/ml)	0.122	41.3	36	0.119	0.0207–0.198	−2.33

Note: θ_{CL} , The population parameters typical value of clearance; θ_V , The population parameters typical value of the volume of distribution; θ_{ALB} , The population parameters typical value of ALB; θ_{eGFR} , The population parameters typical value of eGFR; η_{CL} , Inter-individual variation in clearance; η_V , Inter-individual variation in the volume of distribution; ϵ , Residual variation; CI, Confidence interval; RSE, relative standard error; Bias, prediction error; Bias% = (Bootstrap Median–NONMEM Estimates)/NONMEM Estimates × 100%.

Model evaluation

The goodness-of-fit plots for final model are presented in Figure 1. The results of model diagnosis showed that population predicted versus observed concentrations were evenly distributed around the line of $y = x$, and less scatter points deviated far from the line of $y = x$. The individual

predicted versus observed concentrations were evenly distributed around the line of $y = x$. Conditional weighted residuals versus population predictions and time after the first dose were evenly distributed around the line of $y = 0$. The model diagnostic plots showed that the established model fit the data well, and the selected error model was adequate.

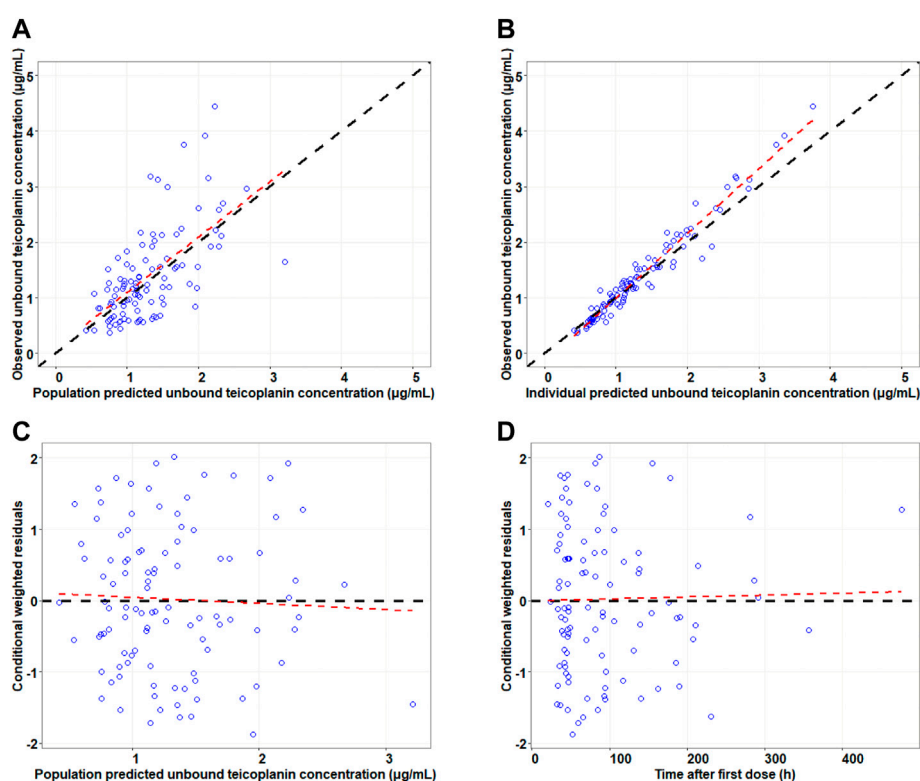


FIGURE 1

Goodness-of-fit plots for the final model. Note: The upper left and upper right panels represent observed versus population and individual predicted concentrations, respectively (A,B); the lower left and lower right panels represent conditional weighted residuals versus population predicted concentrations and the time after the first dose, respectively (C,D). The line in the upper panel is $y = x$; the line in the lower panel is $y = 0$.

The parameter estimates of the final model and the results of non-parametric bootstrap analysis are shown in Table 2. The bootstrap results showed the successful minimization in 875 of the 1,000 simulations. The median values were close to the final parameters estimated by NONMEM program, with $<6.5\%$ bias, and the final model parameter estimates were within the 95% confidence intervals of bootstrap results, indicating that the performance of the model was stable.

Evaluation of the NPDE distribution showed that the mean of the NPDE was not significantly different from 0 (Wilcoxon signed rank, $p = 0.131 > 0.05$), the variance was not significantly different from 1 (Fisher test, $p = 0.142 > 0.05$) and the NPDE distribution was not significantly different from a normal distribution (Shapiro-Wilks, $p = 0.561 > 0.05$). The NPDE plots of the final model are presented in Figure 2. It can be seen that the NPDE followed a normal distribution and no trend in the scatterplots was observed. The results confirmed that the final model could adequately describe the observed data.

Simulation and dosing optimization

Monte Carlo simulations were performed based on the final model and the simulated population was stratified by the various eGFR and serum albumin levels. The PTA for achieving a target unbound C_{through} of 0.75 mg/L (most infection induced by Gram-positive bacteria) or 1.13 mg/L (endocarditis and severe infection) at 48 h or 96 h were calculated. The PTA results for the various teicoplanin loading dose regimen simulations for unbound C_{through} at 48 h are shown in Figure 3. The simulation results showed that PTA decreased as eGFR and serum albumin concentration increased, and PTA increased as the loading dose increased. The standard loading dose regimen of 400 mg for three doses could only achieve $\text{PTA} \geq 80\%$ in patients with low eGFR or serum albumin concentrations, and higher loading doses were required in patients with high eGFR and serum albumin concentrations. In addition, with the same eGFR and serum albumin concentrations, patients with endocarditis and severe infection require a higher loading dose to achieve $\text{PTA} \geq 80\%$. Table 3 summarizes the dosing regimens (loading dose and maintenance dose) with $\geq 80\%$ PTA at 48 h or 96 h, and the probability (risk) of

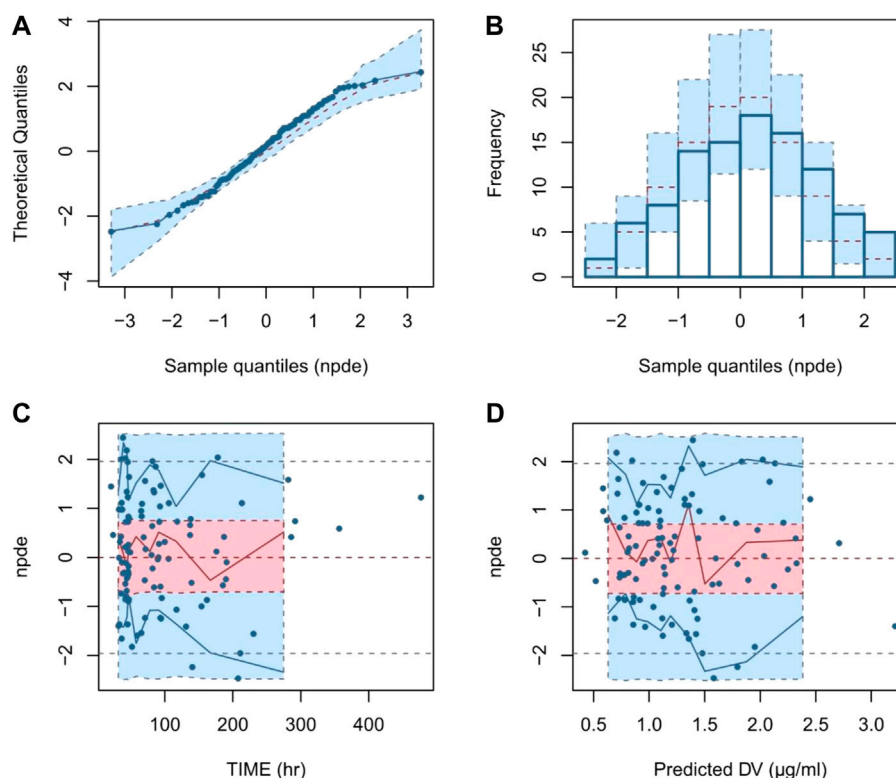


FIGURE 2

Normalized prediction distribution error (NPDE) plots of final model. Note: (A) quantile-quantile plot of the distribution of the NPDE against theoretical distribution; (B) histogram of the distribution of the NPDE against theoretical distribution; (C) scatter plot of NPDE vs. time after the first dose (TAFD); (D) scatter plot of NPDE vs. predicted concentrations.

achieving unbound $C_{\text{through}} \geq 4.5$ mg/L at 96 h for each dosing regimen. The simulation results for the recommended dosing regimens are provided as [Supplementary Material](#).

Discussion

This study was the first to establish a PopPK model of unbound teicoplanin in adult Chinese patients and assess the effect of intrinsic/extrinsic factors on the PK characteristics of unbound teicoplanin. At the same time, the optimal dosing regimens for achieving target unbound C_{trough} were obtained by Monte Carlo simulation, providing a reference for clinical application.

In this study, due to the limitation of clinical circumstances, it was difficult to perform relatively intensive PK sampling to describe the complete concentration-time profiles. The sampling method was sparse sampling, with an average of only 1–5 sampling points per patient, and most were trough concentrations. This was close to the sampling method in the study by [Kasai et al. \(2018\)](#) and [Byrne et al. \(2018\)](#). Such

sampling data could accurately describe the elimination phase. A one-compartment model was optimal and adopted for the modeling of the data. The results of covariate analysis showed the eGFR was a significant covariate on CL, and serum albumin was a significant covariate on V.

The typical value of CL was 11.7 L/h, which was close to the value of 7.29 L/h for the unbound teicoplanin in the previous study ([Byrne et al., 2018](#)). The typical value of V was 811 L, which was greater than the value of total teicoplanin obtained in our previous PopPK study (83.1 L) ([Fu et al., 2021](#)). Because teicoplanin is highly bound to serum albumin (90%–95%), it was justified that only unbound drug could distribute into tissues and was more widely distributed than total drug. The renal function (eGFR) was positive correlation with unbound teicoplanin CL, but the relative standard error of eGFR was relatively large (RSE = 50%). It might be due to the large IIV of patients as well as limited sample size. Considering eGFR could significantly improve the goodness-of-fit of the model and the result was also in keeping with teicoplanin's elimination characteristics ([Wilson, 2000](#)), the final model retained eGFR as a covariate. The finding was consistent with the results

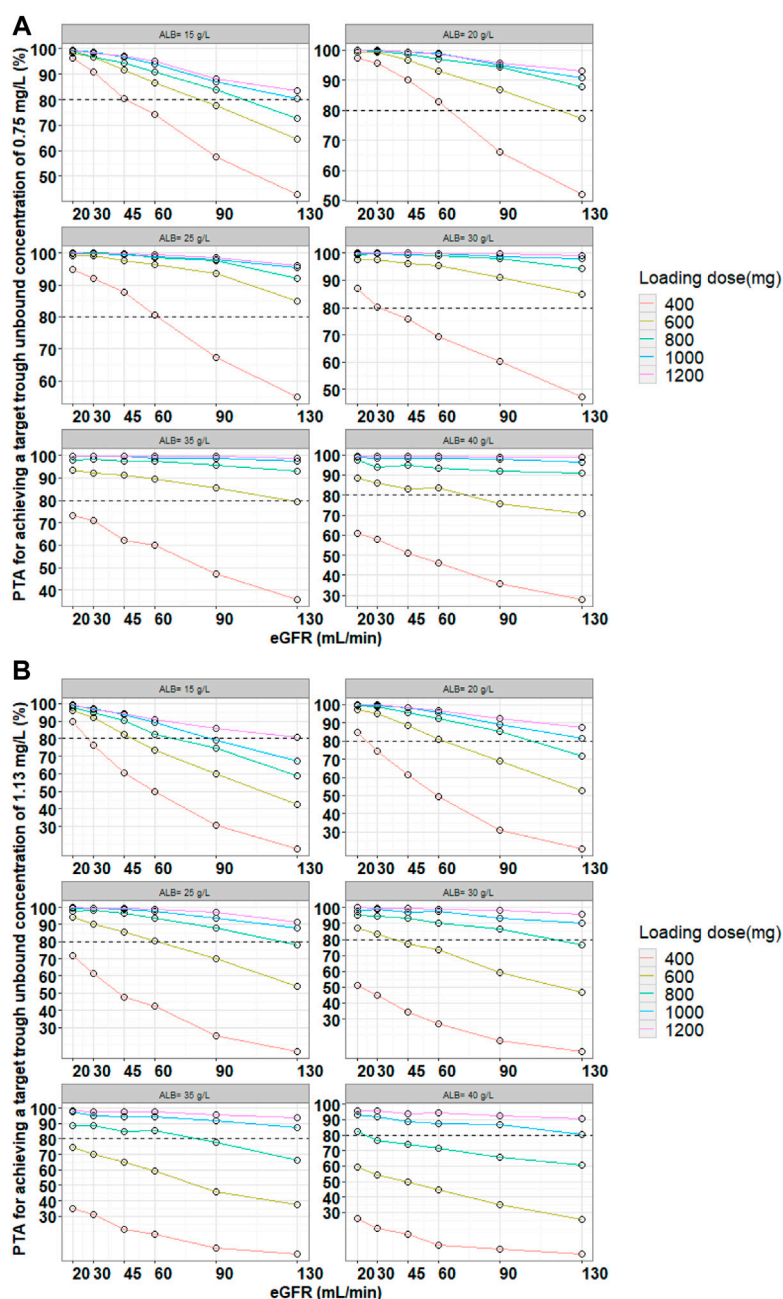


FIGURE 3

Monte Carlo simulations and PTA for unbound trough concentrations at 48 h for various loading dose regimens. Note: Loading doses were administered every 12 h for three doses and unbound trough concentrations were simulated at 48 h. The dash line represented a PTA of 80%. (A) Most infection induced by Gram-positive bacteria, (B) endocarditis and severe infection.

obtained in the previous studies (Soy et al., 2006; Matsumoto et al., 2016; Ogami et al., 2020). In addition, the serum albumin concentrations of patients included in this study ranged from 18.3 to 46 g/L, covering a wide range, and included patients with hypoproteinemia (<25 g/L). The covariate analysis also

revealed that the serum albumin level was positive correlation with V. The volume of distribution was lower in patients with low serum albumin levels, and the unbound concentrations were higher at certain doses. The finding was consistent with the previous studies (Yano et al., 2007; Zhao et al., 2015) that

TABLE 3 Optimal dosing regimens achieving target unbound teicoplanin C_{through} at 48 h for loading dose regimens and at 96 h for maintenance dose regimens (PTA $\geq 80\%$).

eGFR (ml/min)	ALB (g/L)					
	15	20	25	30	35	40
Most infection induced by Gram-positive bacteria						
Loading dose (mg)/maintenance dose (mg) to achieve unbound target C_{through} of 0.75 mg/L [Probability of unbound $C_{\text{through}} \geq 4.5$ mg/L at 96 h (%)]						
20	400/400 (1.7)	400/200 (0)	400/200 (0)	400/200 (0)	600/200 (0)	600/200 (0)
30	400/400 (0.4)	400/400 (0)	400/200 (0)	400/200 (0)	600/200 (0)	600/200 (0)
45	400/400 (0.1)	400/400 (0)	400/400 (0)	600/200 (0)	600/200 (0)	600/200 (0)
60	600/600 (0.8)	400/400 (0)	400/400 (0)	600/400 (0)	600/400 (0)	600/400 (0)
90	800/800 (1.7)	600/600 (0)	600/600 (0)	600/400 (0)	600/400 (0)	800/400 (0)
130	1,000/1,000 (1.7)	800/800 (0.4)	600/600 (0)	600/600 (0)	600/600 (0)	800/400 (0)
Endocarditis and severe infection						
Loading dose (mg)/maintenance dose (mg) to achieve unbound target C_{through} of 1.13 mg/L (Probability of unbound $C_{\text{through}} \geq 4.5$ mg/L at 96 h [%])						
20	400/400 (1.7)	400/400 (0.5)	600/200 (0.2)	600/200 (0.2)	800/200 (0.3)	800/200 (0.4)
30	600/600 (5.3)	600/400 (0.7)	600/400 (0.1)	600/400 (0.1)	800/400 (0.4)	1,000/200 (0)
45	600/600 (2.6)	600/600 (1.5)	600/600 (0.4)	800/400 (0.4)	800/400 (0)	1,000/400 (0.2)
60	800/800 (4.6)	600/600 (0.7)	800/600 (1.0)	800/600 (0.2)	800/600 (0.4)	1,000/400 (0.1)
90	1,000/1,000 (4.6)	800/800 (1.6)	800/800 (0.9)	800/600 (0.2)	1,000/600 (0.2)	1,000/600 (0.1)
130	1,200/1,200 (4.7)	1,000/1,000 (0.2)	1,000/800 (0.4)	1,000/800 (0)	1,000/800 (0)	1,000/800 (0)

Note: ALB, albumin; C_{through} , trough concentration; eGFR, estimated glomerular filtration rate; PTA, probability of target attainment.

suggested there were higher unbound teicoplanin concentrations in patients with lower ALB levels. Ulldemolins et al. (2011) also proposed that serum albumin concentrations significantly impacts CL or V in highly protein-bound drugs.

It was found that body weight significantly affected the volume of distribution of teicoplanin in patients with haematological malignancy in the previous studies (Byrne et al., 2017b). However, this study did not find the significant effect of body weight on PK parameters of unbound teicoplanin. The possible reasons are as follows: 1) the majority of patients' (more than 80%) body weight was centrally distributed between 50 and 70 kg; 2) some patients were long-term bedridden and unable to measure the body weight accurately; 3) small sample size with certain limitations.

Based on the parameters of the final model, the dosing regimens were designed by simulation in patients with different levels of eGFR and serum albumin concentrations to achieve the PTA of no less than 80%. We found that the standard dosing regimen (three loading doses of 400 mg q12h

followed by maintenance doses of 400 mg/200 mg qd) did not meet the treatment needs of all patients and higher PTA could only be achieved in patients with low eGFR and ALB levels. In particular, a dose increase may be necessary in patients with enhanced renal function and high serum albumin levels, or in patients with endocarditis and severe infection. Meanwhile, patients with renal impairment and hypoproteinemia at the same dose had a relatively increased risk of adverse events (probability of attaining trough unbound concentrations ≥ 4.5 mg/L). This suggested that in clinical, it would be useful to measure unbound concentrations, and the dosing regimen needed to be adjusted in time according to the patient's eGFR and serum albumin concentrations.

Several limitations of this study warrant mention. This study was a single center study and a different result may have been obtained if multiple centers had been studied. The main limitation of this study was the sample size of our data set. Although the sample size could meet the needs of PK modeling, it was necessary to expand the sample size while collecting more blood samples obtained by intensive sampling to further evaluate and optimize the model of unbound teicoplanin.

Conclusion

In conclusion, in order to optimize teicoplanin therapy in adult Chinese patients, a PopPK model of the unbound teicoplanin concentrations was developed in this study and recommendations for individualized dosing regimens were made by simulation. The effects of eGFR and serum albumin concentrations on PK parameters of unbound teicoplanin were proposed. Importantly, our study further highlights the importance of guiding dosing through unbound drugs. It was recommended that in clinical, a reasonable dosing regimen should be designed according to the patient's eGFR and serum albumin concentrations, which was a key step to achieve individualized dosing.

Data availability statement

The raw data supporting the conclusion of this article will be made available by the authors, without undue reservation.

Ethics statement

The studies involving human participants were reviewed and approved by Ethics committee of 900th Hospital of Joint Logistics Support Force, Fuzhou, China. The patients/participants provided their written informed consent to participate in this study. Written informed consent was obtained from the individual(s) for the publication of any potentially identifiable images or data included in this article.

Author contributions

L-LZ and W-QF designed the study. W-QF performed the major research. The manuscript was written mainly with the efforts of W-QF and reviewed by L-LZ. The clinical materials were collected by W-QF and T-TT. The determination method of unbound concentration was developed by W-QF and M-XZ. H-TS contributed as consultant. All

authors helped analyze and interpret the data. W-QF, T-TT, M-XZ, H-TS, and L-LZ have given approval to the final version of the manuscript.

Funding

This study is supported by Natural Science Foundation of Fujian Province (2020J05284).

Acknowledgments

We thank all of the patients participating in our study and all supports for the Natural Science Foundation of Fujian Province and 900th Hospital of Joint Logistics Support Force.

Conflict of interest

The authors declare that the research was conducted in the absence of any commercial or financial relationships that could be construed as a potential conflict of interest.

Publisher's note

All claims expressed in this article are solely those of the authors and do not necessarily represent those of their affiliated organizations, or those of the publisher, the editors and the reviewers. Any product that may be evaluated in this article, or claim that may be made by its manufacturer, is not guaranteed or endorsed by the publisher.

Supplementary material

The Supplementary Material for this article can be found online at: <https://www.frontiersin.org/articles/10.3389/fphar.2022.1045895/full#supplementary-material>

References

- Aulin, L. B. S., De Paep, P., Dhont, E., De Jaeger, A., Vande Walle, J., Vandenberghe, W., et al. (2021). Population pharmacokinetics of unbound and total teicoplanin in critically ill pediatric patients. *Clin. Pharmacokinet.* 60, 353–363. doi:10.1007/s40262-020-00945-4
- Brink, A. J., Richards, G. A., Lautenbach, E. E., Rapeport, N., Schillack, V., Van Niekerk, L., et al. (2015). Albumin concentration significantly impacts on free teicoplanin plasma concentrations in non-critically ill patients with chronic bone sepsis. *Int. J. Antimicrob. Agents* 45, 647–651. doi:10.1016/j.ijantimicag.2015.01.015
- Byrne, C. J., Parton, T., Mcwhinney, B., Fennell, J. P., O'Byrne, P., Deasy, E., et al. (2018). Population pharmacokinetics of total and unbound teicoplanin concentrations and dosing simulations in patients with haematological malignancy. *J. Antimicrob. Chemother.* 73, 995–1003. doi:10.1093/jac/dkx473
- Byrne, C. J., Roberts, J. A., Mcwhinney, B., Fennell, J. P., O'Byrne, P., Deasy, E., et al. (2017a). Variability in trough total and unbound teicoplanin concentrations and achievement of therapeutic drug monitoring targets in adult patients with hematological malignancy. *Antimicrob. Agents Chemother.* 61, e0246616. doi:10.1128/AAC.02466-16
- Byrne, C. J., Roberts, J. A., Mcwhinney, B., Ryder, S. A., Fennell, J. P., O'Byrne, P., et al. (2017b). Population pharmacokinetics of teicoplanin and attainment of pharmacokinetic/pharmacodynamic targets in adult patients with haematological malignancy. *Clin. Microbiol. Infect.* 23, e7–e674. doi:10.1016/j.cmi.2017.02.032

- Center for Drug Evaluation (2021). *Guidance for Industry Pharmacokinetics in Patients with Impaired Renal Function*.
- Fu, W., Tian, T., Zhang, M., Song, H., and Zhang, L. (2021). Population pharmacokinetics of teicoplanin in adult patients. *Chin. J. Hosp. Pharm.* 41, 1967–1972.
- Fu, W., Zhang, M., Yao, N., Zhang, L., and Song, H. (2020). Assay of unbound teicoplanin in human plasma by centrifugal ultrafiltration combined with ultra performance liquid chromatography-tandem mass spectrometry. *J. Pharm. Pract.* 38, 547–551.
- Gao, L., Xu, H., Ye, Q., Li, S., Wang, J., Mei, Y., et al. (2020). Population pharmacokinetics and dosage optimization of teicoplanin in children with different renal functions. *Front. Pharmacol.* 11, 552. doi:10.3389/fphar.2020.00552
- Kasai, H., Tsuji, Y., Hiraki, Y., Tsuruyama, M., To, H., and Yamamoto, Y. (2018). Population pharmacokinetics of teicoplanin in hospitalized elderly patients using cystatin C as an indicator of renal function. *J. Infect. Chemother.* 24, 284–291. doi:10.1016/j.jiac.2017.12.002
- Li, G., and Wang, R. (2016). Expert consensus on teicoplanin clinical dose. *Chin. J. Tuberc. Respir.* 39, 500–508.
- Lu, K., and Song, H. (2014). PK/PD characteristics and the progress of research on the dosage regimen of glycopeptides antibiotics in the treatment of MRSA infection. *Chin. J. Hosp. Pharm.* 34, 952–957.
- Matsumoto, K., Watanabe, E., Kanazawa, N., Fukamizu, T., Shigemi, A., Yokoyama, Y., et al. (2016). Pharmacokinetic/pharmacodynamic analysis of teicoplanin in patients with MRSA infections. *Clin. Pharmacol.* 8, 15–18. doi:10.2147/CPAA.S96143
- Ogami, C., Tsuji, Y., Muraki, Y., Mizoguchi, A., Okuda, M., and To, H. (2020). Population pharmacokinetics and pharmacodynamics of teicoplanin and C-reactive protein in hospitalized patients with gram-positive infections. *Clin. Pharmacol. Drug Dev.* 9, 175–188. doi:10.1002/cpdd.684
- Pauluzzi, S., Del Favero, A., Menichetti, F., Baratta, E., Moretti, V. M., Di Filippo, P., et al. (1987). Treatment of infections by staphylococci and other gram-positive bacteria with teicoplanin: An open study. *J. Antimicrob. Chemother.* 20, 431–438. doi:10.1093/jac/20.3.431
- Ramos-Martín, V., Paulus, S., Siner, S., Scott, E., Padmore, K., Newland, P., et al. (2014). Population pharmacokinetics of teicoplanin in children. *Antimicrob. Agents Chemother.* 58, 6920–6927. doi:10.1128/AAC.03685-14
- Roberts, J. A., Stove, V., De Waele, J. J., Sipinkoski, B., McWhinney, B., Ungerer, J. P., et al. (2014). Variability in protein binding of teicoplanin and achievement of therapeutic drug monitoring targets in critically ill patients: Lessons from the DALI study. *Int. J. Antimicrob. Agents* 43, 423–430. doi:10.1016/j.ijantimicag.2014.01.023
- Rowland, M. (1990). Clinical pharmacokinetics of teicoplanin. *Clin. Pharmacokinet.* 18, 184–209. doi:10.2165/00003088-199018030-00002
- Soy, D., López, E., and Ribas, J. (2006). Teicoplanin population pharmacokinetic analysis in hospitalized patients. *Ther. Drug Monit.* 28, 737–743. doi:10.1097/01.ftd.0000249942.14145.ff
- Su, H., Zhang, S., and Chen, W. (2015). Review on population pharmacokinetics and its application. *Anhui Med. Pharm. J.* 205–208, 209.
- Svetitsky, S., Leibovici, L., and Paul, M. (2009). Comparative efficacy and safety of vancomycin versus teicoplanin: Systematic review and meta-analysis. *Antimicrob. Agents Chemother.* 53, 4069–4079. doi:10.1128/AAC.00341-09
- Tobin, C. M., Lovering, A. M., Sweeney, E., and Macgowan, A. P. (2010). Analyses of teicoplanin concentrations from 1994 to 2006 from a UK assay service. *J. Antimicrob. Chemother.* 65, 2155–2157. doi:10.1093/jac/dkq266
- Ulldemolins, M., Roberts, J. A., Rello, J., Paterson, D. L., and Lipman, J. (2011). The effects of hypoalbuminaemia on optimizing antibacterial dosing in critically ill patients. *Clin. Pharmacokinet.* 50, 99–110. doi:10.2165/11539220-000000000-00000
- Wilson, A. P. (2000). Clinical pharmacokinetics of teicoplanin. *Clin. Pharmacokinet.* 39, 167–183. doi:10.2165/00003088-200039030-00001
- Yano, R., Nakamura, T., Tsukamoto, H., Igarashi, T., Goto, N., Wakiya, Y., et al. (2007). Variability in teicoplanin protein binding and its prediction using serum albumin concentrations. *Ther. Drug Monit.* 29, 399–403. doi:10.1097/FTD.0b013e3180690755
- Zhao, W., Zhang, D., Storme, T., Baruchel, A., Declès, X., and Jacqz-Aigrain, E. (2015). Population pharmacokinetics and dosing optimization of teicoplanin in children with malignant haematological disease. *Br. J. Clin. Pharmacol.* 80, 1197–1207. doi:10.1111/bcp.12710



OPEN ACCESS

EDITED BY

Rong Wang,
People's Liberation Army Joint Logistics
Support Force 940th Hospital, China

REVIEWED BY

Yitian Zhou,
Karolinska Institutet (KI), Sweden
Zhongbin Zhang,
Tianjin Children's Hospital, China

*CORRESPONDENCE

Xiaomei Fan,
xmfane@163.com

[†]These authors have contributed equally
to this work

SPECIALTY SECTION

This article was submitted to Drug
Metabolism and Transport,
a section of the journal
Frontiers in Pharmacology

RECEIVED 05 September 2022

ACCEPTED 17 November 2022

PUBLISHED 25 November 2022

CITATION

Shen X, Chen X, Lu J, Chen Q, Li W,
Zhu J, He Y, Guo H, Xu C and Fan X
(2022), Pharmacogenetics-based
population pharmacokinetic analysis
and dose optimization of valproic acid in
Chinese southern children with
epilepsy: Effect of *ABCB1*
gene polymorphism.
Front. Pharmacol. 13:1037239.
doi: 10.3389/fphar.2022.1037239

COPYRIGHT

© 2022 Shen, Chen, Lu, Chen, Li, Zhu,
He, Guo, Xu and Fan. This is an open-
access article distributed under the
terms of the [Creative Commons
Attribution License \(CC BY\)](#). The use,
distribution or reproduction in other
forums is permitted, provided the
original author(s) and the copyright
owner(s) are credited and that the
original publication in this journal is
cited, in accordance with accepted
academic practice. No use, distribution
or reproduction is permitted which does
not comply with these terms.

Pharmacogenetics-based population pharmacokinetic analysis and dose optimization of valproic acid in Chinese southern children with epilepsy: Effect of *ABCB1* gene polymorphism

Xianhuan Shen^{1,2†}, Xinyi Chen^{3†}, Jieluan Lu^{1,2}, Qing Chen¹,
Wenzhou Li¹, Jiahao Zhu^{1,2}, Yaodong He^{1,2}, Huijuan Guo¹,
Chenshu Xu³ and Xiaomei Fan^{1*}

¹Shenzhen Baoan Women's and Children's Hospital, Jinan University, Shenzhen, China, ²College of Pharmacy, Jinan University, Guangzhou, China, ³School of Pharmaceutical Sciences, Health Science Center, Shenzhen University, Shenzhen, China

Objective: The aim of this study was to establish a population pharmacokinetic (PPK) model of valproic acid (VPA) in pediatric patients with epilepsy in southern China, and provide guidance for individualized medication of VPA therapy.

Methods: A total of 376 VPA steady-state trough concentrations were collected from 103 epileptic pediatric patients. The PPK parameter values for VPA were calculated by using the nonlinear mixed-effects modeling (NONMEM) method, and a one-compartment model with first-order absorption and elimination processes was applied. Covariates included demographic information, concomitant medications and selected gene polymorphisms. Goodness-of-fit (GOF), bootstrap analysis, and visual predictive check (VPC) were used for model evaluation. In addition, we used Monte Carlo simulations to propose dose recommendations for different subgroup patients.

Results: A significant effect of the patient age and *ABCB1* genotypes was observed on the VPA oral clearance (CL/F) in the final PPK model. Compared with patients with the *ABCB1* rs3789243 AA genotype, CL/F in patients with GG and AG genotypes was increased by 8% and reduced by 4.7%, respectively. The GOF plots indicated the satisfactory predictive performance of the final model, and the evaluation by bootstrap and VPC showed that a stable model had been developed. A table of individualized

Abbreviations: VPA, Valproic acid; ILAE, International League against Epilepsy; AED, Antiepileptic drug; TDM, Therapeutic drug monitoring; PK, Pharmacokinetic; PPK, Population pharmacokinetic; LEPR, Leptin receptor; SCN1A, Sodium channel neuronal type I alpha subunit; NONMEM, Non-linear mixed-effects modeling; SNP, Single nucleotide polymorphism; OFV, Objective function value; AIC, Akaike information criterion; BIC, Bayesian information criterion; GOF, Goodness-of-fit; CWRES, Conditional weighted residual; VPC, Visual predictive checks; PTA, Probability of target attainment; RSE, Relative standard error; IIV, Inter-individual variability; RV, Residual variability; TDD, Total daily dose.

dosing regimens involving age and *ABCB1* genotype was constructed based on the final PPK model.

Conclusion: This study quantitatively investigated the effects of patient age and *ABCB1* rs3789243 variants on the pharmacokinetic variability of VPA. The PPK models could be beneficial to individual dose optimization in epileptic children on VPA therapy.

KEYWORDS

valproic acid, epileptic children, population pharmacokinetics, NONMEM, genetic polymorphism

1 Introduction

Epilepsy is one of the most common and most disabling chronic neurological disorders, characterized by an enduring predisposition to generate recurrent epileptic seizures (Devinsky et al., 2018). There are more than 70 million people of all age groups worldwide who suffer from epilepsy (Löscher et al., 2020). The prevalence of epilepsy in children is particularly high, ranging from 4 to 9 per 1,000 children, and is increasing each year (Mac et al., 2007). Valproic acid (VPA) is currently recommended by the 'International League against Epilepsy' (ILAE) as a first-line antiepileptic drug (AED) for children (Glauser et al., 2013), due to its broad spectrum of action against various kinds of seizures.

The exact mechanisms of VPA remain to be understood. Nevertheless, several studies have proposed that VPA can intensify the synthesis and release of gamma aminobutyric acid (GABA), an inhibitory neurotransmitter in the central nervous system, thereby suppress seizures (Rogawski and Löscher, 2004; Berg et al., 2008). VPA is rapidly and completely absorbed, and the available data have suggested the nearly total bioavailability (close to 1.0) for oral solutions and capsules (Johannessen and Johannessen, 2003). It is a highly protein-bound drug to albumin, and its protein binding is concentration-dependent (Patsalos et al., 2017). The saturable binding and a higher unbound fraction exhibit when VPA concentrations above 50 mg/L, which results in a non-linear relationship between daily dose and serum concentration (Perucca, 2002; Patsalos et al., 2008). For VPA half-life, an average value is 10–12 h. Additionally, higher VPA clearance and shorter half-life have been reported in children (Methaneethorn, 2018).

VPA is mainly metabolized by the liver, with only a small amount of unchanged form being excreted by the urine (Johannessen and Johannessen, 2003). It includes the following main routes: Glucuronidation *via* uridine diphosphate glucuronosyltransferase (UGT), beta-oxidation in mitochondria (both as major metabolic routes accounting for 50% and 40%, respectively), and a minor route of cytochrome P450 (CYP)-mediated oxidation and hydroxylation (approximately 10%) (Xu et al., 2018).

According to the Consensus Guidelines, the effective VPA therapeutic reference range for epilepsy is 50–100 mg/L with a broad recommended dose range (Hiemke et al., 2018). Some researchers have reported that the rates of adverse reactions (including nausea, vomiting, weight gain, teratogenicity and hepatotoxicity) were higher in patients with VPA levels >125 mg/L (Zang et al., 2022). However, serum concentration levels may vary considerably among patients taking the same dose of VPA (Ferraro and Buono, 2005). Several factors involved in VPA absorption (diet and dosage form), distribution (body weight, age, dose, and protein binding), and metabolism (sex, dose, gene polymorphism of enzymes related to VPA glucuronidation and oxidation, drug-drug interactions with other commonly used AEDs) have a significant influence on VPA clearance, which cause to the high inter- and intra-individual variability of VPA pharmacokinetic (PK) (Mei et al., 2018). The large variability in VPA and narrow therapeutic window necessitate therapeutic drug monitoring (TDM) and individualized dosing regimens, thus ensuring optimal efficacy and avoiding adverse effect, especially in pediatric patients.

A population pharmacokinetic (PPK) modeling approach can help identify the quantitative impact of individual variability on VPA PK in a target population (Kiang et al., 2012). Compared with traditional empirical dosing, model-informed precision dosing (MIPD) can aid in optimizing individual dosing based on patient physiology, pathology, genetics and other characteristics to improve the attainment of the predefined targets (Darwich et al., 2021). In addition, this new approach is more flexible in clinical applications such as non-steady state drug concentrations or clinically unstable patients (Methaneethorn, 2018). Analysis of PPK requires sparse PK sampling from patients and is applicable to children in particular. To date, although there have been a substantial number of PPK studies in the pediatric population addressing the association of demographic factors with PK variability of VPA (Botha et al., 1995; Correa et al., 2008; Ding et al., 2015; Rodrigues et al., 2018), few of them were focused on the effect of genetic polymorphisms (Jiang et al., 2007; Xu et al., 2018; Guo et al., 2020).

With the development of the pharmacogenomics in VPA, it has helped to identify a large number of candidate genes, such as drug metabolizing enzymes, regulating signaling pathways (membrane transporters and nuclear receptors), effect pathways related gene mutations, associating with the increase or decrease of VPA serum concentration (Ghodke-Puranik et al., 2013). Besides, genes that have been demonstrated in influencing its PK behavior could also partly illustrate inter-individual variability among patients taking VPA, including *UGT1A3/1A4/1A6/1A8/1A9/1A10/2B7*, *CYP2A6/2B6/2C9/2C19*, leptin receptor (*LEPR*), ABC transporter, adenosine monophosphate-activated protein kinase (*AMPK*), and sodium channel neuronal type I alpha subunit (*SCN1A*) (Zhu et al., 2017; Xu et al., 2018). However, little is known about the quantitative impact of these genotypes as covariates on variability in the PK parameters of VPA in children with epilepsy.

The purpose of this study is to identify potential covariates (including clinical and genetic factors) that could explain the PK variability of VPA within the Chinese pediatric population, and to establish mathematical modeling reflecting these covariates using the nonlinear mixed-effects modeling (NONMEM) method. It is expected that this PPK model can provide information in the clinic for the individualization of VPA dosage in epileptic children.

2 Materials and methods

2.1 Patients and data collection

All the patients were diagnosed with definitely characterized epilepsy or epileptic syndrome by two independent neurologic clinicians on the basis of the latest version of ILAE commission's classification criterion (Scheffer et al., 2017). Serum samples for VPA trough concentration determination at a steady-state were collected retrospectively from pediatric patients with epilepsy in Baoan Women's and Children's Hospital (Shenzhen, China) from September 2016 to January 2022. VPA was administered orally two to three times a day in the forms of syrup (Depakine, Hangzhou Sanofi Minsheng Pharmaceutical Co. Ltd., Hangzhou, China) or conventional tablets (Hunan Xiangzhong Pharmaceutical Co. Ltd., Hunan, China).

The children with epilepsy aged <16 years old who received VPA alone or in combination with other AEDs were included in this study. Those with a history of pseudo-epileptic seizure, impaired hepatic and/or renal function, or the existence of any diseases which presented gastrointestinal symptoms similar to side effects induced by antiepileptic drugs were excluded. Comprehensive demographic information was collected for the patients at the time of enrollment in the study, including age, weight, sex, VPA dosage regimen details (dose, dosing time, and frequency), VPA total serum concentrations and concurrent medications.

The study was approved by the Baoan Women's and Children's Hospital Ethics Committee (Appr. Number LLSC 2020-10-06-KS, date of approval: 25 September 2020) and performed in accordance with the Declaration of Helsinki and its amendments. Written informed consents were obtained from all patients' guardians.

2.2 Analysis of VPA in serum samples

After at least 1 week of VPA stable dosing regimens, the patients were assumed to have reached steady-state serum concentrations. Given the reported diurnal variation in VPA concentrations, and trough concentration in the morning is the most stable level, so the blood samples were obtained before the morning dose (Methaneethorn, 2018). Serum concentrations of VPA were analyzed by homogeneous enzyme immune assays (Viva-E, Siemens, Erlangen, Germany; commissioned to Kingmed Diagnostics Group Co., Ltd.). The coefficients of variation within and between assays were less than 10%, and the analytic measurement range was 1–600 mg/L with 1 mg/L as the lower limit of quantification.

2.3 Genotype identification

Genomic DNA samples were extracted from 1.5 ml of whole blood. Target gene fragments of single nucleotide polymorphisms (SNPs) were amplified by the polymerase chain reaction (PCR), which was performed as detailed in our previous study (Fan et al., 2020). The following SNPs were selected for genotyping by reviewing the pharmacogenetic studies related to ABC transporters, VPA metabolism, nuclear receptors, and the efficacy of VPA treatment (Kwan et al., 2009; El-Khodary et al., 2012; Nakashima et al., 2015; Queckenberg et al., 2015; Li et al., 2016; Talwar et al., 2017; Chen et al., 2018; Margari et al., 2018; Wang et al., 2018; Xu et al., 2018; Al-Eitan et al., 2019; Chouchi et al., 2019; Shi et al., 2019; Liu et al., 2020; Makowska et al., 2021). Genotyping of all polymorphisms was carried out using Sequenom MassArray System (Agena Bioscience, San Diego, CA, United States) and iPLEX® Gold Assay. The MassArray Typer 4.0 software was used for data acquisition and analysis. All SNPs were calculated to confirm if they were in Hardy–Weinberg equilibrium.

2.4 Population pharmacokinetic model development

The PPK model of VPA for pediatric patients was established using non-linear mixed effect modeling software, NONMEM® program (version 7.5, ICON Development Solutions, Ellicott City, MD, United States), to describe the relationship between

TABLE 1 A summary of demographic information in children with epilepsy.

Characteristics	Values
Number of patients/VPA samplings	103/376
Male/Female	56/47
Age (years)	5.30 ± 3.39 (0.5–15)
Weight (kg)	19.9 ± 10.6 (6.5–52.0)
VPA daily dose (mg/kg/day)	23.8 ± 5.7 (9.9–45.7)
VPA concentration (mg/L)	60.54 ± 19.32 (14.67–110.99)
Co-medicated drugs, <i>n</i> (%)	
Levetiracetam	52 (13.83%)
Oxcarbazepine	42 (11.17%)
Topiramate	16 (4.26%)
Clonazepam	14 (3.72%)
Phenobarbital	12 (3.19%)
Midazolam	10 (2.66%)
Ibuprofen	6 (1.6%)

VPA serum concentrations and time data and to conduct model-based simulations. The output visualizations and the model evaluations were performed in the R programming environment (version 4.1, <http://www.r-project.org>) and Pirana[®] (version 3.0, <http://www.pirana-software.com>). The first-order conditional estimation method with interaction (FOCE-I) was used to estimate the PK pharmacokinetic parameters and their variability.

2.4.1 Base model

Based on previous reports, the VPA concentration-time data were fitted by a one-compartment model with first-order absorption and elimination (Ding et al., 2015). NONMEM subroutines were specified as ADVAN2-TRANS2. Since the majority of the data collected were trough concentration measurements, there is no information to identify the absorption rate constant (K_a). A previous study has shown that the k_a had no significant impact on clearance estimates (Byon et al., 2013). Therefore, K_a was fixed at 1.9 h^{-1} , in accordance with the references (Ding et al., 2015). Moreover, as bioavailability could not be determined either, clearance (CL) and the volume of distribution (V) were regarded as the apparent clearance (CL/F) and apparent distribution volume (V/F), respectively. The inter-individual variability was evaluated on PK parameters using an exponential model. Additive, proportional and combined error models were investigated to describe the residual variability.

2.4.2 Covariate model

The covariate models were developed using a stepwise forward/backward approach. After the construction of the base model, the continuous covariates (AGE, WT, VPA daily

dose) and categorical covariates (SEX, concurrent medications and genotype) were used to establish a stepwise full regression model in the form of linear, power, exponential and piecewise model. As most concentrations collected in this study were trough concentrations, the covariates were investigated only for the CL/F. Covariates included in the model were first identified using graphical methods. Co-medications administered with a proportion of more than 2.5% of the sample were evaluated including levetiracetam (LEV), oxcarbazepine (OXC), topiramate (TPM), clonazepam (CNZ), phenobarbital (PB), and midazolam (MDZL). Polymorphisms of 15 candidate genes were tested for their impacts on VPA CL/F by categorizing patients into genotypic groups (wild type, heterozygous mutation, and homozygous mutation).

During the process of stepwise forward inclusion and backward elimination, criterion for the selection of a model was when the objective function value (OFV) changed at least 3.84 units ($\Delta\text{OFV} > 3.84$) between the two nested models ($p < 0.05$, $\text{df} = 1$), and the covariate was considered to have a significant effect. The differences in OFV, Akaike Information Criterion (AIC), Bayesian Information Criterion (BIC), and parameter estimates rationality of each model were comprehensively compared to select the optimal model. Models with lower AICs and BICs were considered superior. This process was continued until no further change in the OFV was observed (Byon et al., 2013).

2.5 Model evaluation

The appropriateness and stability between the base model and the final model was first evaluated by visual inspection of goodness-of-fit (GOF) plots. GOF diagnostic scatter plots are as follows: observed (DV) vs. predicted concentrations, conditional weighted residual errors (CWRES) vs. time or predicted concentrations. In addition, visual predictive checks (VPC) with 1,000 simulation data sets was performed for the predictive performance of final model, and the 5th, 50th, and 95th percentile of the observations and 95% confidence interval (95% CI) of simulated concentrations were plotted verse time. Furthermore, a bootstrap resampling method (1,000 runs) was applied to calculate the median and 95% CI of parameters, and these values were then compared with the estimated values obtained from the final model so as to assess the robustness and accuracy simultaneously.

2.6 Simulation of dosing regimen

Probability of target attainment (PTA) table was generated by performing Monte Carlo simulations ($n = 10,000$) using the final model. The steady-state trough concentration of VPA was investigated and the goal was to have VPA concentrations within

TABLE 2 Genotype frequencies of selected variants in 103 patients.

Genetic polymorphisms	Genotypes	Values(<i>n</i>)	Frequency(%)	HWE(<i>P</i> -value)
<i>ABCB1</i>				
rs3789243	AA/AG/GG	14/50/39	13%/49%/38%	0.748
rs1128503	AA/AG/GG	42/51/10	41%/50%/9%	0.329
<i>ABCC2</i>				
rs2273697	GG/GA/AA	88/14/1	85%/14%/1%	0.603
<i>CYP1A1</i>				
rs2606345	CC/CA/AA	96/7/0	93%/7%/0%	0.721
<i>CYP2C9</i>				
rs1057910	AA/AC/CC	96/6/1	93%/6%/1%	0.026
<i>LEPR</i>				
rs1137101	AA/AG/GG	2/19/82	2%/18%/80%	0.477
<i>MTHFR</i>				
rs1801133	GG/GA/AA	51/35/17	50%/34%/16%	0.016
rs1801131	TT/TG/GG	67/31/5	65%/30%/5%	0.57
<i>SCN1A</i>				
rs6732655	AA/AT/TT	4/97/2	4%/94%/2%	0
rs6730344	CC/CA/AA	74/26/3	72%/25%/3%	0.699
rs10167228	TT/TA/AA	1/17/85	1%/16%/83%	0.884
rs3812718	CC/CT/TT	17/47/39	16%/46%/38%	0.657
rs2298771	CC/CT/TT	1/18/84	1%/17%/82%	0.974
<i>SCN2A</i>				
rs2304016	AA/AG/GG	82/20/1	80%/19%/1%	0.857
rs17183814	GG/GA/AA	73/28/2	71%/27%/2%	0.715

p > 0.05 represents that the distribution of genotype follows Hardy-Weinberg equilibrium.

50–100 mg/L. Dosing regimens at 15–35 mg/kg/day every 12 h administered orally were considered for determination of initial therapeutic VPA dose. Virtual patients were divided into different subgroups on the basis of the incorporated covariates, and PTA at least 70% probability was considered to be clinically acceptable. In children, VPA dose was mainly depended on the body weight. Therefore, WT of 10–40 kg was constructed for typical pediatric patients based on the China National Survey of Body Weight for children (Li et al., 2009), as we had few patients >40 kg in our cohort (*n* = 8). Simulations were conducted for different WT subgroups to determine the most appropriate scheme to meet the therapeutic criteria. The dose regimens were then compared with those from other PPK studies.

3 Results

3.1 Patient demographic data and genotyping

A total of 376 steady-state trough concentrations (range, 14.67–110.99 mg/L) obtained from 103 pediatric patients (47 females and 56 males) with epilepsy were included in the

final analysis. Table 1 shows the main demographic characteristics of the patients along with concomitant medications. VPA was administered orally two to three times daily, and co-prescribed medications in this population mainly included levetiracetam and oxcarbazepine. Genetic testing was also performed for all 103 patients. The genotype with allele frequencies is illustrated in Table 2. The deviations from Hardy-Weinberg equilibriums for the selected SNPs were assessed using the chi-square test, and 12 genotypes were found to conform to the equilibrium (*p* > 0.05), while *CYP2C9* rs1057910, *MTHFR* rs1801133, *SCN1A* rs6732655 significantly deviated from Hardy-Weinberg proportions (*p* < 0.05) and were excluded in the covariate model development.

3.2 Population pharmacokinetic model development

An additive error model describing residual variability with the lowest AIC and BIC was selected, according to the distribution of residuals in the diagnostic plots of the base model. As only steady-state trough serum concentrations were collected, the relative standard error (RSE) of the inter-individual variability (IIV) for

TABLE 3 Results of hypothesis testing in the model development procedure.

Model no.	Model description	OFV	Δ OFV	P-value
Forward inclusion 1				
1	Base model	2595.456		
2	Add WT on CL/F in Model 1	2435.963	-159.493	<0.001
3	Add AGE on CL/F in Model 1	2417.706	-177.750	<0.001
4	Add TDD on CL/F in Model 1	2595.416	-0.040	NS
5	Add SEX on CL/F in Model 1	2595.347	-0.109	NS
6	Add LEV on CL/F in Model 1	2595.468	0.012	NS
7	Add OXC on CL/F in Model 1	2593.070	-2.386	NS
8	Add TPM on CL/F in Model 1	2593.728	-1.728	NS
9	Add CNZ on CL/F in Model 1	2591.536	-3.920	<0.05
10	Add PB on CL/F in Model 1	2595.455	-0.001	NS
11	Add MDZL on CL/F in Model 1	2591.975	-3.481	NS
12	Add <i>ABCB1</i> rs3789243 on CL/F in Model 1	2586.368	-9.088	<0.01
13	Add <i>ABCB1</i> rs1128503 on CL/F in Model 1	2589.456	-6.000	<0.05
14	Add <i>ABCC2</i> rs2273697 on CL/F in Model 1	2594.987	-0.469	NS
15	Add <i>CYP1A1</i> rs2606345 on CL/F in Model 1	2594.706	-0.750	NS
16	Add <i>LEPR</i> rs1137101 on CL/F in Model 1	2592.391	-3.065	NS
17	Add <i>MTHFR</i> rs1801131 on CL/F in Model 1	2595.074	-0.382	NS
18	Add <i>SCN1A</i> rs6730344 on CL/F in Model 1	2593.524	-1.932	NS
19	Add <i>SCN1A</i> rs10167228 on CL/F in Model 1	2594.216	-1.240	NS
20	Add <i>SCN1A</i> rs3812718 on CL/F in Model 1	2587.310	-8.146	<0.01
21	Add <i>SCN1A</i> rs2298771 on CL/F in Model 1	2593.886	-1.570	NS
22	Add <i>SCN2A</i> rs2304016 on CL/F in Model 1	2592.423	-3.033	NS
23	Add <i>SCN2A</i> rs17183814 on CL/F in Model 1	2594.704	-0.752	NS
Forward inclusion 2				
24	Add CNZ on CL/F in Model 3	2413.940	-3.766	NS
25	Add <i>ABCB1</i> rs3789243 on CL/F in Model 3	2408.473	-9.233	<0.01
26	Add <i>ABCB1</i> rs1128503 on CL/F in Model 3	2415.917	-1.789	NS
27	Add <i>SCN1A</i> rs3812718 on CL/F in Model 3	2415.719	-1.987	NS
Backward elimination				
28	Remove AGE on CL/F from Model 25	2586.368	177.895	<0.001
29	Remove <i>ABCB1</i> rs3789243 on CL/F from Model 25	2417.706	9.233	<0.01

WT, weight; TDD, VPA total daily dose; LEV, levetiracetam; OXC, oxcarbazepine; TPM, topiramate; CNZ, clonazepam; PB, phenobarbital; MDZL, midazolam.

V/F was poor and then removed from the model building process. Furthermore, none of the tested covariates could significantly influence V/F. The population typical value of CL/F and V/F in the base model was 0.205 L/h and 3.43 L, respectively.

The changes of OFV value in the covariate screening process are listed in Table 3. Only 1.6% of the population had concomitant administration of ibuprofen and thus was not included as a covariate. A total of 12 SNPs were selected to test the impact of genetic factors on the CL/F of VPA in children with epilepsy. In the first forward inclusion, clonazepam decreased the OFV by 3.920 ($p < 0.05$). *ABCB1* rs1128503 and *SCN1A* rs3812718 dropped the OFV value from 2595.456 to 2589.456 and 2587.310, respectively ($p < 0.05$). However, there was no significant difference for the above three covariates in the second inclusion. Age and *ABCB1*

rs3789243 were identified as significant covariates on the CL/F and retained in the final model followed by forward inclusion and backward elimination. Further incorporation of other covariates did not improve the fitting performance of the model to the observed data.

Minimization and the covariance step were successful for the final model. Table 4 lists the estimate, RSE, IIV, and residual variability (RV) of the parameters for the base model, final model, and bootstrap validation. These estimates demonstrated an acceptable precision (RSE% < 30%). In the final model, the IIV-shrinkage and RV-shrinkage was 13.0% and 5.9%, respectively. The typical value of CL/F and V/F was 0.214 L/h and 3.63 L, respectively. The final model was listed below:

TABLE 4 PPK parameter estimates from the final model and bootstrap validation.

Description	Parameter	Base model		Final model		Bootstrap ^a		Relative error (%) ^b
		Estimate	RSE (%)	Estimate	RSE (%)	Median	95% CI	
CL/F (L/h)	θ_{CL}	0.205	7.4	0.214	7.4	0.207	0.136–0.245	–3.3
V/F (L)	θ_V	3.43	22.7	3.63	23.8	3.57	1.07–6.14	–1.7
Age on CL/F	θ_{Age}	—	—	0.357	9.6	0.349	0.243–0.423	–2.2
<i>ABCB1</i> rs3789243 AG on CL/F	$\theta_{ABCB1\ AG}$	—	—	0.953	4.7	0.955	0.872–1.06	0.2
<i>ABCB1</i> rs3789243 GG on CL/F	$\theta_{ABCB1\ GG}$	—	—	1.08	5.5	1.08	0.967–1.22	0
IV on CL/F (%)	ω_{CL}	0.302	10.9	0.169	13.0	0.167	0.106–0.42	–1.2
η -shrinkage (%)	$\eta_{shrinkage}$	5.8	—	12.1	—	—	—	—
RV (mg/L)	$\sigma_{additive}$	13.7	6.5	11.9	5.9	11.8	11.3–15.0	–0.8
ϵ -shrinkage (%)	$\epsilon_{shrinkage}$	12.9	—	11.1	—	—	—	—

CL/F, clearance; V/F, distribution volume; IV, inter-individual variability; RV, residual variability; θ , factor describing the relationship between the covariate and the clearance; ω , coefficient variation of inter-individual variability; σ , coefficient variation of residual variability; RSE(%), relative standard error (standard error/estimate \times 100%); 95%CI, 95% confidence interval.

^a995 of 1,000 bootstrap runs were successful and used to calculate the point estimates and 95%CI.

^bRelative error % = (Bootstrap median – estimate in final model)/estimate in final model \times 100%.

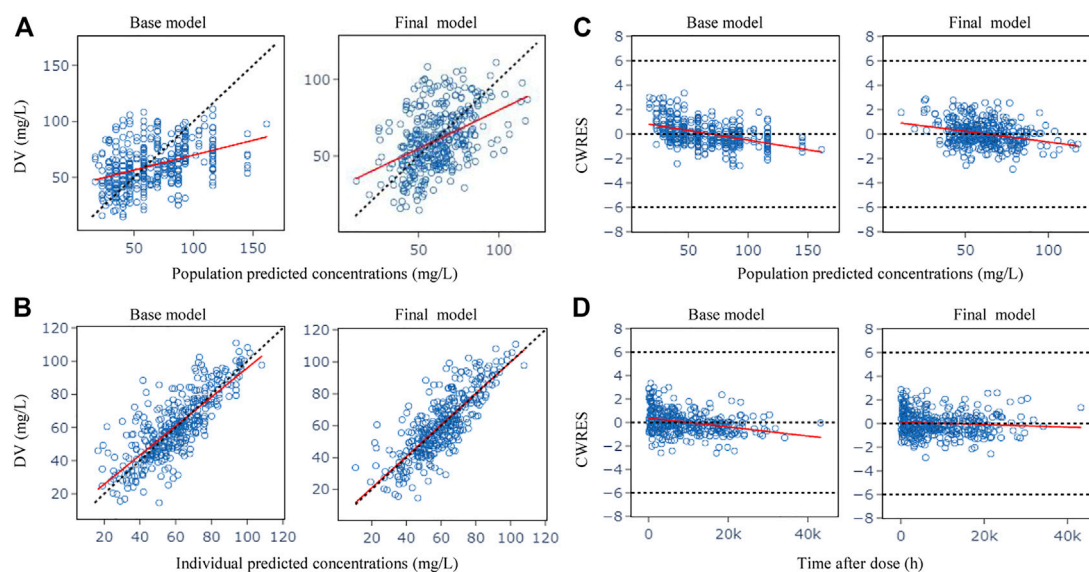


FIGURE 1

Goodness-of-fit plots for the base model and the final model. (A) Observed (DV) vs. population predicted concentrations (PRED); (B) DV vs. individual predicted concentrations (IPRED); (C) Conditional weighted residuals (CWRES) vs. PRED; (D) CWRES vs. time after dose. The red lines in the panel represent linear fit lines.

$$CL/F = 0.214 \times \left(\frac{Age}{5}\right)^{0.357} \times 0.953^{ABCB1\ AG} \times 1.08^{ABCB1\ GG} \quad (1)$$

$$V/F = 3.63 \quad (2)$$

Where *ABCB1* is the *ABCB1* rs3789243 polymorphism, *ABCB1* AG = 0, GG = 0 for patients with wild type, *ABCB1* AG = 1, GG = 0 for patients with heterozygous AG genotype, *ABCB1* GG = 1, AG = 0 for patients with homozygous GG genotype.

3.3 Model evaluation

Figure 1 shows the GOF plots obtained from the base and final model. The PRED and IPRED of the final model were evenly distributed around the reference line when plotted versus observed concentrations, this improved correlation indicated no structural bias and a good fit of the final model prediction. The CWRES showed a distribution around 0 randomly

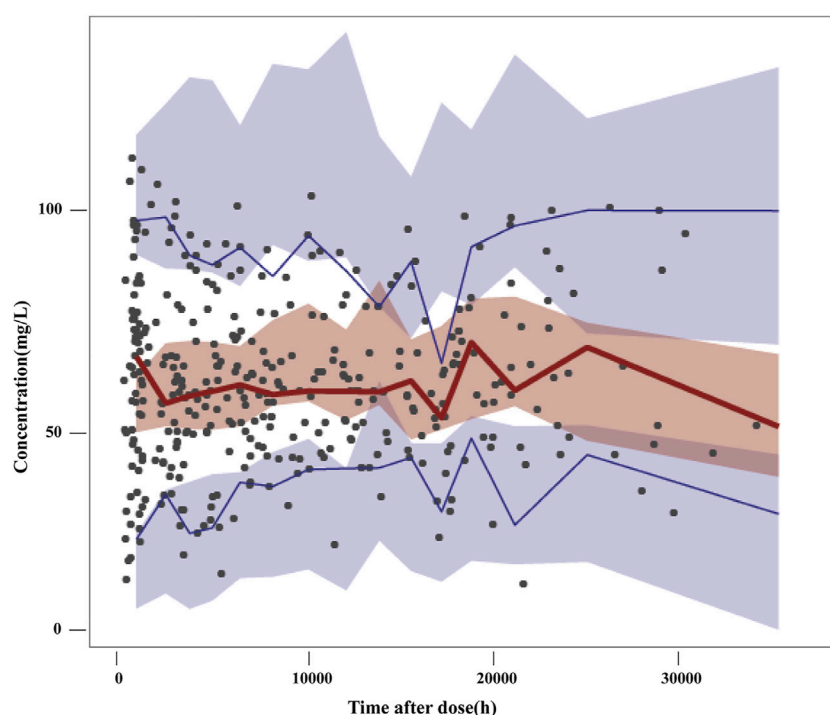


FIGURE 2

Visual predictive checks of the final model. Black dots represent the observed concentrations; the red line represents the 50th percentile of the observations; the blue lines represent the 5th and 95th percentiles of the observations. The shaded areas represent the simulation-based 95% confidence interval for each line.

within ± 2 , and the final model showed no obvious bias or significant trends compared to the base model.

The success rate (successful in minimization) of bootstrap analyses was a satisfactory result of 99.5%. The parameters observed in the final PK model were within the corresponding bootstrap 95% CI results and approximated to the median values from bootstrap with a relative error less than 3.3%, which indicated the accuracy and robustness of the final model parameter estimates (Table 4).

The VPC of the final model is presented in Figure 2. The 5th, 50th and 95th percentiles of the observations were distributed approximately within the 95%CI of the simulated concentrations for each interval. Small outlier areas in 95th percentiles slightly over-predicted had limited impact on the overall predictive ability of the model. This suggested the presence of precise predictive performance in the final model which was judged suitable to predict VPA concentrations.

3.4 Simulation of dosing regimens

The PPK parameters from the final model with two covariates (age, genotype) were used to conduct Monte Carlo simulations with the goal of obtaining VPA trough concentration within 50–100 mg/L during therapy. Patients were, therefore, classified

by age level and *ABCB1* genotype. Table 5 shows the simulation results of different dosing regimens. The results suggested that in children aged 1–4 years, a dose of at least 25 mg/kg/day VPA is required to achieve the PTA >70% target. For children older than 4 years, a smaller dose (around 20 mg/kg/day) is sufficient. In patients with the *ABCB1* rs3789243 homozygous (GG genotype) and heterozygous (AG genotype) types of the variant allele, CL/F was increased by 8% and reduced by 4.7%, respectively, compared with the AA genotype. Therefore, a higher dose was needed for patients with homozygous GG genotype within the same age. Taking typical patients aged 2–3 years as an example, the recommended VPA daily dose for a child with GG genotype is 30 mg/kg/day, and 25 mg/kg/day for other genotypes.

The simulation results of predicted VPA trough concentrations for the typical weight of 10–40 kg in children are presented in Figure 3, and the dosage regimens recommended by the other established model are displayed in Table 6. The VPA concentrations were higher with increasing body weight at the same dosage. In order to achieve the target therapeutic concentrations (50–100 mg/L), a dosing regimen of 20–30 mg/kg twice daily (bid) was required for simulated subjects with a bodyweight of 10–40 kg. Moreover, Figure 3 shows an overdose of 40 mg/kg/day in children weighing >20 kg. VPA predicted trough concentrations in excess of 100 mg/L indicate a possibly increased risk of toxicity.

TABLE 5 Probability of target attainment for various predicted valproic acid daily dose using the final model.

Dose (mg/kg/day)		AGE (year)						
		1–2 (%)	2–3 (%)	3–4 (%)	4–6 (%)	6–8 (%)	8–10 (%)	10–12 (%)
ABCB1 rs3789243 AG	15	21.86	26.17	32.77	45.32	59.71	70.36	73.89
	20	78.80	76.77	77.75	83.3	83.23	71.60	55.89
	25	96.58	97.99	96.56	81.98	63.25	48.59	33.29
	30	78.14	73.83	67.23	54.68	40.29	29.63	15.26
	35	45.17	45.84	42.79	33.68	22.53	13.41	3.95
ABCB1 rs3789243 AA	15	14.76	17.61	26.17	38.00	53.41	64.82	70.56
	20	70.11	67.92	69.04	74.77	80.24	72.57	60.44
	25	95.36	96.13	96.16	83.45	67.62	54.08	39.74
	30	85.22	82.39	73.83	61.98	46.59	35.18	22.22
	35	56.36	54.47	49.82	42.25	29.24	19.25	8.60
ABCB1 rs3789243 GG	15	6.44	7.88	14.43	28.41	43.55	55.60	65.66
	20	55.96	54.69	57.69	64.54	72.46	70.36	60.70
	25	89.00	87.44	86.43	83.22	72.36	60.36	47.03
	30	92.7	91.48	85.21	70.47	56.32	44.40	30.92
	35	70.53	66.16	60.82	51.73	39.96	29.67	17.57

Percentage represents the simulated patients who achieve target steady-state trough concentrations (50–100 mg/L) given the dose mentioned. Numbers in bold font indicate the PTA is greater than 70%.

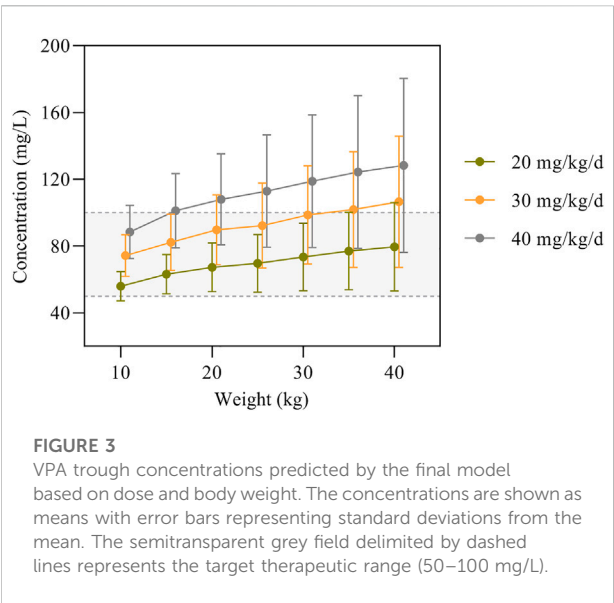


FIGURE 3 VPA trough concentrations predicted by the final model based on dose and body weight. The concentrations are shown as means with error bars representing standard deviations from the mean. The semitransparent grey field delimited by dashed lines represents the target therapeutic range (50–100 mg/L).

4 Discussion

In this study, VPA PPK modeling in 103 Chinese pediatric patients with epilepsy was constructed, where clinical and genetic factors were investigated on the PK parameters of VPA. The final model showed satisfactory predictive performance and was used

to facilitate the development of optimal dosing regimens for children. To the best of our knowledge, this is the first study to report that genetic polymorphisms of *ABCB1* have a significant effect on VPA CL/F in epileptic children.

The patient demographic characteristics, medication details and genotype were carefully documented in this analysis and used for reliable estimates of CL/F and its influential factors. During the modeling process (Table 3), the patient’s body weight and age were both found to have a significant effect on CL/F. However, the very close correlation in the children between weight and age ($r = 0.915$) requires the exclusion of one of these two variables. Age was included in the final regression model due to a greater impact on CL/F than weight.

Glucuronidation is a major pathway of VPA metabolism. The hepatic glucuronidation activities are low in infants, especially in children under 2 years old, and reach the adult levels after 10–15 years of age (Strassburg et al., 2002). VPA is metabolized more quickly in younger children, and declines gradually with age. The CL/F of VPA is similar to those of adults when the child’s weight reaches 40 kg which is the mean weight of 12-year-old children (Ogunbenro and Aarons, 2014; Methaneethorn, 2018). Thus, the age-dependent changes in the VPA CL/F of our study may partially be explained by the abundance of hepatic drug enzymes that changes significantly during growth (Kearns et al., 2003). An age-dependent exponent model was used by Ding et al. (2015) to identify the maturation

TABLE 6 Results of doses simulations from published population pharmacokinetic models in pediatric patients with epilepsy.

Author (publication year)	Country	Target concentration (mg/L)	Weight (kg)	Recommended dose (mg/kg/day)
Yukawa et al.(1997)	Japan	75	≤10	30–40
			10–20	20–30
			>10	10–20
Blanco Serrano et al.(1999)	Spain	60	12	35
			18	27
			21	25
			25	22
			32	20
			40	17
			50	16
Correa et al.(2008)	Mexico	60	10	50
			20	40
			30	35
			40	30
			50	25
			60	20
Ding et al.(2015)	China	50	8.4	14
			10	20
			15	15
			25	10
			≥30	5–10
Gu et al.(2021)	China	4–12 ^a	3.3	50
			10	50
			12.5	60
			20	50
			40	40
			60	40

^aUnbound valproic acid concentration.

processes of VPA CL/F. Furthermore, VPA is high protein binding with albumin (90%–95%). When the albumin content in the blood decreases, the CL/F value of VPA increases due to more unbound VPA (Kearns et al., 2003). The serum albumin concentration increases with age in children, suggesting CL/F of VPA decreases with increasing age (Doré et al., 2017). Albumin levels was reported to be a significant factor affecting VPA CL/F and a table of individualized medication regimens based on albumin levels was constructed by Guo et al. (2020).

Additionally, it is well known that weight is an important cause of PK variation among individuals and is related to the functionality and development of the organs responsible for drug elimination. Several studies have demonstrated that weight is an important factor influencing the PK process of VPA in children

with epilepsy (Correa et al., 2008; Ding et al., 2015; Xu et al., 2018). Notwithstanding the wide usage of the 3/4 allometric exponent method to scale CL/F (Holford et al., 2013; Back et al., 2019), the value of 0.75 remains controversial due to over-predicting CL/F for neonates and under-predicting CL/F for infants (Peeters et al., 2010). Although body weight is known to be an important factor in dosing regimens for the pediatric patient, weight-based dosing may raise concerns of adverse effects in obese children (Löscher, 2002), and the effect of age should be considered as well.

Genetic variants had been proved to influence the pharmacokinetics of VPA and contribute to its IIV, however, only a few studies calculated the PPK parameters of VPA involving genetic polymorphisms as covariates. CYP2C9 and

CYP2C19 genotypes were found to significantly affect VPA CL/F (Jiang et al., 2007; Guo et al., 2020). However, other studies indicated that none of the CYPs or UGTs gene variants affect the VPA PK (Xu et al., 2018). As metabolism by the CYP pathway is not the main route of VPA elimination, other genetic polymorphisms that might cause variations in VPA PK should be considered. CL/F in Chinese epileptic children with the *LEPR* rs1137101 variant (AG and GG genotypes) were much lower than in those with the AA genotype (17.8% and 22.6% lower, respectively) (Xu et al., 2018).

In the present study, 12 selected genes related to ABC transporters, VPA metabolism, nuclear receptors, and the efficacy of VPA treatment were included as covariates to evaluate their influence on VPA CL/F. CL/F in patients with the *ABCB1* rs3789243 GG and AG genotypes differed from those with the AA genotype (8% higher and 4.7% lower, respectively) through the PPK model development. *ABCB1* gene encodes the membrane-associated protein [P-glycoprotein (P-gp/*ABCB1*)], a member of the superfamily of ABC transporters, which limits the intracellular uptake and retention of various molecules. Membrane transporters are important determinants of drug absorption, distribution and elimination (Yee et al., 2010). ABC transporters have been reported to be associated with antiepileptic drug resistance (Kwan et al., 2009; Chen et al., 2018; Al-Eitan et al., 2019; Chouchi et al., 2019). As *ABCB1* genotypes could affect the disposition of VPA, this could explain why it leads to PK diversity of VPA between individuals. It is essential for future research to clearly clarify why heterozygous carriers and homozygous carriers showing functional consequences in two directions.

The *SCN1A* gene encodes the alpha 1 subunit of the voltage-gated Na⁺ channel and plays a crucial role in the pathogenesis of several epilepsy syndromes (Scheffer and Nabbout, 2019). *SCN1A* gene polymorphisms were found to be associated with the therapeutic effects of VPA in the treatment of epilepsy (Wang et al., 2018; Shi et al., 2019). The *SCN1A* gene polymorphisms were selected as covariates in our PPK analysis, but none of them were added to the final model.

Concomitant medications commonly found to influence VPA pharmacokinetic characteristics *in vivo* included carbamazepine, phenobarbitone and phenytoin due to their enzyme-inducing capacity (Methaneethorn, 2018). However, the effect of concomitant medications on VPA CL/F was not significant in this PPK modeling study, partly because of the limited number of subjects receiving these drugs concomitantly. In the forward inclusion, concomitant therapy with clonazepam reduced the OFV by 3.920 ($p < 0.05$), but the effect was removed from the final regression model. Yukawa et al. found that concomitant administration of clonazepam showed a 17.9% decrease in VPA CL/F among 250 Japanese patients aged 0.3–32.6 years with an unknown mechanism of interaction (Yukawa et al., 2003), but other studies have shown that VPA concentrations were not affected by clonazepam (Wang

and Wang, 2002; Zang et al., 2022). Therefore, the interactions between VPA and comedications should be further investigated.

An increase in VPA CL/F with increasing VPA total daily dose (TDD) was reported by several studies in both adult and pediatric patients (Correa et al., 2008; Nakashima et al., 2015; Methaneethorn, 2018). This could be explained by the protein binding saturation, resulting in a higher unbound fraction of VPA concentrations available for elimination and therefore higher CL/F (Kodama et al., 1992). Moreover, the TDM effects should also be considered: patients with high CL/F tend to receive a higher dosage to ensure the concentration within the therapeutic range (Ahn et al., 2005). Therefore, the dose-dependent maximum effect (DDE) model and protein binding model were found to best describe VPA data (Ding et al., 2015). In our analysis, the effect of TDD on VPA CL/F was investigated to describe the characteristics of protein binding and then found to be not significant.

Whether sex affects the CL/F of VPA is controversial in previous studies. Some studies have reported that female patients have lower CL/F of VPA because of the difference in weight between males and females (Ibarra et al., 2013; Nakashima et al., 2015). UGT activity in females lower than in males could also account for the sex-induced differences in VPA CL/F (Court, 2010). However, this finding was confirmed neither by our study, nor by other VPA PPK models (Serrano et al., 1999; Correa et al., 2008; Williams et al., 2012; Ding et al., 2015). Whether the 1:1 male to female ratio affects VPA pharmacokinetic properties should be investigated in further studies in a larger sample size.

The simulations of VPA dosing (Table 5) based on the age and *ABCB1* genotype of patients indicated that 20–25 mg/kg/day bid of VPA oral administration is sufficient to maintain PTA >70% for most patients aged 1–10 years, while the same dose to patients with GG genotype would lead to relatively lower VPA concentrations. As shown in Figure 3, the Monte Carlo simulations evidenced that dose requirements decreased as weight increased for the typical weight of 10–40 kg in children. The model-based recommended doses are 20–30 mg/kg/day in the present study with higher doses such as 40 mg/kg/day for lower weight subgroups of 10–15 kg. Current recommendations indicated a maintenance daily dose of 20–30 mg/kg for children, which is consistent with our simulation results (Braathén et al., 1988; Rodrigues et al., 2018). A summary of the dosage regimens recommended by the other established PPK mode is displayed in Table 6. Dosage regimens based on our model are similar to Ding et al. in China and lower than that of western people (Correa et al., 2008; Ding et al., 2015) because of considering the high variability of VPA concentrations (50–100 mg/L versus around 60 mg/L) in our study. Based on the inter-individual and residual variability in the model, TDM is essential for guaranteeing VPA within the concentration targets and obtaining more accurate estimations with the

Bayesian method as a basis for appropriate dosage adjustments.

Only a relatively small sample size was used in this study, which may result in non-significant differences on the included covariates. The predictive capacity of the final model was not evaluated by external validation, as data with genetic polymorphism could not be obtained from routine clinical information of patients. Moreover, actual clinical practice of the developed model and data on pharmacodynamics (PD) is lacking. Therefore, a further multicenter study with an increased sample size is needed to explore the PPK/PD model of VPA to determine the recommended therapeutic concentration for pediatric population with epilepsy and to verify the role of genetic factors on VPA PPK.

5 Conclusion

In this study, a novel PPK model enrolled Chinese pediatric patients with epilepsy for VPA was developed and proved to be stable with acceptable predictive performance. To the best of our knowledge, this study is the first to report that *ABCB1* genetic polymorphisms were identified as effective covariates for the CL/F of VPA. These findings contribute to a better understanding of the IIV in VPA PK, and a table of individualized medication regimens in consideration of the age and genotype was constructed to improve the therapeutic effect of VPA.

Data availability statement

The original contributions presented in the study are included in the article/supplementary material, further inquiries can be directed to the corresponding author.

Ethics statement

The studies involving human participants were reviewed and approved by the Baoan Women's and Children's Hospital Ethics Committee (Appr. Number LLSC 2020-10-06-KS). Written informed consent to participate in this study was provided by the participant's; legal guardian/next of kin.

References

Ahn, J. E., Birnbaum, A. K., and Brundage, R. C. (2005). Inherent correlation between dose and clearance in therapeutic drug monitoring settings: Possible misinterpretation in population pharmacokinetic analyses. *J. Pharmacokinet. Pharmacodyn.* 32, 703–718. doi:10.1007/s10928-005-0083-6

Al-Eitan, L. N., Al-Dalalah, I. M., Mustafa, M. M., Alghamdi, M. A., Elshammari, A. K., Khreisat, W. H., et al. (2019). Effects of MTHFR and ABCC2 gene polymorphisms on antiepileptic drug responsiveness in Jordanian epileptic patients. *Pharmacogenomics. Pers. Med.* 12, 87–95. doi:10.2147/PGPM.S211490

Author contributions

XS and XC performed the population pharmacokinetics analysis and drafted the manuscript. JL and QC managed the literature searches and participated in patient enrollment. WL undertook the data analysis and manuscript preparation. JZ and YH collected the blood samples, and HG and CX organized the database. XF designed the pharmacokinetic study and participated in manuscript revision. All authors reviewed the analysis and manuscript.

Funding

This work was supported by the National Natural Science Foundation of China (Grant Number. 81603185) and the Natural Science Foundation of Guangdong province (Grant Number. 2020A1515011452).

Acknowledgments

The authors would like to thank the patients who participated in this study, as well as all investigators and the medical, nursing and laboratory staff who were involved in the present work.

Conflict of interest

The authors declare that the research was conducted in the absence of any commercial or financial relationships that could be construed as a potential conflict of interest.

Publisher's note

All claims expressed in this article are solely those of the authors and do not necessarily represent those of their affiliated organizations, or those of the publisher, the editors and the reviewers. Any product that may be evaluated in this article, or claim that may be made by its manufacturer, is not guaranteed or endorsed by the publisher.

Back, H. M., Lee, J. B., Han, N., Goo, S., Jung, E., Kim, J., et al. (2019). Application of size and maturation functions to population pharmacokinetic modeling of pediatric patients. *Pharmaceutics* 11, 259. doi:10.3390/pharmaceutics11060259

Berg, A. T., Langfitt, J. T., Testa, F. M., Levy, S. R., Dimario, F., Westerveld, M., et al. (2008). Global cognitive function in children with epilepsy: A community-based study. *Epilepsia* 49, 608–614. doi:10.1111/j.1528-1167.2007.01461.x

- Botha, J. H., Gray, A. L., and Miller, R. (1995). A model for estimating individualized valproate clearance values in children. *J. Clin. Pharmacol.* 35, 1020–1024. doi:10.1002/j.1552-4604.1995.tb04020.x
- Braathén, G., Theorell, K., Persson, A., and Rane, A. (1988). Valproate in the treatment of absence epilepsy in children: A study of dose-response relationships. *Epilepsia* 29, 548–552. doi:10.1111/j.1528-1157.1988.tb03759.x
- Byon, W., Smith, M. K., Chan, P., Tortorici, M. A., Riley, S., Dai, H., et al. (2013). Establishing best practices and guidance in population modeling: An experience with an internal population pharmacokinetic analysis guidance. *CPT. Pharmacometrics Syst. Pharmacol.* 2, e51. doi:10.1038/psp.2013.26
- Chen, J., Su, Q. B., Tao, Y. Q., Qin, J. M., Zhou, Y., Zhou, S., et al. (2018). ABC2 rs2273697 is associated with valproic acid concentrations in patients with epilepsy on valproic acid monotherapy. *Pharmazie* 73, 279–282. doi:10.1691/ph.2018.7344
- Chouchi, M., Klau, H., Ben-Youssef Turki, I., and Hila, L. (2019). ABCB1 polymorphisms and drug-resistant epilepsy in a Tunisian population. *Dis. Markers* 2019, 1343650. doi:10.1155/2019/1343650
- Correa, T., Rodríguez, I., and Romano, S. (2008). Population pharmacokinetics of valproate in Mexican children with epilepsy. *Biopharm. Drug Dispos.* 29, 511–520. doi:10.1002/bdd.636
- Court, M. H. (2010). Interindividual variability in hepatic drug glucuronidation: Studies into the role of age, sex, enzyme inducers, and genetic polymorphism using the human liver bank as a model system. *Drug Metab. Rev.* 42, 209–224. doi:10.3109/03602530903209288
- Darwich, A. S., Polasek, T. M., Aronson, J. K., Ogungbenro, K., Wright, D. F. B., Achour, B., et al. (2021). Model-informed precision dosing: Background, requirements, validation, implementation, and forward trajectory of individualizing drug therapy. *Annu. Rev. Pharmacol. Toxicol.* 61, 225–245. doi:10.1146/annurev-pharmtox-033020-113257
- Devinsky, O., Vezzani, A., O'Brien, T. J., Jette, N., Scheffer, I. E., De Curtis, M., et al. (2018). Epilepsy. *Nat. Rev. Dis. Prim.* 4, 18024. doi:10.1038/nrdp.2018.24
- Ding, J., Wang, Y., Lin, W., Wang, C., Zhao, L., Li, X., et al. (2015). A population pharmacokinetic model of valproic acid in pediatric patients with epilepsy: A non-linear pharmacokinetic model based on protein-binding saturation. *Clin. Pharmacokinet.* 54, 305–317. doi:10.1007/s40262-014-0212-8
- Doré, M., San Juan, A. E., Frenette, A. J., and Williamson, D. (2017). Clinical importance of monitoring unbound valproic acid concentration in patients with hypoalbuminemia. *Pharmacotherapy* 37, 900–907. doi:10.1002/phar.1965
- El-Khodary, N. M., El-Haggag, S. M., Eid, M. A., and Ebeid, E. N. (2012). Study of the pharmacokinetic and pharmacogenetic contribution to the toxicity of high-dose methotrexate in children with acute lymphoblastic leukemia. *Med. Oncol.* 29, 2053–2062. doi:10.1007/s12032-011-9997-6
- Fan, X., Chen, Y., Li, W., Xia, H., Liu, B., Guo, H., et al. (2020). Genetic polymorphism of ADORA2A is associated with the risk of epilepsy and predisposition to neurologic comorbidity in Chinese southern children. *Front. Neurosci.* 14, 590605. doi:10.3389/fnins.2020.590605
- Ferraro, T. N., and Buono, R. J. (2005). The relationship between the pharmacology of antiepileptic drugs and human gene variation: An overview. *Epilepsy Behav.* 7, 18–36. doi:10.1016/j.yebeh.2005.04.010
- Ghodke-Puranik, Y., Thorn, C. F., Lamba, J. K., Leeder, J. S., Song, W., Birnbaum, A. K., et al. (2013). Valproic acid pathway: Pharmacokinetics and pharmacodynamics. *Pharmacogenet. Genomics* 23, 236–241. doi:10.1097/FPC.0b013e32835ea0b2
- Glauser, T., Ben-Menachem, E., Bourgeois, B., Cnaan, A., Guerreiro, C., Kälviäinen, R., et al. (2013). Updated ILAE evidence review of antiepileptic drug efficacy and effectiveness as initial monotherapy for epileptic seizures and syndromes. *Epilepsia* 54, 551–563. doi:10.1111/epi.12074
- Guo, J., Huo, Y., Li, F., Li, Y., Guo, Z., Han, H., et al. (2020). Impact of gender, albumin, and CYP2C19 polymorphisms on valproic acid in Chinese patients: A population pharmacokinetic model. *J. Int. Med. Res.* 48, 300060520952281. doi:10.1177/0300060520952281
- Hiemke, C., Bergemann, N., Clement, H. W., Conca, A., Deckert, J., Domschke, K., et al. (2018). Consensus guidelines for therapeutic drug monitoring in neuropsychopharmacology: Update 2017. *Pharmacopsychiatry* 51, e1–e62. doi:10.1055/s-0037-1600991
- Holford, N., Heo, Y. A., and Anderson, B. (2013). A pharmacokinetic standard for babies and adults. *J. Pharm. Sci.* 102, 2941–2952. doi:10.1002/jps.23574
- Ibarra, M., Vázquez, M., Fagiolino, P., and Derendorf, H. (2013). Sex related differences on valproic acid pharmacokinetics after oral single dose. *J. Pharmacokinet. Pharmacodyn.* 40, 479–486. doi:10.1007/s10928-013-9323-3
- Jiang, D. C., Wang, L., Wang, Y. Q., Li, L., Lu, W., and Bai, X. R. (2007). Population pharmacokinetics of valproate in Chinese children with epilepsy. *Acta Pharmacol. Sin.* 28, 1677–1684. doi:10.1111/j.1745-7254.2007.00704.x
- Johannessen, C. U., and Johannessen, S. I. (2003). Valproate: Past, present, and future. *CNS Drug Rev.* 9, 199–216. doi:10.1111/j.1527-3458.2003.tb00249.x
- Kearns, G. L., Abdel-Rahman, S. M., Alander, S. W., Blowey, D. L., Leeder, J. S., and Kauffman, R. E. (2003). Developmental pharmacology--drug disposition, action, and therapy in infants and children. *N. Engl. J. Med.* 349, 1157–1167. doi:10.1056/NEJMra035092
- Kiang, T. K., Sherwin, C. M., Spigarelli, M. G., and Ensom, M. H. (2012). Fundamentals of population pharmacokinetic modelling: Modelling and software. *Clin. Pharmacokinet.* 51, 515–525. doi:10.2165/11634080-000000000-00000
- Kodama, Y., Koike, Y., Kimoto, H., Yasunaga, F., Takeyama, M., Teraoka, I., et al. (1992). Binding parameters of valproic acid to serum protein in healthy adults at steady state. *Ther. Drug Monit.* 14, 55–60. doi:10.1097/00007691-199202000-00009
- Kwan, P., Wong, V., Ng, P. W., Lui, C. H., Sin, N. C., Poon, W. S., et al. (2009). Gene-wide tagging study of association between ABCB1 polymorphisms and multidrug resistance in epilepsy in Han Chinese. *Pharmacogenomics* 10, 723–732. doi:10.2217/pgs.09.32
- Li, H., Ji, C. Y., Zong, X. N., and Zhang, Y. Q. (2009). Height and weight standardized growth charts for Chinese children and adolescents aged 0 to 18 years. *Zhonghua Er Ke Za Zhi* 47, 487–492.
- Li, X., Zhang, J., Wu, X., Yan, H., Zhang, Y., He, R. H., et al. (2016). Polymorphisms of ABAT, SCN2A and ALDH5A1 may affect valproic acid responses in the treatment of epilepsy in Chinese. *Pharmacogenomics* 17, 2007–2014. doi:10.2217/pgs-2016-0093
- Liu, M., Mao, J., Xu, H., Wang, J., Zhao, P., Xu, Q., et al. (2020). Effects of SCN1A and SCN2A polymorphisms on responsiveness to valproic acid monotherapy in epileptic children. *Epilepsy Res.* 168, 106485. doi:10.1016/j.eplepsyres.2020.106485
- Löscher, W. (2002). Basic pharmacology of valproate: A review after 35 years of clinical use for the treatment of epilepsy. *CNS Drugs* 16, 669–694. doi:10.2165/00023210-200216100-00003
- Löscher, W., Potschka, H., Sisodiya, S. M., and Vezzani, A. (2020). Drug resistance in epilepsy: Clinical impact, potential mechanisms, and new innovative treatment options. *Pharmacol. Rev.* 72, 606–638. doi:10.1124/pr.120.019539
- Mac, T. L., Tran, D. S., Quet, F., Odermatt, P., Preux, P. M., and Tan, C. T. (2007). Epidemiology, aetiology, and clinical management of epilepsy in asia: A systematic review. *Lancet. Neurol.* 6, 533–543. doi:10.1016/S1474-4422(07)70127-8
- Makowska, M., Smolarz, B., Bryś, M., Forma, E., and Romanowicz, H. (2021). An association between the rs1799853 and rs1057910 polymorphisms of CYP2C9, the rs4244285 polymorphism of CYP2C19 and the prevalence rates of drug-resistant epilepsy in children. *Int. J. Neurosci.* 131, 1147–1154. doi:10.1080/00207454.2020.1781110
- Margari, L., Legrottaglie, A. R., Vincenti, A., Coppola, G., Operto, F. F., Buttiglione, M., et al. (2018). Association between SCN1A gene polymorphisms and drug resistant epilepsy in pediatric patients. *Seizure* 55, 30–35. doi:10.1016/j.seizure.2018.01.002
- Mei, S., Feng, W., Zhu, L., Li, X., Yu, Y., Yang, W., et al. (2018). Effect of CYP2C19, UGT1A8, and UGT2B7 on valproic acid clearance in children with epilepsy: A population pharmacokinetic model. *Eur. J. Clin. Pharmacol.* 74, 1029–1036. doi:10.1007/s00228-018-2440-6
- Methaneethorn, J. (2018). A systematic review of population pharmacokinetics of valproic acid. *Br. J. Clin. Pharmacol.* 84, 816–834. doi:10.1111/bcp.13510
- Nakashima, H., Oniki, K., Nishimura, M., Ogasu, N., Shimomasuda, M., Ono, T., et al. (2015). Determination of the optimal concentration of valproic acid in patients with epilepsy: A population pharmacokinetic-pharmacodynamic analysis. *PLoS One* 10, e0141266. doi:10.1371/journal.pone.0141266
- Ogungbenro, K., and Aarons, L. (2014). A physiologically based pharmacokinetic model for Valproic acid in adults and children. *Eur. J. Pharm. Sci.* 63, 45–52. doi:10.1016/j.ejps.2014.06.023
- Patsalos, P. N., Berry, D. J., Bourgeois, B. F., Cloyd, J. C., Glauser, T. A., Johannessen, S. I., et al. (2008). Antiepileptic drugs—best practice guidelines for therapeutic drug monitoring: A position paper by the subcommission on therapeutic drug monitoring, ILAE commission on therapeutic strategies. *Epilepsia* 49, 1239–1276. doi:10.1111/j.1528-1167.2008.01561.x
- Patsalos, P. N., Zugman, M., Lake, C., James, A., Ratnaraj, N., and Sander, J. W. (2017). Serum protein binding of 25 antiepileptic drugs in a routine clinical setting: A comparison of free non-protein-bound concentrations. *Epilepsia* 58, 1234–1243. doi:10.1111/epi.13802
- Peeters, M. Y., Allegaert, K., Blussé Van Oud-Alblas, H. J., Cella, M., Tibboel, D., Danhof, M., et al. (2010). Prediction of propofol clearance in children from an

allometric model developed in rats, children and adults versus a 0.75 fixed-exponent allometric model. *Clin. Pharmacokinet.* 49, 269–275. doi:10.2165/11319350-000000000-00000

Perucca, E. (2002). Pharmacological and therapeutic properties of valproate: A summary after 35 years of clinical experience. *CNS Drugs* 16, 695–714. doi:10.2165/00023210-200216100-00004

Queckenberg, C., Erlinghagen, V., Baken, B. C., Van Os, S. H., Wargenau, M., Kubeš, V., et al. (2015). Pharmacokinetics and pharmacogenetics of capecitabine and its metabolites following replicate administration of two 500 mg tablet formulations. *Cancer Chemother. Pharmacol.* 76, 1081–1091. doi:10.1007/s00280-015-2840-6

Rodrigues, C., Chhun, S., Chiron, C., Dulac, O., Rey, E., Pons, G., et al. (2018). A population pharmacokinetic model taking into account protein binding for the sustained-release granule formulation of valproic acid in children with epilepsy. *Eur. J. Clin. Pharmacol.* 74, 793–803. doi:10.1007/s00228-018-2444-2

Rogawski, M. A., and Löscher, W. (2004). The neurobiology of antiepileptic drugs. *Nat. Rev. Neurosci.* 5, 553–564. doi:10.1038/nrn1430

Scheffer, I. E., Berkovic, S., Capovilla, G., Connolly, M. B., French, J., Guilhoto, L., et al. (2017). ILAE classification of the epilepsies: Position paper of the ILAE commission for classification and terminology. *Epilepsia* 58, 512–521. doi:10.1111/epi.13709

Scheffer, I. E., and Nabbout, R. (2019). SCN1A-related phenotypes: Epilepsy and beyond. *Epilepsia* 60, S17–s24. doi:10.1111/epi.16386

Serrano, B. B., García Sánchez, M. J., Otero, M. J., Buelga, D. S., Serrano, J., and Domínguez-Gil, A. (1999). Valproate population pharmacokinetics in children. *J. Clin. Pharm. Ther.* 24, 73–80.

Shi, L., Zhu, M., Li, H., Wen, Z., Chen, X., Luo, J., et al. (2019). SCN1A and SCN2A polymorphisms are associated with response to valproic acid in Chinese epilepsy patients. *Eur. J. Clin. Pharmacol.* 75, 655–663. doi:10.1007/s00228-019-02633-0

Strassburg, C. P., Strassburg, A., Kneip, S., Barut, A., Tukey, R. H., Rodeck, B., et al. (2002). Developmental aspects of human hepatic drug glucuronidation in young children and adults. *Gut* 50, 259–265. doi:10.1136/gut.50.2.259

Talwar, P., Kanojia, N., Mahendru, S., Baghel, R., Grover, S., Arora, G., et al. (2017). Genetic contribution of CYP1A1 variant on treatment outcome in epilepsy patients: A functional and interethnic perspective. *Pharmacogenomics J.* 17, 242–251. doi:10.1038/tj.2016.1

Wang, L., and Wang, X. D. (2002). Pharmacokinetic and pharmacodynamic effects of clonazepam in children with epilepsy treated with valproate: A preliminary study. *Ther. Drug Monit.* 24, 532–536. doi:10.1097/00007691-200208000-00012

Wang, Z. J., Chen, J., Chen, H. L., Zhang, L. Y., Xu, D., and Jiang, W. T. (2018). Association between SCN1A polymorphism rs3812718 and valproic acid resistance in epilepsy children: A case-control study and meta-analysis. *Biosci. Rep.* 38, BSR20181654. doi:10.1042/BSR20181654

Williams, J. H., Jayaraman, B., Swoboda, K. J., and Barrett, J. S. (2012). Population pharmacokinetics of valproic acid in pediatric patients with epilepsy: Considerations for dosing spinal muscular atrophy patients. *J. Clin. Pharmacol.* 52, 1676–1688. doi:10.1177/0091270011428138

Xu, S., Chen, Y., Zhao, M., Guo, Y., Wang, Z., and Zhao, L. (2018). Population pharmacokinetics of valproic acid in epileptic children: Effects of clinical and genetic factors. *Eur. J. Pharm. Sci.* 122, 170–178. doi:10.1016/j.ejps.2018.06.033

Yee, S. W., Chen, L., and Giacomini, K. M. (2010). Pharmacogenomics of membrane transporters: Past, present and future. *Pharmacogenomics* 11, 475–479. doi:10.2217/pgs.10.22

Yukawa, E., Nonaka, T., Yukawa, M., Higuchi, S., Kuroda, T., and Goto, Y. (2003). Pharmacoeconomic investigation of a clonazepam-valproic acid interaction by mixed effect modeling using routine clinical pharmacokinetic data in Japanese patients. *J. Clin. Pharm. Ther.* 28, 497–504. doi:10.1046/j.1365-2710.2003.00528.x

Zang, Y. N., Guo, W., Niu, M. X., Bao, S., Wang, Q., Wang, Y., et al. (2022). Population pharmacokinetics of valproic acid in adult Chinese patients with bipolar disorder. *Eur. J. Clin. Pharmacol.* 78, 405–418. doi:10.1007/s00228-021-03246-2

Zhu, M. M., Li, H. L., Shi, L. H., Chen, X. P., Luo, J., and Zhang, Z. L. (2017). The pharmacogenomics of valproic acid. *J. Hum. Genet.* 62, 1009–1014. doi:10.1038/jhg.2017.91



OPEN ACCESS

EDITED BY

Rong Wang,
People's Liberation Army Joint Logistics
Support Force 940th Hospital, China

REVIEWED BY

Jonathan Wolf Mueller,
University of Birmingham,
United Kingdom
Xiaobo Zhong,
University of Connecticut, United States

*CORRESPONDENCE

Liewei Wang,
wang.liewei@mayo.edu

SPECIALTY SECTION

This article was submitted to Drug
Metabolism and Transport,
a section of the journal
Frontiers in Pharmacology

RECEIVED 18 September 2022

ACCEPTED 07 November 2022

PUBLISHED 28 November 2022

CITATION

Zhu X, Gao H, Qin S, Liu D, Cairns J,
Gu Y, Yu J, Weinshilboum RM and
Wang L (2022), Testis- specific Y-
encoded- like protein 1 and cholesterol
metabolism: Regulation of *CYP1B1*
expression through Wnt signaling.
Front. Pharmacol. 13:1047318.
doi: 10.3389/fphar.2022.1047318

COPYRIGHT

© 2022 Zhu, Gao, Qin, Liu, Cairns, Gu,
Yu, Weinshilboum and Wang. This is an
open-access article distributed under
the terms of the [Creative Commons
Attribution License \(CC BY\)](https://creativecommons.org/licenses/by/4.0/). The use,
distribution or reproduction in other
forums is permitted, provided the
original author(s) and the copyright
owner(s) are credited and that the
original publication in this journal is
cited, in accordance with accepted
academic practice. No use, distribution
or reproduction is permitted which does
not comply with these terms.

Testis- specific Y-encoded- like protein 1 and cholesterol metabolism: Regulation of *CYP1B1* expression through Wnt signaling

Xiujuan Zhu, Huanyao Gao, Sisi Qin, Duan Liu, Junmei Cairns,
Yayun Gu, Jia Yu, Richard M. Weinshilboum and Liewei Wang*

Department of Molecular Pharmacology and Experimental Therapeutics, Mayo Clinic, Rochester, MN, United States

The cytochromes P450 (CYPs) represent a large gene superfamily that plays an important role in the metabolism of both exogenous and endogenous compounds. We have reported that the testis-specific Y-encoded-like proteins (TSPYLs) are novel *CYP* gene transcriptional regulators. However, little is known of mechanism(s) by which TSPYLs regulate *CYP* expression or the functional consequences of that regulation. The *TSPYL* gene family includes six members, *TSPYL1* to *TSPYL6*. However, *TSPYL3* is a pseudogene, *TSPYL5* is only known to regulate the expression of *CYP19A1*, and *TSPYL6* is expressed exclusively in the testis. Therefore, *TSPYL1*, 2 and 4 were included in the present study. To better understand how *TSPYL1*, 2, and 4 might influence *CYP* expression, we performed a series of pull-downs and mass spectrometric analyses. Panther pathway analysis of the 2272 pulled down proteins for all 3 *TSPYL* isoforms showed that the top five pathways were the Wnt signaling pathway, the Integrin signaling pathway, the Gonadotropin releasing hormone receptor pathway, the Angiogenesis pathway and Inflammation mediated by chemokines and cytokines. Specifically, we observed that 177 Wnt signaling pathway proteins were pulled down with the TSPYLs. Subsequent luciferase assays showed that *TSPYL1* knockdown had a greater effect on the activation of Wnt signaling than did *TSPYL2* or *TSPYL4* knockdown. Therefore, in subsequent experiments, we focused our attention on *TSPYL1*. HepaRG cell qRT-PCR showed that *TSPYL1* regulated the expression of CYPs involved in cholesterol-metabolism such as *CYP1B1* and *CYP7A1*. Furthermore, *TSPYL1* and β -catenin regulated *CYP1B1* expression in opposite directions and *TSPYL1* appeared to regulate *CYP1B1* expression by blocking β -catenin binding to the TCF7L2 transcription factor on the *CYP1B1* promoter. In β -catenin and *TSPYL1* double knockdown cells, *CYP1B1* expression and the generation of *CYP1B1* downstream metabolites such as 20-HETE could be restored. Finally, we observed that *TSPYL1* expression was associated with plasma cholesterol levels and BMI during previous clinical studies of obesity. In conclusion, this series of experiments has revealed a novel mechanism for regulation of the expression of cholesterol-metabolizing CYPs, particularly *CYP1B1*, by *TSPYL1* via Wnt/ β -catenin signaling, raising the possibility that

TSPYL1 might represent a molecular target for influencing cholesterol homeostasis.

KEYWORDS

TSPYL1, CYP1B1, Wnt, β -catenin, cholesterol, cell signaling, cytochrome P450, obesity

Introduction

The cytochrome P450 (CYP) superfamily consists of a group of enzymes that catalyze the metabolism of numerous endogenous and exogenous compounds including steroids, drugs, carcinogens and natural products (Nebert and Dalton, 2006; Nebert et al., 2013; Nelson et al., 2013). CYPs are expressed in a tissue-specific manner and the expression of many CYPs can be induced by xenobiotics (Esteves et al., 2021). We recently identified members of the testis-specific Y-encoded-like protein (TSPYL) gene family as novel transcription regulators that can influence CYP expression (Liu et al., 2013; Qin et al., 2018; Qin et al., 2020). The TSPYL gene family includes six members, TSPYL1 to TSPYL6. Each TSPYL gene includes a highly conserved Nucleosome Assembly Protein (NAP) domain but, otherwise, they display relatively little sequence homology (Vogel et al., 1998). NAPs help to assemble DNA and histones reversibly into chromatin, a process that is important for cell proliferation and the regulation of gene expression (Gill et al., 2022). Most TSPYL family members are expressed in all human tissues based on the Genotype-Tissue Expression (GTEx) database. However, TSPYL3 is a pseudogene and TSPYL6 is expressed exclusively in the testis. A previous large GWAS study of plasma estradiol concentrations performed by our group reported that single nucleotide polymorphisms (SNPs) in or near TSPYL5 were associated with plasma estradiol concentrations by virtue of an effect on the expression of CYP19A1—an enzyme critical for estrogen biosynthesis (Liu et al., 2013). Estradiol is synthesized from cholesterol *in vivo* through a series of reactions. CYP19A1 is the only CYP with expression that is currently known to be influenced by TSPYL5 (Qin et al., 2018). Subsequently, TSPYL1, 2 and 4 have all been reported to be involved in the regulation of CYP17A1 and CYP3A4 expression which contributes to abiraterone response in metastatic castration-resistant prostate cancer (Qin et al., 2018), and the regulation of CYP2C9 and CYP2C19 which affects the metabolism of selective serotonin reuptake inhibitors (Qin et al., 2020). We have also observed that those TSPYLs can regulate the expression of CYP1B1 and CYP7A1 (Qin et al., 2018). However, the consequence(s) of the regulation of CYP1B1 and CYP7A1 have not been explored, and molecular mechanism(s) by which TSPYLs regulate CYP expression remain unknown.

CYP1B1 metabolizes many important physiological compounds, including estrogens, arachidonic acid, melatonin and retinoids (Li et al., 2017). Hydroxyeicosatetraenoic acids

(HETEs), including 20-HETE and 12-HETE, are the major CYP1B1 arachidonic acid metabolites in humans (Choudhary et al., 2004). Clinical studies have reported elevated levels of plasma and urinary 20-HETE in disease states that include obesity and CYP1B1 knock out in mouse models has been reported to protect against obesity induced by a high-fat diet (Li et al., 2014; Larsen et al., 2015) and lack of CYP1B1 is linked to altered lipid metabolism, an association which may help protect against the negative health effects of obesity.

CYP7A1 catalyzes the initial, rate-limiting step in the bile acid biosynthetic pathway. In mammals, excess cholesterol in the liver is removed mainly by conversion to bile acids. Only a small portion of cholesterol is utilized for steroid hormone synthesis in the adrenal glands, ovaries, testes, placenta and brain. Transgenic mice overexpressing CYP7A1 are resistant to high fat diet-induced obesity, fatty liver and diabetes (Li et al., 2010). Based on this series of observations, the present study has focussed on the possible role of TSPYL1 in cholesterol biosynthesis and metabolism because, as explained subsequently, TSPYL1 displayed a greater effect on Wnt signaling than did TSPYL2 or TSPYL4. Specifically, we found that TSPYL1 interacted with proteins in the Wnt/ β -catenin signaling pathway. Wnt/ β -catenin signaling determines hepatic zonation of CYP expression (Loeppen et al., 2005; Hailfinger et al., 2006; Sekine et al., 2006; Braeuning and Schwarz, 2010) and is involved in the regulation of CYP transcription in response to exposure to xenobiotic agonists for a number of nuclear receptors (Braeuning et al., 2009; Ganzenberg et al., 2013; Vaas et al., 2014). Specifically, β -catenin is a downstream target of Wnt signaling (Kimelman and Xu, 2006). In the nucleus, β -catenin binds to transcriptional activators of the T-cell factor/lymphoid-enhancing factor (TCF/LEF) family to activate the transcription of Wnt signaling target genes.

Wnt/ β -catenin signaling plays an important role in obesity (Wang et al., 2013) as does the TCF/LEF family. This family of transcription factors includes TCF7, LEF1, TCF7L1, and TCF7L2. As described subsequently, we found that both TCF7 and TCF7L2 were also pulled down with TSPYLs (see Supplementary Table S1). Genetic polymorphisms in the TCF7L2 gene have been associated with obesity and increased BMI (Cauchi et al., 2008; Haupt et al., 2010). Although the regulation of CYPs by Wnt/ β -catenin signaling and by TSPYL1 were known, potential interaction of β -catenin with TSPYL1 had not previously been described. Therefore, included among the goals of the present study was a determination of whether Wnt/ β -catenin signaling had an effect on the regulation

of CYP expression by TSPYL1 in human hepatic cell lines. We hypothesized that TSPYL1 might regulate CYP expression through interaction with the Wnt/ β -catenin signaling pathway. Our results—as described subsequently—demonstrated that TSPYL1 can compete with TCF7L2 for binding to β -catenin, reducing Wnt/ β -catenin activity. Taken together, these results suggest that variation in TSPYL1 expression, Wnt/ β -catenin signaling and CYP expression may all contribute to risk for or variation in response to the treatment of obesity.

Materials and methods

Cell culture and transfection

Undifferentiated HepaRG human hepatic cells (HPR101) were obtained from Biopredict (Rennes, France) and were cultured and differentiated into fully functional hepatocyte-like cells according to the manufacture's protocol. HPR101 cells were grown in William's E media (Gibco, Grand Island, NY) supplemented with $\times 1$ GlutaMAX (Gibco, Grand Island, NY) and 10% HepaRG Growth Medium Supplement (Biopredict, Rennes, France) until confluent. Cells were then switched into HepaRG Differentiation media for 2 weeks. Differentiated HepaRG cells were used directly for transfection.

HepG2 cells (the American Type Culture Collection, ATCC) were grown in Eagle's Minimum Essential Medium containing 10% fetal bovine serum (FBS) (HyClone). HEK 293T were grown in Dulbecco's modified Eagle's medium containing 10% FBS. STF cells (ATCC) were cultured in 80% DMEM F12 Medium, (ATCC 30-2006), add 20% Bovine Calf Serum, Iron Fortified (ATCC 30-2030) and 200ug/ml G-418. All cells were cultured at 37°C with 5% CO₂ and used within 30 passages. Cells were transfected with plasmids using lipofectamine 2000 (Thermo scientific). Cells were transfected with siRNA using Lipofectamine RNAiMAX (Invitrogen). Specifically, for 6 well plates, each well used 4 μ l Lipofectamine RNAiMAX reagent and 4 μ l siRNA (10 μ M).

Real-time quantitative reverse transcription polymerase chain reaction

Total RNA was purified using the QIAGEN RNeasy kit (Germantown, MD). Primers for the amplification of TSPYL1, CTNNB1 and CYPs were Prime Time pre-designed qPCR primers (IDT Inc., Coralville, Iowa). All samples were measured in technical triplicates using the SYBR green reagent with an ABI Prism 7000HT sequence detection system (Applied Biosystems). The results were quantified using the Comparative Ct ($\Delta\Delta$ Ct) method with

the housekeeping gene GAPDH as an internal reference control.

Western blot analysis

Protein levels were determined using Western blot analysis. The following primary antibodies were used: Flag (1:1,000, Cell Signaling Technology, cat. #F1804), GAPDH (1:1,000, Cell Signaling Technology, cat. #5174S), β -catenin (1:1,000, Cell Signaling Technology, cat. #9582S), TSPYL1 (1:1,000, Bethyl Laboratories, cat. #A304-852A-M), and TCF7L2 (1:1,000, Cell Signaling Technology, cat. #2569S). The following secondary antibodies were used: Peroxidase- conjugated AffiniPure Goat Anti-Mouse IgG, light chain specific (1:2,000 dilution, Jackson immunoResearch) and Peroxidase- conjugated IgG fraction monoclonal mouse anti-rabbit IgG, light chain specific (1:2,000 dilution, Jackson Immuno Research).

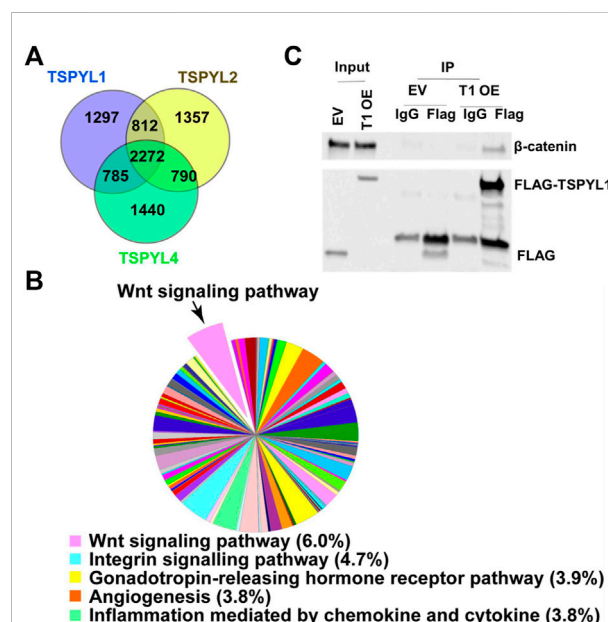
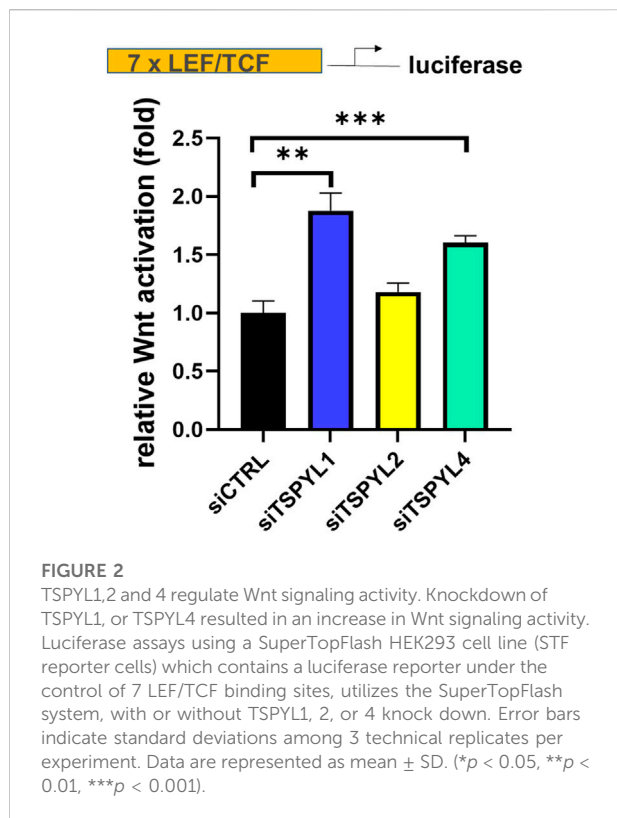


FIGURE 1

TSPYL1, 2 and 4 interact with Wnt signaling pathway proteins. (A) Venn diagram depicting the number of proteins pulled down by TSPYL1 (blue circle), TSPYL2 (yellow circle), or TSPYL4 (green circle) respectively and identified by mass spectrometry in HepaRG cells. (B) Signaling pathway analysis of the 2272 proteins pulled down by all 3 TSPYL isoforms. A pie chart showing the quantity of proteins matched with Panther pathways. The top five pathways are shown in the legend with percentages of input genes noted after the pathway name. The Wnt signaling pathway is shown as a pop-out slice. (C) Co-IP of FLAG-TSPYL1 with endogenous β -catenin in 293T cells. FLAG-TSPYL1 was immunoprecipitated, and the quantity of β -catenin bound to TSPYL1 was determined using immunoblot with an anti- β -catenin antibody. The quantities of TSPYL1 and β -catenin immunoprecipitated were compared with IgG. (EV - empty vector; T1 OE - TSPYL1 over expression).



IP and IB analysis

For Co-IP, 293T cells were grown in 10-cm dishes and were transfected with the appropriate plasmids for 48 h. Cell lysates were incubated with 3 μ g of Flag antibody on a rotator overnight at 4°C. The protein-antibody-protein A/G-agarose complexes were prepared by adding 50 μ l of protein A/G-agarose beads (Thermo scientific) for 2 h at 4°C. After three washings with NETN lysis buffer, the immunoprecipitated complexes were resuspended in reducing sample buffer and elute at 50°C for 10 min. The supernatants were transferred to a clean tube and boiled for 5 min. Supernatants were subjected to SDS-polyacrylamide gel electrophoresis (PAGE) and IB.

Mass spectrometry

Mass Spectrometry was done using differentiated HepaRG cells with IRES-TSPYL1, 2 or 4 plasmids transiently transfected using lipofectamine 2000 for 48 h. TSPYL interacting proteins were immunoprecipitated using Flag antibody. Normal mouse IgG was used as a negative control. The immunoprecipitated protein was eluted using 2X Laemmli buffer and resolved using SDS-PAGE electrophoresis. Protein bands were visualized by Coomassie Blue Staining and were dissected into sections equally. The dissected gel slices were sent for Mass spectrometric analysis

at the Harvard Taplin Mass Spec facility. Proteins uniquely precipitated using Flag antibody but not IgG, and shared among all three TSPYLs were included for further pathway analysis. Pathway analysis was performed using the Panther pathway database.

Clinical data

TSPYL1 expression, cholesterol and BMI data from patients were downloaded from the Gene Expression Omnibus (<https://www.ncbi.nlm.nih.gov/geo/>) by GEO ID GSE48452 and GSE130991. Probe IDs were labeled in the figure legends. For the BMI analysis, samples were divided by TSPYL1 median expression level. The GSE130991 dataset was used for the age-specific LDL-cholesterol level test. Samples were grouped by both the median expression of TSPYL1 and the population median age. Statistical significance was tested by the Mann-Whitney test.

Luciferase assays

SuperTopFlash HEK293 cell line (STF) reporter cells were split into 24-well plates and were transfected 24 h later with 1 μ g of TSPYL overexpression plasmid or siRNA and 0.8 ng of the transfection control Renilla luciferase plasmid pTK-RL (Promega) using lipofectamine 2000 (Thermo scientific). 48 h after transfection, the cells were washed with PBS and luciferase activities were measured with a Dual-Luciferase Assay Kit (Promega, cat# E1960) according to the manufacturer's protocols. Luciferase assays were performed at least in triplicate.

Plasmids and siRNAs and reagents

SMARTpool siRNA duplexes specific for *CTNNB1* (Catalog ID: M-003482-00-0005), *TSPYL1* (Catalog ID: M-028592-01-0005), *TSPYL2* (Catalog ID: M-013880-01-0005), *TSPYL4* (Catalog ID: M-017980-00-0005), and a Non-Targeting siRNA pool (siCTRL, Catalog ID: D-001206-13-05) were purchased from Dharmacon. Recombinant human Wnt-3a was purchased from R&D Systems. Human TSPYL cDNA constructs and empty vector, Pcmv6-XL4, were purchased from Origene Technologies (Rockville, MD).

CHIP assays

HepaRG cells were used to perform ChIP assays to determine possible TSPYL1 binding to the promoter regions of *CYP1B1* or *CYP7A1*. Primer sets (see [Supplementary Table S2](#)) which covered TCF7L2 binding sites of *CYP1B1* or TCF7 binding sites of *CYP7A1*, were designed to "screen" potential TSPYL1-

DNA binding sites. ChIP assay was performed using the SimpleChIP Enzymatic Chromatin IP kit (Cat. #91820, cell signaling technology) followed by quantitative PCR using the TB Green Premix Ex Taq™ PCR master mix reagent (Cat. #RR420A, TaKaRa).

Determination of 20-hydroxyeicosatetraenoic acid levels

The concentration of 20-HETE was determined by an ELISA kit (20H39-K01, Eagle Biosciences) according to the manufacturer's instructions. For measurement of 20-HETE in cultured HepaRG cells, cells were trypsinized in 0.05% trypsin after washing with PBS. Half of the cells were used for PCR. The remainder of the cells were homogenized and sonicated with RIPA buffer containing triphenylphosphine. 50 µl was used for the 20-HETE assay on the day of extraction. The remaining homogenate was frozen at -80°C for protein assay.

Statistics

A two-tailed Student-*t* test was used for statistical analysis for changes across conditions, if not specified. A *p* value < 0.05 was considered to be statistically significant. Statistical significance is indicated by asterisks. **p* < 0.05; ***p* < 0.01; ****p* < 0.001, *****p* < 0.0001.

Results

As stated above, we previously identified TSPYLs as novel CYP gene transcriptional regulators (Qin et al., 2018; Qin et al., 2020). However, relatively little is known with regard to mechanisms by which TSPYLs might regulate CYP expression or how their effect on CYP transcriptional regulation might influence human biology and/or pathophysiology. The studies described subsequently revealed a novel mechanism for regulation of the expression of cholesterol-metabolizing CYPs, particularly CYP1B1, by TSPYL1, in a process mediated by Wnt/β-catenin signaling. These observations also raised the possibility that TSPYL1 might be a novel target for drugs designed to influence cholesterol homeostasis.

TSPYLs interact with Wnt signaling pathway proteins

To study mechanisms and potential signaling pathways that interact with TSPYLs, we performed flag-affinity

purification of 3XFLAG-TSPYL1, 2 and 4 from HepaRG cells after IRES plasmid transient transfection to isolate TSPYL1,2 and 4-associated proteins. A total of 2272 proteins were pulled down for these three TSPYL isoforms as shown by the Venn diagram in Figure 1A. The pie charts and Venn diagram of panther pathway analysis for each individual pull down by TSPYL1, 2 and 4 are shown in Supplementary Figure S1. Panther pathway analysis was performed for these 2272 proteins. Included among the top signaling pathways associated with TSPYLs on the basis of mass spectrometric analysis were Wnt signaling pathway proteins (Figures 1A,B). The other top 4 pathways were the Integrin signaling pathway, the Gonadotropin-releasing hormone receptor pathway, the Angiogenesis pathway, and Inflammation mediated by chemokines and cytokines. All of the protein pull-down information is available in a Supplementary Excel File.

β-Catenin is a key component of Wnt canonical signaling (Mosimann et al., 2009). It is known that β-catenin binds to TCF/LEF family members to activate the transcription of Wnt signaling target genes (Mosimann et al., 2009). Therefore, we confirmed the mass spectrometric results by performing co-immunoprecipitation using 293T cells and found that endogenous β-catenin (Figure 1C) could be co-precipitated with Flag-tagged-TSPYL1.

TSPYL1 knockdown increased Wnt signaling activity

Because of the nuclear localization and the association among TSPYLs, β-catenin and TCF/LEF, we next tested the possibility of a functional link between TSPYLs and Wnt signaling. We used SuperTopFlash (STF) HEK293 reporter cells to determine whether the knockdown of TSPYLs could affect Wnt signaling. TSPYL1 knockdown increased luciferase reporter transcription (Figure 2). TSPYL2 and TSPYL4 knockdown also increased Wnt activity 1.25 and 1.55 fold, respectively, but less than that observed for TSPYL1 (1.73 fold) (Figure 2). These observations raised the possibility that these TSPYLs might be negative regulators of Wnt/β-catenin signaling.

TSPYL1 knockdown regulates cholesterol metabolizing CYPs

CYPs play an important role in the maintenance of cholesterol homeostasis (Pikuleva, 2006). For example, CYP7A1 is the first and the rate-limiting enzyme in the classic bile acid synthesis pathway in which cholesterol is metabolized to form bile acids, while CYP11A1 catalyzes a step in a pathway by which cholesterol serves as a substrate for

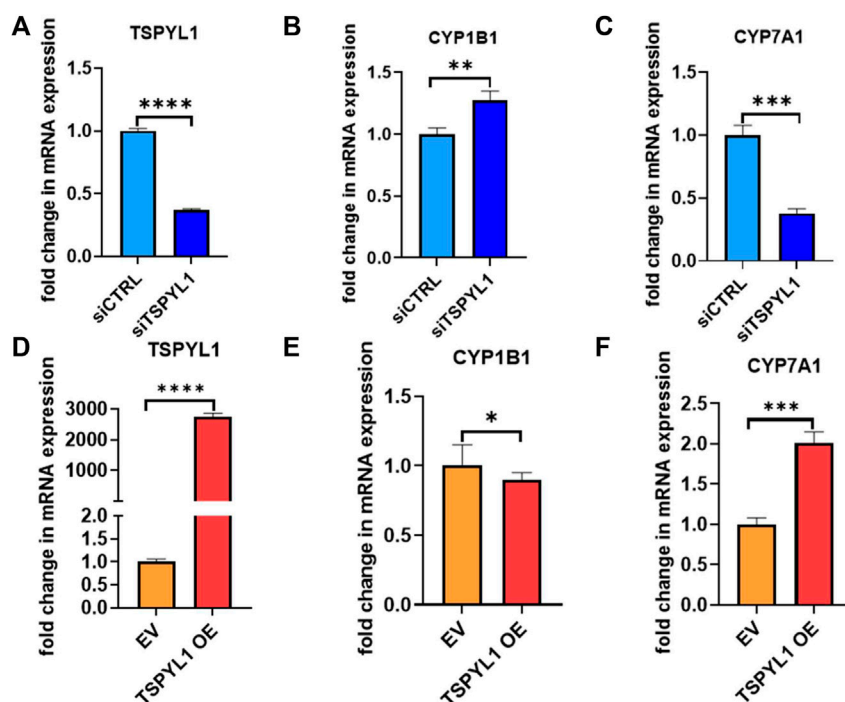


FIGURE 3

TSPYL1 regulates *CYP1B1* and *CYP7A1* expression in HepaRG cells. (A) HepaRG cells with or without TSPYL1 depletion by siRNA were transfected as indicated. *CYP1B1* (B) and *CYP7A1* (C) expression were tested by qRT-PCR. (D) HepaRG cells with or without TSPYL1 overexpression were transfected as indicated. *CYP1B1* (E) and *CYP7A1* (F) expression were tested by qRT-PCR. Gene-specific data were normalized to GAPDH expression. Error bars indicated standard deviations among 3 technical replicates per experiment. Data are represented as mean \pm SD. (* $p < 0.05$, ** $p < 0.01$, *** $p < 0.001$, **** $p < 0.0001$).

the synthesis of steroid hormones (Pikuleva, 2006). *CYP1B1* also has a significant impact on cholesterol metabolism. Consistent with our previous observations (Qin et al., 2018), we found that *CYP1B1* was upregulated by TSPYL1 knockdown (Figures 3A,B) and that it was downregulated by TSPYL1 overexpression in HepaRG cells (Figures 3D,E). *CYP7A1* was significantly downregulated by TSPYL1 knockdown (Figure 3C) and was upregulated by TSPYL1 overexpression in those cells (Figure 3F). PCR results had previously shown that *CYP11A1* was not significantly regulated by TSPYL1 knockdown (Qin et al., 2018), so we did not perform follow up studies on *CYP11A1*. We next analyzed the correlation of TSPYL1 and *CYP1B1* expression, using expression quantitative trait loci (eQTL) data from human hepatic tissue (Innocenti et al., 2011). The expression of TSPYL1 and *CYP1B1* were negatively correlated, with a correlation coefficient of -0.26 (Figure 4A, $p = 1.35e-08$). When we analyzed the correlation of TSPYL1 with *CYP7A1* expression, we observed that TSPYL1 and *CYP7A1* expression were positively correlated, with a correlation coefficient of 0.25 (Figure 4A, $p = 5.54e-08$).

TSPYL1 and TCF7L2 bind to the promoter region of *CYP1B1* in HepaRG cells

According to the TCF7L2 ChIP-seq data in the ENCODE database, TCF7L2 binds to the *CYP1B1* promoter in Panc1 cells (Figure 5A). We hypothesized that TSPYL1, by interacting with β -catenin and TCF7L2, might bind to the same *CYP1B1* promoter region as does TCF7L2 in HepaRG cells. Therefore, we performed CHIP assays with antibodies to both TSPYL1 and TCF7L2 using HepaRG cells because of the high protein expression level of TSPYL1 in HepaRG cells. Specifically, a series of PCR primers was designed to amplify TCF7L2 binding sites in the *CYP1B1* promoter. Our CHIP results showed that TSPYL1 bound to the same *CYP1B1* promoter region as did TCF7L2 (Figure 5B). We next performed co-immunoprecipitation to study possible interactions among TCF7L2-FLAG, TSPYL1 and endogenous β -catenin. The results showed that TSPYL1 overexpression dramatically reduced β -catenin binding to TCF7L2 (Figure 6). These results suggested that the expression of TSPYL1 might influence the interaction between TCF7L2 and β -catenin, specifically that TSPYL1 might interfere with β -catenin binding to TCF7L2.

A putative bile acid responsive element, BAREII (DR1), is present in the human *CYP7A1* gene promoter. TCF7 binds to BAREII to regulate *CYP7A1* gene transcription in HepG2 cells based on ENCODE data (see [Supplementary Figure S2A](#)). Therefore, we performed a CHIP assay to determine whether TSPYL1 might bind to the BAREII element in the *CYP7A1* promoter. Four pairs of primers for PCR of the *CYP7A1* promoter region were used. We failed to detect significant TSPYL1 recruitment to the *CYP7A1* promoter region in HepaRG cells (see [Supplementary Figure S2B](#)).

CYP expression regulation by Wnt signaling in HepG2 cells

The effect of the WNT/ β -catenin pathway on the regulation of the expression of major human P450 enzymes in HepaRG cells has been studied extensively ([Thomas et al., 2015](#)), but *CYP1B1* had not been studied in that context. To obtain additional information on the effect of the WNT/ β -catenin pathway in hepatic cells, we studied an additional cell line, HepG2. To identify CYP genes that were transcriptionally regulated by Wnt, we determined the effect of Wnt pathway activation or inhibition on the expression of a series of CYPs in HepG2 cells. As a first step, we compared the effect of β -catenin siRNA and control siRNA knockdown on CYP expression. siRNA-mediated knockdown of β -catenin resulted in an approximate 75% decrease in the expression of β -catenin (*CTNNB1*) mRNA and its downstream target genes (see [Supplementary Figure S3C](#)). We also tested the effect of stimulation with the canonical Wnt ligand, Wnt-3a. Wnt-3a treatment significantly induced the expression of Wnt signaling downstream genes compared with BSA treatment as a control (see [Supplementary Figure S3D](#)). Changes in CYP mRNA expression in HepG2 cells were also determined. Specifically, PCR analysis revealed that *CYP1B1*, *CYP2A6* and *CYP2B6* were transcriptionally downregulated more than 2-fold by β -catenin knockdown in HepG2 cells (see [Supplementary Figure S3A](#)), whereas expression of *CYP2C9*, *CYP2C18*, *CYP3A7*, *CYP7A1*, *CYP7B1*, and *CYP27A1* were upregulated by β -catenin knock down in HepG2 cells (see [Supplementary Figure S3A](#)). By contrast, *CYP1B1*, *CYP2A6* and *CYP2B6* expression was significantly upregulated after Wnt-3a stimulation, while the expression of *CYP2C9*, *CYP2C19* and *CYP3A7* was downregulated more than 2-fold by Wnt activation (see [Supplementary Figure S3B](#)). These results support the conclusion that the expression of *CYP1B1*, together with that of other CYPs, is regulated by Wnt/ β -catenin signaling in HepG2 cells.

CYP1B1 expression was restored in β -catenin and TSPYL1 double knockdown HepaRG cells

We had demonstrated that TSPYL1 negatively regulated *CYP1B1* expression by blocking β -catenin binding to TCF7L2 on the *CYP1B1* promoter. After β -catenin knockdown, *CYP1B1* expression was down regulated in HepaRG cells ([Figures 7A,B](#)). In summary, TSPYL1 and β -catenin knockdown regulated *CYP1B1* expression in opposite directions.

Therefore, we anticipated that by inhibiting the activity of the Wnt/ β -catenin pathway, we could “rescue” TSPYL1 knockdown-dependent *CYP1B1* upregulation. To test that hypothesis, we conducted a double knockdown experiment. Our PCR results supported the hypothesis that *CYP1B1* expression could be rescued by β -catenin and TSPYL1 double knockdown ([Figure 7C](#)). 20-HETE, a downstream metabolite of *CYP1B1*, was also restored by TSPYL1 and CTNNB1 double knockdown ([Figure 7D](#)). These results supported the conclusion that TSPYL1 regulates *CYP1B1* expression through Wnt/ β -catenin signaling.

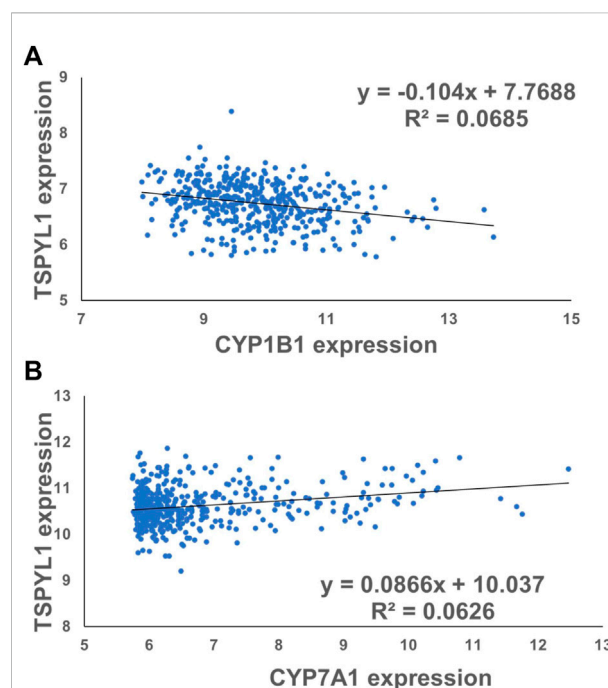


FIGURE 4
TSPYL1 expression associates with *CYP1B1* and *CYP7A1* expression levels in human liver tissue. (A) The expression correlation coefficient for *CYP1B1* and TSPYL1 was -0.26 . ($r = -0.26$, ****, $p = 1.35e-08$). (B) The expression correlation coefficient for *CYP7A1* and TSPYL1 was 0.25 . ($r = 0.25$, ****, $p = 5.54e-08$). These data were obtained from a previous publication [Innocenti et al. \(2011\)](#).

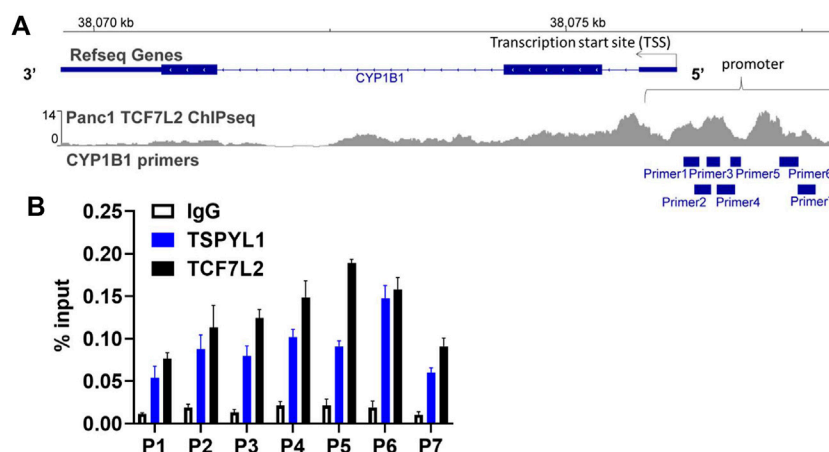


FIGURE 5

TSPYL1 and TCF7L2 bind to the promoter region of *CYP1B1* in HepaRG cells. (A) Seven pairs of primers covering the *CYP1B1* promoter region were used to perform CHIP assays. (B) CHIP assays were performed to test TSPYL1 and TCF7L2 binding to the *CYP1B1* promoter region using HepaRG cells. The binding of TSPYL1 and TCF7L2 to *CYP1B1* promoter regions was detected by qRT-PCR and has been expressed as percent of input.

TSPYL1 has been associated with BMI and cholesterol levels in patients with obesity

Transgenic mice overexpressing CYP7A1 in the liver have been reported to be resistant to high-fat diet induced obesity, fatty liver disease and diabetes (Li et al., 2010), while decreased CYP1B1 expression has been correlated with altered lipid metabolism, especially lysophosphatidylcholines, contributing to protection against the development of obesity (Li et al., 2014). Since TSPYL1 knockdown in hepatic cells resulted in increased CYP1B1 and decreased CYP7A1 expression, we asked whether TSPYL1 expression might be associated with obesity and/or plasma cholesterol concentrations in humans. As an initial step toward systematically testing the hypothesis that hepatic TSPYL1 expression might be associated with obesity, we examined publically available data from two clinical studies addressing obesity in which hepatic mRNA expression had been determined. The first trial entitled “A Biological Atlas of Severe Obesity (Biological Tissue Collection (ABOS))” (ClinicalTrials.gov Identifier: NCT01129297) involved 897 obese patients. Figure 8A shows the results of transcriptomic profiling of hepatic tissue from those 897 obese patients (Mean BMI 46.7). Among those patients, 173 received statin treatment, and differential expression analysis was performed between samples from patients who were treated with or without statins to test possible statin effects on gene expression. TSPYL1 expression levels for those patients were negatively associated with plasma LDL-cholesterol levels. A separate cohort from the “Human Liver Biopsy of Different Phases

of Control to NASH” (GSE48452) study involved 73 severely obese patients with various degrees of non-alcoholic fatty liver disease (NAFLD). Those patients also had transcriptomic profiling of hepatic tissue, and hepatic TSPYL1 expression in this group was negatively associated with BMI (Figure 8B). Both of these datasets were analyzed using non-parametric two-group testing (Mann-Whitney test). These two examples are, of course, merely suggestive, and studies designed to

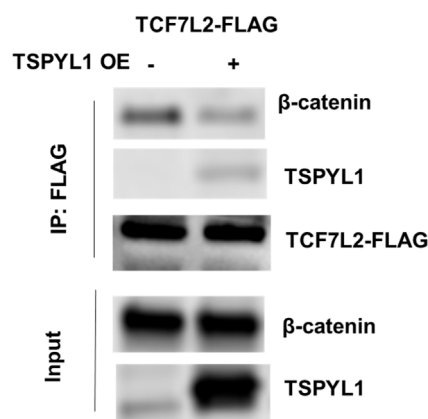


FIGURE 6

TSPYL1 blocks β -catenin binding with TCF7L2. Interaction of endogenous β -catenin with overexpressed TSPYL1 and TCF7L2-FLAG is shown. IP was conducted with whole-cell lysates of 293T cells transfected with TCF7L2-FLAG and an empty vector or TSPYL1 overexpression plasmid. TSPYL1 overexpression reduced β -catenin binding with TCF7L2.

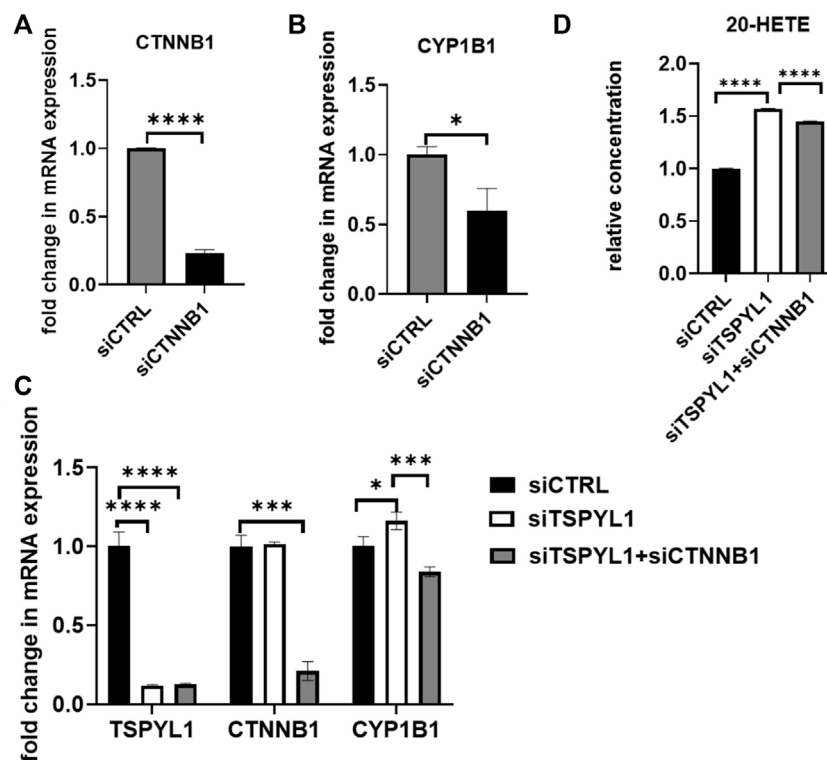


FIGURE 7

β -Catenin knockdown rescues TSPYL1 knockdown-related increase in CYP1B1. (A) HepaRG cells with or without β -catenin (CTNNB1) depletion by siRNA were transfected as indicated. (B) *CYP1B1* expression was tested by qRT-PCR. (C) HepaRG cells with TSPYL1 or CTNNB1 depletion by siRNA were transfected as indicated. *CYP1B1* expression was tested by qRT-PCR. Gene-specific data were normalized to GAPDH expression. (D) 20-HETE was measured by ELISA. Error bars indicate standard deviations among 3 technical replicates per experiment. Data are represented as mean \pm SD. (* $p < 0.05$, ** $p < 0.01$, *** $p < 0.001$, **** $p < 0.0001$).

specifically test hypotheses arising from the present series of studies will have to be performed in the future.

Specifically, our observations raise the possibility that CYP1B1 could represent a therapeutic target for the treatment

Discussion

The results of the experiments described above indicate that TSPYL1 represents one factor regulating the expression of CYPs including, especially, CYP1B1, with a significant effect on cholesterol concentrations. This effect of TSPYL1 appears to be mediated, at least in part, through Wnt/ β -catenin signalling. These observations suggest, among other implications, that TSPYL1 might represent a target for future attempts to influence or modify cholesterol biosynthesis.

As shown schematically in Figure 8A, decreased TSPYL1 expression is associated with elevated LDL-cholesterol plasma levels in patients. This relationship can be explained, at least in part, by the model shown in Figure 9. When TSPYL1 levels decrease, β -catenin binds to TCF/LEF in the nucleus. That binding activates *CYP1B1* transcription which may then alter fatty acid and cholesterol metabolism.

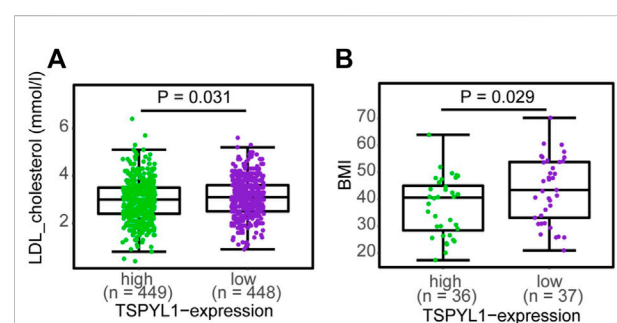
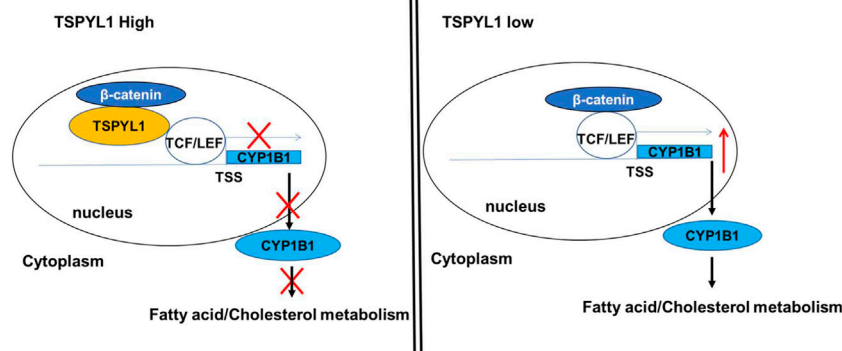


FIGURE 8

TSPYL1 expression and cholesterol levels and BMI in clinical trials. (A) LDL-cholesterol levels subgrouped by median TSPYL1 expression, using hepatic expression array data for the GSE130991 dataset. (B) BMI measurements grouped by median TSPYL1 expression using data from the GSE48452 dataset. Statistical significance was tested by use of the Mann-Whitney test with p -values indicated above the figures.

**FIGURE 9**

Proposed schematic model for the role of TSPYL1 in *CYP1B1* transcription regulation. β -Catenin is a transcriptional activator for *CYP1B1*. TSPYL1 inhibits β -catenin binding with TCF/LEF on the *CYP1B1* promoter. When the TSPYL1 level decreases, β -catenin binds to TCF/LEF in the nucleus. This activates *CYP1B1* transcription and interferes with fatty acid and cholesterol metabolism.

of selected metabolic diseases. CYP1B1 knockdown altered the expression of 560 hepatic genes, including the PPARs, a group of nuclear receptors that play a key role in lipid and glucose homeostasis (Larsen et al., 2015). Metabolic pathways regulated by CYP1B1 include steroid hormone metabolism, fatty acid metabolism, vitamin metabolism and melatonin metabolism (Li et al., 2017). *CYP1B1* is an important gene associated with obesity, based on a review of 49 obesity-related genome-wide sequencing studies covering 16,186 genes (English and Butte, 2007). However, the mechanisms governing that regulation have remained unclear. To our knowledge, the current study is the first to demonstrate that TSPYL1 can influence the expression of cholesterol metabolizing CYPs, particularly CYP1B1, via Wnt/ β -catenin signaling in HepaRG cells. We observed the binding of TCF7L2 to β -catenin and TSPYL1, and that β -catenin binding with TCF7L2 could be reduced by TSPYL1 overexpression. Those observations are compatible with a competition between TSPYL1 and TCF7L2 for binding to β -catenin. Although our CHIP assay showed that TCF7L2 and TSPYL1 bind to the same region of the *CYP1B1* promoter in HepaRG cells, we do not know whether TSPYL1 binds directly or indirectly to the *CYP1B1* promoter region by binding jointly with TCF7L2. Our group had already predicted the TSPYL1 DNA binding motif based on CHIP-PCR assay (Qin et al., 2018). That sequence is not the same as the TCF7L2 binding motif. However, there is a TCF7L2 binding motif (TCAAAG) in the *CYP1B1* promoter. As a result, it is possible that TSPYL1 may bind to the *CYP1B1* promoter as a result of its interaction with TCF7L2. Consistent with a previous publication (Malovannaya et al., 2011), our results suggest that, as transcriptional regulatory proteins, TSPYLs regulate gene transcription by interacting with transcription factors which bind with target gene promoter regions. A transcription factor (TF) is a sequence-specific DNA-binding factor. Specifically, it is

a protein that controls the rate of transcription of genetic information from DNA to messenger RNA by binding to a specific DNA sequence. However, TSPYLs do not bind to a specific DNA sequence, as demonstrated by CHIP-PCR in our current and previous studies (Qin et al., 2018). Instead, transcription regulators influence transcriptional regulation by interacting with other proteins to “fine tune” transcription. As a result, TSPYLs are considered as transcription regulators, but not transcription factors.

In summary, the results of this series of studies indicates that TSPYL1 might be an important modulator of *CYP1B1* and, possibly, of *CYP7A1* expression in human hepatic cells. The identification of an “antagonistic” relationship between β -catenin and TSPYL1 adds a possible new layer of regulation to the complex network involving β -catenin, as well as the role of the TSPYL1 as an important regulator of CYP expression in the human liver. Finally, in summary, our findings suggest that decreased TSPYL1 expression might result in altered cholesterol metabolism through the regulation of cholesterol metabolizing CYPs in a process mediated by Wnt/ β -catenin signaling.

Data availability statement

The original contributions presented in the study are included in the article/Supplementary Material, further inquiries can be directed to the corresponding author.

Author contributions

XZ: Data collection, data analysis, methodology, conceptualization, writing- original draft. HG and SQ:

Data collection, data analysis, conceptualization, methodology, writing-review and editing. DL, JC, YG, and JY: Conceptualization, methodology, writing-review and editing. RW and LW: Funding acquisition, supervision, conceptualization, writing-review and editing.

Funding

This work was supported by National Institutes of Health grants U19 GM61388 (The Pharmacogenomics Research Network), R01 CA196648, R01 GM28157, R01 AA27486, The Minnesota Partnership for Biotechnology and Medical Genomics Grant #14.37, Prostate Cancer Foundation, and Private and philanthropy funding sources: 1) Mayo Clinic Center for Individualized Medicine; 2) A. T. Suharya and Ghan D. H., Gail and Joseph Gassner; 3) Mayo Clinic Schulze Cancer for Novel Therapeutics in Cancer Research.

Conflict of interest

The authors declare that the research was conducted in the absence of any commercial or financial relationships that could be construed as a potential conflict of interest.

Publisher's note

All claims expressed in this article are solely those of the authors and do not necessarily represent those of their affiliated organizations, or those of the publisher, the editors and the reviewers. Any product that may be evaluated in this article, or claim that may be made by its manufacturer, is not guaranteed or endorsed by the publisher.

References

- Braeuning, A., Sanna, R., Huelsken, J., and Schwarz, M. (2009). Inducibility of drug-metabolizing enzymes by xenobiotics in mice with liver-specific knockout of *Cttnb1*. *Drug Metab. Dispos.* 37 (5), 1138–1145. doi:10.1124/dmd.108.026179
- Braeuning, A., and Schwarz, M. (2010). beta-Catenin as a multilayer modulator of zonal cytochrome P450 expression in mouse liver. *Biol. Chem.* 391 (2-3), 139–148. doi:10.1515/BC.2010.012
- Cauchi, S., Choquet, H., Gutierrez-Aguilar, R., Capel, F., Grau, K., Proenca, C., et al. (2008). Effects of TCF7L2 polymorphisms on obesity in European populations. *Obes. (Silver Spring)* 16 (2), 476–482. doi:10.1038/oby.2007.77
- Choudhary, D., Jansson, I., Stoilov, I., Sarfarazi, M., and Schenkman, J. B. (2004). Metabolism of retinoids and arachidonic acid by human and mouse cytochrome P450 1b1. *Drug Metab. Dispos.* 32 (8), 840–847. doi:10.1124/dmd.32.8.840
- English, S. B., and Butte, A. J. (2007). Evaluation and integration of 49 genome-wide experiments and the prediction of previously unknown obesity-related genes. *Bioinformatics* 23 (21), 2910–2917. doi:10.1093/bioinformatics/btm483
- Esteves, F., Rueff, J., and Kranendonk, M. (2021). The central role of cytochrome P450 in xenobiotic metabolism-A brief review on a fascinating enzyme family. *J. Xenobiot.* 11 (3), 94–114. doi:10.3390/jox11030007
- Ganzenberg, K., Singh, Y., and Braeuning, A. (2013). The time point of beta-catenin knockout in hepatocytes determines their response to xenobiotic activation of the constitutive androstane receptor. *Toxicology* 308, 113–121. doi:10.1016/j.tox.2013.03.019
- Gill, J., Kumar, A., and Sharma, A. (2022). Structural comparisons reveal diverse binding modes between nucleosome assembly proteins and histones. *Epigenetics Chromatin* 15 (1), 20. doi:10.1186/s13072-022-00452-9
- Hailfinger, S., Jaworski, M., Braeuning, A., Buchmann, A., and Schwarz, M. (2006). Zonal gene expression in murine liver: Lessons from tumors. *Hepatology* 43 (3), 407–414. doi:10.1002/hep.21082
- Haupt, A., Thamer, C., Heni, M., Ketterer, C., Machann, J., Schick, F., et al. (2010). Gene variants of TCF7L2 influence weight loss and body composition during lifestyle intervention in a population at risk for type 2 diabetes. *Diabetes* 59 (3), 747–750. doi:10.2337/db09-1050

Supplementary material

The Supplementary Material for this article can be found online at: <https://www.frontiersin.org/articles/10.3389/fphar.2022.1047318/full#supplementary-material>

SUPPLEMENTARY FIGURE S1

The pie charts and Venn diagrams for each individual pull down by TSPYL1, 2 and 4. Pie charts depicting the signaling pathways pulled down by TSPYL1 (A), TSPYL2 (B), or TSPYL4 (C), respectively. (D) A Venn diagram of TSPYLs interacting signaling pathways for all three TSPYLs studied. The TSPYL interacting proteins and pathways are listed in a supplementary excel file.

SUPPLEMENTARY FIGURE S2

TSPYL1 binding to the *CYP7A1* promoter region in HepaRG cells was not detected. (A) Four pairs of primers covering the *CYP7A1* promoter region were used for CHIP assays. (B) CHIP assays were performed to test TSPYL1 binding to the *CYP7A1* promoter region using HepaRG cells. The binding of TSPYL1 to the *CYP7A1* promoter is shown as fold enrichment compared with IgG control. A set of control primers targeted to non-protein binding areas were used as a negative control. Compared with the negative control, TSPYL1 was not found to bind to the *CYP7A1* promoter region in HepaRG cells.

SUPPLEMENTARY FIGURE S3

(A,B) Effect of Wnt/ β -catenin signaling on basal CYP expression. For β -catenin knockdown, HepG2 cells were treated with siRNA against β -catenin (C, blue bars). For β -catenin (CTNNB1) activation, HepG2 cells were treated for 24 h with 200 ng/ml Wnt-3a (D, red bars). The levels of the indicated CYPs were measured by PCR. By β -catenin knockdown in HepG2 cells, CYP1B1, CYP2A6 and CYP2B6 were transcriptionally downregulated more than 2-fold, whereas CYP2C9, CYP2C18, CYP3A7, CYP7A1, CYP7B1, and CYP27A1 were upregulated by β -catenin knockdown (A). By contrast, after Wnt-3a stimulation, CYP1B1, CYP2A6, and CYP2B6 expression was significantly upregulated, while the expression of CYP2C9, CYP2C19, and CYP3A7 was downregulated more than 2-fold (B). Vehicle controls (0.1% bovine serum albumin and nontargeting control siRNA, respectively) were used. Data represent means \pm SD of three technical replicates per experiments. Student *t*-test were used for statistical analysis. Statistical significance is indicated by asterisks. **P* < 0.05, ***P* < 0.01, ****P* < 0.001, *****P* < 0.0001.

SUPPLEMENTARY TABLE S1

Summary of mass spectrometric analysis of wnt signaling proteins associated with TSPYLs.

SUPPLEMENTARY TABLE S2

ChIP-qPCR primer sets for promoter regions of *CYP1B1* and *7A1*.

- Innocenti, F., Cooper, G. M., Stanaway, I. B., Gamazon, E. R., Smith, J. D., Mirkov, S., et al. (2011). Identification, replication, and functional fine-mapping of expression quantitative trait loci in primary human liver tissue. *PLoS Genet.* 7 (5), e1002078. doi:10.1371/journal.pgen.1002078
- Kimelman, D., and Xu, W. (2006). beta-catenin destruction complex: insights and questions from a structural perspective. *Oncogene* 25 (57), 7482–7491. doi:10.1038/sj.onc.1210055
- Larsen, M. C., Bushkofsky, J. R., Gorman, T., Adhami, V., Mukhtar, H., Wang, S., et al. (2015). Cytochrome P450 1B1: An unexpected modulator of liver fatty acid homeostasis. *Arch. Biochem. Biophys.* 571, 21–39. doi:10.1016/j.abb.2015.02.010
- Li, F., Jiang, C., Larsen, M. C., Bushkofsky, J., Krausz, K. W., Wang, T., et al. (2014). Lipidomics reveals a link between CYP1B1 and SCD1 in promoting obesity. *J. Proteome Res.* 13 (5), 2679–2687. doi:10.1021/pr500145n
- Li, F., Zhu, W., and Gonzalez, F. J. (2017). Potential role of CYP1B1 in the development and treatment of metabolic diseases. *Pharmacol. Ther.* 178, 18–30. doi:10.1016/j.pharmthera.2017.03.007
- Li, T., Owsley, E., Matozel, M., Hsu, P., Novak, C. M., and Chiang, J. Y. (2010). Transgenic expression of cholesterol 7alpha-hydroxylase in the liver prevents high-fat diet-induced obesity and insulin resistance in mice. *Hepatology* 52 (2), 678–690. doi:10.1002/hep.23721
- Liu, M., Ingle, J. N., Fridley, B. L., Buzdar, A. U., Robson, M. E., Kubo, M., et al. (2013). TSPYL5 SNPs: Association with plasma estradiol concentrations and aromatase expression. *Mol. Endocrinol.* 27 (4), 657–670. doi:10.1210/me.2012-1397
- Loeppen, S., Koehle, C., Buchmann, A., and Schwarz, M. (2005). A beta-catenin-dependent pathway regulates expression of cytochrome P450 isoforms in mouse liver tumors. *Carcinogenesis* 26 (1), 239–248. doi:10.1093/carcin/bgh298
- Malovannaya, A., Lanz, R. B., Jung, S. Y., Bulynko, Y., Le, N. T., Chan, D. W., et al. (2011). Analysis of the human endogenous coregulator complexome. *Cell* 145 (5), 787–799. doi:10.1016/j.cell.2011.05.006
- Mosimann, C., Hausmann, G., and Basler, K. (2009). Beta-catenin hits chromatin: Regulation of wnt target gene activation. *Nat. Rev. Mol. Cell Biol.* 10 (4), 276–286. doi:10.1038/nrm2654
- Nebert, D. W., and Dalton, T. P. (2006). The role of cytochrome P450 enzymes in endogenous signalling pathways and environmental carcinogenesis. *Nat. Rev. Cancer* 6 (12), 947–960. doi:10.1038/nrc2015
- Nebert, D. W., Wikvall, K., and Miller, W. L. (2013). Human cytochromes P450 in health and disease. *Philos. Trans. R. Soc. Lond. B Biol. Sci.* 368 (1612), 20120431. doi:10.1098/rstb.2012.0431
- Nelson, D. R., Goldstone, J. V., and Stegeman, J. J. (2013). The cytochrome P450 *Genesis* locus: The origin and evolution of animal cytochrome P450s. *Philos. Trans. R. Soc. Lond. B Biol. Sci.* 368 (1612), 20120474. doi:10.1098/rstb.2012.0474
- Pikuleva, I. A. (2006). Cytochrome P450s and cholesterol homeostasis. *Pharmacol. Ther.* 112 (3), 761–773. doi:10.1016/j.pharmthera.2006.05.014
- Qin, S., Eugene, A. R., Liu, D., Zhang, L., Neavin, D., Biernacka, J. M., et al. (2020). Dual roles for the TSPYL family in mediating serotonin Transport and the metabolism of selective serotonin reuptake inhibitors in patients with major depressive disorder. *Clin. Pharmacol. Ther.* 107 (3), 662–670. doi:10.1002/cpt.1692
- Qin, S., Liu, D., Kohli, M., Wang, L., Vedell, P. T., Hillman, D. W., et al. (2018). TSPYL family regulates CYP17A1 and CYP3A4 expression: Potential mechanism contributing to abiraterone response in metastatic castration-resistant prostate cancer. *Clin. Pharmacol. Ther.* 104 (1), 201–210. doi:10.1002/cpt.907
- Sekine, S., Lan, B. Y., Bedolli, M., Feng, S., and Hebrok, M. (2006). Liver-specific loss of beta-catenin blocks glutamine synthesis pathway activity and cytochrome p450 expression in mice. *Hepatology* 43 (4), 817–825. doi:10.1002/hep.21131
- Thomas, M., Bayha, C., Vetter, S., Hofmann, U., Schwarz, M., Zanger, U. M., et al. (2015). Activating and inhibitory functions of WNT/ β -Catenin in the induction of cytochromes P450 by nuclear receptors in HepaRG cells. *Mol. Pharmacol.* 87 (6), 1013–1020. doi:10.1124/mol.114.097402
- Vaas, S., Kreft, L., Schwarz, M., and Braeuning, A. (2014). Cooperation of structurally different aryl hydrocarbon receptor agonists and beta-catenin in the regulation of CYP1A expression. *Toxicology* 325, 31–41. doi:10.1016/j.tox.2014.08.010
- Vogel, T., Dittrich, O., Mehraein, Y., Dechend, F., Schnieders, F., and Schmidtke, J. (1998). Murine and human TSPYL genes: Novel members of the TSPY-SET-nap111 family. *Cytogenet. Cell Genet.* 81 (3–4), 265–270. doi:10.1159/000015042
- Wang, J., Liu, R., Wang, F., Hong, J., Li, X., Chen, M., et al. (2013). Ablation of LGR4 promotes energy expenditure by driving white-to-brown fat switch. *Nat. Cell Biol.* 15 (12), 1455–1463. doi:10.1038/ncb2867



OPEN ACCESS

EDITED BY

Rong Wang,
People's Liberation Army Joint Logistics
Support Force 940th Hospital, China

REVIEWED BY

Xuebin Wang,
Second Military Medical University,
China
Li Zhiling,
Shanghai Jiao Tong University, China

*CORRESPONDENCE

Yang Wang,
cattop3211@qq.com
Zhisheng Liu,
liuzsc@126.com

[†]These authors have contributed equally
to this work

SPECIALTY SECTION

This article was submitted to
Drug Metabolism and Transport,
a section of the journal
Frontiers in Pharmacology

RECEIVED 19 September 2022

ACCEPTED 23 November 2022

PUBLISHED 02 December 2022

CITATION

Xin Y, Gao L, Tuo Y, Nie G, Mei Y, Chen C,
Wang J, Li S, Sun D, Qian Q, Fu Y, Wang Y
and Liu Z (2022), Understanding inter-
individual variability in
pharmacokinetics/pharmacodynamics
of aripiprazole in children with tic
disorders: Individualized administration
based on physiological development
and CYP2D6 genotypes.
Front. Pharmacol. 13:1048498.
doi: 10.3389/fphar.2022.1048498

COPYRIGHT

© 2022 Xin, Gao, Tuo, Nie, Mei, Chen,
Wang, Li, Sun, Qian, Fu, Wang and Liu.
This is an open-access article
distributed under the terms of the
[Creative Commons Attribution License](#)
(CC BY). The use, distribution or
reproduction in other forums is
permitted, provided the original
author(s) and the copyright owner(s) are
credited and that the original
publication in this journal is cited, in
accordance with accepted academic
practice. No use, distribution or
reproduction is permitted which does
not comply with these terms.

Understanding inter-individual variability in pharmacokinetics/pharmacodynamics of aripiprazole in children with tic disorders: Individualized administration based on physiological development and CYP2D6 genotypes

Yingying Xin^{1†}, Liulu Gao^{2†}, Yali Tuo², Gang Nie², Yan Mei²,
Chen Chen³, Jun Wang², Sichan Li², Dan Sun¹, Qiaoqiao Qian¹,
Yongli Fu⁴, Yang Wang^{2*} and Zhisheng Liu^{1*}

¹Department of Neurology, Wuhan Children's Hospital, Tongji Medical College, Huazhong University of Science and Technology, Wuhan, China, ²Department of Pharmacy, Wuhan Children's Hospital, Tongji Medical College, Huazhong University of Science and Technology, Wuhan, China, ³Department of Pharmacy, Union Hospital, Tongji Medical College, Huazhong University of Science and Technology, Wuhan, China, ⁴Department of Pharmacy, Wuhan Mental Health Center, Tongji Medical College, Huazhong University of Science and Technology, Wuhan, China

Objective: This study aims to develop a combined population pharmacokinetic (PPK) model for aripiprazole (ARI) and its main active metabolite dehydroaripiprazole (DARI) in pediatric patients with tic disorders (TD), to investigate the inter-individual variability caused by physiological and genetic factors in pharmacokinetics of ARI and optimize the dosing regimens for pediatric patients.

Methods: A prospective PPK research was performed in Chinese children with TD. Totally 84 patients aged 4.83–17.33 years were obtained for the pharmacokinetic analysis. 27 CYP2D6 and ABCB1 gene alleles were detected. Moreover, the clinical efficacy was evaluated according to reduction rate of Yale Global Tic Severity Scale (YGTSS) score at the 12th week comparing with the baseline. Monte Carlo simulations were used to evaluate and optimize dosing regimens.

Results: The PPK model was established to predict the concentrations of ARI and DARI. Body weight and CYP2D6 genotype were the significant covariates affecting the clearance of ARI. The DARI/ARI metabolic ratios (MRs) of AUC_{24h}, C_{min} and C_{max} at the steady state of results were ultra-rapid metabolizers (UMs) > normal metabolizers (NMs) > intermediated metabolizers (IMs). MRs could be used to distinguish UMs or IMs from other patients. The best predictor of clinical efficacy for TD was the trough concentration of ARI and the cut-off point was 101.636 ng/ml.

Conclusion: The pharmacokinetics of ARI and DARI in pediatric TD were significantly influenced by body weight and CYP2D6 genotype. Individualized dosing regimens were recommended for pediatric patients with TD to ensure clinical efficacy.

KEYWORDS

pediatric, tic disorders, aripiprazole, CYP2D6, population pharmacokinetics, pharmacodynamics

Highlights

- 1) A population pharmacokinetic model was firstly established in pediatric tic disorders.
- 2) Body weight and CYP2D6 genotype were the significant covariates.
- 3) Dehydroaripiprazole/aripiprazole ratios could be substituted for CYP2D6 genotyping.
- 4) Trough concentration of aripiprazole could predict clinical efficacy of tic disorders.
- 5) Precise dosing regimens were proposed based on body weight and CYP2D6 genotype.

Introduction

Tic disorders (TD) is one of the most common neurodevelopmental disorders in childhood, which is characterized with sudden, rapid, recurrent, nonrhythmic motor movement or vocalization (Deeb et al., 2019). The Diagnostic and Statistical Manual of Mental Disorders, 5th edition (DSM-5) classifies TD into provisional tic disorders (PTD), chronic motor or vocal tic disorders (CTD) and Tourette syndrome (TS) (Association AP, 2013). According to the national-scale psychiatric epidemiological survey in China in 2021, the prevalence of PTD, CTD, TS in school children and adolescents is 1.2%, 0.9% and 0.4%, respectively (Li et al., 2021). Before treatment, Yale Global Tic Severity Scale (YGTSS) is commonly used to assess the frequency and severity of tic symptoms in clinics (Martino et al., 2017). The treatment of TD contains pharmacological treatment and non-pharmacological treatment and patients with moderate to severe conditions need pharmacological treatment. Tiapride, clonidine adhesive patch and aripiprazole (ARI) are recommended as the first-line pharmacological treatment in the expert consensus (Liu et al., 2020). Recently, the European Society for the Study of Tourette Syndrome (ESSTS) proposed that ARI should be the first choice of drug for TD both in children and adults (Roessner et al., 2022).

ARI is the third-generation atypical antipsychotic which acts as a partial agonist at the dopamine D₂, dopamine D₃ and serotonin 5-HT_{1A} receptors and an antagonist at the serotonin 5-HT_{2A} receptors (Shapiro et al., 2003). The main active metabolite of ARI is dehydroaripiprazole (DARI), which

accounts for 40% ARI exposure in plasma (Kinghorn and Mcevoy, 2005). Due to the long half-life ($T_{1/2}$) of ARI, it usually reaches steady state concentrations after 14 days of treatment or dose adjustment (Prommer, 2017). According to the 2017 Arbeitsgemeinschaft für Neuropsychopharmakologie und Pharmakopsychiatrie (AGNP)-therapeutic drug monitoring (TDM) expert group consensus guidelines for TDM recommendations of ARI, the therapeutic reference ranges are 100–350 ng/ml for ARI, and 150–500 ng/ml for ARI plus DARI (Hiemke et al., 2018). For pediatric patients, the application of TDM in ARI appears to be more important in terms of their development (Rafaniello et al., 2020). However, there are no specific therapeutic reference ranges in ARI or DARI for children with TD. Meanwhile, a few related literatures were reported just in adult patients with schizophrenia (Kirschbaum et al., 2008; Lin et al., 2011).

ARI is mainly metabolized in the liver through three biotransformation pathways: dehydrogenation, hydroxylation and N-dealkylation via CYP2D6 and CYP3A4 enzyme (Belmonte et al., 2018). ARI is metabolized to a lesser extent by CYP3A4 enzyme, recent research progress showed that CYP3A4 genotype did not significantly influence the pharmacokinetics of ARI and DARI (Belmonte et al., 2018; Saiz-Rodríguez et al., 2020). The ATP-binding cassette sub-family B member 1 (ABCB1) gene is located on chromosome 7 at q21 and codes for the P-glycoprotein (P-gp) (Gottesman et al., 1995). P-gp involves in the process of absorption, distribution and elimination of ARI, which transports ARI across intracellular and extracellular membranes (Thiebaut et al., 1987). Both ARI and DARI are possible substrates of P-gp and it was reported that ABCB1 polymorphism was associated with the serum concentrations of ARI or DARI (Gunes et al., 2008; Rafaniello et al., 2018). CYP2D6 is a highly polymorphic gene. According to the classifications of CYP2D6 genotype, subjects are usually divided into four phenotypes as following: poor metabolizers (PMs), intermediated metabolizers (IMs), normal metabolizers (NMs), and ultra-rapid metabolizers (UMs) (Gaedigk et al., 2017; pharmvar, 2022). Previous studies showed that there was high variability in inter- and intra-individual pharmacokinetics of ARI (Molden et al., 2006), which could be mainly explained by CYP2D6 genetic polymorphisms (Jovanovic et al., 2020). Those studies were mainly aimed at psychiatric patients or healthy subjects in adults. However, for

TD patients, especially in children, there were insufficient research data and several limitations. Besides the genetic polymorphisms, the other factors such as physiological developmental index, liver and renal function, or drug combination may influence the pharmacokinetics of ARI. Moreover, the correlation between serum concentrations and treatment response of ARI is still unclear and the therapeutic range of serum concentrations has not been estimated. Furthermore, the dose of ARI is often adjusted on the basis of drug response and side effects in clinics and the optimal dose regimens are under researched.

In this study, a combined population pharmacokinetic (PPK) model of ARI and its metabolite DARI was developed. It investigated the contributions of CYP2D6 and ABCB1 genetic polymorphisms, physiological factors, and drug combinations in ARI and DARI pharmacokinetics. Finally, the precise medication for pediatric patients with TD was promoted and appropriate dosing regimens were proposed.

Materials and methods

Study population

This prospective study was conducted at the Department of Pediatric Neurology of Wuhan Children's hospital, Huazhong University of Science and Technology, from January 2021 to July 2022. The inclusion criteria for patients included in the pharmacokinetic study were listed as follows: 1. The diagnosis complies with the diagnostic criteria of TD in DSM-5; 2. Chinese patients, aged less than 18 years, no matter of sex 3. Pharmacological treatment included ARI monotherapy or ARI add-on therapy; 4. Free from any known organic diseases, normal liver and renal functions, normal electrocardiogram (ECG) and so on. The exclusion criteria for pharmacokinetic study were listed as follows: 1. Subjects participated in other clinical trials in the past 1 month; 2. the clinical data were incomplete; 3. Poor medication adherence or lost follow-up; 4. Patients with epilepsy, encephalitis, schizophrenia, abnormal liver function or other organic diseases. The inclusion criteria for pharmacodynamic study were listed as follows on the basis of above inclusion criteria in pharmacokinetic study: YGTSS total score ≥ 25 at the baseline. The exclusion criteria for pharmacodynamic study were as follows on basis of the above exclusion criteria in pharmacokinetic study: add other drugs for the treatment of TD or adjust the dose of drugs other than ARI during follow-up. The study was approved by the Ethics Committee of Wuhan Children's hospital, Huazhong University of Science and Technology (No: 2021R101-E01). Informed consent was obtained from the guardians of the children involved in this study.

Dosage regimen, blood sampling and data collection

ARI was orally administered to the pediatric patients at a dose of 1.25–5 mg once a day in the first week, with a gradual increase to the target dose of 2.5–20 mg/d. The dose adjustment interval was at least 1 week. A sampling strategy was selected to collect blood samples for pharmacokinetic analysis. The dosing and sampling time was accurately recorded. Blood samples (4 ml) were collected from patients after orally taking ARI for at least 14 consecutive days. The serum concentrations of ARI were tested, subsequently the residual blood samples were separated and stored at -70°C for CYP2D6 and ABCB1 genetic testing.

Individual laboratory and demographic parameters were collected from the electronic medical records database, including age, gender, height, weight, alanine aminotransferase (ALT), aspartate aminotransferase (AST), direct bilirubin (DBIL), total bilirubin (TBIL), albumin (ALB), globulin (GLB), γ -glutamyltranspeptidase (γ -GT), blood urea nitrogen (BUN), serum cystatin C (Cys-C), and serum creatinine concentration (Scr). The body surface area (BSA) was calculated by the Mosteller formula. The estimated glomerular filtration rate (eGFR) was obtained by the modified Schwartz formula.

Quantification of ARI and DARI

The concentrations of ARI and DARI were detected by using the HPLC method. The preparation procedures of the sample were as follows: Blood sample was centrifuged at 1,500 g for 10 min and 0.5 ml serum sample was added into the solid-phase extraction column (Agela Technologies, Cleanert ODS C18), subsequently methanol containing 0.05% hydrochloric acid was used for elution. The Innoval C18 column (Agela Technologies, 5 μm , 4.6 \times 250 mm) was used for separation. Ammonium acetate (0.03 mol/L): methanol = 20:80 was prepared as the mobile phase. The wavelength of ultraviolet (UV) detection was 217 nm. The linear ranges of ARI and DARI detection were 10–1,490 ng/ml and 15–1,070 ng/ml, respectively. The intra- and inter-day precisions for ARI and DARI were within 10%.

CYP2D6 and ABCB1 SNP detection, CYP2D6 allele and genotype frequencies

First-generation sequencing was utilized for genetic detection, consisting of DNA extraction, polymerase chain reaction (PCR) amplification and SNP detection process. DNA extraction was performed by MolPure[®] blood DNA kits (Yeasen Biotechnology, Shanghai). SNP detection was

determined by 3730XL Sequencer (ABI, Inc., USA) by Sangon Biotech (Shanghai, China).

A total of 27 SNPs were detected and consisted of 25 SNPs of CYP2D6 and 2 SNPs of ABCB1, including CYP2D6*3 (rs35742686), CYP2D6*4 (rs3892097), CYP2D6*6 (rs5030655), CYP2D6*9 (rs5030656), CYP2D6*14 (rs5030865), CYP2D6*17 (rs28371706), CYP2D6*33 (rs28371717), CYP2D6*35 (rs769258), CYP2D6*41 (rs28371725), CYP2D6*49 (rs1135822), CYP2D6*51 (rs72549348), CYP2D6*54 (rs267608297), CYP2D6*69 (rs267608289), rs1135840, rs16947, rs1058164, rs28371705, rs28371703, rs28371702, rs28371699, rs29001518, rs1080995, rs1065852, rs1080989, rs1080985, ABCB1 C3435T (rs1045642) and G2677T/A (rs2032582). The frequencies of CYP2D6 allele mutation were shown in gene heat map.

Based on the classification standard (Zhang et al., 2021), patients were categorized into four CYP2D6 metabolizer phenotypes. UMs were defined as carrying more than 2 normal function alleles, e.g., *1*1, *1*2, *2*2. NMs were defined as carrying 1 functional allele, e.g., *1*10, *1*33. IMs were defined as carrying 1 decreased-function allele and 1 non-function allele or carrying 2 decreased-function alleles, e.g., *3*10, *10*10. PMs were defined as carrying 2 non-function alleles, e.g., *3*3.

Clinical efficacy observation

Outpatients and telephone follow-ups were conducted respectively at the baseline and after 12 weeks of ARI treatment. The basic information such as gender, age, height, weight, disease type, comorbidity, dosage, concomitant medication, liver and kidney function, serum concentrations of ARI and metabolite DARI, clinical efficacy was recorded in detail during follow-up. The severity of TD was assessed by Yale Global Tic Severity Scale (YGTSS). The scale includes three parts: motor tic score, vocal tic score and functional impairment score. The sum of the three parts is the total scores of YGTSS. The higher the total scores, the more serious the symptoms of disease. After 12 weeks treatment, the clinical efficacy was assessed by the YGTSS score reduction rate (%). YGTSS score reduction rate (%) = (total scores before treatment – total scores after treatment) / total score before treatment × 100%. Compared with the baseline YGTSS scores, when YGTSS score reduction rate is less than 50%, it is evaluated as ineffective. When YGTSS score reduction rate is more than 50%, it is evaluated as effective. Side effects or adverse events were observed and recorded during treatment.

PPK modeling

The population pharmacokinetics analysis was performed by the software Phoenix® NLME (Version 8.2.0. 4383, Pharsight Corporation, USA) and R program (Version 4.0.2). The first

order conditional estimation-extended least squares (FOCE ELS) method was applied to the estimation of population pharmacokinetic parameters and the variabilities.

Construction of the base model

One- or two-compartment model with first-order elimination were evaluated for ARI and DARI. Since the lack of absorption and distribution phase data, the parameters were difficult to be estimated by two-compartment model. Therefore, two one-compartment tandem models were applied in the construction of the base model for both ARI and DARI. According to the reports in the literature, the absorption rate constant (k_a) was fixed at 1.06 h^{-1} (Jovanovic et al., 2020), and the bioavailability (F) was not estimated. The material balance formulas were shown in Equations 1–3.

$$dA(\text{dose})/dt = -k_a \times A(\text{dose}) \times F \quad (1)$$

$$dA(p)/dt = k_a \times A(\text{dose}) \times F - CL/V_d \times A(p) \quad (2)$$

$$dA(m)/dt = F_m \times k_n \times CL/V_d \times A(p) - CL(m)/V_d(m) \times A(m) \quad (3)$$

where $A(\text{dose})$ represents the dosage of ARI, k_a is the absorption rate constant, F is the oral bioavailability of ARI, $A(p)$ is the amount of ARI in the central compartment, CL/F is the apparent clearance of ARI, V_d/F is the apparent volume of distribution, $A(m)$ is the amount of DARI in the metabolic compartment, F_m is the dosage conversion fraction from ARI to DARI, since the amount of ARI translate to DARI was unknown, F_m was not estimated in this study. k_n is the molecular mass ratio of DARI/ARI (0.995), $CL(m)/F_m$ is the apparent clearance of DARI, $V_d(m)/F_m$ is the apparent volume of distribution of DARI.

The exponential and proportional model were respectively applied to the estimation of inter- and intra-individual variability, which were shown as Equations 4, 5.

$$P_i = \theta \times \exp(\eta_i) \quad (4)$$

$$Y = IPRED \times (1 + \varepsilon) \quad (5)$$

where P_i is regarded as the individual pharmacokinetic parameter, θ represents the typical value of the population pharmacokinetic parameter, η_i is the inter-individual variation, and η_i conforms to a normal distribution with mean 0 and variance ω^2 . Y is the observed drug concentration, $IPRED$ is the individual prediction, ε is the intra-individual variation, and ε conforms to a normal distribution with mean 0 and variance σ^2 .

Covariate analysis

After the construction of the basic structure model, the stepwise method was used to investigate the influence of

covariates on the pharmacokinetic parameters, and the inclusion or exclusion of a covariate depended on the changes of the objective function value (OFV). The forward and backward selections were utilized. In the forward selection, the covariate would be added into the basic structure model if the decrease in OFV was more than 3.84 ($p < 0.05$, $df = 1$). The covariates were removed from the model one by one. In the backward selection, the covariate should be removed if the increase of OFV was less than 6.64 ($p < 0.01$, $df = 1$). Then the final PPK model was established.

The covariates in the final model consisted of continuous variables and categorical variables. Continuous variables included age, height, weight, liver and kidney function indicators. Categorical variables included gender, genotype, and combination medication. The introduction methods of continuous and categorical variables were shown in Equations 6, 7, respectively. Five developmental models were tried to analyze the effect of physiological development on ARI clearance (Ding et al., 2015; Li et al., 2020).

$$\theta_i = \theta \times \left(\frac{Cov-j}{Cov-median} \right)^{\theta_{cov}} \quad (6)$$

$$\theta_i = \theta \times \exp(\theta_{cov}) \quad (7)$$

where θ_i represents the population predicted value of pharmacokinetic parameter, θ is the population typical value, $Cov-j$ is the j th continuous covariate, $Cov-median$ is the median value of the covariate, and θ_{cov} is regarded as the fixed effect of the covariate on the parameter.

Validation of the final model

The prediction performance of the population pharmacokinetic model was usually evaluated by nonparametric bootstrap analysis, goodness-of-fit plots, normalized prediction distribution errors (NPDE), and visual predictive check (VPC). Both bootstrap analysis and VPC tests were run for 1,000 times to assess the accuracy and stability of the final model established in this study. To confirm the reliability of the final model, the bootstrap parameters were required to be within 10% of the final model parameters and the 90% CIs of the VPC predicted values should cover most of the measured values. Goodness-of-fit plots were employed to check the agreement between the predicted and observed value, to verify whether the prediction error has a significant drift with the predicted value or observation time, including observed concentrations vs. individual predictions or population predictions (PRED), conditional weighted residuals (CWRES) vs. PRED or time. The distributional trends and characteristics of the data error were checked by NPDE. The results were generalized graphically by default as obtained from the R package, including Quantile-quantile plot, the NPDE histogram,

and scatterplots of NPDE against time after the last dose or against PRED. The NPDE was expected to follow the normal distribution.

Model-based simulations

The area under the curves over 24 h (AUC_{24h}), peak concentrations (C_{max}) and trough concentration (C_{min}) of ARI and DARI at steady-state were calculated by employing Bayesian maximum posterior probability method. The metabolic ratio (MR, DARI/ARI) was calculated and the comparison of MRs between different groups (UMs, NMs, IMs) was explored. The ROC curve was used to find the diagnostic cut-off point of MR for distinguishing IMs or UMs from other patients. The relationship between steady-state trough concentration of ARI, DARI, ARI plus DARI and clinical efficacy was investigated respectively by ROC method. Otherwise, the relationship between the dose of ARI and clinical efficacy was investigated and the diagnostic cut-off point was determined. The concentrations collected at non-standard valley time point were corrected by Bayesian method.

The target indexes of the simulated trough concentration of ARI and ARI plus DARI were determined on the basis of the observation of clinical efficacy and the standard of AGNP. The Monte Carlo simulations were performed by the parameters and variabilities derived from the final model. Each dose, as well as each scenario, was simulated for 1,000 times to evaluate the clinical efficacy and safety of different dosing regimens under different covariate factors. The steady-state trough concentration and the probability of reaching the target (PTA) of efficacy and toxicity were calculated.

Results

Study population

Totally 84 patients aged 4.83–17.33 years old were included for PPK analysis. These patients consisted of 64 males and 20 females, all of which were diagnosed with TD. The body weight ranged from 17.90 to 100 kg. The demographic and clinical characteristics of the patients for the pharmacokinetics analysis in this study are summarized in Table 1.

Phenotypic and CYP2D6 allele frequencies

All subjects were genotyped for all the variants ($n = 84$ subjects). The results of CYP2D6 genotype and phenotype were shown in Table 2. The results of CYP2D6 allele mutation frequencies were shown in Supplementary Figure S1 in the supplementary document.

TABLE 1 Basic information of patients for the pharmacokinetics analysis in this study.

	n	Mean \pm SD	Median (range)
Patients	84	—	—
Sex (male: female)	64:20	—	—
Age (year)	—	9.62 \pm 2.73	9.17 (4.83–17.33)
Body weight (kg)	—	40.25 \pm 16.76	36.00 (17.90–100.00)
Height (cm)	—	141.92 \pm 15.85	142.00 (108.00–176.00)
Body surface area (m ²)	—	1.24 \pm 0.32	1.21 (0.73–2.21)
ALT (U/L)	—	14.67 \pm 7.81	13.00 (5.00–50.00)
AST (U/L)	—	21.47 \pm 4.60	21.00 (12.00–33.00)
DBIL (mol/L)	—	3.84 \pm 1.36	3.60 (1.90–8.40)
TBIL (μ mol/L)	—	9.39 \pm 3.92	8.65 (3.00–23.70)
γ -GT (U/L)	—	13.14 \pm 4.99	12.00 (7.00–40.00)
GLB (g/L)	—	23.22 \pm 3.15	23.35 (15.40–30.00)
ALB (g/L)	—	48.51 \pm 2.39	48.25 (43.10–55.30)
CRE (μ mol/L)	—	43.77 \pm 10.29	42.05 (28.00–91.70)
BUN (mmol/L)	—	4.54 \pm 0.99	4.59 (2.20–7.60)
Cys-C (mg/L)	—	0.86 \pm 0.11	0.86 (0.62–1.25)
eGFR (mL/min \cdot 1.73m ²)	—	121.72 \pm 18.58	121.56 (66.49–162.39)
Concentration of ARI (ng/ml)	—	137.11 \pm 81.47	123.96 (11.31–346.55)
Concentration of DARI (ng/ml)	—	50.83 \pm 29.39	44.10 (15.19–162.40)
Number of combined medication cases			
Tiapride	26	—	—
Clonidine	41	—	—
Methylphenidate	1	—	—
Topiramate	3	—	—
Trihexyphenidate	1	—	—
Inosine	4	—	—
Chinese traditional medicine	10	—	—

TABLE 2 The distribution of CYP2D6 genotypes and phenotypes.

Genotype/Phenotype	N (%)	Genotype/Phenotype	N (%)
CYP2D6 genotype	—	*10*10	30 (35.71%)
*1*1	1 (1.19%)	*10*14	3 (3.57%)
*1*2	6 (7.14%)	*10*41	2 (2.38%)
*39*39	8 (9.52%)	CYP2D6 phenotype	—
*1*10	27 (32.14%)	UMs	15 (17.86%)
*1*41	3 (3.57%)	NMs	34 (40.48%)
*1*14	1 (1.19%)	IMs	35 (41.67%)
*10*34	1 (1.19%)	PMs	0 (0.00%)
*10*35	1 (1.19%)	—	—
*1*33	1 (1.19%)	—	—

Population pharmacokinetic modeling

The number of samples collected from per patient was 1–5, and finally a total of 143 serum concentrations were collected for

population pharmacokinetic modeling. Most of the blood samples were obtained after continuous administration for at least 14 days in this study, only one blood sample was collected less than 14 days because of adverse reactions. The modeling

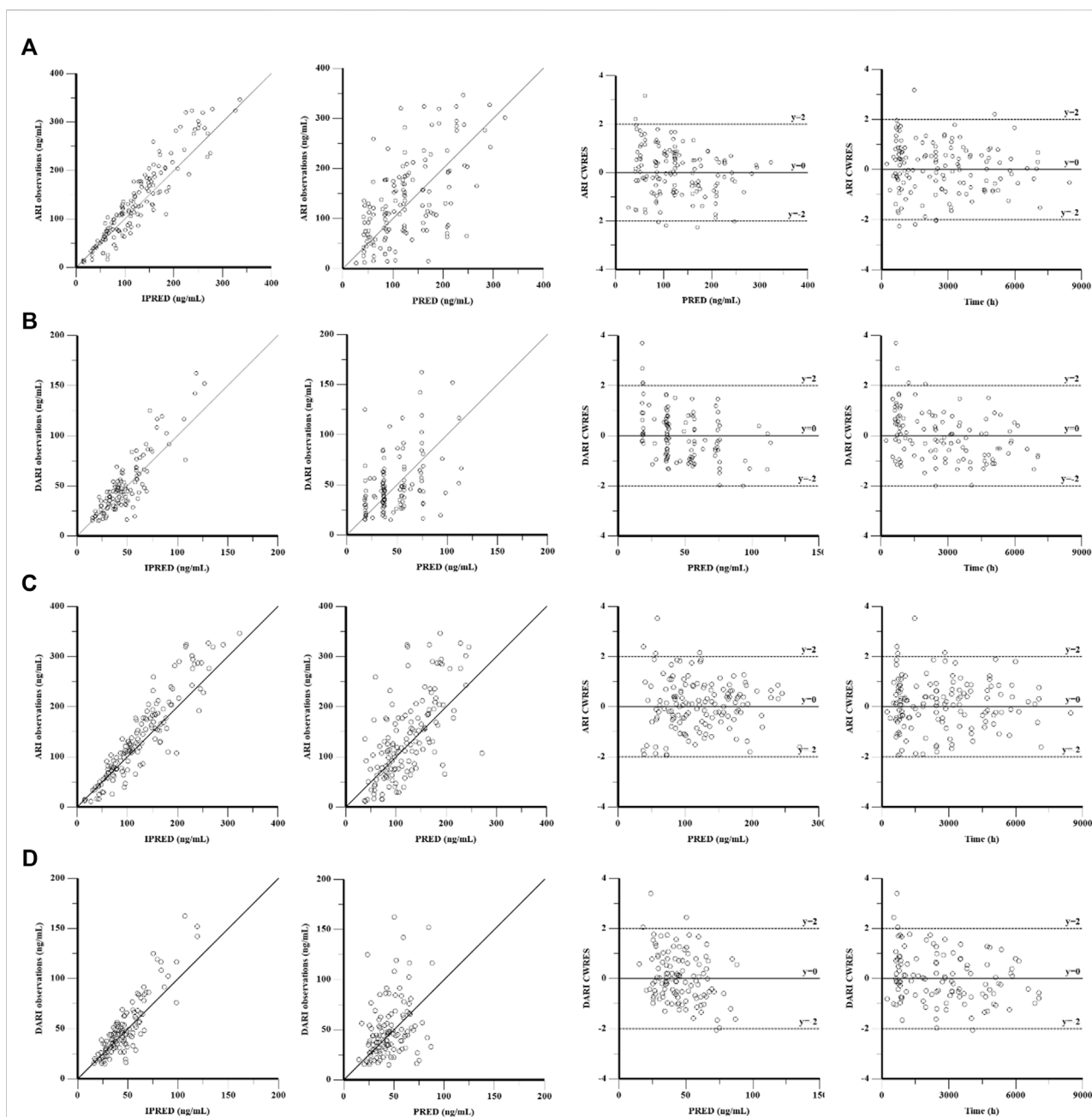


FIGURE 1

Goodness-of-fit plot of the base model and final population pharmacokinetics model for ARI (A,C) and DARI (B,D). From left to right, the plots are observations against individual predictions (IPRED), observations against population predictions (PRED), conditional weighted residuals (CWRES) against PRED, and CWRES against time, respectively.

procedures were shown in [Supplementary Table S1](#) in supplementary document. The simplest exponent model was applied as developmental model resulting from the lowest values of OFV, Akaike information criterion (AIC) and Bayesian information criterion (BIC). Comparing with the basic model, the decrease of OFV, AIC and BIC in the final model integrating

with body weight and CYP2D6 genotype were 33.2, 27.2 and 16.5 units, respectively.

Both body weight and genotype were included in the final PPK model and the final model was expressed using Equations 8 to 12:

$$k_a (h^{-1}) = 1.06 \quad (8)$$

TABLE 3 Pharmacokinetic parameters and bootstrap results of the final model.

Parameter	Final model		Bootstrap analysis	
	Estimate	RSE (%)	Bootstrap median	Bootstrap 95%CI
θ_{ka} (h^{-1})	1.06 (fixed)	—	1.06 (fixed)	—
$\theta_{Vd/F}$ (L)	219.91	23.36	226.07	158.86–370.98
$\theta_{CL/F}$ ($L \cdot h^{-1}$)	3.06	11.92	2.99	2.37–4.05
$\theta_{Vd(m)/Fm}$ (L)	423.78	43.01	431.19	44.47–1,097.35
$\theta_{CL(m)/Fm}$ ($L \cdot h^{-1}$)	8.86	5.56	8.87	7.90–9.78
θ_1	1.00 (fixed)	—	1.00 (fixed)	—
θ_2	0.64	21.86	0.62	0.37–0.89
θ_{NM}	0.00 (fixed)	—	0.00 (fixed)	—
θ_{IM}	-0.23	25.32	-0.23	-0.42–0.03
θ_{UM}	0.21	35.09	0.21	0.01–0.53
θ_3	1.00 (fixed)	—	1.00 (fixed)	—
θ_4	0.75 (fixed)	—	0.75 (fixed)	—
Inter-individual variation				
$\omega_{Vd/F}^2$	79.99	39.38	73.52	12.81–134.22
$\omega_{CL/F}^2$	12.07	24.52	10.90	4.43–17.35
$\omega_{CL(m)/Fm}^2$	15.31	30.63	14.75	5.44–24.05
Intra-individual variation				
σ_{ARI} (%)	35.45	9.34	36.10	25.72–43.17
σ_{DARI} (%)	35.37	7.17	34.66	29.38–39.44

θ_1 , exponent for WT as covariate for V_d/F ; θ_2 , exponent for WT as covariate for CL/F ; θ_3 , exponent for WT as covariate for $V_{d(m)}/F_m$; θ_4 , exponent for WT as covariate for $CL_{(m)}/F_m$.

$$V_d/F(L) = 219.91 \times \left(\frac{WT}{70}\right)^{1.0} \times \exp(\eta_{V_d/F}) \quad (9)$$

$$CL/F(L \cdot h^{-1}) = 3.06 \times \left(\frac{WT}{70}\right)^{0.64} \times \exp(\theta_{genotype}) \times \exp(\eta_{CL/F}) \quad (10)$$

$$V_{d(m)}/F_m(L) = 423.78 \times \left(\frac{WT}{70}\right)^{1.0} \quad (11)$$

$$CL_{(m)}/F_m(L \cdot h^{-1}) = 8.86 \times \left(\frac{WT}{70}\right)^{0.75} \times \exp(\eta_{CL_{(m)}/F_m}) \quad (12)$$

where WT is the body weight, V_d/F is the apparent volume of distribution of ARI, $V_{d(m)}/F_m$ is the apparent volume of distribution of DARI, CL/F is the apparent clearance of ARI, $CL_{(m)}/F_m$ is the apparent clearance of DARI. The clearance of ARI was decreased by 20.55% in IMs, and increased by 23.37% in UMs.

Final model validation

The goodness-of-fit plots were presented in Figure 1. The observed serum concentrations showed closely agreement with the model prediction and conditional prediction residuals mostly located within ± 2 standard deviations without significant drift, suggesting the predictive accuracy

of the final model. The results of the nonparametric bootstrap analysis could be seen in Table 3. The final model estimates distributed in the 95% confidence intervals (CIs) of estimates obtained from the bootstrap procedure and were close to the median parameter estimates with small bias, which indicated good stability of the population pharmacokinetic model. Additionally, the VPCs for both ARI and DARI were shown in Figure 2. Almost all of the observed concentrations were within the 90% CIs, validating the predictive capability of the final model. As shown in Figure 3, the NPDE analysis for ARI and DARI were performed by employing t-test, Shapiro Wilks test, Fisher's variance test, and Global test. The NPDE results were shown in Supplementary Table S2, which suggested that the NPDEs followed a normal distribution with P values larger than 0.05.

Pharmacodynamic observations

As shown in Supplementary Table S3, totally 56 pediatric patients with TD were ultimately enrolled for the pharmacodynamic analysis of ARI. After analyzing and assessing, 73% effective rate and 26.8% adverse reaction incidence rate were acquired (41/56) after 12-week ARI monotherapy or add-on treatment. The relationships

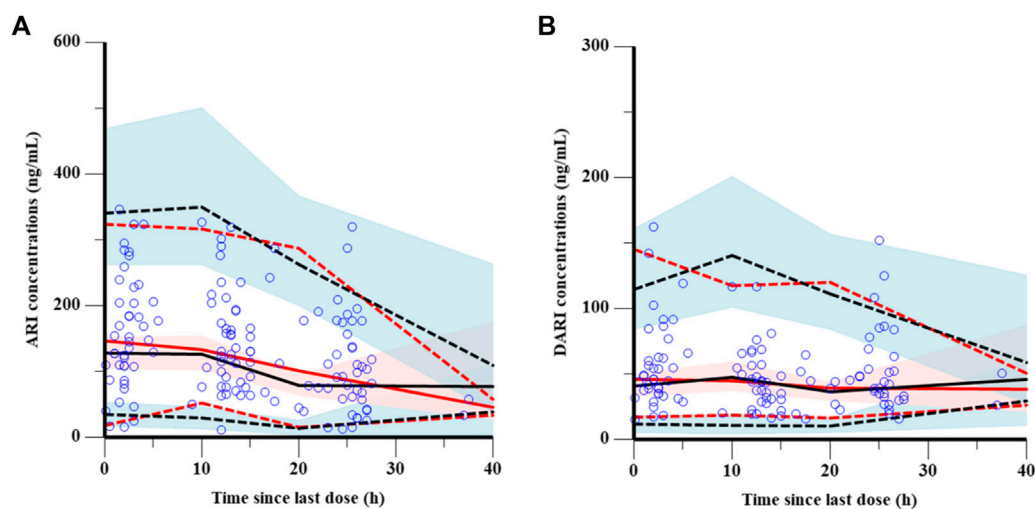


FIGURE 2

Visual prediction checks of the final model for ARI (A) and DARI (B). The blue points represent the observed value. The dashed and solid red lines are the 5th percentile, 95th percentile and the median of the observed concentrations, respectively. The dashed and solid black lines are the 5th percentile, 95th percentile and the median of the simulated concentrations, respectively. The shaded areas represent the 90% predicted intervals of the 5th, 50th and 95th percentiles of the simulated data, respectively.

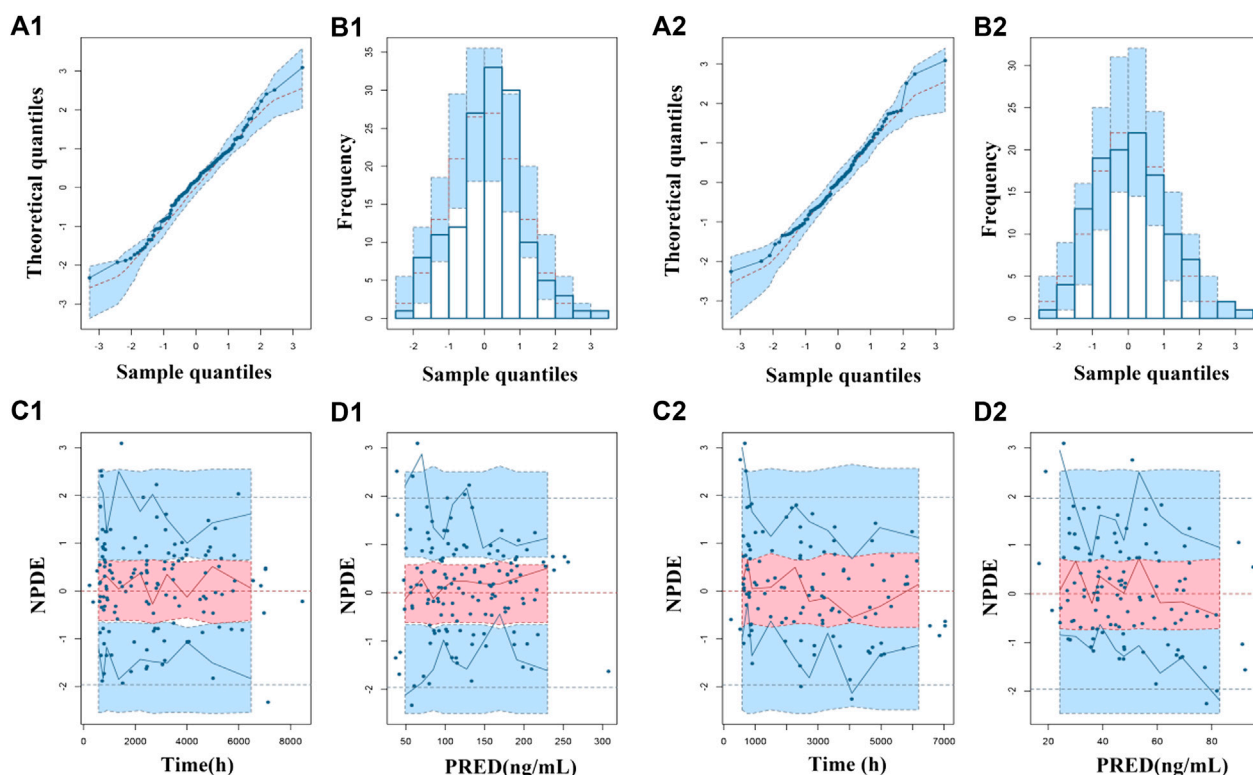
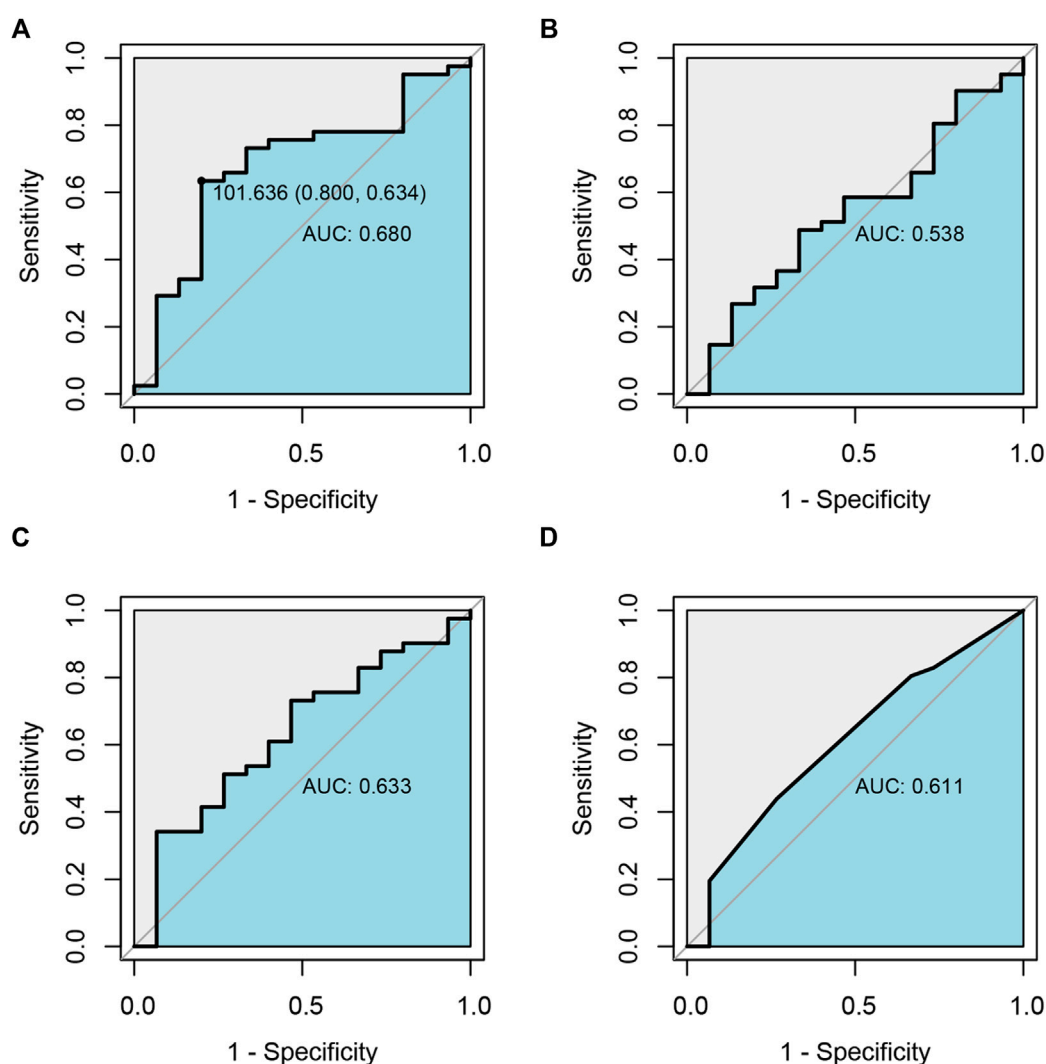


FIGURE 3

Normalized prediction distribution errors (NPDEs) of the final population pharmacokinetic model for ARI (1) and DARI (2). (A1,A2) Quantile-quantile plot vs. the expected standard normal distribution for ARI and DARI; (B1,B2) Histogram of NPDE with the density of the standard normal distribution overlaid; (C1,C2) Scatterplot of NPDE against time; (D1,D2) Scatterplot of NPDE against PRED.

**FIGURE 4**

Receiver operating characteristic curve (ROC) analysis of the relationship between drug exposure of ARI(A), DARI(B), ARI plus DARI(C) and clinical efficacy, and the relationship between the dosage of ARI and clinical efficacy (D).

between drug exposure, the dosage of ARI and clinical efficacy were analyzed by employing ROC diagnostic curve, and the results were shown in Figure 4. The areas under the curve of ARI, DARI, ARI plus DARI and ARI dosage were 0.680, 0.538, 0.633, and 0.611, respectively. The area under the curve of ARI was the largest with the lower limit of 95%CI larger than 0.5, but the lower limits of 95%CI of DARI and ARI plus DARI were less than 0.5, suggesting the best predictor of the clinical efficacy for children with TD was the trough concentration of ARI. In addition, the cut-off point was 101.636 ng/ml, with the sensitivity and specificity of 0.800 and 0.634 respectively, which was very close to the lower limit of 100–350 ng/ml recommended by AGNP for mental disorders in adults. The

intolerable adverse reactions were not observed within 350 ng/ml during the administration in this study. Therefore, 100–350 ng/ml was selected as the target index range of steady-state trough concentration of ARI.

Simulation and dosing regimen optimization

The predicted concentration-time profiles of ARI and DARI during 30 days oral administration were simulated according to the CYP2D6 phenotypes. The median body weight of 36 kg and the median dose of 0.5 mg once a day were applied to simulated.

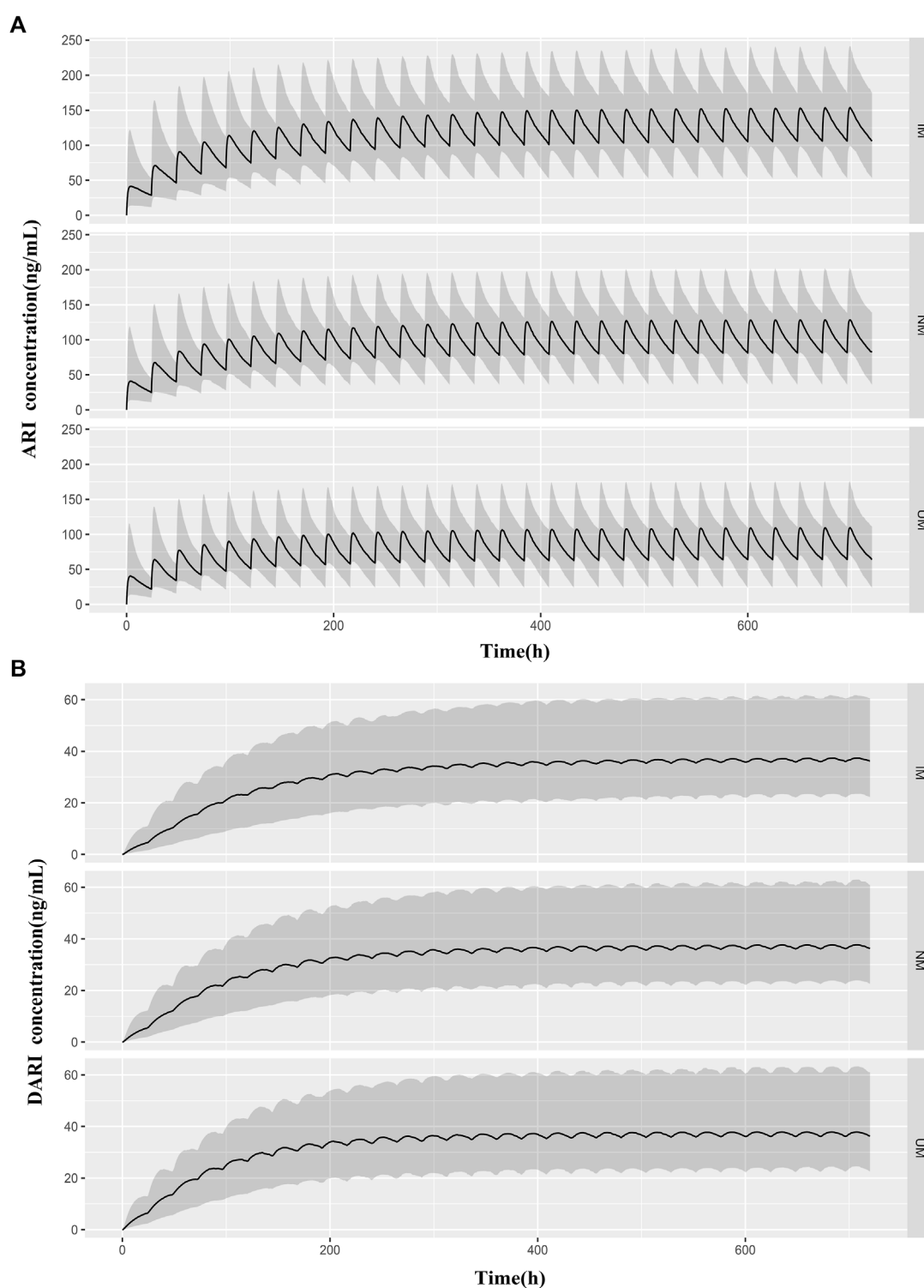
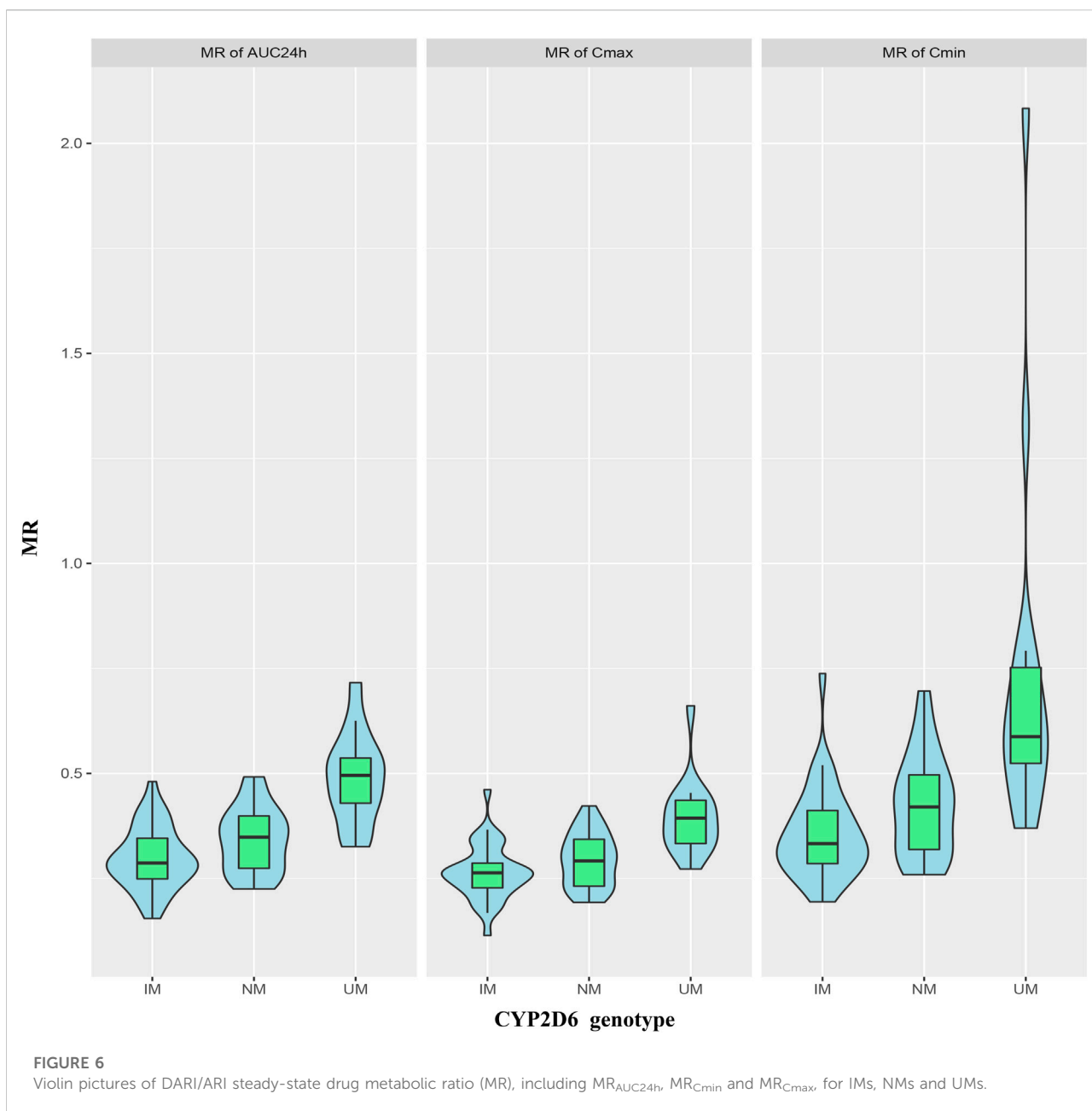


FIGURE 5

Predicted pharmacokinetic profiles of ARI (A) and DARI (B) during the first 20 days of treatment obtained from IMs, NMs, and UMs. The median body weight of 36 kg and the median dose of 0.5 mg were applied to simulated. The black line is the median of the simulated concentrations. The grey shaded area represents the prediction interval (10th-90th percentiles).



As shown in Figure 5, comparing to NMs and UMs, the trough concentrations of ARI at steady state showed significantly elevation in IMs, whereas the trough levels of DARI indicated no difference.

The MRs of AUC_{24h}, C_{min} and C_{max} for all patients were 0.35 ± 0.11 , 0.45 ± 0.25 and 0.30 ± 0.08 , respectively. The MRs of AUC_{24h} for UMs, NMs, IMs were 0.49 ± 0.11 , 0.34 ± 0.08 , and 0.30 ± 0.07 ; the MRs of C_{min} for UMs, NMs, IMs were 0.73 ± 0.44 , 0.43 ± 0.12 , and 0.36 ± 0.11 ; the MRs of C_{max} for UMs, NMs, IMs were 0.40 ± 0.09 , 0.29 ± 0.06 , and 0.26 ± 0.07 , respectively. The comparison of MRs between UMs, NMs, IMs was shown in Figure 6. The violin picture showed that the MR values of AUC_{24h}, C_{min} and C_{max} were UMs >

NMs > IMs ($p < 0.05$). As shown in Table 4, the diagnostic cut-off points of MRs were calculated respectively. The results showed that MRs could be used to distinguish UMs or IMs from other patients.

The PTAs of the trough concentrations of ARI and ARI plus DARI under different dosage regimens for patients with different body weight and CYP2D6 genotypes were shown in Supplementary Table S4, and Figure 7 was drawn based on these results. According to the results of PTAs, we organized the optimal dosage regimens for patients with different body weight and CYP2D6 phenotypes, which was shown in Table 5. Eventually, under the optimal dosage regimens, the PTAs of C_{min} of ARI ≥ 100 ng/ml and C_{min} of ARI plus DARI ≥ 150 ng/ml were larger than 75%; the PTAs of C_{min} of

TABLE 4 The diagnostic cut-off points of MRs for distinguishing UMs or IMs from other patients.

MRs	Area	95%CI	Cut-off point	Sensitivity	Specificity
MRs for UM diagnosis					
MR _{AUC}	0.91 ± 0.04	0.83–0.99	≥0.42	0.80	0.90
MR _{Cmin}	0.88 ± 0.05	0.79–0.97	≥0.52	0.80	0.88
MR _{Cmax}	0.88 ± 0.04	0.79–0.96	≥0.32	0.93	0.71
MRs for IM diagnosis					
MR _{AUC}	0.75 ± 0.05	0.64–0.85	≤0.31	0.69	0.74
MR _{Cmin}	0.75 ± 0.05	0.65–0.85	≤0.40	0.71	0.69
MR _{Cmax}	0.71 ± 0.06	0.60–0.83	≤0.28	0.71	0.71

ARI ≥350 ng/ml and C_{min} of ARI plus DARI ≥500 ng/ml were less than 5%; and the PTA of C_{min} of ARI ≥1,000 ng/ml was less than 1%. The results suggested that it was optimal to determine the dosing regimen of ARI for pediatric patients with TD based on body weight and CYP2D6 genotype.

Discussion

To the best of our knowledge, this research firstly described the PPK analysis of oral ARI in pediatric patients with TD. We found body weight and CYP2D6 genotype were the most important covariates that contributed to the inter-individual variability of ARI pharmacokinetics in children with TD. The study illustrated the relationship between ARI serum concentrations and clinical response, thus playing an instrumental role in proposing personalized dose regimens of ARI.

Clinical response of ARI

In this study, the high response rate and low incidence of side effects of oral ARI reflected the good tolerance of ARI in treatment of TD. Similar findings were also found by other studies. In 2011, a prospective multicenter study on ARI against tiapride for TD suggested that the clinical response and adverse incidence rate of ARI were 60.21% and 29.6%, which paralleled with our results (Liu et al., 2011). The previous placebo-controlled clinical studies showed that oral ARI exhibited a good efficacy and safety profile for the treatment of TD (Sallee et al., 2017; Yang et al., 2019).

To date, drug exposure-efficacy relationship has not been well appreciated in pediatric TD patients. Our study confirmed a significant correlation between drug response and the parent drug (ARI) blood levels, while the correlation would be less vital when DARI or the sum of ARI and DARI were involved, which was consistent with findings from KIRSCHBAUM et al. (Kirschbaum et al.,

2008). In 2011, Lin et al. (Lin et al., 2011) analysed the relationship between the serum concentrations of ARI, DARI, ARI plus DARI and clinical response in 45 patients with schizophrenia and schizoaffective disorder. Responders were found significantly higher serum concentrations of DARI and ARI plus DARI, which might be caused by the large variability of MR (DARI/ARI) in neuropsychiatric patients. The serum concentrations of ARI seem to be more significant than DARI in the dose optimization for TD patients through TDM.

Population pharmacokinetics of ARI

Two one-compartment models were developed for both ARI and DARI to investigate the variability of pharmacokinetics of ARI. The population typical values obtained in the final PPK model were: $ka = 1.06 \text{ h}^{-1}$, $CL/F = 3.06 \text{ L} \cdot \text{h}^{-1}$, $Vd/F = 219.91 \text{ L}$. ka was fixed to 1.06 h^{-1} in accordance with previous researches (Kim et al., 2008; Jovanovic et al., 2020). The population typical value of CL/F in the final model was lower than the previously reported values which ranged from $3.15 \text{ L} \cdot \text{h}^{-1}$ – $3.88 \text{ L} \cdot \text{h}^{-1}$ (Kim et al., 2008; Knights and Rohatagi, 2015) but higher than that of Jeon et al.'s report ($2.69 \text{ L} \cdot \text{h}^{-1}$) (Jeon et al., 2016). As for the distribution volume of ARI, the Vd/F (219.91 L) obtained in this study was larger than the value of Kim et al.'s (193 L) and Knights and Rohatagi et al.'s (192 L) (Kim et al., 2008; Knights and Rohatagi, 2015). Racial differences, different sampling time, methods, physiological and pathological differences may contribute to the difference of the above values.

The researchers proposed that dose of ARI would not be adjusted in liver or renal impairment patients (Mallikaarjun et al., 2008). Though no liver or renal impairment occurred in this study, many other factors were taken into account. Drug combinations such as clonidine or tiapride, the most common drugs that patients used, were not included in the final PPK model in this study. Furthermore, no dose adjustments are

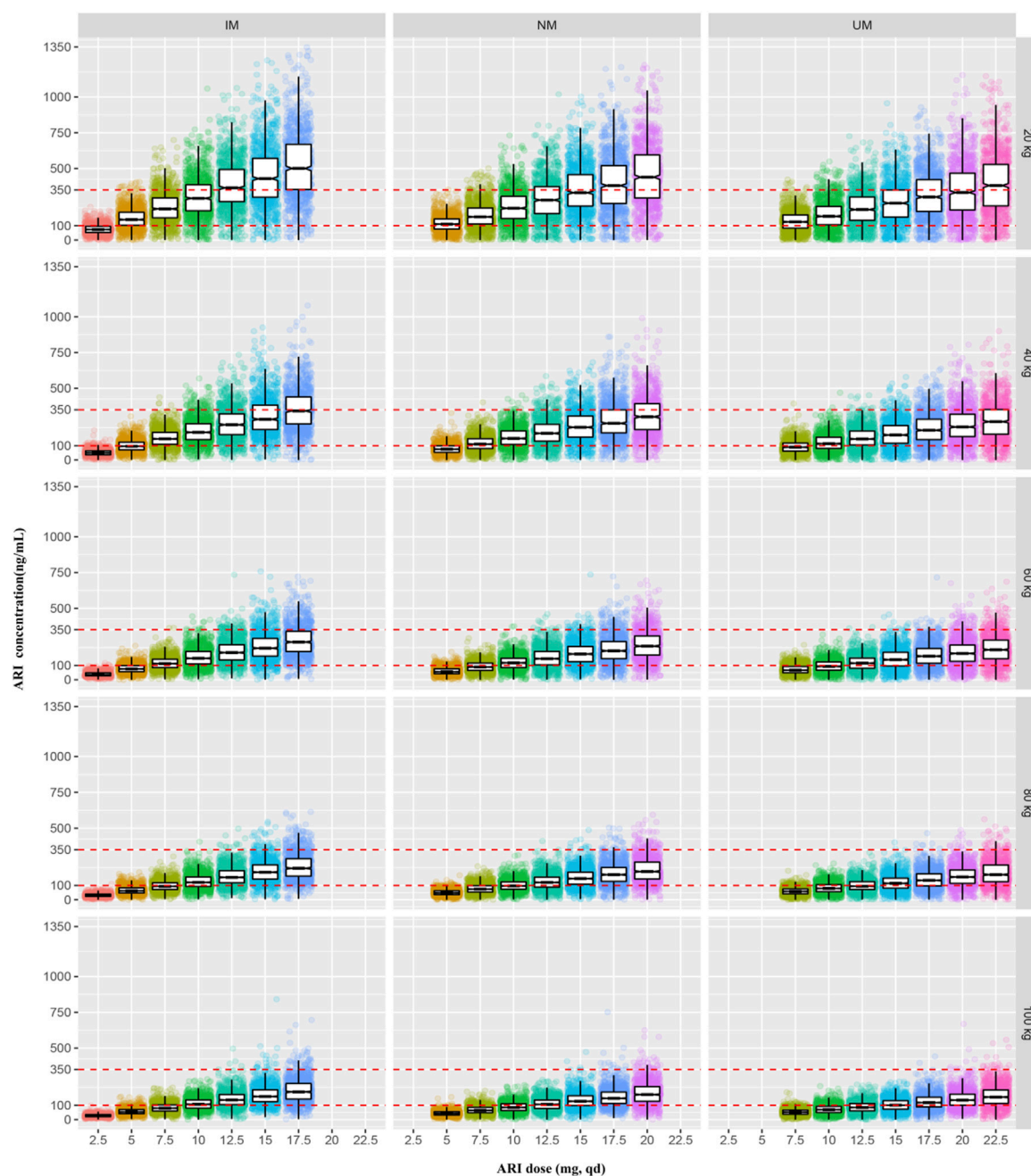


FIGURE 7

The simulated steady-state trough concentrations of ARI for patients with different body weight and CYP2D6 genotypes under the different dosage regimens.

required on the grounds of age, sex, race or smoking (Mauri et al., 2018). Moreover, gene polymorphism is deemed as a remarkable element in the field of pharmacokinetics study of ARI. The relationship between CYP2D6 genotype and ARI pharmacokinetics has been intensively probed over the past decade. Jeon et al. (Jeon et al., 2016) developed a two-

compartment model for ARI in healthy Korean subjects. They proposed that CYP2D6 genotype polymorphisms, height, and weight were the covariates significantly affecting ARI pharmacokinetic parameters such as CL/F, Vc/F and Vp/F. Similarly, Knights and Rohatagi et al. (Knights and Rohatagi, 2015) found that CYP2D6 genotype, weight (<115 kg) and age

TABLE 5 Optimal dosage regimens for patients of different CYP2D6 genotypes.

Group	Weight (kg)				
	20	40	60	80	100
NM	7.5 mg, qd	10.0 mg, qd	12.5 mg, qd	15.0 mg, qd	17.5 mg, qd
IM	5.0 mg, qd	7.5 mg, qd	10.0 mg, qd	12.5 mg, qd	12.5 mg, qd
UM	10.0 mg, qd	12.5 mg, qd	17.5 mg, qd	20.0 mg, qd	20.0 mg, qd

were the important covariates that influenced CL/F of ARI. Regarding the young population, few population models and the pharmacokinetic analyses embraced pediatric patients. The final model established in this study showed that the clearance of ARI in pediatric TD patients could be markedly affected by body weight and CYP2D6 genotype.

CYP2D6 and ABCB1 genetic polymorphisms in ARI

ARI metabolism is mainly mediated by CYP2D6, CYP3A4 and ABCB1 (Belmonte et al., 2018). It has been proved that CYP2D6, ABCB1 C3435T and G2677T/A but not CYP3A4 genotype were the most commonly reported genotypes associated with variability in absorption and excretion of ARI (Belmonte et al., 2018; Rafaniello et al., 2018). Furthermore, it was demonstrated that CYP3A5 polymorphism had no impact on the pharmacokinetics (Kim et al., 2008; Suzuki et al., 2014; Jeon et al., 2016). Although one study showed that subjects with CYP3A5 *3/*3 had a lower dehydro-aripiprazole/aripiprazole ratio (Belmonte et al., 2018), the influence of CYP3A5 on the pharmacokinetics of ARI and DARI is much smaller than that of CYP2D6. Therefore, CYP2D6 and ABCB1 SNPs were detected in this study. As previously reported, IMs comprise a large proportion of the Asian people, especially for CYP2D6*10 which accounts for more than 60% (Zhang et al., 2019). The IMs, NMs, UMs accounted for 41.7%, 40.5%, 17.8% respectively in this study, but no PMs were found. There was evidence that AUC_{0-t} of ARI of PMs was increased by 50% and AUC_{0-t} of DARI was decreased by 33% compared to EMs (Belmonte et al., 2018). In this study, we found that the C_{min} of ARI at steady state were notably increased in IMs in contrast to UMs and NMs, but no difference in the C_{min} of DARI. This suggested that the CYP2D6 genotype had no effect on the clearance of DARI. The critical metabolic rate-limiting step may lie in the metabolism of ARI but not in the clearance of the metabolites. At the same time, we also compared MRs of AUC_{24h}, C_{min} and C_{max} between the UMs, NMs and IMs, results showed that MRs were lower in subjects with lesser active CYP2D6 alleles and this conclusion was in agreement with Belmonte et al.'s report (Belmonte et al., 2018). MRs of

AUC_{24h}, C_{min} and C_{max} helped to distinguish UMs or IMs from other patients. AUC curves of MRs of AUC_{24h}, C_{min} and C_{max} as predictors of IMs or UMs were calculated with high sensitivity and specificity (Table 4). These parameters conferred precious value in clinical. To some extent, we can substitute MRs for CYP2D6 genotyping, which can make up for the large costs of genetic testing in poor areas or families and further promote individual medication.

ABCB1 genes variants may alter transport activities performed by their gene products, thus to influence the serum concentrations of drugs. It was reported that the clearance of ARI in ABCB1 TT/TT subjects would be lower (Moons et al., 2011). In view of already published works, controversial conclusions have been made by many researchers. Rafaniello et al. (Rafaniello et al., 2018) investigated the impact of ABCB1 on ARI concentrations in ninety Caucasian pediatric patients, which displayed that ABCB1 2677TT/3435TT genotype had a statistically significant lower ARI serum concentration/dose ratio compared with other ABCB1 genotypes. Nevertheless, Suzuki et al. (Suzuki et al., 2014) revealed that there was no difference between ABCB1 variants (C3435T and G2677T/A) and the exposure of ARI in Japanese adult patients with schizophrenia. Five ABCB1 TT/TT subjects were detected in this study but no relationship between ABCB1 variants (C3435T and G2677T/A) and the clearance of ARI was found, possibly due to small samples of this research. Therefore, ABCB1 genetic polymorphisms were not included as significant covariates in the final model established in this study. This might be ascribed to differences in races, sample numbers or disease types of subjects in various researches. Further study is required to promote precise dose adjustment of ARI in pediatric TD patients.

Optimal dosing regimens

So far, there is no consensus on clinical dosing regimen recommendations for ARI in tic disorders. Food and Drug Agency (FDA) or the Royal Dutch Pharmacists Association proposed that CYP2D6 PMs should be administered 50% and 67% of maximum recommended daily dosage respectively in psychotics (Sven et al., 2011; US Food and Drug

Administration, 2018). Although there are not recommendations for IMs or UMs, CYP2D6 genetic testing is still necessary in clinical dose adjustment (Bousman, 2019). The previous evidence-based researches also showed that CYP2D6 genetic testing helps to guide antipsychotic ARI medications: Kneller et al. (Kneller et al., 2021) used a physiologically based pharmacokinetic (PBPK) approach to estimate the effects of CYP2D6 phenotype-related physiological changes on the pharmacokinetics of ARI, DARI, and ARI plus DARI. They demonstrated that the daily dose should be adjusted for CYP2D6 PMs and the maximum daily dose recommended should be 10 mg. Meanwhile, the researcher proposed it was unnecessary to adjust dosage for UMs and IMs. However, the above model was developed on basis of data from healthy volunteers. Instead, IMs accounts for 45% in east Asian people, recently Jukic et al. indicated that 30% lower doses than usual should be administered to IMs and PMs (Jukic et al., 2019). This study firstly elucidated optimal and individualized dosing regimens based on different body weight and CYP2D6 genotypes in children with TD, thus ensuring therapy effectiveness and safety. For IMs, the weight of 20 kg, 40 kg, 60 kg, 80 kg, 100 kg should be given 5 mg, 7.5 mg, 10 mg, 12.5 mg, 15 mg, qd, respectively; for NMs, the weight of 20 kg, 40 kg, 60 kg, 80 kg, 100 kg should be given 7.5 mg, 10 mg, 12.5 mg, 15 mg, 17.5 mg, qd, respectively; for UMs, the weight of 20 kg, 40, 60, 80, 100 kg should be given 10, 12.5, 15, 17.5, 20 mg, qd, respectively. In China, ARI is an off-label drug for children with TD. Therefore, the individualized dosing regimens greatly help physicians to make appropriate dosing decisions.

Limitations

The limitations of our study are as follows: 1. Due to the limited sample size, no data on PMs were obtained; 2. It was difficult to estimate pharmacokinetic parameters in absorption and distribution phase because of the limited concentration data; 3. Some of the steady-state trough concentrations of ARI and DARI were corrected according to the pharmacokinetic parameters obtained from the PPK model because the blood samples of some patients were not collected at the time point of trough concentration. Despite these limitations, our study can provide a valuable reference for personalized ARI treatment in pediatric patients with TD.

Conclusions

This study firstly established a combined PPK model of ARI and DARI in pediatric patients with TD. The relationship between serum concentrations of ARI and clinical response was better understood and clinically important in offering a more promising therapeutic strategy for ARI. Furthermore, the

influence of CYP2D6 genotype on serum concentrations of ARI, DARI, and ARI plus DARI was investigated, which offered the first proof of phenotype-weight-guided dose adjustments in pediatric TD patients. ARI has achieved beneficial clinical effects and exhibited good tolerability in the treatment of TD. Finally, we really promoted the safer, proper and more individualized dosing regimens of ARI in clinical practice.

Data availability statement

The datasets presented in this study can be found in online repositories. The names of the repository/repositories and accession number(s) can be found below: NCBI Sequence Read Archive [SRA] (<https://www.ncbi.nlm.nih.gov/sra>), SRR21835902.

Ethics statement

The studies involving human participants were reviewed and approved by Ethics Committee of Wuhan Children's hospital, Huazhong University of Science and Technology (No: 2021R101-E01). Written informed consent to participate in this study was provided by the participants' legal guardian/next of kin.

Author contributions

ZL, DS, and YW: Conceptualization. YW, YX, and LG: Methodology and investigation. CC: Software support. YW: Software, validation, and formal analysis. YX and LG: Writing original draft. ZL, DS, YF, YW, GN, and YM: Supervision, Writing—review and editing. YT, JW, SL, and QQ: Project administration. All authors have read and agreed to the published version of the manuscript.

Funding

This study was supported by: 1. Construction Project of Clinical Medical Research Center for Neurodevelopmental Disabilities in Children in Hubei Province (No. HST2020-19). 2. The medical research project of Wuhan Municipal Health Commission (WX21A14). 3. Health commission of Hubei Province scientific research project (WJ2019H426). 4. The medical research project of Wuhan Municipal Health Commission (WX19B03).

Acknowledgments

We appreciate the assistance of GN and YT for editing the manuscript and CC for providing software support in this study.

Conflict of interest

The authors declare that the research was conducted in the absence of any commercial or financial relationships that could be construed as a potential conflict of interest.

Publisher's note

All claims expressed in this article are solely those of the authors and do not necessarily represent those of their affiliated

organizations, or those of the publisher, the editors and the reviewers. Any product that may be evaluated in this article, or claim that may be made by its manufacturer, is not guaranteed or endorsed by the publisher.

Supplementary material

The Supplementary Material for this article can be found online at: <https://www.frontiersin.org/articles/10.3389/fphar.2022.1048498/full#supplementary-material>

References

- Association AP (2013). *Diagnostic and statistical manual of mental disorders*. Fifth Edition. DSM-5 [M].
- Belmonte, C., Ochoa, D., Roman, M., Saiz-Rodriguez, M., Wojnicz, A., Gomez-Sanchez, C. I., et al. (2018). Influence of CYP2D6, CYP3A4, CYP3A5 and ABCB1 polymorphisms on pharmacokinetics and safety of aripiprazole in healthy volunteers. *Basic Clin. Pharmacol. Toxicol.* 122 (6), 596–605. doi:10.1111/bcpt.12960
- Bousman, C. A. (2019). CYP2D6 testing to guide risperidone and aripiprazole therapy. *Lancet. Psychiatry* 6 (5), 362–364. doi:10.1016/s2215-0366(19)30138-5
- Deeb, W., Malaty, I. A., and Mathews, C. A. (2019). Tourette disorder and other tic disorders. *Handb. Clin. Neurol.* 165, 123–153. doi:10.1016/b978-0-444-64012-3.00008-3
- Ding, J., Wang, Y., Lin, W., Wang, C., Zhao, L., Li, X., et al. (2015). A population pharmacokinetic model of valproic acid in pediatric patients with epilepsy: A non-linear pharmacokinetic model based on protein-binding saturation. *Clin. Pharmacokinet.* 54 (3), 305–317. doi:10.1007/s40262-014-0212-8
- Gaedigk, A., Sangkuhl, K., Whirl-Carrillo, M., Klein, T., and Leeder, J. S. (2017). Prediction of CYP2D6 phenotype from genotype across world populations. *Genet. Med.* 19 (1), 69–76. doi:10.1038/gim.2016.80
- Gottesman, M. M., Hrycyna, C. A., Schoenlein, P. V., Germann, U. A., and Pastan, I. (1995). Genetic analysis of the multidrug transporter. *Annu. Rev. Genet.* 29, 607–649. doi:10.1146/annurev.ge.29.120195.003135
- Gunes, A., Spina, E., Dahl, M. L., and Scordo, M. G. (2008). ABCB1 polymorphisms influence steady-state plasma levels of 9-hydroxyrisperidone and risperidone active moiety. *Ther. Drug Monit.* 30 (5), 628–633. doi:10.1097/FTD.0b013e3181858ca9
- Hiemke, C., Bergemann, N., Clement, H. W., Conca, A., Deckert, J., Domschke, K., et al. (2018). Consensus guidelines for therapeutic drug monitoring in neuropsychopharmacology: Update 2017. *Pharmacopsychiatry* 51 (1-02), 9–62. doi:10.1055/s-0043-116492
- Jeon, J. Y., Chae, S. W., and Kim, M. G. (2016). Population pharmacokinetics of aripiprazole in healthy Korean subjects. *Int. J. Clin. Pharmacol. Ther.* 54 (4), 293–304. doi:10.5414/cp202466
- Jovanovic, M., Vucicevic, K., and Miljkovic, B. (2020). Understanding variability in the pharmacokinetics of atypical antipsychotics - focus on clozapine, olanzapine and aripiprazole population models. *Drug Metab. Rev.* 52 (1), 1–18. doi:10.1080/03602532.2020.1717517
- Jukic, M. M., Smith, R. L., Haslemo, T., Molden, E., and Ingelman-Sundberg, M. (2019). Effect of CYP2D6 genotype on exposure and efficacy of risperidone and aripiprazole: A retrospective, cohort study. *Lancet. Psychiatry* 6 (5), 418–426. doi:10.1016/s2215-0366(19)30088-4
- Kim, J. R., Seo, H. B., Cho, J. Y., Kang, D. H., Kim, Y. K., Bahk, W. M., et al. (2008). Population pharmacokinetic modelling of aripiprazole and its active metabolite, dehydroaripiprazole, in psychiatric patients. *Br. J. Clin. Pharmacol.* 66 (6), 802–810. doi:10.1111/j.1365-2125.2008.03223.x
- Kinghorn, W. A., and Mcevoy, J. P. (2005). Aripiprazole: Pharmacology, efficacy, safety and tolerability. *Expert Rev. Neurother.* 5 (3), 297–307. doi:10.1586/14737175.5.3.297
- Kirschbaum, K. M., Müller, M. J., Malevani, J., Mobascher, A., Burchardt, C., Piel, M., et al. (2008). Serum levels of aripiprazole and dehydroaripiprazole, clinical response and side effects. *World J. Biol. Psychiatry* 9 (3), 212–218. doi:10.1080/15622970701361255
- Kneller, L. A., Zubiaur, P., Koller, D., Abad-Santos, F., and Hempel, G. (2021). Influence of CYP2D6 phenotypes on the pharmacokinetics of aripiprazole and dehydro-aripiprazole using a physiologically based pharmacokinetic approach. *Clin. Pharmacokinet.* 60 (12), 1569–1582. doi:10.1007/s40262-021-01041-x
- Knights, J., and Rohatagi, S. (2015). Development and application of an aggregate adherence metric derived from population pharmacokinetics to inform clinical trial enrichment. *J. Pharmacokinet. Pharmacodyn.* 42 (3), 263–273. doi:10.1007/s10928-015-9414-4
- Li, F., Cui, Y., Li, Y., Guo, L., Ke, X., Liu, J., et al. (2021). Prevalence of mental disorders in school children and adolescents in China: Diagnostic data from detailed clinical assessments of 17, 524 individuals. *J. Child. Psychol. Psychiatry* 63, 34–46. doi:10.1111/jcpp.13445
- Li, S., Shu, C., Wu, S., Xu, H., and Wang, Y. (2020). Population pharmacokinetics and dose optimization of ganciclovir in critically ill children. *Front. Pharmacol.* 11, 614164. doi:10.3389/fphar.2020.614164
- Lin, S. K., Chen, C. K., and Liu, Y. L. (2011). Aripiprazole and dehydroaripiprazole plasma concentrations and clinical responses in patients with schizophrenia. *J. Clin. Psychopharmacol.* 31 (6), 758–762. doi:10.1097/JCP.0b013e3182356255
- Liu, Z. S., Chen, Y. H., Zhong, Y. Q., Zou, L. P., Wang, H., Sun, D., et al. (2011). A multicenter controlled study on aripiprazole treatment for children with Tourette syndrome in China. *Chin. J. Pediatr.* 49 (8), 572–576.
- Liu, Z. S., Cui, Y. H., Sun, D., Lu, Q., Jiang, Y. W., Jiang, L., et al. (2020). Current status, diagnosis, and treatment recommendation for tic disorders in China. *Front. Psychiatry* 11, 774. doi:10.3389/fpsy.2020.00774
- Mallikaarjun, S., Shoaf, S. E., Boulton, D. W., and Bramer, S. L. (2008). Effects of hepatic or renal impairment on the pharmacokinetics of aripiprazole. *Clin. Pharmacokinet.* 47 (8), 533–542. doi:10.2165/00003088-200847080-00003
- Martino, D., Pringsheim, T. M., Cavanna, A. E., Colosimo, C., Hartmann, A., Leckman, J. F., et al. (2017). Systematic review of severity scales and screening instruments for tics: Critique and recommendations. *Mov. Disord.* 32 (3), 467–473. doi:10.1002/mds.26891
- Mauri, M. C., Paletta, S., Di Pace, C., Reggiori, A., Cirnigliaro, G., Valli, I., et al. (2018). Clinical pharmacokinetics of atypical antipsychotics: An update. *Clin. Pharmacokinet.* 57 (12), 1493–1528. doi:10.1007/s40262-018-0664-3
- Molden, E., Lunde, H., Lunder, N., and Refsum, H. (2006). Pharmacokinetic variability of aripiprazole and the active metabolite dehydroaripiprazole in psychiatric patients. *Ther. Drug Monit.* 28 (6), 744–749. doi:10.1097/01.fdt.0000249944.42859.bf
- Moons, T., De Roo, M., Claes, S., and Dom, G. (2011). Relationship between P-glycoprotein and second-generation antipsychotics. *Pharmacogenomics* 12 (8), 1193–1211. doi:10.2217/pgs.11.55
- pharmvar (2022). Pharmacogene variation consortium. .
- Prommer, E. (2017). Aripiprazole. *Am. J. Hosp. Palliat. Care* 34 (2), 180–185. doi:10.1177/1049909115612800
- Rafaniello, C., Sessa, M., Bernardi, F. F., Pozzi, M., Cheli, S., Cattaneo, D., et al. (2018). The predictive value of ABCB1, ABCG2, CYP3A4/5 and CYP2D6 polymorphisms for risperidone and aripiprazole plasma concentrations and the occurrence of adverse drug reactions. *Pharmacogenomics* 18 (3), 422–430. doi:10.1038/tpj.2017.38
- Rafaniello, C., Sullo, M. G., Carnovale, C., Pozzi, M., Stelitano, B., Radice, S., et al. (2020). We really need clear guidelines and recommendations for safer and proper use of aripiprazole and risperidone in a pediatric population: Real-world analysis of EudraVigilance database. *Front. Psychiatry* 11, 550201. doi:10.3389/fpsy.2020.550201

- Roessner, V., Eichele, H., Stern, J. S., Skov, L., Rizzo, R., Debes, N. M., et al. (2022). European clinical guidelines for tourette syndrome and other tic disorders-version 2.0. Part III: Pharmacological treatment. *Eur. Child. Adolesc. Psychiatry* 31 (3), 425–441. doi:10.1007/s00787-021-01899-z
- Saiz-Rodríguez, M., Almenara, S., Navares-Gómez, M., Ochoa, D., Román, M., Zubiaur, P., et al. (2020). Effect of the most relevant CYP3A4 and CYP3A5 polymorphisms on the pharmacokinetic parameters of 10 CYP3A substrates. *Biomedicines* 8 (4), 94. doi:10.3390/biomedicines8040094
- Sallee, F., Kohegyi, E., Zhao, J., McQuade, R., Cox, K., Sanchez, R., et al. (2017). Randomized, double-blind, placebo-controlled trial demonstrates the efficacy and safety of oral aripiprazole for the treatment of tourette's disorder in children and adolescents. *J. Child. Adolesc. Psychopharmacol.* 27 (9), 771–781. doi:10.1089/cap.2016.0026
- Shapiro, D. A., Renock, S., Arrington, E., Chiodo, L. A., Liu, L. X., Sibley, D. R., et al. (2003). Aripiprazole, a novel atypical antipsychotic drug with a unique and robust pharmacology. *Neuropsychopharmacology* 28 (8), 1400–1411. doi:10.1038/sj.npp.1300203
- Suzuki, T., Mihara, K., Nakamura, A., Kagawa, S., Nagai, G., Nemoto, K., et al. (2014). Effects of genetic polymorphisms of CYP2D6, CYP3A5, and ABCB1 on the steady-state plasma concentrations of aripiprazole and its active metabolite, dehydroaripiprazole, in Japanese patients with schizophrenia. *Ther. Drug Monit.* 36 (5), 651–655. doi:10.1097/ftd.0000000000000070
- Swen, J. J., Nijenhuis, M., De Boer, A., Grandia, L., Maitland-Van Der Zee, A. H., Mulder, H., et al. (2011). Pharmacogenetics: From bench to byte-an update of guidelines. *Clin. Pharmacol. Ther.* 89 (5), 662–673. doi:10.1038/clpt.2011.34
- Thiebaut, F., Tsuruo, T., Hamada, H., Gottesman, M. M., Pastan, I., and Willingham, M. C. (1987). Cellular localization of the multidrug-resistance gene product P-glycoprotein in normal human tissues. *Proc. Natl. Acad. Sci. U. S. A.* 84 (21), 7735–7738. doi:10.1073/pnas.84.21.7735
- US Food and Drug Administration (2018). US Food and drug administration. .
- Yang, C., Yi, Q., Zhang, L., Cui, H., and Mao, J. (2019). Safety of aripiprazole for tics in children and adolescents: A systematic review and meta-analysis. *Med. Baltim.* 98 (22), e15816. doi:10.1097/MD.00000000000015816
- Zhang, X., Liu, C., Zhou, S., Xie, R., He, X., Wang, Z., et al. (2021). Influence of CYP2D6 gene polymorphisms on the pharmacokinetics of aripiprazole in healthy Chinese subjects. *Pharmacogenomics* 22 (4), 213–223. doi:10.2217/pgs-2020-0134
- Zhang, X., Xiang, Q., Zhao, X., Ma, L., and Cui, Y. (2019). Association between aripiprazole pharmacokinetics and CYP2D6 phenotypes: A systematic review and meta-analysis. *J. Clin. Pharm. Ther.* 44 (2), 163–173. doi:10.1111/jcpt.12780

Glossary

TD, tic disorders

CTD, chronic motor or vocal tic disorders

PTD, provisional tic disorders

TS, Tourette syndrome

YGTSS, Yale Global Tic Severity Scale

ARI, Aripiprazole

ESSTS, European Society for the Study of Tourette syndrome

DARI, dehydroaripiprazole

AGNP, Arbeitsgemeinschaft für Neuropsychopharmakologie und Pharmakopsychiatrie

TDM, therapeutic drug monitoring

PPK, population pharmacokinetics

DSM-5, the fifth edition of the Diagnostic and Statistical Manual of Mental Disorders

ECG, electrocardiogram

VPC, visual prediction check

NPDE, normalized prediction distribution errors

PRED, population predictions

IPRED, individual prediction

CWRES, conditional weighted residuals

ROC, receiver operating characteristic curve

PTA, the probability of reaching the target

UMs, ultra-rapid metabolizers

NMs, normal metabolizers

IMs, intermediated metabolizers

PMs, poor metabolizers

ABCB1, ATP-binding cassette sub-family B member 1

HPLC, high-performance liquid chromatography

ALT, alanine aminotransferase

AST, aminotransferase

DBIL, direct bilirubin

TBIL, total bilirubin

ALB, albumin

GLB, globulin

γ -GT, γ -glutamyltranspeptidase

BUN, blood urea nitrogen

Cys-C, serum cystatin C

Scr, serum creatinine concentration

BSA, serum creatinine concentrationBSA, body surface area

eGFR, estimated glomerular filtration rate

UV, ultraviolet

PCR, polymerase chain reaction

FOCE ELS, the first order conditional estimation-extended least squares

OFV, the objective function value

MR, metabolic ratio

AUC_{24h}, the area under the curve over 24 hours

C_{max}, peak concentration

C_{min}, trough concentration

AIC, Akaike information criterion

BIC, Bayesian information criterion

CIs, confidence intervals

SNP, single nucleotide polymorphism

P-gp, P-glycoprotein

FDA, Food and Drug Agency

PBPK, physiologically based pharmacokinetic.



OPEN ACCESS

EDITED BY

Junmin Zhang,
Lanzhou University, China

REVIEWED BY

Olga Butranova,
Peoples' Friendship University of Russia,
Russia
Ramazan Rezaei,
Shahid Beheshti University of Medical
Sciences, Iran
Lian-Sheng Wang,
Nanjing Medical University, China

*CORRESPONDENCE

Melisa I. Barliana,
melisa.barliana@unpad.ac.id

SPECIALTY SECTION

This article was submitted to Drug
Metabolism and Transport,
a section of the journal
Frontiers in Pharmacology

RECEIVED 07 October 2022

ACCEPTED 28 November 2022

PUBLISHED 12 December 2022

CITATION

Annisa N, Barliana MI, Santoso P and
Ruslami R (2022), Transporter and
metabolizer gene polymorphisms affect
fluoroquinolone
pharmacokinetic parameters.
Front. Pharmacol. 13:1063413.
doi: 10.3389/fphar.2022.1063413

COPYRIGHT

© 2022 Annisa, Barliana, Santoso and
Ruslami. This is an open-access article
distributed under the terms of the
[Creative Commons Attribution License](#)
(CC BY). The use, distribution or
reproduction in other forums is
permitted, provided the original
author(s) and the copyright owner(s) are
credited and that the original
publication in this journal is cited, in
accordance with accepted academic
practice. No use, distribution or
reproduction is permitted which does
not comply with these terms.

Transporter and metabolizer gene polymorphisms affect fluoroquinolone pharmacokinetic parameters

Nurul Annisa^{1,2}, Melisa I. Barliana^{1,3*}, Prayudi Santoso⁴ and
Rovina Ruslami⁵

¹Department of Biological Pharmacy, Biotechnology Pharmacy Laboratory, Faculty of Pharmacy, Universitas Padjadjaran, Sumedang, Indonesia, ²Unit of Clinical Pharmacy and Community, Faculty of Pharmacy, Universitas Mulawarman, Samarinda, Indonesia, ³Center of Excellence for Pharmaceutical Care Innovation, Universitas Padjadjaran, Sumedang, Indonesia, ⁴Division of Respiratory and Critical Care, Department of Internal Medicine, Faculty of Medicine, Universitas Padjadjaran-Hasan Sadikin Hospital, Bandung, Indonesia, ⁵Division of Pharmacology and Therapy, Department of Biomedical Sciences, Faculty of Medicine, Universitas Padjadjaran, Bandung, Indonesia

Tuberculosis (TB) is an infectious disease that occurs globally. Treatment of TB has been hindered by problems with multidrug-resistant strains (MDR-TB). Fluoroquinolones are one of the main drugs used for the treatment of MDR-TB. The success of therapy can be influenced by genetic factors and their impact on pharmacokinetic parameters. This review was conducted by searching the PubMed database with keywords polymorphism and fluoroquinolones. The presence of gene polymorphisms, including *UGT1A1*, *UGT1A9*, *SLCO1B1*, and *ABCB1*, can affect fluoroquinolones pharmacokinetic parameters such as area under the curve (AUC), creatinine clearance (C_{Cr}), maximum plasma concentration (C_{max}), half-life ($t_{1/2}$) and peak time (t_{max}) of fluoroquinolones.

KEYWORDS

pharmacogenetics, *UGT1A1*, *UGT1A9*, *SLCO1B1*, *ABCB1*, moxifloxacin, sitafloxacin, trovafloxacin

Introduction

Multidrug Resistant-Tuberculosis (MDR-TB) is a severe problem in various parts of the world, and Tuberculosis (TB) cases are particularly prevalent in India and Indonesia (WHO, 2020a). However, the use of pharmacogenomic and pharmacokinetic aspects as therapeutic parameters were expected to have a positive impact on treatment and may achieve an 80% reduction in TB incidence rates by 2030 as described in the WHO End TB strategy.

Drug responses of individual patients can be determined by the drug pharmacokinetic parameters, and these responses can be affected by single nucleotide polymorphisms (SNPs) in genes that encode drug-metabolizing enzymes and transporters; the influence of these SNPs on drug response is called pharmacogenetics. Therefore, comprehensive molecular understanding and clinical information for precise treatment of individuals are

needed to improve the outcome therapy (Roden and Tyndale, 2011). Genetic polymorphism is due to naturally existing variants in genes that occur in more than 1% of the population. Polymorphism may influence the action of a drug by changing the pharmacokinetic or pharmacodynamic profile (Belle and Singh, 2008).

Transport proteins or transporters are membrane channels and molecular pumps that facilitate the movement of ions, small molecules, macromolecules, and drugs across membranes (Nelson et al., 2008). The movement of biochemical compounds through biological membranes is critical to the absorption, distribution, metabolism, and excretion of nutrients, neurotransmitters, and drugs (Overington et al., 2006; Ware, 2006; Giacomini et al., 2010; Yan, 2010; Rask-Andersen et al., 2011). The dynamic partnerships of transporters with other signaling molecules in subcellular locations are regarded as essential processes for cellular function. The attenuation of transporter gene sequence by polymorphisms often contributes to complex human diseases and individual drug responses (Ware, 2006; Cardoso et al., 2010; Yan, 2010; Longo et al., 2011; Rask-Andersen et al., 2011; Ueda, 2011).

In shorter MDR-TB treatment regimens, fluoroquinolones such as levofloxacin (L-isomer ofloxacin) and moxifloxacin (8-methoxy fluoroquinolone) are an important class of drugs (group A) used in the initial treatment phase for 4–6 months and the continuation phase for 5 months (WHO, 2020b). Fluoroquinolones such as levofloxacin and moxifloxacin are effective against gram-positive and gram-negative anaerobic bacteria through bactericidal action that acts *via* inhibition of the topoisomerase II (DNA gyrase) and topoisomerase IV enzymes required for bacterial DNA replication, transcription, repair, and recombination (FDA, 2008; Fàbrega et al., 2009; FDA, 2016).

Fluoroquinolone antibiotics play a significant role in the elimination of bacteria in the treatment of infections, necessitating accuracy in drug administration to maintain their efficacy and safety, which can be influenced by several circumstances. Therefore, the objective of this study was to determine explicitly how human genetic variation can alter the pharmacokinetic profile of fluoroquinolone antibiotic and how it also impact in clinical implication.

Materials and methods

This narrative review used articles published in PubMed obtained using the combination of “polymorphism” OR “single nucleotide polymorphism” OR “SNP” AND “fluoroquinolone” AND “pharmacokinetic” as keywords and found 387 articles. Finally, 6 out of 387 studies were reviewed to identify gene polymorphisms and their effect on the pharmacokinetic parameters of fluoroquinolones. Due to the limitations of

published studies, we also searched several other studies that have been performed on other drugs for more comprehensive approaches to gene polymorphisms.

Result and discussion

Metabolic processes in the liver play an important role in influencing drug levels in the body. Drug metabolism in the liver can result in the formation of drugs that are more hydrophilic and that are then excreted through the liver, kidneys, and/or intestines. Drug metabolism involves the chemical biotransformation of drug molecules by enzymes present in the body. In addition, drug transporters facilitate the movement of drugs and metabolites in and out of cells and organs (Taxax and Bhartam, 2014).

Drug metabolism pathways consist of phases I and II and may include phase III. The phase I pathway is generally controlled by the Cytochrome P450 (CYP450) family, the main group of enzymes that chemically modify drugs so that they are more soluble in water and are then easily excreted by the kidneys and/or liver. The phase II pathway of drugs/metabolites involves enzymatic conjugation with endogenous hydrophilic compounds assisted by transferase enzymes; phase II metabolic enzymes are UDP-glucuronosyltransferase (UGT), Sulfotransferases, N-acyl transferases, Glutathione S-transferases, N-acetyl transferases, and Methyl transferases (Taxax and Bhartam, 2014). Phase III pathways are classified into two main superfamilies: ATP-binding cassette (ABC) proteins and solute carrier (SLC) transporters. The phase III pathway is facilitated by drug transporters that in general are transmembrane proteins that facilitate the transport of large molecules and/or ionized molecules into or out of the cell. ABC transporters require energy (ATP) to actively absorb or efflux the drug from one side of the cell membrane to the other, whereas SLCs enable the passage of certain solutes (e.g., sugars and amino acids) across the membrane while actively transporting other solutes despite their electrochemical gradients by coupling the process with another solute or ion (Almazroo et al., 2017). Fifty-two percent of moxifloxacin's oral or intravenous dose is metabolized by glucuronide and sulfate conjugation (phase II metabolism). While the CYP450 system is not involved in the metabolic process of the moxifloxacin (FDA, 2016).

The pharmacokinetic profile of a drug can be influenced by internal factors that cannot be modified, such as genetic components, and several genes are known to be involved in the pharmacokinetic profile of fluoroquinolones. We found the study in fluoroquinolones antibiotics group are moxifloxacin, sitafloxacin, and trovafloxacin as fourth-generation fluoroquinolones. The gene found were uridine 5'-diphospho-glucuronosyltransferase family 1 member A1 (*UGT1A1*), 5'-diphospho-glucuronosyltransferase family 1 member A9 (*UGT1A9*), solute carrier organic anion

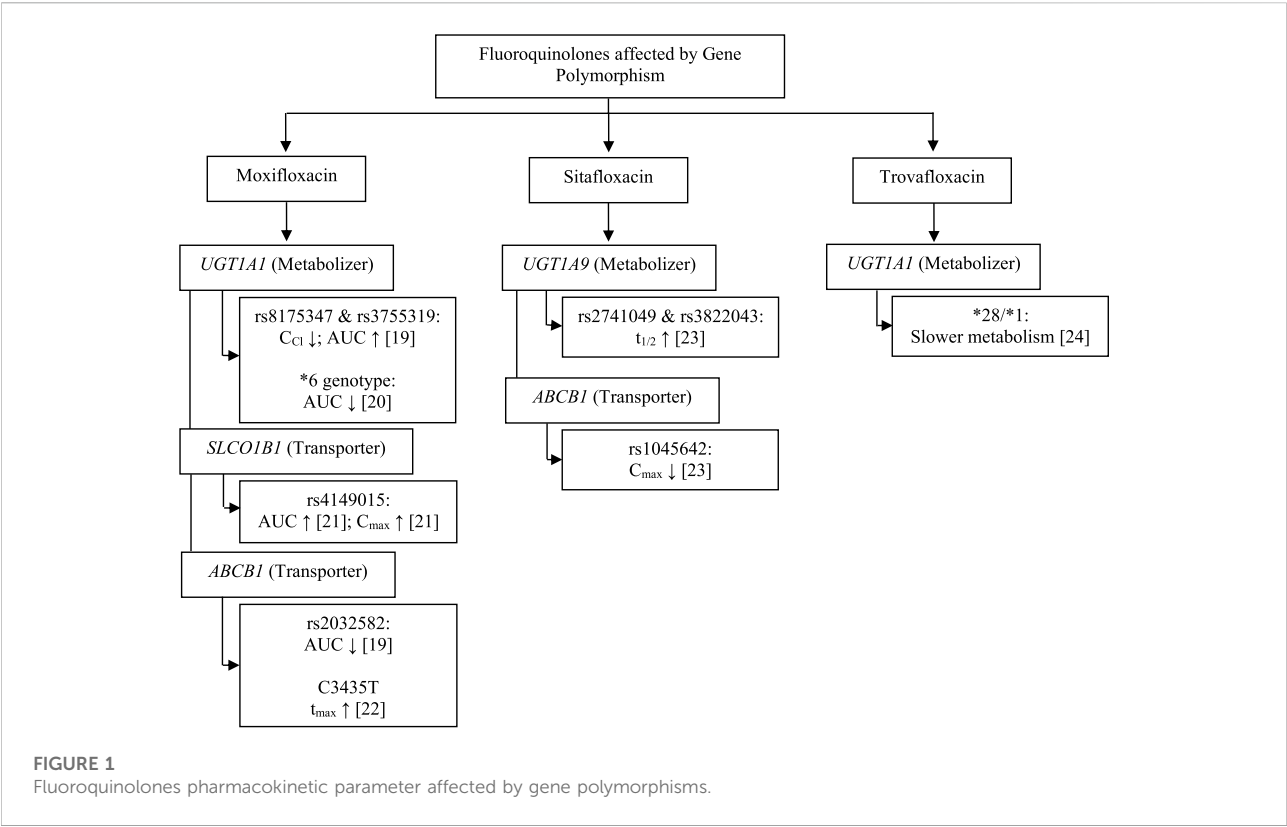


TABLE 1 The effect of transporter and metabolizer human gene polymorphism on moxifloxacin pharmacokinetic parameter.

Gene	Genotyping method	Polymorphism	Study population		Discussion	References
			Number	Ethnic		
UGT1A1	Taqman® Genotyping OpenArray™	rs8175347 rs3755319	230	African	Association between gene polymorphism and moxifloxacin pharmacokinetics (reducing C_{Cr} and increasing AUC)	Naidoo et al. (2018)
	TaqMan SNP Genotyping Assay, Life Technologies Japan	*6 Genotype	79	Japanese, Chinese, Korean and Caucasian	*6 carriers had a significantly lower AUC_{inf} of M2 moxifloxacin compared with the other genotypes	Hasunuma et al. (2016)
SLCO1B1	Allelic Discrimination Assay (TaqMan C_32325356), Thermo Fisher Scientific	rs4149015 g.-11187G>A	49	African and American	The median moxifloxacin AUC_{0-24} was 46% higher and the median C_{max} was 30% higher in 4 (8%) participants who had the SLCO1B1 g.-11187 AG genotype	Weiner et al. (2018)
ABCB1	Taqman® Genotyping OpenArray™	rs2032582	230	African	The area under the concentration-time curve from 0 to 24 h (AUC_{0-24}) for moxifloxacin decreased 27%	Naidoo et al. (2018)
	TaqMan Real Time PCR	C3435T	16	Black, White non-Hispanic, White Hispanic, Asian	Significant increase in peak time (T_{max}) in subjects with MDRI 3435CC compared to other genotypes	Weiner et al. (2007)

transporter family member 1B1 (*SLCO1B1*), and ATP-binding cassette subfamily B member 1 (*ABCB1*) may affect fluoroquinolones pharmacokinetic parameters, including

creatinine clearance (C_{Cr}), area under the curve (AUC), maximum plasma concentration (C_{max}), half-life ($t_{1/2}$) and time to the maximum plasma concentration (t_{max}).

TABLE 2 The effect of transporter and metabolizer human gene polymorphism on sitafloxacin and trovafloxacin pharmacokinetic parameter.

Gene	Genotyping method	Polymorphism	Study population		Discussion	References
			Number	Ethnic		
<i>ABCB1</i>	Sanger Sequencing, Shanghai Sangon Bio-Tech Co., Ltd.	rs1045642 (sitafloxacin)	30	Chinese	Had a significant effect on the C_{max} dose sitafloxacin	Sun et al. (2021)
<i>UGT1A9</i>		rs2741049 (sitafloxacin)			Had a significant effect on the sitafloxacin $t_{1/2}$	
		rs3822043 (sitafloxacin)			Had a significant effect on the sitafloxacin $t_{1/2}$	
<i>UGT1A1</i>	Enzyme assay: UGT Isoforms-expressing Systems	*28/*1 (trovafloxacin)	Human liver microsome	The trovafloxacin glucuronidation in liver microsomes from UGT1A1*28/*28 carriers was significantly slower than that in microsomes from UGT1A1*1/*1		Fujiwara et al. (2015)

Thus, the pharmacokinetic profile of fluoroquinolones may be affected by proteins expressed by the *UGT1A1*, *UGT1A9*, *SLCO1B1*, and *ABCB1* genes (Figure 1; Tables 1, 2). UGT functions as a drug metabolizer, while the roles of SLC and ABC as transporters will certainly affect the pharmacokinetic profile. The metabolism of moxifloxacin by UGT with SNPs at rs8175347 and rs3755319 reduces C_{Cr} and increases AUC in healthy subjects, in contrast to studies that show a reduction in AUC with the *UGT1A1**6 genotype. *SLCO1B1* encodes organic anion transporting polypeptide 1B1 (OATP1B1), which acts as a moxifloxacin drug transporter. The rs4149015 SNP of *SLCO1B1* increases the AUC and C_{max} of moxifloxacin, whereas the p-glycoprotein drug transporter encoded by *ABCB1* decreases the AUC, C_{max} , and increases T_{max} . Studies have shown a similar decrease in drug exposure and a prolonged time to reach the peak drug level in the body (Weiner et al., 2007; Hasunuma et al., 2016; Naidoo et al., 2018; Weiner et al., 2018).

Polymorphism of *UGT1A1*, *UGT1A9*, and *ABCB1* also affects the pharmacokinetic profile in sitafloxacin and trovafloxacin (Figure 1; Table 2). A study on sitafloxacin showed that there was an association of genetic polymorphism of the human drug transporter *ABCB1* rs1045642 in subjects with heterozygous or homozygous genotype variants with a lower C_{max} of sitafloxacin than that in subjects without variants ($p < 0.05$) (Sun et al., 2021). SNPs in *UGT1A9* rs2741049 and rs3822043 have a longer half-life ($t_{1/2}$) than those in subjects without the variant; this was thought to occur due to decreased metabolism and disposition of sitafloxacin. However, this study did not show significant changes in AUC in either the *ABCB1* or *UGT1A9* groups (Sun et al., 2021). Acyl glucuronidation of trovafloxacin has been studied in human liver microsomes and also in UGT isoform-expressing systems in human liver microsomes.

*UGT1A1**28/*28 carriers were significantly slower metabolism than that in microsomes from *UGT1A1**1/*1, suggesting that *UGT1A1* is the main contributor to the glucuronidation of trovafloxacin (Fujiwara et al., 2015). At the molecular level, an influx transporter implicated in the membrane transport of quinolone antibacterial drugs (levofloxacin) has been identified for the first time as a result of the current work, in conclusion. OATP1A2, the discovered transporter molecule, is expressed in several tissues, including the small intestine, blood-brain barrier, liver, lung, and testis. As a result, it may play a part in regulating the intestinal absorption, tissue distribution, and hepatic excretion of these substances (Maeda et al., 2007).

Covariates can have an impact on the pharmacokinetic profile of fluoroquinolones in addition to genetic variables. According to a study conducted in Africa, gender, height, and body size (fat-free mass) may affect the pharmacokinetic characteristics of moxifloxacin, but these variables were adjusted before the pharmacokinetic analysis (Naidoo et al., 2018). Studies on the body weight, body mass index (BMI), and C_{Cr} of subjects of Japanese, Chinese, Korean, and Caucasian ancestry have been adjusted for pharmacokinetic moxifloxacin outcomes at a body weight of 70 kg (Hasunuma et al., 2016). Age, race, and weight were all correlated with geographic origin (African and American). The moxifloxacin AUC_{0-24} and C_{max} were significantly increased by the moxifloxacin milligrams per kilogram dosage and genotype of variant g.11187G.A in the *SLCO1B1* gene (rs4149015), but not by geographic location (Weiner et al., 2018). To adjust factors that can impact the pharmacokinetic profile of moxifloxacin, values from monitored univariate tests, sex, ethnicity (Black, White non-Hispanic, White Hispanic, and Asian), and univariate test results were employed (Weiner et al., 2007). Sitafloxacin can reduce C_{max} by 50% when

TABLE 3 *UGT1A1* gene polymorphism on telmisartan, irinotecan, dolutegavir, latermovir, axitinib pharmacokinetic parameter.

Polymorphism	Genotyping method	Study population			Drug	Disussion	References
		Number	Ethnic	Condition			
rs4124874	Matrix-Assisted Laser Desorption/Ionization Time-of Flight Mass Spectrometry	58	Chinese	Hypertension	Telmisartan	Affected telmisartan bioavailability, Lower creatinine clearance and higher bioavailability in female with CC and CA genotype (high triglyceride)	Huang et al. (2019)
*28	Real-Time Allelic Discrimination PCR Assays on a DNA Engine Chromo4 System Bio-Rad Lab, United States)	93	European	HIV	Dolutegravir	Homozygosity was associated with a 79% increase in AUC ₀₋₂₄ ($p = 0.001$; 27% if analyzed individually)	Elliot et al. (2020)
rs4148323	BioProcessing Solutions Alliance in Piscataway, New Jersey	296	Asian, Black, White & Other	Prevention CMV Infection	Letermovir	An allele was present predominantly in Asian participants and was associated with an increase in AUC compared with non-carriers	Kobie et al. (2019)
*6 and *28	Pyrosequencing or Direct Sequencing	176	Japanese	Cancer	Irinotecan	Significantly reduce AUC ratios	Minami et al. (2007)
*6 221GA (rs4148323)	Tm Analysis Using a Quenching Probe	46	Japanese	Cancer	Axitinib	C ₀ dan AUC ₀₋₁₂ in patients with <i>UGT1A1</i> poor metabolizer were significantly higher than those in patients with <i>UGT1A1</i> extensive metabolizers (polymorphism were significantly associated with the plasma axitinib level)	Igarashi et al. (2018)
*27 686CA (rs35350960)							

consumed by subjects who are fasting or having high fat foods intake, but it does not affect t_{max} , $t_{1/2}$ elimination, or total exposure (AUC_{0-t} and AUC_{0-∞}). Despite only being possible in one dosing group of 10 participants, it is possible to affect the pharmacokinetic properties of ciprofloxacin, including $t_{1/2}$ and C_{max} (Sun et al., 2021).

UGT1A1 and UGT1A9

UGT1A1 is a member of the UGT family and encodes a UDP-glucuronosyltransferase, an enzyme of the glucuronidation pathway (Genecards, 2022), (National Library of Medicines, 2022). This enzyme catalyzes glucuronidation during phase II of drug metabolism, especially in conjugate reactions (Guillemette et al., 2000; Balram et al., 2002; Zhang et al., 2007). Moxifloxacin and trovafloxacin are metabolized via glucuronide and sulfate conjugation by glucuronosyltransferase and sulfotransferase (Moise et al., 2000), (Vincent et al., 1998). Therefore, genetic variations of *UGT1A1* may affect the pharmacokinetic profile and clinical response of moxifloxacin and trovafloxacin.

Studies in South African patients (of black African ethnicity) with TB (Naidoo et al., 2018), *UGT1A1* rs8175347, and rs3755319 were significantly associated with the alteration of pharmacokinetic parameters for moxifloxacin. After controlling for other factors, it was shown that having the TA 5/6 repeat in rs8175347 was linked to a 20.6% poorer clearance and roughly a 26% higher AUC ($p = 0.001$). Subjects with the AC and AA rs3755319 genotypes had 11.6% higher clearance than those with the CC genotype in the model ($p = 0.032$) (Naidoo et al., 2018). Other studies showed that *UGT1A1**6 (211G > A; G71R) carriers had a significantly lower total exposure to the drug (AUC_{inf}) for the glucuronide conjugate (M2 metabolite) moxifloxacin than that in the other genotypes ($p < 0.0001$), although the metabolism of moxifloxacin itself was not influenced by variation of the *UGT1A1* genotype. There were significant differences between Japanese, Chinese, Korean, and Caucasian populations in C_{max} , AUC_{inf}, and C_{Cr} of moxifloxacin. The average AUC_{inf} and C_{max} compared to the parent compound in this study showed significant differences between the Japanese and Korean groups. AUC_{inf} M2 in Caucasian races showed a higher value than in East Asian population groups (Japanese, Chinese and Korean) and was associated with differences in the frequency of

*UGT1A1**6 genotypes. These studies showed that ethnic differences may affect the pharmacokinetic parameters of drugs (Hasunuma et al., 2016). In a study using human liver microsomes, trovafloxacin glucuronidation was substantially slower in liver microsomes from *UGT1A1**28/*28 carriers than it was in *UGT1A1**1/*1 carriers (Fujiwara et al., 2015). According to these findings, *UGT1A1**28/*28, rs8175347, and rs3755319 carriers have a poor metabolizer phenotype, while carriers of the *6 genotype have a hyper metabolizer phenotype (Naidoo et al., 2018), (Hasunuma et al., 2016), (Fujiwara et al., 2015).

The genetic variations of *UGT1A1* also affected the pharmacokinetic profile of other drugs, such as telmisartan, irinotecan, dolutegravir, letermovir, and axitinib (Table 3). In general, the effect of the *UGT1A1* polymorphism on other drugs also has an influence on the pharmacokinetic profile (AUC and C_{Cr}) and moxifloxacin.

A study on the hypertension drug telmisartan showed that there was a genotype difference (rs4124874) associated with decreased clearance and increased bioavailability, and studies of dolutegravir and letermovir showed similar results with an increase in AUC (Huang et al., 2019; Kobie et al., 2019; Elliot et al., 2020). Studies on irinotecan (*UGT1A1**6 and *8) and axitinib (*UGT1A1**6 221GA and *27 686CA) showed a reduction in AUC (Minami et al., 2007), (Igarashi et al., 2018).

Similarly with *UGT1A1*, *UGT1A9* also encodes a UDP-glucuronosyltransferase, an enzyme of the glucuronidation pathway that transforms small lipophilic molecules. UDP-glucuronosyltransferases (UGT) as a catalyst for the phase II biotransformation reaction in a lipophilic substrate conjugated with glucuronic acid to increase the polarity of the metabolite, which in turn can facilitate excretion in urine or bile. In addition, it has an important role in the elimination of drugs, xenobiotics, and endogenous compounds (Gene Cards, 2022a). Studies on sitafloxacin at rs2741049 and rs3832043 showed a significant effect on longer drug half-life $t_{1/2}$ ($p < 0.05$). Inferring a poor metabolizer, rs2741049 and rs3822043 may play a part in the pharmacokinetic profile of the drug (Sun et al., 2021), another study at rs3832043 showed a possible effect on acetaminophen metabolism in neonates (Linakis et al., 2018). Thus, *UGT1A9* may have a role in the pharmacokinetic profile of the drug.

It can be summarized the effect of *UGT1A1* and *UGT1A9* can affect metabolic processes that have an impact on decreasing C_{Cr} , decreasing $t_{1/2}$, and increasing AUC in the fluoroquinolone antibiotics (moxifloxacin, sitafloxacin, and trovafloxacin) (Naidoo et al., 2018), (Sun et al., 2021), (Fujiwara et al., 2015). An increase in AUC needs to be considered to avoid drug side effects and can be considered in treatment interventions such as lowering drug doses for the safety of drug use and the effectiveness of therapy.

SLCO1B1

The *SLCO1B1* gene is located on chromosome 12p12.1, 796 base pairs, and is an important pharmacokinetic gene. The function of the OATP1B1 protein, encoded by *SLCO1B1*, is to enable the transport of several compounds (hormones, toxins, and drugs) from the blood to the liver for elimination (Genetic Home Reference, 2022), (Ensembl Asia, 2022). OATP1B1 is located on the sinusoidal membrane of human hepatocytes, where it mediates the uptake of its substrates from portal blood into the hepatocytes (Takaaki et al., 1999), (Oshiro et al., 2010).

4 (8%) persons with the *SLCO1B1* g.11187 AG genotype had a median moxifloxacin AUC_{0-24} that was 46% higher and a median C_{max} that was 30% higher than 45 participants with the wild-type GG genotype (median AUC_{0-24} from the model [p 0.005, ANCOVA]; median C_{max} from the model [p 0.009, ANCOVA]) (Weiner et al., 2018). This suggests that subject with g.-11187G>A shows poor metabolizer phenotype. Elevated levels of moxifloxacin can lead to risk for blood and lymphatic system disorders (anemia), gastrointestinal disorders (nausea, diarrhea, vomiting, constipation, abdominal pain, dyspepsia), metabolic and nutritional disorders (hypokalemia), nervous system disorders (headache, dizziness) and QT prolongation (FDA, 2016). Increased AUC and C_{max} need to be seen to avoid drug side effects and can be considered in treatment interventions such as lowering doses for the safety of drug use.

SNPs of *SLCO1B1* may affect the pharmacokinetic profiles of other drugs (Table 4). Studies on atorvastatin polymorphisms in (*SLCO1B1**15) and fluvastatin (c.521TA>G) showed an AUC-enhancing effect. Similarly, studies on methotrexate (388A>G and wild-type (AA) for 388A>G) showed the largest decrease in clearance in this genotype (Lee et al., 2010; Hirvensalo et al., 2019; Schulte et al., 2021). Conversely, studies on rifampin (c.388AA) and repaglinide/nateglinide (*SLCO1B1**1B/*1B) in the Finnish ethnic group showed a decrease in drug concentrations in the body. In addition, the same study on repaglinide (*SLCO1B1**1B/*1B) in ethnic Chinese was consistent with previous studies showing decreased AUC (Kalliokoski et al., 2008; He et al., 2011; Dompereh et al., 2018). Several studies also showed an effect of increasing the AUC that was similar to that of moxifloxacin.

ABCB1

ABCB1 is a member of the ABC family. *ABCB1* is a member of the ABC family. ABC proteins are divided into seven subfamilies, namely, ATP binding cassette subfamily A (ABC1), ATP binding cassette subfamily B (MDR/TAP), ATP binding cassette subfamily C (ABCC), ATP binding cassette

TABLE 4 *SLCO1B1* gene polymorphism on atorvastatin, 2-hydroxyatorvastatin, rifampin, repaglinide, nateglinide, methotrexate, fluvastatin & repaglinide pharmacokinetic parameter.

Polymorphism	Genotyping method	Study population			Drug	Discussion	References
		Number	Ethnic	Condition			
*15 for c.388A > G	Direct Sequencing, Using an Automated Genetic Analyzer	290	Korean	Heathy subject	Atorvastatin and 2-Hydroxyatorvastatin	<i>SLCO1B1</i> *15 allele increased the AUC of atorvastatin	Lee et al. (2010)
388A>G (rs2306283)	VANTAGE Using custom Designed Multiplexed MassARRAY IPLEX Gold SNP Paels, Evaluated in a MassArray Typer 4.0	106	American	Lymphoblastic Lymphoma	Methotrexate	388A>G and 521T>C affect methotrexate clearance variability	Schulte et al. (2021)
521T>C (rs4149056)							
c.521T>C (rs4149056)	TaqMan Assays on QuantStudio 12Kflex Real-Time PCR System	200	Finnish	Healthy subject	Fluvastatin	c.521T>C has an enantiospecific effect on active 3R,5S-fluvastatin increased AUC.	Hirvensalo et al. (2019)
c.388AA c.463AA	Taqman Genotyping on ViiA 7 Real-Time PCR	113	Ghanaian	Tuberculosis	Rifampin	c.388AA genotype (found in 2 children) was associated with low rifampin concentration compared with c.388GG.	Dompreh et al. (2018)
*1A/*1B	TaqMan Allelic Discrimination with Applied Biosystems 7300 Real-Time PCR System	16	Finnish	Heathy subject	Repaglinide & Nateglinide	The <i>SLCO1B1</i> *1B/*1B genotype is associated with reduced plasma concentrations of repaglinide, consistent with an enhanced hepatic uptake by OATP1B1, but has limited effects on the pharmacokinetics of nateglinide	Kalliokoski et al. (2008)
*1B/*1B	Polymerase Chain Reaction-Restriction Fragment Length Polymorphism (PCR-RFLP), with Little Modification	22	Chinese	Healthy subject	Repaglinide	<i>SLCO1B1</i> *1A/*1B or *1A/*1A genotype and <i>SLCO1B1</i> *15/*1A or *5/*1A genotype had significantly higher AUC _{0-∞} than participants with <i>SLCO1B1</i> *1B/*1B genotype	He et al. (2011)
*1A/*1B or *1A/*1A						There was a difference in clearance between the two genotype groups but it was not significant	

subfamily D (ABCD), ATP binding cassette subfamily E (ABCE), ATP binding cassette subfamily F (GCN20), and ATP binding cassette subfamily G (WHITE) (*Gene Cards*, 2022b), (*Human Genome Organisation*, 2022). ABC proteins are found on chromosome 7q21.12, 323 base pairs that span 209.6 kb with 29 exons (*Gene Cards*, 2022b). The p-glycoprotein encoded by *ABCB1* plays a key role in the elimination of drugs in the first pass of orally administered drugs, thereby limiting their bioavailability by excreting the drug through the epithelium that faces the lumen of the small intestine and colon and from the canaliculi facing the hepatic bile. The drug substrate will be removed from the systemic circulation through urine *via* the proximal renal tubule and through biliary excretion (Fromm, 2004). The expression and

function of p-glycoprotein are *ABCB1* SNPs-dependent. Changes in p-glycoprotein expression and function will affect the absorption, tissue distribution, and excretion of drug substances. Therefore, transporters genetic variations potentially affected the fate of drugs as well as the effectiveness of therapy (Marzolini et al., 2004).

For the *ABCB1* SNP rs2032582, only one person in the cohort under study had the CA genotype. The patient with the CA genotype had a 40% lower prehepatic bioavailability and a comparable decrease in AUC when the effect of the rs2032582 SNP was taken into account in the population PK model ($p = 0.01$) (Naidoo et al., 2018). However, in another study, in univariate analyses of the pharmacogenetic data obtained with moxifloxacin plus rifampin, cases with the

TABLE 5 *ABCB1* gene polymorphism on aripiprazole, azithromycin, sunitinib, clopidogrel, and tacrolimus pharmacokinetic parameter.

Polymorphism	Genotyping method	Study population			Drug	Discussion	References
		Number	Ethnic	Condition			
1236TT	Real-Time Polymerase Chain Reaction (PCR)	148	Spanish	Healthy subject	Aripiprazole	1236TT had lower clearance of aripiprazole ($p = 0.023$) and AUC ($p = 0.039$) and C_{max} of dehydro-aripiprazole ($p = 0.036$) compared to C/C	Belmonte et al. (2018)
2677GG/3435CC 2677GT/3435CT 2677TT/3435TT	Polymerase Chain Reaction-Restriction Fragment Length Polymorphism (PCR-RFLP)	16	Pakistani	Healthy subject	Azithromycin	C_{max} was significantly higher in 2677GG/3435CC as compared to 2677GT/3435CT and 2677TT/3435TT (p -value = 0.02)	Nazir et al. (2020)
C3435T, rs1045642	High-Performance Liquid Chromatography (HPLC)	31	Asian	Metastatic renal cell carcinoma	Sunitinib	Mutant genotype CT/TT on Cl/F of sunitinib was higher than 31.14% ($p = 0.006$) as compared with the wild genotype (CC)	Woo et al. (2016)
C3435T, rs1045642	Seqnom MassArray Technology (San Diego, United States)	401	Chinese	Acute Coronary Syndrome	Clopidogrel	The carriers of C3435T were associated with lower levels of plasma clopidogrel and its active (clopi-H4) and inactive (CLPM) metabolites (all $p = 0.05$ vs non-carriers)	Wang et al. (2015)
3435 T	Polymerase Chain Reaction-Restriction Fragment Length Polymorphism (PCR-RFLP)	70	Japanese	Rheumatoid Arthritis	Tacrolimus	The 3435TT group had higher dose-normalized blood concentrations of tacrolimus and 13-O-demethylate	Naito et al. (2015)

MDR1 3435CC genotype showed a significant increase in the time to the peak concentration of moxifloxacin (T_{max}) compared to cases with the other genotypes, but there were no differences in the mean peak concentration of moxifloxacin [a 23% lower geometric mean for the 3435 CC genotype ($p = 0.08$)] (Weiner et al., 2007).

Two studies showed in-line results in the *ABCB1* gene. A decrease in AUC and an increase in T_{max} occurred with moxifloxacin, whereas in sitafloxacin there was a decrease in C_{max} ($p < 0.05$) (Naidoo et al., 2018), (Weiner et al., 2007), (Sun et al., 2021). According to the moxifloxacin pharmacokinetics results, *ABCB1* rs2032582 and C3435T suggest a hyper metabolizer phenotype, while rs1045642 on sitafloxacin suggests a poor metabolizer. Low levels of drugs in the blood in the use of antibiotics will risk the occurrence of drug resistance and failed treatment. This data can be taken into consideration in treatment interventions such as increasing or adjusting the drug dose until it reaches the expected level.

Genetic variations of *ABCB1* may also affect the pharmacokinetic profiles of other drugs (Table 5). *ABCB1* polymorphism studies have been performed using other drugs and show that lower drug levels are in line with those used for moxifloxacin and sitafloxacin (decreased C_{max}). Studies on other drugs showed similar results where variations in pharmacokinetic parameters tended to decrease the blood

levels of the drug. Studies on aripiprazole showed that the 1236TT genotype compared with the CC genotype had a lower clearance of aripiprazole, and also lower AUC and C_{max} of dehydro-aripiprazole (it is an active metabolite). The azithromycin study showed that individuals with a heterozygous genotype of 2677GT/3435CC could inhibit intermediate levels of AUC and C_{max} . In the sunitinib study, the mutant genotype (CT/TT) had a greater Cl/F compared with that of the wild genotype (CC). Clopidogrel (C3435) and tacrolimus (3435T) studies have revealed decreased plasma drug levels (Belmonte et al., 2018; Nazir et al., 2020; Woo et al., 2016; Wang et al., 2015; Naito et al., 2015).

Clinical implications

Treatment of MDR-TB is critical to eradicating *tuberculosis*. Genetic variations (SNPs) in genes that encode drug metabolizers or transporter proteins may affect the response to treatment. Identification of these SNPs is expected to provide specific information on the alteration of pharmacokinetic profiles, especially that of fluoroquinolones, a key drug in MDR-TB therapy (group A). Therefore, dose adjustments for the phenotype that appears (hyper metabolizer or poor metabolizer) may be required. In addition, it is also possible to consider changing

the drug, because in antibiotic therapy a certain dose must be reached for efficacy without causing toxic effects. Therefore, it is deemed necessary to carry out pharmacogenetic studies to see the genetic profile of a population. Hence, genetic profile information can be used as a database for genetic screening for personalized treatment recommendations.

Limitation of the review

A limitation of this review is that studies on relevant SNPs and their effect on the pharmacokinetic profile of fluoroquinolones are limited. Hence, the number of subjects in those included studies are also limited and this may not be representative enough for the population. We also discovered that SNPs variation in the same gene can influence the pharmacokinetic profile of other drugs. This information also enriched the description of altered functions of transporters (*ABCB1* and *SLCO1B1*) and metabolizers (*UGT1A1* and *UGT1A9*) although their effect on fluoroquinolones still needs further study.

Conclusion

SNP polymorphisms that have been known to affect the pharmacokinetic parameters of fluoroquinolone as an important drug in the treatment of MDR-TB are found in the *UGT1A1*, *UGT1A9*, *SLCO1B1*, and *ABCB1* genes. *UGT1A1* and *UGT1A9*, genes that encode enzyme metabolizers for fluoroquinolones, can reduce C_{Cr} , $t_{1/2}$, and influence AUC. *SLCO1B1*, a gene that encodes the OATP1B1 protein as a drug transporter for moxifloxacin, can increase the AUC and C_{max} . *ABCB1*, a gene

that encodes p-glycoprotein as a drug transporter for fluoroquinolones, has the effect of decreasing AUC and C_{max} and increasing T_{max} .

Author contributions

NA writing original draft; NA and MB conceptualization and design; PS and MB editing draft manuscript; RR critical revision and supervision.

Funding

This research was funded by grants-in-aid from the Ministry of Research, Technology, and the Higher Education Republic of Indonesia for MB [1827/UN6.3.1/LT/2020].

Conflict of interest

The authors declare that the research was conducted in the absence of any commercial or financial relationships that could be construed as a potential conflict of interest.

Publisher's note

All claims expressed in this article are solely those of the authors and do not necessarily represent those of their affiliated organizations, or those of the publisher, the editors and the reviewers. Any product that may be evaluated in this article, or claim that may be made by its manufacturer, is not guaranteed or endorsed by the publisher.

References

- Almazroo, O. A., Miah, M. K., and Venkataramanan, R. (2017). Drug metabolism in the liver. *Clin. Liver Dis.* 21, 1–20. doi:10.1016/j.cld.2016.08.001
- Balam, C., Sabapathy, K., Fei, G., Khoo, K. S., and Lee, E. J. D. (2002). Genetic polymorphisms of UDP-glucuronosyltransferase in asians: UGT1A1*28 is a common allele in Indians. *Pharmacogenetics* 12 (1), 81–83. doi:10.1097/00008571-200201000-00012
- Belle, D. J., and Singh, H. (2008). Genetic factors in drug metabolism. *Am. Fam. Physician* 77 (11), 1553–1560.
- Belmonte, C., Ochoa, D., Roman, M., Saiz-Rodriguez, M., Wojnicz, A., Gomez-Sanchez, C. I., et al. (2018). Influence of CYP2D6, CYP3A4, CYP3A5 and ABCB1 polymorphisms on pharmacokinetics and safety of aripiprazole in healthy volunteers. *Basic Clin. Pharmacol. Toxicol.* 122 (6), 596–605. doi:10.1111/bcpt.12960
- Cardoso, A. R., Queliconi, B. B., and Kowaltowski, A. J. (2010). Mitochondrial ion transport pathways: Role in metabolic diseases. *Biochim. Biophys. Acta* 1797 (7), 832–838. doi:10.1016/j.bbapbio.2009.12.017
- Dompereh, A., Tang, X., Zhou, J., Yang, H., Topletz, A., Adu Ahwireng, E., et al. (2018). Effect of genetic variation of NAT2 on isoniazid and SLCO1B1 and CES2 on rifampin pharmacokinetics in Ghanaian children with tuberculosis. *Antimicrob. Agents Chemother.* 62 (3), e02099–e02117. doi:10.1128/AAC.02099-17
- Elliot, E. R., Neary, M., Else, L., Khoo, S., Moyle, G., Carr, D. F., et al. (2020). Genetic influence of ABCG2, UGT1A1 and NR1I2 on dolutegravir plasma pharmacokinetics. *J. Antimicrob. Chemother.* 75 (5), 1259–1266. doi:10.1093/jac/dkz558
- Ensembl Asia (2022). Ensembl Asia, rs4149015 SNP. [Online]. Available: http://asia.ensembl.org/Homo_sapiens/Variation/Population?db=core;r=12:21129888-21130888;v=rs4149015;vdb=variation;vf=418101832.
- Fàbrega, A., Madurga, S., Giral, E., and Vila, J. (2009). Mechanism of action of and resistance to quinolones. *Microb. Biotechnol.* 2 (1), 40–61. doi:10.1111/j.1751-7915.2008.00063.x
- FDA (2016). Highlights of prescribing information. Avelox® (moxifloxacin hydrochloride). [Online]. Available: https://www.accessdata.fda.gov/drugsatfda_docs/label/2016/021085s063lbl.pdf.
- FDA (2008). Highlights of prescribing information. Levaquin® (levofloxacin). [Online]. Available: https://www.accessdata.fda.gov/drugsatfda_docs/label/2006/020634s040,020635s043,021721s007lbl.pdf.
- Fromm, M. F. (2004). Importance of P-glycoprotein at blood-tissue barriers. *Trends Pharmacol. Sci.* 25 (8), 423–429. doi:10.1016/j.tips.2004.06.002
- Fujiwara, R., Sumida, K., Kutsuno, Y., Sakamoto, M., and Itoh, T. (2015). UDP-glucuronosyltransferase (UGT) 1A1 mainly contributes to the glucuronidation of trovafloxacin. *Drug Metab. Pharmacokinet.* 30 (1), 82–88. doi:10.1016/j.dmpk.2014.09.003
- Gene Cards (2022). Human gene database index: ABCB1 gene. [Online]. Available: <https://www.genecards.org/cgi-bin/carddisp.pl?gene=ABCB1>.
- Gene Cards (2022). Human gene database: UGT1A9. [Online]. Available: <https://www.genecards.org/cgi-bin/carddisp.pl?gene=UGT1A9>.

- Genecards (2022). Human gene database index: UGT1A1. [Online]. Available: <https://www.genecards.org/cgi-bin/carddisp.pl?gene=UGT1A1>.
- Genetic Home Reference (2022). SLCO1B1 gene. [Online]. Available: <https://ghr.nlm.nih.gov/gene/SLCO1B1>.
- Giacomini, K. M., Huang, S. M., Tweedie, D. J., Benet, L. Z., Brouwer, K. L. R., Chu, X., et al. (2010). Membrane transporters in drug development. *Nat. Rev. Drug Discov.* 9 (3), 215–236. doi:10.1038/nrd3028
- Guillemette, C., Millikan, R. C., Newman, B., and Housman, D. E. (2000). Genetic polymorphisms in uridine diphospho-glucuronosyltransferase 1A1 and association with breast cancer among African Americans. *Cancer Res.* 60 (4), 950–956.
- Huang, L., Yang, L., Huang, J., Tan, H. Y., Liu, S. K., Guo, C. X., et al. (2019). Effects of UGT1A1 polymorphism, gender and triglyceride on the pharmacokinetics of telmisartan in Chinese patients with hypertension: A population pharmacokinetic analysis. *Eur. J. Drug Metab. Pharmacokinet.* 44 (6), 797–806. doi:10.1007/s13318-019-00567-7
- Hasunuma, T., Tohkin, M., Kaniwa, N., Jang, I. J., Yimin, C., Kaneko, M., et al. (2016). Absence of ethnic differences in the pharmacokinetics of moxifloxacin, simvastatin, and meloxicam among three East Asian populations and Caucasians. *Br. J. Clin. Pharmacol.* 81 (6), 1078–1090. doi:10.1111/bcp.12884
- He, J., Qiu, Z., Li, N., Yu, Y., Lu, Y., Han, D., et al. (2011). Effects of SLCO1B1 polymorphisms on the pharmacokinetics and pharmacodynamics of repaglinide in healthy Chinese volunteers. *Eur. J. Clin. Pharmacol.* 67 (7), 701–707. doi:10.1007/s00228-011-0994-7
- Hirvensalo, P., Tornio, A., Neuvonen, M., Kiander, W., Kidron, H., Paile-Hyvarinen, M., et al. (2019). Enantiospecific pharmacogenomics of fluvastatin. *Clin. Pharmacol. Ther.* 106 (3), 668–680. doi:10.1002/cpt.1463
- Human Genome Organisation (2022). HUGO gene nomenclature. [Online]. Available: <https://www.hugo-international.org/standards/>.
- Igarashi, R., Inoue, T., Fujiyama, N., Tsuchiya, N., Numakura, K., Kagaya, H., et al. (2018). Contribution of UGT1A1 genetic polymorphisms related to axitinib pharmacokinetics to safety and efficacy in patients with renal cell carcinoma. *Med. Oncol.* 35, 51. doi:10.1007/s12032-018-1113-8
- Kallikowski, A., Backman, J. T., Neuvonen, P. J., and Niemi, M. (2008). Effects of the SLCO1B1*1B haplotype on the pharmacokinetics and pharmacodynamics of repaglinide and nateglinide. *Pharmacogenet. Genomics* 18 (11), 937–942. doi:10.1097/FPC.0b013e32830d733e
- Kobie, J., Guo, Z., Cho, C. R., Menzel, K., McCrea, J. B., Blanchard, R., et al. (2019). Pharmacogenetic analysis of OATP1B1, UGT1A1, and BCRP variants in relation to the pharmacokinetics of letermovir in previously conducted clinical studies. *J. Clin. Pharmacol.* 59 (9), 1236–1243. doi:10.1002/jcph.1420
- Lee, Y. J., Lee, M. G., Lim, L. A., Jang, S. B., and Chung, J. Y. (2010). Effects of SLCO1B1 and ABCB1 genotypes on the pharmacokinetics of atorvastatin and 2-hydroxyatorvastatin in healthy Korean subjects. *Int. J. Clin. Pharmacol. Ther.* 48 (1), 36–45. doi:10.5414/cpp48036
- Linakis, M. W., Cook, S. F., Kumar, S. S., Liu, X., Wilkins, D. G., Gaedigk, R., et al. (2018). Polymorphic expression of UGT1A9 is associated with variable acetaminophen glucuronidation in neonates: A population pharmacokinetic and pharmacogenetic study. *Clin. Pharmacokinet.* 57 (10), 1325–1336. doi:10.1007/s40262-018-0634-9
- Longo, N., Ardon, O., Vanzo, R., Schwartz, E., and Pasquali, M. (2011). Disorders of creatine transport and metabolism. *Am. J. Med. Genet. C Semin. Med. Genet.* 157 (1), 72–78. doi:10.1002/ajmg.c.30292
- Maeda, T., Takahashi, K., Ohtsu, N., Oguma, T., Ohnishi, T., Atsumi, R., et al. (2007). Identification of influx transporter for the quinolone antibacterial agent levofloxacin. *Mol. Pharm.* 4 (1), 85–94. doi:10.1021/mp060082j
- Marzolini, C., Paus, E., Buclin, T., and Kim, R. B. (2004). Polymorphisms in human MDR1 (P-glycoprotein): Recent advances and clinical relevance. *Clin. Pharmacol. Ther.* 75 (1), 13–33. doi:10.1016/j.clpt.2003.09.012
- Minami, H., Sai, K., Saeki, M., Saito, Y., Ozawa, S., Suzuki, K., et al. (2007). Irinotecan pharmacokinetics/pharmacodynamics and UGT1A genetic polymorphisms in Japanese: Roles of UGT1A1*6 and *28. *Pharmacogenet. Genomics* 17 (7), 497–504. doi:10.1097/FPC.0b013e328014341f
- Moise, P., Birmingham, M., and Schentang, J. (2000). Pharmacokinetics and metabolism of moxifloxacin. *Metabolism Moxifloxacin Drugs Today* 36 (4), 229–244. doi:10.1358/dot.2000.36.4.570201
- Naidoo, A., Ramsuran, V., Chirehwa, M., Denti, P., McIlerron, H., Naidoo, K., et al. (2018). Effect of genetic variation in UGT1A and ABCB1 on moxifloxacin pharmacokinetics in South African patients with tuberculosis. *Pharmacogenomics* 19 (1), 17–29. doi:10.2217/pgs-2017-0144
- Naito, T., Mino, Y., Aoki, Y., Hirano, K., Shimoyama, K., Ogawa, N., et al. (2015). ABCB1 genetic variant and its associated tacrolimus pharmacokinetics affect renal function in patients with rheumatoid arthritis. *Clin. Chim. Acta.* 445, 79–84. doi:10.1016/j.cca.2015.03.021
- National Library of Medicines (2022). Gene summary: UGT1A1-UDP glucosyltransferase family 1 member A1 (human). Available at: <https://www.ncbi.nlm.nih.gov/gene/54658>.
- Nazir, S., Adnan, K., Gul, R., Ali, G., Saleha, S., and Khan, A. (2020). The effect of gender and ABCB1 gene polymorphism on the pharmacokinetics of azithromycin in healthy male and female Pakistani subjects. *Can. J. Physiol. Pharmacol.* 98 (8), 506–510. doi:10.1139/cjpp-2019-0569
- Nelson, D., Lehninger, A., and Cox, M. (2008). *Lehninger principles of biochemistry*. New York: W. H. Freeman.
- Oshiro, C., Mangravite, L., Klein, T., and Altman, R. (2010). PharmGKB very important pharmacogene: SLCO1B1. *Pharmacogenet. Genomics* 20 (3), 211–216. doi:10.1097/FPC.0b013e328333b99c
- Overington, J. P., Al-Lazikani, B., and Hopkins, A. L. (2006). How many drug targets are there? *Nat. Rev. Drug Discov.* 5 (12), 993–996. doi:10.1038/nrd2199
- Rask-Andersen, M., Almén, M. S., and Schiöth, H. B. (2011). Trends in the exploitation of novel drug targets. *Nat. Rev. Drug Discov.* 10 (8), 579–590. doi:10.1038/nrd3478
- Roden, D. M., and Tyndale, R. F. (2011). Pharmacogenomics at the Tipping Point: Challenges and Opportunities. *Clinical Pharmacology and Therapeutics* 89 (3), 323–327. doi:10.1038/clpt.2010.340
- Schulte, R. R., Choi, L., Utreja, N., Van Driest, S. L., Stein, C. M., and Ho, R. H. (2021). Effect of SLCO1B1 polymorphisms on high-dose methotrexate clearance in children and young adults with leukemia and lymphoblastic lymphoma. *Clin. Transl. Sci.* 14 (1), 343–353. doi:10.1111/cts.12879
- Sun, L. N., Sun, G. X., Yang, Y. Q., Shen, Y., Huang, F. R., Xie, L. J., et al. (2021). Effects of ABCB1, UGT1A1, and UGT1A9 genetic polymorphisms on the pharmacokinetics of sitafloxacin granules in healthy subjects. *Clin. Pharmacol. Drug Dev.* 10 (1), 57–67. doi:10.1002/cpdd.848
- Takaaki, A., Kakyom, T., Tokui, T., Nakagomi, R., Nishio, T., Nakai, D., et al. (1999). Identification of a novel gene family encoding human liver-specific organic anion transporter LST-1. *J. Biol. Chem.* 274 (24), 17159–17163. doi:10.1074/jbc.274.24.17159
- Taxax, N., and Bhartam, P. (2014). Drug metabolism: A fascinating link between chemistry and biology resonance. *Reson.* 19, 259–282. doi:10.1007/s12045-014-0031-0
- Ueda, K. (2011). ABC proteins protect the human body and maintain optimal health. *Biosci. Biotechnol. Biochem.* 75 (3), 401–409. doi:10.1271/bbb.100816
- Vincent, J. T., R Dalvie, D. K., and Friedman, H. L. (1998). Pharmacokinetics and metabolism of single oral doses of trovafloxacin. *Am. J. Surg.* 176 (6), 8S–13S. doi:10.1016/s0002-9610(98)00213-x
- Wang, X. Q., Shen, C. L., Wang, B. N., Huang, X. H., Hu, Z. L., and Li, J. (2015). Genetic polymorphisms of CYP2C19*2 and ABCB1 C3435T affect the pharmacokinetic and pharmacodynamic responses to clopidogrel in 401 patients with acute coronary syndrome. *Gene* 558 (2), 200–207. doi:10.1016/j.gene.2014.12.051
- Ware, J. A. (2006). Membrane transporters in drug discovery and development: A new mechanistic adme era. *Mol. Pharm.* 3 (1), 1–2. doi:10.1021/mp058084b
- Weiner, M., Burman, W., Luo, C. C., Peloquin, C. A., Engle, M., Goldberg, S., et al. (2007). Effects of rifampin and multidrug resistance gene polymorphism on concentrations of moxifloxacin. *Antimicrob. Agents Chemother.* 51 (8), 2861–2866. doi:10.1128/AAC.01621-06
- Weiner, M., Gelfond, J., Johnson-Pais, T. L., Engle, M., Peloquin, C. A., Johnson, J. L., et al. (2018). Elevated plasma moxifloxacin concentrations and SLCO1B1 g-11187G>A polymorphism in adults with pulmonary tuberculosis. *Antimicrob. Agents Chemother.* 62 (5), e01802–e01817. doi:10.1128/AAC.01802-17
- WHO (2020a). *Global tuberculosis report 2020*. Geneva: World Health Organization. Licence: CC BY-NC-SA 3.0 IGO.
- WHO (2020b). *WHO operational handbook on tuberculosis. Module 4: treatment -drug-resistant tuberculosis treatment*. Geneva: World Health Organization. Licence: CC BY-NC-SA 3.0 IGO.
- Woo, C. J., Teo, Y. L., Ho, H. K., Lee, J., Back, H. M., Yun, H. Y., et al. (2016). BSA and ABCB1 polymorphism affect the pharmacokinetics of sunitinib and its active metabolite in Asian mRCC patients receiving an attenuated sunitinib dosing regimen. *Cancer Chemother. Pharmacol.* 78 (3), 623–632. doi:10.1007/s00280-016-3104-9
- Yan, Q. (2010). Membrane transporters and drug development: Relevance to pharmacogenomics, nutrigenomics, epigenetics, and systems biology. *Methods Mol. Biol.* 637, 1–21. doi:10.1007/978-1-60761-700-6_1
- Zhang, A., Xing, Q., Qin, S., Du, J., Wang, L., Yu, L., et al. (2007). Intra-ethnic differences in genetic variants of the UGT-glucuronosyltransferase 1A1 gene in Chinese populations. *Pharmacogenomics* 7 (5), 333–338. doi:10.1038/sj.tp.6500424



OPEN ACCESS

EDITED BY
Junmin Zhang,
Lanzhou University, China

REVIEWED BY
Zhonggao Gao,
Institute of Chinese Materia Medica,
China Academy of Chinese Medical
Sciences, China
Ryan Williams,
City College of New York (CUNY),
United States

*CORRESPONDENCE
Zhihui Liu,
✉ dr_lzhh@163.com
Xinying Ji,
✉ 10190096@vip.henu.edu.cn

[†]These authors have contributed equally
to this work and share first authorship

SPECIALTY SECTION
This article was submitted
to Drug Metabolism and Transport,
a section of the journal
Frontiers in Pharmacology

RECEIVED 05 November 2022
ACCEPTED 05 December 2022
PUBLISHED 14 December 2022

CITATION
Zhang L, Liang Y, Liang G, Tian Z,
Zhang Y, Liu Z and Ji X (2022), The
therapeutic prospects of N-
acetylgalactosamine-siRNA conjugates.
Front. Pharmacol. 13:1090237.
doi: 10.3389/fphar.2022.1090237

COPYRIGHT
© 2022 Zhang, Liang, Liang, Tian, Zhang,
Liu and Ji. This is an open-access article
distributed under the terms of the
[Creative Commons Attribution License](#)
(CC BY). The use, distribution or
reproduction in other forums is
permitted, provided the original
author(s) and the copyright owner(s) are
credited and that the original
publication in this journal is cited, in
accordance with accepted academic
practice. No use, distribution or
reproduction is permitted which does
not comply with these terms.

The therapeutic prospects of N-acetylgalactosamine-siRNA conjugates

Lei Zhang^{1†}, Yayu Liang^{2†}, Guohui Liang³, Zhili Tian³,
Yue Zhang⁴, Zhihui Liu^{5*} and Xinying Ji^{1*}

¹Henan International Joint Laboratory of Nuclear Protein Regulation, School of Basic Medical Sciences, Henan University, Kaifeng, China, ²School of Stomatology, Henan University, Kaifeng, China, ³School of Clinical Medical Sciences, Henan University, Kaifeng, China, ⁴Department of Obstetrics and Gynecology, Zhengzhou, China, ⁵Department of General Practice, Henan Provincial People's Hospital, Zhengzhou University, Zhengzhou, China

RNA interference has become increasingly used for genetic therapy following the rapid development of oligonucleotide drugs. Significant progress has been made in its delivery system and implementation in the treatment of target organs. After a brief introduction of RNA interference technology and siRNA, the efficiency and stability of GalNAc-siRNA conjugates are highlighted since several oligonucleotide drugs of GalNAc have been approved for clinical use in recent years. The structure and features of GalNAc-siRNA conjugates are studied and the clinical efficiency and limitations of oligonucleotide-based drugs are summarized and investigated. Furthermore, another delivery system, lipid nanoparticles, that confer many advantages, is concluded, including stability and mass production, compared with GalNAc-siRNA conjugates. Importantly, developing new approaches for the use of oligonucleotide drugs brings hope to genetic therapy.

KEYWORDS

RNAi, GalNAc-siRNA, delivery system, ASGPR, LNPs

1 Introduction

RNA interference (RNAi) is a natural defense mechanism widely present in organisms to protect against exogenous gene invasion (Svoboda, 2014; Swevers et al., 2018). It is one of the most important methods, together with zinc-finger nucleases, transcription activator-like effector nucleases and clustered regularly interspaced short palindromic repeat/associated protein, for regulating gene expression and growth and offers significant application value for the research of gene function and the development of gene therapeutics (Hannon, 2002; Xu et al., 2022). Specifically, RNAi primarily downregulates target gene expression via sequence specificity involving specific enzymatic degradation of target mRNA by the RNA-induced silencing complex (RISC) mediated by the siRNA antisense chain (Han, 2018). In other words, siRNA is a highly specific biomolecule that can inhibit or silence the expression of its complementary genes. In addition, this inhibition or silencing effect (degradation reaction) has a cascade effect (Liu et al., 2017). The benefits of RNA interference

technology include high efficiency, targeting and low toxicity, accounting for its widespread use in drug research (Saw and Song, 2019; Setten et al., 2019). In August 2018, the US Food and Drug Administration and the European Commission approved ONPATRO (Patisiran), which is the first approved for clinical use, developed by Alnylam Pharmaceuticals, to treat peripheral neuropathy with hereditary transthyroxine protein-mediated (hATTR) amyloidosis (Hoy, 2018). This RNAi milestone for the pharmaceutical industry represents one of the breakthroughs of oligonucleotide drug development, from research to clinical application.

N-acetylgalactosamine (GalNAc) conjugated to siRNA is considered as a promising solution of siRNA delivery system. The GalNAc GalNAc is targeting ligand binds highly selectively to asialoglycoprotein (ASGPR), which is abundantly expressed on hepatocyte cell, resulting in rapid endocytosis (Nair et al., 2014; Crooke et al., 2018; Jeon et al., 2022). The formed GalNAc-siRNA conjugates target ASGPR specifically expressed on the surface of hepatocytes, assisting in cleaving and separating approved drugs including Leqvio® (inclisiran), GIVLAARI™ (givosiran), Oxlumo™ (lumasiran), and AMVUTTRA™ (vutrisiran) as targeted RNA strands. These RNA strands can silence mRNA to lowering abnormal metabolites level and eventually ease the symptoms and pain (Bissell et al., 2017; German and Shapiro, 2020; Zhang et al., 2021a; Cui et al., 2021; Dobrowolski et al., 2021; Scott and Keam, 2021; Storjerd, 2021; Yu and Tu, 2021; Keam, 2022).

In this manuscript, several critical features are included. The structure and mechanism of action are priorly mentioned, following by the chemical modification, clinical and preclinical advances as well as challenges and limitations of GalNAc-siRNA conjugates. Finally, the features of GalNAc-siRNA conjugates are concluded by comparing GalNAc-siRNA conjugates to lipid nanoparticles (LNPs) to highlight the safety and efficiency of GalNAc-siRNA conjugates.

2 Challenge and siRNA delivery system

Despite its potential advantages, siRNA is beset with difficulties in clinical application (Xu and Anchordoquy, 2011; Khan, 2019). The main difficulty that restricts the implementation of siRNAs into clinical practice is drug delivery, given the poor molecular stability, wide distribution *in vivo*, difficulty in cell uptake, high dose, poor targeting, and wide variety of biological barriers, such as the GI tract mucosal epithelium, nasal/lung epithelia and skin, which affect oral, nose/pulmonary and dermal/transdermal administration, respectively (Antimisiaris et al., 2021). Moreover, naked siRNA can be easily degraded by RNases, thus failing to perform targeted knockdown (Springer and Dowdy, 2018). Additionally, the negatively charged

hydrophilic phosphate groups in the double-stranded skeleton structure of siRNA make it difficult for the cell membrane to absorb naked siRNA. Therefore, siRNA needs to be chemically modified or delivered with the help of vectors. In the meantime, exogenous siRNA may compete with endogenous RNA, resulting in supersaturation. Exogenous siRNA also causes an “off-target effect”, leading to the silenced expression of nontarget functional genes, significant siRNA side effects, and intracellular trafficking, which is a significant contributing factor to oligonucleotide delivery (Juliano, 2018; Marinho et al., 2018). Importantly, the above problems can be minimized or avoided by designing reasonable, efficient and specific siRNA sequences or chemical modifications (such as pentose modification and base modification). Oligonucleotide drugs have achieved sustained significant progress in treating various diseases in the recent decade. As therapeutics that selectively suppress target genes through the mechanism of RNA interference, oligonucleotide drugs have been granted market approval (Cui et al., 2021). For instance, Leqvio® (inclisiran), GIVLAARI™ (givosiran), Oxlumo™ (lumasiran), and AMVUTTRA™ (vutrisiran) that are approved for clinical usage, can target liver mRNAs for the treatment of hypercholesterolemia, mixed dyslipidemia, acute hepatic porphyria (AHP), primary hyperoxaluria type 1 (PH1) and hATTR amyloidosis (Lamb, 2021; Scott and Keam, 2021; Subhan et al., 2021; Adams et al., 2022). Importantly, more oligonucleotide drugs that target metabolic dysfunction symptoms and subsequent complications are under development, providing hope for more genetic solutions.

Common nonviral vectors based on RNAi include LNPs, cationic polymers that represent polymer-based delivery systems and siRNA-carbohydrate bioconjugates such as GalNAc-siRNA conjugates (Subhan et al., 2021; Tian et al., 2021; Thapa Magar et al., 2022). At present, GalNAc-siRNA conjugates and LNPs are the most studied and discussed delivery systems in RNAi therapy owing to their practicality, stability, and safety (Paunovska et al., 2022).

3 GalNAc-siRNA Conjugates

Twenty years after RNAi discovery, siRNA therapy has begun to be implemented in clinical practice. In recent years, unprecedented progress has been achieved in developing various delivery technologies. One giant leap in delivery technology is the GalNAc-siRNA conjugate, which specifically delivers to and targets the liver. In November 2019, GIVLAARI® (givosiran), as the first GalNAc siRNA drug, was approved to be marketed in the United States for the treatment of acute hepatic porphyria, followed by inclisiran and lumasiran (Table 1) (Scott, 2020). The nature of the chemical mechanism of these approved drugs is the binding of siRNA to GalNAc.

TABLE 1 Marketed GalNAc-conjugated RNA drugs.

Brand name	Generic name	Target	Molecular mechanism	Condition
Leqvio	Inclisiran	proprotein convertase subtilisin/kexin type 9 (PCSK9)	PCSK9 Expression Inhibitors	atherosclerosis, dyslipidemia, hypercholesterolemia, familial hypercholesterolemia, hyperlipidemia
Oxlumo	Lumasiran	hydroxyacid oxidase 1 (HAO1)	HAO1 Expression Inhibitors	end-stage renal disease, hyperoxaluria, primary hyperoxaluria type 1
Givlaari	Givosiran	5'-aminolevulinate synthase 1 (ALAS1)	ALAS1 Expression Inhibitors	porphyria, acute porphyria
Amvuttra	Vutrisiran	transthyretin (TTR)	TTR (Mutant) Expression Inhibitors	amyloidosis, transthyretin-related amyloidosis

TABLE 2 Comparison of GalNAc- siRNA and LNP loaded siRNA.

	GalNAc-siRNA	LNPs loaded siRNA (Aldosari et al., 2021; Zhang et al., 2021a; Lokugamage et al., 2021)
Benefits & Challenges	-can be injected subcutaneously, with only small chances of plasma siRNA degradation, rapid absorption, high uptake, and long half-life, (Springer and Dowdy, 2018)-endosomal escape, hepatotoxicity from off-target effects, acidic subcellular compartments, and extensive clearance, affect GalNAc efficiency and sequence barriers (Ayyar et al., 2021; Fairman et al., 2021; Fattal and Fay, 2021; Fumoto et al., 2021; Liu et al., 2021; Nanavati et al., 2021; Schlich et al., 2021)	-avoid siRNA degradation of and the stimulation of the immune system by siRNA-lack efficient nuclear penetration and sustainable transgene expression (limitations such as poor biodistribution and possible toxic discharge), immunogenic and pose safety concerns of liposome molecules and limited efficacy and biosafety since unconjugated liposomes cannot achieve targeted delivery (Ickenstein and Garidel, 2019; Hu et al., 2020; Blakney et al., 2021; Hassett et al., 2021; Maestro et al., 2021)
Composition	Specific arrangement of nucleoside, pO/PS linkage and monovalent GalNAc (Matsuda et al., 2015)	polyethylene glycol-lipid conjugates (PEG-DMG), ionizable amino lipids (DLin-MC3-DMA), distearyl phosphatidylcholine (DSPC) and cholesterol
Attachment	Triantennary GalNAc ligand	PEGylated surface
Target	ASGPR on hepatocyte	Liver and Triple-negative breast cancer (TNBC) (Wang et al., 2021b)
RNAi activity (Brown et al., 2020)	slower	faster
RNAi action time (Brown et al., 2020)	longer	shorter
Approved drugs	Inclisiran, Lumasiran, Givosiran, Vutrisiran etc.	Patisiran (Weng et al., 2019), etc.

3.1 Structure and mechanism of action

The coupling of drugs with cell surface receptor ligands has been reported as a promising pathway for targeted drug delivery. These receptors are only expressed in particular cell types and are overexpressed in specific organs or tissues in certain diseases. GalNAc is an efficient nucleic acid therapeutic ligand with a high affinity for ASGPR. ASGPR, also called the Ashwell-Morell receptor, has been established to feature liver specificity and species specificity. It is chiefly expressed on the surface of liver parenchyma cells in the hepatic sinusoid space and exhibits calcium-dependent ligand binding (Gabba et al., 2021). Due to the evolution of human defense mechanisms, negatively charged siRNAs with large molecular weights cannot enter the cell itself. Accordingly, siRNAs with GalNAc have been modified for

targeted siRNA delivery to the liver and siRNA entry into the cell *via* ASGPR-mediated cellular endocytosis (Figure 1) (Ayyar et al., 2021; Zhou et al., 2021; Paunovska et al., 2022).

The GalNAc trimer is mainly synthesized by D-(+)-galactosamine (I), 2-amino-2-hydroxymethyl-1,3-propanediol (II), and trans-4-hydroxy-L-proline methyl ester (III). Solid carrier IV plus tyrosine can be used as a radioactive marker to evaluate the *in vivo* receptor-ligand interactions and GalNAc-siRNA conjugate uptake (Nair et al., 2014). Subsequently, the synthesized three-antenna GalNAc can combine with the 3' end of the antisense chain of siRNA to form a GalNAc-siRNA conjugate (Shchegrovina et al., 2021). siRNA can be synthesized directly by a chemical approach or by breaking long double-stranded RNA obtained by enzyme transcription into 21–23 nt siRNA under the action of the

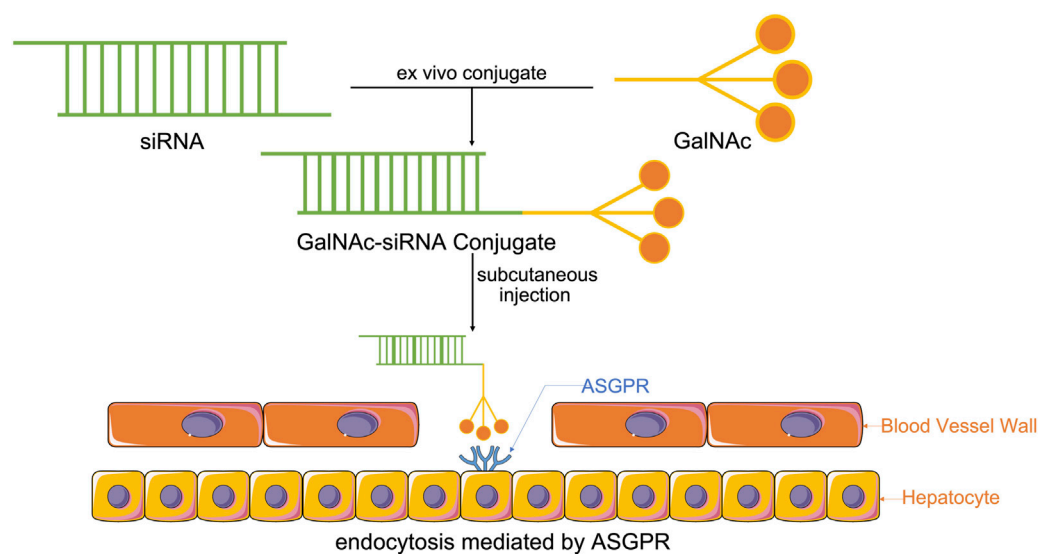


FIGURE 1
Synthesis of GalNAc-siRNA conjugates. Through chemically synthesized conjugates, modified siRNAs with GalNAc enter the system by subcutaneous injection, which is the most effective way to help GalNAc-siRNA conjugates attach to ASGPR, the receptor, that is, chiefly expressed on the surface of liver parenchyma cells in the hepatic sinusoid space, thus enabling ASGPR-mediated cellular endocytosis to cause siRNA to enter the cell and perform its function.

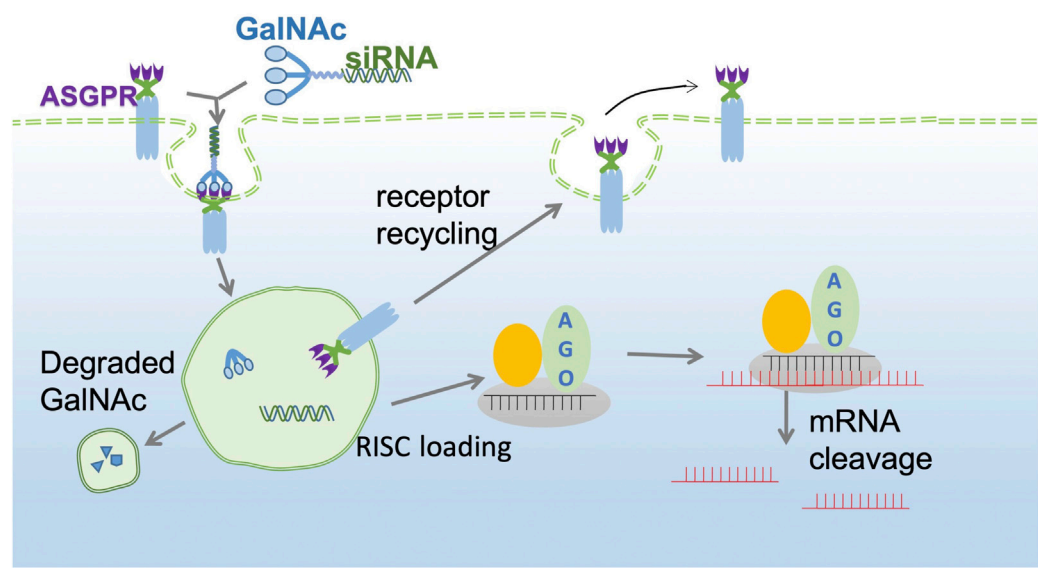


FIGURE 2
GalNAc-siRNA conjugate pathway. The GalNAc-siRNA conjugate binds to ASGPR receptors on the surface of hepatocytes and is then endocytosed into the cytoplasm to form endosomes. Due to the decrease in pH in endosomes, the siRNA GalNAc-ASGPR complex is decomposed, and less than 1% of free siRNA escapes to the cytoplasm to exert an RNAi effect. ASGPR will return to the surface of liver cells for recycling, while GalNAc will be degraded and excluded. The negative chain of siRNA, Ago2 protein and related enzymes together constitute RISC and guide RISC to bind to target mRNA to achieve target mRNA gene silencing.

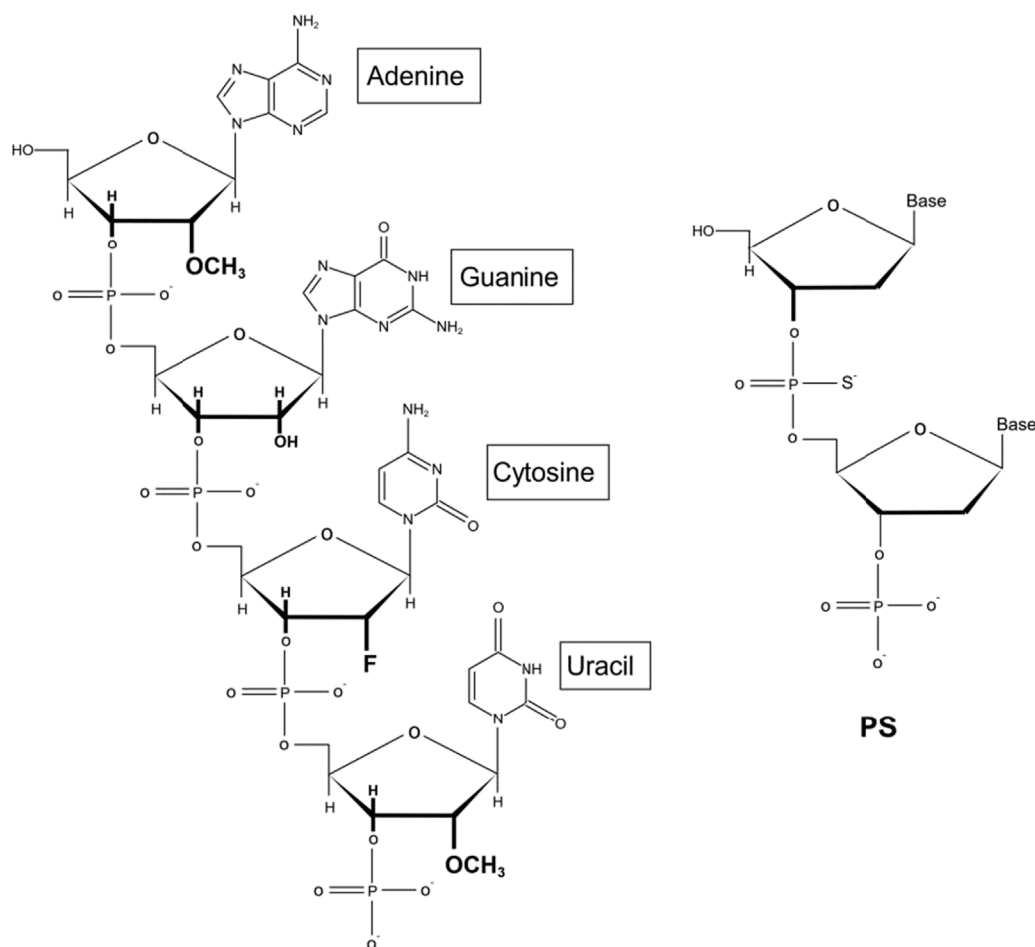


FIGURE 3
Schemes of siRNA chemical modification.

cytoplasmic RNase III endonuclease Dicer, which has two protruding nucleotides at the 3' hydroxyl end, a phosphate terminal at the 5' end and a complementary double-stranded region of 19 nt in the middle (Adachi et al., 2021; Paro et al., 2021). When GalNAc-siRNA is introduced into the body and binds to ASGPR on the surface of hepatocytes, the siRNA GalNAc-ASGPR complex is separated in the endosome (Holland et al., 2021; Shchegravina et al., 2021). Thereafter, siRNA escapes from the endosome, and GalNAc is degraded and excreted out of the endosome. Vesicles enclosing the ASGPR are fused with the cell membrane to return to the surface of hepatocytes to complete the ASGPR cycle (van den Berg et al., 2021; Damase et al., 2021). After the escaped or released siRNA molecules separate the double strand under the action of helicase, the negative strand binds to Ago2 proteins and related enzymes to form RISC and guide RISC to bind to the complementary regions of the target dsRNA. Under the action of Ago2 protein, the newly combined double-stranded complex can break the

phosphodiester bond between the 10th and 11th bases at the 5' end of antisense RNA to achieve siRNA-mediated gene silencing of specific target mRNAs (Figure 2) (Alshaer et al., 2021; Iwakawa and Tomari, 2021; Montañés et al., 2021; Zhao et al., 2021).

3.2 Chemical modification

Moreover, the chemical modification of siRNA is conducive to further application of siRNA in the clinic. Initially, the experimenters try to modify the phosphate skeleton, base, terminal groups and ribose according to the structure of siRNA. The results show that ribose modification is more advantageous to some extent. Among them, the chemical modification of ribose 2'-OH is the most important. It is widely acknowledged that oligonucleotide nuclease stability can be significantly refined by adjusting the 2' position of the

RNA. In addition, it has been shown that by further improving the siRNA chemically, such as through optimizing the position of ribose modification of 2'-deoxy-2'-fluoro (2'-F) and 2'-O-methyl (2'-OMe) on the two strands of double-stranded siRNA (Figure 3), the stability can be improved without affecting inherent RNAi activity to achieve substantial therapeutic improvement (Foster et al., 2018). This phenomenon has also led to the development of standard template chemistry (STC) toward enhanced stabilization chemistry (ESC) and advanced ESC. Early GalNAc-siRNA conjugates (STC) modified with 2'-F or 2'-OMe are stable enough to stimulate activity *in vivo* but require high doses. ESC is designed to add two phosphorothioate (PS) bonds at the 5' ends of the siRNA guide chain and the guest chain (Foster et al., 2018; Brown et al., 2020). An increasing body of evidence suggests that ESC siRNA exhibits enhanced effectiveness and duration in preclinical and clinical trials. However, the good tolerance of siRNA containing 2'-F and 2'-OMe modifications has led to advanced ESC designs, which achieve optimal results by adjusting the position and ratio of 2'-F and 2'-OMe in the double strand (Nair et al., 2017; Gupta et al., 2021a). Although both designs yield steady results during *ex vivo* studies, it is worth noting that compared with *in vivo* ESC templates, the efficacy and duration of advanced ESC designs are superior (Brown et al., 2020; Kulkarni et al., 2021). In conclusion, the above results demonstrate that the covalent bonding of the GalNAc trimer with optimal, chemically modified siRNAs yields a conjugate with nuclease stability and improves the pharmacokinetics compared to uncoupled siRNAs, resulting in a steady increase in the potency and duration of GalNAc-siRNA conjugate activity (Lundin et al., 2015; Freitag and Wagner, 2021).

Furthermore, nonclinical studies on ultratherapeutic doses of GalNAc-siRNA have shown that some typical molecules (six enhanced stable chemical GalNAc-siRNAs) exhibit similar safety signals and histological findings in the liver, as well as the kidney and lymph nodes (Janas et al., 2018a; Sutherland et al., 2020). Most of these conjugates have no side effects, which can be attributed to their pharmacokinetics and intracellular distribution, which usually reflect the cumulative dose efficiency (Debacker et al., 2020). In addition, all GalNAc-siRNAs assessed thus far have been shown to be nongenotoxic and have undergone pharmacological safety studies (Janas et al., 2018a).

3.3 Clinical and preclinical advances in approved or ongoing GalNAc-siRNA therapeutics

To date, three GalNAc-siRNA therapeutics, Leqvio® (inclisiran), GIVLAARI™ (givosiran) and Oxlumo™ (lumiasiran), have been approved for commercial applications, with 13 GalNAc-siRNA products undergoing clinical trials

(Supplementary Table S1). Abundant preclinical studies are implementing or awaiting further improvements (Supplementary Table S2). The clinical advances of GalNAc conjugates for treating AHP, hypercholesterolemia, PH1, etc. are concluded.

3.3.1 Clinical efficacy of several approved GalNAc-siRNA conjugates drugs: Leqvio® (inclisiran), GIVLAARI™ (givosiran), Oxlumo™ (lumiasiran), and AMVUTTRA™ (vutrisiran)

As previously mentioned, GalNAc-siRNA conjugates are commonly used in liver diseases (Springer and Dowdy, 2018; Willoughby et al., 2018; Thangamani et al., 2021). The development of GalNAc-siRNA conjugates can help to boost oligonucleotide drug popularity by removing barriers such as poor drug safety, efficacy, and specificity posed by other delivery systems. Promptly internalized by high-capacity ASGPR, GalNAc conjugates can internalize within clathrin-coated vesicles and enter endosomal compartments, leading to the disruption of ionic interactions caused by endosomal acidification. In this regard, decreasing the pH of endosomal compartments can help to release GalNAc-siRNAs from ASGPRs to transfer GalNAc-siRNAs back to the cell surface every 10–15 min, ensuring transport efficacy (Brown et al., 2020; Abdelal and Kasinski, 2021). However, it has been shown that only a few (<1%) GalNAc-siRNA conjugates are distributed from pH-decreasing endosomal compartments to the cytoplasm, making endosomal escape an important rate-determining step for the efficient delivery of siRNAs and antisense oligonucleotides (ASOs) (Gilleron et al., 2013; Springer and Dowdy, 2018; Ayyar et al., 2021; Holland et al., 2021). Potential endosomal-escape promoters such as chloroquine and nigericin, also known as osmotic agents, along with other approaches and techniques, have been associated with cytotoxicity that has limited their therapeutic application, making GalNAc-siRNA conjugates more promising solutions (Lechanteur et al., 2018).

Givosiran is an FDA-approved therapeutic siRNA based on GalNAc-siRNA technology. As previously discussed, givosiran is indicated for AHP caused by a disorder of hepatic ALAS1 and acute intermittent porphyria (AIP), which can result in the accumulation of several components, including toxic metabolites such as porphyrin precursors, ALA and PBG, leading to multiorgan and multisystem injury, including nervous system injury, along with conditions such as chronic kidney disease, hepatocellular carcinoma and hypertension (Lazareth et al., 2021). Iron overload and vein thrombosis are the predominant limitations of intravenous hemin application to suppress ALAS1 induction and cure palindromic attacks. After incorporation into RISC, givosiran then adopts the RNAi mechanism to silence the mRNA of hepatic ALAS1, thus thwarting the synthesis of ALAS1 integrin (Bissell and Wang, 2015; Sawicki et al., 2015; Agarwal et al., 2020; de Paula Brandão

et al., 2020; Lazareth et al., 2021). During phase three testing of the ENVISION trial, the givosiran-injected group exhibited a lower rate of annual attacks, lower urinary ALA levels, and less pain than the placebo. Nonetheless, higher serum transaminase levels and creatinine levels were observed, attributed to glomerular filtration changes (Balwani et al., 2020; Bonkovsky et al., 2020; Ventura et al., 2021). Overall, givosiran is still paving the way for the clinical application of GalNAc-siRNA conjugates and represents an excellent AIP oligonucleotide therapeutic option that can promote siRNA development.

Inclisiran is another GalNAc-siRNA conjugate approved by the FDA that can bind to hepatically expressed PCSK9 proteins, representing ideal targets that affect systemic and regional lipid metabolism and plasma cholesterol level regulation (Leiter et al., 2019; German and Shapiro, 2020; Kam et al., 2020; Scicchitano et al., 2021). Inclisiran has been documented to be effective in lowering LDL-C in cases of high cholesterol levels. Importantly, drug elimination 24 h after injection and liver uptake selectivity and efficiency suggest inclisiran to be a promising drug (Tomlinson et al., 2021). Research has shown that inclisiran and bempedoic acid can resolve limitations associated with pH treatment (Aguilar-Salinas et al., 2021). Moreover, it has been shown that inclisiran can decrease LDL-C levels; the published ORION trials demonstrated that combining inclisiran and the maximum tolerated dose of statins led to a 150% decline in LDL-C (Stoekenbroek et al., 2018; Gallego-Colon et al., 2020; Bardolia et al., 2021; Hardy et al., 2021).

Lumasiran targeting glycolate oxidase is a promising therapeutic agent shown to effectively lower oxalate levels in the liver, resulting in less deposition of calcium oxalate crystals in the kidneys and lower probability of kidney failure, systemic oxalosis and other systemic organ failure due to metabolic dysfunction (Perazella and Herlitz, 2021; Scott and Keam, 2021; Shah et al., 2021). Glyoxylic acid is obtained by glycolic acid conversion catalyzed by glycolate oxidase and is inhibited by limiting glyoxylate availability, leading to increased glycolate levels (Dutta et al., 2016; Liebow et al., 2017; Frishberg et al., 2021). A phase 1/2 randomized placebo-controlled study showed that lumasiran was biologically safe and effectively reduced urinary oxalate excretion in all cases with PH1 during the trial (Frishberg et al., 2021). In a phase three double-blind trial where urinary oxalate excretion patients with PH1 were studied, lumasiran effectively reduced progression to kidney failure (Garrelfs et al., 2020; Garrelfs et al., 2021; Frishberg et al., 2022).

Vutrisiran is a transthyretin-directed siRNA therapeutic for the treatment of amyloid transthyretin-mediated (ATTR) amyloidosis, including hATTR amyloidosis and wild-type ATTR (wtATTR) amyloidosis (Keam, 2022). Vutrisiran reduces serum TTR levels by reducing synthesis of variant and wild-type TTR which primarily synthesis in liver. Via ESC design of GalNAc-siRNA conjugates, Vutrisiran is able to bind ASGPR effectively, allowing for once every 3 months

subcutaneous injection with better metabolic stability and improved potency in a phase three study (Soprano et al., 1985; Holmgren et al., 1991; Habtemariam et al., 2021; Alnylam Pharmaceuticals Inc, 2022).

3.3.2 Clinical and preclinical advances in GalNAc-siRNA therapeutics

As the representative of GalNAc conjugates clinical usage, Fitusiran, developed by Alnylam and Sanofi Genzyme, is a synthetic siRNA targeting liver antithrombin to increase thrombin generation developed for the treatment of coagulation factor VIII deficiency (hemophilia A) and coagulation factor IX deficiency (hemophilia B) and is ongoing. In a phase 1 inhibitor cohort, monthly fitusiran lowered antithrombin levels from baseline, resulting in thrombin generation improvements, suggesting that monthly subcutaneous injections of fitusiran may lead to bleeding episode reduction and improved quality of life in participants with hemophilia A or B treated with inhibitors (Pasi et al., 2021).

The phase three ATLAS trial design consists of major branches including 1) ATLAS-A/B (NCT03417245), assessing fitusiran or on-demand factor replacement therapy, and 2) ATLAS-INH (NCT03417102), assessing fitusiran or on-demand bypassing agent therapy (Zhang et al., 2021a). A phase three results for 1) ATLAS-A/B (Genzyme, 2021) and 2) ATLAS-INH (Genzyme, 2020) are completed, with outcomes summarized. In ATLAS-A/B and ATLAS-INH, the observed annualized bleeding rate (ABR) for treated bleeds during the efficacy period and the treatment period and the onset period of the fitusiran 80 mg prophylaxis group are significantly reduced compared to the on-demand group. The same tendency also appears in the observed annualized spontaneous bleeding rate and annualized joint bleeding rate for treated bleeds during the efficacy period, representing less spontaneous bleeding events appearing after subcutaneous administration of 80 mg (mg) of fitusiran as prophylaxis once monthly compared to the on-demand or bypassing agents (BPA) on-demand group.

Additionally, preclinical undergone experiments with published papers are listed, with comparisons on years, models, animals, etc. (Willoughby et al., 2018; Brown et al., 2020; Ayyar et al., 2021; Iwakawa and Tomari, 2021; Yang et al., 2021) (Supplementary Table S3).

3.4 Challenges and limitations

Although GalNAc conjugates possess better stability, other crucial factors, such as endosomal escape, hepatotoxicity from off-target effects, acidic subcellular compartments, and extensive clearance, affect GalNAc efficiency and sequence barriers (Ayyar et al., 2021; Fairman et al., 2021; Fattal and Fay, 2021; Fumoto et al., 2021; Liu et al., 2021; Nanavati et al., 2021; Schlich et al., 2021).

3.4.1 Endosomal escape

When GalNAc conjugates are functional *in vivo*, only a few free siRNAs can escape into the hepatocyte cytoplasm and cross the endosomal lipid bilayer membrane, allowing siRNA to transactivate reactive RNA-binding proteins and resulting in a rapid, robust and sustained RNAi response by loading onto the host cell Ago (Springer and Dowdy, 2018). Endosomal escape is considered the rate-limiting step, preventing GalNAc conjugates from exerting their effects. Cell-penetrating peptides (CPPs) are short peptides that cross cellular membranes, facilitating endosomal escape (Oyama et al., 2021). Lonn et al. (2016) hypothesized that the insertion of a lipid bilayer with a hydrophobic patch into PTD/CPP-EED domains resulted in localized membrane destabilization that enhanced endosomal escape into the cytoplasm. CPPs exhibit heterogeneous rates of toxicity, penetration, and membrane leakage (Lonn et al., 2016; Benizri et al., 2019).

3.4.2 Hepatotoxicity from off-target effects

Janas et al. (2018b) hold a point of view that during supratherapeutic exposures, instead of chemical modifications or the perturbation of RNAi pathways, the observed rodent hepatotoxicity can be largely attributed to RNAi-mediated off-target effects. Theoretically, full-length pairing targets mRNA distinctively, while in the siRNA guide strand at positions 2–8 of the seed region (g2–g8), there are complementary sites that bind to the 3' untranslated region (3'-UTR) of mRNAs: thereby, unexpected off-target effects occur through the combination of the two, which is capable of leading to enormous dysregulation of transcription through a manner similar to miRNA (Schlegel et al., 2021; Varley and Desaulniers, 2021). Hepatotoxicity not only results from off-target effects caused by genetic changes, but is also related to intracellular oligonucleotide accumulation and chemical reactivity with metabolites. Moreover, although hepatotoxicity can be associated with disturbances during the RNAi process, it is mainly attributed to off-target effects (Janas et al., 2018b).

To eliminate hepatotoxicity, several solutions have been found. Janas et al. provide compelling evidence that off-target effects play key roles in hepatotoxicity during GalNAc treatment in rats (Janas et al., 2018a; Janas et al., 2018b). It was found that during seed-mediated binding, thermal destabilization is a feasible option to reduce *in vivo* siRNA off-target effects, thereby reducing hepatotoxicity. It is possible to selectively infuse a single thermally destabilizing GNA nucleotide into the seed region of the antisense strand to reduce seed-mediated off-target binding, thereby improving the safety of GalNAc-conjugated siRNA in rats (Janas et al., 2018b). Xu et al. (2004) suggested that among the factors that determine siRNA efficiency, siRNA molecular structural characteristics, such as single or duplex-stranded nature, might be more significant than cellular persistence. In this regard, it has been shown that the duplex siRNA yielded better efficiency of RISC

reconstitution versus single-stranded siRNA, which paved the way for further investigations due to concerns about the use of structural features to improve transfection efficiency (Xu et al., 2004).

3.4.3 Acidic subcellular compartment

It is shown that the results of GalNAc-siRNA conjugate loading into RISC match the corresponding model of GalNAc-siRNA conjugate liberation from the acidic subcellular compartment (Fairman et al., 2021; Schlich et al., 2021). Since less stable siRNA designs degrade faster in acidic subcellular compartments, such as lysosomes, they are unable to support continuous RISC loading over time. Brown et al. (2020) found that the predominant driver for the extended duration of activity is increasing the half-life of chemically stabilized siRNA in acidic subcellular compartments. They also proposed that a slow release of stabilized siRNA from acidic subcellular compartments enables continuous loading of RISC and prolonged target silencing. Nonetheless, enhancing siRNA can counter aggressive degradation of the intracellular compartments by nucleases, leading to better knockdown efficiency and a prolonged effective period.

3.4.4 Extensive enzymatic and/or systemic clearance

Given the wide range of nuclease degradation, sufficient RNA packaging is crucial to ensure that modified RNA can properly access receptors. Additionally, inadequate oligonucleotides exhibit quick renal filtration and elimination, leading to less intracellular residues and a lower half-life, significantly limiting treatment efficacy (Kovacevic et al., 2018; Ayyar et al., 2021; Fairman et al., 2021; Nanavati et al., 2021; Yan et al., 2022).

3.4.5 Sequence barriers

For many siRNA targets, the use of animal models to predict clinical results is prohibited because of the differential sequences between preclinical species. Therefore, new preclinical approaches are necessary in the development of oligonucleotide therapeutics to allow evaluation of target cell delivery as well as RNA silencing efficacy in species-relevant systems (Li, 2010). Primary human hepatocytes, which are considered the “gold standard” *in vitro* experimental model for the evaluation of small molecule drug metabolism, drug-drug interactions, and toxicity, are recommended for siRNA with hepato-cellular targets based on the limitations of the animal models.¹¹⁰ Primary human hepatocytes enable good effects with respect to potency and duration for the evaluation of GalNAc-siRNA efficacy due to the significant species (human) and organ (liver) relevance. Yang et al. collected findings that demonstrate the potential utility of prolonged cultured human hepatocytes (PCHH) as a preclinical tool for the translation of hepatocyte-targeted siRNA, with advantages such as long culture duration, lack of cell division and

prolonged expression of hepatic transcripts in a species, organ and pharmacologically relevant system. In their POC study, robust, durable, HPRT1 mRNA knockdown was demonstrated with a GalNAc-conjugated, stability-enhanced siRNA molecule, indicating that all biochemical systems required to facilitate siRNA delivery and activity are intact and functional in the cryopreserved 999 Elite Human Hepatocytes used in the establishment of PCHH. This *in vitro* model may serve as a valid alternative for siRNA prioritization and selection to reduce overall animal usage in addition to the provision of human hepatocyte-specific results, which may not be readily obtainable from *in vivo* animal models (Yang et al., 2021).

4 Other delivery systems

However, it was found that after years of development, available siRNA drugs still cannot solve problems associated with endosomal escape barriers, off-target effects and extensive enzymatic and/or systemic clearance. The targeting precision needs to be further improved (Xu et al., 2004; Lonn et al., 2016; Janas et al., 2018b; Kovacevic et al., 2018; Zhang et al., 2018; Benizri et al., 2019; Jahns et al., 2021; Schlegel et al., 2021; Yan et al., 2022). Accordingly, further research and development efforts are needed to apply this technology in the clinic.

4.1 LNPs loaded siRNA

The LNP delivery system, also known as the second-generation delivery system of RNAi drugs, is mainly composed of four parts: polyethylene glycol-lipid conjugates (such as PEG-DMG), ionizable amino lipids (such as DLin-MC3-DMA), distearyl phosphatidylcholine (DSPC) and cholesterol (Aldosari et al., 2021; Lokugamage et al., 2021). PEG-lipid on the outside helps protect the contents, while the cationic lipids inside can electrostatically adsorb genetic materials. The oligonucleotide drugs are protected by encapsulation, forming a cationic lipid package (Eygeris et al., 2021; Li et al., 2022; Paunovska et al., 2022; Yan et al., 2022). Cholesterol near the cationic lipid package can help stabilize the structure of nanoparticles and assist endocytosis induced by LDL (Gupta et al., 2021b; Zhang et al., 2021b; Chaudhary et al., 2021; Huang et al., 2021). Overall, the LNP delivery system is currently one of the most effective siRNA delivery methods and is mainly used for intravenous administration (Carrasco et al., 2021; Everton et al., 2021). During the transport of LNP-encapsulated siRNA into the body, LNP first fuses with the lipid bilayer of the cell membrane and then releases siRNA into the cell, allowing systemic siRNA administration (Table 2) (Wang et al., 2021a; Yan et al., 2022).

4.2 ESC and advanced ESC loaded by LNPs

GalNAc-siRNA conjugates are transmitted by ASGPR-mediated endocytosis and accumulate in acidic cells. It is mentioned that high metabolic stability is the most vital factor for GalNAc-siRNA to achieve optimal activity *in vivo* (Foster et al., 2018). Moreover, after subcutaneous injection of a certain dose of ESC and advanced ESC conjugate, significantly different pharmacodynamic characteristics were observed; the stability of advanced ESC was higher than that of ESC. Although studies have shown that ESC conjugates yield a stronger effect at maximum knockout after a threefold increase in the dose, advanced ESC conjugates exhibit more enduring activity, which proves that greater stability of the chemical properties of GalNAc-siRNA enables longer duration of action (Springer and Dowdy, 2018). Furthermore, a study that directly compared the effects of GalNAc coupling and LNP delivery on the siRNAs of traditional and advanced ESC targeting mouse factor 7 indicated that during LNP delivery, ESC and advanced ESC with similar intrinsic efficacy exhibited similar behaviors, which indicates that LNP delivery eliminated the differences in time and efficiency between traditional and advanced ESC. Besides, the exposure levels of total siRNA in the liver after subcutaneous injection of ESC and advanced ESC were lower than those of ESC and advanced ESC delivered by LNPs. It is worth noting that the delivery mode of ESC and advanced ESC loaded with LNPs occurred *via* intravenous injection, substantiating that the delivery mode can significantly affect the activity and duration of GalNAc-siRNA (Brown et al., 2020; Kulkarni et al., 2021; Naito et al., 2021; Salim and Desaulniers, 2021).

5 Conclusion

Many chronic or acute serious diseases are associated with the liver, such as liver cancer, hepatitis, hepatic hemangioma, etc., which remain among the leading causes that seriously affect the quality of human life and even lead to human death. The immense potential of GalNAc siRNA conjugates in the treatment of liver-related diseases involving gene expression provides a new strategy for this purpose. Through years of improvement, siRNA therapeutics have achieved superior advances in delivery accuracy and targeting precision, and both LNP siRNA and GalNAc siRNA delivery systems have enabled siRNA systemic delivery. However, GalNAc conjugate-based siRNA capable of direct targeted delivery offers the advantages of being safer and more efficient than the second-generation delivery system LNP siRNA. Additionally, the results of intravenous injection of GalNAc-siRNA highlighted the durability of RNAi, while subcutaneous injection increased target gene knockout and prolonged the duration of RNAi activity. Moreover, studies have shown that chemically stable siRNA persists in highly acidic subcellular compartments after administration, with chemical stability contributing to prolonging the activity of RNAi. The progress in siRNA design and chemical

modification is the crucial step in improving the stability of siRNA metabolism when designing oligonucleotides with continuously increased efficacy and enhancing the half-life of the GalNAc conjugates. To date, with several approved drugs and ongoing clinical and preclinical trials, it is promising that with more contributions taken into account, more delicate designs and modifications can lead GalNAc conjugates to not only longer duration but also higher efficiency, reduced toxicity and tighter attachment. Challenges such as endosomal escape barriers, off-target effects, and a lack of safety profile remain hindrances to actualizing the full opportunity and potential of oligonucleotide drugs. Thankfully, massive research is underway to investigate these obstacles, including the development of hepatic and extrahepatic delivery platforms, paving the way for further design and development. It is believed that state-of-the-art siRNA technology will surely be a boon to clinical medicine.

Author contributions

Conceptualization, ZL, LZ, YL, and XJ; methodology, GL; data curation, YZ; writing—original draft preparation, LZ, YL, and ZT; writing—review and editing, ZL, LZ, YL, XJ, GL, and ZT. All authors have read and agreed to the published version of the manuscript.

Funding

This work has been financed by the National Natural Science Foundation of China (No. 81870591), Key R&D and Promotion

Projects in Henan Province (Nos. 212102310874 and 222102310013), Key Scientific Research Projects of Colleges and Universities in Henan Province (No. 23A310011), National College Students' Innovation and Entrepreneurship Training Program (Nos. 202110475021, 202110475048 and 202110475037).

Conflict of interest

The authors declare that the research was conducted in the absence of any commercial or financial relationships that could be construed as a potential conflict of interest.

Publisher's note

All claims expressed in this article are solely those of the authors and do not necessarily represent those of their affiliated organizations, or those of the publisher, the editors and the reviewers. Any product that may be evaluated in this article, or claim that may be made by its manufacturer, is not guaranteed or endorsed by the publisher.

Supplementary material

The Supplementary Material for this article can be found online at: <https://www.frontiersin.org/articles/10.3389/fphar.2022.1090237/full#supplementary-material>

References

- Abdelaal, A. M., and Kasinski, A. L. (2021). Ligand-mediated delivery of RNAi-based therapeutics for the treatment of oncological diseases. *Nar. Cancer* 3 (3), zcab030. doi:10.1093/narcan/zcab030
- Adachi, H., Hengesbach, M., Yu, Y. T., and Morais, P. (2021). From antisense RNA to RNA modification: Therapeutic potential of RNA-based technologies. *Biomedicine* 9 (5), 550. doi:10.3390/biomedicine9050550
- Adams, D., Tournev, I. L., Taylor, M. S., Coelho, T., Plante-Bordeneuve, V., Berk, J. L., et al. (2022). Efficacy and safety of vutrisiran for patients with hereditary transthyretin-mediated amyloidosis with polyneuropathy: A randomized clinical trial. *Amyloid*, 1–9. doi:10.1080/13506129.2022.2091985
- Agarwal, S., Simon, A. R., Goel, V., Habtemariam, B. A., Clausen, V. A., Kim, J. B., et al. (2020). Pharmacokinetics and pharmacodynamics of the small interfering ribonucleic acid, givosiran, in patients with acute hepatic porphyria. *Clin. Pharmacol. Ther.* 108 (1), 63–72. doi:10.1002/cpt.1802
- Aguilar-Salinas, C. A., Gomez-Diaz, R. A., and Corral, P. (2021). New therapies for primary hyperlipidaemia. *J. Clin. Endocrinol. Metab.*
- Aldosari, B. N., Alfagih, I. M., and Almurshedi, A. S. (2021). Lipid nanoparticles as delivery systems for RNA-based vaccines. *Pharmaceutics* 13 (2), 206. doi:10.3390/pharmaceutics13020206
- Alnylam Pharmaceuticals Inc (2022). US prescribing information:AMVUTTRA (vutrisiran) injection, for subcutaneous use. Available from https://www.accessdata.fda.gov/drugsatfda_docs/label/2022/215515s000lbl.pdf.
- Alshaer, W., Zureigat, H., Al Karaki, A., Al-Kadash, A., Gharaibeh, L., Hatmal, M. M., et al. (2021). Corrigendum to "siRNA: Mechanism of action, challenges, and therapeutic approaches" [Eur. J. Pharmacol. 905 (2021) 174178]. *Eur. J. Pharmacol.* 916, 174741. doi:10.1016/j.ejphar.2022.174741
- Antimisiaris, S. G., Marazioti, A., Kannavou, M., Natsaridis, E., Gkartzou, F., Kogkos, G., et al. (2021). Overcoming barriers by local drug delivery with liposomes. *Adv. Drug Deliv. Rev.* 174, 53–86. doi:10.1016/j.addr.2021.01.019
- Ayyar, V. S., Song, D., Zheng, S., Carpenter, T., and Heald, D. L. (2021). Minimal physiologically based pharmacokinetic-pharmacodynamic (mPBPK-PD) model of N-Acetylgalactosamine-Conjugated small interfering RNA disposition and gene silencing in preclinical species and humans. *J. Pharmacol. Exp. Ther.* 379 (2), 134–146. doi:10.1124/jpet.121.000805
- Balwani, M., Sardh, E., Ventura, P., Peiro, P. A., Rees, D. C., Stolzel, U., et al. (2020). Phase 3 trial of RNAi therapeutic givosiran for acute intermittent porphyria. *N. Engl. J. Med.* 382 (24), 2289–2301. doi:10.1056/NEJMoa1913147
- Bardolia, C., Amin, N. S., and Turgeon, J. (2021). Emerging non-statin treatment options for lowering low-density lipoprotein cholesterol. *Front. Cardiovasc. Med.* 8, 789931. doi:10.3389/fcvm.2021.789931
- Benizri, S., Gissot, A., Martin, A., Vialat, B., Grinstaff, M. W., and Barthelemy, P. (2019). Bioconjugated oligonucleotides: Recent developments and therapeutic applications. *Bioconjug. Chem.* 30 (2), 366–383. doi:10.1021/acs.bioconjchem.8b00761
- Bissell, D. M., Anderson, K. E., and Bonkovsky, H. L. (2017). *N. Engl. J. Med.* 377 (9), 862–872. doi:10.1056/NEJMra1608634
- Bissell, D. M., and Wang, B. (2015). Acute hepatic porphyria. *J. Clin. Transl. Hepatol.* 3 (1), 17–26. doi:10.14218/JCTH.2014.00039

- Blakney, A. K., McKay, P. F., Hu, K., Samnuan, K., Jain, N., Brown, A., et al. (2021). Polymeric and lipid nanoparticles for delivery of self-amplifying RNA vaccines. *J. Control. Release* 338, 201–210. doi:10.1016/j.jconrel.2021.08.029
- Bonkovsky, H. L., Balwani, M., Sardh, E., Gouya, L., Rees, D. C., Stein, P., et al. (2020). S1154 clinical outcomes in patients with acute hepatic porphyria treated with givosiran who stopped hemin prophylaxis at study entry: A post hoc analysis of data from the phase 3 ENVISION study through month 12. *Am. J. Gastroenterol.* 115, S578. doi:10.14309/01.ajg.0000706664.77192.9e
- Brown, C. R., Gupta, S., Qin, J., Racie, T., He, G., Lentini, S., et al. (2020). Investigating the pharmacodynamic durability of GalNAc-siRNA conjugates. *Nucleic Acids Res.* 48 (21), 11827–11844. doi:10.1093/nar/gkaa670
- Carrasco, M. J., Alishetty, S., Alameh, M. G., Said, H., Wright, L., Paige, M., et al. (2021). Ionization and structural properties of mRNA lipid nanoparticles influence expression in intramuscular and intravascular administration. *Commun. Biol.* 4 (1), 956. doi:10.1038/s42003-021-02441-2
- Chaudhary, N., Weissman, D., and Whitehead, K. A. (2021). mRNA vaccines for infectious diseases: Principles, delivery and clinical translation. *Nat. Rev. Drug Discov.* 20 (11), 817–838. doi:10.1038/s41573-021-00283-5
- Crooke, S. T., Witztum, J. L., Bennett, C. F., and Baker, B. F. (2018). RNA-targeted therapeutics. *Cell Metab.* 27 (4), 714–739. doi:10.1016/j.cmet.2018.03.004
- Cui, H., Zhu, X., Li, S., Wang, P., and Fang, J. (2021). Liver-targeted delivery of oligonucleotides with N-acetylgalactosamine conjugation. *ACS Omega* 6 (25), 16259–16265. doi:10.1021/acsomega.1c01755
- Damase, T. R., Sukhovshin, R., Boada, C., Taraballi, F., Pettigrew, R. I., and Cooke, J. P. (2021). The limitless future of RNA therapeutics. *Front. Bioeng. Biotechnol.* 9, 628137. doi:10.3389/fbioe.2021.628137
- de Paula Brandão, P. R., Titz-de-Almeida, S. S., and Titz-de-Almeida, R. (2020). Leading RNA interference therapeutics part 2: Silencing delta-aminolevulinic acid synthase 1, with a focus on givosiran. *Mol. Diagn. Ther.* 24 (1), 61–68. doi:10.1007/s40291-019-00438-6
- Debacker, A. J., Voutila, J., Catley, M., Blakey, D., and Habib, N. (2020). Delivery of oligonucleotides to the liver with GalNAc: From research to registered therapeutic drug. *Mol. Ther.* 28 (8), 1759–1771. doi:10.1016/j.ymthe.2020.06.015
- Dobrowolski, C., Paunovska, K., Hatit, M. Z. C., Lokugamage, M. P., and Dahlman, J. E. (2021). Therapeutic RNA delivery for COVID and other diseases. *Adv. Healthc. Mat.* 10, 2002022. doi:10.1002/adhm.202002022
- Dutta, C., Avitahl-Curtis, N., Pursell, N., Larsson Cohen, M., Holmes, B., Diwanji, R., et al. (2016). Inhibition of glycolate oxidase with dicer-substrate siRNA reduces calcium oxalate deposition in a mouse model of primary hyperoxaluria type 1. *Mol. Ther.* 24 (4), 770–778. doi:10.1038/mt.2016.4
- Everton, E., Rizvi, F., Smith, A. R., Beattie, M., Tam, Y., Pardi, N., et al. (2021). Transient yet robust expression of proteins in the mouse liver via intravenous injection of lipid nanoparticle-encapsulated nucleoside-modified mRNA. *Bio. Protoc.* 11 (19), e4184. doi:10.21769/BioProtoc.4184
- Eygeris, Y., Gupta, M., Kim, J., and Sahay, G. (2021). Chemistry of lipid nanoparticles for RNA delivery. *Acc. Chem. Res.* 55, 2–12. doi:10.1021/acs.accounts.1c00544
- Fairman, K., Li, M., Ning, B., and Lumen, A. (2021). Physiologically based pharmacokinetic (PBPK) modeling of RNAi therapeutics: Opportunities and challenges. *Biochem. Pharmacol.* 189, 114468. doi:10.1016/j.bcp.2021.114468
- Fattal, E., and Fay, F. (2021). Nanomedicine-based delivery strategies for nucleic acid gene inhibitors in inflammatory diseases. *Adv. Drug Deliv. Rev.* 175, 113809. doi:10.1016/j.addr.2021.05.019
- Foster, D. J., Brown, C. R., Shaikh, S., Trapp, C., Schlegel, M. K., Qian, K., et al. (2018). Advanced siRNA designs further improve *in vivo* performance of GalNAc-siRNA conjugates. *Mol. Ther.* 26 (3), 708–717. doi:10.1016/j.ymthe.2017.12.021
- Freitag, F., and Wagner, E. (2021). Optimizing synthetic nucleic acid and protein nanocarriers: The chemical evolution approach. *Adv. Drug Deliv. Rev.* 168, 30–54. doi:10.1016/j.addr.2020.03.005
- Frishberg, Y., Cochat, P., Talamudupula, S., McGregor, T., Tamimi, N., Illuminate, C., et al. ILLUMINATE-C: A phase 3 single-arm study to evaluate efficacy, safety, pharmacokinetics, and pharmacodynamics of lumasiran in patients with advanced primary hyperoxaluria type. 2022.
- Frishberg, Y., Deschênes, G., Grothoff, J. W., Hulton, S.-A., Magen, D., Harambat, J., et al. (2021). Phase 1/2 study of lumasiran for treatment of primary hyperoxaluria type 1: A placebo-controlled randomized clinical trial. *Clinical Journal of the American Society of Nephrology*.
- Fumoto, S., Yamamoto, T., Okami, K., Maemura, Y., Terada, C., Yamayoshi, A., et al. (2021). Understanding *in vivo* fate of nucleic acid and gene medicines for the rational design of drugs. *Pharmaceutics* 13 (2), 159. doi:10.3390/pharmaceutics13020159
- Gabba, A., Bogucka, A., Luz, J. G., Diniz, A., Coelho, H., Corzana, F., et al. (2021). Crystal structure of the carbohydrate recognition domain of the human macrophage galactose C-type lectin bound to GalNAc and the tumor-associated tn antigen. *Biochemistry* 60 (17), 1327–1336. doi:10.1021/acs.biochem.1c00009
- Gallego-Colon, E., Daum, A., and Yosefy, C. (2020). Statins and PCSK9 inhibitors: A new lipid-lowering therapy. *Eur. J. Pharmacol.* 878, 173114. doi:10.1016/j.ejphar.2020.173114
- Garrelfs, S. F., Frishberg, Y., Hulton, S. A., Koren, M. J., O'Riordan, W. D., Cochat, P., et al. (2021). Lumasiran, an RNAi therapeutic for primary hyperoxaluria type 1. *N. Engl. J. Med.* 384 (13), 1216–1226. doi:10.1056/NEJMoa2021712
- Garrelfs, S., Frishberg, Y., Hulton, S., Koren, M., O'Riordan, W., Cochat, P., et al. (2020). LB002 illuminate-a, a phase 3 study of lumasiran, an investigational rna therapeutic, in children and adults with primary hyperoxaluria type 1 (PH1). *Nephrol. Dial. Transplant.* 35 (3), gfaa146. doi:10.1093/ndt/gfaa146.lb002
- Genzyme, A. S. C. (2020). A study of fitusiran (ALN-AT3SC) in severe hemophilia A and B patients with inhibitors. Available at: <https://ClinicalTrials.gov/show/NCT03417102>.
- Genzyme, A. S. C. (2021). A study of fitusiran (ALN-AT3SC) in severe hemophilia A and B patients without inhibitors. Available at: <https://ClinicalTrials.gov/show/NCT03417245>.
- German, C. A., and Shapiro, M. D. (2020). Small interfering RNA therapeutic inclisiran: A new approach to targeting PCSK9. *BioDrugs* 34 (1), 1–9. doi:10.1007/s40259-019-00399-6
- Gilleron, J., Querbes, W., Zeigerer, A., Borodovsky, A., Marsico, G., Schubert, U., et al. (2013). Image-based analysis of lipid nanoparticle-mediated siRNA delivery, intracellular trafficking and endosomal escape. *Nat. Biotechnol.* 31 (7), 638–646. doi:10.1038/nbt.2612
- Gupta, A., Andresen, J. L., Manan, R. S., and Langer, R. (2021). Nucleic acid delivery for therapeutic applications. *Adv. Drug Deliv. Rev.* 178, 113834. doi:10.1016/j.addr.2021.113834
- Gupta, S. V., Fanget, M. C., MacLauchlin, C., Clausen, V. A., Li, J., Cloutier, D., et al. (2021). Clinical and preclinical single-dose pharmacokinetics of VIR-2218, an RNAi therapeutic targeting HBV infection. *Drugs R. D.* 21 (4), 455–465. doi:10.1007/s40268-021-00369-w
- Habtemariam, B. A., Karsten, V., Attarwala, H., Goel, V., Melch, M., Clausen, V. A., et al. (2021). Single-dose pharmacokinetics and pharmacodynamics of transthyretin targeting N-acetylgalactosamine-Small interfering ribonucleic acid conjugate, vutrisiran, in healthy subjects. *Clin. Pharmacol. Ther.* 109 (2), 372–382. doi:10.1002/cpt.1974
- Han, H. (2018). RNA interference to knock down gene expression. *Methods Mol. Biol.* 1706, 293–302. doi:10.1007/978-1-4939-7471-9_16
- Hannon, G. J. (2002). RNA interference. *nature* 418 (6894), 244–251. doi:10.1038/418244a
- Hardy, J., Niman, S., Pereira, E., Lewis, T., Reid, J., Choksi, R., et al. (2021). A critical review of the efficacy and safety of inclisiran. *Am. J. Cardiovasc. Drugs* 21, 629–642. doi:10.1007/s40256-021-00477-7
- Hassett, K. J., Higgins, J., Woods, A., Levy, B., Xia, Y., Hsiao, C. J., et al. (2021). Impact of lipid nanoparticle size on mRNA vaccine immunogenicity. *J. Control. Release* 335, 237–246. doi:10.1016/j.jconrel.2021.05.021
- Holland, R. J., Lam, K., Ye, X., Martin, A. D., Wood, M. C., Palmer, L., et al. (2021). Ligand conjugate structure activity relationships and enhanced endosomal escape with a targeted polymer micelle in non-human primates. *Mol. Ther.* 29, doi:10.1016/j.ymthe.2021.06.002
- Holmgren, G., Steen, L., Ekstedt, J., Groth, C. G., Ericzon, B. G., Eriksson, S., et al. (1991). Biochemical effect of liver transplantation in two Swedish patients with familial amyloidotic polyneuropathy (FAP-met30). *Clin. Genet.* 40 (3), 242–246. doi:10.1111/j.1399-0004.1991.tb03085.x
- Hoy, S. M. (2018). Patisiran: First global approval. *Drugs* 78 (15), 1625–1631. doi:10.1007/s40265-018-0983-6
- Hu, B., Zhong, L., Weng, Y., Peng, L., Huang, Y., Zhao, Y., et al. (2020). Therapeutic siRNA: State of the art. *Signal Transduct. Target. Ther.* 5 (1), 101. doi:10.1038/s41392-020-0207-x
- Huang, J., Yuen, D., Mintern, J. D., and Johnston, A. P. R. (2021). Opportunities for Innovation: Building on the success of lipid nanoparticle vaccines. *Curr. Opin. Colloid Interface Sci.* 55, 101468. doi:10.1016/j.cocis.2021.101468
- Ickenstein, L. M., and Garidel, P. (2019). Lipid-based nanoparticle formulations for small molecules and RNA drugs. *Expert Opin. Drug Deliv.* 16 (11), 1205–1226. doi:10.1080/17425247.2019.1669558

- Iwakawa, H.-o., and Tomari, Y. (2021). Life of RISC: Formation, action, and degradation of RNA-induced silencing complex. *Mol. Cell* 82, 30–43. doi:10.1016/j.molcel.2021.11.026
- Jahns, H., Degaonkar, R., Podbevsek, P., Gupta, S., Bisbe, A., Aluri, K., et al. (2021). Small circular interfering RNAs (sciRNAs) as a potent therapeutic platform for gene-silencing. *Nucleic Acids Res.* 49 (18), 10250–10264. doi:10.1093/nar/gkab724
- Janas, M. M., Harbison, C. E., Perry, V. K., Carito, B., Sutherland, J. E., Vaishnav, A. K., et al. (2018). The nonclinical safety profile of GalNAc-conjugated RNAi therapeutics in subacute studies. *Toxicol. Pathol.* 46 (7), 735–745. doi:10.1177/0192623318792537
- Janas, M. M., Schlegel, M. K., Harbison, C. E., Yilmaz, V. O., Jiang, Y., Parmar, R., et al. (2018). Selection of GalNAc-conjugated siRNAs with limited off-target-driven rat hepatotoxicity. *Nat. Commun.* 9 (1), 723. doi:10.1038/s41467-018-02989-4
- Jeon, J. Y., Ayyar, V. S., and Mitra, A. (2022). Pharmacokinetic and pharmacodynamic modeling of siRNA therapeutics - a minireview. *Pharm. Res.* 39 (8), 1749–1759. doi:10.1007/s11095-022-03333-8
- Juliano, R. L. (2018). Intracellular trafficking and endosomal release of oligonucleotides: What we know and what we don't. *Nucleic Acid. Ther.* 28 (3), 166–177. doi:10.1089/nat.2018.0727
- Kam, N., Perera, K., Zomer, E., Liew, D., and Ademi, Z. (2020). Inclisiran as adjunct lipid-lowering therapy for patients with cardiovascular disease: A cost-effectiveness analysis. *Pharmacoeconomics* 38 (9), 1007–1020. doi:10.1007/s40273-020-00948-w
- Keam, S. J. (2022). Vutrisiran: First approval. *Drugs* 82 (13), 1419–1425. doi:10.1007/s40265-022-01765-5
- Khan, S. H. (2019). Genome-editing technologies: Concept, pros, and cons of various genome-editing techniques and bioethical concerns for clinical application. *Mol. Ther. Nucleic Acids* 16, 326–334. doi:10.1016/j.omtn.2019.02.027
- Kovacevic, K. D., Gilbert, J. C., and Jilma, B. (2018). Pharmacokinetics, pharmacodynamics and safety of aptamers. *Adv. Drug Deliv. Rev.* 134, 36–50. doi:10.1016/j.addr.2018.10.008
- Kulkarni, J. A., Witzigmann, D., Thomson, S. B., Chen, S., Leavitt, B. R., Cullis, P. R., et al. (2021). The current landscape of nucleic acid therapeutics. *Nat. Nanotechnol.* 16 (6), 630–643. doi:10.1038/s41565-021-00898-0
- Lamb, Y. N. (2021). Inclisiran: First approval. *Drugs* 81 (3), 389–395. doi:10.1007/s40265-021-01473-6
- Lazareth, H., Poli, A., Bignon, Y., Mirmiran, A., Rabant, M., Cohen, R., et al. (2021). Renal function decline with small interfering RNA silencing aminolevulinic acid synthase 1 (ALAS1). *Kidney Int. Rep.* 6 (7), 1904–1911. doi:10.1016/j.ekir.2021.04.004
- Lechanteur, A., Sanna, V., Duchemin, A., Evrard, B., Mottet, D., and Piel, G. (2018). Cationic liposomes carrying siRNA: Impact of lipid composition on physicochemical properties, cytotoxicity and endosomal escape. *Nanomater. (Basel)* 8 (5), 270. doi:10.3390/nano8050270
- Leiter, L. A., Teoh, H., Kallend, D., Wright, R. S., Landmesser, U., Wijngaard, P. L. J., et al. (2019). Inclisiran lowers LDL-C and PCSK9 irrespective of diabetes status: The ORION-1 randomized clinical trial. *Diabetes Care* 42 (1), 173–176. doi:10.2337/dc18-1491
- Li, A. P. (2010). "Evaluation of drug metabolism, drug-drug interactions, and *in vitro* hepatotoxicity with cryopreserved human hepatocytes," in *Hepatocytes* (Humana: Springer), 281–294. doi:10.1007/978-1-60761-688-7_15
- Li, M., Li, Y., Li, S., Jia, L., Wang, H., Li, M., et al. (2022). The nano delivery systems and applications of mRNA. *Eur. J. Med. Chem.* 227, 113910. doi:10.1016/j.ejmech.2021.113910
- Liebow, A., Li, X., Racie, T., Hettinger, J., Bettencourt, B. R., Najafian, N., et al. (2017). An investigational RNAi therapeutic targeting glycolate oxidase reduces oxalate production in models of primary hyperoxaluria. *J. Am. Soc. Nephrol.* 28 (2), 494–503. doi:10.1681/ASN.2016030338
- Liu, Y., Xu, C. F., Iqbal, S., Yang, X. Z., and Wang, J. (2017). Responsive nanocarriers as an emerging platform for cascaded delivery of nucleic acids to cancer. *Adv. Drug Deliv. Rev.* 115, 98–114. doi:10.1016/j.addr.2017.03.004
- Liu, Z., Wang, S., Tapeinos, C., Torrieri, G., Känkänen, V., El-Sayed, N., et al. (2021). Non-viral nanoparticles for RNA interference: Principles of design and practical guidelines. *Adv. Drug Deliv. Rev.* 174, 576.
- Lokugamage, M. P., Vanover, D., Beyersdorf, J., Hatit, M. Z. C., Rotolo, L., Echeverri, E. S., et al. (2021). Optimization of lipid nanoparticles for the delivery of nebulized therapeutic mRNA to the lungs. *Nat. Biomed. Eng.* 5 (9), 1059–1068. doi:10.1038/s41551-021-00786-x
- Lonn, P., Kacsinta, A. D., Cui, X. S., Hamil, A. S., Kaulich, M., Gogoi, K., et al. (2016). Enhancing endosomal escape for intracellular delivery of macromolecular biologic therapeutics. *Sci. Rep.* 6, 32301. doi:10.1038/srep32301
- Lundin, K. E., Gissberg, O., and Smith, C. E. (2015). Oligonucleotide therapies: The past and the present. *Hum. Gene Ther.* 26 (8), 475–485. doi:10.1089/hum.2015.070
- Maestro, S., Weber, N. D., Zabaleta, N., Aldabe, R., and Gonzalez-Aseguinolaza, G. (2021). Novel vectors and approaches for gene therapy in liver diseases. *JHEP Rep.* 3 (4), 100300. doi:10.1016/j.jhepr.2021.100300
- Marinho, H. S., Marcelino, P., Soares, H., and Corvo, M. L. (2018). Gene silencing using siRNA for preventing liver ischaemia-reperfusion injury. *Curr. Pharm. Des.* 24 (23), 2692–2700. doi:10.2174/1381612824666180807124356
- Matsuda, S., Keiser, K., Nair, J. K., Charisse, K., Manoharan, R. M., Kretschmer, P., et al. (2015). siRNA conjugates carrying sequentially assembled trivalent N-acetylglucosamine linked through nucleosides elicit robust gene silencing *in vivo* in hepatocytes. *ACS Chem. Biol.* 10 (5), 1181–1187. doi:10.1021/cb501028c
- Montañés, J. C., Rojano, C., Ylla, G., Piulachs, M. D., and Maestro, J. L. (2021). siRNA enrichment in Argonaute 2-depleted *Blattella germanica*. *Biochim. Biophys. Acta. Gene Regul. Mech.* 1864 (6–7), 194704. doi:10.1016/j.bbagr.2021.194704
- Nair, J. K., Attarwala, H., Sehgal, A., Wang, Q., Aluri, K., Zhang, X., et al. (2017). Impact of enhanced metabolic stability on pharmacokinetics and pharmacodynamics of GalNAc-siRNA conjugates. *Nucleic Acids Res.* 45 (19), 10969–10977. doi:10.1093/nar/gkx818
- Nair, J. K., Willoughby, J. L. S., Chan, A., Charisse, K., Alam, M. R., Wang, Q., et al. (2014). Multivalent N-acetylglucosamine-conjugated siRNA localizes in hepatocytes and elicits robust RNAi-mediated gene silencing. *J. Am. Chem. Soc.* 136 (49), 16958–16961. doi:10.1021/ja505986a
- Naito, M., Chaya, H., Toh, K., Kim, B. S., Hayashi, K., Fukushima, S., et al. (2021). Structural tuning of oligonucleotides for enhanced blood circulation properties of unit polyion complexes prepared from two-branched poly (ethylene glycol)-block-poly (l-lysine). *J. Control. Release* 330, 812–820. doi:10.1016/j.jconrel.2021.01.001
- Nanavati, C., McMullen, G., Yu, R., Geary, R. S., Henry, S. P., and Wang, Y. (2021). Interspecies scaling of human clearance and plasma trough exposure for antisense oligonucleotides: A retrospective analysis of GalNAc3-conjugated and unconjugated-antisense oligonucleotides. *Nucleic Acid. Ther.* 31, 298–308. doi:10.1089/nat.2020.0911
- Oyama, S., Yamamoto, T., and Yamayoshi, A. (2021). Recent advances in the delivery carriers and chemical conjugation strategies for nucleic acid drugs. *Cancers* 13 (15), 3881. doi:10.3390/cancers13153881
- Paro, R., Grossniklaus, U., Santoro, R., Wutz, A., et al. (2021). "RNA-based mechanisms of gene silencing," in *Introduction to epigenetics* (Cham: Springer), 117–133.
- Pasi, K. J., Lissitchkov, T., Mamonov, V., Mant, T., Timofeeva, M., Bagot, C., et al. (2021). Targeting of antithrombin in hemophilia A or B with investigational siRNA therapeutic fitusiran-Results of the phase 1 inhibitor cohort. *J. Thromb. Haemost.* 19 (6), 1436–1446. doi:10.1111/jth.15270
- Paunovska, K., Loughrey, D., and Dahlman, J. E. (2022). Drug delivery systems for RNA therapeutics. *Nat. Rev. Genet.* 23, 265–280. doi:10.1038/s41576-021-00439-4
- Perazella, M. A., and Herlitz, L. C. (2021). The crystalline nephropathies. *Kidney Int. Rep.* 6 (12), 2942–2957. doi:10.1016/j.ekir.2021.09.003
- Salim, L., and Desaulniers, J.-P. (2021). To conjugate or to package? A look at targeted siRNA delivery through folate receptors. *Nucleic Acid. Ther.* 31 (1), 21–38. doi:10.1089/nat.2020.0893
- Saw, P. E., and Song, E.-W. (2019). siRNA therapeutics: a clinical reality. *Sci. China. Life Sci.* 63 (4), 485–500. doi:10.1007/s11427-018-9438-y
- Sawicki, K. T., Chang, H. C., and Ardehali, H. (2015). Role of heme in cardiovascular physiology and disease. *J. Am. Heart Assoc.* 4 (1), e001138. doi:10.1161/JAHA.114.001138
- Schlegel, M. K., Matsuda, S., Brown, C. R., Harp, J. M., Barry, J. D., Berman, D., et al. (2021). Overcoming GNA/RNA base-pairing limitations using isonucleotides improves the pharmacodynamic activity of ESC+ GalNAc-siRNAs. *Nucleic Acids Res.* 49, 10851. doi:10.1093/nar/gkab916
- Schlich, M., Palomba, R., Costabile, G., Mizrahy, S., Pannuzzo, M., Peer, D., et al. (2021). Cytosolic delivery of nucleic acids: The case of ionizable lipid nanoparticles. *Bioeng. Transl. Med.* 6, e10213. doi:10.1002/btm2.10213
- Scicchitano, P., Milo, M., Mallamaci, R., De Palo, M., Caldarola, P., Massari, F., et al. (2021). Inclisiran in lipid management: A literature overview and future perspectives. *Biomed. Pharmacother.* 143, 112227. doi:10.1016/j.biopha.2021.112227

- Scott, L. J. (2020). Givosiran: First approval. *Drugs* 80 (3), 335–339. doi:10.1007/s40265-020-01269-0
- Scott, L. J., and Keam, S. J. (2021). Lumasiran: First approval. *Drugs* 81 (2), 277–282. doi:10.1007/s40265-020-01463-0
- Setten, R. L., Rossi, J. J., and Han, S.-p. (2019). The current state and future directions of RNAi-based therapeutics. *Nat. Rev. Drug Discov.* 18 (6), 421–446. doi:10.1038/s41573-019-0017-4
- Shah, A., Leslie, S. W., and Ramakrishnan, S. (2021). Hyperoxaluria. StatPearls [Internet]. Available at: <https://www.ncbi.nlm.nih.gov/books/NBK558987/>.
- Shchegrovina, E., Sachkova, A. A., Usova, S. D., Nyuchev, A. V., Gracheva, Y. A., and Fedorov, A. Y. (2021). Carbohydrate systems in targeted drug delivery: Expectation and reality. *Russ. J. Bioorg. Chem.* 47 (1), 71–98. doi:10.1134/s1068162021010222
- Soprano, D. R., Herbert, J., Soprano, K. J., Schon, E. A., and Goodman, D. S. (1985). Demonstration of transthyretin mRNA in the brain and other extrahepatic tissues in the rat. *J. Biol. Chem.* 260 (21), 11793–11798. doi:10.1016/s0021-9258(17)39100-7
- Springer, A. D., and Dowdy, S. F. (2018). GalNAc-siRNA conjugates: Leading the way for delivery of RNAi therapeutics. *Nucleic Acid. Ther.* 28 (3), 109–118. doi:10.1089/nat.2018.0736
- Stoekenbroek, R. M., Kallend, D., Wijngaard, P. L., and Kastelein, J. J. (2018). Inclisiran for the treatment of cardiovascular disease: The ORION clinical development program. *Future Cardiol.* 14 (6), 433–442. doi:10.2217/fca-2018-0067
- Storjord, E. (2021). Acute intermittent porphyria. Inflammation, diet and biomarkers in acute intermittent porphyria. Available at: <https://munin.uit.no/handle/10037/20120?locale-attribute=en>.
- Subhan, M. A., Attia, S. A., and Torchilin, V. P. (2021). Advances in siRNA delivery strategies for the treatment of MDR cancer. *Life Sci.* 274, 119337. doi:10.1016/j.lfs.2021.119337
- Sutherland, J. E., Hettinger, J. L., Chan, A., Gilbert, J., Warner, G. L., and Davis, W. P. (2020). Nonclinical safety profile of revusiran, a 1st-generation GalNAc-siRNA conjugate for treatment of hereditary transthyretin-mediated amyloidosis. *Nucleic Acid. Ther.* 30 (1), 33–49. doi:10.1089/nat.2019.0796
- Svoboda, P. (2014). Renaissance of mammalian endogenous RNAi. *FEBS Lett.* 588 (15), 2550–2556. doi:10.1016/j.febslet.2014.05.030
- Swevers, L., Liu, J., and Smagghe, G. (2018). Defense mechanisms against viral infection in Drosophila: RNAi and non-RNAi. *Viruses* 10 (5), 230. doi:10.3390/v10050230
- Thangamani, L., Balasubramanian, B., Easwaran, M., Natarajan, J., Pushparaj, K., Meyyazhagan, A., et al. (2021). GalNAc-siRNA conjugates: Prospective tools on the frontier of anti-viral therapeutics. *Pharmacol. Res.* 173, 105864. doi:10.1016/j.phrs.2021.105864
- Thapa Magar, K., Boaf, G. F., Li, X., Chen, Z., and He, W. (2022). Liposome-based delivery of biological drugs. *Chin. Chem. Lett.* 33 (2), 587–596. doi:10.1016/j.ccl.2021.08.020
- Tian, Z., Liang, G., Cui, K., Liang, Y., Wang, Q., Lv, S., et al. (2021). Insight into the prospects for RNAi therapy of cancer. *Front. Pharmacol.* 12 (308), 644718. doi:10.3389/fphar.2021.644718
- Tomlinson, B., Chow, E., Chan, P., and Lam, C. W. K. (2021). An evaluation of the pharmacokinetics of inclisiran in the treatment of atherosclerotic cardiovascular disease. *Expert Opin. Drug Metab. Toxicol.* 17 (12), 1353–1361. doi:10.1080/17425255.2021.2029402
- van den Berg, A. I., Yun, C. O., Schifflers, R. M., and Hennink, W. E. (2021). Polymeric delivery systems for nucleic acid therapeutics: Approaching the clinic. *J. Control. Release* 331, 121–141. doi:10.1016/j.jconrel.2021.01.014
- Varley, A. J., and Desaulniers, J.-P. (2021). Chemical strategies for strand selection in short-interfering RNAs. *RSC Adv.* 11 (4), 2415–2426. doi:10.1039/d0ra07747j
- Ventura, P., Bonkovsky, H. L., Gouya, L., Aguilera-Peiró, P., Montgomery Bissell, D., Stein, P. E., et al. (2021). Efficacy and safety of givosiran for acute hepatic porphyria: 24-month interim analysis of the randomized phase 3 ENVISION study. *Liver Int.* 42, 161. doi:10.1111/liv.15090
- Wang, C., Zhang, Y., and Dong, Y. (2021). Lipid nanoparticle-mRNA formulations for therapeutic applications. *Acc. Chem. Res.* 54 (23), 4283–4293. doi:10.1021/acs.accounts.1c00550
- Wang, J., Zhu, M., and Nie, G. (2021). Biomembrane-based nanostructures for cancer targeting and therapy: From synthetic liposomes to natural biomembranes and membrane-vesicles. *Adv. Drug Deliv. Rev.* 178, 113974. doi:10.1016/j.addr.2021.113974
- Weng, Y., Xiao, H., Zhang, J., Liang, X. J., and Huang, Y. (2019). RNAi therapeutic and its innovative biotechnological evolution. *Biotechnol. Adv.* 37 (5), 801–825. doi:10.1016/j.biotechadv.2019.04.012
- Willoughby, J. L., Chan, A., Sehgal, A., Butler, J. S., Nair, J. K., Racie, T., et al. (2018). Evaluation of GalNAc-siRNA conjugate activity in pre-clinical animal models with reduced asialoglycoprotein receptor expression. *Mol. Ther.* 26 (1), 105–114. doi:10.1016/j.ymthe.2017.08.019
- Xu, L., and Anchordoquy, T. (2011). Drug delivery trends in clinical trials and translational medicine: Challenges and opportunities in the delivery of nucleic acid-based therapeutics. *J. Pharm. Sci.* 100 (1), 38–52. doi:10.1002/jps.22243
- Xu, Y., Linde, A., Larsson, O., Thormeyer, D., Elmen, J., Wahlestedt, C., et al. (2004). Functional comparison of single- and double-stranded siRNAs in mammalian cells. *Biochem. Biophys. Res. Commun.* 316 (3), 680–687. doi:10.1016/j.bbrc.2004.02.100
- Xu, Z., Wang, Q., Zhong, H., Jiang, Y., Shi, X., Yuan, B., et al. (2022). Carrier strategies boost the application of CRISPR/Cas system in gene therapy. *Exploration* 2 (2), 20210081. doi:10.1002/exp.20210081
- Yan, Y., Liu, X. Y., Lu, A., Wang, X. Y., Jiang, L. X., and Wang, J. C. (2022). Non-viral vectors for RNA delivery. *J. Control. Release* 342, 241–279. doi:10.1016/j.jconrel.2022.01.008
- Yang, Q., Humphreys, S. C., Lade, J. M., and Li, A. P. (2021). Prolonged cultured human hepatocytes as an *in vitro* experimental system for the evaluation of potency and duration of activity of RNA therapeutics: Demonstration of prolonged duration of gene silencing effects of a GalNAc-conjugated human hypoxanthine phosphoribosyl transferase (HPRT1) siRNA. *Biochem. Pharmacol.* 189, 114374. doi:10.1016/j.bcp.2020.114374
- Yu, A.-M., and Tu, M.-J. (2021). Deliver the promise: RNAs as a new class of molecular entities for therapy and vaccination. *Pharmacol. Ther.* 230, 107967. doi:10.1016/j.pharmthera.2021.107967
- Zhang, L., Liang, D., Chen, C., Wang, Y., Amu, G., Yang, J., et al. (2018). Circular siRNAs for reducing off-target effects and enhancing long-term gene silencing in cells and mice. *Mol. Ther. Nucleic Acids* 10, 237–244. doi:10.1016/j.omtn.2017.12.007
- Zhang, M. M., Bahal, R., Rasmussen, T. P., Manautou, J. E., and Zhong, X. B. (2021). The growth of siRNA-based therapeutics: Updated clinical studies. *Biochem. Pharmacol.* 189, 114432. doi:10.1016/j.bcp.2021.114432
- Zhang, Y., Sun, C., Wang, C., Jankovic, K. E., and Dong, Y. (2021). Lipids and lipid derivatives for RNA delivery. *Chem. Rev.* 121 (20), 12181–12277. doi:10.1021/acs.chemrev.1c00244
- Zhao, Y., Shu, R., and Liu, J. (2021). The development and improvement of ribonucleic acid therapy strategies. *Mol. Ther. Nucleic Acids* 26, 997–1013. doi:10.1016/j.omtn.2021.09.002
- Zhou, Y., Teng, P., Montgomery, N. T., Li, X., and Tang, W. (2021). Development of triantennary N-acetylgalactosamine conjugates as degraders for extracellular proteins. *ACS Cent. Sci.* 7 (3), 499–506. doi:10.1021/acscentsci.1c00146



OPEN ACCESS

EDITED BY
Junmin Zhang,
Lanzhou University, China

REVIEWED BY
Yurong Lai,
Gilead, United States
Mei-Hua Qu,
Weifang Second People's Hospital,
China

*CORRESPONDENCE
Weina Li,
liweina@fmmu.edu.cn
Meng Li,
limeng@fmmu.edu.cn

[†]These authors have contributed equally
to this work

SPECIALTY SECTION
This article was submitted to Drug
Metabolism and Transport,
a section of the journal
Frontiers in Pharmacology

RECEIVED 23 August 2022
ACCEPTED 23 November 2022
PUBLISHED 14 December 2022

CITATION
He L, Feng D, Guo H, Zhou Y, Li Z,
Zhang K, Zhang W, Wang S, Wang Z,
Hao Q, Zhang C, Gao Y, Gu J, Zhang Y,
Li W and Li M (2022), Pharmacokinetics,
distribution, metabolism, and excretion
of body-protective compound 157, a
potential drug for treating various
wounds, in rats and dogs.
Front. Pharmacol. 13:1026182.
doi: 10.3389/fphar.2022.1026182

COPYRIGHT
© 2022 He, Feng, Guo, Zhou, Li, Zhang,
Zhang, Wang, Wang, Hao, Zhang, Gao,
Gu, Zhang, Li and Li. This is an open-
access article distributed under the
terms of the [Creative Commons
Attribution License \(CC BY\)](https://creativecommons.org/licenses/by/4.0/). The use,
distribution or reproduction in other
forums is permitted, provided the
original author(s) and the copyright
owner(s) are credited and that the
original publication in this journal is
cited, in accordance with accepted
academic practice. No use, distribution
or reproduction is permitted which does
not comply with these terms.

Pharmacokinetics, distribution, metabolism, and excretion of body-protective compound 157, a potential drug for treating various wounds, in rats and dogs

Lei He^{1†}, Donglin Feng^{1,2†}, Hui Guo², Yueyuan Zhou¹,
Zhaozhao Li¹, Kuo Zhang¹, Wangqian Zhang¹, Shuning Wang¹,
Zhaowei Wang¹, Qiang Hao¹, Cun Zhang¹, Yuan Gao¹,
Jintao Gu¹, Yingqi Zhang¹, Weina Li^{1*} and Meng Li^{1*}

¹State Key Laboratory of Cancer Biology, Department of Biopharmaceutics, School of Pharmacy, Air Force Medical University, Xi'an, China, ²School of Pharmacy, Shaanxi University of Chinese Medicine, Xi'an, China

Body-protective compound (BPC) 157 demonstrates protective effects against damage to various organs and tissues. For future clinical applications, we had previously established a solid-phase synthesis process for BPC157, verified its biological activity in different wound models, and completed preclinical safety evaluations. This study aimed to investigate the pharmacokinetics, excretion, metabolism, and distribution profiles of BPC157. After a single intravenous (IV) administration, single intramuscular (IM) administrations at three doses in successive increments along with repeated IM administrations, the elimination half-life ($t_{1/2}$) of prototype BPC157 was less than 30 min, and BPC157 showed linear pharmacokinetic characteristics in rats and beagle dogs at all doses. The mean absolute bioavailability of BPC157 following IM injection was approximately 14%–19% in rats and 45%–51% in beagle dogs. Using [³H]-labeled BPC157 and radioactivity examination, we proved that the main excretory pathways of BPC157 involved urine and bile. [³H]BPC157 was rapidly metabolized into a variety of small peptide fragments *in vivo*, thus forming single amino acids that entered normal amino acid metabolism and excretion pathways. In conclusion, this study provides the first analysis of the pharmacokinetics of BPC157, which will be helpful for its translation in the clinic.

KEYWORDS

BPC157, pharmacokinetics, absorption, distribution, metabolism, excretion, wounds

1 Introduction

Body-protective compound (BPC) 157 is a peptide isolated from human gastric juice (Sikiric et al., 1993). BPC157 comprises 15 amino acids (Gly-Glu-Pro-Pro-Pro-Gly-Lys-Pro-Ala-Asp-Asp-Ala-Gly-Leu-Val) and has a molecular weight of 1419 Da. Also known as BPC-15, PL-10, PLD-116, or PL14736 (Keremi et al., 2009), BPC157 has demonstrated remarkable potential as a therapeutic agent for severe trauma and stress damage and can promote the healing of wounds, ligament injuries, tendon injuries, and fractures. BPC157 exerts a significant protective effect on various tissues and organs, such as the esophagus, stomach, duodenum (Drmic et al., 2017), colorectal mucosa (Duzel et al., 2017), liver, pancreas (Konturek and Brzozowski, 2008), muscle (Lai et al., 2019), cornea (Lazic et al., 2005), heart (Sikiric et al., 2016) and nerves (Grabarevic et al., 1997; Klicek et al., 2013; Wang et al., 2019). Apart from its protective effect against multiple organ injuries, BPC157 has also demonstrated cytoprotective (Sikiric et al., 2018) and anti-inflammatory properties and plays a role in maintaining epithelial integrity (Mota et al., 2018). Although the mechanism of action of BPC157 remains unclear, BPC157 has demonstrated significant effects at very low doses with very good stability (Sikiric et al., 2018). It can be stored at room temperature and is resistant to hydrolysis, enzyme digestion, and even gastric juice. Based on the stability and pleiotropy of BPC157, it is an ideal candidate for the treatment of all types of severe trauma and may be superior to the widely used cytokine drugs in wound therapy.

Previously, we established a solid-phase synthesis process for BPC157 (Xue et al., 2004) and verified its biological activity in rat gastric ulcer models and various skin wound models (Huang et al., 2015). At the same time, our preclinical safety evaluation studies showed that BPC157 was well tolerated and did not demonstrate any serious toxic effects in mice, rats, rabbits, or dogs (Xu et al., 2020). For evaluating its future clinical use as a therapeutic drug and follow-up clinical trials, the present study was undertaken to evaluate the pharmacokinetics, tissue distribution, metabolism, and drug excretion of BPC157 in Sprague-Dawley (SD) rats and beagle dogs as well as in associated *in vitro* studies. The experiments were performed according to the criteria of the new investigational drug application. This study is the first preclinical pharmacokinetic study of BPC157, and the results are of considerable importance, as they demonstrate not only the pharmacokinetic parameters of BPC157 but also show the implications for its systemic application as a novel drug for various injuries.

2 Results

2.1 Pharmacokinetic studies of BPC157 in rats

The effective dose of BPC157 for the treatment of various injuries in mice, rats, and rabbits ranges from 6 to 50 $\mu\text{g/kg}$ (Huang et al., 2015; Mota et al., 2018; Sikiric et al., 2018). Our proposed clinical dose of BPC157 was 200 $\mu\text{g/person/day}$, and its equivalent dose in rats was 20 $\mu\text{g/kg}$ (converted based on body surface area). Therefore, we performed pharmacokinetic studies of BPC157 in rats following a single intravenous (IV) administration of 20 $\mu\text{g/kg}$, single intramuscular (IM) administration of doses 20, 100, or 500 $\mu\text{g/kg}$, and repeated IM administrations of 100 $\mu\text{g/kg}$ of BPC157 for seven consecutive days. The administration of BPC157 was well tolerated by all rats, and no visual signs of toxicity were observed, consistent with our previous safety evaluation studies (Xu et al., 2020). In addition, no noticeable difference in the plasma concentration of BPC157 was observed between male and female rats.

The mean (\pm SD) plasma concentration of BPC157 versus time curves following administration of various BPC157 doses in rats are shown in Figures 1A–C, and the corresponding pharmacokinetic parameters are presented in Tables 1–Tables 3. After a single IV administration, BPC157 was rapidly eliminated from the plasma of rats, and the average elimination half-life ($t_{1/2}$) was 15.2 min. The average area under the plasma concentration-time curve (AUC_{0-t}) was 399 ng min/ml . After single IM administrations of doses 20, 100, or 500 $\mu\text{g/kg}$, the peak time (T_{max}) of each dose was 3 min. The maximum concentrations (C_{max}) of each dose were 12.3, 48.9, and 141 ng/ml , respectively, and the AUC_{0-t} values were 75.1, 289, and 1930 ng min/ml , respectively. Linear relationships were observed between AUC_{0-t} and BPC157 doses, as well as between C_{max} and BPC157 doses (Figures 1D,E). The absolute bioavailability after IM administration of each dose was 18.82%, 14.49%, and 19.35%, respectively. After repeated IM administration of BPC157 at 100 $\mu\text{g/kg}$ for seven consecutive days, the plasma concentration versus time curve (Figure 1C) and pharmacokinetic parameters (Table 3) were similar to those observed after a single IM injection at a dose of 100 $\mu\text{g/kg}$, except for a slight increase in C_{max} and AUC_{0-t} . The aforementioned results showed that BPC157 reached its peak rapidly in rats and was rapidly eliminated after reaching its peak. The prototype drug could not be detected 4 h after administration, and its elimination half-life was less than 30 min. BPC157 showed linear pharmacokinetic characteristics in rats at the experimental dose.

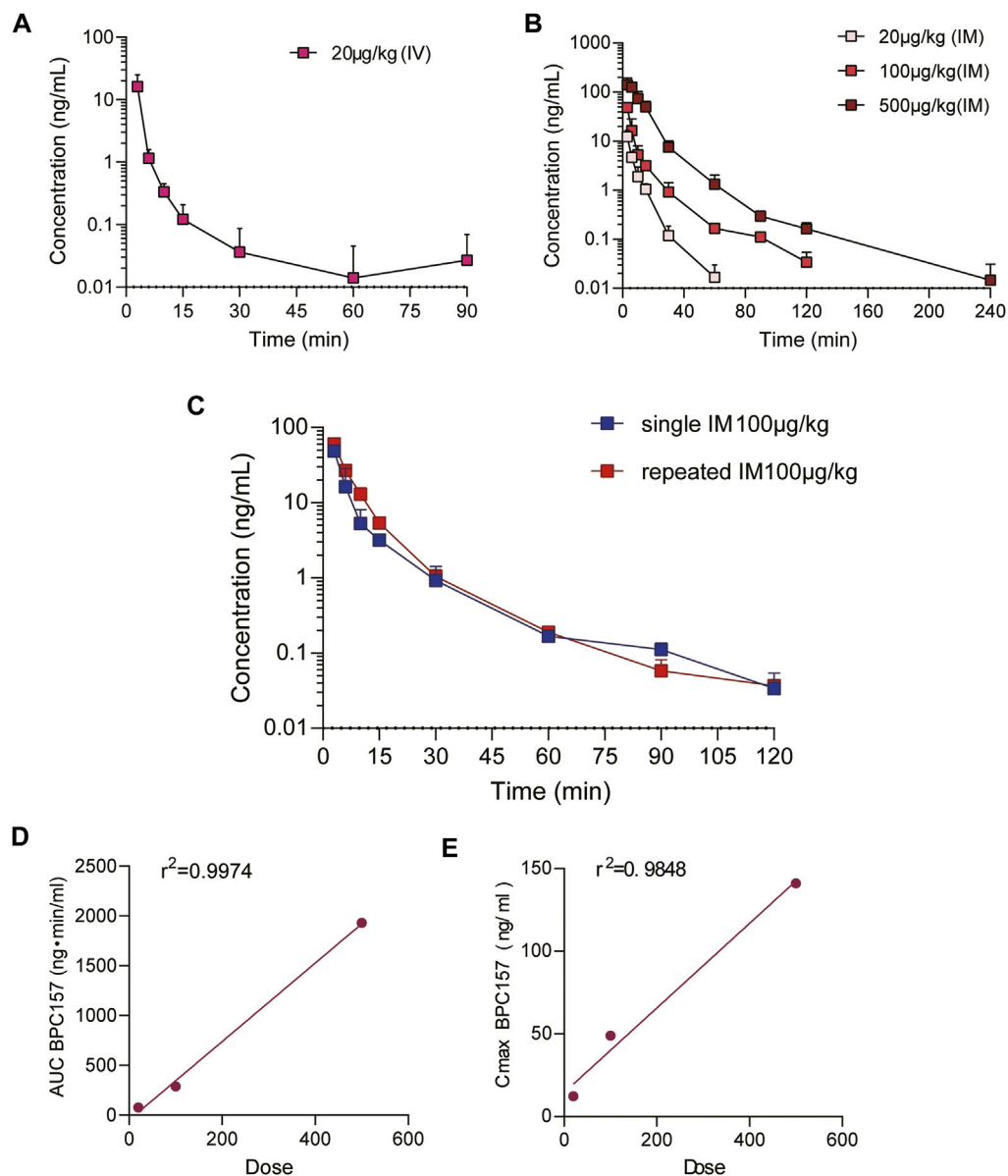


FIGURE 1

Pharmacokinetic studies of BPC157 in rats (mean \pm SD, $n = 6$). (A) Total plasma concentration versus time profiles of BPC157 following intravenous administration at a dose of 20 µg/kg; (B) Total plasma concentration versus time profiles of BPC157 following intramuscular administration at the doses of 20, 100, or 500 µg/kg; (C) Total plasma concentration versus time profiles of BPC157 following repeat intramuscular administration at a dose of 100 µg/kg for seven consecutive days (red) or a single intramuscular administration at a dose of 100 µg/kg (blue). (D) Linear regression between BPC157 AUC and doses evaluated following intramuscular administration of doses 20, 100, or 500 µg/kg. (E) Linear regression between BPC157 C_{max} and doses evaluated following intramuscular administration of doses 20, 100, or 500 µg/kg. The goodness of fit was estimated by the coefficient of determination (r^2). Data are representative of three independent experiments.

2.2 Pharmacokinetic studies of BPC157 in beagle dogs

Our proposed clinical dose of BPC157 was 200 µg/person/day, and its equivalent dose in dogs was 6 µg/kg (converted based on body surface area). Therefore, we performed pharmacokinetic studies of BPC157 in beagle dogs

following single IV administration at a dose of 6 µg/kg, single IM administration at doses of 6, 30, or 150 µg/kg, and repeated IM administration at a dose of 30 µg/kg for seven consecutive days. The administration of BPC157 was well tolerated by all dogs, and no visual signs of toxicity were observed, which was consistent with our previous safety evaluation studies. No noticeable difference in the plasma

TABLE 1 Pharmacokinetic parameters of BPC157 in rats following a single intravenous administration (mean \pm SD, $n = 6$).

$AUC_{0-90min}$	$AUC_{0-\infty}$	MRT	$t_{1/2}$	V_{ss}	CL
(ng·min/ml)	(ng·min/ml)	(min)	(min)	(ml/kg)	(ml/min/kg)
399	400	0.727	15.2	36.4	50.1

$AUC_{0-90min}$, area under the concentration/time curve at last observation; $AUC_{0-\infty}$, area under the concentration/time curve from 0 h to infinity; $t_{1/2}$, half-life; V_{ss} , volume of distribution (steady state); CL, clearance.

TABLE 2 Pharmacokinetic parameters of BPC157 in rats following intramuscular administrations of doses ranging between 5 and 120 μ g/kg (mean \pm SD, $n = 6$).

Dosage	T_{max}	C_{max}	AUC_{0-t}	$AUC_{0-\infty}$	MRT	$t_{1/2}$	F_a
(μ g/kg)	(min)	(ng/ml)	(ng·min/ml)	(ng·min/ml)	(min)	(min)	(%)
20	3.00	12.3	75.1	75.3	7.27	7.87	18.82
100	3.00	48.9	289	290	9.61	17.1	14.49
500	3.00	141	1930	1931	12.8	29.7	19.35

T_{max} , time to peak concentration of drug in plasma; C_{max} , peak concentration of drug in plasma; $F_a = (AUC_{0-t,IM-DoseIV})/(AUC_{0-t,IV-DoseIM}) \times 100\%$.

TABLE 3 Pharmacokinetic parameters of BPC157 in rats following repeat intramuscular administration of 100 μ g/kg BPC157 for seven consecutive days (mean \pm SD, $n = 6$).

T_{max}	C_{max}	AUC_{0-t}	$AUC_{0-\infty}$	$t_{1/2}$	C_{ssav}	C_{ssmin}
(min)	(ng/ml)	(ng·min/ml)	(ng·min/ml)	(min)	(ng/ml)	(ng/ml)
3.00	60.4	418	419	18.5	0.290	0

$C_{ssav} = AUC_{0-\tau}/\tau$, τ is the interval of administration; $C_{ssmin} = (C_{-48h} + C_{-24h} + C_{0h})/3$.

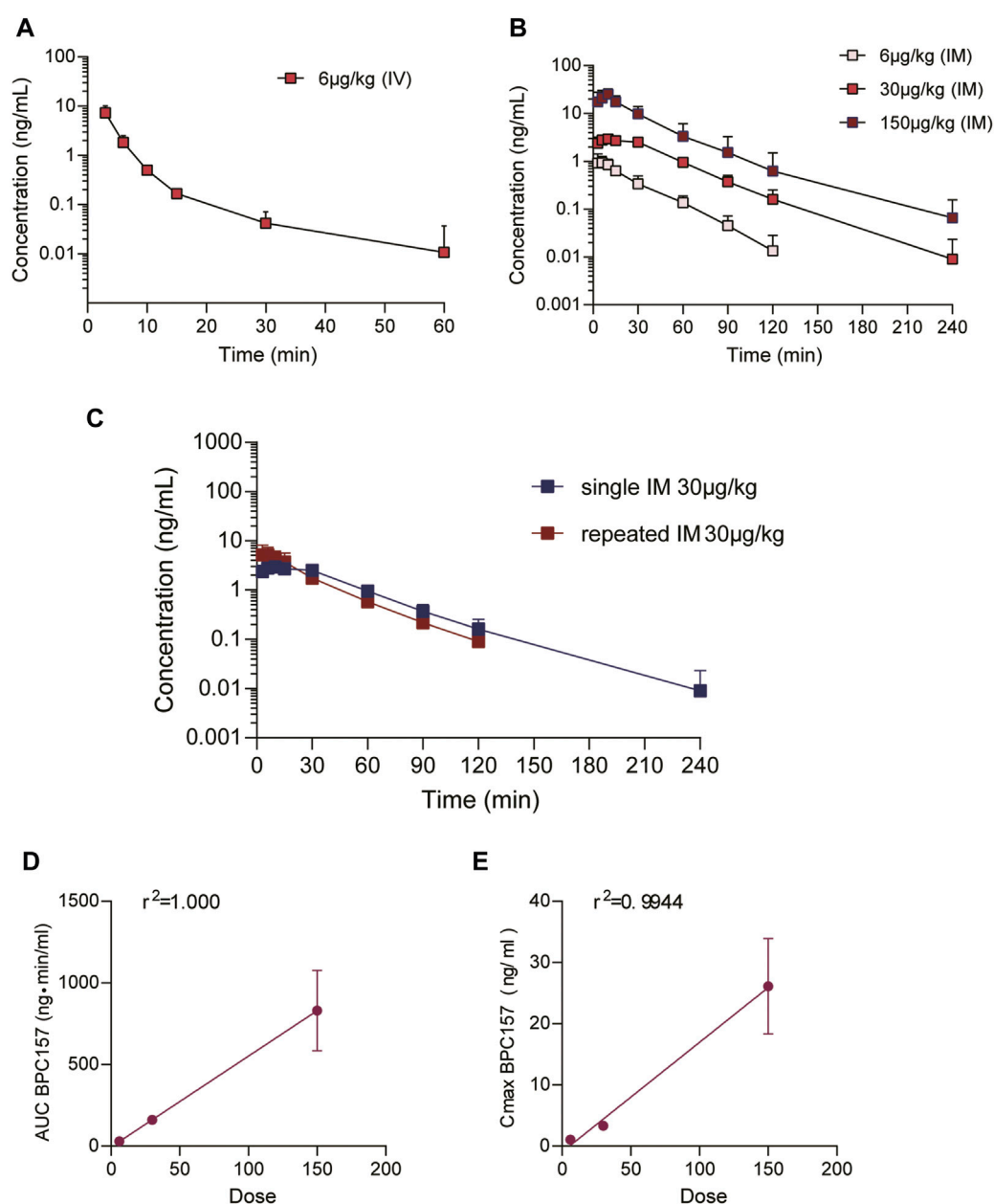
concentration of BPC157 was found between male and female dogs.

The mean (\pm SD) BPC157 plasma concentration versus time curves following administration of various BPC157 doses in dogs are shown in Figures 2A–C, and the corresponding pharmacokinetic parameters are presented in Tables 4–Tables 6. After single IV administration, the $t_{1/2}$ and AUC_{0-t} of BPC157 in dogs were 5.27 min and 76.4 ± 30.2 ng min/ml. After single IM administration at doses of 6, 30, or 150 μ g/kg, the T_{max} values of each dose were 6.33, 8.67, and 8.17 min, respectively. The C_{max} values of each dose were 1.05 ± 0.429 , 3.30 ± 0.508 , and 26.1 ± 7.82 ng/ml, respectively, and the AUC_{0-t} values were 29.0 ± 2.68 , 160 ± 21.0 , and 830 ± 247 ng min/mL respectively. Linear relationships were observed between AUC_{0-t} and BPC157 doses, as well as between C_{max} and BPC157 doses (Figures 2D,E). The absolute bioavailability observed after IM administration of each dose in dogs was 45.27%, 47.64%, and 50.56%, respectively. After repeated IM administration of BPC157 at 30 μ g/kg for seven consecutive days, the plasma concentration versus time curve was similar to that observed

after a single IM injection of 30 μ g/kg (Figure 2C). However, the pharmacokinetic parameters after repeated IM administration changed slightly compared to those observed after a single IM injection, with a small decrease in C_{max} and $t_{1/2}$ and an increase in T_{max} . The area under the curve (AUC) values did not change significantly (Table 6). The aforementioned results showed that BPC157 reached its peak rapidly in beagle dogs and was rapidly eliminated after reaching its peak. The prototype drug could not be detected 4 h after administration, and its elimination half-life was less than 30 min. BPC157 showed linear pharmacokinetic characteristics in beagle dogs at the experimental dose.

2.3 Excretion, metabolism, and tissue distribution of BPC157

In the aforementioned studies, we characterized the pharmacokinetic profile of prototype BPC157 using high-performance liquid chromatography (HPLC) in rats and dogs. Next, we evaluated the excretion, metabolism, and tissue

**FIGURE 2**

Pharmacokinetic studies of BPC157 in beagle dogs (mean \pm SD, $n = 6$). (A) Total plasma concentration versus time profiles of BPC157 following intravenous administration at a dose of 6 μ g/kg; (B) Total plasma concentration versus time profiles of BPC157 following intramuscular administration of doses 6, 30, or 150 μ g/kg; (C) Total plasma concentration versus time profiles of BPC157 following repeated intramuscular administration at a dose of 30 μ g/kg for seven consecutive days (red) or a single intramuscular administration at a dose of 30 μ g/kg (blue). (D) Linear regression analysis between BPC157 AUC and doses following intramuscular administration of doses 6, 30, or 150 μ g/kg. (E) Linear regression analysis between BPC157 C_{max} and doses following intramuscular administration of doses 6, 30, or 150 μ g/kg. The goodness of fit was estimated by coefficients of determination (r^2). Data are representative of three independent experiments.

distribution of BPC157 in rats after a single IM injection of 100 μ g/300 μ Ci/kg [3 H]BPC157. [3 H]BPC157 was well tolerated by all rats, and no visual signs of toxicity were observed. Prolines of BPC157 were labeled with [3 H] and the structure of [3 H]-labeled BPC157 is shown in Figure 3A.

2.3.1 BPC157 excretion in rats evaluated by examination of total radioactivity

The average recovery rates of total radioactivity in urine, feces, and cage cleaning fluid collected from 0 to 72 h after [3 H] BPC157 administration in intact rats were $15.88\% \pm 2.99\%$,

TABLE 4 Pharmacokinetic parameters of BPC157 in dogs following a single intravenous administration (mean \pm SD, $n = 6$).

$AUC_{0-t_{min}}$	$AUC_{0-\infty}$	MRT	$t_{1/2}$	V_{ss}	CL
(ng·min/ml)	(ng·min/ml)	(min)	(min)	(ml/kg)	(ml/min/kg)
76.4 \pm 30.2	76.9 \pm 30.2	2.49 \pm 0.822	5.27 \pm 2.25	243 \pm 162	90.8 \pm 40.1

$AUC_{0-90min}$, area under the concentration/time curve at last observation; $AUC_{0-\infty}$, area under the concentration/time curve from 0 h to infinity; $t_{1/2}$, half-life; V_{ss} , volume of distribution (steady state); CL, clearance.

TABLE 5 Pharmacokinetic parameters of BPC157 in dogs following intramuscular administration of doses ranging between 6 and 150 μ g/kg (mean \pm SD, $n = 6$).

Dosage (μ g/kg)	T_{max}	C_{max}	AUC_{0-t}	$AUC_{0-\infty}$	MRT	$t_{1/2}$	F_a
	(min)	(ng/ml)	(ng·min/ml)	(ng·min/ml)	(min)	(min)	(%)
6	6.33 \pm 3.14	1.05 \pm 0.429	29.0 \pm 2.68	30.0 \pm 3.11	25.8 \pm 7.35	20.0 \pm 5.53	45.27 \pm 24.85
30	8.67 \pm 5.54	3.30 \pm 0.508	160 \pm 21.0	164 \pm 21.5	37.0 \pm 7.77	25.5 \pm 7.08	47.64 \pm 18.09
150	8.17 \pm 2.99	26.1 \pm 7.82	830 \pm 247	831 \pm 246	31.4 \pm 15.2	29.3 \pm 5.06	50.56 \pm 27.01

T_{max} , time to peak concentration of drug in plasma; C_{max} , peak concentration of drug in plasma; $F_a = (AUC_{0-t, IM-DoseIV}) / (AUC_{0-t, IV-DoseIM}) \times 100\%$.

TABLE 6 Pharmacokinetic parameters of BPC157 in dogs following repeated intramuscular administration at a dose of 30 μ g/kg for seven consecutive days (mean \pm SD, $n = 6$).

T_{max} (min)	C_{max} (ng/ml)	AUC_{0-t} (ng·min/ml)	$AUC_{0-\infty}$ (ng·min/ml)	$t_{1/2}$ (min)	C_{ssav} (ng/ml)	C_{ssmin} (ng/ml)
10.5 \pm 10.5	5.89 \pm 2.41	155 \pm 25.2	158 \pm 26.0	19.6 \pm 3.72	0.108 \pm 0.0177	0.00285 \pm 0.00698

$C_{ssav} = AUC_{0-t} / \tau$, τ is the interval of administration; $C_{ssmin} = (C_{-48h} + C_{-24h} + C_{0h}) / 3$.

2.25% \pm 0.67%, and 1.41% \pm 1.04%, respectively, and the proportion of residual radioactivity in the cadavers was 54.31% \pm 3.04% (Table 7; Figure 3B). Furthermore, in bile duct-cannulated (BDC) rats, the average recovery rates of total radioactivity in bile, urine, feces, and cage cleaning fluid collected during 72 h after dosing were 9.08% \pm 0.86%, 17.77% \pm 6.35%, 2.73% \pm 0.40%, and 0.91% \pm 0.13%, respectively (Table 8; Figure 3C). These results suggest that urinary excretion is the dominant route of elimination following IM administration of BPC157.

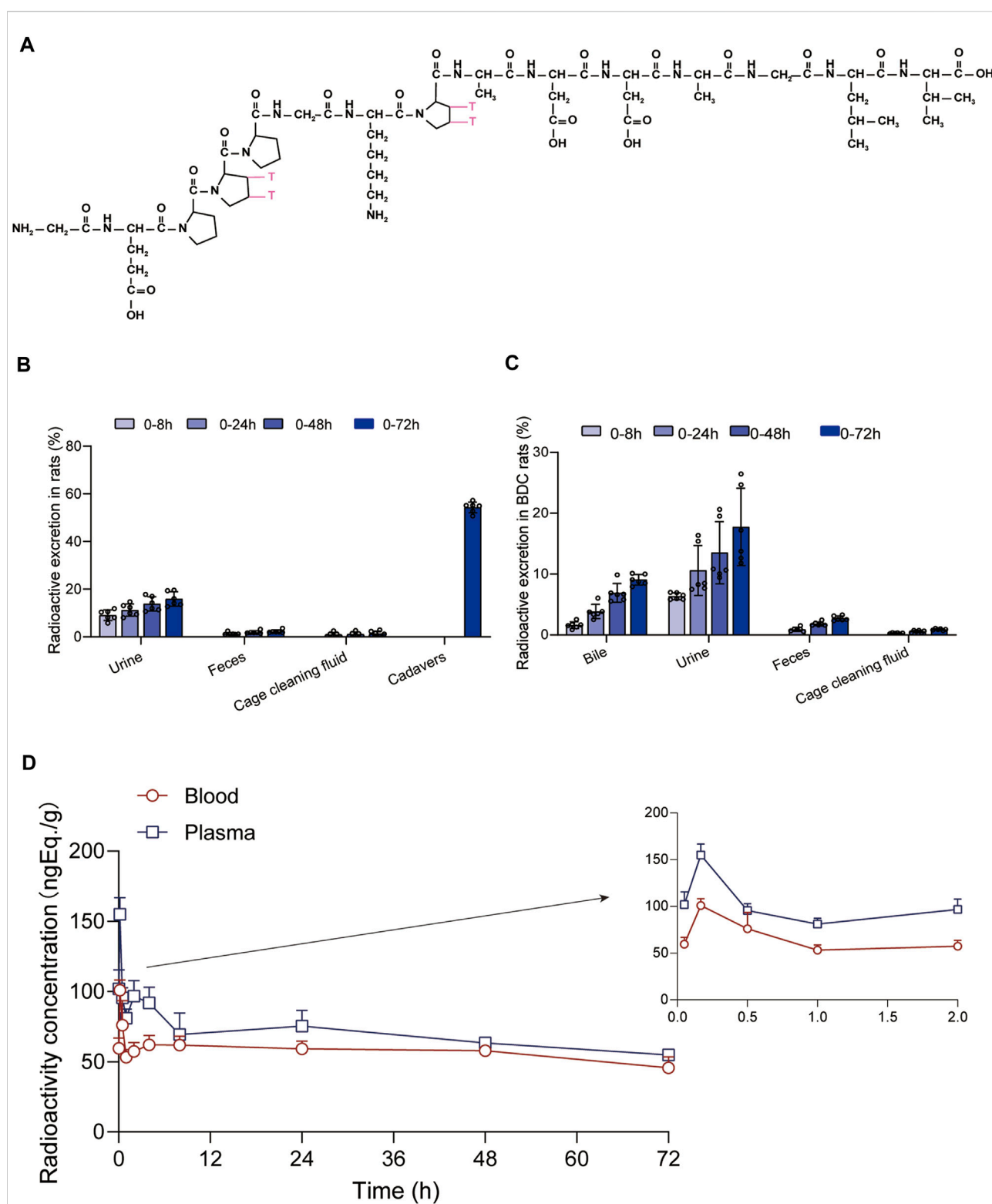
2.3.2 Plasma pharmacokinetic parameters of BPC157 in rats evaluated based on total radioactivity

After a single IM injection of 100 μ g/300 μ Ci/kg [3 H] BPC157 in jugular vein-cannulated (JVC) rats, the total radioactivity concentrations in the whole blood and plasma were similar between males and females. The total radioactivity concentration versus time curve is shown in Figure 3D. The corresponding pharmacokinetic parameters are listed as follows: $T_{max} = 0.167$ h, $C_{max} = 155 \pm 11.8$ ng Eq./ml, $AUC_{0-t} = 4945 \pm 417$ h ng Eq./ml, $AUC_{0-\infty} = 12956 \pm$

2074 h•ng Eq./ml, average residence time (MRT_{0-t}) of plasma total radioactivity = 33.2 ± 1.03 h, and $t_{1/2} = 102$ h (Table 9). Compared with the results of prototype BPC157 in rats, the pharmacokinetic parameters of [3 H]BPC157 evaluated based on total radioactivity changed markedly, indicating the significant metabolism and decomposition process of BPC157 *in vivo*.

2.3.3 Metabolite analysis of BPC157

We analyzed the metabolites of [3 H]BPC157 in rat plasma, bile, urine, and feces using the samples collected during the aforementioned extraction and plasma pharmacokinetic studies. First, using HPLC and HPLC-associated radioactive detector, we identified six radioactive components, in addition to prototype [3 H]BPC157, in rat plasma collected at 0.05, 0.167, 1, 8, and 24 h after administration (Supplementary Figure S1). Through high-performance liquid chromatography-tandem mass spectrometry (LC-MS/MS)-based molecular weight identification, standard molecular weight comparison, and characteristic HPLC profiles of the [3 H]proline and [3 H]BPC157 standards (Supplementary Figure S2), we speculated the structures of these six components and designated them as M1–M6 (Table 10). M1 was identified as [3 H]proline and

**FIGURE 3**

Evaluation of BPC157 excretion in rats by examination of total radioactivity. **(A)** The structure of [^3H]-labeled BPC157. [^3H]-labeled sites are indicated by T (red). **(B)** The average recovery of total radioactivity in the urine, feces, cage cleaning fluid, and cadavers during 0–72 h after [^3H] BPC157 administration in intact rats (mean \pm SD, $n = 6$). **(C)** The average recovery of total radioactivity in the urine, feces, and cage cleaning fluid collected during 0–72 h after [^3H] BPC157 administration in bile duct cannulated rats (mean \pm SD, $n = 6$). **(D)** Total radioactivity concentration versus time curve for [^3H] BPC157 in jugular vein cannulated rats following a single intramuscular injection at a dose of 100 $\mu\text{g}/300 \mu\text{Ci}/\text{kg}$ (mean \pm SD, $n = 6$). Data are representative of three independent experiments.

TABLE 7 The recovery of total radioactivity in the urine, feces, and cage cleaning fluid during 0–72 h after intramuscular administration of [³H]BPC157 in rats.

Time interval (hour)	Recovery of radioactivity (%)			
	Urine	Feces	Cage cleaning fluid	Cadavers
0–8	9.11 ± 2.21	—	—	—
0–24	11.25 ± 2.54	1.31 ± 0.54	0.94 ± 0.91	—
0–48	13.84 ± 3.00	1.92 ± 0.61	1.08 ± 0.93	—
0–72	15.88 ± 2.99	2.25 ± 0.67	1.41 ± 1.04	54.31 ± 2.27

TABLE 8 The recovery of total radioactivity in bile, urine, feces, and cage cleaning fluid during 0–72 h after intramuscular administration of [³H]BPC157 in BDC rats.

Time interval (hour)	Recovery of radioactivity (%)			
	Bile	Urine	Feces	Cage cleaning fluid
0–8	1.61 ± 0.55	6.37 ± 0.54	—	—
0–24	3.86 ± 1.18	10.62 ± 4.10	0.92 ± 0.34	0.29 ± 0.08
0–48	6.92 ± 1.55	13.53 ± 5.11	1.84 ± 0.33	0.59 ± 0.17
0–72	9.08 ± 0.86	17.77 ± 6.35	2.73 ± 0.40	0.91 ± 0.13

TABLE 9 Plasma pharmacokinetic parameters examined based on total radioactivity following a single intramuscular administration of 100 µg/300 µCi/kg of [³H]BPC157 in rats (mean ± SD, *n* = 6).

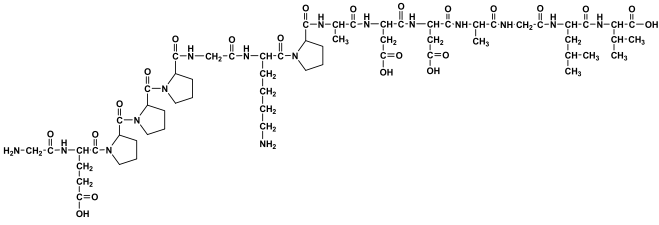
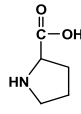
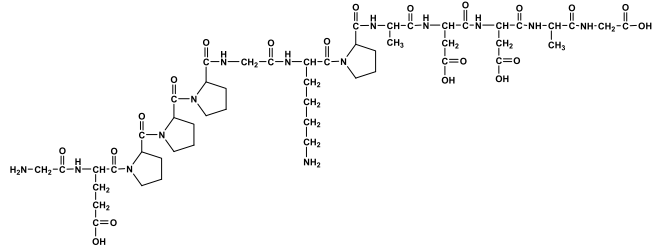
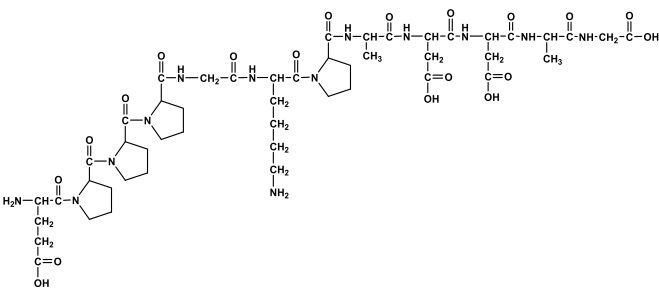
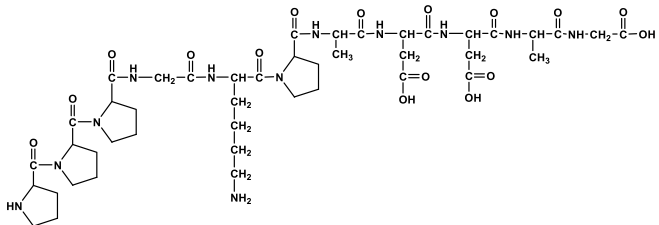
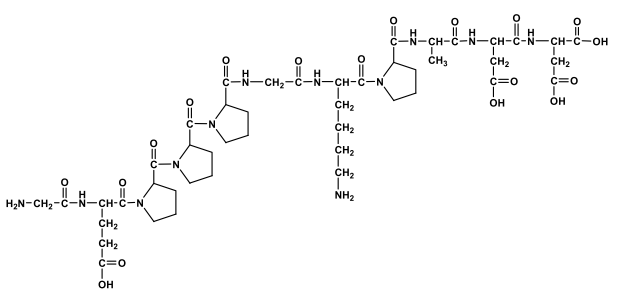
T _{max} (h)	C _{max} (ng-Eq./ml)	AUC _{0–t} (ng-Eq./ml)	AUC _{0–∞} (h·ng·min/ml)	t _{1/2} (h)	MRT _{0–t} (h)
0.167	155 ± 11.8	4945 ± 417	12956 ± 2074	102 ± 32	33.2 ± 1.03

M2–M6 were identified as a variety of small molecular peptides generated upon the degradation of [³H]BPC157. Based on the structures of the M1–M6 metabolites, we proposed the metabolic process of BPC157 *in vivo* (Figure 4). The proportions of M1–M6 and [³H]BPC157 in plasma radioactive components at different sampling times demonstrated that [³H]BPC157 was the main plasma component at 0.05 h (3 min) after administration and was subsequently degraded into small molecular peptide fragments in the following 0.167 h (10 min) (Figure 5A). At 1 h after administration, [³H]proline accounted for 86.65% of the plasma radioactive components. Subsequently, the proportion of tritium water increased and that of [³H]proline decreased gradually with time.

Next, we analyzed the main metabolites of [³H]BPC157 in urine collected from 0 to 8 h and from 8 to 72 h and in bile and feces collected from 0 to 72 h after administration. No new metabolites were found in urine, bile, and fecal samples other than the six components found in the plasma. In the mixed urine

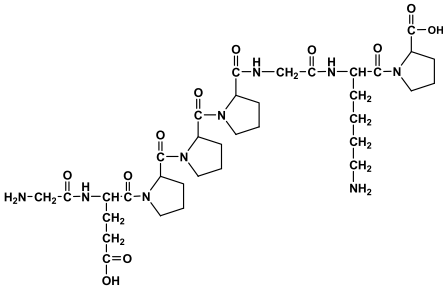
samples collected from 0 to 8 h, the content of [³H]proline (M1), the main metabolite, was higher, accounting for 13.9% (female) and 11.7% (male) of the total radioactivity. In mixed urine samples collected between 8 and 72 h, the proportion of tritium water was higher, accounting for 69.5% (female) and 75.3% (male) of the total radioactivity, and [³H]proline (M1) accounted for 3.11% (female) and 4.17% (male) of the total radioactivity (Figure 5B). The total radioactivity excretion in mixed bile samples collected between 0 and 72 h was low, and tritium water was primarily detected, accounting for 91.2% (females) and 91.0% (males) of the sample. The main metabolite, [³H]proline (M1), accounted for 4.96% (female) and 3.93% (male) of the bile samples (Figure 5C). Small amounts of [³H]BPC157 were detected in feces, accounting for 0.63% (female) and 2.26% (male) of the total fecal radioactivity. The tritium water content was 30.1% (female) and 29.3% (male), and the content of [³H]proline (M1) was higher, accounting for 20.7% (female) and 30.2% (male) of the total radioactivity

TABLE 10 Structures of six metabolites identified by high-performance liquid chromatography-tandem mass spectrometry in rat plasma, bile, urine, and feces following a single intramuscular administration of 100 µg/300 µCi/kg of [3H]BPC157.

Designation	Structure	Molecular weight (Da)	Retention time (min)
BPC157		1419.5	~39.8
M1(Proline)		115.1	~5.1
M2		1207.3	~19.5
M3		1150.2	~19.4
M4		1021.1	~19.1
M5		1079.1	~18.7

(Continued on following page)

TABLE 10 (Continued) Structures of six metabolites identified by high-performance liquid chromatography-tandem mass spectrometry in rat plasma, bile, urine, and feces following a single intramuscular administration of 100 µg/300 µCi/kg of [3H]BPC157.

Designation	Structure	Molecular weight (Da)	Retention time (min)
M6		777.9	~19.0

Rt, Retention time on LC-MS/MS.

(Figure 5D). The contents of other metabolites in feces were all lower than 0.06% of the administered amount, and it was impossible to perform structural identification because of the extremely low content. These results suggest that BPC157 was rapidly metabolized into low levels of a variety of small peptide fragments, finally resulting in a single amino acid represented by [³H]proline, which entered the normal amino acid metabolism and excretion pathway in the body.

2.3.4 Tissue distribution of BPC157 in rats

The total radioactivity concentrations in the rat tissues were similar after a single IM injection of 100 µg/300 µCi/kg of [3H] BPC157. Tissue distributions at different time points are summarized in Figure 6. After 3 min of administration, total radioactivity concentration was detected in all rat tissues; however, it was significantly lower than that observed in the plasma. After 10 min of administration, the total radioactivity concentration increased significantly in all tissues, with the mean renal tissue concentration reaching 223 ng (Eq. µg/ml), which was higher than the mean plasma concentration (150 ng, Eq./ml). After 1 h of administration, the total radioactivity peaked in most tissues, and the average concentration in the kidney was the highest, reaching 560 ng (Eq. µg/ml), followed by that in the liver, stomach wall, spleen, and thymus. All average concentrations were higher than those in the plasma. The total radioactivity concentrations in the intestine, skin, and lungs were similar to those in the plasma, and the mean concentrations in the gonads, myocardium, skeletal muscle, brain, and body fat were all lower than the mean concentrations in the plasma. At 24 h after administration, the mean concentrations of total radioactivity in the kidney, thymus, liver, spleen, and gastric wall decreased significantly but were still higher than the mean concentrations in the plasma at the same time. The concentrations in other tissues were lower than the average concentration in the plasma and are presented in the descending order as follows: intestinal tract, lung, gonad, skin, skeletal muscle, cardiac muscle, whole

blood, brain, and body fat. The total radioactivity concentrations in the kidney, liver, stomach wall, thymus, spleen, intestine, lung, skin, and body fat were reduced by approximately 50% compared with the peak concentration in the same tissue (1 h after administration).

3 Discussion

Pharmacokinetic evaluations are necessary and vital for the development of new drugs. To translate BPC157 into the clinic, we previously conducted preclinical safety studies and found that BPC157 was well tolerated and did not demonstrate serious toxicity (Xu et al., 2020). This study aimed to investigate the pharmacokinetics of BPC157. Experiments were performed to characterize the pharmacokinetics, absorption, distribution, metabolism, and excretion characteristics of BPC157 in rats and dogs.

We studied the pharmacokinetics of BPC157 after its IV and IM administration in rats and beagle dogs. According to the results, the elimination half-life (*t*_{1/2}) of the prototype BPC157 was less than 30 min, and BPC157 showed linear pharmacokinetic characteristics in rats and beagles at all experimental doses. After IM injections of 20, 100, and 500 µg/kg of BPC157 in rats and 6, 30, and 150 µg/kg of BPC157 in beagles, plasma BPC157 reached its peak rapidly (within 9 min). The pharmacokinetic parameters of BPC157 did not significantly change after repeated administration of BPC157 compared to those observed after a single IM injection of the same dose administered daily for 7 days. The mean absolute bioavailability observed after IM injections was approximately 14%–19% in rats and 45%–51% in beagle dogs. In contrast to small-molecule compounds, peptide drugs demonstrate pharmacokinetic characteristics of short elimination half-life and poor metabolic stability *in vivo*. Generally, *t*_{1/2} values of peptide

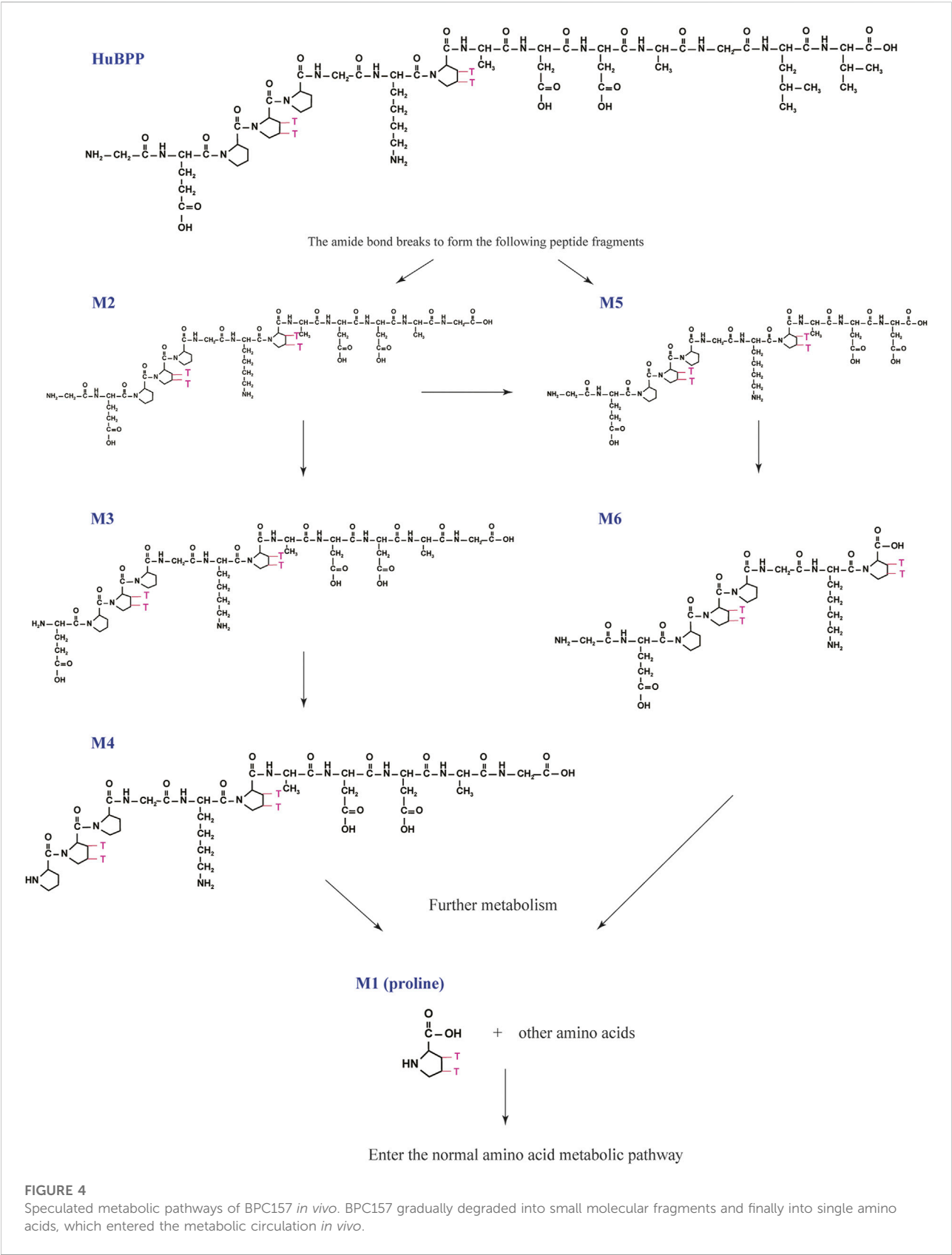
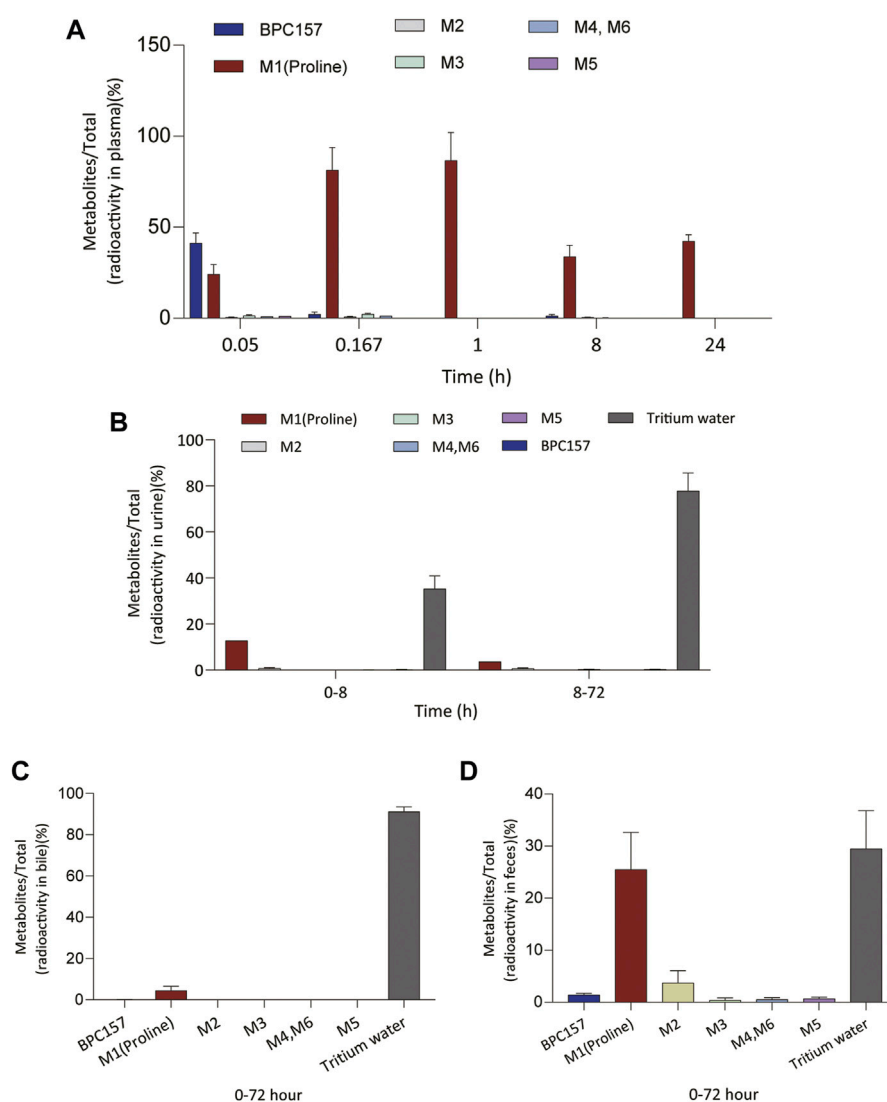


FIGURE 4
Speculated metabolic pathways of BPC157 *in vivo*. BPC157 gradually degraded into small molecular fragments and finally into single amino acids, which entered the metabolic circulation *in vivo*.

**FIGURE 5**

Changes in the proportion of six metabolites (M1–M6) with time in plasma (A), urine (B), bile (C), and feces (D) after a single intramuscular administration of 100 µg/300 µCi/kg of [3H]BPC157 in rats (mean ± SD, $n = 6$). Data are representative of three independent experiments.

drugs range from a few minutes to an hour (Wang et al., 2016). The presence of a large number of proteolytic enzymes and peptidases in the body is the primary reasons for this phenomenon (Sharma et al., 2013). Therefore, in terms of the elimination half-life, BPC157 conformed to the characteristics of general peptide drugs. Our previous work has shown that IM injection of prototype BPC157 can effectively promote wound healing, and we aim to conduct clinical trials examining BPC157 for the treatment of severe trauma and burns in China. Nevertheless, extending the half-life of BPC157 and further improving its pharmacokinetic characteristics are important directions for the future development of this drug.

The radioisotope probe assay is a cost-effective and fast method for generating informative data for early preclinical/pharmacokinetic absorption, digestion, metabolism, and excretion studies of biotherapeutics (Roffey et al., 2007; Khalil et al., 2011; Chen et al., 2014). We labeled the proline of BPC157 with tritium and then studied the metabolism, excretion, and tissue distribution characteristics of BPC157 by examining the total radioactivity. The results of the excretion experiment showed that the main excretory pathways of BPC157 involve the liver and kidney, which was also consistent with the excretion characteristics of peptide drugs (Czock et al., 2012; Li et al., 2015). The tissue distribution results showed that the radioactivity intensity in most tissues peaked 1 h

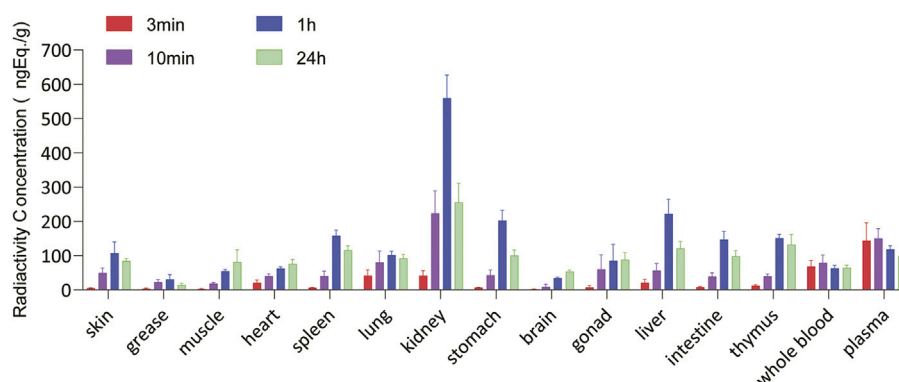


FIGURE 6

Tissue and organ distribution of [^3H]BPC157 after a single intramuscular administration of 100 μg /300 μCi /kg of [^3H]BPC157 in rats (mean \pm SD $n = 6$ per time point), expressed as the content of BPC157 per gram of tissue/organ. Data are representative of three independent experiments.

after administration, which was slightly later than the peak time of the total radioactivity concentration in plasma (0.167 h). The peak concentrations of radioactivity in the kidney, liver, stomach wall, thymus, and spleen were significantly higher than those in the plasma. The concentrations in the intestinal tract, lungs, and skin were similar to those in the plasma, followed by those in the gonads, cardiac muscle, skeletal muscle, and whole blood. The concentrations were lowest in the brain and body fat. These results suggested that BPC157 can enter tissues and cells to perform biological functions.

Determination of metabolites was the most challenging aspect of this study. The metabolism of peptides and proteins usually starts from the action of endopeptidase and then undergoes multi-step enzymatic degradation to produce the final metabolite amino acids, which enter the amino acid pool *in vivo* (Vugmeyster et al., 2012). In rat plasma, we identified six radioactive components, in addition to the prototype [^3H]BPC157, and their structures were predicted by LC-MS/MS molecular weight identification and comparison with standards. Through the analysis of possible hydrolysis sites, we predicted the metabolic process of BPC157 and proved that BPC157 was finally metabolized into a single amino acid, represented by [^3H]proline, in plasma, urine, and feces. These results show that BPC157 conforms to the metabolic process of peptide drugs, further proving its metabolic safety. However, analysis of the proportions of various metabolites in plasma over time once again suggested a short half-life and rapid degradation of prototype BPC157. In addition, we did not conduct metabolite analysis in tissues, especially in target organs, owing to the small sample size. The analysis of metabolites in tissues is important for further pharmacodynamic examination of BPC157 and explanation of its efficacy.

In conclusion, the present study is the first systematic report evaluating the pharmacokinetics, tissue distribution, metabolism,

and excretion of BPC157. Many methodological validations were not included because of the limited space of the article. The results showed that the pharmacokinetic characteristics of BPC15 were consistent with the general properties of peptide drugs. In the future, we will conduct clinical trials for examining BPC157 for the treatment of severe trauma and burns. The observations of the present study and previous safety evaluation and pharmacodynamic research will provide basic information for further comprehensive clinical research. This study also provides a reference for the development of various peptide drugs.

4 Materials and methods

4.1 Test article and materials

BPC157 was synthesized and purified *via* HPLC in our laboratory with 99% purity. This compound was sterilized and lyophilized to meet the regulatory requirements of preclinical studies. [^3H]BPC157 was synthesized by Moravek Biochemicals Inc. The specific radioactivity was 71.7 Ci/mmol, the radioactive purity was 99.6%, and the total amount was approximately 10 Mcurie. The tritium labeling sites were located on two prolines.

BPC157 solution for administration was prepared by diluting the required amount of concentrated BPC157 solution in 0.9% NaCl injection solution prior to administration. The clinical dose of 200 μg /person/day of BPC157 was converted to 20 μg /kg for rats and 6 μg /kg for dogs. Based on its conversion according to body surface area and detection sensitivity, 100 μg /300 μCi /kg [^3H]BPC157 was used for tritium labeling experiment in rats, 20, 100, and 500 μg /kg of BPC157 was used for unlabeled experiment in rats, and 6, 30, and 150 μg /kg of BPC157 was used for unlabeled experiment in dogs.

Warfarin sodium was purchased from Tokyo Chemical Industry Co. Ltd., Lot: 340JE. Heparin sodium and normal saline were obtained from Sinopharm Chemical Reagents Co. Ltd. (Shanghai, China). 3H scintillation solution was purchased from R.J. Harvey Co. (Tappan, NY). Ultima Gold scintillation solution was purchased from Perkin Elmer (Waltham, MA, United States). HPLC-grade acetonitrile, formic acid, and methanol were obtained from Merck (Darmstadt, Germany). HPLC-grade water was produced using a Milli-Q® ultrapure water purification system (Bedford, MA, United States).

4.2 Animals

Approximately six-week-old SD rats weighing approximately 220 g were purchased from Beijing Vital River Laboratory Animal Technology Co., Ltd. The rats were maintained in an animal room with an air-conditioned barrier system at an ambient temperature of $25^{\circ}\text{C} \pm 2^{\circ}\text{C}$, relative humidity of $50\% \pm 10\%$, and a 12 h light/dark cycle. Ten-to-twelve-month-old beagle dogs weighing between 9.8 and 12.8 kg were purchased from YaDong Experimental Animal Research Centre, Nanjing, China. The dogs were raised in an open feeding farm under conditions involving natural light. The animals were provided with *ad libitum* access to clean drinking water and a standard pellet diet. The dogs were acclimatized to the housing conditions for at least 7 days prior to the initiation of the experiment. All animals were treated humanely, and all studies were carried out in accordance with good laboratory practice (GLP) (China Food and Drug Administration, CFDA) guidelines for nonclinical laboratory studies of drugs issued by the National Scientific and Technological Committee of the People's Republic of China. Animal care and welfare were performed in accordance with the Guide for the Care and Use of Laboratory Animals.

4.3 Pharmacokinetic parameters in Sprague-Dawley rats after intravenous and intramuscular administration

A total of 324 SD rats were randomly divided into five groups, including 66 rats in group one, 60 rats each in groups two to four, and 78 rats in group five, with each group comprising half male and half female subjects. Group one was administered 20 $\mu\text{g/kg}$ BPC157 saline solution intravenously. Groups two, three, and four were administered 20, 100, and 500 $\mu\text{g/kg}$ BPC157 saline solutions *via* single IM injections, respectively. Group five was administered 100 $\mu\text{g/kg}$ BPC157 normal saline solution by IM injection once a day for seven consecutive days. Blood samples were collected from rats in groups one to four at the corresponding time points before (0 h) and within 6 h after BPC157 administration. Blood samples were collected from rats

in group five before the last three doses and within 6 h after the last dose. Three male and three female rats were selected at each time point, and approximately 7 ml of whole blood was collected by heart puncture. Blood was centrifuged at 4°C to obtain plasma and stored at 20°C until further analysis. The concentration of BPC157 in the animal plasma at different time points was determined by high-performance liquid chromatography-tandem mass spectrometry (LC-MS/MS). The calibration and quality control samples of BPC157 were prepared using animal plasma with K3EDTA as anticoagulant, and dextromethorphan was used as the internal standard of BPC157. The analyte and internal standard were extracted from 50 μl of plasma by solid phase extraction. BPC157 and internal standard were separated by reverse-phase chromatographic column, and the analyte was quantified by electrospray ionization (ESI) on a tandem four-stage mass spectrometer. The confirmed linear quantification range of BPC157 was 4.00 and 4,000 ng/ml. The pharmacokinetic parameters were calculated using the mean concentration and Watson LIMS software according to the non-atrioventricular model.

4.4 Pharmacokinetic parameters in beagle dogs after intravenous and intramuscular administration

In this part of the experiment, three male and three female beagles were examined for four cycles. In the first cycle, a normal saline solution (6 $\mu\text{g/kg}$) of BPC157 was administered intravenously. In the second and fourth cycles, the animals were administered 6, 30, and 150 $\mu\text{g/kg}$ BPC157 saline solutions *via* single IM injections. In the third cycle, the dogs were administered 30 $\mu\text{g/kg}$ BPC157 saline solution by IM injection once a day for seven consecutive days. Blood samples were collected at the corresponding time points before (0 h) and within 6 h of a single administration. Blood samples were collected from dogs administered multiple doses at corresponding time points before the first dosing (0 h), within 6 h after dosing, before the last three doses, and at corresponding time points after the last dosing. Approximately 3 ml of whole blood was collected at each time point through the venous plexus of the forelimb. The plasma was stored at -20°C for analysis.

4.5 Pharmacokinetic, tissue distribution, and excretion studies in rats administered radioactive-labeled BPC157

Thirty intact SD rats, six JVC rats, and six BDC rats (half male and half female subjects) were injected intramuscularly with 100 $\mu\text{g}/300 \mu\text{Ci/kg}$ of $[3\text{H}]\text{BPC157}$. Whole blood and plasma samples of six JVC rats were collected at 0.05, 0.167, 0.5, 1, 2, 4, 8,

24, 48, and 72 h after administration (three males and three females at each time point) for the examination of radio pharmacokinetics of total plasma. Six intact SD rats were used for urinary, fecal, and biliary excretion studies. Urine and fecal samples were collected from each rat at 0–8, 8–24, 24–48, and 48–72 h. Animal carcasses were collected 72 h after administration. Bile excretion was studied in six SD rats with BDC. Bile, urine, and feces were collected 0–72 h after administration. Tissue distribution of BPC was studied in 24 intact SD rats. The rats were euthanized, and tissue samples (brain, heart, kidneys, liver, spleen, lung, stomach, intestine, muscle, grease, ovaries, womb, testicles, and thymus) were collected at 3 min, 10 min, 1 h, and 24 h after administration (three males and three females at each time point). Male SD rats were administered a single IM injection of blank solvent (excipient), and biological samples, including whole blood, plasma, urine, feces, and tissues, were collected for background control. The radioactivity of the plasma, tissue, bile, urinary, and fecal samples was analyzed using a liquid scintillation counter.

4.6 Metabolism

Plasma, bile, urine, and fecal samples of intact SD rats or BDC rats after a single administration of [3H]BPC157 were analyzed by HPLC combined with a low-energy radionuclide detection technique to obtain the radiometabolite profiles of [3H] BPC157. The structures of the main metabolites of [3H] BPC157 in rat plasma, bile, urine, and feces were analyzed and identified using LC-MS/MS and standard molecular weight comparison.

4.7 Statistical analysis

All data are expressed as mean \pm standard deviation. Pharmacokinetic parameters were evaluated using the WinNonlin software (version 5.3) according to a non-atrioventricular model. Linear regression was examined between AUC values obtained after BPC157 IM administration and BPC157 doses and between C_{\max} values and BPC157 doses. The goodness of fit was estimated using the coefficients of determination (r^2).

Data availability statement

The original contributions presented in the study are included in the article/Supplementary Material, further inquiries can be directed to the corresponding authors.

Ethics statement

The animal study was reviewed and approved by the Laboratory Animal Welfare and Ethics Committee of Fourth Military Medical University.

Author contributions

Conceptualization, YZ, WL, and ML. Methodology, LH and DF. Validation, HG, KZ, WZ, and SW. Formal analysis, CZ, ZL, and QH. Investigation, LH and DF. Data curation, YG, and JG. Writing original draft preparation, WL. Writing review and editing, ML, WL, and YZ. Supervision, YZ. Project administration, KZ;. Funding acquisition, WL, YYZ, and ML. All the authors have read and agreed to the published version of the manuscript.

Funding

This work was supported by grants from the National Natural Science Foundation of China (NSFC Numbers 81672800, 81603009, 81673020, 81802632, and 82173830), Natural Science Foundation of Shaanxi (2020JQ-445), and the Key Research and Development Program of Shaanxi Province (2021SF-207, 2021SF-223, and 2022ZDLSF05-19).

Conflict of interest

The authors declare that the research was conducted in the absence of any commercial or financial relationships that could be construed as a potential conflict of interest.

Publisher's note

All claims expressed in this article are solely those of the authors and do not necessarily represent those of their affiliated organizations, or those of the publisher, the editors and the reviewers. Any product that may be evaluated in this article, or claim that may be made by its manufacturer, is not guaranteed or endorsed by the publisher.

Supplementary material

The Supplementary Material for this article can be found online at: <https://www.frontiersin.org/articles/10.3389/fphar.2022.1026182/full#supplementary-material>

References

- Chen, J., Wang, M., Joyce, A., DeFranco, D., Kavosi, M., Xu, X., et al. (2014). Comparison of succinimideyl [(125)I]iodobenzoate with iodogen iodination methods to study pharmacokinetics and ADME of biotherapeutics. *Pharm. Res.* 31, 2810–2821. doi:10.1007/s11095-014-1378-3
- Czock, D., Keller, F., and Seidling, H. M. (2012). Pharmacokinetic predictions for patients with renal impairment: Focus on peptides and protein drugs. *Br. J. Clin. Pharmacol.* 74, 66–74. doi:10.1111/j.1365-2125.2012.04172.x
- Drmic, D., Kolenc, D., Ilic, S., Bauk, L., Sever, M., Zenko Sever, A., et al. (2017). Celecoxib-induced gastrointestinal, liver and brain lesions in rats, counteraction by BPC 157 or L-arginine, aggravation by L-NAME. *World J. Gastroenterol.* 23, 5304–5312. doi:10.3748/wjg.v23.i29.5304
- Duzel, A., Vlainic, J., Antunovic, M., Malekinusic, D., Vrdoljak, B., Samara, M., et al. (2017). Stable gastric pentadecapeptide BPC 157 in the treatment of colitis and ischemia and reperfusion in rats: New insights. *World J. Gastroenterol.* 23, 8465–8488. doi:10.3748/wjg.v23.i48.8465
- Grabarevic, Z., Tisljar, M., Artukovic, B., Bratulic M.Dzaja, P., Seiwert, S., et al. (1997). The influence of BPC 157 on nitric oxide agonist and antagonist induced lesions in broiler chicks. *J. Physiol. Paris* 91, 139–149. doi:10.1016/s0928-4257(97)89478-8
- Huang, T., Zhang, K., Sun, L., Xue, X., Zhang, C., Shu, Z., et al. (2015). Body protective compound-157 enhances alkali-burn wound healing *in vivo* and promotes proliferation, migration, and angiogenesis *in vitro*. *Drug Des. devel. Ther.* 9, 2485–2499. doi:10.2147/DDDT.S82030
- Keremi, B., Lohinai, Z., Komora, P., Duhaj, S., Borsi, K., JobbaGy-Ovari, G., et al. (2009). Antiinflammatory effect of BPC 157 on experimental periodontitis in rats. *J. Physiol. Pharmacol.* 60 (7), 115–122.
- Khalil, M. M., Tremoleda, J. L., Bayomy, T. B., and Gsell, W. (2011). Molecular SPECT imaging: An overview. *Int. J. Mol. Imaging* 2011, 796025. doi:10.1155/2011/796025
- Klicek, R., Kolenc, D., Suran, J., Drmic, D., Brcic, L., Aralica, G., et al. (2013). Stable gastric pentadecapeptide BPC 157 heals cysteamine-colitis and colon-colon-anastomosis and counteracts cuprizone brain injuries and motor disability. *J. Physiol. Pharmacol.* 64, 597–612.
- Konturek, S. J., and Brzozowski, T. (2008). Gastrointestinal and liver physiology. Preface. *J. Physiol. Pharmacol.* 59 (2), 3–5.
- Lai, T. T., Yip, O. M., and Sham, M. M. K. (2019). Clinical parameters of wound healing in patients with advanced illness. *Ann. Palliat. Med.* 8, S5–S14. doi:10.21037/apm.2019.01.05
- Lazic, R., Gabric, N., Dekaris, I., Bosnar, D., Boban-Blagaic, A., and Sikiric, P. (2005). Gastric pentadecapeptide BPC 157 promotes corneal epithelial defects healing in rats. *Coll. Antropol.* 29, 321–325.
- Li, Z. G., Jia, L., Guo, L. F., Yu, M., Sun, X., Nie, W., et al. (2015). Pharmacokinetics of PEGylated recombinant human endostatin (M2ES) in rats. *Acta Pharmacol. Sin.* 36, 847–854. doi:10.1038/aps.2015.16
- Mota, A. P., Menezes, C. A., Alpoim, P. N., Cardoso, C. N., Martins, S. R., Alves, L. V., et al. (2018). Regulatory and pro-inflammatory cytokines in Brazilian living-related renal transplant recipients according to creatinine plasma levels. *Nephrology* 23, 867–875. doi:10.1111/nep.13114
- Roffey, S. J., Obach, R. S., Gedge, J. I., and Smith, D. A. (2007). What is the objective of the mass balance study? A retrospective analysis of data in animal and human excretion studies employing radiolabeled drugs. *Drug Metab. Rev.* 39, 17–43. doi:10.1080/03602530600952172
- Sharma, R., McDonald, T. S., Eng, H., Limberakis, C., Stevens, B. D., Patel, S., et al. (2013). *In vitro* metabolism of the glucagon-like peptide-1 (GLP-1)-derived metabolites GLP-1 (9-36) amide and GLP-1 (28-36) amide in mouse and human hepatocytes. *Drug Metab. Dispos.* 41, 2148–2157. doi:10.1124/dmd.113.054254
- Sikiric, P., Rucman, R., Turkovic, B., Sever, M., Klicek, R., Radic, B., et al. (2018). Novel cytoprotective mediator, stable gastric pentadecapeptide BPC 157. Vascular recruitment and gastrointestinal tract healing. *Curr. Pharm. Des.* 24, 1990–2001. doi:10.2174/1381612824666180608101119
- Sikiric, P., Seiwert, S., Grabarevic, Z., Rucman, R., PetekM.RotkvIc, I., et al. (1993). Hepatoprotective effect of BPC 157, a 15-amino acid peptide, on liver lesions induced by either restraint stress or bile duct and hepatic artery ligation or CCl4 administration. A comparative study with dopamine agonists and somatostatin. *Life Sci.* 53, PL291–296. doi:10.1016/0024-3205(93)90589-u
- Sikiric, P., Seiwert, S., Rucman, R., Kolenc, D., Vuletic, L. B., Drmic, D., et al. (2016). Brain-gut Axis and pentadecapeptide BPC 157: Theoretical and practical implications. *Curr. Neuropharmacol.* 14, 857–865. doi:10.2174/1570159x13666160502153022
- Vugmeyster, Y., Xu, X., Theil, F. P., Khawli, L. A., and Leach, M. W. (2012). Pharmacokinetics and toxicology of therapeutic proteins: Advances and challenges :advances and challenges. *World J. Biol. Chem.* 26, 73–92. doi:10.4331/wjbc.v3.i4.73
- Wang, X. Y., Qu, M., Duan, R., Shi, D., Jin, L., Gao, J., et al. (2019). Cytoprotective mechanism of the novel gastric peptide BPC157 in gastrointestinal tract and cultured enteric neurons and glial cells. *Neurosci. Bull.* 35, 167–170. doi:10.1007/s12264-018-0269-8
- Wang, Y., Lomakin, A., Kanai, S., Alex, R., Belli, S., Donzelli, M., et al. (2016). The molecular basis for the prolonged blood circulation of lipidated incretin peptides :peptide oligomerization or binding to serum albumin. *J. Control. Release* 241, 25–33. doi:10.1016/j.jconrel.2016.08.035
- Xu, C., Sun, L., Ren, F., Huang, P., Tian, Z., Cui, J., et al. (2020). Preclinical safety evaluation of body protective compound-157, a potential drug for treating various wounds. *Regul. Toxicol. Pharmacol.* 114, 104665. doi:10.1016/j.yrtph.2020.104665
- Xue, X. C., Wu, Y. J., Gao, M. T., Li, W. G., Zhao, N., Wang, Z. L., et al. (2004). Protective effects of pentadecapeptide BPC 157 on gastric ulcer in rats. *World J. Gastroenterol.* 10, 1032–1036. doi:10.3748/wjg.v10.i7.1032



OPEN ACCESS

EDITED BY

Junmin Zhang,
Lanzhou University, China

REVIEWED BY

Cao YingYing,
Shanghai Dermatology Hospital, China
Letizia Angioletti,
Sapienza University of Rome, Italy

*CORRESPONDENCE

Yongbing Cao,
✉ ybcao@vip.sina.com
Hui Lu,
✉ luhui2019@tongji.edu.cn
Yuanying Jiang,
✉ 19851@tongji.edu.cn

SPECIALTY SECTION

This article was submitted to Drug
Metabolism and Transport,
a section of the journal
Frontiers in Pharmacology

RECEIVED 18 November 2022

ACCEPTED 12 December 2022

PUBLISHED 21 December 2022

CITATION

Wang H, Ji Z, Feng Y, Yan T, Cao Y, Lu H
and Jiang Y (2022), Myriocin enhances
the antifungal activity of fluconazole by
blocking the membrane localization of
the efflux pump Cdr1.
Front. Pharmacol. 13:1101553.
doi: 10.3389/fphar.2022.1101553

COPYRIGHT

© 2022 Wang, Ji, Feng, Yan, Cao, Lu and
Jiang. This is an open-access article
distributed under the terms of the
[Creative Commons Attribution License
\(CC BY\)](https://creativecommons.org/licenses/by/4.0/). The use, distribution or
reproduction in other forums is
permitted, provided the original
author(s) and the copyright owner(s) are
credited and that the original
publication in this journal is cited, in
accordance with accepted academic
practice. No use, distribution or
reproduction is permitted which does
not comply with these terms.

Myriocin enhances the antifungal activity of fluconazole by blocking the membrane localization of the efflux pump Cdr1

Hongkang Wang^{1,2}, Zhe Ji³, Yanru Feng³, Tianhua Yan²,
Yongbing Cao^{1*}, Hui Lu^{3*} and Yuanying Jiang^{3*}

¹Institute of Vascular Anomalies, Shanghai TCM-Integrated Hospital, Shanghai University of Traditional Chinese Medicine, Shanghai, China, ²Department of Physiology and Pharmacology, School of Basic Medicine and Clinical Pharmacy, China Pharmaceutical University, Nanjing, China, ³Department of Pharmacy, Shanghai Tenth People's Hospital, School of Medicine, Tongji University, Shanghai, China

Introduction: Extrusion of azoles from the cell, mediated by an efflux pump Cdr1, is one of the most frequently used strategies for developing azole resistance in pathogenic fungi. The efflux pump Cdr1 is predominantly localized in lipid rafts within the plasma membrane, and its localization is sensitive to changes in the composition of lipid rafts. Our previous study found that the calcineurin signal pathway is important in transferring sphingolipids from the inner to the outer membrane.

Methods: We investigated multiple factors that enhance the antifungal activity of fluconazole (FLC) using minimum inhibitory concentration (MIC) assays and disk diffusion assays. We studied the mechanism of action of myriocin through qRT-PCR analysis and confocal microscopy analysis. We tested whether myriocin enhanced the antifungal activity of FLC and held therapeutic potential using a mouse infection model.

Results: We found that this signal pathway has no function in the activity of Cdr1. We found that inhibiting sphingolipid biosynthesis by myriocin remarkably increased the antifungal activity of FLC with a broad antifungal spectrum and held therapeutic potential. We further found that myriocin potently enhances the antifungal activity of FLC against *C. albicans* by blocking membrane localization of the Cdr1 rather than repressing the expression of Cdr1. In addition, we found that myriocin enhanced the antifungal activity of FLC and held therapeutic potential.

Discussion: Our study demonstrated that blocking the membrane location and inactivating Cdr1 by inhibiting sphingolipids biogenesis is beneficial for enhancing the antifungal activity of azoles against azole-resistant *C. albicans* due to Cdr1 activation.

KEYWORDS

efflux pump Cdr1, membrane localization, myriocin, fluconazole, *Candida albicans*

Introduction

Fluconazole (FLC), as a represent azole, is widely used to treat invasive fungal infections due to its broad antifungal spectrum, good safety profile, and multiple administration routes (Lu et al., 2021). However, FLC is a fungistatic agent that cannot kill pathogenic fungi; fungi easily acquire azole resistance (Perlin et al., 2017). Extrusion of FLC from the cell, mediated by an efflux pump Cdr1, is one of the most frequently used strategies for developing FLC resistance in pathogenic fungi (Kim et al., 2019; Teo et al., 2019; Borgeat et al., 2021). Therefore, pharmacological inactivation of Cdr1 through suppressing the expression of Cdr1, blocking membrane localization of Cdr1, and inhibiting the combination of Cdr1 and antifungal agents, is beneficial to overcoming fungal FLC resistance (Monk and Goffeau, 2008). However, few compounds enhance the antifungal activity of FLC by inactivating Cdr1.

The activation of Cdr1 depends on the expression level of Cdr1, which is regulated by the Tac1 transcriptional regulator (Liu and Myers, 2017), and the membrane location of Cdr1, which is predominantly localized in lipid rafts within the plasma membrane (Pasrija et al., 2008). The activity and localization of Cdr1 are sensitive to changes in the composition of sphingolipids and ergosterol of lipid rafts (Pasrija et al., 2008). Our previous study showed that the calcineurin signaling pathway plays an important role in sphingolipid transport from the inner to the outer membrane. Still, it is unclear whether the influence on sphingolipid membrane transport can affect the integrity of lipid rafts and thus affect the membrane location and activity of Cdr1. Other factors that may affect the location and activity of the Cdr1 membrane also need further study.

In this study, we found that the calcineurin signaling pathway has no function in the activity of Cdr1. We further investigated multiple factors that enhance the antifungal activity of FLC. We found that inhibiting sphingolipid biosynthesis by myriocin remarkably increased the antifungal activity of FLC with a broad antifungal spectrum and held therapeutic potential. We further found that myriocin could enhance the antifungal activity of FLC by blocking membrane localization of Cdr1 rather than inhibiting the expression level of Cdr1. Our findings will help get specific small molecule inhibitors of Cdr1 and open the way for developing new antifungal therapeutics targeted at inhibiting the activity of Cdr1.

Results

Calcineurin has no function on the activation of Cdr1

The Cdr1 is predominantly localized in lipid rafts, composed of sphingolipids and ergosterol (Hurst and Fratti, 2020). The calcineurin signal pathway transfers sphingolipids from the inner

to the outer membrane (Jia et al., 2009). Therefore, we hypothesize that the calcineurin pathway may regulate the membrane localization and the activity of Cdr1 by affecting the transfer of sphingolipids and the composition of lipid rafts. To test this hypothesis, we successfully constructed null mutants of calcineurin signal pathway genes generating *cmp1Δ/cmp1Δ*, *crz1Δ/crz1Δ*, and *rta2Δ/rta2Δ* null mutants (Supplementary Figure S1A). We also constructed the homogenesis gene deletion of the *CDR1* gene null mutant (*cdr1Δ/cdr1Δ*) (Supplementary Figure S1A). We found that loss of the Cdr1 led to increased susceptibility of *C. albicans* to fluconazole (FLC). Compared to the wild-type strain, the minimum inhibitory concentration (MIC) value of FLC decreased from 1 to 0.5 μg/ml, but the *cdr1Δ/cdr1Δ* null mutant could still grow in the presence of FLC (Figure 1A). However, contrary to the *cdr1Δ/cdr1Δ*, the *cmp1Δ/cmp1Δ* mutant is inviable in the presence of FLC, rather than decreased FLC MIC value (Figure 1A). Losses of the Crz1 and Rta2 do not affect the susceptibility to FLC in *C. albicans* because that *crz1Δ/crz1Δ* and *rta2Δ/rta2Δ* null mutants and wild-type strain SN152 have the same value of FLC (1 μg/ml) and trailing growth in the presence of FLC (Figure 1A). Due to the tolerance of *C. albicans* to FLC, disk diffusion assays showed noticeable growth of cells in the zone of inhibition of 25 μg FLC on YPD plates incubated at 30°C for 48 h for SN152, *crz1Δ/crz1Δ* null mutant, and *rta2Δ/rta2Δ* null mutant (Figure 1B) (Rosenberg et al., 2018). It is worth noting that the zones of inhibition for 25 μg FLC treatments were clear on YPD plates for *cmp1Δ/cmp1Δ* rather than for the *cdr1Δ/cdr1Δ* null mutant (Figure 1B). The discrepant phenotypes between the *cdr1Δ/cdr1Δ* and *cmp1Δ/cmp1Δ*, *crz1Δ/crz1Δ*, and *rta2Δ/rta2Δ* null mutants in susceptibility to FLC suggested that the calcineurin signal pathway has no function in the activation of Cdr1. To confirm this founding, we then created ectopic over-expression constructs of the *CDR1* gene in null mutants (*cmp1Δ/cmp1Δ*, *crz1Δ/crz1Δ*, and *rta2Δ/rta2Δ*) and wild-type strain (SN152) by expressing the *CDR1* gene using the potent *ADHI* promoter (Chang et al., 2018). We used PCR to verify the insertion position of the *ADHI* promoter in these mutants (Supplementary Figure S1B) and qRT-PCR to confirm the expression level of the *CDR1* gene (Supplementary Figure S1C). We found that over-expression of the *CDR1* gene can enhance the resistance of *C. albicans* to FLC in all null mutants and the wild-type strain because the MIC values of FLC increased from 1 to 2 μg/ml (Figure 1A). Further, we found that cyclosporin A, an inhibitor of a catalytic subunit of calcineurin (Sanglard et al., 2003), did not affect the increase of the MIC value of FLC caused by over-expression of the *CDR1* gene (Figure 1C) (Marchetti et al., 2003). Similarly, we induced over-expression of the *CDR1* gene by 10 μg/ml fluphenazine (FNZ) (Liu and Myers, 2017). We found that FNZ can increase the MIC value of FLC from 1 to 4 μg/ml against both the wild-type strain and the *cmp1Δ/cmp1Δ* null mutant (Figure 1D), suggesting that the impaired calcineurin signal

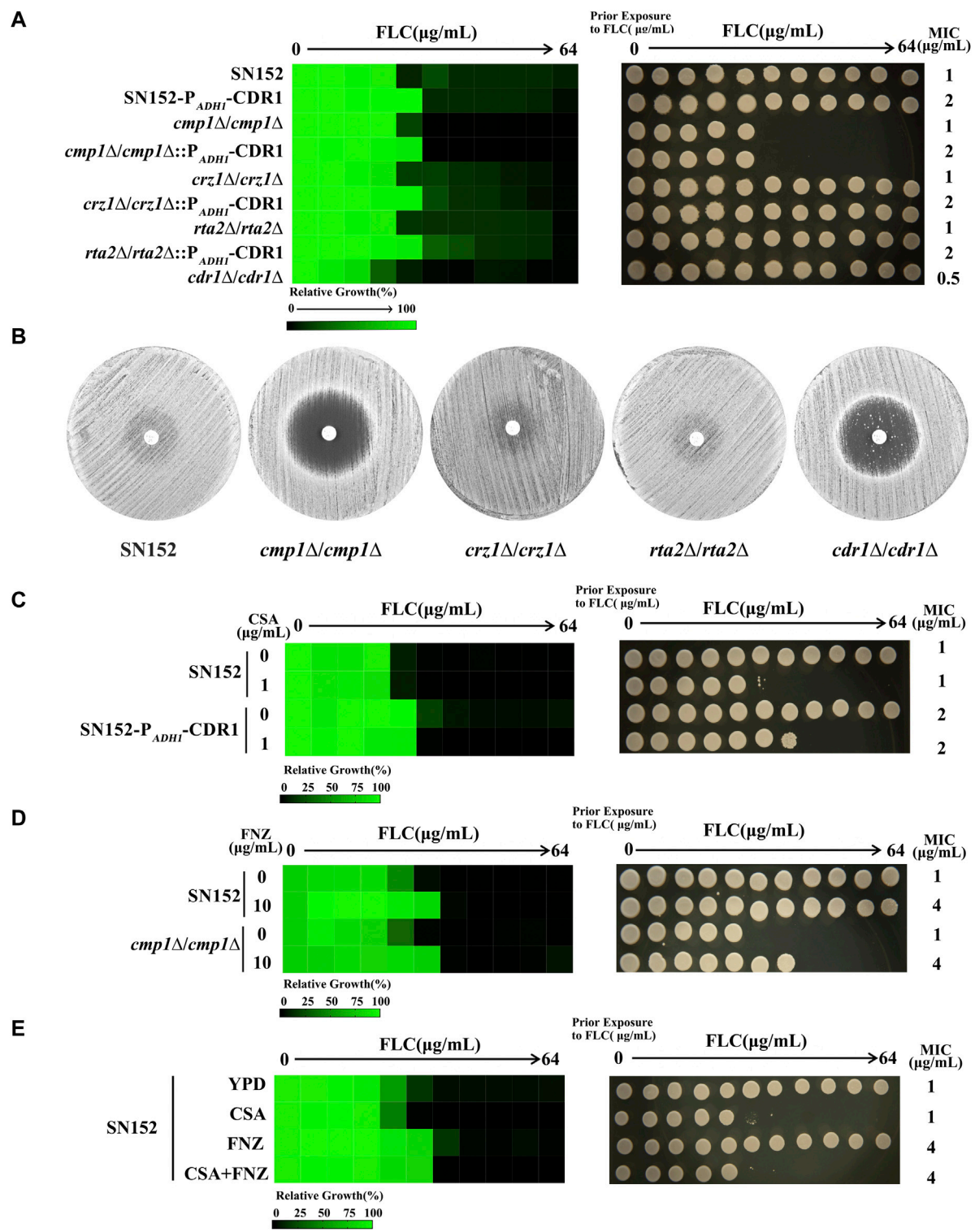
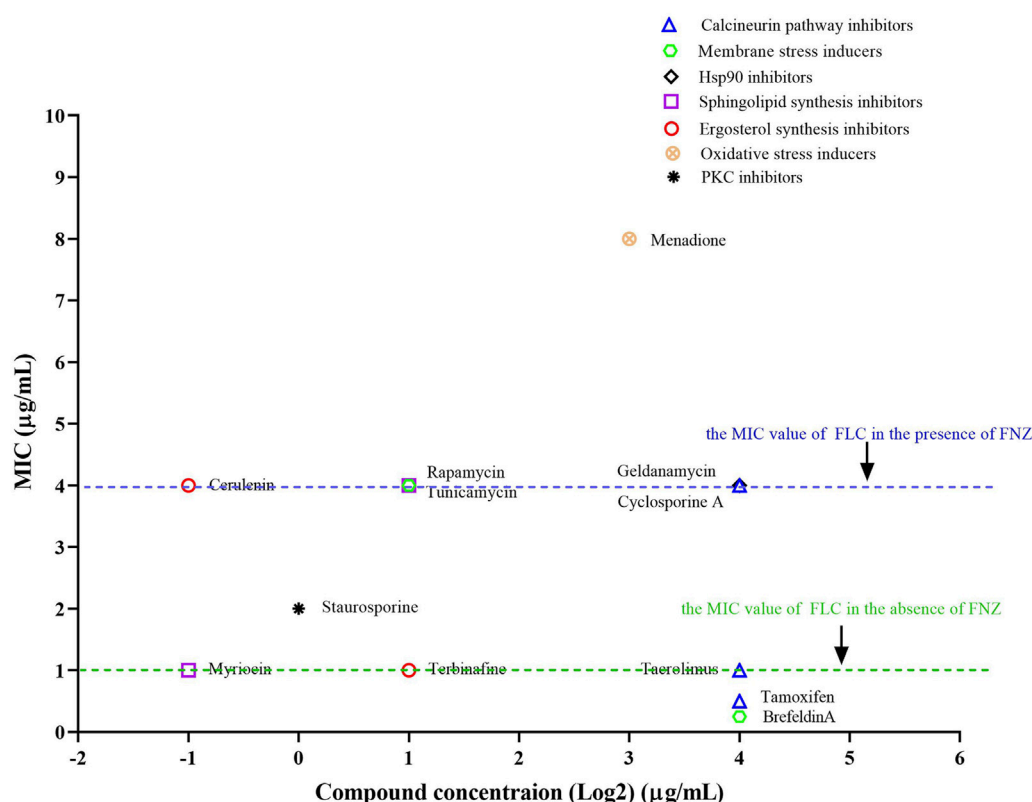


FIGURE 1
The impaired calcineurin signal pathway did not affect the function of Cdr1. **(A)** The sensitivities of *C. albicans* wild-type strain (SN152) and mutants (*P_{ADHI}*-CDR1, *cmp1Δ/cmp1Δ*, *cmp1Δ/cmp1Δ::P_{ADHI}*-CDR1, *crz1Δ/crz1Δ*, *crz1Δ/crz1Δ::P_{ADHI}*-CDR1, *rta2Δ/rta2Δ*, *rta2Δ/rta2Δ::P_{ADHI}*-CDR1, *cdr1Δ/cdr1Δ*) to FLC were tested by the broth microdilution assays in a YPD medium incubated at 30°C for 48 h (Left). Cells from the broth microdilution assays were spotted onto YPD medium and incubated at 30°C for 48 h before the plate was photographed (Right). **(B)** Disk diffusion assays showed that the loss of the *CMP1* gene, but not the *CDR1* gene, cleared the inhibition zones of 25 μg FLC. In brief, cells (2×10^5 cells) (Continued)

FIGURE 1 (Continued)

were spread onto YPD plates. A single 25 μg FLC disk (6 mm, Liofilchem, Italy) was placed in the center of each plate. Plates were then incubated at 30°C for 48 h before plates were photographed. **(C)** The MIC values of FLC of the SN152 strain and the $P_{ADH1}\text{-CDR1}$ mutant in a YPD medium without or with 1 $\mu\text{g}/\text{ml}$ cyclosporin A were tested by the broth microdilution assays (at 30°C for 48 h) (Left). Cells from the broth microdilution assays were spotted onto YPD medium and incubated at 30°C for 48 h before the plate was photographed (Right). **(D)** The MIC values of FLC of the SN152 strain and the $cmp1\Delta/cmp1\Delta$ null mutant in a YPD medium without or with 10 $\mu\text{g}/\text{ml}$ fluphenazine (FNZ) were tested by the broth microdilution assays (at 30°C for 48 h) (Left). Cells from the broth microdilution assays were spotted onto YPD medium and incubated at 30°C for 48 h before the plate was photographed (Right). **(E)** The MIC values of FLC of the SN152 strain in a YPD medium with 1 $\mu\text{g}/\text{ml}$ cyclosporin A, 10 $\mu\text{g}/\text{ml}$ FNZ, 1 $\mu\text{g}/\text{ml}$ cyclosporin A+10 $\mu\text{g}/\text{ml}$ FNZ or without any compound (control) were tested by the broth microdilution assays (at 30°C for 48 h) (Left). Cells from the broth microdilution assays were spotted onto YPD medium and incubated at 30°C for 48 h before the plate was photographed (Right).

**FIGURE 2**

The synergistic antifungal activity of FLC and some compounds. Dose-matrix titration assays showed that some compounds (concentration range from 0.25 to 16 $\mu\text{g}/\text{ml}$) enhanced the antifungal activity of FLC in the presence of FNZ (10 $\mu\text{g}/\text{ml}$) (The MIC values of FLC reduced from 4 to 1 $\mu\text{g}/\text{ml}$ or lower).

pathway cannot affect the function of Cdr1. Finally, in the presence of cyclosporin A (1 $\mu\text{g}/\text{ml}$), FNZ (10 $\mu\text{g}/\text{ml}$) can increase the MIC value of FLC against *C. albicans* (from 1 to 4 $\mu\text{g}/\text{ml}$) (Figure 1E); In the presence of FNZ (10 $\mu\text{g}/\text{ml}$), cyclosporin A (1 $\mu\text{g}/\text{ml}$) can still eliminate the FLC tolerance of *C. albicans* (Figure 1E). In summary, the calcineurin signal pathway functions in the transfer of sphingolipids from the inner to the outer membrane (Jia et al., 2009) and may affect the composition of lipid rafts but have no role in the activity of Cdr1.

Myriocin enhanced the antifungal activity of FLC by inactivation of the Cdr1

The activation of Cdr1 plays an important role in the azole resistance in pathogenic fungi. Therefore, the inactivation of Cdr1 will enhance the antifungal activity of azoles against fungal infection. It is reported that ergosterol and sphingolipid contents can affect the membrane localization of Cdr1 (Pasrija et al., 2008). Therefore, we investigated the inactivation of FNZ-

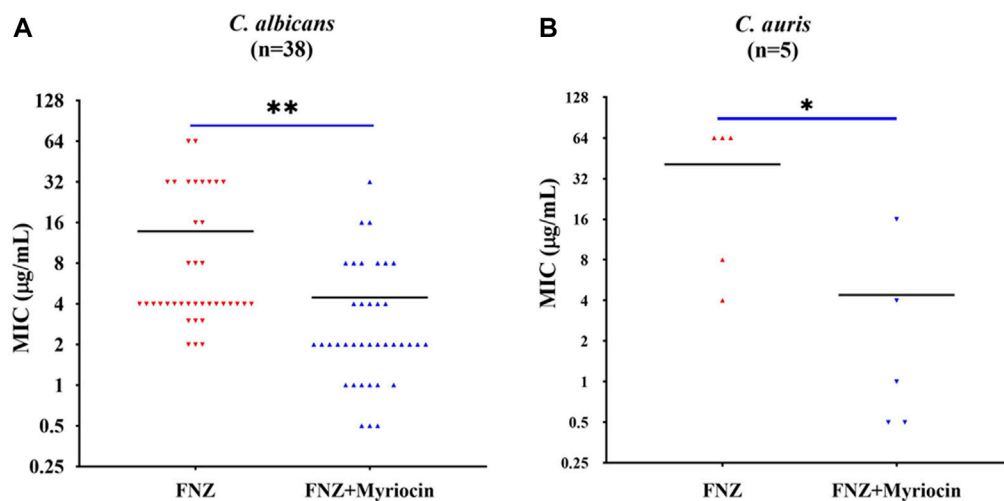


FIGURE 3

Myriocin can significantly reduce the MIC values of FLC against (A) *C. albicans* isolates ($n = 38$) (** $p = 0.0017$, the FNZ (10 $\mu\text{g/mL}$) + myriocin (0.5 $\mu\text{g/mL}$) treated group compared to the FNZ (10 $\mu\text{g/mL}$) group, t-Test) and (B) *C. auris* isolates ($n = 5$) (* $p = 0.036$, the FNZ (10 $\mu\text{g/mL}$) + myriocin (0.5 $\mu\text{g/mL}$) treated group compared to the FNZ (10 $\mu\text{g/mL}$) group, t-Test).

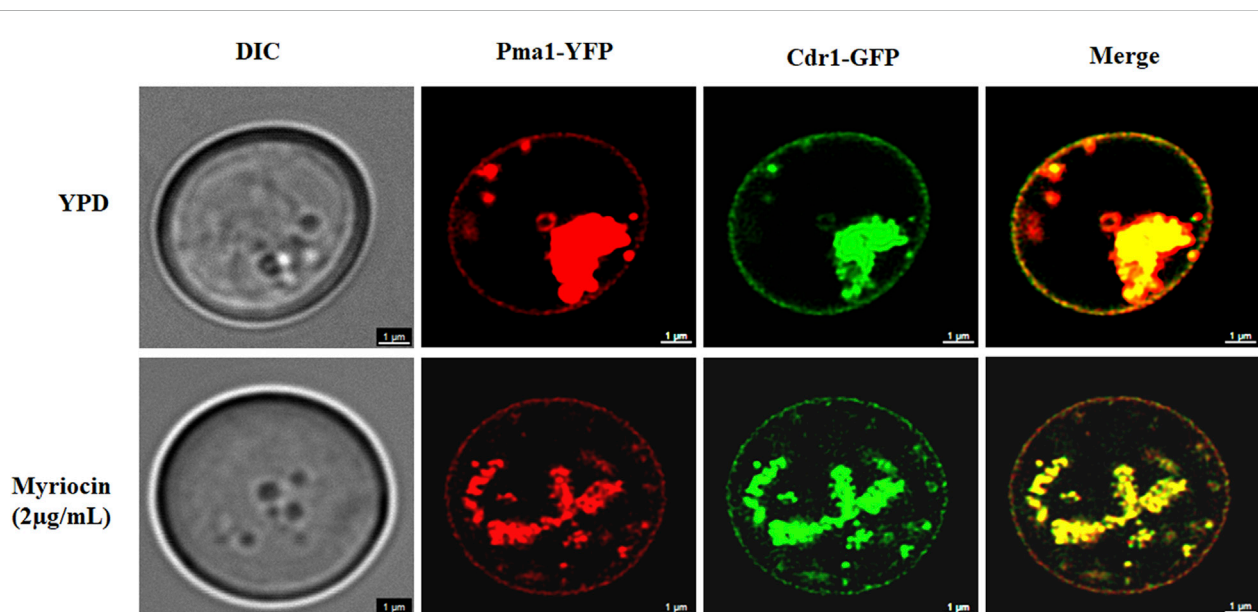
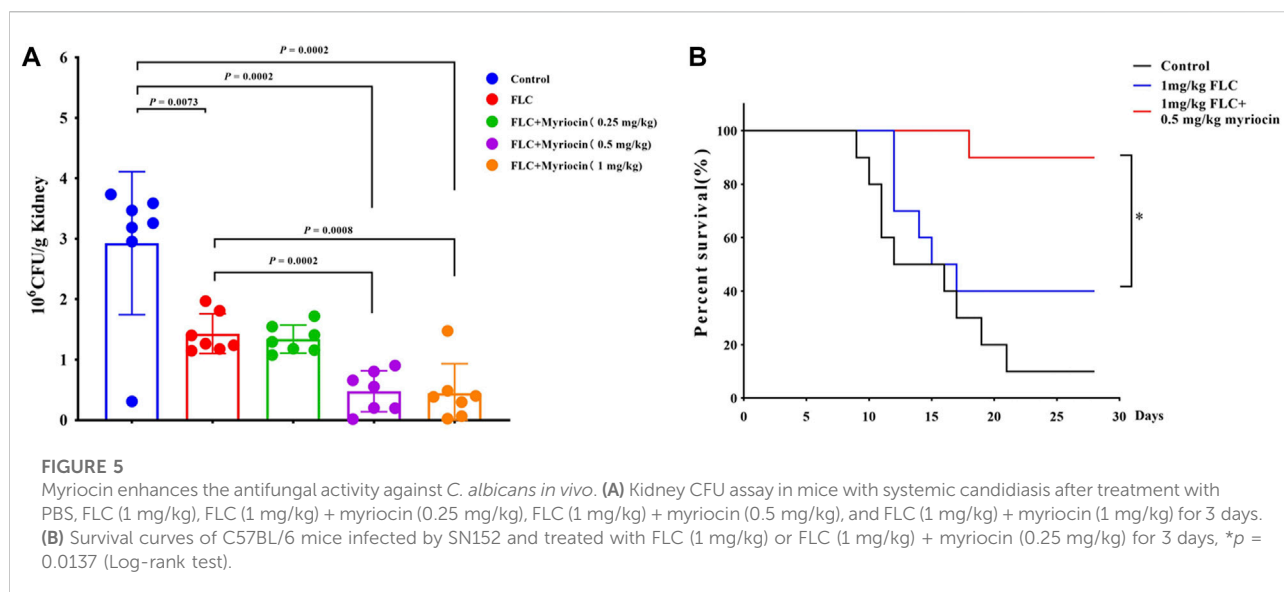


FIGURE 4

Confocal micrographs of cell membrane staining (Pma1-YFP) and membrane localization of Cdr1-GFP in the Cdr1-GFP::Pma1-YFP mutant after treatment with or without 2 $\mu\text{g/mL}$ myriocin for 16 h in YPD medium. DIC, differential interference contrast; YFP, yellow fluorescent protein; GFP, green fluorescent protein. Scale bar = 1 μm .

induced over-expression of the *CDR1* gene by sphingolipid biosynthesis inhibitors (myriocin and rapamycin) (He et al., 2004; Teixeira and Costa, 2016) and ergosterol biosynthesis inhibitors (cerulenin and terbinafine) (Nomura et al., 1972; Ryder, 1992). Previous studies demonstrated that

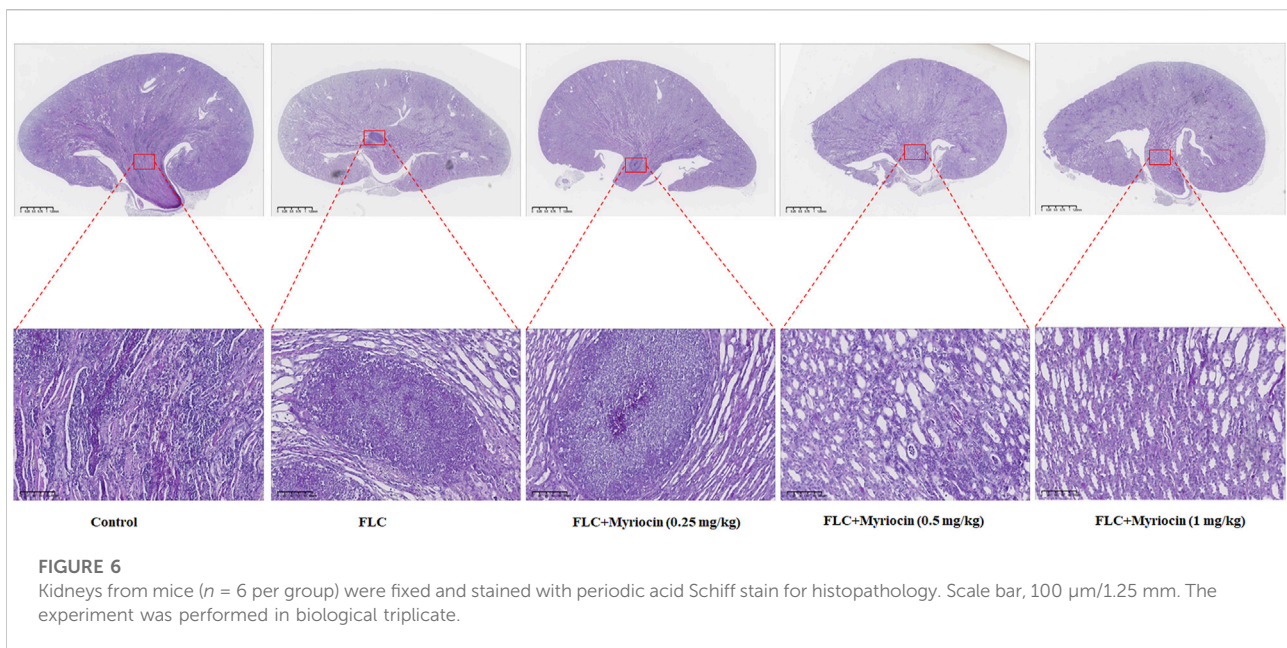
geldanamycin [an inhibitor of heat shock protein 90 (Hsp90)] (Rosenberg et al., 2018), brefeldin A (a Golgi stress inducer) (Epp et al., 2010), tunicamycin (an endoplasmic reticulum stress inducer) (Sellam et al., 2009), staurosporine (a protein kinase C (PKC) inhibitor) (LaFayette et al., 2010), menadione (an



oxidative stress inducer (Sa et al., 2017), and tamoxifen (a calmodulin inhibitor) (Dolan et al., 2009), can enhance the antifungal activity of FLC. Still, it is unclear whether these compounds can affect the activity of Cdr1. In this study, we used 10 μ g/ml FNZ to increase the MIC value of FLC from 1 to 4 μ g/ml (Liu and Myers, 2017) and then examined which of these compounds could significantly reduce the MIC value of FLC against *C. albicans* in the presence of FNZ.

As discussed above, pharmacological compromise of the calcineurin pathway by cyclosporine A (16 μ g/ml) did not change the MIC of FLC in the presence of FNZ (Figure 2, Supplementary Figure S2A). Tacrolimus binds to an FK506-binding protein (FKBP12) and inhibits calcineurin, and targets of rapamycin complex 1 (TORC1), which is important for ribosome biosynthesis (Azzi et al., 2013; Kasahara, 2021). Therefore, a high concentration of tacrolimus (16 μ g/ml) inhibited both calcineurin and TORC1 and decreased the MIC value (from 4 to 1 μ g/ml) of FLC in the presence of FNZ (Figure 2, Supplementary Figure S2B). Tamoxifen targets calmodulin (Dolan et al., 2009), then blocks the calcineurin pathway and inhibits NADPH-cytochrome P450 reductase Ccr1 (Liu et al., 2020) and ergosterol biosynthesis in fission yeast. Therefore, tamoxifen could improve the antifungal activity of FLC at a high concentration (16 μ g/ml) (Figure 2, Supplementary Figure S2C) due to inhibiting ergosterol biosynthesis and then inactivation Cdr1 (Pasrija et al., 2008). Blocking the PKC pathway could enhance the antifungal activity of FLC and even make FLC fungicidal (LaFayette et al., 2010). We found that staurosporine (1 μ g/ml) could decrease the MIC value of FLC from 4 to 2 μ g/ml in the presence of FNZ (Figure 2, Supplementary Figure S2D), suggesting that the PKC pathway contributes to the activity of Cdr1. Hsp90 is an important molecular chaperone that regulates fungal drug resistance via physically interacts with the catalytic subunit of calcineurin and

Mkc1 and maintains their stable conformations (Cowen, 2009; Singh et al., 2009; LaFayette et al., 2010). Indeed, geldanamycin made FLC act as fungicidal against *C. albicans* (Cowen and Lindquist, 2005; Rosenberg et al., 2018). However, in this study, we found that geldanamycin (16 μ g/ml) did not decrease the MIC value of FLC in the presence of FNZ (Figure 2, Supplementary Figure S2E), suggesting that geldanamycin enhances the antifungal activity of FLC do not depend on inactivation of Cdr1. Membrane trafficking is important in maintaining cell membrane function and fungal drug resistance. Brefeldin A could inhibit the ADP ribosylation factor cycling, disrupt the membrane trafficking, and make FLC fungicidal against *C. albicans* (Epp et al., 2010). In the present study, we found that brefeldin A at a high concentration (16 μ g/ml) could remarkably decrease the MIC value of FLC from 4 to 0.25 μ g/ml (Figure 2 Supplementary Figure S2F), suggesting that the membrane trafficking process plays a vital role in the activity of Cdr1. It is reported that tunicamycin, as an endoplasmic reticulum stress inducer, had a synergistic antifungal activity with FLC against *C. albicans* (Sellam et al., 2009; Yu et al., 2013); however, which is not achieved through the inhibition of Cdr1 activity by tunicamycin (Figure 2 Supplementary Figure S2G). Oxidative stress could increase *C. albicans*' susceptibility to FLC (Xu et al., 2009). However, in the presence of FNZ, menadione (8 μ g/ml), as an oxidative stress inducer, antagonizes the antifungal activity of FLC (the MIC value of FLC increased from 4 to 8 μ g/ml) (Figure 2, Supplementary Figure S2H). Intracellular ergosterol is important for membrane localization and the activity of Cdr1 (Pasrija et al., 2008). We found that terbinafine (an inhibitor of Erg1) (Ryder, 1992) could decrease the MIC value of FLC in the presence of FNZ (Figure 2, Supplementary Figure S2I), but cerulenin (an inhibitor of 3-hydroxy-3-methylglutaryl coenzyme A) (Nomura et al., 1972) could not (Figure 2, Supplementary Figure S2J). In addition, sphingolipids also play an important role in *C. albicans*'



resistance to FLC (Gao et al., 2018). However, rapamycin, as an inhibitor of the target of rapamycin (TOR) signal pathway and able to inhibit sphingolipid synthesis (Teixeira and Costa, 2016), did not enhance the antifungal activity of FLC in the presence of FNZ (Figure 2, Supplementary Figure S2K). Notably, myriocin, which is an inhibitor of serine-palmitoyl-transferase that is essential for sphingolipid synthesis (He et al., 2004), at a concentration as low as 0.5 $\mu\text{g/ml}$ could significantly reduce the MIC value of FLC from 4 to 1 $\mu\text{g/ml}$ in the presence of FNZ (Figure 2, Supplementary Figure S2L). To sum up, myriocin is the most potential adjuvant to enhance the antifungal activity of FLC.

To examine whether the inhibitory effect of myriocin on the activity of the Cdr1 enhancing the antifungal activity of FLC is conserved across other *C. albicans* strains and pathogenic *Candida* species, we tested the antifungal activity of FLC plus 0.5 $\mu\text{g/ml}$ myriocin combinations compared to FLC alone in the presence of 10 $\mu\text{g/ml}$ FNZ in clinical isolates of *C. albicans* ($n = 38$), *C. auris* ($n = 5$), *C. glabrata* ($n = 13$), *C. krusei* ($n = 9$), *C. parapsilosis* ($n = 43$), and *C. tropicalis* ($n = 12$). Myriocin significantly reduced the MIC value of FLC against *C. albicans* and *C. auris* strains (Figure 3). However, myriocin did not enhance the antifungal activity of FLC against *C. glabrata*, *C. krusei*, *C. parapsilosis*, and *C. tropicalis* (Supplementary Figure S3).

Myriocin inactivated the Cdr1 via blocking membrane localization of Cdr1

We speculated that myriocin might inactivate Cdr1 by inhibiting the expression or membrane localization of Cdr1.

We tested the expression level of the *CDR1* gene by quantitative real-time PCR (qRT-PCR) analysis. Compared with FNZ treated (10 $\mu\text{g/ml}$) or untreated *C. albicans* cells, myriocin (0.5 $\mu\text{g/ml}$) treated *C. albicans* cells had significantly higher expression of the *CDR1* gene (Supplementary Figure S4). The qRT-PCR analysis demonstrated that myriocin induces the expression of the *CDR1* gene rather than suppresses its expression, suggesting that myriocin inactivated Cdr1 by blocking membrane localization of Cdr1 and consequently compensatively causing the expression of the *CDR1* gene. To verify this hypothesis, we tagged the C-termini of Cdr1 with a GFP tag (Chang et al., 2018) (Supplementary Figure S5A) and Pma1 (a marker protein of lipid rafts) (Shukla et al., 2003) with a YFP tag (Gola et al., 2003) (Supplementary Figure S5B). Without myriocin, like Pma1, Cdr1 is located on the cell membrane. However, in the presence of myriocin (2 $\mu\text{g/ml}$), the amount of Cdr1 located on the membrane is reduced (Figure 4). In summary, these results suggested that myriocin inactivated Cdr1 and enhanced the antifungal activity of FLC by blocking membrane localization of Cdr1 rather than suppressing the expression of Cdr1.

Myriocin enhanced the antifungal activity of FLC against invasive infection caused by *C. albicans*

We employed a mouse candidiasis model to evaluate whether myriocin enhances the antifungal activity against *C. albicans* *in vivo*. Female C57BL/6 mice have been infected with *C. albicans* (the wild-type SN152 strain) cells *via* tail vein injection. After 2 h

of infection, PBS, FLC (1 mg/kg), FLC (1 mg/kg) + myriocin (0.25 mg/kg), FLC (1 mg/kg) + myriocin (0.5 mg/kg), and FLC (1 mg/kg) + myriocin (1 mg/kg) treatment was given intraperitoneally. The antifungal drug treatment lasted for 3 days. After being infected for 5 days, seven mice from each group were euthanized and enumerated for *C. albicans*' burden in kidneys. Lower kidney fungal burden was observed from the kidneys of mice treated with FLC compared to a control group ($p = 0.0073$, t -test) (Figure 5A). Of note, the fungal burden was significantly lower after being treated with the FLC (1 mg/kg) + myriocin (0.5 mg/kg) treated group ($p = 0.0002$, t -test) and FLC (1 mg/kg) + myriocin (1 mg/kg) treated group ($p = 0.0008$, t -test) in comparison with the FLC (1 mg/kg) treated group (Figure 5A).

To test whether myriocin enhanced the antifungal activity of FLC and held therapeutic potential, we randomly divided the mice into three groups 1) no drug-treated group (as control), 2) 1 mg/kg FLC treated group, and 3) 1 mg/kg FLC plus 0.5 mg/kg myriocin treated group, with ten mice in each group. We found that the mortality of the control group was 90% during the 28-day observation, and the median survival time of the control group was 14 days (Figure 5B). After being treated with 1 mg/kg FLC, the mortality of infected mice decreased to 60%, and the median survival time extended to 16 days (p -value is 0.1533 for comparison between FLC treated group and control group. Log-rank test) (Figure 5B). It is worth noting that myriocin (0.5 mg/kg) enhanced the antifungal activity of FLC (1 mg/kg) against *C. albicans* infection because the mortality of 1 mg/kg FLC plus 0.5 mg/kg myriocin-treated group decreased to 10% (Figure 5B) (p -value is 0.0002 for comparison between FLC plus myriocin treated group and control group. p -value is 0.0137 for comparison between FLC plus myriocin-treated and FLC-treated groups. Log-rank test). For histopathology, the kidneys of mice were fixed and stained with periodic acid Schiff (PAS) stain. Compared to no drug-treated group, after FLC (1 mg/kg) or FLC (1 mg/kg) + myriocin (0.25 mg/kg) treatment, the number of fungal infection lesions in the kidneys of mice infected with *C. albicans* decreased, but remained. In contrast, after treatment with FLC (1 mg/kg) and myriocin (0.5 mg/kg or 1 mg/kg) combination, the infection focuses of the fungal-infected mouse kidney disappeared (Figure 6). In summary, these *in vivo* experiments suggested that myriocin enhanced the antifungal activity of FLC against fungal infection caused by *C. albicans*.

Discussion

FLC is widely used to treat invasive fungal infections because of its broad antifungal spectrum, well safety profile, and multiple routes of administration. However, it is easy for fungi to obtain FLC resistance because FLC is a fungistatic agent (Lu et al., 2021). The activation of Cdr1 and the reduction of intracellular FLC concentration is one of the important mechanisms of FLC

resistance in fungi (Monk and Goffeau, 2008). There are three strategies to inactivate Cdr1: 1) inhibiting the expression of Cdr1, 2) using azole analogs to inhibit the binding of azoles to Cdr1, and 3) blocking membrane localization of Cdr1. Indeed, loss of Cdr1 resulted in remarkably increased susceptibility of *C. albicans* to FLC, miconazole, ketoconazole, and itraconazole (Sanglard et al., 1996; Jha et al., 2004; Xu et al., 2007; Tsao et al., 2009; Xu et al., 2021). Similarly, the efflux pump protein Cdr1 also plays an important role in the azole resistance of *C. glabrata* (Galkina et al., 2020), *C. auris* (Carolus et al., 2021), *Candida lusitanae* (Borgeat et al., 2021), *Fusarium keratoplasticum* (James et al., 2021). In this study, myriocin significantly enhanced the antifungal activity of FLC by blocking membrane localization and inactivating Cdr1. Therefore, the inactivation of Cdr1 is an important and promising antifungal strategy (Prasad et al., 2019).

Sphingolipids play an important role in fungal azole resistance (Song et al., 2020). Altering sphingolipid composition makes *C. albicans* gain azole resistance (Gao et al., 2018). Our previous study found that blocking the transfer of sphingolipids from the inner to the outer membrane by genetic inactivation (deletion of the *RTA2* gene) increased the FLC susceptibility of *C. albicans* (Jia et al., 2009). Inhibiting sphingolipid and ergosterol biosynthesis can change the composition of lipid rafts in the plasma membrane and block the membrane localization of Cdr1 (Pasrija et al., 2005; Prasad et al., 2005; Pasrija et al., 2008). In *C. albicans*, the deletion of the *ERG11* gene led to ergosterol deficiency and a decrease in plasma membrane fluidity (Suchodolski et al., 2019). In the *erg11* Δ /*erg11* Δ null mutant, Cdr1 falls off the plasma membrane to the vacuole in the early logarithmic growth phase, and there is a positioning error (Suchodolski et al., 2019). Similarly, lactic acid can reduce the expression of the *ERG11* gene, thereby affecting the location of Cdr1 and blocking the activity of Cdr1 (Suchodolski et al., 2021). In *C. albicans*, when functional mitochondria are damaged, Cdr1 will be misplaced on the vacuole membrane (Thomas et al., 2013), indicating that functional mitochondria exert post-translational regulation on the level of Cdr1, thus affecting the biological function of Cdr1. The research on the role of Cdr1 in *C. albicans* shows that when cysteine at positions 1056, 1091, 1106 and 1294 is replaced separately, Cdr1 cannot be correctly located on the cell membrane (Prasad et al., 2012). In this study, we found that the calcineurin signaling pathway does not affect the activity of Cdr1, suggesting that the process of sphingolipid transfer has little effect on the integrity of lipid rafts and the membrane localization of Cdr1. In this study, we used FNZ to induce the expression of Cdr1 and increase the MIC values of FLC against pathogenic fungi (Liu and Myers, 2017). We found that pharmacological compromise of sphingolipid biosynthesis by myriocin could occur in the inactivation of Cdr1. It is worth noting that myriocin at sub-MIC could significantly enhance the antifungal activity against clinical *C. albicans* isolates.

Our present study demonstrated that inhibiting sphingolipid biosynthesis by myriocin remarkably increased the antifungal activity of FLC with a broad antifungal spectrum and held therapeutic potential. The synergistic antifungal activity of FLC and myriocin depends on the fact that myriocin blocks membrane localization of Cdr1. Our findings will help overcome the fungal azole resistance caused by Cdr1 activation and open the way for developing new antifungal therapeutics targeted at inhibiting the activity of Cdr1.

Materials and methods

Strains, primers, agents, and cultural conditions

All strains used in this study are listed in [Supplementary Table S1](#). All primers used in this study are listed in [Supplementary Table S2](#). We routinely used a YPD medium (1% (W/V) yeast extract, 2% (W/V) peptone, and 2% (W/V) dextrose) to culture *Candida* strains at 30°C. To prepare the solid medium plates, we added 2% (W/V) agar to the liquid medium. To construct mutant strains, we used a synthetic complete dropout medium (0.67% (W/V) yeast nitrogen base without amino acids, 2% (W/V) dextrose, 2% (W/V) agar, and appropriate amino acid mix) to screen positive colonies. Drug stock solutions were prepared using dimethyl sulfoxide (DMSO) (Sangon Biotech, Shanghai, China) as a solvent for brefeldin A (6.4 mg/ml) (MCE, Shanghai, China), cerulenin (6.4 mg/ml) (MCE, Shanghai, China), cyclosporin A (6.4 mg/ml) (Aladdin, Shanghai, China), FLC (6.4 mg/ml) (Aladdin, Shanghai, China), FNZ (6.4 mg/ml) (MCE, Shanghai, China), geldanamycin (Sangon Biotech, Shanghai, China), menadione (Aladdin, Shanghai, China), myriocin (6.4 mg/ml) (MCE, Shanghai, China), rapamycin (6.4 mg/ml) (MCE, Shanghai, China), staurosporine (6.4 mg/ml) (MCE, Shanghai, China), tacrolimus (6.4 mg/ml) (Aladdin, Shanghai, China), and terbinafine (6.4 mg/ml) (MCE, Shanghai, China).

MIC assays

MIC assays were carried out according to a modified version of the CLSI procedure (M27, fourth edition). Briefly, 100 µl of drugs at two-fold the final concentrations were serially diluted in YPD medium in 96-well culture plates and combined with 100 µl of fungal cultures in which the fungal cell concentration was adjusted to 1×10^3 cells/ml. Plates were incubated at 30°C, and optical densities were read after 48 h with a Spectra Max ID3 plate reader (Molecular Devices, MD, United States); the MIC is defined as the first well with more than 50% growth reduction in terms of OD₆₀₀ values compared to the drug-free cells. Before the 48 h OD₆₀₀ readings, we carefully shook the plates and spotted a representative aliquot of 5 µl of each well on fresh YPD solid medium plates. Recovery plates were incubated

at 30°C for 48 h before being photographed. All assays were performed and repeated three times.

Disk diffusion assays

We carried out disk diffusion assays according to the CLSI M44-A2 guidelines with slight modifications. In short, strains were cultured overnight in a YPD medium at 30°C, cell density was adjusted to 1×10^6 cells/ml in sterile PBS, and 100 µl of cell suspension was streaked on YPD solid medium plates. One paper disk supplemented with 25 µg FLC (Liofilchem, Italy) was placed in the center of each plate. The plates were then incubated for 48 h and photographed.

RNA extractions and quantitative real-time PCR assays

C. albicans strains were grown overnight in YPD medium at 30°C with shaking. Total RNA was extracted using a YeaStar RNA Kit (ZymoResearch, United States). Reverse transcription of the isolated RNA samples was performed by using the PrimeScript™ RT reagent Kit with gDNA Eraser (Takara Bio, Japan). The cDNA abundance was relatively quantified using TB Green® Premix DimerEraser™ (Takara Bio, Japan) in a CFX96™ Real-Time PCR Detection System (Bio-Rad, United States) with the following strategy: 1) 95°C for 30 s; 2) 95°C for 5 s, 50°C for 30 s, and 72°C for 30 s, for 40 cycles. The relative expression level of the *CDR1* gene was normalized to that of the reference *ACT1* gene, and the data were interpreted as fold changes based on the untreated control according to the $2^{-\Delta\Delta C_t}$ method and triplicate measurements were conducted with each sample (Lu et al., 2015).

Disruption of target genes

We used a fusion PCR method to delete the two alleles of target genes from the strain SN152 (Noble and Johnson, 2005). Briefly, the first round of PCR reactions involved the amplification of the flanking sequences (approximately 350-bp) of target genes (with a genomic DNA of SN152 strain and primers P1 and P3 or P4 and P6, in separate reactions) and the selectable marker (*HIS1* or *ARG4*) with a template of plasmid pSN52 or pSN69 and primers universal primer two and universal primer 5. We used primers P1 and P6 to amplify gene deletion cassettes with all three first-round PCR products. We then transformed gene deletion cassettes into the SN152 strain or heterozygous mutant strain using Yeastmaker™ Yeast Transformation System two kit (Clontech Laboratories, United States) and selected on synthetic media containing the necessary auxotrophic supplements for heterozygous or homozygous mutant strains. The primers used for diagnosis of target genes knockouts were, for the 5' junctions, a primer

UCheck plus a primer HIS1left or ARG4left; for the 3' junctions, a primer Dcheck plus a primer HIS1right or ARG4right.

Over-expression of the *CDR1* gene

The over-expressed *CDR1* gene mutant was constructed (Chang et al., 2018). The pCPC158 backbone is amplified using F1/R1 primers, generating a product with a 39 bp flank homology region to the *CDR1* gene. Using this PCR product as a PCR template, the second round of PCR using F2/R2 primers generates the ectopic expression cassette, an N-terminal tagging cassette with 78 bp homology regions to the *CDR1* gene. After transformation and integration, the constitutive *ADH1* promoter located upstream of the *CDR1* gene increased the expression of the *CDR1* gene. Verification primers VP42 and VP43 were used for diagnostic PCR.

C-terminal of proteins tagging GFP and YFP

To tag the C-terminal of Cdr1 using GFP, we adopted a PCR strategy to amplify the desired DNA cassettes in a plasmid pCPC64 (Chang et al., 2018). For the first round of PCR using F1/R1 primers, a product with 39 bp homology regions is generated. Using this product as a PCR template directly, the second round of PCR using F2/R2 primers yields DNA cassettes with 78 bp homology regions to the *CDR1* gene. This product could be transformed into *C. albicans* cells to generate a mutant with the C-terminal tagged Cdr1 with GFP. We used primers Cdr1CUpCheck plus VP8 to check the 5' integration and VP19 plus Cdr1CDnCheck for the 3' integration. We further tagged the C-terminal of Pma1 with YFP in the Cdr1-GFP mutant using a pFA-YFP-ARG4 plasmid as described previously (Gola et al., 2003). Diagnostic PCR used primers Pma1Upcheck plus A2 and A3 plus Pma1Dncheck to confirm the C-terminal of Pma1 tagged with YFP mutant.

Confocal microscopy analysis

The effect of myriocin on the membrane localization of Cdr1 was determined by a confocal laser scanning microscopy (Stellaris, Leica, Germany) in the Cdr1-GFP::Pma1-YFP mutant. *C. albicans* cells were cultured at 30°C and treated without or with 2 µg/ml myriocin for 16 h. The fluorescence of GFP was excited by the laser of 488 nm with an emission of 500–560 nm, and the fluorescence of YFP was excited by the laser of 510 nm with an emission of 527 nm.

Mouse infection model

Groups of C57BL/6 female mice (6–8 weeks) were inoculated via lateral tail vein with 100 µl PBS containing 1×10^5 *C. albicans*

cells. FLC (1 mg/kg) and myriocin (0.5 mg/kg) were administered to the infected mice once a day intraperitoneally for 3 days, starting 2 h after the injection with *C. albicans*. Mice were monitored daily for survival for 28 days. Kaplan-Meier analyses were used to indicate the survival probabilities, and Log-rank testing was used to evaluate the significance of survival curves. The mice were sacrificed 2 days after the last administration; the left kidney of each mouse was taken and homogenized in sterile PBS, diluted and coated on the YPD solid medium plates, and incubated at 30°C for 48 h before counting colonies; The right kidney of the animal was taken for histopathology by periodic acid-Schiff (PAS) staining to visualize the fungal burden. The Tongji University Animal Care Committee approved all experimental procedures involving animals (No.: TJAA00322102).

Data availability statement

The raw data supporting the conclusion of this article will be made available by the authors, without undue reservation.

Ethics statement

The animal study was reviewed and approved by the Tongji University Animal Care Committee.

Author contributions

HW conducted most of the experiments and performed data analysis. ZJ, YF, and TY helped to construct and confirm mutant strains. HL and HW wrote the manuscript draft. HW, ZJ, YF, HL, YC, and YJ discussed and analyzed the data. YJ, YC, and HL conceived the idea. YJ directed the experiments.

Funding

This study was supported by the National Key Research and Development Program of China (2021YFC2300404), the National Natural Science Foundation of China (No. 81673478 and No. 82020108032), the Shanghai Key Basic Research Project (No. 19JC1414900) and the Innovation Program of Shanghai Municipal Education Commission (202101070007-E00094).

Acknowledgments

We thank Dr. Suzanne M. Noble (University of California-San Francisco) for providing *C. albicans* strain

SN152 and plasmids pSN52 and pSN69. We acknowledge Dr. Peng Chang for providing a plasmid pCPC64 and pCPC158.

Conflict of interest

The authors declare that the research was conducted in the absence of any commercial or financial relationships that could be construed as a potential conflict of interest.

Publisher's note

All claims expressed in this article are solely those of the authors and do not necessarily represent those of their affiliated organizations, or those of the publisher, the editors and the reviewers. Any product that may be evaluated in this article, or claim that may be made by its manufacturer, is not guaranteed or endorsed by the publisher.

Supplementary material

The Supplementary Material for this article can be found online at: <https://www.frontiersin.org/articles/10.3389/fphar.2022.1101553/full#supplementary-material>

References

- Azzi, J. R., Sayegh, M. H., and Mallat, S. G. (2013). Calcineurin inhibitors: 40 years later, can't live without. *J. Immunol.* 191, 5785–5791. doi:10.4049/jimmunol.1390055
- Borgeat, V., Brandalise, D., Grenouillet, F., and Sanglard, D. (2021). Participation of the ABC transporter CDR1 in azole resistance of *Candida lusitanae*. *J. Fungi (Basel)* 7, 760. doi:10.3390/jof7090760
- Carolus, H., Pierson, S., Munoz, J. F., Subotic, A., Cruz, R. B., Cuomo, C. A., et al. (2021). Genome-Wide analysis of experimentally evolved *Candida auris* reveals multiple novel mechanisms of multidrug resistance. *mBio* 12, 033333–e3420. doi:10.1128/mBio.03333-20
- Chang, P., Wang, W., Igarashi, Y., Luo, F., and Chen, J. (2018). Efficient vector systems for economical and rapid epitope-tagging and overexpression in *Candida albicans*. *J. Microbiol. Methods* 149, 14–19. doi:10.1016/j.mimet.2018.04.016
- Cowen, L. E. (2009). Hsp90 orchestrates stress response signaling governing fungal drug resistance. *PLoS Pathog.* 5, e1000471. doi:10.1371/journal.ppat.1000471
- Cowen, L. E., and Lindquist, S. (2005). Hsp90 potentiates the rapid evolution of new traits: Drug resistance in diverse fungi. *Science* 309, 2185–2189. doi:10.1126/science.1118370
- Dolan, K., Montgomery, S., Buchheit, B., Didone, L., Wellington, M., and Krysan, D. J. (2009). Antifungal activity of tamoxifen: *In vitro* and *in vivo* activities and mechanistic characterization. *Antimicrob. Agents Chemother.* 53, 3337–3346. doi:10.1128/AAC.01564-08
- Epp, E., Vanier, G., Harcus, D., Lee, A. Y., Jansen, G., Hallett, M., et al. (2010). Reverse genetics in *Candida albicans* predicts ARF cycling is essential for drug resistance and virulence. *PLoS Pathog.* 6, e1000753. doi:10.1371/journal.ppat.1000753
- Galkina, K. V., Okamoto, M., Chibana, H., Knorre, D. A., and Kajiura, S. (2020). Deletion of CDR1 reveals redox regulation of pleiotropic drug resistance in *Candida glabrata*. *Biochimie* 170, 49–56. doi:10.1016/j.biochi.2019.12.002
- Gao, J., Wang, H., Li, Z., Wong, A. H., Wang, Y. Z., Guo, Y., et al. (2018). *Candida albicans* gains azole resistance by altering sphingolipid composition. *Nat. Commun.* 9, 4495. doi:10.1038/s41467-018-06944-1
- Gola, S., Martin, R., Walther, A., Dunkler, A., and Wendland, J. (2003). New modules for PCR-based gene targeting in *Candida albicans*: Rapid and efficient gene targeting using 100 bp of flanking homology region. *Yeast* 20, 1339–1347. doi:10.1002/yea.1044
- He, Q., Johnson, V. J., Osuchowski, M. F., and Sharma, R. P. (2004). Inhibition of serine palmitoyltransferase by myriocin, a natural mycotoxin, causes induction of c-myc in mouse liver. *Mycopathologia* 157, 339–347. doi:10.1023/b:myco.0000024182.04140.95
- Hurst, L. R., and Fratti, R. A. (2020). Lipid rafts, sphingolipids, and ergosterol in yeast vacuole fusion and maturation. *Front. Cell Dev. Biol.* 8, 539. doi:10.3389/fcell.2020.00539
- James, J. E., Lamping, E., Santhanam, J., Cannon, R. D., Abd Razak, M. F., Zakaria, L., et al. (2021). A 23 bp cyp51A promoter deletion associated with voriconazole resistance in clinical and environmental isolates of *Neocosmospora keratoplastica*. *Front. Microbiol.* 12, 272. doi:10.3389/fmicb.2020.00272
- Jha, S., Dabas, N., Karnani, N., Saini, P., and Prasad, R. (2004). ABC multidrug transporter Cdr1p of *Candida albicans* has divergent nucleotide-binding domains which display functional asymmetry. *FEMS Yeast Res.* 5, 63–72. doi:10.1016/j.femsyr.2004.07.002
- Jia, X. M., Wang, Y., Jia, Y., Gao, P. H., Xu, Y. G., Wang, L., et al. (2009). RTA2 is involved in calcineurin-mediated azole resistance and sphingoid long-chain base release in *Candida albicans*. *Cell Mol. Life Sci.* 66, 122–134. doi:10.1007/s00018-008-8409-3
- Kasahara, K. (2021). Physiological function of FKBP12, a primary target of rapamycin/FK506: A newly identified role in transcription of ribosomal protein genes in yeast. *Curr. Genet.* 67, 383–388. doi:10.1007/s00294-020-01142-3
- Kim, S. H., Iyer, K. R., Pardeshi, L., Munoz, J. F., Robbins, N., Cuomo, C. A., et al. (2019). Genetic analysis of *Candida auris* implicates Hsp90 in morphogenesis and azole tolerance and Cdr1 in azole resistance. *mBio* 10, 025299–e2618. doi:10.1128/mBio.02529-18
- LaFayette, S. L., Collins, C., Zaas, A. K., Schell, W. A., Betancourt-Quiroz, M., Gunatilaka, A. A., et al. (2010). PKC signaling regulates drug resistance of the fungal pathogen *Candida albicans* via circuitry comprised of Mkc1, calcineurin, and Hsp90. *PLoS Pathog.* 6, e1001069. doi:10.1371/journal.ppat.1001069
- Liu, Q., Guo, X., Jiang, G., Wu, G., Miao, H., Liu, K., et al. (2020). NADPH-cytochrome P450 reductase Ccr1 is a target of tamoxifen and participates in its

SUPPLEMENTARY FIGURE S1

Deletions of target genes (the CMP1, CRZ1, RTA2, CDR1 genes) were diagnosed by PCR, for the 5' junctions, a primer UCheck plus a primer HIS1left or ARG4left; (A) for the 3' junctions, a primer Dcheck plus a primer HIS1right or ARG4right. (B) PADH1-CDR1, cmp1Δ/cmp1Δ::PADH1-CDR1, crz1Δ/crz1Δ::PADH1-CDR1, and rta2Δ/rta2Δ::PADH1-CDR1 mutants ectopic over-expression the CDR1 gene were checked by the primers Cdr1NUpcheck plus VP42 and the primers VP43 plus Cdr1NDncheck. (C) We determined the expression of the CDR1 gene in the wild-type strain (SN152) and mutants using qRT-PCR.

SUPPLEMENTARY FIGURE S2

Dose-matrix titration assays (incubated in a YPD medium at 30°C for 48 h) were used to evaluate the synergistic antifungal activity of FLC and antifungal agents, (A) including cyclosporine A, (B) tacrolimus, (C) Tamoxifen, (D) staurosporine, (E) geldanamycin, (F) brefeldin A, (G) tunicamycin, (H) menadione, (I) terbinafine, (J) cerulenin, (K) rapamycin, (L) myriocin.

SUPPLEMENTARY FIGURE S3

Myriocin did not enhance the antifungal activity of FLC against *C. glabrata* ($n = 13$), *C. krusei* ($n = 9$), *C. parapsilosis* ($n = 43$), and *C. tropicalis* ($n = 12$).

SUPPLEMENTARY FIGURE S4

The qRT-PCR analysis demonstrated that myriocin (0.5 μg/mL) induced the expression of the CDR1 gene.

SUPPLEMENTARY FIGURE S5

(A) The C-termini of Cdr1 with a GFP tag mutant was checked by PCR using the Cdr1CUpCheck plus VP8 and the primers VP19 plus Cdr1CDnCheck. (B) The C-termini of Pma1 with a YFP tag mutant was diagnosed by PCR using the primers Pma1UpCheck plus A2 and the primers A3 plus Pma1DnCheck.

antifungal activity via regulating cell wall integrity in fission yeast. *Antimicrob. Agents Chemother.* 64, 000799–e120. doi:10.1128/AAC.00079-20

Liu, Z., and Myers, L. C. (2017). Mediator tail module is required for *tac1*-activated CDR1 expression and azole resistance in *Candida albicans*. *Antimicrob. Agents Chemother.* 61, 013422–e1417. doi:10.1128/AAC.01342-17

Lu, H., Shrivastava, M., Whiteway, M., and Jiang, Y. (2021). *Candida albicans* targets that potentially synergize with fluconazole. *Crit. Rev. Microbiol.* 47, 323–337. doi:10.1080/1040841x.2021.1884641

Lu, H., Yao, X. W., Whiteway, M., Xiong, J., Liao, Z. B., Jiang, Y. Y., et al. (2015). Loss of RPS41 but not its paralog RPS42 results in altered growth, filamentation and transcriptome changes in *Candida albicans*. *Fungal Genet. Biol.* 80, 31–42. doi:10.1016/j.fgb.2015.03.012

Marchetti, O., Moreillon, P., Entenza, J. M., Vouillamoz, J., Glauser, M. P., Bille, J., et al. (2003). Fungicidal synergism of fluconazole and cyclosporine in *Candida albicans* is not dependent on multidrug efflux transporters encoded by the CDR1, CDR2, CaMDR1, and FLU1 genes. *Antimicrob. Agents Chemother.* 47, 1565–1570. doi:10.1128/aac.47.5.1565-1570.2003

Monk, B. C., and Goffeau, A. (2008). Outwitting multidrug resistance to antifungals. *Science* 321, 367–369. doi:10.1126/science.1159746

Noble, S. M., and Johnson, A. D. (2005). Strains and strategies for large-scale gene deletion studies of the diploid human fungal pathogen *Candida albicans*. *Eukaryot. Cell* 4, 298–309. doi:10.1128/EC.4.2.298-309.2005

Nomura, S., Horiuchi, T., Omura, S., and Hata, T. (1972). The action mechanism of cerulenin. I. Effect of cerulenin on sterol and fatty acid biosynthesis in yeast. *J. Biochem.* 71, 783–796. doi:10.1093/oxfordjournals.jbchem.a129827

Pasrija, R., Panwar, S. L., and Prasad, R. (2008). Multidrug transporters CaCdr1p and CaMdr1p of *Candida albicans* display different lipid specificities: Both ergosterol and sphingolipids are essential for targeting of CaCdr1p to membrane rafts. *Antimicrob. Agents Chemother.* 52, 694–704. doi:10.1128/AAC.00861-07

Pasrija, R., Prasad, T., and Prasad, R. (2005). Membrane raft lipid constituents affect drug susceptibilities of *Candida albicans*. *Biochem. Soc. Trans.* 33, 1219–1223. doi:10.1042/BST20051219

Perlin, D. S., Rautemaa-Richardson, R., and Alastruey-Izquierdo, A. (2017). The global problem of antifungal resistance: Prevalence, mechanisms, and management. *Lancet Infect. Dis.* 17, e383–e392. doi:10.1016/S1473-3099(17)30316-X

Prasad, R., Balzi, E., Banerjee, A., and Khandelwal, N. K. (2019). All about CDR transporters: Past, present, and future. *Yeast* 36, 223–233. doi:10.1002/yea.3356

Prasad, R., Shah, A. H., Sanwal, H., and Kapoor, K. (2012). Alanine scanning of all cysteines and construction of a functional cysteine-less Cdr1p, a multidrug ABC transporter of *Candida albicans*. *Biochem. Biophys. Res. Commun.* 417, 508–513. doi:10.1016/j.bbrc.2011.11.150

Prasad, T., Saini, P., Gaur, N. A., Vishwakarma, R. A., Khan, L. A., Haq, Q. M., et al. (2005). Functional analysis of CalPT1, a sphingolipid biosynthetic gene involved in multidrug resistance and morphogenesis of *Candida albicans*. *Antimicrob. Agents Chemother.* 49, 3442–3452. doi:10.1128/AAC.49.8.3442-3452.2005

Rosenberg, A., Ene, I. V., Bibi, M., Zakin, S., Segal, E. S., Ziv, N., et al. (2018). Antifungal tolerance is a subpopulation effect distinct from resistance and is associated with persistent candidemia. *Nat. Commun.* 9, 2470. doi:10.1038/s41467-018-04926-x

Ryder, N. S. (1992). Terbinafine: Mode of action and properties of the squalene epoxidase inhibition. *Br. J. Dermatol.* 126 (39), 2–7. doi:10.1111/j.1365-2133.1992.tb00001.x

Sa, N. P., Lima, C. M., Lino, C. I., Barbeira, P. J. S., Baltazar, L. M., Santos, D. A., et al. (2017). Heterocycle thiazole compounds exhibit antifungal activity through increase in the production of reactive oxygen species in the cryptococcus neoformans-cryptococcus gattii species complex. *Antimicrob. Agents Chemother.* 61, e02700–e02716. doi:10.1128/AAC.02700-16

Sanglard, D., Ischer, F., Marchetti, O., Entenza, J., and Bille, J. (2003). Calcineurin A of *Candida albicans*: Involvement in antifungal tolerance, cell morphogenesis and virulence. *Mol. Microbiol.* 48, 959–976. doi:10.1046/j.1365-2958.2003.03495.x

Sanglard, D., Ischer, F., Monod, M., and Bille, J. (1996). Susceptibilities of *Candida albicans* multidrug transporter mutants to various antifungal agents and other metabolic inhibitors. *Antimicrob. Agents Chemother.* 40, 2300–2305. doi:10.1128/AAC.40.10.2300

Sellam, A., Askew, C., Epp, E., Lavoie, H., Whiteway, M., and Nantel, A. (2009). Genome-wide mapping of the coactivator Ada2p yields insight into the functional roles of SAGA/ADA complex in *Candida albicans*. *Mol. Biol. Cell* 20, 2389–2400. doi:10.1091/mbc.e08-11-1093

Shukla, S., Saini, P., Smriti, A., Jha, S., Ambudkar, S. V., and Prasad, R. (2003). Functional characterization of *Candida albicans* ABC transporter Cdr1p. *Eukaryot. Cell* 2, 1361–1375. doi:10.1128/ec.2.6.1361-1375.2003

Singh, S. D., Robbins, N., Zaas, A. K., Schell, W. A., Perfect, J. R., and Cowen, L. E. (2009). Hsp90 governs echinocandin resistance in the pathogenic yeast *Candida albicans* via calcineurin. *PLoS Pathog.* 5, e1000532. doi:10.1371/journal.ppat.1000532

Song, J., Liu, X., and Li, R. (2020). Sphingolipids: Regulators of azole drug resistance and fungal pathogenicity. *Mol. Microbiol.* 114, 891–905. doi:10.1111/mmi.14586

Suchodolski, J., Muraszko, J., Bernat, P., and Krasowska, A. (2019). A crucial role for ergosterol in plasma membrane composition, localisation, and activity of Cdr1p and H(+)-ATPase in *Candida albicans*. *Microorganisms* 7, 378. doi:10.3390/microorganisms7100378

Suchodolski, J., Muraszko, J., Bernat, P., and Krasowska, A. (2021). Lactate like fluconazole reduces ergosterol content in the plasma membrane and synergistically kills *Candida albicans*. *Int. J. Mol. Sci.* 22, 5219. doi:10.3390/ijms22105219

Teixeira, V., and Costa, V. (2016). Unraveling the role of the Target of Rapamycin signaling in sphingolipid metabolism. *Prog. Lipid Res.* 61, 109–133. doi:10.1016/j.plipres.2015.11.001

Teo, J. Q., Lee, S. J., Tan, A. L., Lim, R. S., Cai, Y., Lim, T. P., et al. (2019). Molecular mechanisms of azole resistance in *Candida* bloodstream isolates. *BMC Infect. Dis.* 19, 63. doi:10.1186/s12879-019-3672-5

Thomas, E., Roman, E., Claypool, S., Manzoor, N., Pla, J., and Panwar, S. L. (2013). Mitochondria influence CDR1 efflux pump activity, Hog1-mediated oxidative stress pathway, iron homeostasis, and ergosterol levels in *Candida albicans*. *Antimicrob. Agents Chemother.* 57, 5580–5599. doi:10.1128/AAC.00889-13

Tsao, S., Rahkhoodae, F., and Raymond, M. (2009). Relative contributions of the *Candida albicans* ABC transporters Cdr1p and Cdr2p to clinical azole resistance. *Antimicrob. Agents Chemother.* 53, 1344–1352. doi:10.1128/AAC.00926-08

Xu, D., Jiang, B., Ketela, T., Lemieux, S., Veillette, K., Martel, N., et al. (2007). Genome-wide fitness test and mechanism-of-action studies of inhibitory compounds in *Candida albicans*. *PLoS Pathog.* 3, e92. doi:10.1371/journal.ppat.0030092

Xu, Y., Lu, H., Zhu, S., Li, W. Q., Jiang, Y. Y., Berman, J., et al. (2021). Multifactorial mechanisms of tolerance to ketoconazole in *Candida albicans*. *Microbiol. Spectr.* 9, e0032121. doi:10.1128/Spectrum.00321-21

Xu, Y., Wang, Y., Yan, L., Liang, R. M., Dai, B. D., Tang, R. J., et al. (2009). Proteomic analysis reveals a synergistic mechanism of fluconazole and berberine against fluconazole-resistant *Candida albicans*: Endogenous ROS augmentation. *J. Proteome Res.* 8, 5296–5304. doi:10.1021/pr9005074

Yu, Q., Ding, X., Xu, N., Cheng, X., Qian, K., Zhang, B., et al. (2013). *In vitro* activity of verapamil alone and in combination with fluconazole or tunicamycin against *Candida albicans* biofilms. *Int. J. Antimicrob. Agents* 41, 179–182. doi:10.1016/j.ijantimicag.2012.10.009



OPEN ACCESS

EDITED BY

Rong Wang,
People's Liberation Army Joint Logistics
Support Force 940th Hospital, China

REVIEWED BY

Li Zhiling,
Shanghai Jiao Tong University, China
Mohammed E. El-Asrag,
University of Birmingham, United Kingdom

*CORRESPONDENCE

Masato Kobayashi,
✉ kobayashi@mhs.mp.kanazawa-u.ac.jp

SPECIALTY SECTION

This article was submitted to Drug
Metabolism and Transport,
a section of the journal
Frontiers in Pharmacology

RECEIVED 13 October 2022

ACCEPTED 29 December 2022

PUBLISHED 11 January 2023

CITATION

Sato K, Seki T, Mizutani A, Muranaka Y,
Hirota S, Nishi K, Yamazaki K, Nishii R,
Nakanishi T, Tamai I, Kawai K and
Kobayashi M (2023), A single high-dose
irradiation changes accumulation of
methotrexate and gene expression levels
of SLC and ABC transporters in
cancer cells.
Front. Pharmacol. 13:1069321.
doi: 10.3389/fphar.2022.1069321

COPYRIGHT

© 2023 Sato, Seki, Mizutani, Muranaka,
Hirota, Nishi, Yamazaki, Nishii, Nakanishi,
Tamai, Kawai and Kobayashi. This is an
open-access article distributed under the
terms of the [Creative Commons
Attribution License \(CC BY\)](https://creativecommons.org/licenses/by/4.0/). The use,
distribution or reproduction in other
forums is permitted, provided the original
author(s) and the copyright owner(s) are
credited and that the original publication in
this journal is cited, in accordance with
accepted academic practice. No use,
distribution or reproduction is permitted
which does not comply with these terms.

A single high-dose irradiation changes accumulation of methotrexate and gene expression levels of SLC and ABC transporters in cancer cells

Kakeru Sato¹, Tatsuya Seki¹, Asuka Mizutani², Yuka Muranaka¹,
Shiho Hirota¹, Kodai Nishi³, Kana Yamazaki⁴, Ryuichi Nishii⁴,
Takeo Nakanishi⁵, Ikumi Tamai⁶, Keiichi Kawai^{2,7} and
Masato Kobayashi^{2*}

¹Division of Health Sciences, Graduate School of Medical Sciences, Kanazawa University, Kanazawa, Japan, ²Faculty of Health Sciences, Institute of Medical, Pharmaceutical and Health Sciences, Kanazawa University, Kanazawa, Japan, ³Department of Radioisotope Medicine, Atomic Bomb Disease Institute, Nagasaki University, Nagasaki, Japan, ⁴Department of Molecular Imaging and Theranostics, Institute for Quantum Medical Science, Quantum Life and Medical Science Directorate, National Institutes for Quantum Science and Technology, Chiba, Japan, ⁵Faculty of Pharmacy, Takasaki University of Health and Welfare, Takasaki, Gunma, Japan, ⁶Faculty of Pharmaceutical Sciences, Institute of Medical, Pharmaceutical and Health Sciences, Kanazawa University, Kanazawa, Japan, ⁷Biomedical Imaging Research Center, University of Fukui, Fukui, Japan

Chemoradiotherapy is frequently used to treat cancer. Stereotactic body radiotherapy (SBRT) is a single high-dose radiotherapy used to treat a variety of cancers. The anticancer drug methotrexate (MTX) shows affinity for solute carrier (SLC) and ATP-binding cassette (ABC) transporters. This study investigated relationships between accumulation of methotrexate and gene expression levels of solute carrier and ATP-binding cassette transporters in cancer cells after a single and high-dose X-ray irradiation. Cancer cell lines were selected from lung and cervical cancer cell line that are commonly used for stereotactic body radiotherapy and effective with methotrexate. We examined expression levels of organic anion-transporting polypeptide (OATP)1B1, OATP1B3, OATP1B7, and organic anion transporter (OAT)1 as solute carrier transporters and multidrug resistance-associated protein (MRP)1 and MRP2 as ATP-binding cassette transporters, using real-time polymerase chain reaction and accumulation of ³H-MTX in cancer cells after 10-Gy irradiation, assuming stereotactic body radiotherapy. Cells were divided into three groups: Control without irradiation; 4 h after irradiation; and 24 h after irradiation. In control, gene expression levels of OAT1 in all cells was below the limit of measurement. After irradiation, gene expression levels of OATP1B1/1B3/1B7 showed changes in each cell line. Gene expression levels of MRP1/2 tended to increase after irradiation. Gene expression levels of OATP1B1/1B3/1B7 were much lower than those of MRP1/2. Accumulation of ³H-MTX tended to decrease over time after irradiation. Irradiation of cancer cells thus alters gene expression levels of both solute carrier transporters (OATP1B1/1B3/1B7) and ABC transporters (MRP1/2) and decreases accumulation of ³H-MTX in cancer cells over time due to elevated expression of MRP1/2.

KEYWORDS

chemoradiotherapy, methotrexate, SLC transporter, ABC transporters, stereotactic body radiotherapy, x-ray, irradiation

1 Introduction

Chemoradiotherapy combines chemotherapy with anticancer drugs and radiotherapy to treat cancer. Chemoradiotherapy can be divided into three categories according to the timing of anticancer drug administration: Neoadjuvant; concurrent; and adjuvant (Baldini et al., 2018). The accumulation of anticancer drugs in cancer cells usually depends on gene expression levels of solute carrier (SLC) and ATP-binding cassette (ABC) transporters (Nakanishi, 2007; Carmichael and Day, 2022). SLC transporters mainly contribute to the uptake of anticancer drugs, while ABC transporters are involved in their excretion (Nakanishi, 2007; Carmichael and Day, 2022).

In radiotherapy, stereotactic radiotherapy involves the delivery of higher doses (7–18 Gy or more) than the usual single-beam dose (1.8–2 Gy) and is used to treat various cancers (Marcrom et al., 2017; Jardel et al., 2020; Sarudis et al., 2021; Ugurluer et al., 2021). Stereotactic radiotherapy was originally used to treat brain cancers, with stereotactic body radiotherapy (SBRT) representing the application of this technology to the trunk of the body, such as for lung and liver cancers (Song et al., 2004; Donovan and Swaminath, 2018; Tandberg et al., 2018; Sarudis et al., 2021; Ugurluer et al., 2021). SBRT has also been shown to be effective against cervical cancer, which is still frequently treated using intracavitary small-source radiotherapy (Ito et al., 2019; Facondo et al., 2021).

Methotrexate (MTX) is a folate antagonist used as an anticancer drug (Visentin et al., 2012). This agent stops cancer growth by preventing the uptake of folic acid, which is necessary in DNA synthesis (Yu et al., 2020). MTX is effective against lung and cervical cancers, where SBRT also appears useful (Conroy et al., 1976; Smyth and Ford, 1981). MTX has shown affinity for the SLC transporters organic anion-transporting polypeptide (OATP) and organic anion transporter (OAT), and the ABC transporters multidrug resistance-associated protein (MRP), multidrug resistance protein (MDR), and breast cancer resistance protein (BCRP) (Hagenbuch and Meier, 2004; Nakanishi, 2007; Murakami and Mori, 2012; Gao et al., 2021). While irradiation increases the expressions of MRP1 and MRP2, contributing to the efflux of MTX (Henness et al., 2002; Bartkowiak et al., 2009), the effects of irradiation on SLC transporters have not been examined. Further, correlations between the kinetics of anticancer drugs including MTX and SLC and ABC transporters after irradiation have yet to be clarified. The purpose of this study was thus to investigate the relationships between accumulation of MTX and expression levels of the genes for SLC and ABC transporters in cancer cells after irradiation. Temporal changes in MTX accumulation in cancer cells after a single and high-dose irradiations assuming SBRT were examined.

2 Material and methods

2.1 Cancer cell lines

The human-derived lung adenocarcinoma cancer cell lines NCI-H441 (American Type Culture Collection, Manassas, VA, United States) and PC-14 (RIKEN Cell Bank, Tsukuba, Japan) were used. The HeLa human-derived cervical cancer line (RIKEN Cell Bank) was also used. H441, PC-14 and HeLa cell lines were cultivated using RPMI-1640 (FUJIFILM Wako Chemical, Osaka, Japan), Dulbecco's Modified Eagle's Medium (FUJIFILM Wako

Chemicals) and Eagle's minimum essential medium (FUJIFILM Wako Chemicals) mixed with 10% fetal bovine serum and 1% sodium pyruvate at 37°C under conditions of 5% CO₂.

2.2 Irradiation of cell lines

After achieving 70–80% confluence in a 10-cm diameter plate, each cell line was irradiated with a single 10-Gy X-ray (dose rate, 1.0 Gy/min) using X-ray irradiation equipment (MBR1520R-3; Hitachi, Tokyo, Japan). Cells were divided into three groups: Control without irradiation; 4 h after irradiation; and 24 h after irradiation.

2.3 RNA extraction and quality assessment

An RNeasy Plus Mini Kit (QIAGEN, Hilden, Germany) was used to extract RNA from the cancer cells used in this study. The quality of the extracted RNA was evaluated using the RNA integrity number (RIN) as an indicator of quality. The RIN is expressed as a number from 1 to 10, with a higher number reflecting higher quality of RNA. An Affinity Script QPCR cDNA Synthesis kit (Agilent Technologies, Tokyo, Japan) was used for synthesizing cDNA.

2.4 Conducting real-time polymerase chain reaction (PCR)

Real-time PCR was performed using an AriaMx 5P system (Agilent Technologies). *OATP1B1/1B3/1B7* as the combination of *OATP1B1*, *OATP1B3* and *OATP1B7* for SLC transporters (because the primer sequences of these transporters are quite similar) and *MRP1* and *MRP2* for ABC transporters were selected as the targets of PCR. The gene *ACBT* for β -actin was used as the internal control gene, as a housekeeping gene that is constantly expressed in all cells. Also, *ACBT* was used to correct for differences in the amounts of initial RNA and cDNA due to differences in sample organization and purification methods. Primer design was outsourced to Eurofins Genomics (Tokyo, Japan). Preparation of cloned plasmids used for the creation of standard curves was outsourced to GenScript (Tokyo, Japan). Primer sequences and concentrations of the genes used are shown in Table 1. A 20- μ L volume of PCR reaction solution contained 10 μ L of Brilliant III Ultra-Fast SYBR Green QPCR Master Mix (Agilent Technologies), .4 μ L of primer, 1 μ L of template (10–50 ng of cDNA or cloned plasmid) and 8.6 μ L of nuclease-free water. The thermal profile of reaction conditions was: 95°C hot start for 3 min, then 45 cycles of amplification at 95°C for 5 s and 62°C for 15 s, ending with 95°C for 1 min, 55°C for 30 s and 95°C for 30 s.

2.5 Accumulation of ³H-MTX in cancer cells

Each cell was seeded at 1.0 $\times 10^5$ cells/well in 12-well plastic plates. At about 24 h after seeding, cells were irradiated and divided into three groups: 4 h after irradiation; 24 h after irradiation; and control without irradiation. Each group was pre-incubated for 5 min in phosphate-buffered saline (PBS), then incubated with ³H-MTX (10 kBq/well) for 5, 10, 30, or 60 min. After incubation, cells were washed twice with

TABLE 1 Primer sequences and concentrations of the used genes.

Transporters/Housekeeping gene		Gene symbol	Primer sequence		Concentration (nM)
			Forward	Reverse	
OATP1B1/1B3/1B7	OATP1B1	<i>SLCO1B1</i>	GCACTGGGTTTCCACTCAAT	CAGTTGTTGGTGGACCACTTT	200
	OATP1B3	<i>SLCO1B3</i>	GCAATGGGTTTCCAGTCAAT	AGCTGTTGGTGGACCACTTC	
	OATP1B7	<i>SLCO1B7</i>	GCAATCGGCTTCCATTCAAT	AGCTGTTGGTGGACCACTTC	
OAT1		<i>SLC22A6</i>	GCGCCTTTTTCCTTCT	TTCCCGCTTCCCATGATC	300
MRP1		<i>ABCC1</i>	GACCATGAATGTGCAGAAGG	GCCTCATCCAACACAAGGAT	100
MRP2		<i>ABCC2</i>	CTGCGGCTCTCATTCACTCT	GCCAAGTTGGATAGGGTCAA	
ACTB		<i>ACTB</i>	CCAACCGCGAGAAGATGA	CCAGAGGCGTACAGGGATAG	

TABLE 2 Gene expression levels of measured drug transporter in each cell by conducting Real-time PCR.

Transporter	Condition	Gene expression level ($\times 10^5$)		
		H441	PC-14	HeLa
OATP1B1/1B3/1B7	Control	13.0	0.01	0.04
	4 h after irradiation	10.5	0.05	0.06
	24 h after irradiation	10.0	0.04	0.09
MRP1	Control	64.5	56.1	34.5
	4 h after irradiation	50.3	78.9	51.0
	24 h after irradiation	79.3	90.3	70.8
MRP2	Control	0.30	1.80	56.7
	4 h after irradiation	0.40	2.30	60.2
	24 h after irradiation	0.80	2.70	98.0
MRP1/2	Control	64.8	57.9	91.2
	4 h after irradiation	50.7	81.2	111.2
	24 h after irradiation	80.1	93.0	168.8

600 μ L of PBS and lysed by 500 μ L of .1 M NaOH. Three hundred microliters of cell lysate were mixed with 5 mL of ULTIMA GOLD (Perkin Elmer, Waltham, MA, United States) and the radioactivity of the mixture was measured using a liquid scintillation counter (LSC-5100; Hitachi Aloka Medical, Tokyo, Japan). The results are shown as the percent injected dose/number of living cells measured by an automatic cell counter (LUNA FX7TM; Logo Biosystems, Gyeonggi-do, South Korea).

3 Results

All cell lines showed RIN >9, indicating high-quality RNA. Measured expression levels of drug transporter genes in each cell line in the three groups by conducting Real-time PCR are shown in Table 2. For SLC transporters, the total gene expression level of OATP1B1/1B3/1B7 was higher in H441 cells than in PC-14 or

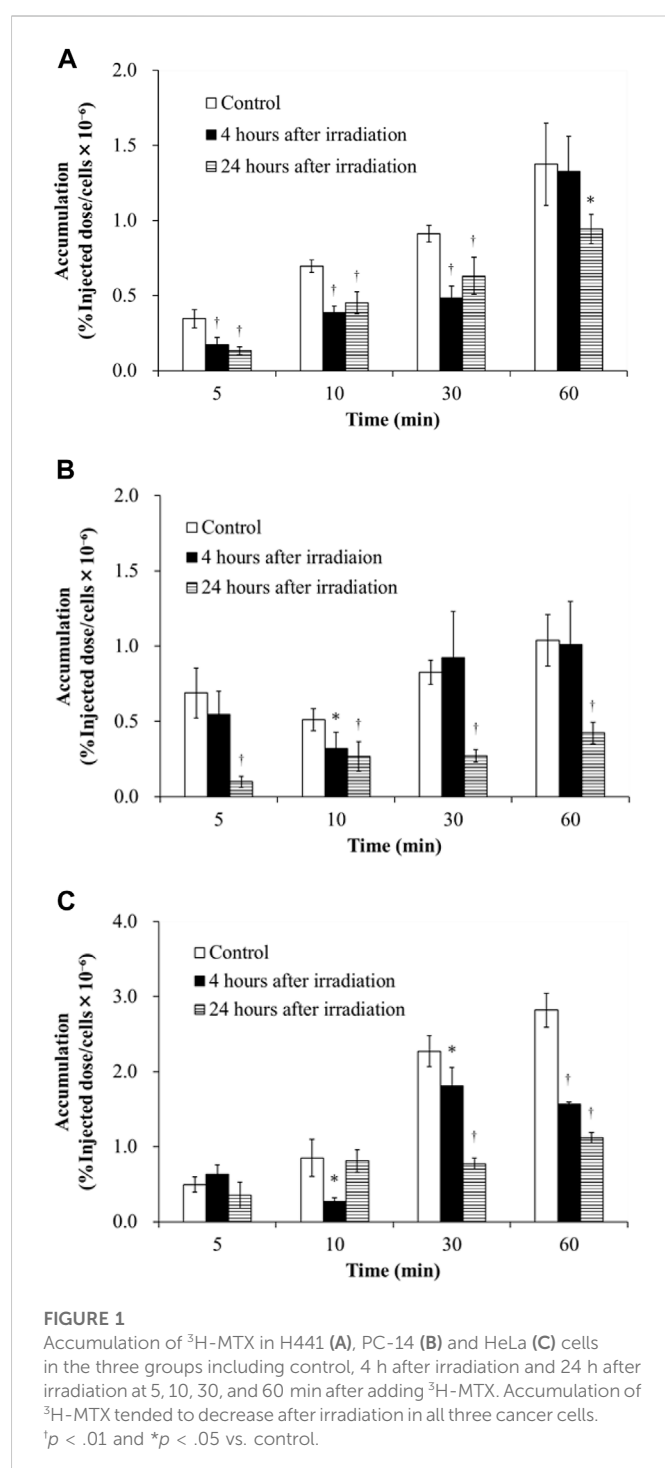
HeLa cells, but OAT1 in all cells was below the limit of measurement. After cell irradiation, total gene expression levels of OATP1B1/1B3/1B7 decreased in H441 in comparison to before irradiation (control), but increased slightly in PC-14 and HeLa cells.

For ABC transporters, expression levels of MRP1/2, as the combination of MRP1 and MRP2, were higher than levels of OATP1B1/1B3/1B7 and OAT1 in control samples of all cancer cells. In control samples, MRP1/2 showed higher expression in HeLa than in H441 or PC-14. In addition, H441 and PC-14 showed higher gene expression levels of MRP1 than MRP2, while HeLa displayed higher gene expression levels of MRP2 than MRP1. After irradiation, gene expression levels of MRP1/2 tended to increase over time in all cancer cell lines.

Figure 1 shows the accumulation of ³H-MTX in H441, PC-14 and HeLa cells in the control, 4 h after irradiation and 24 h after irradiation groups at 5, 10, 30, and 60 min after ³H-MTX injection. Accumulation of ³H-MTX was decreased at 4 and 24 h after irradiation in H441 cells and at 24 h after irradiation in PC-14 cells. In HeLa cells, accumulation of ³H-MTX was significantly decreased compared to control from 10 min after ³H-MTX injection in the 4 h after irradiation group and from 30 min after ³H-MTX injection in the 24 h after irradiation group.

4 Discussion

Consideration of the effects of irradiation on the kinetics of anticancer drugs in chemoradiotherapy is important. This study examined how the accumulation of ³H-MTX in cancer cells was impacted by the effects of gene expression levels for SLC and ABC transporters after X-ray irradiation. Since the degree to which gene expression levels of SLC and ABC transporters are changed under the influence of irradiation was unknown, we examined these gene expressions after irradiation by conducting Real-time PCR (Table 2). Total gene expression levels of OATP1B1/1B3/1B7 decreased after irradiation in H441 cells compared to control, but increased slightly in PC-14 and HeLa cells. For ABC transporters, total gene expression levels of MRP1/2 were higher than OATP1B1/1B3/1B7 and OAT1 in all cancer cell lines under the control conditions. Accumulation of ³H-MTX tended to decrease over time after irradiation in all cancer cell lines (Figure 1), and accumulation was significantly decreased at 24 h.



The correlation between accumulation of ^3H -MTX and gene expression levels of drug transporters is discussed for each cell line. In H441 cells (Table 2), gene expression levels of OATP1B1/1B3/1B7 decreased over time, and MRP1/2 was slightly decreased at 4 h after irradiation in comparison with control and increased further at 24 h after irradiation. Accumulation of ^3H -MTX in H441 cells was significantly decreased compared to control at 5, 10, and 30 min after adding ^3H -MTX (Figure 1A). Although we selected MRP1/2 as representative ABC transporters for MTX, changes in MDR and BCRP gene expressions might also influence the accumulation of ^3H -MTX in H441 (Ji et al., 2013). Henness

et al. (2002) reported that expressions of MRP1 and MRP2 were increased after fractionated irradiation, but these expression levels might change over time after a single high-dose irradiation. In PC-14 and HeLa cells (Table 2), gene expression levels of MRP1/2 were much greater than those of OATP1B1/1B3/1B7. After irradiation, the difference between OATP1B1/1B3/1B7 and MRP1/2 became greater over time.

In PC-14 (Figure 1B), accumulation of ^3H -MTX showed little change between control and 4 h after irradiation, but was significantly decreased at all time points after adding ^3H -MTX in cells at 24 h after irradiation. Since gene expression levels of OATP1B1/1B3/1B7 were slightly greater in PC-14 cells, the effects on gene expression levels of OATP1B1/1B3/1B7 may be greater than the effects on accumulation of ^3H -MTX at 4 h after irradiation. At 24 h after irradiation, a correlation was noted between decrease in accumulation of ^3H -MTX and much higher gene expression levels of MRP1/2.

In HeLa cells (Figure 1C), accumulation of ^3H -MTX was significantly decreased compared to control at 4 h after irradiation from 10 min after adding ^3H -MTX, and at 24 h after irradiation from 30 min after adding ^3H -MTX. Although the effects of drug transporters are usually seen at 5 min after adding ^3H -MTX, no significant differences at this time points were seen between control and groups at 4 and 24 h after irradiation. An equilibrium state appears to exist between functions of OATP1B1/1B3/1B7 and MRP1/2 at around 5 min after adding ^3H -MTX, but gene expression levels of MRP1/2 were higher than those of OATP1B1/1B3/1B7 (Table 2). With greater expression of MRP1/2 over time, accumulation of ^3H -MTX decreased significantly compared to control (Figure 1C). From 10 min after adding ^3H -MTX, accumulation of ^3H -MTX was higher in HeLa than in H441 and PC-14. Gene expression levels of MRP2 were also higher in HeLa than in H441 or PC-14, and expression of MRP2 was also higher than that of MRP1. These results may suggest that ^3H -MTX has higher affinity for MRP1 than for MRP2.

This study was performed assuming SBRT, in which a single exposure provides a higher dose than conventional radiotherapy (Marcrom et al., 2017; Jardel et al., 2020; Sarudis et al., 2021; Ugurluer et al., 2021). Since Lei et al. (2021) reported that the survival rate of HeLa was less than 50% after a single 10-Gy irradiation, we selected a single high-dose of 10-Gy irradiation. In our experiments, cancer cells after a single high-dose irradiation have shown a tendency to excrete anticancer drugs as a foreign body. Neoadjuvant chemotherapy, which administers anticancer drugs prior to radiation, may therefore prove effective in the combination of SBRT and chemotherapy. However, these results only reflect temporal changes following a single irradiation. Future experiments will need to consider fractional irradiation at high dose. In addition, *in vivo* experiments will be required to confirm our *in vitro* results for the accumulation of ^3H -MTX and expression of drug transporters.

For a more detailed examination, next-generation sequencers might be useful in the future because this method is capable of comprehensively quantifying multitude of various genes (Slatko et al., 2018). However, we intentionally selected MTX which has affinity primarily for OATP and MRP transporters as an anti-cancer drug. Therefore, Real-time PCR, which can accurately quantify gene expression levels of specific transporters, would be

appropriate in this study. The Real-time PCR was also used in the study of (Sutherland et al., 2020). They examined the relationship between accumulation of anti-cancer drugs in cancer cells and gene expression levels of specific SLC transporters by Real-time PCR.

5 Conclusion

X-ray irradiation with a single, high dose to cancer cells alters gene expression levels of both SLC transporters (OATP1B1/1B3/1B7) and ABC transporters (MRP1/2). In particular, changes in MRP1/2 were much greater than those in OATP1B1/1B3/1B7. Irradiation decreased accumulation of ³H-MTX in cancer cells over time due to higher expression of MRP1/2.

Data availability statement

The original contributions presented in the study are included in the article/supplementary materials, further inquiries can be directed to the corresponding author.

Author contributions

Conceptualization, MK; methodology, KS, TS, and SH; investigation, KS, TS, AM, SH, YM, KN, and MK; resources, KY and RN; writing—original draft preparation, KS; writing—review and editing, TN, IT, KK, and MK; supervision, TN, IT, KK, and MK. All authors have read and agreed to the published version of the manuscript.

References

- Baldini, E. H., Le Cesne, A., and Trent, J. C. (2018). Neoadjuvant chemotherapy, concurrent chemoradiation, and adjuvant chemotherapy for high-risk extremity soft tissue sarcoma. *Am. Soc. Clin. Oncol. Educ. Book* 23 (38), 910–915. doi:10.1200/EDBK_201421
- Bartkowiak, D., Stempfhuber, M., Wiegel, T., and Bottke, D. (2009). Radiation- and chemoinduced multidrug resistance in colon carcinoma cells. *Strahlenther. Onkol.* 185 (12), 815–820. doi:10.1007/s00066-009-1993-9
- Carmichael, Natasha, and Day, Philip J. R. (2022). Cell surface transporters and novel drug developments. *Front. Pharmacol.* 13, 852938. doi:10.3389/fphar.2022.852938
- Conroy, J. F., Lewis, G. C., Brady, L. W., Brodsky, I., Kahn, S. B., Ross, D., et al. (1976). Low dose bleomycin and methotrexate in cervical cancer. *Cancer* 37 (2), 660–664. doi:10.1002/1097-0142(197602)37:2<660::aid-cnrc2820370208>3.0.co;2-v
- Donovan, E. K., and Swaminath, A. (2018). Stereotactic body radiation therapy (SBRT) in the management of non-small-cell lung cancer: Clinical impact and patient perspectives. *Cancer* 9, 13–23. doi:10.2147/LCTT.S129833
- Facondo, G., Vullo, G., De Sanctis, V., Valeriani, M., Ascolese, A. M., Massaro, M., et al. (2021). Stereotactic body radiation therapy boost in patients with cervical cancer ineligible for brachytherapy. *Cancer Diagn. Progn.* 1 (2), 53–60. doi:10.21873/cdp.10008
- Gao, J., Wang, C., and Wei, W. (2021). The effects of drug transporters on the efficacy of methotrexate in the treatment of rheumatoid arthritis. *Life Sci.* 268, 118907. doi:10.1016/j.lfs.2020.118907
- Hagenbuch, B., and Meier, P. J. (2004). Organic anion transporting polypeptides of the OATP/SLC21 family: Phylogenetic classification as OATP/SLCO superfamily, new nomenclature and molecular/functional properties. *Pflügers Arch.* 447 (5), 653–665. doi:10.1007/s00424-003-1168-y
- Henness, S., Davey, M. W., Harvie, R. M., and Davey, R. A. (2002). Fractionated irradiation of H69 small-cell lung cancer cells causes stable radiation and drug resistance with increased MRP1, MRP2, and topoisomerase IIalpha expression. *Int. J. Radiat. Oncol. Biol. Phys.* 54 (3), 895–902. doi:10.1016/s0360-3016(02)03037-7
- Ito, K., Kito, S., Nakajima, Y., Shimizuguchi, T., Ogawa, H., Nihei, K., et al. (2019). Determining the recommended dose of stereotactic body radiotherapy boost in patients with cervical cancer who are unsuitable for intracavitary brachytherapy: a phase I dose-escalation study. *Jpn. J. Clin. Oncol.* 49 (9), 856–861. doi:10.1093/jjco/hyz074
- Jardel, P., Kammerer, E., Villeneuve, H., and Thariat, J. (2020). Stereotactic radiation therapy for breast cancer in the elderly. *Transl. Cancer Res.* 9 (1), 86–96. doi:10.21037/tcr.2019.07.18
- Ji, X. N., Yang, F., Sui, X. M., Wang, F. G., Ge, R. G., Quan, X. L., et al. (2013). Effect of fractionated irradiation on the expression of multidrug resistance genes in the CNE1 human nasopharyngeal carcinoma cell line. *Mol. Med. Rep.* 7 (1), 187–194. doi:10.3892/mmr.2012.1148
- Lei, H., Shi, J., Teng, Y., Song, C., Zou, L., Ye, F., et al. (2021). Baicalein modulates the radiosensitivity of cervical cancer cells *in vitro* via miR-183 and the JAK2/STAT3 signaling pathway. *Adv. Clin. Exp.* 30 (7), 727–736. doi:10.17219/acem/135478
- Marcrom, S. R., McDonald, A. M., Thompson, J. W., Popple, R. A., Riley, K. O., Markert, J. M., et al. (2017). Fractionated stereotactic radiation therapy for intact brain metastases. *Adv. Radiat. Oncol. metastases* 2 (4), 564–571. doi:10.1016/j.adro.2017.07.006
- Murakami, T., and Mori, N. (2012). Involvement of multiple transporters-mediated transports in mizoribine and methotrexate pharmacokinetics. *Pharmaceuticals* 5 (8), 802–836. doi:10.3390/ph5080802
- Nakanishi, T. (2007). Drug transporters as targets for cancer chemotherapy. *Cancer Genomics Proteomics* 4 (3), 241–254.

Funding

This study was funded in part by Grants-in-Aid for Scientific Research from the Japan Society for the Promotion of Science (Nos 21H02865, 22H03016, and 22K19504) and the Network-type Joint Usage/Research Center for Radiation Disaster Medical Science.

Acknowledgments

The authors would like to thank Mikie Ohtake and other staff of the Faculty of Health Sciences, Kanazawa University.

Conflict of interest

The authors declare that the research was conducted in the absence of any commercial or financial relationships that could be construed as a potential conflict of interest.

Publisher's note

All claims expressed in this article are solely those of the authors and do not necessarily represent those of their affiliated organizations, or those of the publisher, the editors and the reviewers. Any product that may be evaluated in this article, or claim that may be made by its manufacturer, is not guaranteed or endorsed by the publisher.

- Sarudis, S., Karlsson, A., and Bäck, A. (2021). Surface guided frameless positioning for lung stereotactic body radiation therapy. *J. Appl. Clin. Med. Phys.* 22 (9), 215–226. doi:10.1002/acm2.13370
- Slatko, B. E., Gardner, A. F., and Ausubel, F. M. (2018). Overview of next generation sequencing Technologies. *Curr. Protoc. Mol. Biol.* 122 (1), e59. doi:10.1002/cpmb.59
- Smyth, J. F., and Ford, H. T. (1981). Methotrexate in the chemotherapy of lung cancer. *Cancer Treat. Rep.* 65 (1), 161–163.
- Song, D. Y., Kavanagh, B. D., Benedict, S. H., and Schefter, T. (2004). Stereotactic body radiation therapy. Rationale, techniques, applications, and optimization. *Oncology* 18 (11), 1419–1430. discussion 1430, 1432, 1435–6.
- Sutherland, R., Meeson, A., and Lowes, S. (2020). Solute transporters and malignancy: Establishing the role of uptake transporters in breast cancer and breast cancer metastasis. *Cancer Metastasis Rev.* 39 (3), 919–932. doi:10.1007/s10555-020-09879-6
- Tandberg, D. J., Tong, B. C., Ackerson, B. G., and Kelsey, C. R. (2018). Surgery versus stereotactic body radiation therapy for stage I non-small cell lung cancer: A comprehensive review. *Cancer* 124 (4), 667–678. doi:10.1002/cncr.31196
- Ugurluer, G., Mustafayev, T. Z., Gungor, G., Atalar, B., Abacioglu, U., Sengoz, M., et al. (2021). Stereotactic MR-guided online adaptive radiation therapy (SMART) for the treatment of liver metastases in oligometastatic patients: Initial clinical experience. *Radiat. Oncol. J.* 39 (1), 33–40. doi:10.3857/roj.2020.00976
- Visentin, M., Zhao, R., and Goldman, I. D. (2012). The antifolates. *Hematol. Oncol. Clin. North Am.* 26 (3), 629–648. doi:10.1016/j.hoc.2012.02.002
- Yu, W. J., Huang, D. X., Liu, S., Sha, Y. L., Gao, F. H., and Liu, H. (2020). Polymeric nanoscale drug carriers mediate the delivery of methotrexate for developing therapeutic interventions against cancer and rheumatoid arthritis. *Front. Oncol.* 10, 1734. doi:10.3389/fonc.2020.01734



OPEN ACCESS

EDITED BY

Junmin Zhang,
Lanzhou University, China

REVIEWED BY

Xuan Qin,
Baylor College of Medicine, United States
Runbin Sun,
Nanjing Drum Tower Hospital, China

*CORRESPONDENCE

Guangming Luo,
✉ Jzlgm88@163.com
Yangjing Luo,
✉ lyj_20080819@126.com

[†]These authors share first authorship

SPECIALTY SECTION

This article was submitted to Drug
Metabolism and Transport,
a section of the journal
Frontiers in Pharmacology

RECEIVED 03 November 2022

ACCEPTED 29 December 2022

PUBLISHED 18 January 2023

CITATION

Song D, Zhu P, Dong Y, Wang M, Zhao A,
Xia H, Chen Y, Zhou Q, Xiang L, Zhang J,
Luo G and Luo Y (2023), Mechanism of
crocin I on ANIT-induced intrahepatic
cholestasis by combined metabolomics
and transcriptomics.
Front. Pharmacol. 13:1088750.
doi: 10.3389/fphar.2022.1088750

COPYRIGHT

© 2023 Song, Zhu, Dong, Wang, Zhao, Xia,
Chen, Zhou, Xiang, Zhang, Luo and Luo.
This is an open-access article distributed
under the terms of the [Creative Commons
Attribution License \(CC BY\)](#). The use,
distribution or reproduction in other
forums is permitted, provided the original
author(s) and the copyright owner(s) are
credited and that the original publication in
this journal is cited, in accordance with
accepted academic practice. No use,
distribution or reproduction is permitted
which does not comply with these terms.

Mechanism of crocin I on ANIT-induced intrahepatic cholestasis by combined metabolomics and transcriptomics

Dandan Song^{1†}, Pei Zhu^{1†}, Yankai Dong², Mengchao Wang¹,
Anna Zhao¹, Hongdong Xia¹, Yunting Chen¹, Qingguang Zhou³,
Lun Xiang¹, Junyi Zhang¹, Guangming Luo^{1*} and Yangjing Luo^{1*}

¹Jiangxi University of Chinese Medicine, Nanchang, Jiangxi, China, ²Northwest University, Xi'an, Shaanxi, China, ³Nanchang University, Nanchang, Jiangxi, China

Background: Intrahepatic cholestasis (IC) is a disorder of bile production, secretion, and excretion with various causes. Crocin I (CR) is effective in the treatment of IC, but its underlying mechanisms need to be further explored. We aimed to reveal the therapeutic mechanism of crocin I for IC by combining an integrated strategy of metabolomics and transcriptomics.

Methods: The hepatoprotective effect of CR against cholestasis liver injury induced by α -naphthylisothiocyanate (ANIT) was evaluated in rats. The serum biochemical indices, including alanine aminotransferase (ALT), aspartate aminotransferase (AST), total bile acid (TBA), total bilirubin (TBIL), direct bilirubin (DBIL), tumor necrosis factor- α (TNF- α), interleukin 6 (IL-6), and interleukin 1 β (IL-1 β), as well as the liver oxidative stress indexes and the pathological characteristics of the liver were analyzed. In addition, we also performed a serum metabolomics study using UPLC-Q Exactive HF-X technology to investigate the effect of CR on the serum of rats with ANIT-induced IC and screened potential biomarkers. The enrichment analysis of differential expressed genes (DEGs) was performed by transcriptomics. Finally, the regulatory targets of CR on potential biomarkers were obtained by combined analysis, and the relevant key targets were verified by western blotting.

Results: CR improved serum and liver homogenate indexes and alleviated liver histological injury. Compared with ANIT group, the CR group had 76 differential metabolites, and 10 metabolic pathways were enriched. There were 473 DEGs significantly changed after CR treatment, most of which were enriched in the retinol metabolism, calcium signaling pathway, PPAR signaling pathway, circadian rhythm, chemokine signaling pathway, arachidonic acid metabolism, bile secretion, primary bile acid biosynthesis, and other pathways. By constructing the "compound-reaction-enzyme-gene" interaction network, three potential key-target regulation biomarkers were obtained, including 3-hydroxy-3-methylglutaryl-coenzyme A reductase (HMGCR), ATP-binding cassette transporter G5 (ABCG5), and sulfotransferase2A1(SULT2A1), which were further verified by western blotting. Compared with the ANIT group, the CR group significantly increased the expression of ABCG5 and SULT2A1, and the expression of HMGCR significantly decreased.

Conclusion: Combined metabolomic and transcriptomic analyses show that CR has a therapeutic effect on IC through regulation of the biosynthesis of bile acids and bilirubin in the bile secretion pathway and regulation of the expression of HMGCR, ABCG5, and SULT2A1.

KEYWORDS

crocin I, intrahepatic cholestasis, metabolomics, transcriptomics, comprehensive strategy

1 Introduction

A common type of liver disease, intrahepatic cholestasis (IC) is a primary hepatocellular disease. Bile formation and blood flow are blocked due to damage to hepatocytes and bile duct cells. In particular, bile acids are trapped, and bile components such as cholesterol and bilirubin continue to accumulate (Yang et al., 2018). Disturbances in bile acid metabolism and inflammation are common features of IC, with clinical symptoms of jaundice, itchy skin, darkened urine, and physical frailty. If the cholestatic state is not effectively treated, it will develop into liver fibrosis, and even liver cirrhosis (Zhang et al., 2022). Ursodeoxycholic acid, obeticholic acid, S-adenosylmethionine, and other drugs are often used for the clinical treatment of intrahepatic cholestasis. However, the use of ursodeoxycholic acid will cause intolerance in patients. Obecholic acid can produce side effects such as itching (Samant et al., 2019; Fujita et al., 2021). Therefore, the search for an effective drug with few side effects to treat IC is an important topic. Chinese medicines and their monomers have the advantage of being widely applied and have few side effects. Terpenoids have various anti-inflammatory, antioxidant, and anti-fibrosis pharmacological activities that can effectively alleviate IC, and terpenoids are expected to become new drugs for the treatment of cholestatic liver disease (Ji et al., 2022).

Crocin I (CR), as a diterpenoid, is the main active component of saffron (Figure 1). In recent years, many studies have shown that CR has hepatoprotection (Lari et al., 2015), antitumor (Tang et al., 2022), anticardiovascular disease (Motlagh et al., 2021), anti-inflammatory (Teng et al., 2021), and hypoglycemic (Qiu et al., 2020) effects. In addition, it has less toxicity and fewer side effects, and its medical value

has received increasing attention. However, the mechanism of how CR alleviates IC is still unclear. Combining the relevant gene expression information provided by transcriptomics with the statistical information of metabolomics data variables is a reliable method of studying the material basis and mechanism of action of the pharmacological effects of Chinese medicine monomers. Currently, integrating the two techniques to explore the mechanism of CR in the treatment of IC remains a void.

Metabolomics is an important part of systems biology. By revealing the metabolic trends and laws of the body under the influence of internal and external factors, metabolomics can qualitatively and quantitatively determine the dynamic changes of metabolites in the living system caused by pathological, physiological stimulation, or genetic modification (Alarcon-Barrera et al., 2022). The mechanism of how CR protects the liver can be elucidated through metabolomics. Genes are closely related to changes in metabolites, so transcriptomics is used to explain changes in gene expression after drug administration. In addition, combined metabolomic and transcriptomic analysis can reveal phenotype-related metabolic pathways and gene functions through the identified metabolites and differential genes to further gain potential therapeutic targets for various types of liver injury and elucidate disease pathogenesis.

In this study, metabolomics and transcriptomics were integrated. The effects of treating IC with CR on essential metabolites were determined with untargeted metabolomics. We then developed a novel integrated strategy to explore the key targets and mechanisms of CR in treating acute IC based on metabolomics and transcriptomics. This study provided new insights into the

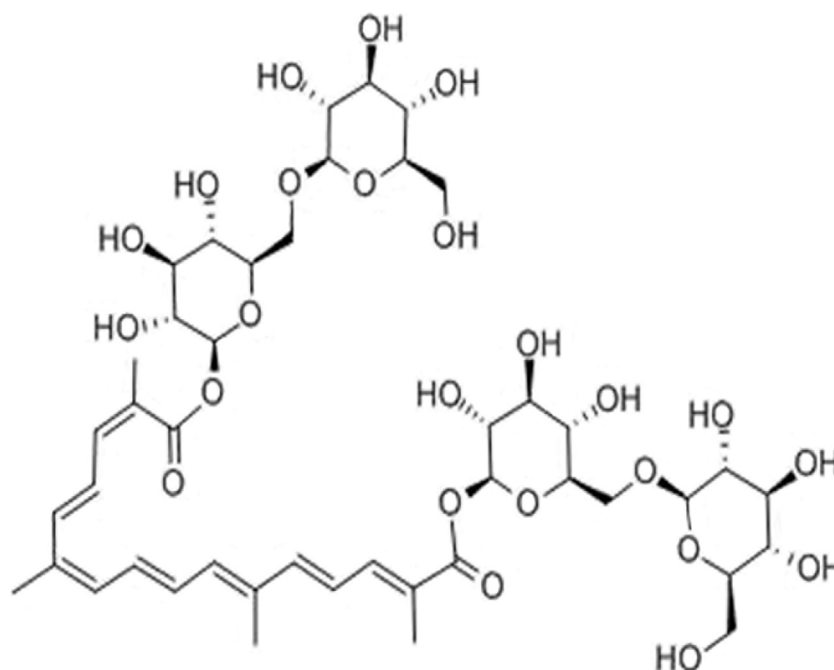
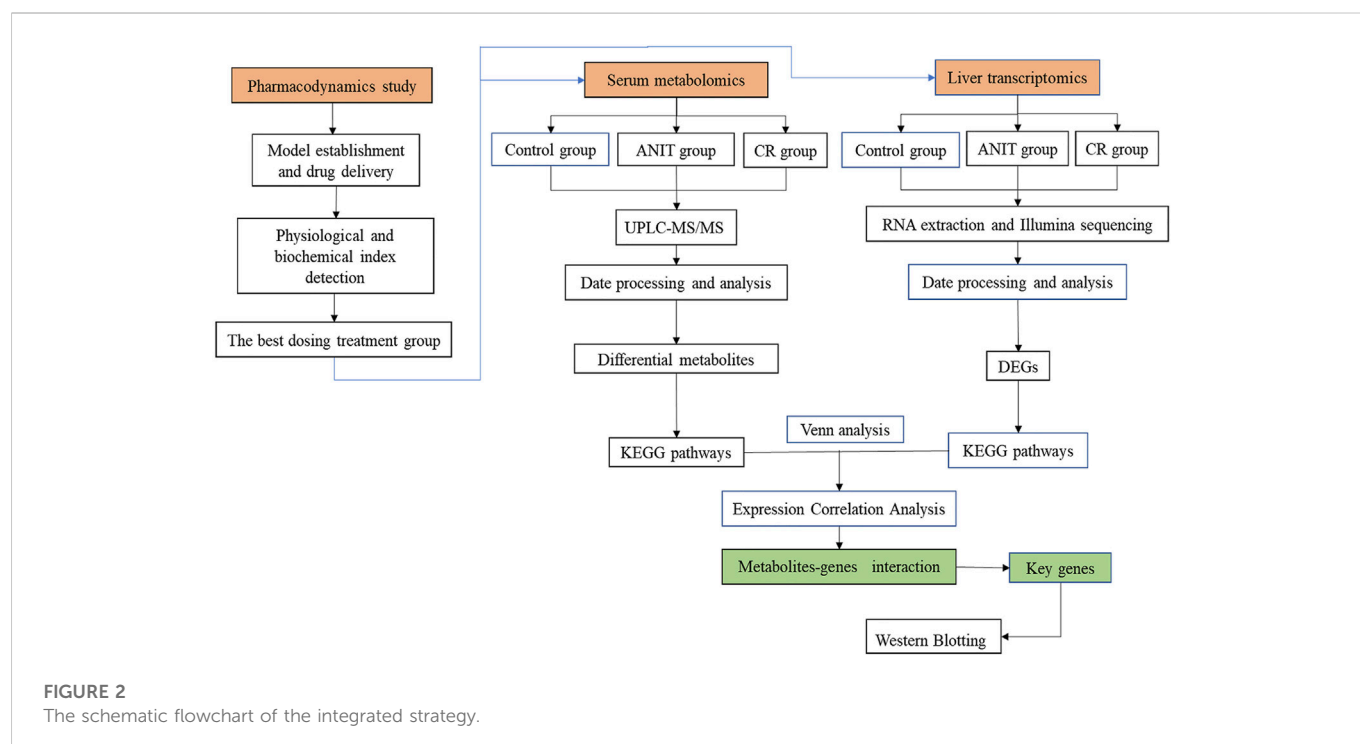


FIGURE 1
The structure of crocin I.



protective effects of CR in the treatment of IC. The research flowchart is shown in Figure 2.

2 Materials and methods

2.1 Chemicals and reagents

Crocin I (C₄₄H₆₄O₂₄, purity>98%, BCTG-0315) was purchased from the National Engineering Research Center of Traditional Chinese Medicine Solid Preparation Manufacturing Technology (Nanchang, China). ANIT and ursodeoxycholic acid (UDCA) were purchased from Shanghai McLean Biochemical Technology Co., Ltd. (Shanghai, China). The alanine aminotransferase (ALT), aspartate transaminase (AST), total bile acid (TBA), total bilirubin (TBIL), and direct bilirubin (DBIL) kits were purchased from Nanjing Jiancheng Bioengineering Institute (Nanjing, China). The tumor necrosis factor- α (TNF- α), interleukin-6 (IL-6), interleukin-1 β (IL-1 β) kits were purchased from Xinhosheng Biotechnology Co., Ltd. (Shenzhen, China).

2.2 Animals

Male Sprague–Dawley rats weighing 200 ± 20 g were obtained from Huiji District (Zhengzhou) Experimental Animal Farm (Zhengzhou, China, Permission No. SCXK(Yu)2019–0002). All rats were housed in a well-ventilated room at 25°C, 60% humidity with a 12-h dark-light cycle and free access to food and water. Animal experiments were carried out in accordance with the guidelines for animal experiments at Jiangxi University of Traditional Chinese Medicine.

After all the rats were allowed to acclimate for 1 week, 48 rats were randomly divided into six groups ($n = 8/\text{group}$): CON group, ANIT group, UDCA group, CR-L group, CR-M group, and CR-H group. The CR groups and the UDCA group were given corresponding drugs by prophylactic gavage. The UDCA group received 60 mg/kg (Li et al., 2020), the CR-L group received 10 mg/kg, the CR-M group received 30 mg/kg, and the CR-H received 90 mg/kg for seven consecutive days, once a day. The CON group and the ANIT group were given an equal volume of .5% CMC-Na. Two hours after administration on the fifth day, the CON group received olive oil, and other groups were given 75 mg/kg ANIT olive oil, respectively.

2.3 Sample collection and preparation

After anesthesia with 3% pentobarbital sodium, blood samples were taken from the abdominal aorta and liver. Next, the blood was centrifuged at 3,000 rpm for 10 min to separate the serum and transferred to -80°C for preservation. Then, the relevant indexes were measured using the appropriate kits. The changes in the physiological and biochemical indexes of rats after CR treatment were observed through histopathological and biochemical analysis.

2.4 Histological examination

The liver tissue was fixed with 4% tissue cell fixative solution. The fixed liver tissue was taken out for routine dehydration, paraffin embedding, sectioning, HE staining, microscopy, and image acquisition.

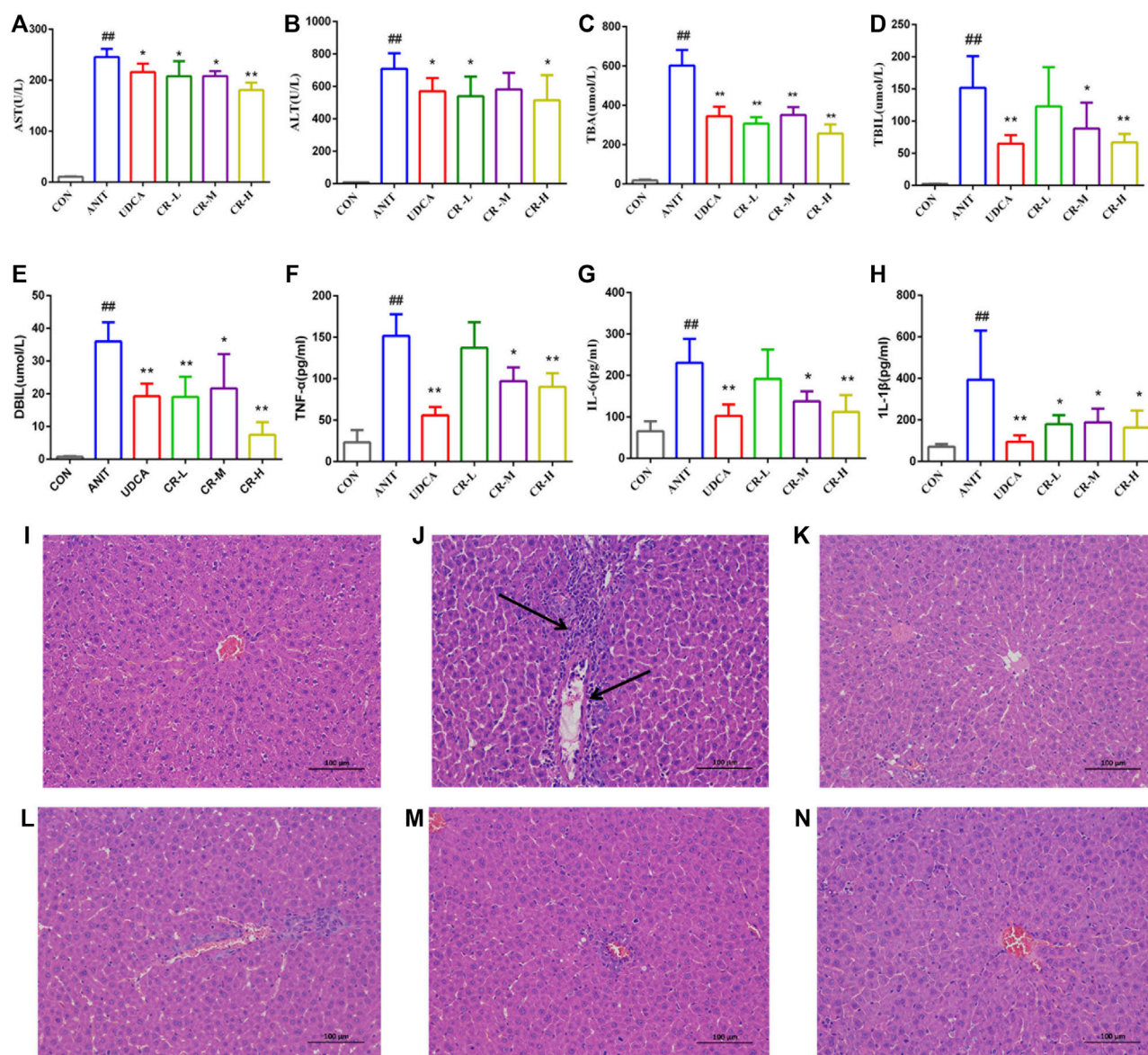


FIGURE 3

Effect of crocin I on serum biochemical indexes and histological (H&E stained, 100× magnification). Hepatocyte damage is indicated by black arrows. (A) Serum AST level, (B) serum ALT level, (C) serum TBA level, (D) serum TBIL level, (E) serum DBIL level, (F) serum TNF- α level, (G) serum IL-6 level, (H) serum IL-1 β level, (I) CON group, (J) ANIT group, (K) UDCA group, (L) CR-L group, (M) CR-M group, (N) CR-H group. Data are presented as means \pm SD ($n = 6$). # $p < .05$, ## $p < .01$ compared with the CON group; * $p < .05$, ** $p < .01$ compared with ANIT group.

2.5 Metabolomics analysis based on UPLC-Q-Exactive HF-X MS

2.5.1 Sample collection and preparation

According to the results of 3.1, the CON group, the ANIT group, and the CR-H group were selected for follow-up analysis of serum. A 100 μ L aliquot of the sample was precisely pipetted into a 1.5 mL centrifuge tube, and 400 μ L of extraction solution was added (methanol: acetonitrile = 1:1 (v:v)), containing .02 mg/mL internal standard (L-2-chlorophenylalanine). After vortexing for 30 s, low-temperature ultrasonic extraction was performed for 30 min (5°C, 40 KHz). The sample was placed at -20°C for 30 min and centrifuged for 15 min (13000g, 4°C). The supernatant was removed, and was

blown dry with nitrogen; 100 μ L of the reconstituted solution was added (acetonitrile: water = 1:1) for reconstitution, vortexed for 30 s, extracted by low-temperature ultrasonic extraction for 5 min (5°C, 40 KHz), and centrifuged for 10 min (13,000 g, 4°C). The supernatant was transferred to a sample vial with an inner cannula for analysis on the computer. The supernatant was stored at -20°C for LC-MS analysis.

2.5.2 Chromatography and mass spectrometry

Serum samples were analyzed using a Thermo Fisher Scientific UPLC-Q Exactive HF-X system. The chromatographic column was ACQUITY UPLC HSS T3 (100 mm \times 2.1 mm id, 1.8 μ m; Waters, Milford, USA), and the column temperature was 40°C. The mobile

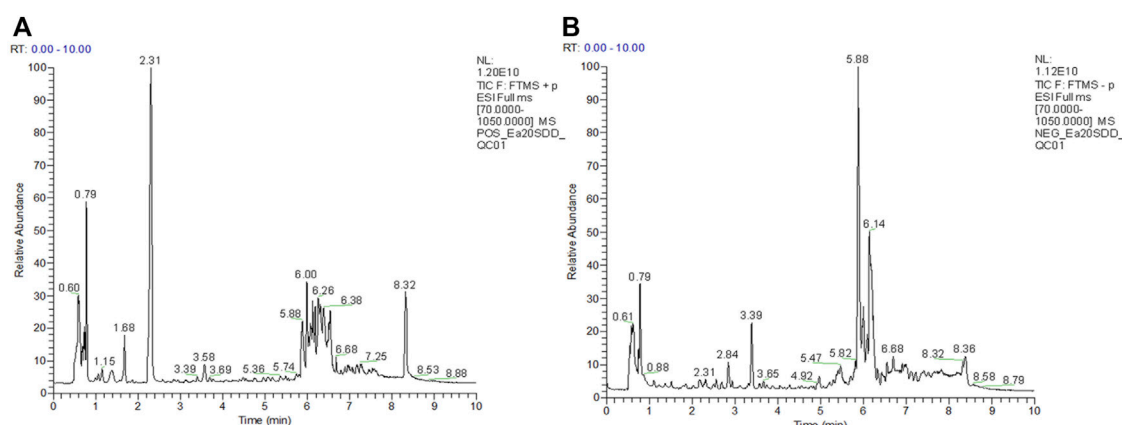


FIGURE 4

Typical chromatograms of positive and negative modes. (A) UPLC-QE ESI(+) total ion current diagram of quality control, (B) UPLC-QE ESI(-) total ion current diagram of quality control.

phase A was 95% water and 5% acetonitrile (containing .1% formic acid). Phase B was 47.5% acetonitrile, 47.5% isopropanol, and 5% water (containing .1% formic acid), and the injection volume was 2 μ L.

In positive and negative ion mode, the linear gradient of the elution column is 0–3.5 min, 0%–24.5% B; 3.5–5 min, 24.5%–65% B; 5–5.5 min, 65%–100% B; 5.5–7.4 min, 100% B; 7.4–7.6 min, 100%–51.5% B; 7.6–7.8 min, 51.5%–0% B; 7.8–10 min, 0% B. The flow rate was 0.4 mL/min. The scanning range (m/z) was 70–1050 Da; the sheath gas flow rate was 50 arb; the auxiliary gas flow rate was 13 arb, the spray voltage (positive and negative mode) was 3500V, –3500V, the heating temperature was 425°C; the capillary temperature was 325°C, and the collision energy was 20, 40, 60 eV.

2.5.3 Method validation

A 20 μ L aliquot of the supernatant was pipetted from each sample and mixed as a quality control sample (QC). The volume of each QC was the same as that of the sample, and it was processed and detected in the same way as the analytical sample. During the instrument analysis process, a QC sample was inserted after every 10 analysis samples to examine the stability of the entire detection process.

2.5.4 Data preprocessing and differential metabolite analysis

The raw data were imported into the metabolomics processing software Progenesis Q1 (Waters Corporation, Milford, USA) for baseline filtering, peak identification, integration, retention time correction, and peak alignment. A data matrix containing information such as retention time, mass charge ratio, and peak intensity was obtained (Trezzini et al., 2015; Vignoli et al., 2020). The R software package ropls (Version 1.6.2) was used to perform multivariate statistical analysis of PLS-DA and OPLS-DA on the processed data. VIP > 1 indicated that the metabolites had an important effect on the classification between groups. The model was tested for overfitting by permuting 200 times. The MS and MS/MS mass spectral information was matched and identified using the HMDB (<http://www.hmdb.ca/>) database and the Metlin (<https://metlin.scripps.edu/>) database to meet the

VIP > 1 and $p < .05$ differential metabolites through metabolic pathway enrichment analysis on data by the KEGG database and SciPy (Python) (Chong & Xia, 2018).

2.5.5 RNA extraction and sequencing

The liver tissue was taken from the –80 °C refrigerator, and the total RNA was extracted by the TRIzol (Invitrogen) method. The sequencing experiment was performed using the Illumina Truseq™ RNA sample prep kit method for library construction. Seqprep and Sickel software programs were used for preprocessing to obtain clean data. The data after quality control were compared with the published rat genome sequence for *Rattus norvegicus*. The DEGseq2 software was used to analyze the differential expression of the CON group, the ANIT group, and the CR-H group, and the differentially expressed genes (DEGs) were screened. Then, the GO and KEGG databases were used for the enrichment analysis of the DEGs.

2.5.6 Western blotting

Three samples from each group were selected for western blot analysis and comparison. The total protein of the samples was extracted with RIPA tissue cell rapid lysis buffer, centrifuged at 12000g at 4°C for 15 min, and the supernatant was collected for protein quantification and stored in a –80°C refrigerator. Then, the BCA kit was used to measure the protein concentration. The protein was separated with 10% SDS polyacrylamide gel and transferred to a polyvinylidene fluoride PVDF membrane. The PVDF membrane was blocked with 5% nonfat milk powder at room temperature for 1 h or overnight at 4°C. Afterward, it was washed with TBST, the primary antibody was incubated at 4°C overnight, and the membrane was incubated with the primary antibody three times, 5 min each time. Then, according to the dosage, the HRP-labeled secondary antibody was diluted 1:1000 and incubated with the membrane at 37°C for 1 h. TBST was used to wash three times for 5 min each. Finally, ECL chemiluminescence detection was performed for development. GAPDH was selected as the internal reference, and Image J software was used for gray value analysis.

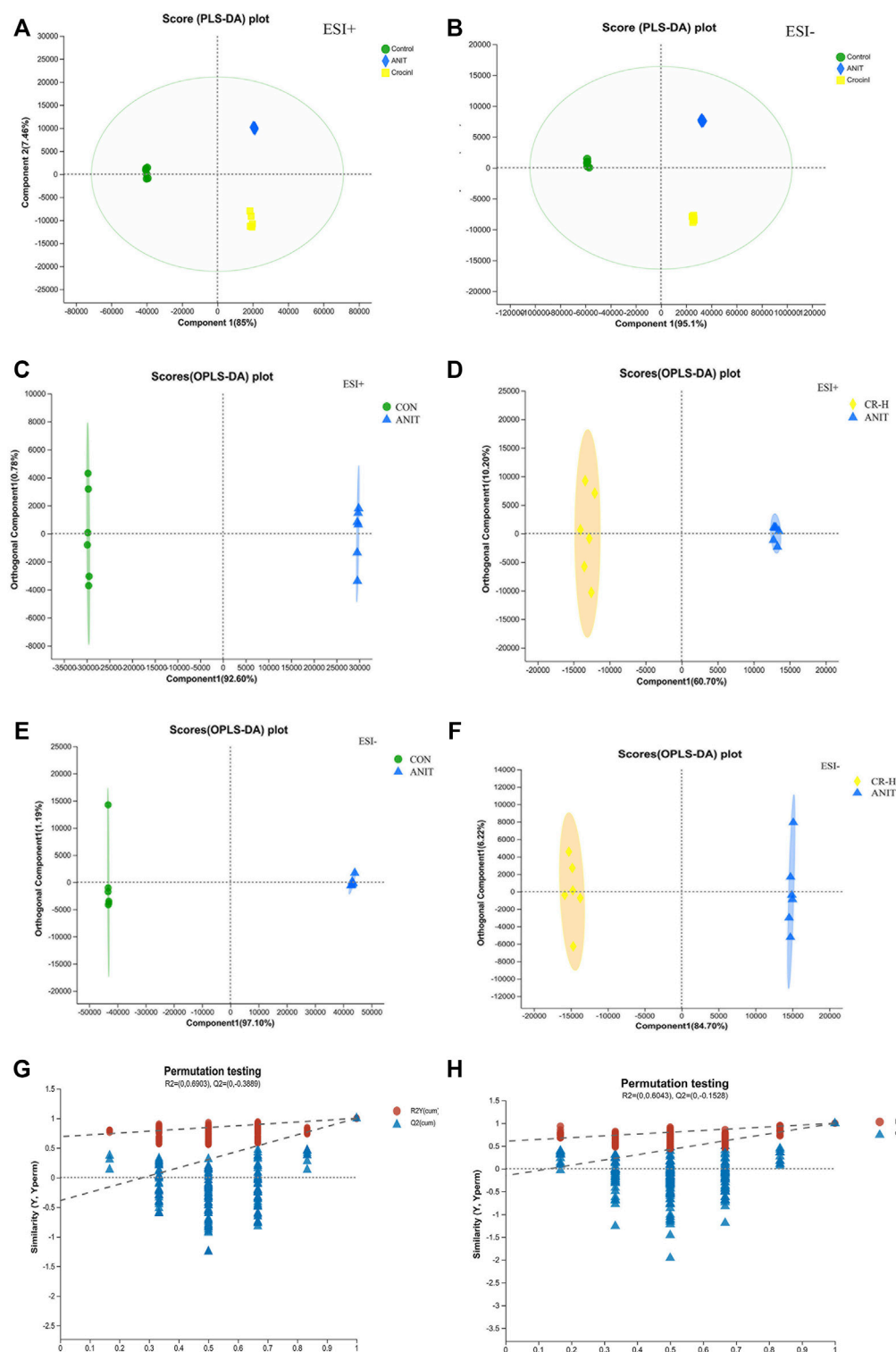


FIGURE 5

Multivariate statistical analysis of serum metabolomics. (A),(B) PLS-DA score plots of serum metabolomics analysis in the ESI + model and ESI- ANIT; (C) OPLS-DA score plots of CON and ANIT in positive mode; (D) OPLS-DA score plots of CON and CR-H in positive mode; (E) OPLS-DA score plots of CON and ANIT in negative mode; (F) OPLS-DA score plots of CON and CR-H in negative mode; (G) 200-permutation test of the OPLS-DA model for the CON and ANIT groups; (H) 200-permutation test of the OPLS-DA model for the CR and ANIT groups.

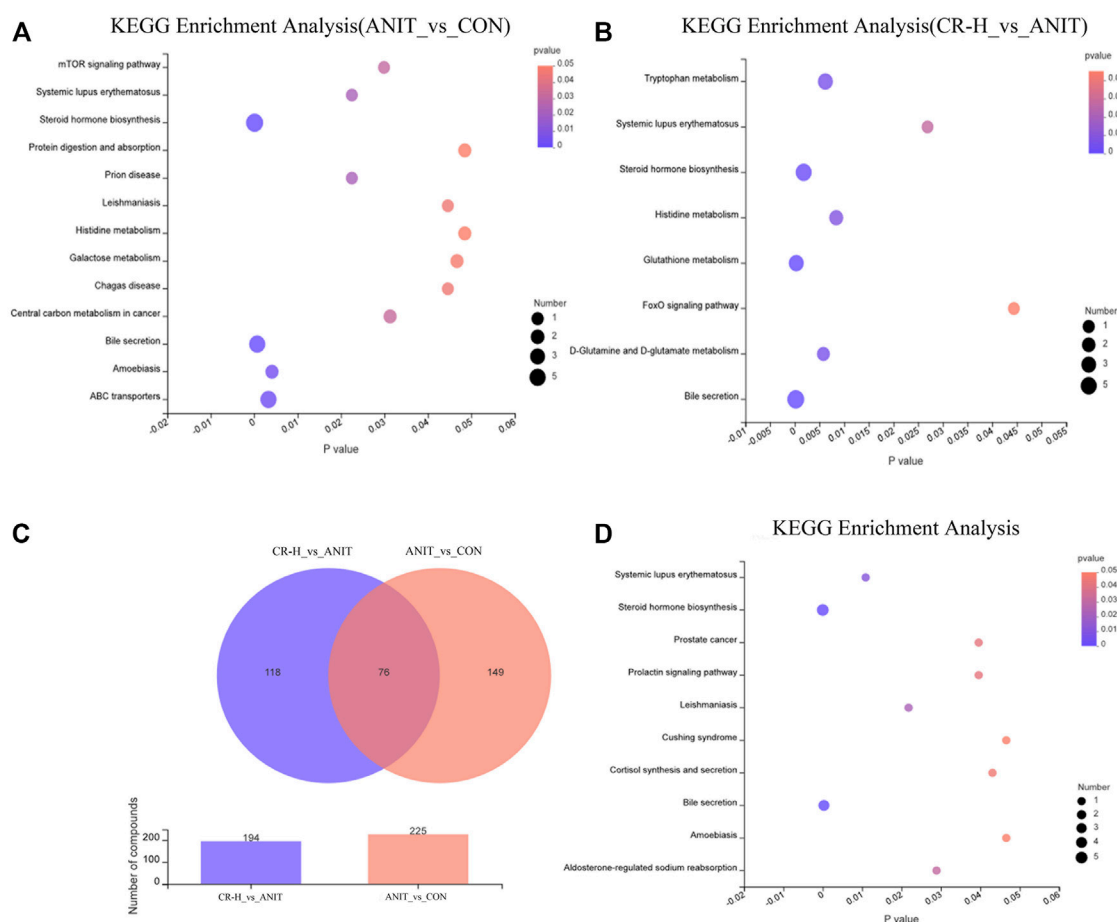


FIGURE 6

Metabolomics pathway enrichment analysis results. (A, B) KEGG pathway enrichment analysis of differential metabolites between the CON group, the ANIT group, and the CR group by bubble plot; (C) Venn diagram of differential metabolites between the groups; (D) pathway enrichment bubble map for 76 shared metabolites.

2.5.7 Statistical analysis

Statistical analysis of the data was performed using Graphpad Prism 8.0 software, and the results were expressed as mean \pm standard deviation ($X \pm S$). One-way ANOVA was used for statistical differences among each group, and Scheffe was used for the *post hoc* test for comparing every two groups; $p < .05$ indicated statistical significance, and $p < .01$ indicated extremely significant differences.

3 Results

3.1 Effects of CR on ANIT-induced IC in rats

Biochemical and histological analyses were used to evaluate the pharmacodynamics of CR in the treatment of IC.

As shown in Figures 3A–H, compared with the CON group, the levels of AST, ALT, TBA, TBIL, and DBIL in the serum of the ANIT group significantly increased, indicating that the ANIT group had a severe liver injury. Compared with the ANIT group, the middle- and high-dose CR and UDCA groups showed significantly reduced levels

of AST, ALT, TBA, TBIL, DBIL, IL-1 β , IL-6, and TNF- α ($p < .05$). The CR-H group showed the most significant effect ($p < .01$).

The histological evaluation provided more intuitive evidence for the protective effect of CR on ANIT-induced IC. As shown in Figure 3I–N, the liver tissue of the CON group showed a standard cellular structure, and the ANIT group showed typical pathological changes, including inflammatory infiltration and necrosis of liver cells and a small amount of hepatic fibrosis and connective tissue proliferation. The degeneration of hepatocytes in the UDCA group and the CR-L, CR-M, and CR-H groups was alleviated, the infiltration of neutrophils was less, and the CR-H group had the most obvious therapeutic effect, which indicated that CR had a certain protective effect on IC.

3.2 Multivariate statistical analysis

UPLC-Q Exactive HF-X/MS was used for the metabolite separation and data collection of serum samples. The serum metabolic profiles of rats in each group were obtained and indicated that some rat metabolites changed. Figure 4 shows typical chromatograms of positive and negative modes. As shown in Figures

TABLE 1 Identification of potential biomarkers in serum.

Metabolite	Library id	Formula	tR/ min	M/Z	Mode	VIP	p_value	Trend	
								M/ K	CR/ M
Naphthalene epoxide	HMDB0006215	C ₁₀ H ₈ O	5.36	186.091	pos	2.15	9.99E-17	↑**	↓**
Cervonoyl ethanolamide	HMDB0013627	C ₂₄ H ₃₆ O ₃	5.85	337.252	pos	1.08	1.95E-09	↑**	↓**
4,4'-Dihydroxy-5,5'-diisopropyl-2,2'-dimethyl-3,6-biphenyldione	HMDB0040760	C ₂₀ H ₂₄ O ₄	6.00	311.164	pos	4.79	5.93E-12	↑**	↑**
Dityrosine	HMDB0006045	C ₁₈ H ₂₀ N ₂ O ₆	5.96	424.150	pos	1.07	6.38E-06	↑**	—
7-beta-D-Glucopyranosyloxybutyridenephthalide	HMDB0034752	C ₁₈ H ₂₂ O ₈	5.26	367.140	pos	1.12	6.97E-07	↑**	—
5'-Carboxy-gamma-chromanol	HMDB0012799	C ₁₈ H ₂₆ O ₄	.51	345.148	pos	1.34	3.29E-09	↑**	↓**
Quillaic acid 3-[xylosyl-(1->3)]-galactosyl-(1->2)]-glucuronide]	HMDB0033406	C ₄₇ H ₇₂ O ₂₀	2.05	490.232	pos	1.00	8.95E-07	↓**	↑**
4-(3-Pyridyl)-3-butenic acid	HMDB0001424	C ₉ H ₉ NO ₂	2.57	164.071	pos	1.28	2.83E-08	↓**	↑**
Estrone	HMDB0000145	C ₁₈ H ₂₂ O ₂	3.33	315.134	pos	1.46	.001057	↑**	↑**
Bilirubin	HMDB0000054	C ₃₃ H ₃₆ N ₄ O ₆	5.88	585.270	pos	1.17	.001869	↑**	↓**
Matricin	HMDB0036643	C ₁₇ H ₂₂ O ₅	5.92	613.302	pos	1.33	1.20E-05	↑**	↓**
Dehydroabietic acid	HMDB0061925	C ₂₀ H ₂₈ O ₂	6.08	301.216	pos	2.29	1.76E-11	↑**	↓**
2-Amino-14,16-dimethyloctadecan-3-ol	LMSP01080031	C ₂₀ H ₄₃ NO	6.11	314.341	pos	1.09	4.35E-05	↓**	↑**
PS (18:0/20:4 (8Z,11Z,14Z,17Z))	HMDB0010165	C ₄₄ H ₇₈ NO ₁₀ P	6.55	812.541	pos	1.57	5.36E-06	↑**	↓**
Suspensolide F	HMDB0031918	C ₂₁ H ₃₄ O ₁₂	6.70	501.196	pos	1.26	1.27E-06	↓**	↑**
Lithocholyltaurine	HMDB0000722	C ₂₆ H ₄₅ NO ₅ S	8.41	466.298	pos	1.55	1.49E-08	↑**	↓**
Cucurbitacin D	HMDB0034695	C ₃₀ H ₄₄ O ₇	7.33	580.327	pos	1.90	1.36E-05	↑**	↓**
PE-NMe2 (20:2 (11Z,14Z)/18:4 (6Z,9Z,12Z,15Z))	HMDB0114250	C ₄₅ H ₇₈ NO ₈ P	6.96	814.536	pos	1.51	4.45E-05	↓**	↑**
PE-NMe2 (11D3/11M5)	HMDB0114663	C ₄₈ H ₈₄ NO ₁₀ P	6.68	848.576	pos	2.06	2.96E-08	↑**	↓**
6-Hydroxyshogaol	HMDB0041249	C ₁₇ H ₂₄ O ₄	6.16	331.130	pos	1.02	7.54E-06	↑**	↓**
Gamma-Glutamyl-4-hydroxybenzene	HMDB0029451	C ₁₁ H ₁₄ N ₂ O ₄	6.15	494.228	pos	1.66	.0001696	↑**	↓**
LysoPC (10:0)	HMDB0003752	C ₁₈ H ₃₉ NO ₇ P+	6.14	413.254	pos	1.40	8.94E-07	↑**	↓**
Physalin O	HMDB0039081	C ₂₈ H ₃₂ O ₁₀	6.11	529.208	pos	1.08	9.38E-06	↑**	—
C17 Sphinganine	LMSP01040003	C ₁₇ H ₃₇ NO ₂	6.01	288.289	pos	1.13	1.99E-09	↓**	↑**
Fumonisin B2	HMDB0034703	C ₃₄ H ₅₉ NO ₁₄	5.94	670.379	pos	1.88	9.94E-11	↑**	↑**
Cortisol	HMDB0000063	C ₂₁ H ₃₀ O ₅	5.88	345.206	pos	1.02	.006046	↓**	↑**
Tauroursodeoxycholic acid	HMDB0000874	C ₂₆ H ₄₅ NO ₆ S	5.69	464.283	pos	1.21	1.38E-10	↑**	—
Isoleucyl-methionine	HMDB0028913	C ₁₁ H ₂₂ N ₂ O ₃ S	5.62	301.100	pos	1.18	8.57E-09	↑**	↓**
31-Hydroxy rifabutin	HMDB0060754	C ₄₆ H ₆₂ N ₄ O ₁₂	5.40	904.477	pos	1.96	6.93E-06	↓**	↑**
Cysteinylglycine	HMDB0000078	C ₅ H ₁₀ N ₂ O ₃ S	5.34	242.058	pos	2.12	.000165	↓**	↑**
Glutathione episulfonium ion	HMDB0060479	C ₁₂ H ₂₀ N ₃ O ₆ S ⁺	5.02	367.140	pos	1.08	5.89E-06	↑**	↓**
(9Z,11E,13E,15Z)-4-Oxo-9,11,13,15-octadecatetraenoic acid	HMDB0031098	C ₁₈ H ₂₆ O ₃	4.49	329.149	pos	1.04	2.79E-06	↑**	—
Isoleucyl-cysteine	HMDB0028904	C ₉ H ₁₈ N ₂ O ₃ S	4.06	273.069	pos	1.94	4.32E-13	↑**	↓**
Myricanone	HMDB0030798	C ₂₁ H ₂₄ O ₅	3.73	379.150	pos	1.64	7.88E-10	↑**	↓**
L,L-Cyclo (leucylprolyl)	HMDB0034276	C ₁₁ H ₁₈ N ₂ O ₂	3.70	211.144	pos	1.06	1.23E-05	↑**	↓**
Isoquinoline	HMDB0034244	C ₉ H ₇ N	3.70	130.065	pos	1.20	4.91E-10	↑**	↓**
N-Deschlorobenzoyl indomethacin	HMDB0013988	C ₁₂ H ₁₃ NO ₃	2.45	202.086	pos	1.33	2.39E-11	↑**	—

(Continued on following page)

TABLE 1 (Continued) Identification of potential biomarkers in serum.

Metabolite	Library id	Formula	tR/ min	M/Z	Mode	VIP	p_value	Trend	
								M/ K	CR/ M
N-(1-Deoxy-1-fructosyl)phenylalanine	HMDB0037846	C ₁₅ H ₂₁ NO ₇	2.21	328.139	pos	1.43	1.06E-07	↓**	↑**
6-(4-Ethyl-2-hydroxyphenoxy)-3,4,5-trihydroxyoxane-2-carboxylic acid	HMDB0124984	C ₁₄ H ₁₈ O ₈	1.89	356.134	pos	1.46	1.52E-07	↑**	↓**
Niazirinin	HMDB0032808	C ₁₆ H ₁₉ NO ₆	1.47	339.155	pos	2.26	8.69E-09	↓**	↑**
Isovalerylalanine	HMDB0000747	C ₈ H ₁₅ NO ₃	.99	174.112	pos	1.28	1.79E-06	↓**	↑**
1-[(5-Amino-5-carboxypentyl)amino]-1-deoxyfructose	HMDB0034879	C ₁₂ H ₂₄ N ₂ O ₇	.51	353.129	pos	1.32	3.71E-06	↓**	↑**
Carnosine	HMDB0000033	C ₉ H ₁₄ N ₄ O ₃	.50	227.114	pos	1.35	2.25E-10	↓**	↑**
Taurolithocholic acid 3-sulfate	HMDB0002580	C ₂₆ H ₄₅ NO ₈ S ₂	6.02	280.621	neg	1.22	2.07E-13	↑**	—
12-Ketodeoxycholic acid	HMDB0000328	C ₂₄ H ₃₈ O ₄	6.15	435.275	neg	1.12	.001512	↓**	↑**
4-Chloro-1H-indole-3-acetic acid	HMDB0032936	C ₁₀ H ₈ ClNO ₂	6.00	208.016	neg	1.08	2.14E-07	↓**	↑**
2-trans-4-trans-7-cis-Decatrienal	HMDB0032213	C ₁₀ H ₁₄ O	4.49	195.102	neg	1.51	.02487	↓**	↓*
Pinocembrin	LMPK12140214	C ₁₅ H ₁₂ O ₄	5.76	255.066	neg	5.85	4.39E-10	↑**	↓**
Taurochenodeoxycholate-7-sulfate	HMDB0002498	C ₂₆ H ₄₅ NO ₉ S ₂	5.92	560.234	neg	1.20	1.42E-07	↑**	—
Rac-5,6-Epoxy-retinoyl-beta-D-glucuronide	HMDB0060123	C ₂₆ H ₃₆ O ₉	6.04	491.228	neg	1.93	1.35E-14	↑**	↓**
Protoporphyrinogen IX	HMDB0001097	C ₃₄ H ₄₀ N ₄ O ₄	6.11	567.297	neg	1.35	1.59E-07	↑**	↑**
1,11-Undecanedicarboxylic acid	HMDB0002327	C ₁₃ H ₂₄ O ₄	6.12	243.160	neg	1.89	7.54E-06	↓**	↑**
CPA (18:2 (9Z,12Z)/0:0)	HMDB0007007	C ₂₁ H ₃₇ O ₆ P	8.11	415.225	neg	2.34	4.05E-13	↓**	↑**
Ganoderic acid eta	HMDB0036309	C ₃₀ H ₄₄ O ₈	6.78	553.283	neg	1.61	2.07E-09	↑**	—
Frangulanine	HMDB0030199	C ₂₈ H ₄₄ N ₄ O ₄	6.70	537.288	neg	1.44	9.63E-07	↑**	—
Androsterone glucuronide	HMDB0002829	C ₂₅ H ₃₈ O ₈	6.70	501.222	neg	1.07	1.71E-06	↓**	↑**
Janthitrem C	HMDB0040684	C ₃₇ H ₄₇ NO ₄	6.14	604.325	neg	2.25	.0001456	↓**	↑**
3-Hydroxytetradecanedioic acid	HMDB0000394	C ₁₄ H ₂₆ O ₅	6.12	255.160	neg	1.54	2.55E-06	↓**	↑**
Allixin	HMDB0040705	C ₁₂ H ₁₈ O ₄	6.08	207.102	neg	1.01	4.04E-06	↓**	↑**
Kinetin-7-N-glucoside	HMDB0012243	C ₁₆ H ₁₉ N ₅ O ₆	5.95	422.135	neg	1.36	1.28E-08	↑**	↑**
Ganglioside GT3 (d18:1/20:0)	HMDB0012073	C ₈₃ H ₁₄₆ N ₄ O ₃₇	5.79	894.469	neg	2.85	8.92E-10	↓**	↑**
Melleolide	HMDB0035689	C ₂₃ H ₂₈ O ₆	5.55	445.189	neg	1.31	3.37E-11	↑**	↑**
Imazamethabenz	HMDB0034885	C ₁₅ H ₁₈ N ₂ O ₃	3.57	255.113	neg	2.01	4.13E-09	↑**	↑**
5-Hydroxyindoleacetic acid	HMDB0000763	C ₁₀ H ₉ NO ₃	3.49	190.050	neg	1.05	1.04E-07	↓**	↓**

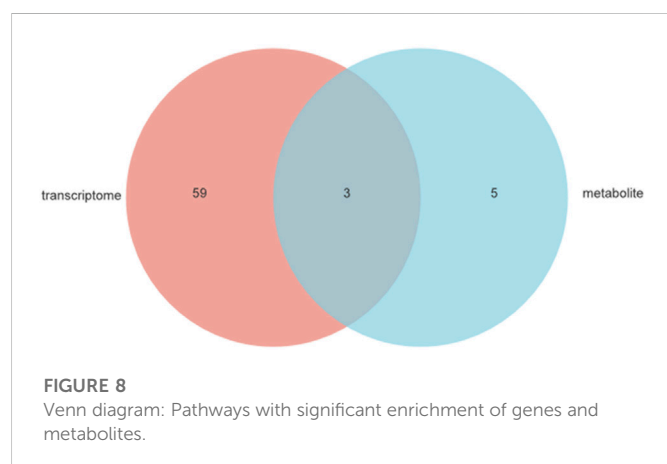
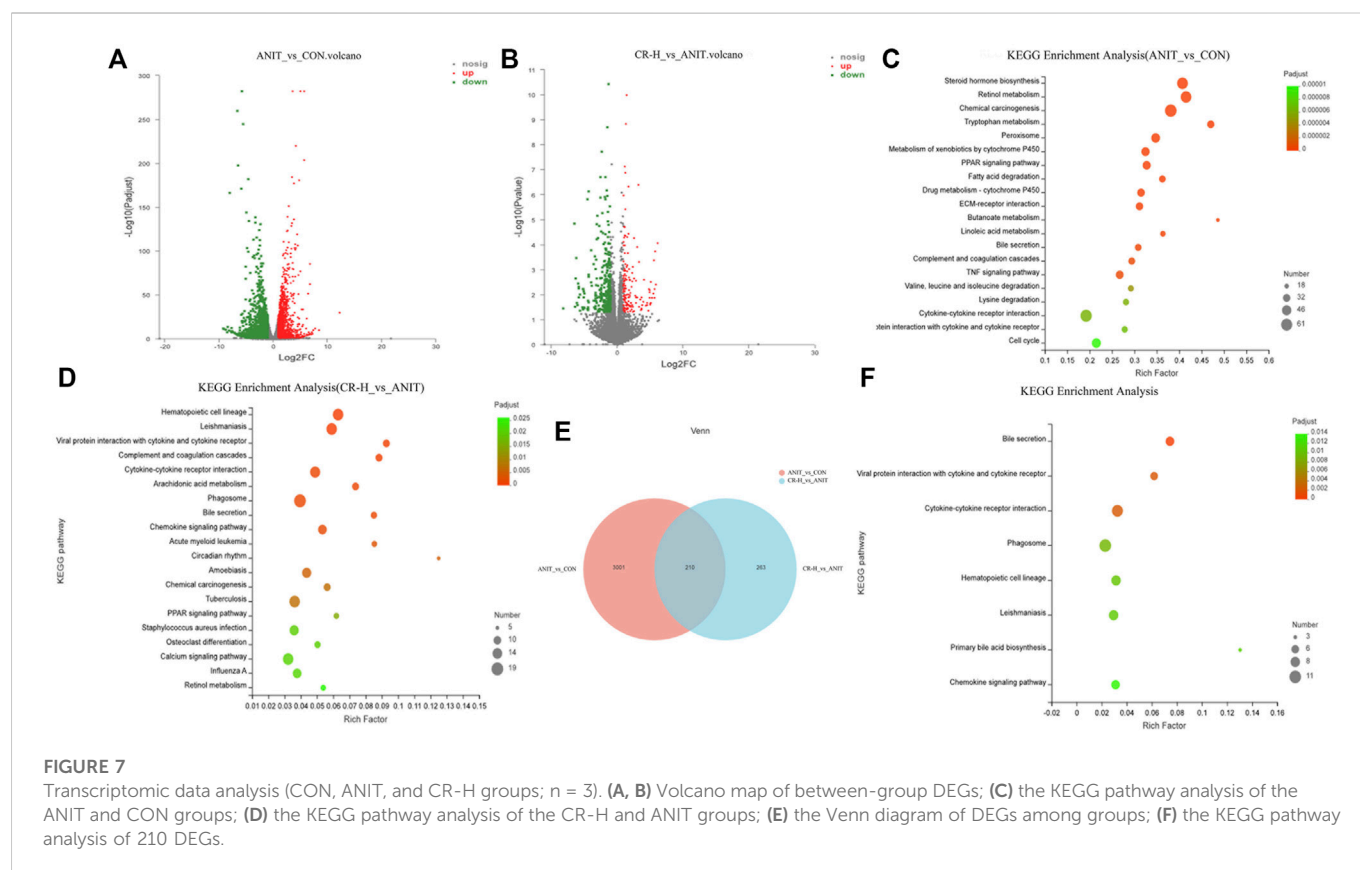
Note: M/K: ANIT versus CON, CR/M: CR-H versus ANIT; ↑:content increased, ↓:content decreased; * $p < .05$, ** $p < .01$.

5A,B, 85% and 95.1% of metabolites had a relative standard deviation (RSD)% \leq 30%, indicating that the separation among the different groups was good in the positive and negative ion modes, and the degree of polymerization within the group was high, indicating that there were remarkable differences in metabolites among the groups. The R^2X (cum), R^2Y (cum), and Q^2 (cum) of OPLS-DA in our positive model were .926, 1, and 1, respectively, using the data from the CON and ANIT groups and .607, .993, and .986, respectively, using the data from the ANIT and CR groups (Figures 5C,D). The OPLS-DA was seen to be accurate and reliable. The R^2X (cum), R^2Y (cum), and Q^2 (cum) of OPLS-DA in our negative model were .971, 1, and 1, respectively, using the data from the CON and ANIT groups and

.847, .993, and .992, respectively, using the data from the ANIT and CR groups (Figures 5E,F). The OPLS-DA was seen to be accurate and reliable. After 200 replacements, Figures 5G,H show values of $R^2 > 0$ and $Q^2 < 0$, indicating that the model did not have overfitting, and that the OPLS-DA model is reliable.

3.3 Identification of potential metabolite of CR in the treatment of ANIT-induced IC

Based on Student's t-test combined with the OPLS-DA analysis method, potential biomarkers were screened according to the



conditions of $VIP > 1$ and $p\text{-value} < .05$. A total of 225 significantly different metabolomics was identified between the ANIT group and the CON group, and 194 significantly different metabolites were obtained between the ANIT group and the CR-H group. To further reveal the metabolic pathways of potential metabolites related to CR in the treatment of IC, we analyzed the metabolic pathway using the KEGG database. Figure 6A shows the top 20 pathways involved in IC: three were significantly affected ($p < .05$), including bile secretion, steroid hormone biosynthesis, and ABC transporters.

The differential metabolites between the CR group and the ANIT group involved eight metabolic pathways, including bile secretion,

glutathione metabolism, steroid hormone biosynthesis, d-glutamine and d-glutamate metabolism, tryptophan metabolism, histidine metabolism, systemic lupus erythematosus, and the foxo signaling pathway (Figure 6B). Venn analysis identified 76 metabolites as differential metabolites in the CR-treated IC rats (Figure 6C), which enriched 10 metabolic pathways (Figure 6D). Table 1 shows the identified intersected metabolites; these differential metabolites in serum may be potential target biomarkers for IC.

3.4 Transcriptomic data analysis

The DEGs were screened using the software DESeq2, with $|\log_2(\text{Fold Change})| > 1$ and $p\text{-value}_{\text{adjust}} < .05$ as the screening conditions. Compared ANIT group with the CON group, 1806 DEGs were significantly upregulated, and 1405 DEGs were significantly downregulated (Figure 7A). Compared with the ANIT group, 153 genes were upregulated, and 320 genes were downregulated in the CR-H group (Figure 7B). With $p\text{-value}_{\text{adjust}} < .05$ as the filter condition, the DEGs between the ANIT group and the CON group were mainly enriched in tryptophan metabolism, chemical carcinogenesis, retinol metabolism, steroid hormone biosynthesis, cell cycle, bile secretion, linoleic acid metabolism, butanoate metabolism, ECM-receptor interaction, drug metabolism-cytochrome P450, fatty acid degradation, PPAR signaling pathway, and the TNF signaling pathway (Figure 7C). These findings show that the pathways that cause cholestasis are closely related to these factors. With $p\text{-value}_{\text{adjust}} < .05$ as the filter condition, the DEGs between the CR group and the ANIT group were mainly enriched in the retinol

TABLE 2 KEGG shared pathway data table.

Pathway id	Pathway description	First category	Second category	Metabolite list	Gene list	p-value_ corrected
rno00140	Steroid hormone biosynthesis	Metabolism	Lipid metabolism	Androsterone glucuronide; cortisol; estrone	gene29387(Ugt2b7); gene1452(Cyp2b2)	.1571
rno05322	Systemic lupus erythematosus	Human diseases	Immune disease	PS (18:0/20:4 (8Z,11Z,14Z,17Z))	gene36403 (RT1-Db1); gene36402 (RT1-Ba)	.0529
					gene36406 (RT1-Da); gene36267(C4a)	
					gene36497 (Tnf); gene28554(Fcgr3a)	
rno04976	Bile secretion	Organismal systems	Digestive system	6-Hydroxy-5-methoxyindole glucuronide; bilirubin; 5-hydroxy-6-methoxyindole glucuronide; estrone; cortisol; glycocholic acid; taurothiocholic acid 3-sulfate	gene13714(Acnat1); gene1200(Sult2a1); gene1197(Sult2a2); gene15392 (Abcg8); gene24758 (Abcc3); gene15391 (ABCG5); gene5199(HMGCR)	.0015

metabolism, calcium signal pathway, PPAR signaling pathway, circadian rhythm, chemokine signal pathway, arachidonic acid metabolism, bile secretion, and primary bile acid biosynthesis (Figure 7D). A total of 3,211 DEGs were obtained between the CON group and the ANIT group, and 210 DEGs were regulated after administration (Figure 7E). Figure 7F shows the KEGG pathway enriched by 210 DEGs.

3.5 Integrated analysis of transcriptomics and metabolomics

Venn analysis was performed to reflect the common pathways annotated between the DEGs of the transcriptome and the differential metabolites of the metabolomics, and three shared pathways were obtained, including steroid hormone biosynthesis, systemic lupus erythematosus, and bile secretion (Figure 8). With p -value_{adjust}<.05 as the filter condition, one pathway was significantly enriched: bile secretion (Table 2).

3.6 Expression correlation analysis

Spearman rank correlation was applied to analyze the DEGs and metabolites. Corr values greater than 0 identify a positive correlation between the differential metabolite and the differential gene. Corr values less than 0 identify a negative correlation between the differential metabolite and the differential gene. The redder the color, the stronger the positive correlation, and the bluer the color, the stronger the negative correlation. A Corr value of 0 indicates no correlation. The correlation between HMGCR, SULT2A1, Sult2a2, Abcc3, and metabolites was strong, and Acnat1, ABCG5, and Abcg8 had a potential correlation with some metabolites (Figure 9A).

The DEGs and differential metabolites on key pathways were imported into Cytoscape 3.8.2 software for gene-metabolite interaction network analysis. The interaction relationship between differential metabolites and DEGs was displayed using the network diagram. As shown in Figure 9B, the relationship between genes and metabolites was established. The results showed that the HMGCR, ABCG5, and Abcg8 genes interacted with most metabolites, while the Abcc3 and SULT2A1 genes interacted with a few metabolites.

3.7 The effect of CR on the expression of key targets

We used immunoblotting to validate the targets that directly modulate potential metabolites and verify some differential genes in the bile secretion pathway. The results showed that the expression of HMGCR in the liver tissue of rats in the ANIT group was significantly increased compared with the CON group. The expressions of ABCG5 and SULT2A1 levels were significantly decreased, and the expressions of these proteins were significantly regulated in CR ($p < .01$ or $p < .05$, Figure 10).

4 Discussion

Metabolomics is a qualitative or quantitative analysis of all small molecule metabolites in the organism with a relative molecular mass between 50 and 1500 to find the links between metabolites and physiological/pathological changes (Zhao et al., 2014). We identified 76 significant metabolites of the CR group in the serum, as well as their related pathways. In view of the one-sidedness of single omics, data analysis and interpretation were performed using transcriptomic conjoint analysis methods. We found three key targets (ABCG5, HMGCR, SULT2A1) and one pathway (bile secretion). Integration of metabolomics and transcriptomics was designed to study the metabolite profiles and gene expression profiles in biological systems under administration conditions and analyze the internal changes of biological systems from two levels (Chen et al., 2020).

In this study, we investigated the mechanism of the effect of CR against IC through metabolomics and transcriptomics. The IC model was successfully established by the administration of ANIT olive oil solution. Compared with the CON group, the serum levels of AST, TBA, and TBIL in the ANIT group were significantly increased, while they were significantly inhibited in the CR groups, which was consistent with the result of Xiong et al. (2016). In addition, compared with the ANIT group, the levels of TNF- α , 1L-L β , and 1L-6 in serum were significantly inhibited after CR administration, indicating that CR could play a protective and therapeutic role by alleviating inflammation, which was consistent with histological analysis.

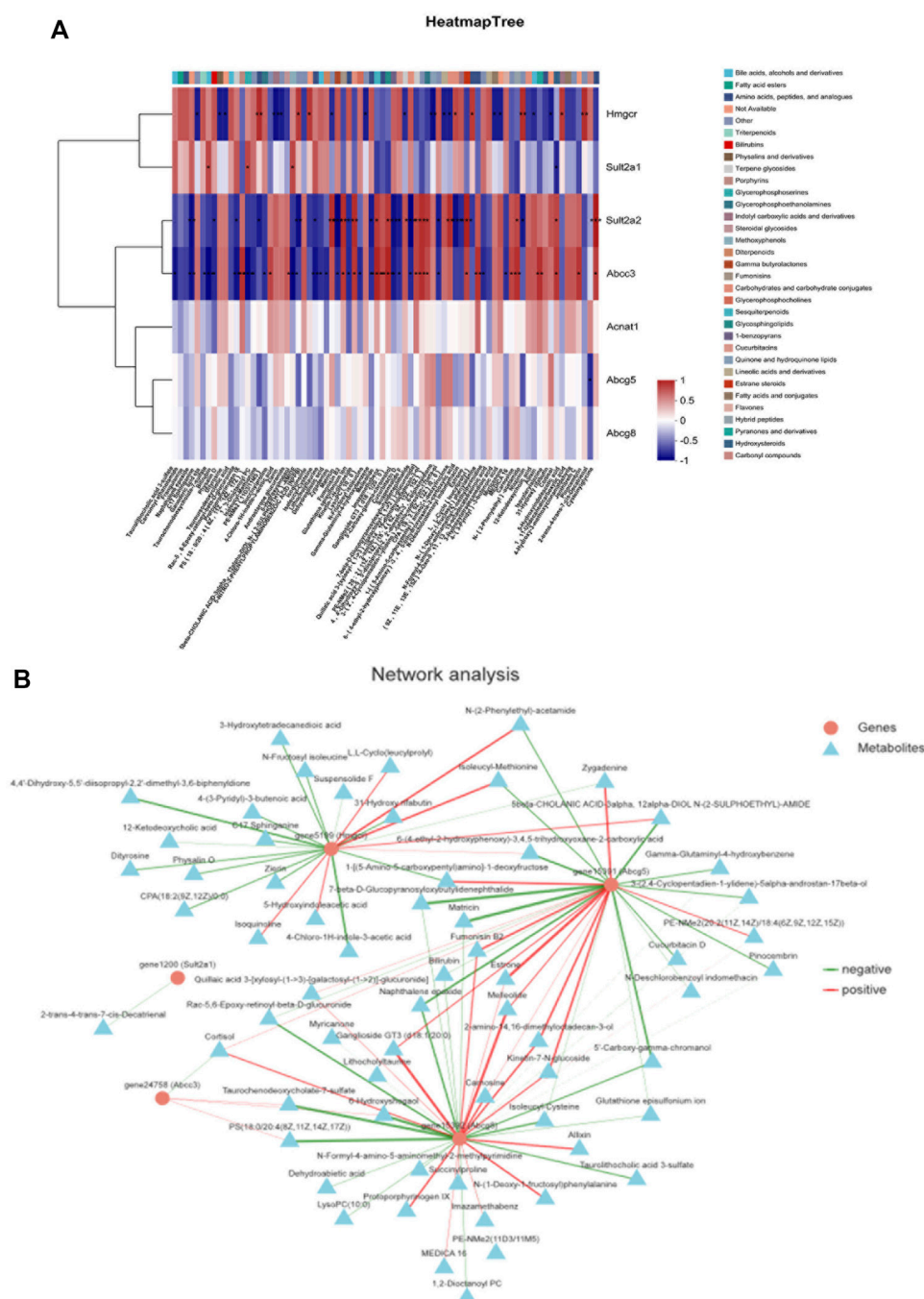


FIGURE 9

Correlation analysis of metabolic biomarkers and DEGs based on Spearman rank. (A) Correlation heat map, (B) correlation network map.

Cholestasis is closely related to metabolic disorders. Metabolomics can reveal the changes in the spectrum of endogenous metabolites in the body and further analyze the overall biological status and functional regulation of the body (S. Chen et al., 2022; Lin et al., 2020). After CR treatment, 45 metabolites in the serum were regulated. These candidate biomarkers and pathways suggest that the pathogenesis of cholestasis disease is a complex process. Therefore, the transcriptomic analysis was applied to explore the mechanism of CR when treating IC. In our study, 3,211 DEGs were obtained between the CON and the ANIT group. Compared with the ANIT group,

148 genes were regulated in the CR group. In addition, the enrichment pathways were mainly involved with endocrine system-related pathways, signal transduction pathways, and lipid metabolism pathways. Using an integrated strategy of transcriptomic and metabolomic analysis revealed the mechanism of CR in the treatment of IC.

To further understand the regulation of potential biomarkers in the CR group, we used the Spearman correlation algorithm to perform correlation analysis on DEGs and differentially expressed metabolites. The targets and potential biomarkers of the CR group were analyzed,

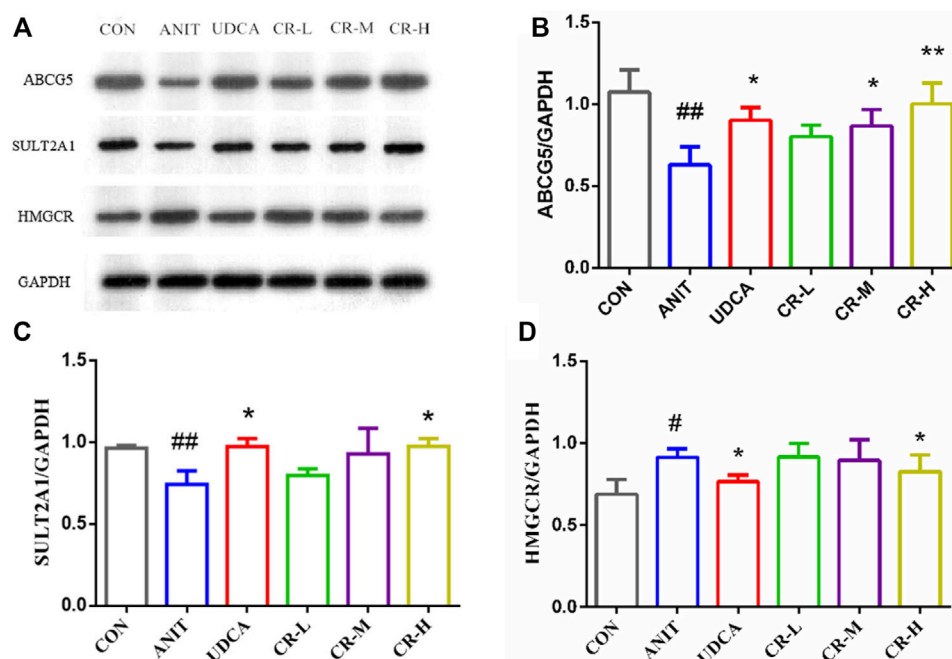


FIGURE 10

Expression levels of different proteins in the liver tissue of rats after administration. (A) Electrophoretic diagram of different groups, (B) expression level of ABCG5 protein, (C) expression level of SULT2A1 protein, (D) expression level of HMGCR protein.

and an interactive network of “potential-biomarker-target-components” was constructed. The results showed that the bile secretion pathway was the most important pathway in IC, and the most closely potential biomarkers were HMGCR, SULT2A1, ABCG5, ABCG8, and ABCC3.

The increase of bilirubin is one of the important phenomena of IC. Direct bilirubin is produced by indirect bilirubin through the transformation of bilirubin in the blood by hepatocytes in the liver (Kong et al., 2021). Further correlation analysis of DEGs and DEMs revealed that SULT2A1, HMGCR, are positively correlated with bilirubin, and ABCG5 are negatively correlated with bilirubin. The corresponding proteins of these three genes were verified by western blot. The analysis of expression of ABCG5, SULT2A1, and HMGCR was consistent with the western blot results, indicating that the results at the gene level and protein level were consistent, and the results of the bioinformatics analysis were reliable.

Synthetic and metabolic enzymes of bile acids also play significant roles in bile acid homeostasis. SULT2A1 can play an important role in the bile secretion pathway (Wu et al., 2021). This study found that the expression level of SULT2A1 in the ANIT group was significantly lower than that in the CON group. The expression of SULT2A1 can be significantly increased after the high-dose intervention of CR, indicating that CR at a dose of 90 mg/kg can exert a detoxification effect by regulating bile acid metabolism. Cholestasis can also lead to abnormal cholesterol metabolism. The liver cholesterol transporter ABCG5/8 is a member of the ABC transporter family, and it is highly expressed in the liver. In this study, the expression of ABCG5/8 in the ANIT group was lower than that of the CON group, and cholestasis developed. In the CR group, the expression of ABCG5/8 could be reversed, and the liver injury was relieved. Multidrug resistance-related protein 3 (MRP3/ABCC3) belongs to the ABC transporter

superfamily, which can combine ATP and utilize energy to drive a variety of different molecules across cell membranes (Wang et al., 2021). MRP3 is responsible for the transfer of certain specific bile acids, and the part of MRP3 may be compensated for by other transporters (Perez-Pineda et al., 2021). In this study, the expression level of HMGCR protein in the ANIT group was increased. In the CR-H group, this protein was significantly downregulated, indicating that the cholesterol synthesis ability was inhibited, and the secretion of bile acids was relatively reduced.

The concentration of 12-ketodeoxycholic acid in the bile of rats in the ANIT group was significantly higher than that in the control group, suggesting that bile acid metabolism in rats was significantly interfered with, thus causing lipid metabolism dysfunction. Due to liver function injury, bilirubin secretion and synthesis of primary bile acid in liver cells increased, which promoted the excretion of 12-ketodeoxycholic acid and increased the detected amount of 12-ketodeoxycholic acid in bile. In the ANIT group, the levels of sulfated cholate in the liver and serum were significantly increased, suggesting that the body had a compensatory detoxification process and alleviated the hepatocyte accumulation toxicity of cholate.

5 Conclusion

In this study, a novel integrated method was designed to investigate the key targets and mechanisms of CR when treating IC according to metabolomics and transcriptomics. The current results showed that CR has the effect of improving IC. The integrated analysis revealed three key targets as well as related metabolites and pathways. The targets were further verified by western blotting. This study has provided data and theoretical support for an in-depth study of the

mechanism and has laid the foundation for clinical application. Further systematic molecular biology experiments are needed to verify the accurate mechanisms. The study has also provided a novel paradigm to identify the potential mechanisms of pharmacological effects derived from a natural compound.

Data availability statement

The raw data supporting the conclusions of this article will be made available by the authors without undue reservation.

Ethics statement

The animal study was reviewed and approved by Jiangxi University of Traditional Chinese Medicine.

Author contributions

DS and PZ contributed to the design of this study and writing the draft of the manuscript. DS and PZ contributed equally to this manuscript. DS, AZ, HX, and YC conducted the experiments. YD, QZ, LX, and MW handled the data analysis. GL and YL contributed to the editing and review of the manuscript. JZ put forward suggestions on the revision of the manuscript after submission. All the authors approved the final version for publication.

References

- Alarcon-Barrera, J. C., Kostidis, S., Ondo-Mendez, A., and Giera, M. (2022). Recent advances in metabolomics analysis for early drug development. *Drug Discov. Today* 27 (6), 1763–1773. doi:10.1016/j.drudis.2022.02.018
- Chen, S., Huang, Y., Su, H., Zhu, W., Wei, Y., Long, Y., et al. (2022). The integrated analysis of transcriptomics and metabolomics unveils the therapeutic effect of asiatic acid on alcoholic hepatitis in rats. *Inflammation* 45 (4), 1780–1799. doi:10.1007/s10753-022-01660-x
- Chen, Y., Gao, Y., Yi, X., Zhang, J., Chen, Z., and Wu, Y. (2020). Integration of transcriptomics and metabolomics reveals the antitumor mechanism underlying shikonin in colon cancer. *Front. Pharmacol.* 11, 544647. doi:10.3389/fphar.2020.544647
- Chong, J., and Xia, J. (2018). MetaboAnalystR: an R package for flexible and reproducible analysis of metabolomics data. *Bioinformatics* 34 (24), 4313–4314. doi:10.1093/bioinformatics/bty528
- Fujita, Y., Sugaya, T., Inui, A., and Yoshihara, S. (2021). Effectiveness of ursodeoxycholic acid in the treatment of primary sclerosing cholangitis with ulcerative colitis: A pediatric case. *Tohoku J. Exp. Med.* 253 (2), 109–112. doi:10.1620/tjem.253.109
- Ji, L., Li, Q., He, Y., Zhang, X., Zhou, Z., Gao, Y., et al. (2022). Therapeutic potential of traditional Chinese medicine for the treatment of nafld: A promising drug potentilla discolor bunge. *Acta Pharm. Sin. B* 12 (9), 3529–3547. doi:10.1016/j.apsb.2022.05.001
- Kong, L., Dong, R., Huang, K., Wang, X., Wang, D., Yue, N., et al. (2021). Yanganonin modulates lipid homeostasis, ameliorates cholestasis and cellular senescence in alcoholic liver disease via activating nuclear receptor FXR. *Phytomedicine* 90, 153629. doi:10.1016/j.phymed.2021.153629
- Lari, P., Abnous, K., Imenshahidi, M., Rashedinia, M., Razavi, M., and Hosseinzadeh, H. (2015). Evaluation of diazinon-induced hepatotoxicity and protective effects of crocin. *Toxicol. Industrial Health* 31 (4), 367–376. doi:10.1177/0748233713475519
- Li, Y. X., Li, X. P., Gu, J., Li, J. C., Gong, P. Y., Shi, Z. L., et al. (2020). Study on protective mechanism of Tibetan medicine Ershiwuwei Songshi Pills on cholestatic liver injury in rats based on FXR signaling pathway. *China J. Chin. Materia Medica* 45 (21), 5273–5279. doi:10.19540/j.cnki.cjcm.20200727.401
- Lin, M., Chen, X., Wang, Z., Wang, D., and Zhang, J.-L. (2020). Global profiling and identification of bile acids by multi-dimensional data mining to reveal a way of eliminating abnormal bile acids. *Anal. Chim. Acta* 1132, 74–82. doi:10.1016/j.aca.2020.07.067
- Motlagh, P. E., Novin, A. G., Ghahari, F., Nikzad, A., Khoshandam, M., Mardani, S., et al. (2021). Evaluation of the effect of crocin on doxorubicin-induced cardiotoxicity. *Adv. Exp. Med. Biol.* 1328, 143–153. doi:10.1007/978-3-030-73234-9_10
- Perez-Pineda, S. I., Baylon-Pacheco, L., Espiritu-Gordillo, P., Tsutsumi, V., and Rosales-Encina, J. L. (2021). Effect of bile acids on the expression of MRP3 and MRP4: An *in vitro* study in HepG2 cell line. *Ann. Hepatology* 24, 100325. doi:10.1016/j.aohep.2021.100325
- Qiu, Y., Jiang, X., Liu, D., Deng, Z., Hu, W., Li, Z., et al. (2020). The hypoglycemic and renal protection properties of crocin via oxidative stress-regulated NF-kappa B signaling in db/db mice. *Front. Pharmacol.* 11, 541. doi:10.3389/fphar.2020.00541
- Samant, H., Manatsathit, W., Dies, D., Shokouh-Amiri, H., Zibari, G., Bektor, M., et al. (2019). Cholestatic liver diseases: An era of emerging therapies. *World J. Clin. Cases* 7 (13), 1571–1581. doi:10.12998/wjcc.v7.i13.1571
- Tang, Y., Yang, H., Yu, J., Li, Z., Xu, Q., Ding, B., et al. (2022). Crocin induces ROS-mediated papillary thyroid cancer cell apoptosis by modulating the miR-34a-5p/PTPN4 axis *in vitro*. *Toxicol. Appl. Pharmacol.* 437, 115892. doi:10.1016/j.taap.2022.115892
- Teng, S., Hao, J., Bi, H., Li, C., Zhang, Y., Zhang, Y., et al. (2021). The protection of crocin against ulcerative colitis and colorectal cancer via suppression of NF-kappa B-mediated inflammation. *Front. Pharmacol.* 12, 639458. doi:10.3389/fphar.2021.639458
- Trezzi, J.-P., Vlassis, N., and Hiller, K. (2015). The role of metabolomics in the study of cancer biomarkers and in the development of diagnostic tools. *Adv. Cancer Biomarkers Biochem. Clin. a Crit. Revis.* 867, 41–57. doi:10.1007/978-94-017-7215-0_4
- Vignoli, A., Muraro, E., Miolo, G., Tenori, L., Turano, P., Di Gregorio, E., et al. (2020). Effect of estrogen receptor status on circulatory immune and metabolomics profiles of

Funding

This research was supported by the National Key Research and Development Program of TCM Modernization Research Key Project (2017YFC1700902).

Acknowledgments

We thank Jiangxi University of Chinese Medicine for its equipment.

Conflict of interest

The authors declare that the research was conducted in the absence of any commercial or financial relationships that could be construed as a potential conflict of interest.

Publisher's note

All claims expressed in this article are solely those of the authors and do not necessarily represent those of their affiliated organizations, or those of the publisher, the editors, and the reviewers. Any product that may be evaluated in this article, or claim that may be made by its manufacturer, is not guaranteed or endorsed by the publisher.

- HER2-positive breast cancer patients enrolled for neoadjuvant targeted chemotherapy. *Cancers* 12 (2), 314. doi:10.3390/cancers12020314
- Wang, W., Zeng, S., Hu, M., Liu, Z., and Gong, L. (2021). The function of multidrug resistance-associated protein 3 in the Transport of bile acids under normal physiological and lithocholic acid-induced cholestasis conditions. *Curr. Drug Metab.* 22 (5), 353–362. doi:10.2174/1389200222666210118101715
- Wu, P., Qiao, L., Yu, H., Ming, H., Liu, C., Wu, W., et al. (2021). Arbutin alleviates the liver injury of alpha-Naphthylisothiocyanate-induced cholestasis through farnesoid X receptor activation. *Front. Cell Dev. Biol.* 9, 758632. doi:10.3389/fcell.2021.758632
- Xiong, X.-L., Yan, S.-Q., Qin, H., Zhou, L.-S., Zhang, L. L., Jiang, Z.-X., et al. (2016). Protective effect of emodin pretreatment in young rats with intrahepatic cholestasis. *Zhongguo dang dai er ke za zhi Chin. J. Contemp. Pediatr.* 18 (2), 165–171. doi:10.7499/j.issn.1008-8830.2016.02.013
- Yang, F., Wang, Y., Li, G., Xue, J., Chen, Z.-L., Jin, F., et al. (2018). Effects of corilagin on alleviating cholestasis via farnesoid X receptor-associated pathways *in vitro* and *in vivo*. *Br. J. Pharmacol.* 175 (5), 810–829. doi:10.1111/bph.14126
- Zhang, H., Li, C., Liao, S., Tu, Y., Sun, S., Yao, F., et al. (2022). PSMD12 promotes the activation of the MEK-ERK pathway by upregulating KIF15 to promote the malignant progression of liver cancer. *Cancer Biol. Ther.* 23 (1), 1–11. doi:10.1080/15384047.2022.2125260
- Zhao, Y. Y., Cheng, X. L., Vaziri, N. D., Liu, S. M., and Lin, R. C. (2014). UPLC-based metabolomic applications for discovering biomarkers of diseases in clinical chemistry. *Clin. Biochem.* 47 (15), 16–26. doi:10.1016/j.clinbiochem.2014.07.019



OPEN ACCESS

EDITED BY

Junmin Zhang,
Lanzhou University, China

REVIEWED BY

Lianguo Chen,
First Affiliated Hospital of Wenzhou
Medical University, China
Masato Takahashi,
Chiba Institute of Science, Japan
Yuan Wei,
Jiangsu University, China
Jie Hou,
Dalian Medical University, China

*CORRESPONDENCE

Kewu Zeng,
✉ zkw@bjmu.edu.cn
Qi Wang,
✉ wangqi@bjmu.edu.cn

SPECIALTY SECTION

This article was submitted to Drug
Metabolism and Transport,
a section of the journal
Frontiers in Pharmacology

RECEIVED 09 November 2022

ACCEPTED 16 January 2023

PUBLISHED 25 January 2023

CITATION

Li Y, Liu X, Li L, Zhang T, Gao Y, Zeng K and
Wang Q (2023), Characterization of the
metabolism of eupalinolide A and B by
carboxylesterase and cytochrome P450 in
human liver microsomes.
Front. Pharmacol. 14:1093696.
doi: 10.3389/fphar.2023.1093696

COPYRIGHT

© 2023 Li, Liu, Li, Zhang, Gao, Zeng and
Wang. This is an open-access article
distributed under the terms of the [Creative
Commons Attribution License \(CC BY\)](#).
The use, distribution or reproduction in
other forums is permitted, provided the
original author(s) and the copyright
owner(s) are credited and that the original
publication in this journal is cited, in
accordance with accepted academic
practice. No use, distribution or
reproduction is permitted which does not
comply with these terms.

Characterization of the metabolism of eupalinolide A and B by carboxylesterase and cytochrome P450 in human liver microsomes

Yingzi Li¹, Xiaoyan Liu¹, Ludi Li¹, Tao Zhang¹, Yadong Gao¹,
Kewu Zeng^{2*} and Qi Wang^{1,3,4*}

¹Department of Toxicology, School of Public Health, Peking University, Beijing, China, ²State Key Laboratory of Natural and Biomimetic Drugs, School of Pharmaceutical Sciences, Peking University, Beijing, China, ³Key Laboratory of State Administration of Traditional Chinese Medicine for Compatibility Toxicology, Beijing, China, ⁴Key Laboratory of Toxicological Research and Risk Assessment for Food Safety, Beijing, China

Eupalinolide A (EA; Z-configuration) and eupalinolide B (EB; E-configuration) are bioactive cis-trans isomers isolated from *Eupatorii Lindleyani Herba* that exert anti-inflammatory and antitumor effects. Although one pharmacokinetic study found that the metabolic parameters of the isomers were different in rats, metabolic processes relevant to EA and EB remain largely unknown. Our preliminary findings revealed that EA and EB are rapidly hydrolyzed by carboxylesterase. Here, we investigated the metabolic stability and enzyme kinetics of carboxylesterase-mediated hydrolysis and cytochrome P450 (CYP)-mediated oxidation of EA and EB in human liver microsomes (HLMs). We also explored differences in the hydrolytic stability of EA and EB in human liver microsomes and rat liver microsomes (RLMs). Moreover, cytochrome P450 reaction phenotyping of the isomers was performed *via in silico* methods (i.e., using a quantitative structure-activity relationship model and molecular docking) and confirmed using human recombinant enzymes. The total normalized rate approach was considered to assess the relative contributions of five major cytochrome P450s to EA and EB metabolism. We found that EA and EB were eliminated rapidly, mainly by carboxylesterase-mediated hydrolysis, as compared with cytochrome P450-mediated oxidation. An inter-species difference was observed as well, with faster rates of EA and EB hydrolysis in rat liver microsomes. Furthermore, our findings confirmed EA and EB were metabolized by multiple cytochrome P450s, among which CYP3A4 played a particularly important role.

KEYWORDS

eupalinolide A, eupalinolide B, human liver microsomes, carboxylesterase, cytochrome P450, metabolic stability, enzyme kinetics, CYP phenotyping

1 Introduction

Eupalinolide A (EA) and eupalinolide B (EB), a pair of cis-trans isomers (Figure 1), are bioactive sesquiterpenoids found in *Eupatorii Lindleyani Herba* (Wang X. et al., 2020). As potential drug candidates, these isomers have been reported to exert anti-inflammatory and antitumor effects (Zhang et al., 2022a; Zhang et al., 2022b; Yang et al., 2022). Recently, EB was reported to exert anti-neuroinflammatory activity *via* targeting ubiquitin-specific protease 7 in the setting of neurodegenerative disease (Zhang et al., 2022c).

Currently, the United States Food and Drug Administration (FDA) recommended that all new chemical entities under development be identified on the basis of their metabolic properties

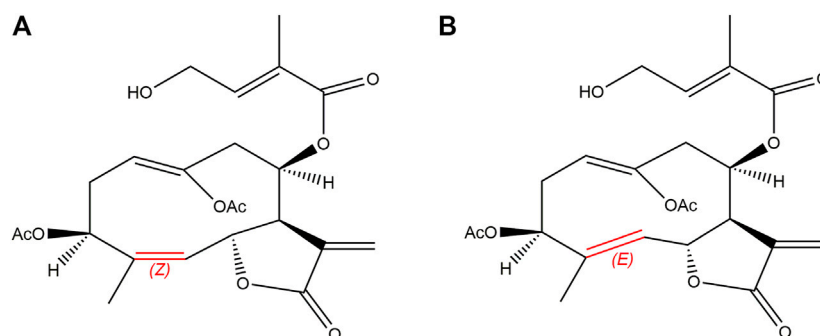


FIGURE 1
Chemical structures of EA [(A); Z-configuration] and EB [(B); E-configuration].

before administration to humans¹. Assessment of candidate compound pharmacokinetics and pharmacodynamics is critical for successful drug development (Kumar and Surapaneni, 2001; Meng and Liu, 2014). Poor metabolic stability *in vitro* is generally predictive for unfavorable pharmacokinetic properties such as rapid compound metabolism *in vivo*, low bioavailability and short duration of action (Liang et al., 2015). To date, few studies have investigated the metabolism of EA and EB. One pharmacokinetic study in rats revealed that these isomers exhibit different metabolic parameters, with EB having a higher bioavailability and thus greater potential for clinical use (Zhang et al., 2015). Importantly, significant differences exist between human and rodent enzymatic function and metabolism. As an ideal *in vitro* human-based test system, human liver microsomes (HLMs) offer numerous advantages for evaluating drug metabolism such as low cost, robustness, low lot-to-lot variability and wide commercial availability (Harper and Brassil, 2008; Miners et al., 2010; Caldwell and Yan, 2014). Our preliminary findings revealed that EA and EB are largely metabolized by carboxylesterase. In this study, we investigated the metabolic stability and kinetics of EA and EB in HLMs, focusing particularly on cytochrome P450 (CYP)-mediated oxidation and carboxylesterase-mediated hydrolysis. We also compared the hydrolytic stability of EA and EB in HLMs and rat liver microsomes (RLMs) to explore possible inter-species differences in metabolism among humans and rats.

Enzyme phenotyping, another important step in the drug development process, is performed to avoid undesirable drug interactions. Recombinant human cytochrome P450s (rhCYPs) are widely used for enzyme phenotyping in early drug development (Chen et al., 2011). In addition, advances in computing methods such as quantitative structure-activity relationship (QSAR) model construction and molecular docking analysis have facilitated isozyme prediction. A QSAR model is established based on structural characteristics and properties of known compounds and is used to predict metabolism of compounds with similar structures under the assumption that molecules with similar structures likely exhibit similar biochemical properties (Wu et al., 2013). The FDA as well as the Registration, Evaluation and Authorization of Chemicals

issued by the European Union consider QSAR predictions to be highly reliable (Gertrudes et al., 2012; Hong et al., 2016). Molecular docking, another computational approach, has become widely used in the early stage of drug development to simulate interactions among proteins and ligands for the purposes of elucidating compound enzymatic metabolism (Kaur et al., 2019; Kazmi et al., 2019).

In this study, we investigated the metabolic stability and kinetics of CYP-mediated oxidation and carboxylesterase-mediated hydrolysis of EA and EB using HLMs. Moreover, CYP phenotyping of the isomers was explored using *in silico* methods including a QSAR model and molecular docking analysis. Findings were confirmed with rhCYPs.

2 Materials and methods

2.1 Reagents and materials

EA (purity $\geq 98\%$) and sulfaphenazole were purchased from Beijing Mreda Technology Co., Ltd. (Beijing, China), while EB (purity $\geq 98\%$) was purchased from Chengdu Push Biotechnology Co., Ltd. (Chengdu, China). Carbamazepine was purchased from Shanghai Yuanye Biotechnology Co., Ltd. (Shanghai, China). Nicotinamide adenine dinucleotide phosphate (NADPH) was purchased from Sigma Aldrich (St. Louis, MO, United States). Midazolam was purchased from Beijing Gersion Biotechnology Co., Ltd. (Beijing, China). Phenacetin and tolbutamide were purchased from Aladdin Industrial Corp. (Shanghai, China). (S)-Mephentoin, dextromethorphan, dextrorphan and 1'-OH-midazolam were purchased from Glpbio (Montclair, CA, United States). Paracetamol and bis(4-nitrophenyl) phosphoric acid (BNPP) were purchased from Beijing Innochem Technology Co., Ltd. (Beijing, China). The 4-OH-tolbutamide was purchased from J&K Scientific Technology Co., Ltd. (Beijing, China), while 4-OH-mephentoin was purchased from Bioplastics (Landgraaf, Netherlands). Acetonitrile and methanol for high-performance liquid chromatography (HPLC) and mass spectrometry (MS) were obtained from Thermo Fisher Scientific (Waltham, MA, United States). All other chemicals and reagents, including $MgCl_2$, potassium phosphate dibasic and dimethyl sulfoxide, were of analytical grade and commercially available.

Pooled HLMs were purchased from Xeno Tech (Kansas City, KS, United States); HLM donors were individuals without hepatic disease

¹ FDA. M12 Drug Interaction Studies (2022). <https://www.fda.gov/regulatory-information/search-fda-guidance-documents/m12-drug-interaction-studies> [Accessed 26 August 2022].

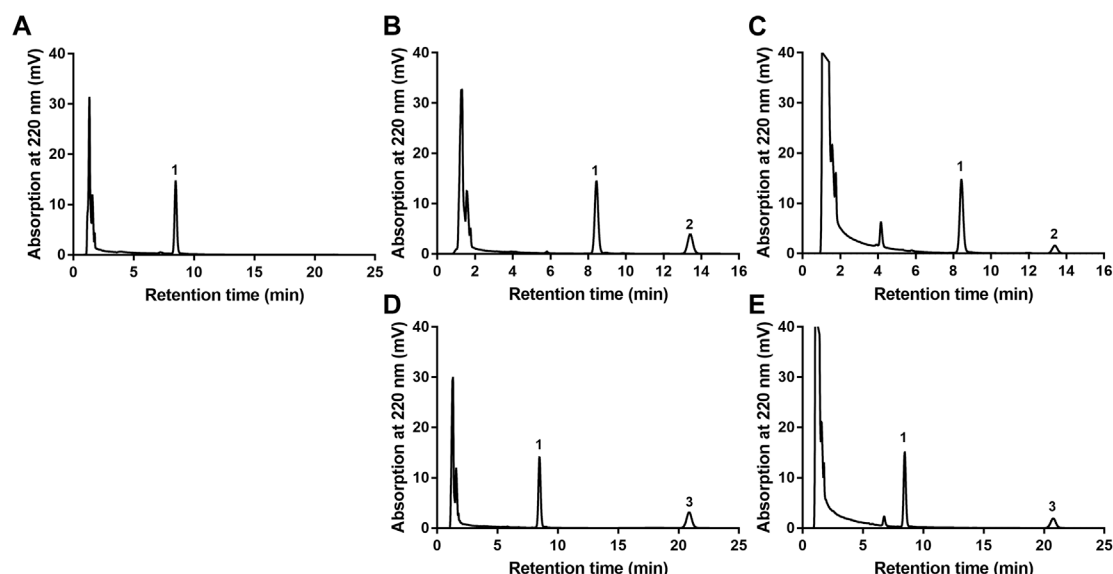


FIGURE 2

HPLC chromatograms of EA or EB in HLMs. (A) blank HLMs; (B) blank HLMs spiked with EA; (C) incubation of EA with HLMs; (D) blank HLMs spiked with EB; (E) incubation of EB with HLMs; 1: IS, 2: EA, 3: EB.

and included 100 men and 100 women aged 16–78 years (lot no. 1910096). Pooled RLMs were purchased from IPHASE (Beijing, China). Activity of HLM and RLM was confirmed *via* the detection of major metabolic enzymes. The cDNA-expressed human CYP1A2, 2C9, 2C19, 2D6 and 3A4 were purchased from Cypex (Dundee, United Kingdom).

2.2 Metabolic stability of EA and EB oxidation and hydrolysis in HLMs

2.2.1 Determination of flavin-containing monooxygenase (FMO) contribution to EA and EB metabolism

To explore CYP-mediated oxidation, we first determined how FMO affects EA and EB metabolism. An incubation system consisting of 100 mM phosphate buffer solution at pH 7.4, HLMs (0.5 g/L), MgCl_2 (5 mM) and NADPH (1 mM) was utilized. The mixture was preincubated at 37°C for 5 min. To initiate the metabolic reaction, EA or EB (dissolved in methanol at a final concentration of 10 μM) was added. To inactivate FMO, HLMs were heated at 50°C for 90 s (Zhuang et al., 2014). HLMs in positive control group were not subjected to heat treatment while negative control groups contained deactivated HLMs. Organic solvent content in the incubation system did not exceed 0.5%. The metabolic reaction was terminated by adding 200 μL of stop solution [ice-cold acetonitrile/methanol (1:1) containing internal standard (IS) carbamazepine] at 0, 2, 5, 10, 20, and 30 min, respectively. Samples were vortexed and centrifuged at 17,000 g for 15 min. Supernatant was collected and subjected to HPLC analysis. All incubations were performed in triplicate.

Data were expressed as means \pm SD and analyzed using SPSS software (IBM, New York, NY, United States). Student's *t*-test was used to compare differences between groups at various time points, and $p < 0.05$ was considered to be statistically significant.

2.2.2 Selection of carboxylesterase inhibitor BNPP concentration in HLMs

To determine ideal BNPP concentration for inhibiting carboxylesterase activity in HLMs, an incubation system consisting of 100 mM phosphate buffer solution at pH 7.4, HLMs (0.5 g/L), MgCl_2 (5 mM) and BNPP (0.5, 1, 1.5 and 2 mM) was prepared (Zhuang et al., 2014; Wang Y. Q. et al., 2020; Zhang et al., 2022d; Jin et al., 2022). The mixture was preincubated at 37°C for 5 min and the metabolic reaction was initiated by addition of EA or EB (at a final concentration of 10 μM). Positive control groups lacked BNPP while negative control groups contained deactivated HLMs. Organic solvent content in the incubation system did not exceed 0.5%. The above reaction was terminated by adding 200 μL of ice-cold stop solution at 30 min. Sample preparation and evaluation were as described in 2.2.1. All incubations were performed in triplicate. The percentage of EA or EB hydrolysis inhibition was calculated using the following Eq. 1:

$$\text{Inhibition\%} = [1 - (\Delta \text{substrate in the presence of chemical inhibitor} / \Delta \text{substrate in the absence of chemical inhibitor})] \times 100\%$$

Data were expressed as means \pm SD and analyzed using SPSS. Student's *t*-test was used to compare differences between groups, and $p < 0.05$ was considered to be statistically significant.

2.2.3 Metabolic stability of EA and EB in HLMs to oxidation and hydrolysis

The metabolic stability of EA and EB was determined by using the most conventional method of measuring test compound depletion over time (Caldwell and Yan, 2014). For determination of metabolic stability to oxidation, a system composed of 100 mM phosphate buffer solution at pH 7.4, HLMs (0.5 g/L), MgCl_2 (5 mM), NADPH (1 mM) and BNPP (0.5 mM) was preincubated at 37°C for 5 min. Then, EA or EB (at a final concentration of 10 μM) was added to initiate the metabolic reaction. For determination of metabolic stability to

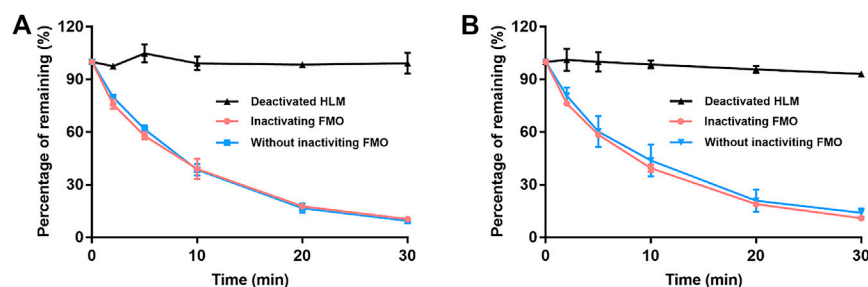


FIGURE 3

The contribution of FMO to EA (A) and EB (B) metabolism in HLMs with NADPH. Deactivated HLMs were used as negative control (mean \pm SD; $n = 3$).

hydrolysis, the incubation system was prepared either without NADPH or BNPP (mixture containing NADPH and lacking BNPP evaluated CYP and carboxylesterase co-mediated metabolic reactivity). Organic solvent content in the incubation system did not exceed 0.5%. Negative control groups contained deactivated HLMs. The above reactions were terminated by adding 200 μ l of ice-cold stop solution at 0, 2, 5, 10, 20, and 30 min, respectively. Sample preparation and determination were as described in 2.2.1. All incubations were performed in triplicate.

The natural logarithm of the remaining percentage of EA or EB and reaction time were plotted to obtain the slope (k) by linear regression; EA and EB elimination half-lives ($t_{1/2}$) were calculated using Eq. 2. The well-stirred model (Obach, 1997; Slaughter et al., 2003; Reddy et al., 2005; Zhao et al., 2005) was used to extrapolate both intrinsic (CL_{int}) [ml/(min·kg)] and hepatic (CL_h) [ml/(min·kg)] clearance of EA and EB from the human liver.

$$t_{1/2} = -0.693/k \quad (2)$$

$$CL_{int} = 0.693/t_{1/2} (G_{HLM}/W_{liver})(W_{liver}/W_{body})/C_{protein} \quad (3)$$

$$CL_h = \frac{Q_h \times CL_{int}}{Q_h + CL_{int}} \quad (4)$$

G_{HLM} represents average liver microsomal protein concentration (mg); W_{liver} represents liver weight (g); W_{body} represents body weight (kg); $C_{protein}$ represents reaction system protein concentration (mg/mL); Q_h represents liver blood flow velocity. Empirical values of relevant human physical and chemical parameters were 48.8, 25.7 and 20.7 for W_{liver}/W_{body} , G_{HLM}/W_{liver} and Q_h , respectively (Slaughter et al., 2003).

2.3 Kinetics of EA and EB oxidation and hydrolysis in HLMs

Experiments were conducted under conditions of linear substrate depletion (0.5 g/L HLMs; 10 min) (Zhang et al., 2008). For assay of CYP-mediated oxidation kinetics, HLMs (0.5 g/L) were incubated with NADPH (1 mM), BNPP (0.5 mM), $MgCl_2$ (5 mM) and 100 mM phosphate buffer solution at pH 7.4. After preincubation at 37°C for 5 min, the metabolic reaction was initiated by adding EA or EB (2.5, 5, 10, 25, 50 or 100 μ M). For assay of carboxylesterase-mediated hydrolysis kinetics, the incubation system was prepared lacking either NADPH or BNPP. Negative controls contained deactivated HLMs. Organic solvent content in the incubation

system did not exceed 0.5%. The above reactions were terminated by adding 200 μ l of ice-cold stop solution at 10 min. Sample preparation and evaluation were as described in 2.2.1. All incubations were performed in triplicate.

The elimination rate of EA and EB was fit with Michaelis-Menten kinetics. Enzyme kinetic parameters, the Michaelis-Menten constant (K_m) and maximum velocity (V_{max}) were calculated using GraphPad Prism 7 to obtain a non-linear least-square fit to the Michaelis-Menten equation. *In vitro* CL_{int} was calculated as $CL_{int} = V_{max}/K_m$ (Yu et al., 2013).

2.4 Hydrolytic stability of EA and EB in RLMs

Male and female RLMs were mixed in a 1:1 ratio for incubation. A system composed of 100 mM phosphate buffer solution at pH 7.4, RLMs (0.5 g/L), $MgCl_2$ (5 mM) and NADPH (1 mM) was preincubated at 37°C for 5 min. Then, EA or EB (at a final concentration of 10 μ M) was added to initiate hydrolysis. Procedures were as described in 2.2.3. All incubations were performed in triplicate. Hydrolytic stability parameters were calculated as described in 2.2.3. Empirical values of relevant rat physical and chemical parameters were 44.8, 40 and 55.2 for W_{liver}/W_{body} , G_{HLM}/W_{liver} and Q_h , respectively (Slaughter et al., 2003).

2.5 CYP phenotyping

2.5.1 QSAR model prediction of CYP phenotyping

The QSAR-based software ADMET Predictor 8.5 (Simulation Plus, Lancaster, CA, United States) was used to predict metabolic phenotyping for CYP1A2, CYP2A6, CYP2B6, CYP2C8, CYP2C9, CYP2C19, CYP2D6, CYP2E1 and CYP3A4 as relevant to EA and EB. The 2D structures of EA and EB were input into the software in MDL Mol file format and analyzed in metabolic modules.

2.5.2 Molecular docking analysis of CYP isozymes

The molecular docking software SYBYL-X 2.0 (Tripos, St Louis, MO, United States) was used to determine whether EA and EB could bind each of the five main CYP isoforms (CYP1A2, CYP2C9, CYP2C19, CYP2D6 and CYP3A4). The 3D structures of proteins [PDB ID: 2HI4 (CYP1A2), 5W0C (CYP2C9), 4GQS (CYP2C19), 3TBG (CYP2D6), and 6MA7 (CYP3A4)] were retrieved from the Protein Data Bank. Protein pretreatment involved removal of metal

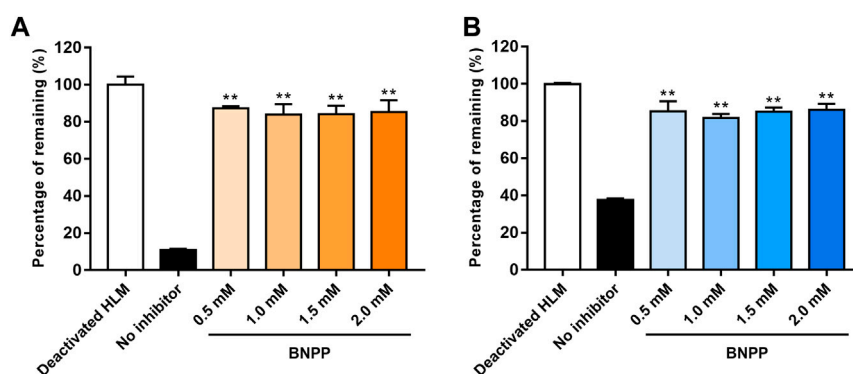


FIGURE 4

Influence of BNPP on EA (A) and EB (B) stability in HLMs in the absence of NADPH. Incubation with deactivated HLMs was performed for negative controls (100% remained). Incubation of HLMs without inhibition was performed for positive control. Significant differences from positive control were analyzed using the *t*-test. **p* < 0.05, ***p* < 0.01 (mean ± SD; *n* = 3).

ions, removal of water and solvent molecules, addition of hydrogen atoms, as well as repair of side-chains and side-chain amides. The 3D structures of EA and EB, which were used as ligands, were input into SYBYL-X in mol2 format. A Gasteger-Hückel charge was added to the third-order force field to minimize EA and EB energy. Surflex-Dock Geom mode was used for molecular docking. The root-mean-square deviation (RMSD) is the average distance between the highest-ranking docked and reference structures. A protein is considered appropriate for molecular docking when the RMSD value is less than 2 Å. The total score is the most important evaluation index for molecular docking, which comprehensively considers polar complementarity, solvation terms, entropic terms and hydrophobic complementarity. It is considered a stable interaction when the total score is greater than 6 (Gao et al., 2016).

2.5.3 Determination of rhCYP activity

Each of the probe substrates (50 μM phenacetin for CYP1A2; 120 μM tolbutamide for CYP2C9; 40 μM (S)-mephenytoin for CYP2C19; 5 μM dextromethorphan for CYP2D6; 5 μM midazolam for CYP3A4) was incubated with 100 pmol ml⁻¹ of rhCYPs (CYP1A2, 2C9, 2C19, 2D6 and 3A4) for 30 min. The incubation system also included MgCl₂ (5 mM) and 100 mM potassium phosphate buffer at pH 7.4. Control groups were treated with stop solution prior to rhCYP addition. Organic solvent content in the incubation system did not exceed 0.5%. Sample preparation was as described in 2.2.1. Supernatant was collected and analyzed for specific metabolites via liquid chromatography-tandem mass spectrometry (LC-MS/MS). All incubations were performed in triplicate.

2.5.4 CYP phenotyping of EA and EB with rhCYPs

Because CYP1A2, 2C9, 2C19, 2D6 and 3A4 are the most important human CYP isoforms involved in drug metabolism (Zhang et al., 2008), we investigated whether the above isoforms were the metabolic enzymes of these isomers. Either EA or EB (10 μM) was incubated with each of the rhCYPs (100 pmol ml⁻¹; CYP1A2, 2C9, 2C19, 2D6 or 3A4), NADPH (1 mM) and MgCl₂ (5 mM) in 100 mM potassium phosphate buffer at pH 7.4 for 10 min. Control groups contained deactivated rhCYPs. Organic solvent content in the incubation system did not exceed 0.5%. Sample preparation and

determination were as described in 2.2.1. All incubations were performed in triplicate.

Relative contribution of CYP isoforms to EA and EB metabolism was estimated using the total normalized rate (TNR) approach as described by Rodrigues (Rodrigues, 1999) and as shown in Eq. 5. The metabolism rate (pmol/min/pmol CYP) for each rhCYP isoform (rCYP_n) was multiplied by the mean specific content of the corresponding CYP isoform in native HLMs (mCYP_n) to yield the normalized rate (NR). Then, NR values were summed to obtain the TNR and percentages of TNRs calculated for each rCYP_n.

$$\begin{aligned} \text{TNR\%} &= \frac{\text{NR}}{\text{TNR}} \times 100 \\ &= \frac{\text{pmol/min/pmolrCYP}_n \times \text{pmolmCYP}_n/\text{mg}}{\sum (\text{pmol/min/pmolrCYP}_n \times \text{pmolmCYP}_n/\text{mg})} \times 100 \end{aligned} \quad (5)$$

2.6 Determination of residual EA and EB by HPLC

Quantification of EA and EB was accomplished via HPLC using an Agilent 1200 Infinity series instrument (Waldbronn, Germany) fitted with a Zorbax SB-C18 HPLC column (4.6 mm × 150 mm, 5 μm; Agilent, Santa Clara, CA, United States). Column temperature was maintained at 40°C with a mobile phase flow rate of 1 ml/min. The detection wavelength was 220 nm. The two compounds were separated by isocratic elution with a mobile phase consisting of 30% acetonitrile and 70% H₂O. Retention times of EA and EB were 13.55 min and 20.91 min, respectively. Incubation sample EA and EB concentrations were quantified using standard curves prepared from samples over a concentration range of 0.5–100 μM.

2.7 Quantification of CYP isoform activity by UFLC-MS/MS

The quantification of five CYP-specific substrate metabolites (paracetamol for CYP1A2; 4-OH-tolbutamide for CYP2C9; 4-OH-mephenytoin for CYP2C19; dextromethorphan for CYP2D6; 1'-OH-midazolam for CYP3A4) was performed according to a method

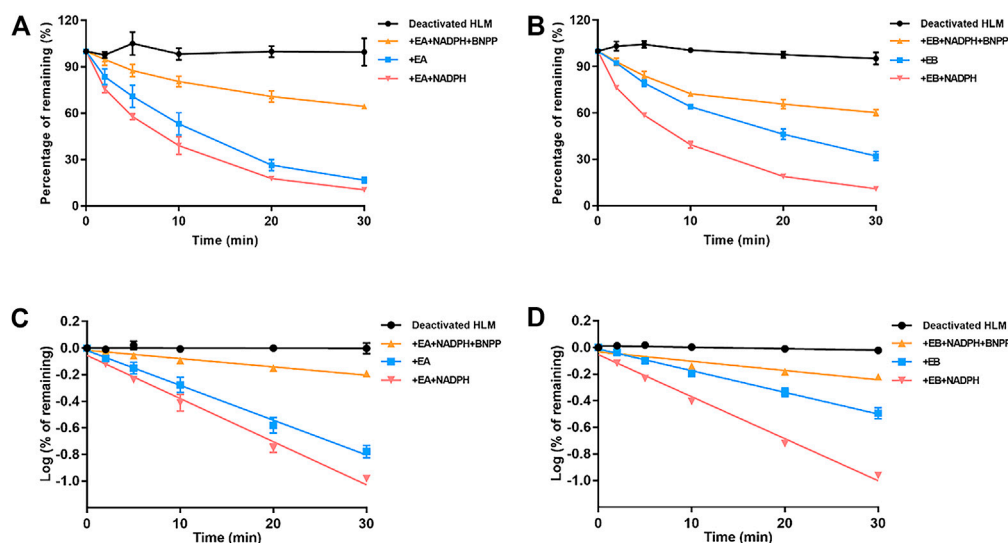


FIGURE 5

Contributions of carboxylesterase and CYP to EA (A,C) and EB (B,D) metabolism in HLMs. Deactivated HLMs were used as negative control (mean \pm SD; $n = 3$).

previously reported but with slight modification (Shen et al., 2013). Metabolites were analyzed by a UFLC–MS/MS 8050 system (Shimadzu Corp., Kyoto, Japan) consisting of an LC-30AD binary pump, an SPD M30A PDA detector, an SIL-30AC autosampler, a CTO-20AC column oven and an 8,050 triple quadrupole mass spectrometer outfitted with a heated ESI source. Samples were separated on an ACQUITY UPLC[®] BEH Shield RP-C₁₈ VanGuard[™] column (100 mm \times 2.1 mm, 1.7 μ m; Waters, Milford, MA, United States) with an ACQUITY UPLC[®] BEH Shield RP-C₁₈ VanGuard[™] precolumn (5 mm \times 2.1 mm, 1.7 μ m; Waters, Milford, MA, United States).

3 Results

3.1 HPLC method validation

The newly developed detection method of EA or EB in HLMs was robust. As shown in Figure 2, endogenous substances within HLMs did not interfere with EA, EB or IS quantification, which were completely separated with good peak shape. Calibration curve regression equations were $Y = 24.823X + 0.5169$, $r^2 = 0.9999$ for EA, and $Y = 18.215X + 0.73$, $r^2 = 0.9998$ for EB over a range of 0.5–100 μ M. The limit of quantification (LOQ) of the method used was 0.5 μ M. Intraday and interday precision were within 0.62% and 6.84% for EA, and 1.16% and 5.86% for EB, respectively, at low, middle and high levels of quality control (1.5, 10 and 75 μ M; $n = 3$). Accuracy ranged from –1.23%–8.77% for EA and 2.86%–9.51% for EB. The extraction recoveries of EA and EB were over a range of 95.89%–104.13% and 95.09%–106.04%, respectively, at the above quality control concentrations. The matrix effect was within the range of 95.54%–102.51% for EA and 102.28%–106.74% for EB. The two isomers were stable at ambient temperature for 6 h, at –20°C for 3 days or after three freeze-thaw cycles.

3.2 FMO was not involved in EA and EB metabolism

Figure 3 details the depletion profiles of EA and EB in HLMs with or without FMO inactivation. No significant differences in EA or EB elimination at each time point were noted whether or not FMO was inactivated by heat treatment. Our findings suggest that FMO was not involved in EA or EB metabolism. These results were consistent with the fact that the molecular structures of the two isomers do not contain heteroatoms such as nucleophilic nitrogen, sulfur or phosphorus atoms, which can be oxidized by FMO. Thus, FMO was not inactivated in subsequent experiments.

3.3 BNPP concentration selection in HLMs

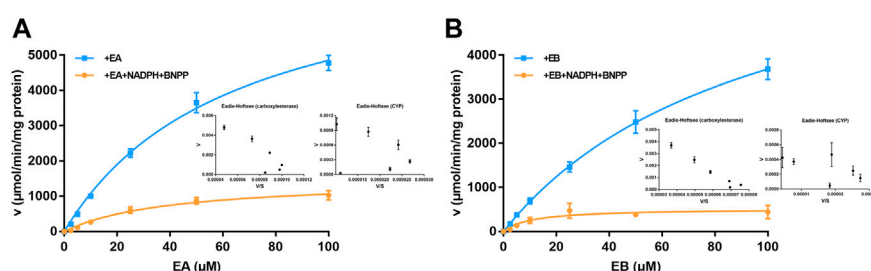
The influence of different BNPP concentrations on EA and EB stability in the absence of NADPH is shown in Figure 4. Compared with the positive control group (without inhibitor), hydrolysis elimination rates of EA and EB decreased significantly in the presence of BNPP. The strongest inhibitory effect on hydrolysis of EA was observed at a BNPP concentration of 0.5 mM (inhibitory percentage of 87.38%). The greatest inhibitory rate of EB hydrolysis was observed at a BNPP concentration of 2 mM (86.11%). Our findings suggest that carboxylesterase was the main enzyme responsible for hydrolysis of EA and EB in HLMs. Moreover, 0.5 mM BNPP was selected to inhibit carboxylesterase activity and thus EA and EB hydrolysis in HLMs.

3.4 Stability of EA and EB to oxidation and hydrolysis in HLMs

Stability of EA and EB to oxidation and hydrolysis in HLMs was evaluated at a concentration of 10 μ M by incubation with and without NADPH or BNPP. Plots of percentages of EA and EB remaining in HLMs

TABLE 1 Metabolic clearance parameters of EA and EB incubated with HLMs in the absence or presence of NADPH, or inhibitor of carboxylesterase BNPP (mean \pm SD; $n = 3$).

Group	Enzyme involved	$t_{1/2}$ (min)	CL_{int} [ml/(min·kg)]	CL_h [ml/(min·kg)]	Metabolism rate (%)
+EA+NADPH+BNPP	CYP	111.36 \pm 5.55	8.90 \pm 0.77	9.04 \pm 0.25	55.32 \pm 1.20
+EA	Carboxylesterase	26.70 \pm 2.93	65.63 \pm 7.15	15.71 \pm 0.41	83.26 \pm 1.80
+EA+NADPH	CYP and carboxylesterase	21.37 \pm 0.40	81.35 \pm 1.53	16.50 \pm 0.06	89.56 \pm 0.60
+EB+NADPH+BNPP	CYP	94.50 \pm 6.36	18.44 \pm 1.24	9.75 \pm 0.35	47.98 \pm 4.00
+EB	Carboxylesterase	42.66 \pm 3.09	40.89 \pm 2.85	13.73 \pm 0.33	67.82 \pm 3.00
+EB+NADPH	CYP and carboxylesterase	21.93 \pm 0.30	79.26 \pm 1.09	16.41 \pm 0.05	89.07 \pm 0.40

**FIGURE 6**

Michaelis–Menten curves of EA (A) and EB (B) in HLMs metabolized by carboxylesterase or CYP and their corresponding Eadie–Hofstee plots (as insert) (mean \pm SD; $n = 3$).

TABLE 2 Oxidative and hydrolysis kinetic parameters of EA and EB in HLMs (mean \pm SD; $n = 3$).

	Compound	K_m (μ M)	V_{max} (μ mol/min/mg protein)	CL_{int} [L/(min·mg)]
Oxidative kinetic parameters	EA	41.02 \pm 8.05	1,497.67 \pm 186.98	36.87 \pm 3.12
	EB	10.68 \pm 1.02	515.97 \pm 124.03	49.26 \pm 15.47
hydrolysis kinetic parameters	EA	63.86 \pm 3.88	7,945.00 \pm 291.66	124.75 \pm 9.56
	EB	104.86 \pm 37.46	7,567.00 \pm 1471.38	75.00 \pm 11.99

versus time are shown in Figure 5. In control samples with deactivated HLMs, negligible reductions in EA and EB were noted, suggesting that the non-specific protein binding can be ignored. Moreover, addition of BNPP to the incubation system markedly slowed EA and EB depletion, indicating that HLM metabolism of EA and EB occurred mainly by hydrolysis. The metabolism rate and clearance parameters of the isomers are shown in Table 1. In the presence of BNPP, the $t_{1/2}$ of EA increased from 26.70 \pm 2.93 to 111.36 \pm 5.55 min, and of EB from 42.66 \pm 3.09 to 94.50 \pm 6.36 min, suggesting that rapid metabolism of EA and EB occurred primarily by carboxylesterase. Furthermore, our findings confirmed metabolic stereoselectivity of EA and EB.

3.5 Kinetics of EA and EB oxidation and hydrolysis in HLMs

Michaelis–Menten curves of EA and EB HLM metabolism by carboxylesterase or CYP are shown in Figure 6; parameters relevant

to oxidation and hydrolysis of EA and EB in HLMs are listed in Table 2. The values of carboxylesterase-mediated CL_{int} of EA and EB were 124.75 \pm 9.56 and 75.00 \pm 11.99 L/(min·mg), respectively, which were markedly higher than corresponding clearance values of CYP (36.87 \pm 3.12 and 49.26 \pm 15.47 L/(min·mg) for EA and EB). The above results were consistent with metabolic stability findings and suggest that hydrolysis by carboxylesterase played a dominant role in EA and EB metabolism. Moreover, differences in K_m and V_{max} between EA and EB further highlight metabolic stereoselectivity of the isomers.

3.6 Hydrolytic stability of EA and EB in HLMs and RLMs

Because EA and EB were metabolized mainly by hydrolysis, we compared their hydrolytic stability in both HLMs and RLMs. Both isomers were hydrolyzed much more rapidly in RLMs than in

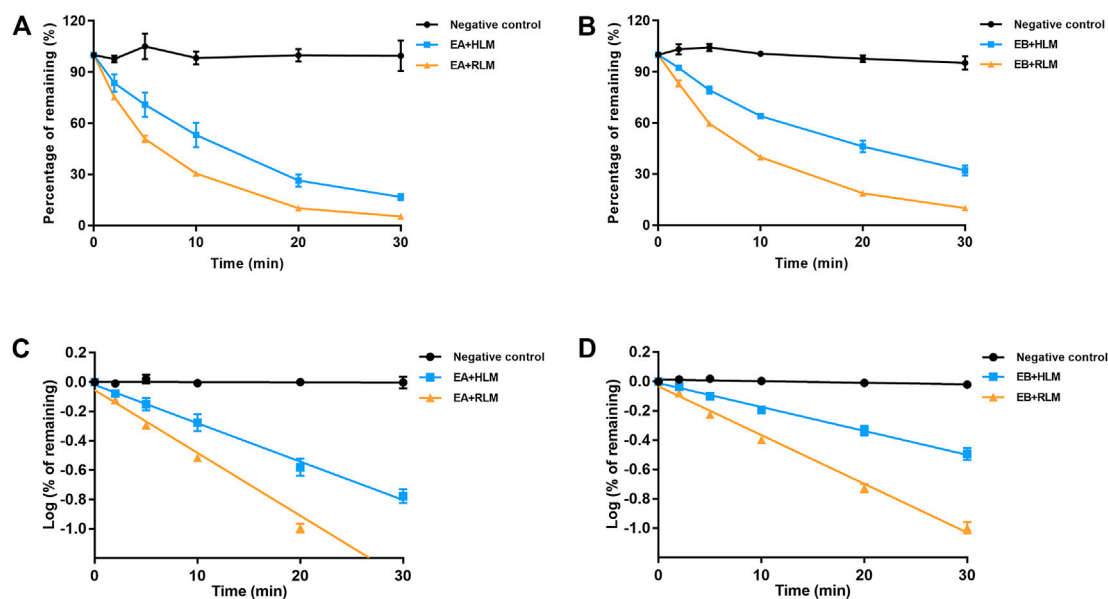


FIGURE 7

Comparison of EA (A,C) and EB (B,D) hydrolysis in HLMs or RLMs. Deactivated microsomes were used as negative control (mean \pm SD; $n = 3$).

TABLE 3 Hydrolytic clearance parameters of EA and EB incubated with RLMs (mean \pm SD; $n = 3$).

Compound	$t_{1/2}$ (min)	CL_{int} [ml/(min·kg)]	CL_h [ml/(min·kg)]	Metabolism rate (%)
EA	16.19 \pm 0.51	153.51 \pm 4.94	40.60 \pm 0.34	94.61 \pm 0.4
EB	20.89 \pm 0.81	118.99 \pm 4.69	37.70 \pm 0.46	89.90 \pm 0.9

TABLE 4 Interactions between EA or EB and CYP isozymes by molecular docking.

Compound	Isozymes	PDB ID	RMSD	Total score	H-bond number	Residues involved in H-bond formation
EA	CYP2C9	5W0C	1.73	10.33	1	A/Asn204
	CYP2C19	4GQS	1.03	11.89	1	A/Ala297
	CYP2D6	3TBG	1.49	8.38	2	A/Ser304, A/Gol750
	CYP3A4	6MA7	1.68	9.66	1	A/Arg212
EB	CYP2C9	5W0C	1.73	10.15	0	-
	CYP2C19	4GQS	1.03	9.37	1	A/Asn204
	CYP2D6	3TBG	1.49	7.99	1	A/Asp301
	CYP3A4	6MA7	1.68	10.57	1	A/Phe304

HLMs (Figure 7). The CL_{int} values for EA were 65.63 ± 7.15 and 153.51 ± 4.94 [ml/(min·kg)] in HLMs and RLMs, respectively (Tables 1, 3). The CL_{int} values for EB were 40.89 ± 2.85 and 118.99 ± 4.69 [ml/(min·kg)] in HLMs and RLMs, respectively. Interestingly, EA was hydrolyzed more rapidly than EB both in HLMs and RLMs.

3.7 CYP phenotyping

3.7.1 QSAR model prediction of CYP phenotyping

ADMET Predictor 8.5 was used to predict CYPs relevant to EA and EB. The prediction results for both isomers were identical, suggesting that CYP3A4 was involved in metabolism of both EA and EB.

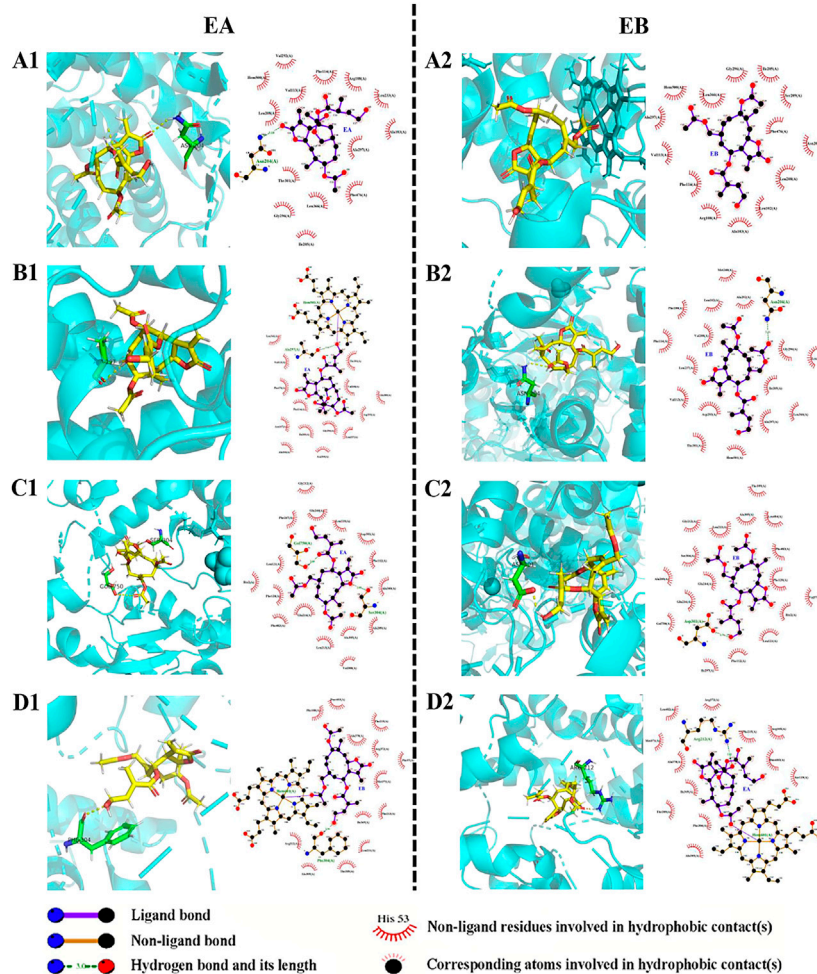


FIGURE 8

Interactions between EA (1) or EB (2) and CYP isoforms (left, 3D and right, 2D). (A) CYP2C9; (B) CYP2C19; (C) CYP2D6; (D) CYP3A4.

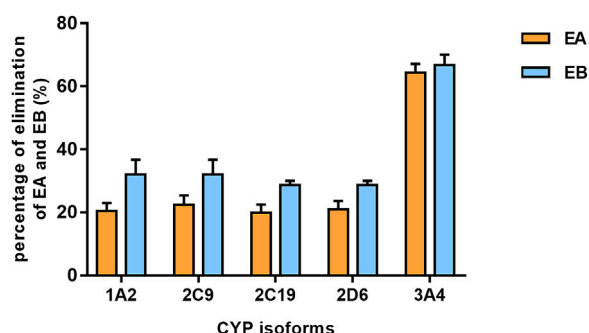


FIGURE 9

The elimination percentage of EA and EB after incubation with various cDNA-expressed human CYP isoforms for 30 min at $10 \mu\text{mol L}^{-1}$ (mean \pm SD; $n = 3$).

3.7.2 Molecular docking analysis

Molecular docking data for CYP2C9, CYP2C19, CYP2D6 and CYP3A4 are shown in Table 4 and Figure 8 (the RMSD of CYP1A2 did

not meet docking standards and the result was excluded). These four enzymes had reasonable RMSD values less than 2 and total scores greater than 6, indicating that direct binding with EA and EB was likely. Bonds were formed primarily by hydrogen bonds; weak interactions were also involved. As such, CYP2C9, CYP2C19, CYP2D6 and CYP3A4 were likely involved in EA and EB metabolism.

3.7.3 CYP phenotyping of EA and EB with rhCYPs

Findings revealed that rhCYP isozyme activity was significant. As shown in Figure 9, both EA and EB were metabolized by human recombinant CYP1A2, CYP2C9, CYP2C19, CYP2D6 and CYP3A4, although to different extents. Table 5 shows the relative contributions of CYP isoforms involved in the metabolism of EA and EB. Findings for EA in descending order were as follows: CYP3A4 (66.20%) > CYP2C9 (19.87%) > CYP1A2 (8.48%) > CYP2C19 (3.50%) > CYP2D6 (1.94%). Findings for EB in descending order were as follows: CYP3A4 (58.18%) > CYP2C9 (23.65%) > CYP1A2 (11.62%) > CYP2C19 (4.39%) > CYP2D6 (2.15%). Our results indicate that EA and EB were metabolized by multiple CYP isoforms, of which CYP3A4 was the main isozyme responsible for oxidative metabolism.

TABLE 5 Contributions of rhCYPs to EA or EB metabolism assessed by the TNR approach ($n = 3$).

Compound	CYPs	Metabolic rate/ $\text{pmol}\cdot\text{min}^{-1}/(\text{pmol}$ $\text{rhCYP})$	Mean CYP content/ $\text{pmol}\cdot\text{mg}^{-1}$ (protein)	Normalized metabolic rate/ $\text{pmol}\cdot\text{mg}^{-1}\cdot\text{min}^{-1}$ (protein)	TNR relative contribution (%)
EA	1A2	0.96	45	43.00	8.48
	2C9	1.05	96	100.74	19.87
	2C19	0.93	19	17.76	3.50
	2D6	0.98	10	9.82	1.94
	3A4	3.11	108	335.60	66.20
EB	1A2	1.46	45	65.71	11.62
	2C9	1.39	96	133.69	23.65
	2C19	1.31	19	24.81	4.39
	2D6	1.22	10	12.17	2.15
	3A4	3.05	108	328.89	58.18

4 Discussion

We explored the metabolic elimination of EA and EB by carboxylesterase and CYP in HLMs. The CYP-mediated oxidation of EA and EB was NADPH-dependent. During this reaction, one O atom in O_2 is incorporated into the substrate, while another is reduced to H_2O via a proton supplied by NADPH (McLean et al., 2015). However, carboxylesterase-mediated hydrolysis does not require NADPH (Zhuang et al., 2014). In the setting of combined metabolism by carboxylesterase and CYP, CL_{int} values for EA and EB were $81.35 \text{ ml}/(\text{min}\cdot\text{kg})$ and $79.26 \text{ ml}/(\text{min}\cdot\text{kg})$, respectively. Generally, a drug is considered to have a high clearance if its hepatic clearance exceeds $14 \text{ ml}/(\text{min}\cdot\text{kg})$ (Liang et al., 2015). As such, our findings suggest that both EA and EB exhibit high clearance. The low metabolic stability of these isomers implies that they are likely to exert short-acting effects; structural modification may be required to enhance their bioavailability. Based on our unpublished findings, EA and EB metabolites are primarily products of carboxylesterase-mediated hydrolysis, where the main hydrolytic sites are the three ester bonds on branched chains. Thus, the preservation of active groups and structural modification involving side-chain ester bonds may be the most important.

Our findings revealed that carboxylesterase-mediated hydrolysis was the main pathway via which EA and EB were metabolized, as opposed to CYP oxidation. Metabolic stability analysis revealed that the CL_{int} of hydrolysis was about seven times that of oxidation for EA and approximately twice that of oxidation for EB. Moreover, enzyme kinetic studies further confirmed the dominant role of carboxylesterase in the metabolism of these isomers with significantly higher hydrolytic V_{max} values as compared to oxidation in HLMs both for EA and EB. Co-administration of carboxylesterase inhibitors with the isomers should thus likely be avoided. Comparison of the hydrolytic stability of EA and EB between HLMs and RLMs revealed significant differences in the rate of hydrolysis between humans and rats. Many studies have suggested metabolic variation of carboxylesterase-substrate compounds among different species. This phenomenon was likely observed due to interspecies differences of distribution, substrate preference and

inhibitor response of carboxylesterase (Wang X. et al., 2020; Zou et al., 2020; Jin et al., 2022). Therefore, caution should be exercised in predicting human clinical pharmacokinetics and pharmacodynamics solely based on rat metabolic parameters.

We found the metabolic parameters of EA and EB to have been different based on our analyses of metabolic stability and enzyme kinetics. The oxidation $t_{1/2}$ of EB was shorter than that of EA, although the hydrolytic $t_{1/2}$ of EB was approximately twice that of EA. Furthermore, the oxidative V_{max} of EA was approximately three times that of EB. Significantly more rapid hydrolysis of EA as compared to EB both in HLMs and RLMs suggest that the Z-configuration in cis-trans isomers for EA and EB was more easily hydrolyzed by carboxylesterase. The different metabolic properties of EA and EB, collectively termed stereoselectivity, were observed likely due to enzymes differing in their affinity toward chiral drugs (Lu, H., 2007; Marzo and Balant, 1996; Rentsch, 2002). As such, pharmacodynamic and/or pharmacokinetic properties of isomers require detailed evaluation in the context of clinical pharmacology (Marzo and Balant, 1996).

Identification of metabolic enzyme subtypes is essential in predicting potential drug interactions. The CYPs mediate metabolism of approximately 75% of all drugs and play a vital role in metabolic functions (Lu et al., 2015). Identification of CYP isoforms responsible for EA and EB metabolism was performed using both *in silico* methods and *in vitro* experimentation with rhCYPs. The QSAR model predicted that both isomers underwent metabolism by CYP3A4. Because different spatial configurations of isomers can lead to distinct metabolic characteristics, we then used 3D structures of EA and EB to confirm QSAR predictions via molecular docking. Our findings confirmed that EA and EB could directly bind CYP2C9, CYP2C19, CYP2D6 and CYP3A4, suggesting that these enzymes contain metabolic sites for these isomers. Interestingly, residues relevant to H-bond formation, H-bond number and degree of CYP isozyme binding were found to differ between EA and EB, implying that differences in metabolism among these isomers manifest on binding. Experimentation using rhCYPs further verified our prediction results. The CYP isozymes CYP1A2, CYP2C9, CYP2C19, CYP2D6 and CYP3A4 were selected because they

are involved in most drug metabolism (Zhang et al., 2008). Our findings indicate that EA and EB were metabolized mainly by CYP3A4 at relative contributions of 66.20% and 58.18%, respectively, although other CYP isozymes also contributed to their metabolism to different extents.

5 Conclusion

Although the structures of EA and EB are similar, the metabolic characteristics of the isomers exhibit stereoselectivity. We found that rapid carboxylesterase-mediated hydrolysis of EA and EB was responsible for their rapid elimination. Importantly, significant differences were noted in metabolic parameters among humans and rats, as well as more rapid hydrolysis in rats. Finally, CYP3A4 was confirmed to be the main CYP isoform responsible for EA and EB oxidation.

Data availability statement

The raw data supporting the conclusion of this article will be made available by the authors, without undue reservation.

Author contributions

YL: methodology, formal analysis, investigation, data curation, as well as writing, reviewing and editing the original draft of this manuscript. XL: methodology as well as writing, reviewing and

editing this manuscript. LL: formal analysis as well as writing, review and editing this manuscript. TZ: visualization. YG: molecular docking. KZ: conceptualization, data validation, as well as writing, reviewing and editing this manuscript. QW: conceptualization, data validation, supervision of experiments, funding acquisition, as well as writing, reviewing and editing this manuscript.

Funding

This work was financially supported by the National Natural Science Foundation of China (No. 82174068 and 81973505).

Conflict of interest

The authors declare that the research was conducted in the absence of any commercial or financial relationships that could be construed as a potential conflict of interest.

Publisher's note

All claims expressed in this article are solely those of the authors and do not necessarily represent those of their affiliated organizations, or those of the publisher, the editors and the reviewers. Any product that may be evaluated in this article, or claim that may be made by its manufacturer, is not guaranteed or endorsed by the publisher.

References

- Caldwell, G. W., and Yan, Z. Y. (2014). *Optimization in drug discovery in vitro methods*. New York: Springer.
- Chen, Y., Liu, L., Nguyen, K., and Fretland, A. J. (2011). Utility of intersystem extrapolation factors in early reaction phenotyping and the quantitative extrapolation of human liver microsomal intrinsic clearance using recombinant cytochromes P450. *Drug Metab. Dispos.* 39, 373–382. doi:10.1124/dmd.110.035147
- Gao, J., Liang, L., Zhu, Y., Qiu, S., Wang, T., and Zhang, L. (2016). Ligand and structure-based approaches for the identification of peptide deformylase inhibitors as antibacterial drugs. *Int. J. Mol. Sci.* 17, 1141. doi:10.3390/ijms17071141
- Gertrudes, J. C., Maltarollo, V. G., Silva, R. A., Oliveira, P. R., Honório, K. M., and da Silva, A. B. (2012). Machine learning techniques and drug design. *Curr. Med. Chem.* 19, 4289–4297. doi:10.2174/092986712802884259
- Harper, T. W., and Brassil, P. J. (2008). Reaction phenotyping: Current industry efforts to identify enzymes responsible for metabolizing drug candidates. *Aaps J.* 10, 200–207. doi:10.1208/s12248-008-9019-6
- Hong, H. X., Chen, M. J., Ng, H. W., and Tong, W. D. (2016). QSAR models at the US FDA/NCTR. *Methods Mol. Biol.* 1425, 431–459. doi:10.1007/978-1-4939-3609-0_18
- Jin, Q., Li, Z., Zhang, M. J., Liu, W. C., Zou, L. W., Sui, H., et al. (2022). Deciphering the species differences in CES1A-mediated hydrolytic metabolism by using a bioluminescence substrate. *Chem. Biol. Interact.* 368, 110197. doi:10.1016/j.cbi.2022.110197
- Kaur, T., Madgulkar, A., Bhalekar, M., and Asgaonkar, K. (2019). Molecular docking in formulation and development. *Curr. Drug Discov. Technol.* 16, 30–39. doi:10.2174/1570163815666180219112421
- Kazmi, S. R., Jun, R., Yu, M. S., Jung, C., and Na, D. (2019). *In silico* approaches and tools for the prediction of drug metabolism and fate: A review. *Comput. Biol. Med.* 106, 54–64. doi:10.1016/j.combiomed.2019.01.008
- Kumar, G. N., and Surapaneni, S. (2001). Role of drug metabolism in drug discovery and development. *Med. Res. Rev.* 21, 397–411. doi:10.1002/med.1016
- Liang, S. C., Ge, G. B., Xia, Y. L., Zhang, J. W., Qi, X. Y., Tu, C. X., et al. (2015). *In vitro* evaluation of the effect of 7-methyl substitution on glucuronidation of daphnetin: Metabolic stability, isoform selectivity, and bioactivity analysis. *J. Pharm. Sci.* 104, 3557–3564. doi:10.1002/jps.24538
- Lu, H. (2007). Stereoselectivity in drug metabolism. *Expert Opin. Drug Metab. Toxicol.* 3, 149–158. doi:10.1517/17425255.3.2.149
- Lu, T. L., Su, L. L., Ji, D., Gu, W., and Mao, C. Q. (2015). Interaction between CYP450 enzymes and metabolism of traditional Chinese medicine as well as enzyme activity assay. *China J. Chin. materia medica* 40, 3524–3529. doi:10.4268/cjcmm.20151802
- Marzo, A., and Balant, L. P. (1996). Investigation of xenobiotic metabolism by CYP2D6 and CYP2C19: Importance of enantioselective analytical methods. *J. Chromatogr. B Biomed. Appl.* 678, 73–92. doi:10.1016/0378-4347(95)00229-4
- McLean, K. J., Luciakova, D., Belcher, J., Tee, K. L., and Munro, A. W. (2015). Biological diversity of cytochrome P450 redox partner systems. *Adv. Exp. Med. Biol.* 851, 299–317. doi:10.1007/978-3-319-16009-2_11
- Meng, Q., and Liu, K. (2014). Pharmacokinetic interactions between herbal medicines and prescribed drugs: Focus on drug metabolic enzymes and transporters. *Curr. Drug Metab.* 15, 791–807. doi:10.2174/1389200216666150223152348
- Miners, J. O., Mackenzie, P. I., and Knights, K. M. (2010). The prediction of drug-glucuronidation parameters in humans: UDP-glucuronosyltransferase enzyme-selective substrate and inhibitor probes for reaction phenotyping and *in vitro-in vivo* extrapolation of drug clearance and drug-drug interaction potential. *Drug Metab. Rev.* 42, 196–208. doi:10.3109/03602530903210716
- Obach, R. S. (1997). Nonspecific binding to microsomes: Impact on scale-up of *in vitro* intrinsic clearance to hepatic clearance as assessed through examination of warfarin, imipramine, and propranolol. *Drug Metab. Dispos.* 25, 1359–1369.
- Reddy, A., Heimbach, T., Freiwald, S., Smith, D., Winters, R., Michael, S., et al. (2005). Validation of a semi-automated human hepatocyte assay for the determination and prediction of intrinsic clearance in discovery. *J. Pharm. Biomed. Anal.* 37, 319–326. doi:10.1016/j.jpba.2004.09.030
- Rentsch, K. M. (2002). The importance of stereoselective determination of drugs in the clinical laboratory. *J. Biochem. Biophys. Methods* 54, 1–9. doi:10.1016/s0165-022x(02)00124-0
- Rodrigues, A. D. (1999). Integrated cytochrome P450 reaction phenotyping: Attempting to bridge the gap between cDNA-expressed cytochromes P450 and native human liver microsomes. *Biochem. Pharmacol.* 57, 465–480. doi:10.1016/s0006-2952(98)00268-8

- Shen, G. L., Zhong, Y. H., Yuan, M., Zhuang, X. M., and Li, H. (2013). Simultaneous quantitation of six cytochrome P450 enzyme probe metabolites by ultra-high performance liquid chromatography tandem mass spectrometry. *Chin. J. Anal. Chem.* 41, 488–493. doi:10.3724/sp.j.1096.2013.20780.J.1096.2013.20780
- Slaughter, D., Takenaga, N., Lu, P., Assang, C., Walsh, D. J., Arison, B. H., et al. (2003). Metabolism of rofecoxib *in vitro* using human liver subcellular fractions. *Drug Metab. Dispos.* 31, 1398–1408. doi:10.1124/dmd.31.11.1398
- Wang, X., Ma, S., Lai, F., Wang, Y., and Lou, C. (2020). Traditional applications, phytochemistry, and pharmacological activities of eupatorium lindleyanum dc.: A comprehensive review. *Front. Pharmacol.* 8, 577124. doi:10.3389/fphar.2020.577124
- Wang, Y. Q., Shang, X. F., Wang, L., Zhang, P., Zou, L. W., Song, Y. Q., et al. (2020). Interspecies variation of clopidogrel hydrolysis in liver microsomes from various mammals. *Chem. Biol. Interact.* 315, 108871. doi:10.1016/j.cbi.2019.108871
- Wu, H., Peng, Y., Sun, J. G., Zhang, X. Y., Zhong, Y. X., and Wang, G. J. (2013). Application and development of *in vitro* metabolism study at early drug discovery stage. *Acta Pharm. Sin.* 48, 1071–1079. doi:10.16438/j.0513-4870.2013.07.024
- Yang, L., Chen, H., Hu, Q., Liu, L., Yuan, Y., Zhang, C., et al. (2022). Eupalinolide B attenuates lipopolysaccharide-induced acute lung injury through inhibition of NF- κ B and MAPKs signaling by targeting TAK1 protein. *Int. Immunopharmacol.* 111, 109148. doi:10.1016/j.intimp.2022.109148
- Yu, M., Zhang, S. Q., Wen, N., and Li, Z. G. (2013). *In vitro* research progress on cytochrome P450 for drug metabolism. *Chin. Pharm. Aff.* 27, 81–87. doi:10.16153/j.1002-7777.2013.01.024
- Zhang, D. L., Zhu, M. S., and Humphreys, W. G. (2008). *Drug metabolism in drug design and development: Basic concepts and practice*. Beijing: People's Military Medical Press.
- Zhang, F., Li, H. X., Zhang, T. T., Xiong, Y., Wang, H. N., Lu, Z. H., et al. (2022a). Human carboxylesterase 1A plays a predominant role in the hydrolytic activation of remdesivir in humans. *Chem. Biol. Interact.* 351, 109744. doi:10.1016/j.cbi.2021.109744
- Zhang, J., Zhao, F., Yu, X., Lu, X., and Zheng, G. (2015). Pharmacokinetics of eupalinolide A, eupalinolide B and hyperoside from Eupatorium lindleyanum in rats by LC/MS/MS. *J. Chromatogr. B Anal. Technol. Biomed. Life Sci.* 995–996, 1–7. doi:10.1016/j.jchromb.2015.04.038
- Zhang, X. W., Feng, N., Liu, Y. C., Guo, Q., Wang, J. K., Bai, Y. Z., et al. (2022b). Neuroinflammation inhibition by small-molecule targeting USP7 noncatalytic domain for neurodegenerative disease therapy. *Sci. Adv.* 8, eabo0789. doi:10.1126/sciadv.abo0789
- Zhang, Y., Dong, F., Cao, Z., Wang, T., Pan, L., Luo, W., et al. (2022c). Eupalinolide A induces autophagy via the ROS/ERK signaling pathway in hepatocellular carcinoma cells *in vitro* and *in vivo*. *Int. J. Oncol.* 61, 131. doi:10.3892/ijo.2022.5421
- Zhang, Y., Zhang, H., Mu, J., Han, M., Cao, Z., Dong, F., et al. (2022d). Eupalinolide B inhibits hepatic carcinoma by inducing ferroptosis and ROS-ER-JNK pathway. *Acta Biochim. Biophys. Sin. (Shanghai)* 54, 974–986. doi:10.3724/abbs.2022082
- Zhao, S. X., Forman, D., Wallace, N., Smith, B. J., Meyer, D., Kazolias, D., et al. (2005). Simple strategies for reducing sample loads in *in vitro* metabolic stability high-throughput screening experiments: A comparison between traditional, two-time-point and pooled sample analyses. *J. Pharm. Sci.* 94, 38–45. doi:10.1002/jps.20213
- Zhuang, X. M., Wei, X., Tan, Y., Xiao, W. B., Yang, H. Y., Xie, J. W., et al. (2014). Contribution of carboxylesterase and cytochrome P450 to the bioactivation and detoxification of isocarbophos and its enantiomers in human liver microsomes. *Toxicol. Sci.* 140, 40–48. doi:10.1093/toxsci/kfu067
- Zou, X. W., Sheng, L., and Li, Y. (2020). The effect of species difference in carboxylesterase on the drug metabolism. *J. Int. Pharm. Res.* 47, 91–96. doi:10.13220/j.cnki.jipr.2020.02.002



OPEN ACCESS

EDITED BY

Junmin Zhang,
Lanzhou University, China

REVIEWED BY

Thomas Hsueh,
Taipei City Hospital, Taiwan
Bing Chen,
Fujian Medical University, China

*CORRESPONDENCE

E. Sun,
✉ sune0825@163.com
Xiaobin Jia,
✉ jiaxiaobin2015@163.com

[†]These authors have contributed equally to this work and share first authorship

SPECIALTY SECTION

This article was submitted to Drug Metabolism and Transport, a section of the journal Frontiers in Pharmacology

RECEIVED 01 December 2022

ACCEPTED 16 January 2023

PUBLISHED 25 January 2023

CITATION

Sun E, Huang R, Ding K, Wang L, Hou J, Tan X, Wei Y, Feng L and Jia X (2023), Integrating strategies of metabolomics, network pharmacology, and experiment validation to investigate the processing mechanism of Epimedium fried with suet oil to warm kidney and enhance yang. *Front. Pharmacol.* 14:1113213. doi: 10.3389/fphar.2023.1113213

COPYRIGHT

© 2023 Sun, Huang, Ding, Wang, Hou, Tan, Wei, Feng and Jia. This is an open-access article distributed under the terms of the [Creative Commons Attribution License \(CC BY\)](https://creativecommons.org/licenses/by/4.0/). The use, distribution or reproduction in other forums is permitted, provided the original author(s) and the copyright owner(s) are credited and that the original publication in this journal is cited, in accordance with accepted academic practice. No use, distribution or reproduction is permitted which does not comply with these terms.

Integrating strategies of metabolomics, network pharmacology, and experiment validation to investigate the processing mechanism of Epimedium fried with suet oil to warm kidney and enhance yang

E. Sun^{1,2†*}, Ran Huang^{1,3†}, Ke Ding¹, Ling Wang¹, Jian Hou², Xiaobin Tan^{1,2}, Yingjie Wei^{1,2}, Liang Feng⁴ and Xiaobin Jia^{1,4*}

¹The Third Clinical Medical College, Nanjing University of Chinese Medicine, Nanjing, China, ²Key Laboratory of New Drug Delivery System of Chinese Materia Medica, Jiangsu Academy of Traditional Chinese Medicine, Nanjing, China, ³Affiliated Hospital of Nanjing University of Chinese Medicine, Nanjing, China, ⁴School of Traditional Chinese Pharmacy, China Pharmaceutical University, Nanjing, China

Introduction: Epimedium, a traditional Chinese medicine (TCM) commonly used in ancient and modern China, is one of the traditional Chinese medicines clinically used to treat kidney yang deficiency syndrome (KYDS). There are differences in the efficacy of Epimedium before and after processing, and the effect of warming the kidney and enhancing yang is significantly enhanced after heating with suet oil. However, the active compounds, corresponding targets, metabolic pathways, and synergistic mechanism of frying Epimedium in suet oil to promote yang, remain unclear.

Methods: Herein, a strategy based on comprehensive GC-TOF/MS metabolomics and network pharmacology analysis was used to construct an “active compounds-targets-metabolic pathways” network to identify the active compounds, targets and metabolic pathways involved. Subsequently, the targets in kidney tissue were further validated by real-time quantitative polymerase chain reaction (RT-qPCR). Histopathological analysis with physical and biochemical parameters were performed.

Results: Fifteen biomarkers from urine and plasma, involving five known metabolic pathways related to kidney yang deficiency were screened. The network pharmacology results showed 37 active compounds (13 from Epimedium and 24 from suet oil), 159 targets, and 267 pathways with significant correlation. Importantly, integrated metabolomics and network pharmacologic analysis revealed 13 active compounds (nine from Epimedium and four from suet oil), 7 corresponding targets (ALDH2, ARG2, GSTA3, GSTM1, GSTM2, HPGDS, and NOS2), two metabolic pathways (glutathione metabolism, arginine and proline metabolism), and two biomarkers (Ornithine and 5-Oxoproline) associated with improved kidney yang deficiency by Epimedium fried with suet oil.

Discussion: These finds may elucidate the underlying mechanism of yang enhancement *via* kidney warming effects. Our study indicated that the mechanism of action mainly involved oxidative stress and amino acid metabolism. Here, we demonstrated the novel strategies of integrating

metabolomics and network pharmacology in exploring of the mechanisms of traditional Chinese medicines.

KEYWORDS

Epimedium, metabolomics, network pharmacology, processing mechanism, kidney yang deficiency syndrome

1 Introduction

Epimedium, also known as Xianlingpi, is the dried leaves of a Berberis plant *Epimedium brevicornum* Maxim., *Epimedium sagittatum* (Sieb. et Zucc.) Maxim., *Epimedium pubescens* Maxim., or the dried leaves of *Epimedium koreanum* Nakai, which was first recorded in Shennong Materia Medica Classic and listed as a medium product, with functions of tonifying the liver and kidney, strengthening muscles and bones, and removing wind and dampness (Chinese Pharmacopoeia Commission [CPC], 2020). There are more than 20 processing methods for Epimedium, including stir-frying, wine roasting, salt roasting, ghee roasting, and suet oil roasting, among which suet oil roasting is the most commonly used and has been included in The Chinese Pharmacopoeia 2020 edition. According to traditional processing theory, suet oil is sweet and warm, possessing tonifying effects to treat deficiency syndromes. Epimedium fried with suet oil can play a synergistic role in strengthening its effect of warming the kidney and enriching the yang, mainly for impotence and infertility treatments. Clinical studies showed that Epimedium raw product focuses on dispelling rheumatism, and strengthening muscles and bones.

Kidney yang deficiency syndrome (KYDS) is a common syndrome type in Chinese medicine consultation, and it is also the basic syndrome type of various diseases. Insufficient kidney Yang may cause somnolence, cold, cold limbs, impotence, infertility in women, diarrhea, along with other symptoms of Yang deficiency (Wu et al., 2022). In the pharmacological research on kidney-yang deficiency, glucocorticoids, sex hormones, adenine, and kidney/bilateral adrenalectomy are often used to establish animal models of kidney-yang deficiency. Conventionally, they are supplemented with large doses of exogenous glucocorticoids (hydrocortisone) to further establish the model (Sun et al., 2017).

In previous studies, our research mainly focused on the mechanism of “heating” and “suet oil” processing factors from the perspective of the absorption and metabolism of flavonoids in Epimedium, indicating that there were differences in the absorption and metabolism of flavonoid glycosides in Epimedium (Chen et al., 2009). In the processing process, “heating” could change the content of main active flavonoids of Epimedium, hence produced more easily absorbed bioactive flavonoids (Chen et al., 2007; Sun et al., 2014). The excipient “suet oil” could further promote the formation of self-assembled micelles of Epimedium flavonoids *in vivo*, increased the solubility of active flavonoids, and improved the absorption of active flavonoids, to achieve the purpose of synergism (Gu et al., 2019). However, the effect of traditional Chinese medicine on human body is a biological process of interaction and integration between “intervention system (TCM) and response system (biological organism)” (Xiang et al., 2012). It is difficult to match corresponding disease targets through the disease database for TCM diseases, especially for deficiency diseases. Therefore, it is

necessary to adopt new methods and strategies to systematically and comprehensively explore the processing mechanism of TCM.

Metabolomics can analyze all metabolites in the whole sample and comprehensively monitor the changes of metabolites in the body. Applying the methods and ideas of metabolomics to the processing of TCM can reveal the changes of metabolism pathway and action network of TCM before and after processing as a whole (Kui et al., 2022). Network pharmacology is a new method to systematically and integrally study drugs from the perspective of biological network stability. It can systematically study the molecular relationship between TCM components and complex diseases (Xie et al., 2019). Metabolomics can be used to construct the target database of disease metabolites, hence the combined application of metabolomics and network pharmacology is gradually increasing (Chen et al., 2019). The multi-omics technology in systems biology may elucidate the processing mechanism of TCM, from the active components to the target genes, proteins, metabolites and metabolic pathways of the body. Therefore, the integration of multi-omics technology is vital to clarify the mechanism of action in TCM and provide insights into the processing mechanism of Epimedium.

Epimedium treatment may cause the linkage effect of “active component group, target *in vivo* and biological metabolism”, so the changes of downstream biological metabolites directly reflect the status of upstream targets. Therefore, based on previous research, this study used metabonomics—Network pharmacology—Real-time quantitative polymerase chain reaction (RT qPCR) integration technology to obtain reasonable and objective data from biomarkers, metabolic pathways, active ingredient groups and potential targets, and build a “component—target—metabolism” network, thereby revealing the processing and synergistic mechanism of Epimedium fried with suet oil for warming the kidney and promoting yang on the whole. This study provides new insights for studying processing mechanism of traditional Chinese medicine.

2 Materials and methods

2.1 Reagents and materials

Epimedium was purchased from Shanxi, identified as *Epimedium brevicornum* Maxim., courtesy of Professor Baolin Guo, Institute of Pharmaceutical Botany, Chinese Academy of Medical Sciences (batch number: 161231). Hydrocortisone injections were bought from Tianjin King York Group Co., Ltd. (batch number: 1407271; Tianjin, China). Suet oil was purchased from Inner Mongolia Xilin Gol Grassland Co., Ltd. (Inner Mongolia, China). Formalin solution was purchased from Shanghai Aladdin Bio-Chem Technology Co., LTD. (batch number: F140859, Shanghai, China). Hydrochloric Acid was purchased from Nanjing Aojia Chemical Co., Ltd. (batch number: 2013050203, Nanjing, China). 2-Chloro-L-phenylalanine

(content $\geq 98\%$) was purchased from Shanghai Hengbo Biological Technology Co., Ltd. (Shanghai, China). Bis(trimethylsilyl) trifluoroacetamide (99% BSTFA +1% TMCS) was provided by Regis Technologies, Inc. (Morton Grove, United States). Sodium azide was bought from Shandong Xiya Chemical Industry Co., Ltd. (batch number: S7470, Jinan, China). Urease was bought from Sigma-Aldrich (batch number: SLBB0100V, St. Louis, MO, United States). Pyridine was purchased from Adamas Reagent, Ltd. (batch number: 030928, Shanghai, China). Chromatography grade methanol was purchased from TEDIA (batch number: 1603253, State of Ohio, United States). Ethanol (analytically pure) was purchased from Nanjing Chemical Reagent Co., Ltd. (batch number: 1603233, Nanjing, China). Trichloromethane (batch number: 10006818) and propan-2-ol (batch number: 80109218) were purchased from Sinopharm Chemical Reagent Co., Ltd. (Shanghai, China). HyPure TMMolecular Biology Grade Water was provided by HyClone (batch number: SH30538.02, Logan, United States).

Corticosterone (CORT), Adrocorticotropin (ACTH), 17-Hydroxysteroids (17-OHCS), trifluorothyronine (T3), Thyroxine (T4), thyroid-stimulating hormone (TSH), luteinizing hormone (LH), testosterone (T), and follicle-stimulating hormone (FSH) kits were purchased from Nanjing Herbaceous Source Biotechnology Co., LTD.

Agilent 7890B gas chromatography system (Agilent, United States) coupled with a LECO Chroma TOF Pegasus HT mass spectrometer (LECO, United States) were employed for metabonomics analysis. Ultrapure water was prepared by a Milli-Q water purifier (Merck Millipore, Germany). Heraeus Fresco 17 Centrifuge (Thermo Scientific, United States). BPG-9050AH high temperature blast drying oven (HASUC, China). Vortex Genie® 2 Vortex instrument (Scientific Industries, United States). CX23 electron microscope (Olympus, Japan). TNG-T98 Frozen Concentration Centrifugal Dryer (Taicang Huamei, China). ELISA (Spectra max 190, Shanghai Meigu Molecular Instrument Co., Ltd., shanghai, china). Quantitative Real-time PCR LightCycler instrument was provided by Bio-Rad Laboratories, Inc. (California, United States). Servicebio® RT First Strand cDNA Synthesis Kit and 2×SYBR Green qPCR Master Mix (None ROX) were obtained from Wuhan servicebio technology Co., LTD. (Wuhan, China).

2.2 Preparation of Epimedium processing and extraction

The prepared Epimedium decoction pieces (1 kg) were selected and made three copies in parallel. One sample was evenly added with hot melted suet oil (200 g), and mixed well. Then, it was oven-baked at 170°C for 7 min to get the Epimedium fried with suet oil. The second sample was placed into the oven without oil to obtain a similarly heated Epimedium. The third decoction piece was reserved as raw control.

All three samples were immersed in boiling water (1:30) for 1 h before extraction. Then it was extracted three times, 30 min for each time, filtered through gauze, respectively. The next three filtrates were merged and concentrated under vacuum, thus extracting solution was obtained respectively. The extraction flow chart is shown in [Supplementary Figure S1](#).

2.3 Animals and treatments

Thirty-six adult male Sprague-Dawley rats (body weight 230 ± 20 g, animal licence No. SCXK(HU)2014-0001) were provided by Animal Experiment Center of Soochow University (Suzhou, China), and raised in the Experimental Animal Center of Jiangsu Academy of Traditional Chinese Medicine (Nanjing, China). Rats were housed in a climate-controlled room (relative humidity of 45% and ambient temperature 22°C–24°C), kept on a 12 h/12 h light-dark cycle, with free access to food and drinking water.

After a 2-week habituation, all rats were randomly divided into 6 groups with 6 rats in each; Control group (N, No. N1~N6), Model group (M, No. M1~M6), Suet oil group (A, No. A1~A6), Epimedium raw product group (B, No. B1~B6), Epimedium heating product group (C, No. C1~C6), Epimedium fried with suet oil group (D, No. D1~D6). M, A, B, C, and D group rats were injected intraperitoneally with hydrocortisone once daily for the following 10 days. The injection dose was 15 mg kg^{-1} on the first day, the dose was halved to 7.5 mg kg^{-1} on the second day and subsequent 9 days. N group was injected intraperitoneally with an equal volume of 0.9% sodium chloride injection. A, B, C, and D group rats were administered *via* intragastric with suet oil emulsion (0.144 g kg^{-1} , 20% of Epimedium content, dispersed in water with CMC-Na), the Epimedium raw product extract (0.72 g kg^{-1}), the Epimedium heating product extract (0.72 g kg^{-1}), and the Epimedium fried with suet oil extract (0.72 g kg^{-1}), respectively. N and M groups were orally administered with the same volume of pure water. The intragastric administration was performed once a day for 10 days. Meanwhile, body weights of the rats in each group were recorded daily. All animal treatments and experiments were approved by the Animal Ethics Committee of Jiangsu Provincial Academy of Chinese Medicine, and were strictly performed in accordance with the National Institutes of Health Guide for the Care and Use of Laboratory Animals (AEWC-20200702-119).

2.4 Collection of samples

After the 10th day of administration, all rats were fasted but had free access to water for 12 h while urine samples were collected. The 12 h urines of all rats were collected into a 50 mL centrifuge tube containing 20 μL of 1% sodium azide (NaN_3). After centrifugation at $4,500 \text{ rpm min}^{-1}$ for 10 min in a 4°C low-temperature centrifuge, the supernatant was taken and stored at -80°C until metabonomics analysis. Afterwards, blood samples were drawn from the orbit and collected in two 2 mL centrifuge tubes, one of which contained 20 μL heparin sodium solution for preparing plasma samples, the other for preparing serum samples. Then, centrifugation was performed at $4,000 \text{ rpm min}^{-1}$ for 10 min in a 4°C low-temperature centrifuge, and the supernatant was taken to obtain plasma samples and serum samples. The plasma and serum samples were stored at -80°C until plasma metabonomics analysis and serum biochemical analysis.

Biochemical indicators included the hypothalamus-pituitary-adrenal axis in kidney-yang deficiency rats ([Chen and Wang, 2015](#); [Liu et al., 2016](#); [Zhang et al., 2020](#)): CORT, ACTH and 17-OHCS;

Hypothalamus-pituitary-thyroid axis related indicators: T3, T4, and TSH; Hypothalamus-pituitary-gonad axis related indicators: LH, T, and FSH.

Thereafter, all rats were euthanized in parallel. The kidney tissues were quickly excised, directly frozen in liquid nitrogen, and stored at -80°C for subsequent quantitative real-time PCR assays. Simultaneously, the hypothalamus, pituitary, thyroid, adrenal gland, testis and kidney of all rats were collected and fixed in formalin solution for histopathological analysis.

2.5 Preparation of metabonomic samples

The urine samples were thawed before analysis and 100 μL aliquots of urine sample were added to 20 μL urease (80 mg mL^{-1}). Then the mixture was shaken and mixed for 30 s, and incubated in an oven at 37°C for 1 h. Subsequently, urine sample mixture and 100 μL aliquots of plasma sample were mixed with 350 μL methanol and 20 μL L-2-chlorophenylalanine. Post vortex-mixing for 30 s and centrifugation at 16000 rpm for 20 min at 4°C , the supernatant of urine sample and plasma sample were transferred into a 2 mL gas sample bottle (siliconized methane). Moreover, 11 μL of each urine sample and plasma sample were accurately pipetted and mixed as the urine and plasma quality control (QC) sample, respectively. After the supernatants of the urine sample and plasma samples were completely dry in a vacuum concentrator, 60 μL of methoxyamine salt reagent (methoxyamine hydrochloride, dissolved in 20 mg mL^{-1} pyridine) was added and mixed well, and incubated in an oven at 80°C for 30 min. Thereafter, 80 μL of BSTFA (containing 1% TCMS, v/v) were quickly added to each sample. The mixture was incubated in an oven at 70°C for 2 h and cooled to 25°C . Finally, 10 μL saturated fatty acid methyl ester standard mixture was added and mixed well for GC-MS analysis.

2.6 Metabonomics analysis

The analysis of plasma and urine samples was performed on an Agilent 7890B gas chromatography system (Agilent, United States) coupled with a LECO Chroma TOF Pegasus HT mass spectrometer (LECO, United States), which was equipped with Agilent DB-5MS capillary column ($30\text{ m} \times 0.25\text{ mm} \times 0.25\text{ }\mu\text{m}$, J&W Scientific, Folsom, CA, United States). GC-TOF-MS analysis conditions were set as follows: the injection volume was 1 μL with non-split mode. Carrier gas was helium used with a column flow rate of 1.0 mL min^{-1} , the column temperature maintained at 50°C for 1 min and then heated at a rate of $20^{\circ}\text{C}\cdot\text{min}^{-1}$ up to 310°C maintained for 6 min. The forward inlet purge flow rate was 3 mL min^{-1} and the forward inlet temperature was 280°C . Transmission line temperature and ion source temperature were 270°C and 220°C respectively. The ionization voltage was -70 eV . The scan range and speed were 50–500 m/z , 20 spectra/sec. The solvent delays of urine and plasma samples were 455 S and 366 S, respectively.

Random urine samples (N2), plasma samples (N5) and the internal standard sample (L-2-chlorophenylalanine) were tested according to the above conditions. Thereafter, a comparative analysis of the GC-TOF-MS total ion characteristics (TIC) between the random urine sample (N2), plasma samples (N5) and the internal

standard sample were analyzed in order to corroborate and validate our experimental methodologies as well as the instrument platforms. The 45 urine samples (including 9 urine QC samples) and plasma samples (including 9 plasma QC samples) were also tested according to the above conditions, and TIC of urine and plasma GC-TOF-MS were obtained for all samples. The retention time of the internal standard (L-2-chlorophenylalanine) in each TIC was extracted to investigate the stability of the system.

First, the raw data collected by the GC-TOFMS system were preprocessed. Single data and single peak in the original data were filtered, the missing value in the original data were recoded, and the internal standard (IS) were utilized to normalize each group of data. Meanwhile, both TOF 4.3X software (LECO Corporation, United States) and LECO Fiehn Rtx5 database were used for raw peak exact matching, baseline filtering and calibration, peak alignment, deconvolution analysis, peak identification and integration of peak area. Finally, the standardized data were imported into SIMCA software (V14.1, MKS Data Analytics Solutions, Umea, Sweden) for multivariate statistical analysis, such as, principal component analysis (PCA) and orthogonal projection to latent structures-discriminant analysis (OPLS-DA) analysis. Prior to PCA, all variables obtained from GC-MS data sets went through logarithmic (LOG) transformation and centralization (CTR) scaling. Meanwhile, prior to OPLS-DA, all variables obtained from GC-MS data sets underwent logarithmic (LOG) transformation and unit variance (UV) scaling. Afterwards, the validity of the OPLS-DA model was tested by 7-fold cross validation and permutation test (random 200 times). Multivariate statistical analysis was conducted, combined with traditional univariate statistical analysis, with variable importance in the projection of the first principal component of the OPLS-DA model greater than 1 ($\text{VIP} > 1$), while the p -value of Student's t -test is less than 0.05 ($p < 0.05$), was used to screen significantly different metabolites, and the result was visualized in the form of a volcano graph. Thereafter, significantly different metabolites were subjected to pathway analysis with KEGG (<https://www.kegg.jp/>) and MetaboAnalyst 5.0 (<https://www.metaboanalyst.ca/>), which is a web-based tool for visualization of metabolomics, to identify related metabolic pathways. Metabolic pathways with $p < 0.05$ or Impact > 0.10 were screened as the most relevant metabolic pathways and may be used to distinguish the kidney-yang deficiency model group from the normal control group.

2.7 Network pharmacology

The active ingredients of Epimedium fried with suet oil mainly include two parts: the active ingredients of Epimedium flavonoids and the chemical ingredients of “suet oil” as the processing auxiliary material. Based on the previous research of the research group (Jiang et al., 2014; Li et al., 2020), 32 flavonoids were identified in raw and processed Epimedium products and 25 fatty acids were identified in suet oil, and made available via PubChem database (<https://pubchem.ncbi.nlm.nih.gov/>) to be downloaded in SDF format for the 2D or 3D structure of each component. The components were then screened with a definite 2D or 3D structure as the component library of Epimedium fried with suet oil. Thereafter, based on the PharmMapper database (<http://www.lilab-ecust.cn/pharmmapper/>), the species was set to “Homo Sapiens”, and the potential targets of Epimedium pilaris were predicted. According to the z

score value, the top 15 targets of each component corresponding to the score were screened as the action targets of chemical components in Epimedium. Targets were canonicalized to standard gene names *via* the UniProt database (<https://www.uniprot.org>). The targets of chemical constituents in Epimedium fried with suet oil are imported into the STRING database (<https://www.string-db.org/>) to construct a PPI network, and then the targets are imported into Cytoscape 3.6.1 to construct an active ingredient-potential target network. Finally, these targets were uploaded to the Metascape database (<https://metascape.org/gp/index>) for KEGG pathway analysis.

2.8 Integrated metabolomics and network pharmacology analysis

The metabolic pathways of $p < 0.05$ or Impact > 0.1 obtained from the metabolomics analysis were mapped to pathways acquired by the network pharmacology to uncover pathways in which the two correlates. Afterwards, target proteins and active compounds corresponding to Epimedium fried with suet oil from network pharmacology were reversely searched from the overlapping pathways, and finally the potential active compounds, target proteins, and metabolic pathways of Epimedium fried with suet oil affecting KYDS were obtained. On this basis, these potential targets were further verified *via* RT-qPCR, and differential target proteins were shown.

2.9 Quantitative real-time PCR analysis

Firstly, total RNA was isolated and extracted from flash-frozen kidney tissues. 100 mg of tissue was taken and added into a pre-cooled homogenized tube (containing 1 mL RNA extract). Grind thoroughly with the grinder until no tissue is visible, and then take the supernatant after centrifuging 10 min at 12,000 rpm. Then 250 μ L of trichloromethane was added, the centrifuge tube was inverted for 15 s, mixed well, and left for 3 min. After separating the cores at 12,000 rpm at 4°C for 10 min, 400 μ L of supernatant was transferred to a new centrifugal tube, adding 0.8 times the volume of propan-2-ol and mixing it upside-down. After being placed at -20°C for 15 min and centrifuged at 12,000°C for another 10 min, the white precipitate at the bottom of the tube was RNA. The liquid was removed by suction, and 1.5 mL of 75% ethanol was added to wash the precipitate, and then centrifuged at 4°C at 12,000 rpm for 5 min. After removing the liquid by suction, the centrifuge tube was placed on the ultra-clean table and blown for 3 min. The RNA was dissolved by adding 15 μ L of RNase-free water and incubated at 55°C for 5 min. The concentration and purity of total RNA samples were determined by Nanodrop 2000. Thereafter, RNA was reversely transcribed to cDNA by using Servicebio® RT Enzyme Mix. Finally, RT-qPCR and data collection were performed with PCR Master Mix (Bio-rad). The samples were exposed to pre-denaturation at 95°C for 10 min, followed by 40 cycles of denaturation at 95°C for 15 s and annealing at 60°C for 30 s. The dissolution curve conditions were from 65°C to 95°C, and the fluorescence signal was collected for every 0.5°C increase in temperature. Target mRNA expression in each sample was normalized to the housekeeping gene (GAPDH) to normalize the starting cDNA levels. The $2^{-\Delta\Delta CT}$ method was used to calculate relative mRNA expression levels. The PCR primers were listed in [Supplementary Table S1](#). The experiment was repeated thrice.

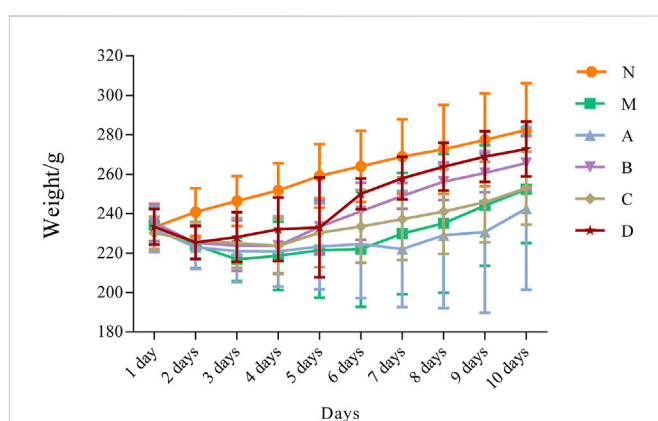


FIGURE 1

Line chart of changes in body weight of rats during the experiment N, normal group; M, model group; A, suet oil group; B, Epimedium raw product group; C, Epimedium heating product group; D, Epimedium fried with suet oil group.

2.10 Statistical analysis

The data from body weight and biochemical indicators were screened by SPSS 26.0 statistical software package (IBM, Armonk, NY, United States) and GraphPad Prism 6.01 (GraphPad Software, Inc., San Diego, CA, United States) software with Student's t-test or one-way analysis of variance (ANOVA). Data were presented as the mean \pm standard deviation. In all experiments, confidence level was set at 95% and 99% to determine the significance of difference ($p < 0.05$, $p < 0.01$).

3 Results

3.1 Weight changes

The weight changes of rats in each group were shown in [Figure 1](#), indicating gradual increase of the body weight of rats in the N group from day 1 until day 10 of the experiment. After modeling, the body weight of rats in the M group decreased to the lowest at day 3, and gradually recovered to the original body weight at day 10. The weight of rats in all treatment groups showed initial decrease followed by a gradual recovery, and the weight changes of rats in the D group was approximate to that of N group.

3.2 Biochemical and histopathological results

[Figure 2](#) showed that compared with the N group, the levels of CORT, ACTH, 17-OHCS, T3, T4, TSH, LH, T, and FSH in the M group were significantly decreased ($p < 0.05$, $p < 0.01$). Apart from ACTH, the A group had a callback effect on other indicators, although there was no significant difference. The B group has significant callback to T3, T and FSH ($p < 0.05$). The C group had significant callback to 17-OHCS, T3, TSH ($p < 0.05$, $p < 0.01$). All biochemical indexes were significantly increased in the D group.

As shown in [Figure 3](#), in the kidney-yang deficiency group M, multiple mild hemorrhages were observed in the hypothalamus tissue. Pituitary tissue was slightly bleeding, the boundary between nucleus

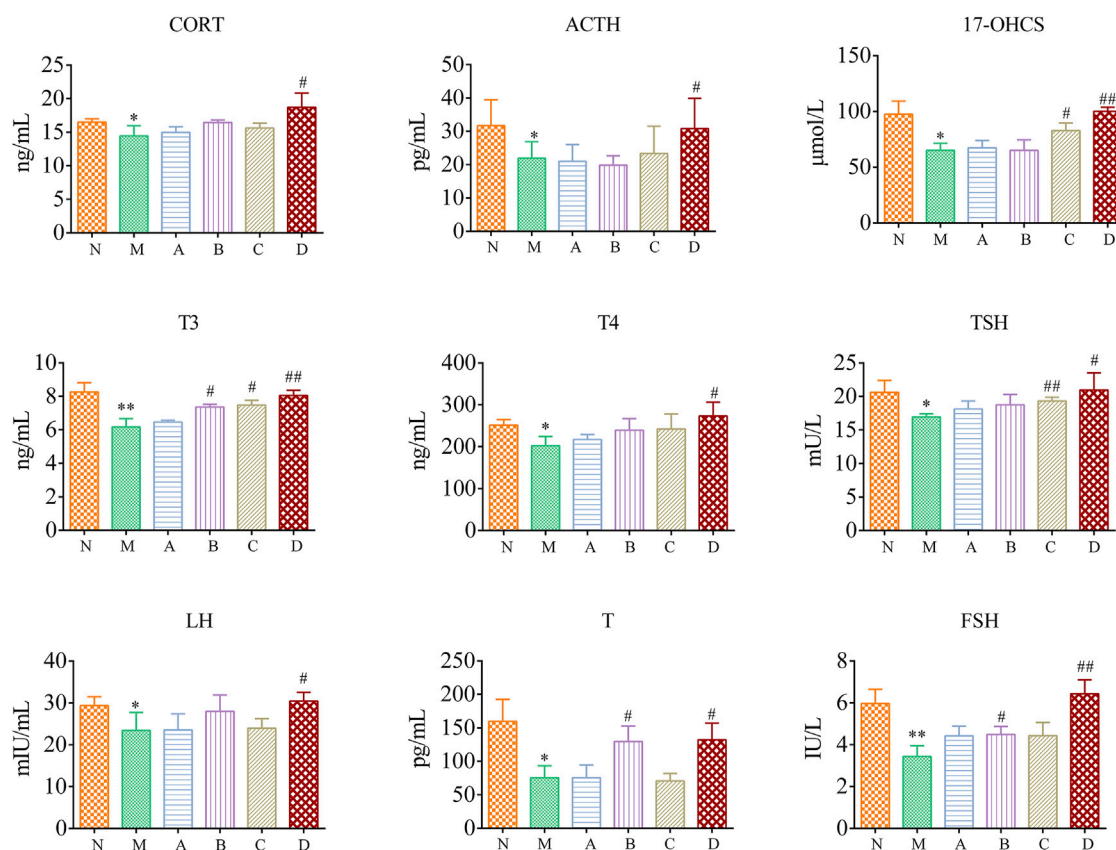


FIGURE 2

Biochemical indexes in kidney-yang deficiency rats N, normal group; M, model group; A, suet oil group; B, Epimedium raw product group; C, Epimedium heating product group; D, Epimedium fried with suet oil group. Significance compared to N group, * $p < 0.05$, ** $p < 0.01$; Significance compared to M group, # $p < 0.05$, ## $p < 0.01$.

and cytoplasm was unclear. In the thyroid tissue, a large number of follicular matrix was reduced, many epithelial cells were necrotic and exfoliated, and nuclear fragmentation was observed. Hemorrhage was observed locally in adrenal tissue, a large number of parenchymal cells had granular degeneration, cells were swollen, and the cytoplasm was loose and lightly stained, showing fine granularity. A small amount of eosinophilic serous material exuded from multiple interstitial areas of testis tissue. In the renal medulla, the renal tubules were significantly dilated, accompanied by mild connective tissue hyperplasia, and punctate infiltration of lymphocytes and macrophages. These were consistent with the results of Tang et al. (Xiang et al., 2012). Except for group A, the hypothalamus-pituitary-target gland axis (hypothalamus, pituitary, thyroid, adrenal gland, testis) in group B/C/D was improved to a certain extent after administration, and the improvement effect of group D was better than that of group B/C. Taken together, these results suggested that the hypothalamic, pituitary, thyroid, adrenal, testis and kidney tissue and cell structures could be altered in the kidney-yang deficiency induced by intraperitoneal injection of hydrocortisone, again demonstrating that the hypothalamic-pituitary gland—the target gland axis was inhibited. After the intervention treatment of Epimedium processed by heating and suet oil, the pathological changes of tissue cell structure caused by kidney yang deficiency was shown to have improved, which further

revealed the mechanism of Epimedium fried with suet oil to warm the kidney and promote yang.

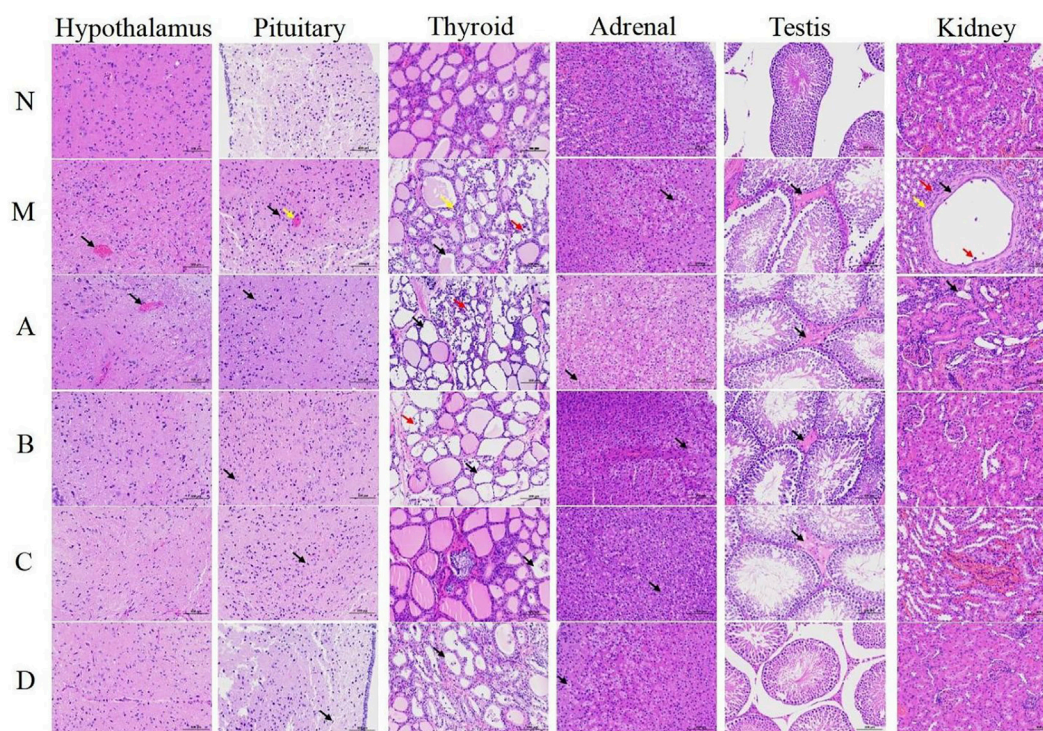
3.3 Metabonomics results

3.3.1 Metabolic profile analysis of urine and plasma in rats

The internal standard (L-2-chlorophenylalanine) retention time, the GC-TOFMS TIC of the random sample (N2, N5) and internal standard (L-2-chlorophenylalanine) were shown in [Supplementary Tables S2, S3, Supplementary Figures S2–S5](#). The results showed that the experimental method was viable; the instrument platform was justified, and corroborated with the conditions in the experimental methodologies. Six groups of total ion current diagrams of the urine samples and serum samples analyzed by GC-MS were shown in [Supplementary Figures S6, S7](#). A total of 759 active peaks were detected in urine and 261 active peaks in plasma.

3.3.2 Multivariate statistical analysis and potential biomarkers exploring

An unsupervised PCA was performed first to characterize between-group differences in rat urine and plasma samples, respectively. As

**FIGURE 3**

H&E staining of hypothalamus, pituitary, thyroid, adrenal, testis and kidney tissue sections (magnification $\times 200$). N, normal group; M, model group; A, suet oil group; B, Epimedium raw product group; C, Epimedium heating product group; D, Epimedium fried with suet oil group. Hypothalamus: Black arrow represents the bleeding. Pituitary: Yellow arrow represents the bleeding. Black arrow represents the cell nucleus and the cytosolic boundary. Thyroid: Black arrow represents the follicular matrix. Yellow arrow represents epithelial cell necrosis. Red arrow represents nuclear fragmentation. Adrenal: Black arrow represents eosinophilic serous material. Yellow arrow represents the connective tissue. Red arrow represents the cellular infiltration. Kidney: Black arrow represents the renal tubules. Yellow arrow represents the connective tissue. Red arrow represents the cellular infiltration.

displayed in Figure 4A, B, the urine and plasma samples of the rats in the control group and the model group were clustered into two categories on the PCA score plots, indicating that after modeling, the urine and plasma endogenous metabolites of the rats in the two groups existed significant differences. As shown in Figures 4C, D, the rat urine and plasma QC samples were well-aggregated, indicating that the detection system was stable and reliable, and the obtained differences could reflect the biological differences between samples. The urine and plasma samples of the A group, the B group, the C group, and the D group were all separated from the M group in the PCA score plots and approached the N group, indicating that each administration group could regulate the metabolic disorder of hydrocortisone-induced kidney-yang deficiency rats to normal to different degrees, and the regulation trend was as follows: D group > C group > B group > A group.

To further determine the differences of endogenous metabolites in the urine and plasma of rats after administration, OPLS-DA analysis was performed on the M group and the N group, respectively. As shown in Figure 5A, B, both in the urine samples and in the plasma samples, the N group and the M group were respectively clustered into one category in the OPLS-DA scores plots, indicating a significant difference between the N group and the M group. Then, a random permutation test ($n = 200$) was performed under the established OPLS-DA model to evaluate the model's interpretation rate (R^2Y), predictive ability (Q^2) and other parameters. The results were arranged

in the experiment. $R^2 = 0.900$, $Q^2 = -0.330$ (urine, Figure 5C); $R^2 = 0.850$, $Q^2 = -0.430$ (plasma, Figure 5D). The results show that the model has good stability and prediction ability, and no overfitting occurs. Combined with VIP > 1 and $p < 0.05$ in the Volcano plot (Figures 5E, F), the differential variables with the largest contribution were screened as biomarkers related to kidney-yang deficiency syndrome, and were identified by LECO Fiehn Rtx5 database and combined with HMDB databases. Twenty-eight relevant biomarkers (13 in urine and 15 in plasma) were finally screened, of which 15 were identified (5 in urine and 10 in plasma). The results are listed in Table 1. Compared with the N group, nine biomarkers were upregulated in the M group, four of which were Tyramine, Galacturonic acid, Gulonate, 3-Hydroxyproline in urine. And 5 in plasma were D-Mannose, Ornithine, Sucrose, 2,4,6-trimethylPyridine, Cholesterol. Six biomarkers in the M group were downregulated, 1 in urine was downregulated as Ribitol, and five in plasma were downregulated as 5-Oxoproline, Citric acid, L-Tryptophan, Glycerol, Threonine acid.

3.3.3 Regulation of differential metabolites

Column charts were drawn according to the relative contents and change trends of the biomarkers in urine and plasma of rats in each group (Figure 6). After the treatment intervention, the B, C, and D group biomarker contents demonstrated certain

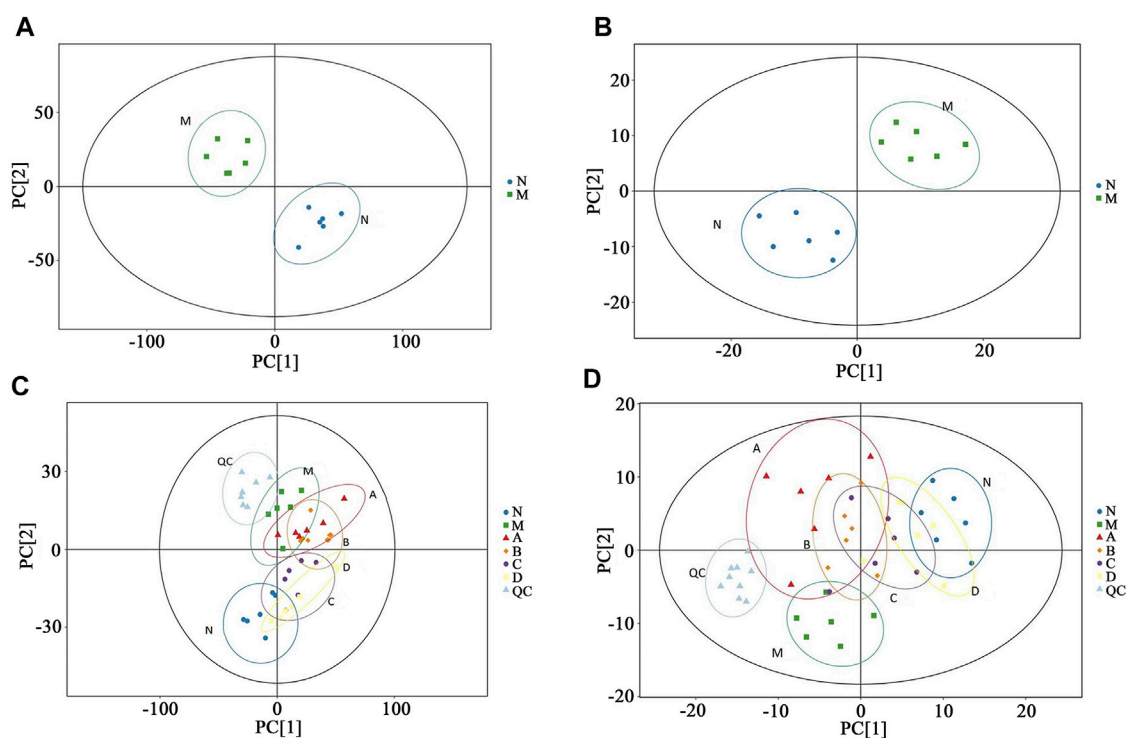


FIGURE 4

PCA scores plots of urine and plasma samples in rats N: Control group; M: Model group; A: Suet oil group; B: Epimedium raw product group; C: Epimedium heating product group; D: Epimedium fried with suet oil group. (N VS. M, (A) Urine, (B) Plasma; the PCA scores plots of six group, (C) Urine, (D) Plasma.)

normalizing trends, with that of the D group being the most significant. The Sucrose and Galacturonic acid could be significantly recalled in the A group ($p < 0.05$, $p < 0.01$), suggesting that the suet oil had some intervention effect on kidney-yang deficiency syndrome. The B group could significantly recall six differential metabolites, especially Ornithine and Sucrose ($p < 0.01$). The C group could significantly recall seven differential metabolites, especially Sucrose and 2,4,6-trimethyl-Pyridine ($p < 0.01$). The D group could significantly recall 13 differential metabolites, especially Tyramine, Ornithine, Sucrose, 2,4,6-trimethyl-Pyridine and Glycerol ($p < 0.01$). Compared with B and C groups, D group had the most different metabolites in callbacks, indicating that the effect of Epimedium fried with suet oil group was the best. It is possible that Epimedium fried with suet oil regulated kidney-yang deficiency in rats through the above-described metabolites, thereby enhancing the warming effect on the kidneys and strengthen yang.

3.3.4 Metabolic pathway analysis

The biomarkers in Table 1 were imported into MetaboAnalyst 5.0 (<http://www.metaboanalyst.ca>) for pathway analysis, and the metabolic pathways with $p < 0.05$ or Impact > 0.1 were screened out as potential kidney-yang deficiency metabolic pathways. As shown in Figure 7, five related metabolic pathways were finally screened out, namely Galactose metabolism, Glutathione metabolism, Glycerolipid metabolism, Arginine and proline metabolism and Tryptophan metabolism.

Analysis of potential biomarkers of kidney-yang deficiency and related metabolic pathways suggested that the processing excipient of suet oil might play a role in warming kidney and promoting Yang by regulating Galactose metabolism. Epimedium raw product and Epimedium heating product might improve kidney-yang deficiency through Galactose metabolism, Glutathione metabolism and Arginine and proline metabolism. Meanwhile, the metabolic pathways above were the metabolic pathways of Epimedium fried with suet oil to improve the kidney yang deficiency syndrome in rats, which further explained that the processing mechanism of epimedium could enhance its effect of warming kidney and promoting Yang after heating with the auxiliary material suet oil.

3.4 Network pharmacological analysis

Thirty-seven compounds were screened out as the active compounds library of Epimedium fried with suet oil, including 13 from Epimedium and 24 from suet oil. The specific results are listed in Supplementary Table S4. *Homo sapiens* species were selected to draw the protein-protein interaction (PPI) network of 159 common targets (Supplementary Figure S8). Then in order to reflect the relationship between the active compounds of Epimedium and suet oil and target genes in Epimedium fried with suet oil, a drug-active compounds-target network was constructed, as shown in the Figure 8. KEGG enrichment analysis was performed on 159 potential targets of active components of Epimedium fried with suet oil using Metascape database, and 267 pathways were obtained (Supplementary Figure S9).

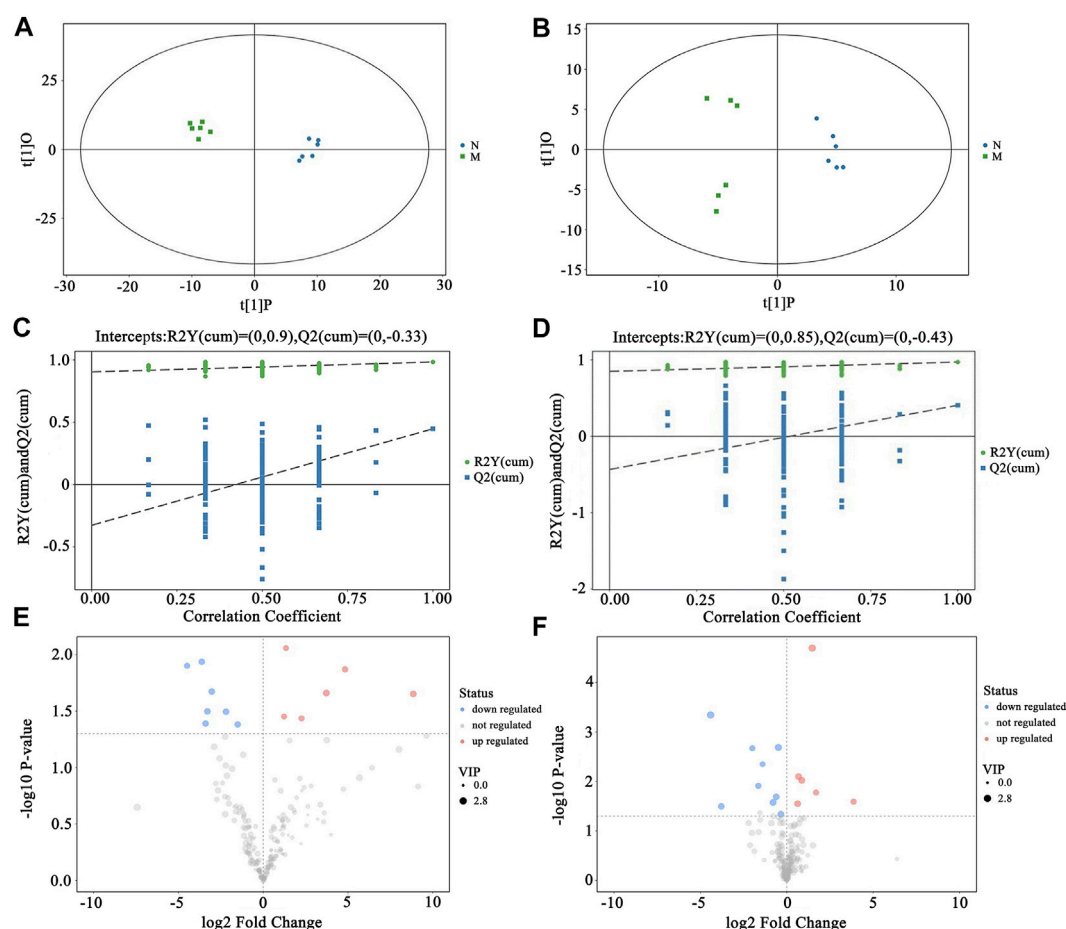


FIGURE 5

Screening of biomarkers in rats with kidney-yang deficiency. N VS. M, (A) Urine OPLS-DA scores plots, (B) Plasma OPLS-DA scores plots, (C) Urine OPLS-DA permutation test, (D) Plasma OPLS-DA permutation test, (E) Urine Volcano plot, (F) Plasma Volcano plot. Red represents upregulation of differential metabolites. Blue represents downregulation of differential metabolites. Gray represents metabolites with no statistical difference.

3.5 Integrative analysis of the network pharmacology and metabolomics

The five key metabolic pathways in metabolomics were mapped to the pathways of network pharmacology for analysis as shown in the Figure 9. It was found that two metabolic pathways (glutathione metabolism, arginine and proline metabolism) overlapped with it, and the corresponding 13 active compounds (9 active compounds in Epimedium and 4 in suet oil) and 7 target genes were obtained by reverse mapping analysis. Thirteen active compounds were Quercetin, Epimedin A, Caohuoside B, Korepimidoside C, Hexandraside E, Epimedin B, Epimedeside E, Baohuoside I, 2''-O-Rhamnosylcariside II, Methyl tetradecanoate, Methyl (Z)-heptadec-10-enoate, Methyl (9E)-9-octadecenoate, Methyl (E)-nonadec-10-enoate. The seven target genes were acetaldehyde dehydrogenase 2 (ALDH2), arginase type II (ARG2), glutathione S-transferase A3 (GSTA3), glutathione S-transferase M1 (GSTM1), glutathione S-transferase M2 (GSTM2), hematopoietic prostaglandin D synthase (HPGDS), Nitric Oxide Synthase 2 (NOS2). The drug-active compounds-target genes-pathways network was constructed as shown in Figure 10.

3.6 Experiment validation

The RT-qPCR verification results were shown in Figure 11. Seven target genes were expressed in kidney tissue. Compared with the N group, the expression levels of two target genes (ARG2 and NOS2) in the M group were significantly increased ($p < 0.01$). The expression of five target genes was decreased, and which of three target genes (ALDH2, GSTA3, HPGDS) were significantly decreased ($p < 0.01$). Compared with the M group, the A, B, C and D groups had different degrees of callback effect on seven target genes. ALDH2, ARG2, GSTA3, HPGDS, NOS2 had a callback trend in the A group, but there was no significant difference. The expression of HPGDS target genes was significantly increased in the B group ($p < 0.05$). The expression of ARG2 and NOS2 were significantly decreased in the B and C groups ($p < 0.05$). The expression levels of GSTM1, GSTM2 and HPGDS were significantly increased ($p < 0.05$, $p < 0.01$), ARG2 and NOS2 expressions were significantly decreased ($p < 0.01$) in the D group.

The callback results of the target genes in each administration group showed that the improvement effect of Epimedium fried with suet oil on kidney-yang deficiency was better than that of the other three administration groups. Notably, the five target genes with

TABLE 1 Biomarkers of urine and plasma in kidney-yang deficiency rats (n = 6, Mean ± SD).

Sample	Metabolite	t_R / min	Formulas	Similarity	Database ID	VIP	P	Variation between groups				
								M vs. N	A vs. M	B vs. M	C vs. M	D vs. M
Urine	Ribitol	17.776	C ₅ H ₁₂ O ₅	864	HMDB0000508	2.103	0.022	↓*	↑	↑	↑	↑
Urine	Tyramine	22.732	C ₈ H ₁₁ NO	920	HMDB0000306	1.990	0.032	↑*	↑	↓	↓	↓
Urine	Galacturonic acid	23.108	C ₆ H ₁₀ O ₇	791	HMDB0002545	1.250	0.009	↑**	↓	↓	↓	↓
Urine	Gulonate	29.778	C ₆ H ₁₂ O ₇	909	HMDB0003290	2.468	0.022	↑*	↓	↓	↓	↓
Urine	3-Hydroxyproline	26.867	C ₅ H ₉ NO ₃	986	HMDB0245903	1.478	0.037	↑*	↓	↓	↓	↓
Plasma	5-Oxoproline	10.037	C ₅ H ₇ NO ₃	954	HMDB0000267	2.122	0.042	↓*	↑	↑	↑	↑
Plasma	D-Mannose	11.970	C ₆ H ₁₂ O ₆	942	HMDB0000169	2.097	0.046	↑*	↑	↓	↓	↓
Plasma	Ornithine	11.657	C ₅ H ₁₂ N ₂ O ₂	935	HMDB0000214	2.202	0.027	↑*	↓	↓	↓	↓
Plasma	Citric acid	11.616	C ₆ H ₈ O ₇	916	HMDB0000094	1.918	0.021	↓*	↓	↑	↑	↑
Plasma	L-Tryptophan	13.690	C ₁₁ H ₁₂ N ₂ O ₂	762	HMDB0000929	2.185	0.008	↓**	↑	↑	↑	↑
Plasma	Sucrose	15.340	C ₁₂ H ₂₂ O ₁₁	733	HMDB0000258	2.768	0.000	↑**	↓	↓	↓	↓
Plasma	2,4,6-trimethylPyridine	6.477	C ₈ H ₁₁ N	895	HMDB0245482	1.642	0.012	↑*	↓	↓	↓	↓
Plasma	Glycerol	8.229	C ₃ H ₈ O ₃	779	HMDB0000131	2.018	0.020	↓*	↑	↑	↑	↑
Plasma	Threonic acid	10.115	C ₄ H ₈ O ₅	745	HMDB0000943	2.184	0.010	↓*	↓	↑	↑	↑
Plasma	Cholesterol	19.184	C ₂₇ H ₄₆ O	872	HMDB0000067	2.427	0.002	↑**	↓	↓	↓	↓

‘↑’ and ‘↓’ represent compounds which are up- and downregulated in the M group compared with the N group or in the administration group (A/B/C/D) compared with the M group. * $p < 0.05$, ** $p < 0.01$ (one-way ANOVA, with a Bonferroni correction). Similarity: Score the match between the substance and the peak detected by mass spectrometry.

significant callback effects in Epimedium fried with suet oil were derived from the target genes corresponding to the active compounds of Epimedium (GSTM1, GSTM2, ARG2 and NOS2) and the target gene corresponding to the active compounds of suet oil (HPGDS). Furthermore, the synergistic mechanism of Epimedium fried with suet oil to warm the kidney and enhance yang was clarified.

3.7 Overall interactive network diagram of drugs, active compounds, targets, pathways, and metabolites

Figure 12 showed the overall interaction network diagram of drugs, active compounds, targets, pathways and metabolites. Integrating network pharmacology, metabolomics and RT-qPCR analysis, it was found that Epimedium fried with suet oil mainly affects 13 active compounds, seven targets, and two biomarkers in two metabolic pathways, thereby improving kidney-yang deficiency. Its mechanism of action may mainly involve amino acid metabolism and oxidative stress.

4 Discussion

Epimedium is a TCM for kidney-yang deficiency. The most common processing method is suet oil processing, which aims to enhance the kidney-warming and yang-boosting effects of Epimedium. Previous studies have shown that the model of kidney

yang deficiency was established through glucocorticoid, and its mechanism was to simulate the pathological state when the hypothalamic-pituitary-target gland axis (adrenal gland, thyroid gland, gonad) was inhibited, thereby producing deficiency symptoms similar to “kidney yang deficiency” (Zhang et al., 2014). Kidney-yang deficiency is manifested in macroscopic characterization (e.g., weight loss), biochemical standards (e.g., decreased hormone levels of CORT, 17-OHCS, T3, T4, and T), and organ histopathology (e.g., pathological changes in the hypothalamus, pituitary gland, thyroid gland, adrenal gland, and testis). This study found that compared with the N group, the body weight of the M group rats was reduced, and the levels of hypothalamic-pituitary-adrenal axis hormones (CORT, ACTH, 17-OHCS), hypothalamic-pituitary-thyroid axis hormones (T3, T4, TSH) and hypothalamic-pituitary-gonadal axis hormones (LH, T, FSH) were inhibited. Pathological changes occurred in the tissues and cellular structures of hypothalamus, pituitary gland, thyroid gland, adrenal gland, testis and kidney. Compared with M group, in addition to the A group, B, C, and D groups could reverse this inhibition of different level and improve the pathological changes of the organization, and the reverse effect of Epimedium fried with suet oil was better than that of raw epimedium and heated epimedium, suggesting that the effect of warming the kidney and promoting yang of epimedium is enhanced after being heated and processed with suet oil.

Subsequently, in this study, we analyzed the processing synergistic mechanism of Epimedium fried with suet oil through metabolomics combined with network pharmacology. In the metabolomic results, 15 biomarkers related to kidney-yang deficiency were screened in

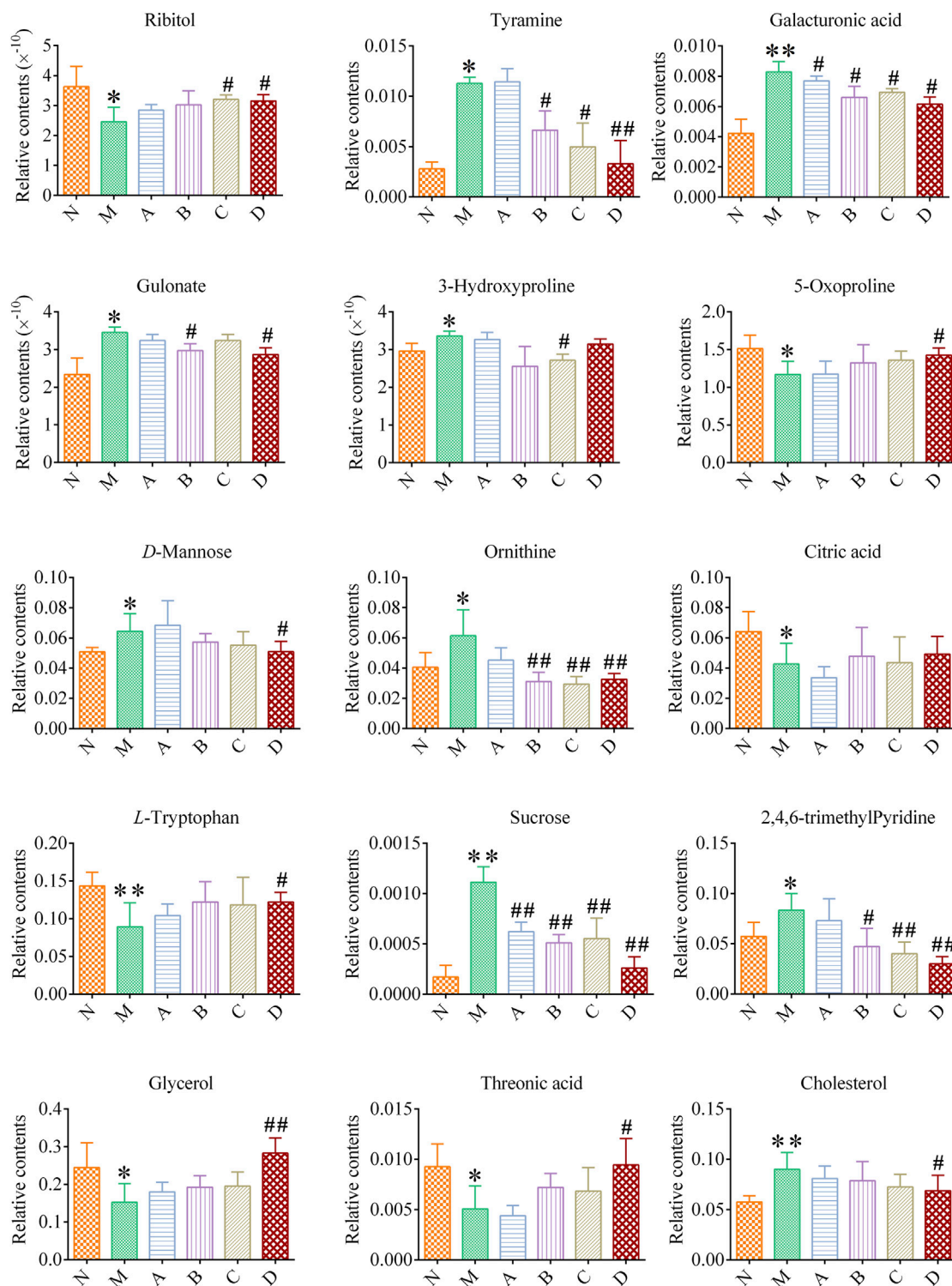
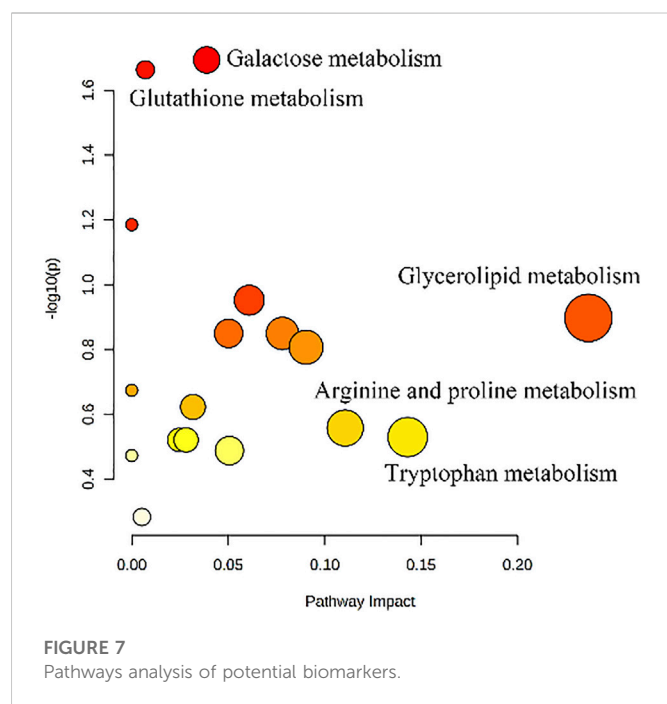


FIGURE 6

The levels of potential biomarkers of kidney-yang deficiency in each group Compared with the N group, * $p < 0.05$, ** $p < 0.01$; compared with the M group, # $p < 0.05$, ## $p < 0.01$.

urine and plasma, involving five metabolic pathways, namely Galactose metabolism, Glutathione metabolism, Glycerolipid metabolism, Arginine and proline metabolism, Tryptophan metabolism. Among them, Galactose metabolism was related to energy metabolism, while Glutathione metabolism, Glycerolipid

metabolism, Arginine and proline metabolism, and Tryptophan metabolism were closely related to amino acid metabolism and oxidative stress. Galactose metabolism regulated by suet oil and Galactose metabolism, Glutathione metabolism, Arginine and proline metabolism regulated by Epimedium heating product were

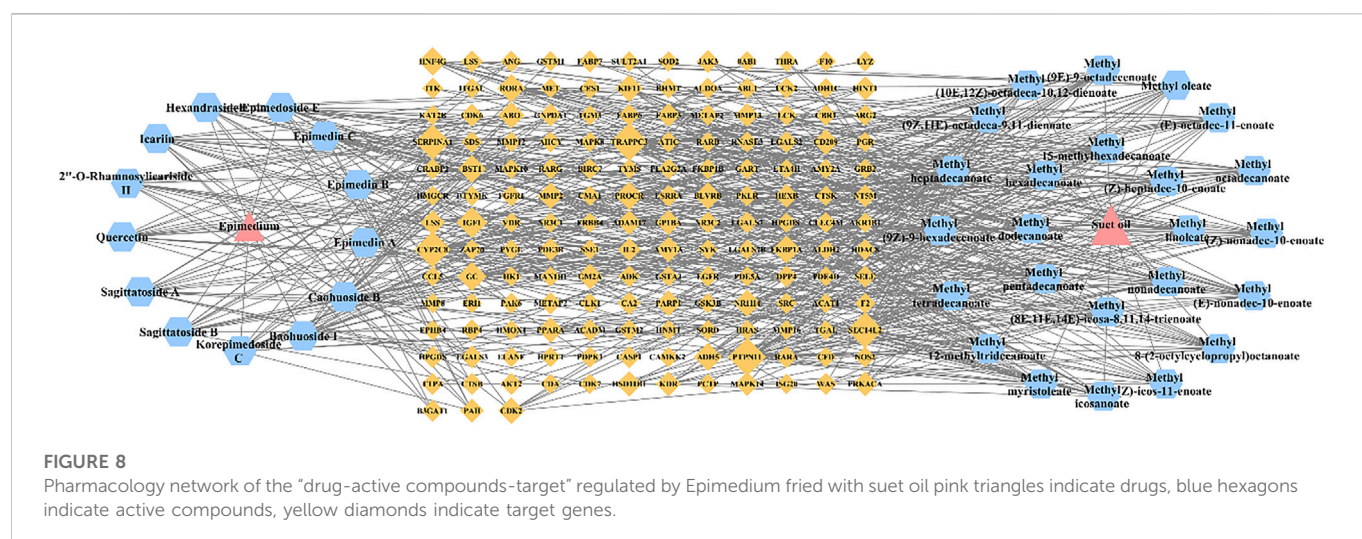


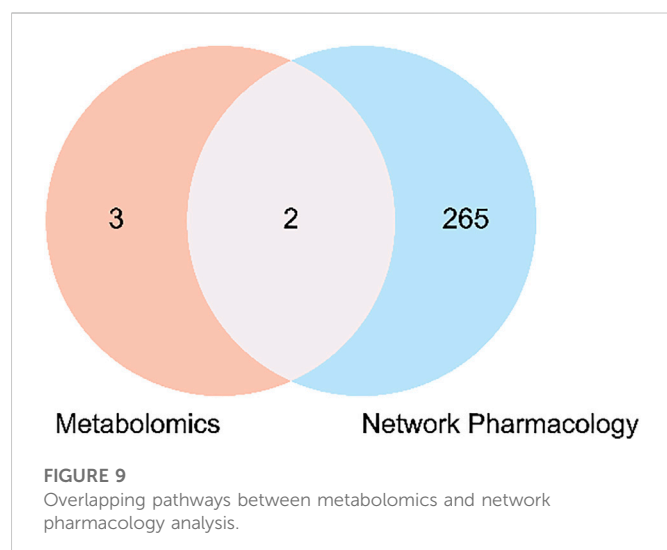
the metabolic pathways of Epimedium fried with suet oil group to improve kidney yang deficiency in rats. In the network pharmacology results, seven target genes (ALDH2, ARG2, GSTA3, HPGDS, GSTM1, GSTM2, and NOS2) and two linked metabolic pathways (glutathione metabolism, arginine and proline metabolism) were identified by the drug-active compounds-target genes-pathways network.

Glutathione comprises cysteine, glutamic acid and glycine. The main metabolic pathways of glutathione include glutathione producing glutathione disulfide (GSSG) under the action of glutathione peroxidase (GSHPx) and cross-linking complex under the action of glutathione transferase (GST). It plays a role in oxidative stress, participating in cell apoptosis and regulating signal transduction (Xu et al., 2014). Studies have found that genes related to kidney-yang deficiency in the aged are closely related to aging (Dong et al., 2013), and glutathione deficiency can induce oxidative stress in the aging process. Increasing the uptake of the

glutathione, precursors glycine and cysteine, can restore the synthesis and concentration of glutathione and reduce oxidative stress and oxidative damage in the aging process (Sekhar et al., 2011). (Du et al., 2020) used LC-MS metabolomics method to identify 31 biomarkers related to kidney Yang deficiency from testicular tissue, and 26 of them could be significantly recovered after Gulingji intervention. It was speculated that they might improve kidney Yang deficiency syndrome by regulating glutathione metabolism, arginine and proline metabolism, glyoxylate and dicarboxylic acid metabolism and other pathways. In this study, it was found that Ornithine and 5-Oxoproline are both products of glutathione metabolism and biomarkers of kidney Yang deficiency. Epimedium fried with suet oil could play its role in warming kidney and helping Yang by regulating these two biomarkers of kidney Yang deficiency. GSTA3, GSTM1 and GSTM2 are transferases of glutathione metabolism, which can catalyze the cross-linking complex between glutathione and electron-philic complex to protect cells from free radical damage. HPGDS, also known as glutathione dependent prostaglandin D synthetase, is involved in the biosynthesis of prostaglandin in adult testis, thereby affecting the production of spermatogenesis and the normal function of testis (Körber and Goericke-Pesh, 2019). The active components of Epimedium fried with suet oil, Quercetin, Epimedin A, Caohuoside B and Korepimidoside C, mainly acted on glutathione sulfur transferases (GSTA3, GSTM1 and GSTM2). Methyl tetradecanoate, Methyl (Z)-heptadec-10-enoate, Methyl (9E)-9-octadecenoate and Methyl (E)-nonadec-10-enoate mainly acted on HPGDS, and then affected glutathione metabolism.

Arginine and proline metabolism is the core process of the biosynthesis and metabolism of arginine, ornithine, proline, citrulline and glutamate (Feng et al., 2022). Arginine is a semi-essential amino acid synthesized from glutamine, glutamate, and proline *via* the gut-kidney axis in humans and most mammals, and plays an important role in the human body as a precursor of various physiologically important substances (Ma et al., 2019). Several studies have shown that arginine and its derivatives may be involved in the pathogenesis of kidney diseases and are markers of pathological progression (Feng et al., 2020). Arginine is the precursor of the synthesis of ornithine, which participates in the ornithine cycle under the action of ornithine carbamoyl transferase, promotes the synthesis of urea and accelerates the degradation of blood ammonia.

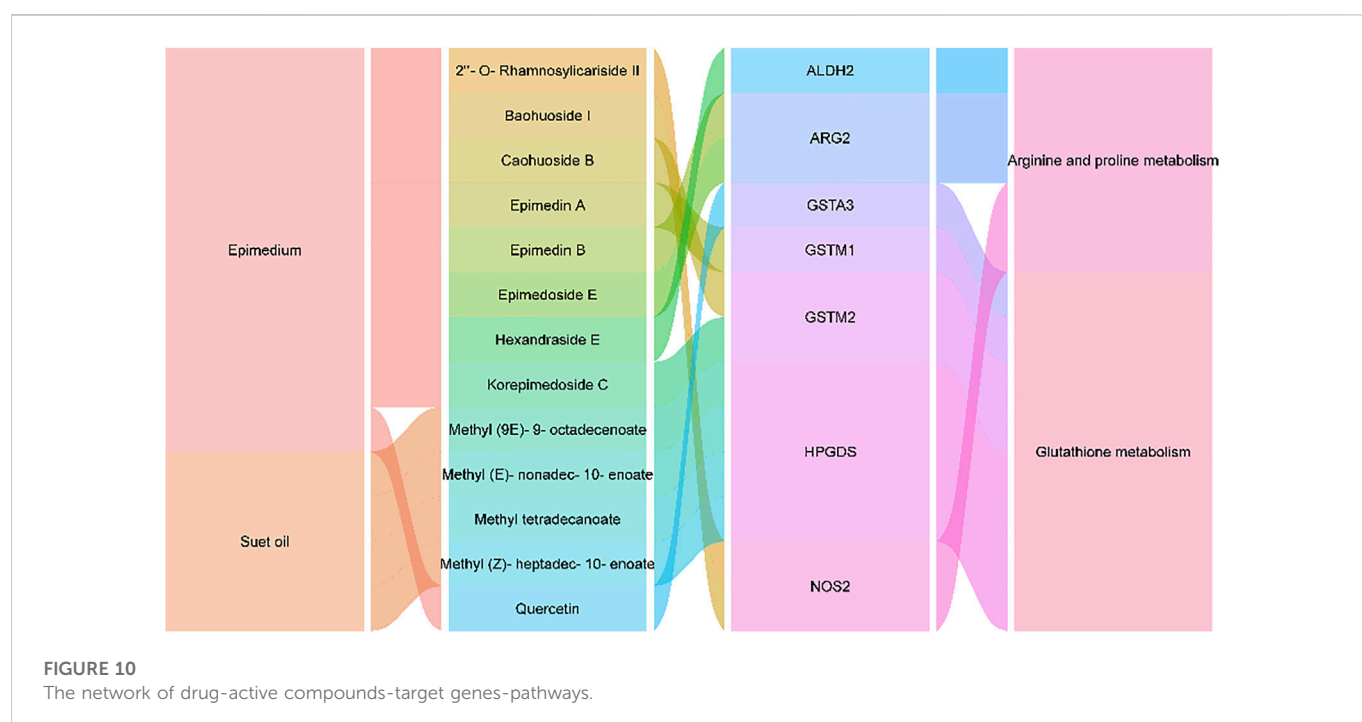




Arginine can form ornithine and urea under the action of arginase, and produce nitric oxide under the action of nitric oxide synthase (Castilho-Martins et al., 2015). These pathways are involved in biochemical processes such as ammonia detoxification, hormone secretion and immune system regulation (Chang et al., 2020). The level of ornithine increased in kidney-yang deficiency rats. It was speculated that the regulation of ornithine in Epimedium fried with suet oil group might be related to the adjustment of gut microbiota balance, the reduction of renal tubulointerstitial fibrosis and the improvement of renal function. In this study, Hexandraside E, the active component of Epimedium fried with suet oil, mainly acted on ALDH2. Epimedin B and Epimedeside E mainly acted on ARG2. Baohuoside I and 2''-O-Rhamnosylcariside II mainly acted on NOS2. Thus, they jointly regulated arginine and proline metabolism.

Galactose metabolism is closely related to glycolytic metabolic pathways, which can reflect the level of energy metabolism of the body and is important for stabilizing the structure of the whole branched carbohydrate chain (Guo et al., 2016; Jin et al., 2019). Galactose metabolism is not only important for energy production in cells, but also contributes to the modification of glycolipids and glycoproteins (Petry and Reichardt, 1998). Galactose metabolism may be associated with chronic inflammation. When galactose metabolism is disrupted, it also promotes the release some inflammatory factors to participate in the body's inflammatory response (Nikolac Perkovic et al., 2014). It is found that the liver and kidney of KYDS rats may be damaged due to the effect of hydrocortisone, thus affecting galactose metabolism (Chen et al., 2018). In this paper, the rats with kidney yang deficiency have cold phobia, kidney damage and other deficiency symptoms, indicating that their energy metabolism is abnormal. After administration, the abnormal galactose metabolism in the body gradually returned to normal, the body's energy metabolism also tended to return to normal, and the inflammation was improved.

Glycerolipid metabolism is one of the important ways of lipid metabolism in the body, and the core reaction is the acetylation of glycerol and the degradation of triacylglycerol (Li et al., 2022). Lipids are divided into eight groups, including fatty acids, triglycerides, glycerolipids, sphingolipids, glycolipids, polyketones, sterolipids, and isopentenol lipids (Fahy et al., 2005). Changes in lipid metabolites can lead to a series of pathophysiological phenomena, including obesity (Nam et al., 2018), inflammation etc, (Ralston et al., 2017). Disturbance of Glycerolipid metabolism was observed in the early, middle and late stages of Aristolochic acid nephropathy (Zhao et al., 2015). Glycerol, as an important small molecule, participates in the Glycerolipid metabolism (Liu et al., 2019). The results of this experiment showed that glycerol, a differential marker screened, had an effect on Glycerolipid metabolism. Compared with the Control group, glycerol content in the kidney-yang deficiency model group was significantly decreased. Different



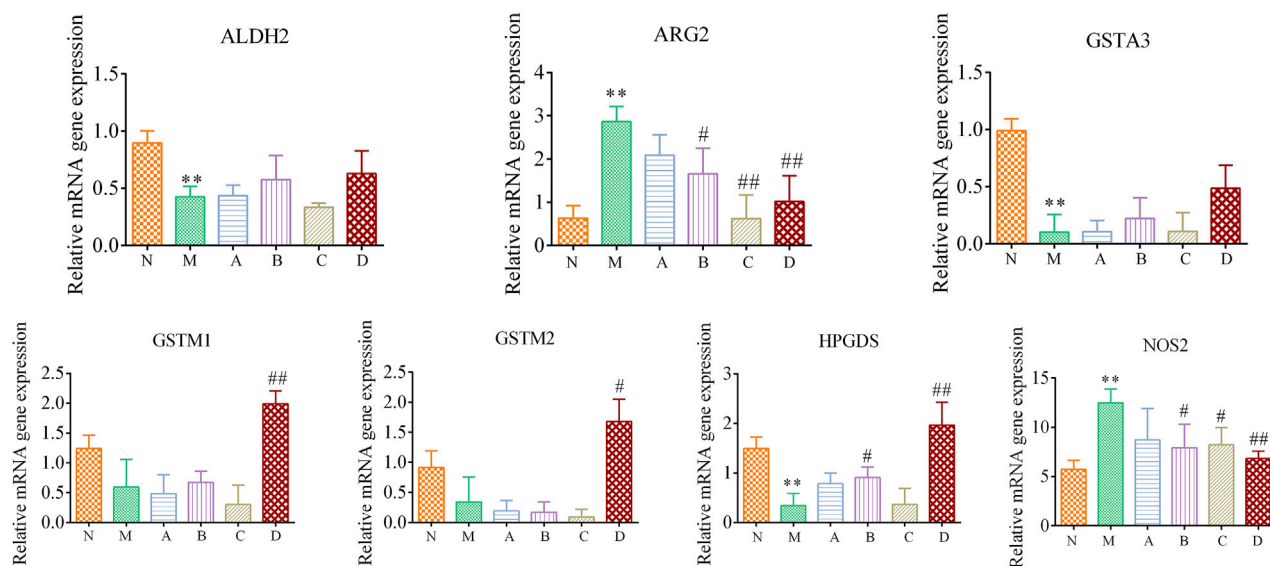


FIGURE 11

Epimedium fried with suet oil regulates differential gene expression associated with kidney yang deficiency. All genes expression were examined by RT-qPCR and normalized to GAPDH expression. Data represent mean \pm SD for at least three independent experiments. Compared with the N group, * $p < 0.05$, ** $p < 0.01$; compared with the M group # $p < 0.05$, ## $p < 0.01$.

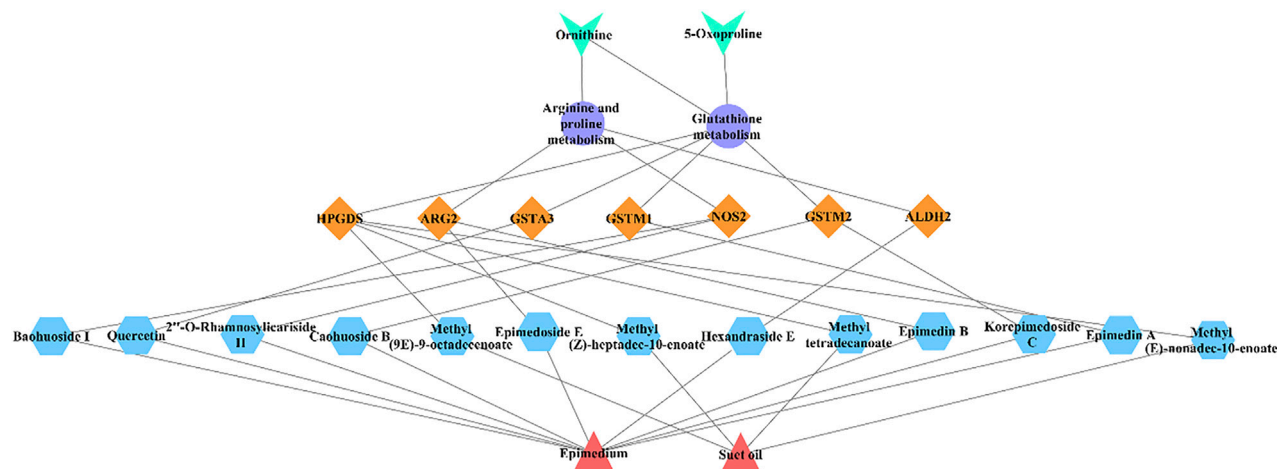


FIGURE 12

The overall interactive network diagram pink triangles indicate drugs, blue hexagons indicate active compounds, yellow diamonds indicate target genes, purple ellipses indicate pathways, green "V" indicates biomarkers.

administration groups could adjust the contents to different degrees, especially the callback effect of the D group had the most significant.

Tryptophan, as an essential amino acid, is involved in tryptophan metabolism (Liu et al., 2022). Tryptophan metabolism is closely related to the central nervous system because tryptophan is involved in serotonin synthesis (Kałużna-Czaplińska et al., 2019). Tryptophan metabolism is related to the activity of inflammatory bowel disease and has significant effects on gastrointestinal physiology (Hua et al., 2019). Zhou et al. found that tryptophan metabolism was seriously disturbed in KYDS state in the study of the therapeutic effect of ShenQiWan on kidney yang deficiency (Zhou et al., 2016). Tong

et al. found that tryptophan is a precursor of serotonin, which is closely related to KYDS metabolic disorders requiring the participation of intestinal flora (Tong et al., 2022). In this study, tryptophan metabolism was disturbed in the model group of kidney-yang deficiency rats. This is consistent with the results of the literature. Compared with the control group, the tryptophan level in the model group decreased significantly. Epimedium fried with suet oil could improve the disorder of tryptophan metabolism by significantly regulating the tryptophan metabolite, showing obvious anti KYDS effect.

To further verify the results, RT-qPCR was used to analyze the expression levels of the seven selected targets in the kidney tissues of

the six groups of rats. GSTA3, GSTM1, GSTM2, and HPGDS belong to the glutathione sulfur transferase series, which are related to prostaglandin synthesis and participates in glutathione metabolism. GSTA3, GSTM1, and GSTM2 are widely present in various tissues and cells of the body, and are related to the occurrence of cell damage, oxidative stress, poisoning, aging and other disease processes (Chen et al., 2018). Glutathione thiotransferase A3 (GSTA3), as one of the most important members of the glutathione transferase family, is involved in detoxication and cell protection (Ilic et al., 2010). GSTA3 has a protective effect on Tubular epithelial-mesenchymal transition in renal fibrosis (Xiao et al., 2016). Glutathione S transferase M1 (GSTM1) is an important member of phase II toxic metabolizing enzyme GST family, which plays a detoxification role by binding with glutathione (Mehdi et al., 2019). It is reported that GSTM1 can repair acute kidney injury by reducing endoplasmic reticulum and oxidative stress (Dai et al., 2021). Glutathione S-transferase M2 (GSTM2) is a protein involved in the detoxification of reactive oxygen species (Zhou et al., 2008). GSTM2 has the activity of prostaglandin E synthetase (PGES) and can participate in the synthesis of prostaglandin E2 (PGE2) (Beuckmann et al., 2000).

HPGDS is a member of the glutathione S-transferases (GSTs) family that is closely associated with inflammatory diseases (Huang et al., 2021). HPGDS is mainly expressed in hematopoietic cell lines, catalyzes the synthesis of prostaglandin D2, and reduces inflammation by regulating the apoptosis of T cells and B cells (Rittchen and Heinemann, 2019). It was found that icariin can increase the levels of glutathione sulfotransferase and glutathione, and decrease the levels of malondialdehyde and nitric oxide (Amanat et al., 2022). In this study, the expression levels of GSTA3, GSTM1, GSTM2 and HPGDS were decreased in kidney tissues after modeling, suggesting that kidney Yang deficiency was accompanied by apoptosis, oxidative stress injury and inflammation of kidney tissue cells, and then caused kidney injury. This is consistent with the kidney histopathological results described above. However, D group could reverse the above level expression. Therefore, it could be speculated that Epimedium fried with suet oil might alleviate kidney injury caused by apoptosis of kidney tissue by increasing the level of glutathione transferase, and then played the role of warming kidney and helping Yang.

ALDH2 is related to the body's energy metabolism and carbohydrate metabolism (Guo et al., 2020). ALDH2 is an important endogenous cardioprotective factor in mitochondria (Xia et al., 2023). Studies have shown that acetaldehyde dehydrogenase ALDH2, as a key enzyme in alcohol metabolism in human body, may affect the occurrence and development of coronary heart disease by affecting the level of blood glucose metabolism (You et al., 2018). ALDH2 plays an important regulatory role in the occurrence and development of tumors, and has a key role in maintaining tumor cell stemness (Toledo-Guzmán et al., 2019). ALDH2 is related to glycolysis and affects the level of blood glucose metabolism, which is consistent with the results of kidney yang deficiency involving Galactose metabolism pathway in this study. In this study, it was found that the expression level of ALDH2 in the kidney tissue of the M group was significantly decreased. It was speculated that the expression level of these related target genes was decreased during the occurrence of kidney Yang deficiency, resulting in the inhibition of the body's energy metabolism, which was consistent with the literature that kidney Yang deficiency caused the body's low energy metabolism (Chen et al., 2018). After administration, the callback trend of D group was closest

to that of the N group. This suggested that Epimedium fried with suet oil could promote the expression of ALDH2, improve the body's energy metabolism, and then improve the state of kidney Yang deficiency.

ARG2 is mainly expressed in kidney, brain and prostate, and located in mitochondria. In clinical studies, arginase activation is closely related to the occurrence and development of heart, lung and kidney ischemia-reperfusion injury, hypertension, erectile dysfunction, atherosclerosis, aging and other diseases (Wu et al., 2015). Studies have shown that cell aging caused by aging is associated with increased intracellular ARG2 activity/expression (Meng and Xiong, 2016). Inhibition of arginase I leads to increased expression of NOS2, thus promoting the production of NO (Raber et al., 2012). In this study, it was found that ARG2 expression level was significantly increased in the M group, suggesting that kidney Yang deficiency might be related to the increased expression level of ARG2 in the kidney tissue, the decreased content of NO and the increased level of superoxide production, which may lead to renal endothelial dysfunction. However, Epimedium fried with suet oil could significantly reduce the ARG2 expression levels, indicating that it might play its role by reducing ARG2 expression levels and alleviating the endothelial dysfunction caused by its overexpression.

NOS2 is the rate-limiting enzyme of NO synthesis, which plays its biological role by producing NO and has important clinical significance in the occurrence and development of diseases (Mount and Power, 2006). Excessive production of NO by NOS2 will lead to cell damage and tissue necrosis, and further promote the occurrence and development of inflammatory diseases. NOS2 is an important intracellular messenger and molecular marker in the mechanism of inflammation (Jiang et al., 2016). In the kidney, NO is involved in the regulation of renal vascular resistance, glomerular filtration rate and maintenance of renal structural integrity (Da Silva et al., 2021). Many studies have shown that NOS2 plays a key role in the pathogenesis of metabolic nephropathy, and it has been found in the pathogenesis of chronic nephropathy that elevated NOS2 levels produce highly reactive NO, which is associated with chronic low-grade inflammatory states (Zhang et al., 2021). In this study, the expression level of NOS2 in the D group was significantly decreased. It suggested that Epimedium fried with suet oil could reduce the production of NO, reduce the inflammatory state of kidney tissue and maintain the integrity of kidney structure by reducing the overexpression of NOS2 in the kidney tissue.

5 Conclusion

In this study, 15 differential metabolites in urine and plasma were screened by GC-MS technique. The regulatory effect of Epimedium on abnormal metabolism of kidney Yang deficiency was related with Galactose metabolism, Glutathione metabolism, Glycerolipid metabolism, Arginine and proline metabolism, Tryptophan metabolism. The processing excipient "suet oil" regulated Galactose metabolism, and "heating" regulated Galactose metabolism, Glutathione metabolism, Arginine and proline metabolism. Together, the two factors enhanced the role of Epimedium fried with suet oil in warming kidney and enriching yang. This further explained the processing mechanism of synergistic effect of Epimedium processed by heating and suet oil.

Based on the results of metabolomics and network pharmacology, combined with RT-PCR verification, the results showed that the 13 active components of Epimedium fried with suet oil played the role of warming kidney and promoting Yang by acting on the seven target genes, two pathways and two biomarkers of kidney Yang deficiency, which further elucidated the processing and synergistic mechanism of Epimedium fried with suet oil. In view of the characteristics of multi-component, multi-target and overall synergy of TCM, this study comprehensively characterized the mechanism of processing effect of Epimedium, which would help to systematically and profoundly reveal the processing mechanism of Epimedium fried with suet oil. At the same time, it provides a research strategy for studying the processing mechanism of TCM and the action mechanism of TCM in treating deficiency syndrome.

Data availability statement

The original contributions presented in the study are included in the article/[supplementary material](#), further inquiries can be directed to the corresponding authors.

Ethics statement

The animal study was reviewed and approved by the Animal Ethics Committee of Jiangsu Provincial Academy of Chinese Medicine.

Author contributions

ES: Conceptualization, funding acquisition, design, supervision. RH: Data processing analysis and writing. KD: Formal analysis. LW: Experiments and database retrieval and analysis. JH: Experiments and writing. XT: Conceptualization, investigation. YW: Project administration. LF: Resources. XJ: Conceptualization, resources, funding acquisition.

References

- Amanat, S., Shal, B., Kyoung-Seo, E., Ali, H., and Khan, S. (2022). Icarin attenuates cyclophosphamide-induced cystitis via down-regulation of NF- κ B and up-regulation of Nrf-2/HO-1 signaling pathways in mice model. *Int. Immunopharmacol.* 106, 108604. doi:10.1016/j.intimp.2022.108604
- Beuckmann, C. T., Fujimori, K., Urade, Y., and Hayaishi, O. (2000). Identification of mu-class glutathione transferases M2-2 and M3-3 as cytosolic prostaglandin E synthases in the human brain. *Neurochem. Res.* 25 (5), 733–738. doi:10.1023/a:1007579507804
- Castilho-Martins, E. A., Canuto, G., Muxel, S. M., daSilva, M., Floeter-Winter, L. M., Del-Aguila, C., et al. (2015). Capillary electrophoresis reveals polyamine metabolism modulation in *Leishmania (Leishmania) amazonensis* wild-type and arginase-knockout mutants under arginine starvation. *Electrophoresis* 36 (18), 2314–2323. doi:10.1002/elps.201500114
- Chang, H., Liu, Q., Bai, W. F., Bai, Y. C., Jia, X. Y., Gao, C., et al. (2020). Protective effects of *Amygdalus mongolica* on rats with renal fibrosis based on serum metabolomics. *J. Ethnopharmacol.* 257, 112858. doi:10.1016/j.jep.2020.112858
- Chen, R. Q., Wang, J., Liao, C. B., Zhang, L., Guo, Q., and Wang, X. F. (2018). Exploring the biomarkers and therapeutic mechanism of kidney-yang deficiency syndrome treated by You-gui pill using systems pharmacology and serum metabolomics. *RSC Adv.* 8 (2), 1098–1115. doi:10.1039/c7ra12451a
- Chen, R. Q., Wang, J., Zhan, R. H., Zhang, L., and Wang, X. F. (2019). Integrated systems pharmacology, urinary metabolomics, and quantitative real-time PCR analysis to uncover targets and metabolic pathways of the you-gui pill in treating kidney-yang deficiency syndrome. *Int. J. Mol. Sci.* 20 (15), 3655. doi:10.3390/ijms20153655
- Chen, S., and Wang, X. F. (2015). Progress on metabolomics studies of the Kidney Yang deficiency syndrome. *Acad. J. Guangdong Coll. Pharm.* 31 (06), 829–832. doi:10.3969/j.issn.1006-8783.2015.06.030
- Chen, Y., Jia, X. B., Cai, Y., and Ding, A. W. (2007). Temperature and heating time - two key factors affecting icariin content. *Chin. Tradit. Pat. Med.* 2007 (07), 1038–1041. doi:10.3969/j.issn.1001-1528.2007.07.030
- Chen, Y., Jia, X. B., Tan, X. B., Fan, C. Y., and Hu, M. (2009). Absorption and metabolism of flavonoids in *Herba Epimedii* via rat intestinal perfusion model. *Chin. J. Chin. Mater Med.* 34 (22), 2928–2931.
- Chinese Pharmacopoeia Commission [CPC] (2020). *Pharmacopoeia of people's Republic of China*. Beijing: Science and Technology Press.
- Da-Silva, C. B. P., Ceron, C. S., Mendes, A. S., de-Martinis, B. S., Castro, M. M., and Tirapelli, C. R. (2021). Inducible nitric oxide synthase (iNOS) mediates ethanol-induced redox imbalance and upregulation of inflammatory cytokines in the kidney. *Can. J. Physiol. Pharmacol.* 99 (10), 1016–1025. doi:10.1139/cjpp-2021-0108
- Dai, T., Yang, P., Liu, B., and Zhang, S. C. (2021). Effect of paeonol on the survival of ischemia and reperfusion induced cardiomyocytes by regulating miR-122-5p/GSTM1 molecular Axis. *China Pharm.* 24 (02), 232–236. doi:10.3969/j.issn.1008-049X.2021.02.005

Funding

This work was supported by the National Natural Science Foundation of China (No. 81503253, 81573833), the Jiangsu Provincial Medical Youth Talent (No. QNRC2016635), Natural Science Foundation of Nanjing University of Chinese Medicine (No. XZR2020028), Medical Innovation Team Project of Jiangsu Province (No. CXTDB2017003), National Administration of traditional Chinese medicine key research laboratory capacity improvement project (No. 2022GJJZDYJS-01), “Major New Drug Innovation” Science and Technology major project (No. 2017ZX09301056), and 2021 Postgraduate Research and Practice Innovation Project of Jiangsu Province (No. SJCX21-0715, SJCX21-0717).

Conflict of interest

The authors declare that the research was conducted in the absence of any commercial or financial relationships that could be construed as a potential conflict of interest.

Publisher's note

All claims expressed in this article are solely those of the authors and do not necessarily represent those of their affiliated organizations, or those of the publisher, the editors and the reviewers. Any product that may be evaluated in this article, or claim that may be made by its manufacturer, is not guaranteed or endorsed by the publisher.

Supplementary material

The Supplementary Material for this article can be found online at: <https://www.frontiersin.org/articles/10.3389/fphar.2023.1113213/full#supplementary-material>

- Dong, Y., Ding, Y., Liu, P. Z., Song, H. Y., Zhao, Y. P., Li, M., et al. (2013). Investigation of the material basis underlying the correlation between presbycusis and kidney deficiency in traditional Chinese medicine via GC/MS metabolomics. *Evid. Based Complement. Altern. Med.* 2013, 762092. doi:10.1155/2013/762092
- Du, K., Gao, X. X., Feng, Y., Li, J., Wang, H., Lv, S. L., et al. (2020). Integrated adrenal and testicular metabolomics revealed the protective effects of Guilingji on the Kidney-Yang deficiency syndrome rats. *J. Ethnopharmacol.* 255, 112734. pii: S0378-8741(19)34453-8. doi:10.1016/j.jep.2020.112734
- Fahy, E., Subramaniam, S., Brown, H. A., Glass, C. K., Merrill, A. H., Murphy, R. C., et al. (2005). A comprehensive classification system for lipids. *J. Lipid Res.* 46 (5), 839–861. doi:10.1194/jlr.E400004-JLR200
- Feng, Q., Li, Y. M., Yang, Y. W., and Feng, J. F. (2020). Urine metabolomics analysis in patients with normoalbuminuric diabetic kidney disease. *Front. Physiol.* 11, 578799. doi:10.3389/fphys.2020.578799
- Feng, Q. S., Tong, L., Lu, Q., Liu, S., Zhao, L. S., and Xiong, Z. L. (2022). 1H NMR serum metabolomics and its endogenous network pharmacological analysis of Gushudan on kidney-yang-deficiency-syndrome rats. *Anal. Biochem.* 643, 114580. doi:10.1016/j.ab.2022.114580
- Gu, H. M., Sun, E., Li, J., Hou, J., and Jia, X. B. (2019). Effect of processing excipient suet oil on formation and absorption of baohuoside -bile salt self-assembled micelles. *Chin. J. Chin. Mater Med.* 44 (23), 5143–5150. doi:10.19540/j.cnki.cjcm.20190916.311
- Guo, G. L., Wang, S., Sun, P., Li, X. L., Wang, X., Cao, G. S., et al. (2020). Research progress on processing mechanism of epimedium fried with sheep fat oil based on warming kidney and promoting yang. *J. Liaoning Univ. Tradit. Chin. Med.* 22 (07), 1–5. doi:10.13194/j.issn.1673-842x.2020.07.001
- Guo, H., Niu, X., Gu, Y., Lu, C., Xiao, C., Yue, K., et al. (2016). Differential amino acid, carbohydrate and lipid metabolism perpetuations involved in a subtype of rheumatoid arthritis with Chinese medicine cold pattern. *Int. J. Mol. Sci.* 17 (10), 1757. doi:10.3390/ijms17101757
- Hua, Y. L., Ma, Q., Li, W., Zhang, X. S., Cheng, X. H., Jia, Y. Q., et al. (2019). Metabolomics analysis of Pulsatilla decoction on treatment of wetness-heat-induced diarrhea in rats based on UPLC-Q/TOF-MS/MS. *Biomed. Chromatogr.* 33 (11), e4629. doi:10.1002/bmc.4629
- Huang, C., Ge, F., Ren, W., Zhang, Y., Wu, X., Zhang, Q., et al. (2021). Copy number variation of the HPGDS gene in the Ashidan yak and its associations with growth traits. *Gene* 772, 145382. doi:10.1016/j.gene.2020.145382
- Ilic, Z., Crawford, D., Vakharia, D., Egner, P. A., and Sell, S. (2010). Glutathione-S-transferase A3 knockout mice are sensitive to acute cytotoxic and genotoxic effects of aflatoxin B1. *Toxicol. Appl. Pharmacol.* 242 (3), 241–246. doi:10.1016/j.taap.2009.10.008
- Jiang, J., Feng, L., Li, J., Sun, E., Ding, S. M., and Jia, X. B. (2014). Multielemental composition of suet oil based on quantification by ultrawave/ICP-MS coupled with chemometric analysis. *Molecules* 19 (4), 4452–4465. doi:10.3390/molecules19044452
- Jiang, Q. Y., Zheng, M. S., Yang, X. J., and Sun, X. S. (2016). Analysis of molecular networks and targets mining of Chinese herbal medicines on anti-aging. *BMC Complement. Altern. Med.* 16 (1), 520. doi:10.1186/s12906-016-1513-2
- Jin, H., Ma, N., Li, X., Kang, M., Guo, M., and Song, L. (2019). Application of GC/MS-Based metabolomic profiling in studying the therapeutic effects of aconitum carmichaeli with ampeleopsis japonica extract on collagen-induced arthritis in rats. *Molecules* 24 (10), 1934. doi:10.3390/molecules24101934
- Kaluźna-Czaplińska, J., Gątarek, P., Chirumbolo, S., Chartrand, M. S., and Björklund, G. (2019). How important is tryptophan in human health? *Crit. Rev. Food Sci. Nutr.* 59 (1), 72–88. doi:10.1080/10408398.2017.1357534
- Körber, H., and Goerick-Pesch, S. (2019). Expression of prostaglandin (PG) D synthase lipocalin and hematopoietic type and PG D receptor during restart of spermatogenesis following downregulation using a slow release GnRH agonist implant in the dog. *Cell Tissue Res.* 378 (2), 359–370. doi:10.1007/s00441-019-03059-x
- Kui, X. T., Wang, J., Chen, W., Wei, Y. P., Lv, Y. H., Zu, X. P., et al. (2022). Metabolomics and its application of in Chinese medicine processing. *Chin. J. Chin. Mater Med.* 47 (03), 593–602. doi:10.19540/j.cnki.cjcm.20210927.601
- Li, B., Ma, J., Zhu, L., Yan, Y., Wu, Y., Zheng, C., et al. (2022). Metabolomic profiling and alleviation of oxidative stress of Huangjing Zanyu capsule treating oligoasthenospermia. *Transl. Androl. Urol.* 11 (5), 659–674. doi:10.21037/tau-22-293
- Li, M. Y., Sun, E., Xu, F. J., Xu, J. D., and Jiao, X. B. (2020). Analysis changes of Epimedium Folium's flavonoids before and after processing based on UPLC-Q/TOF-MS. *Chin. Tradit. Herb. Drugs* 51 (11), 2900–2907. doi:10.7501/j.issn.0253-2670.2020.11.007
- Liu, H., Yang, L., Wan, C., Li, Z., Yan, G., Han, Y., et al. (2022). Evaluation of the pharmacological effects and exploration of the mechanism of traditional Chinese medicine preparation Ciwujia tablets in treating insomnia based on ethology, energy metabolism, and urine metabolomic approaches. *Front. Pharmacol.* 13, 1009668. doi:10.3389/fphar.2022.1009668
- Liu, Q., Zhao, H. W., Zhang, A. H., Sun, H., Zhou, X. H., Nan, Y., et al. (2016). Chinmedomics strategy to discover effective constituents and elucidate action mechanism of Nanshi capsule against kidney-yang deficiency syndrome. *China J. Chin. Mater Med.* 41 (15), 2901–2914. doi:10.4268/cjcm.20161526
- Liu, Z., Zhang, C., Lee, S., Kim, W., Klevstig, M., Harzandi, A. M., et al. (2019). Pyruvate kinase L/R is a regulator of lipid metabolism and mitochondrial function. *Metab. Eng.* 52, 263–272. doi:10.1016/j.ymben.2019.01.001
- Ma, P., Zhang, Z. M., Zhou, X. Y., Luo, J. K., Lu, H. M., and Wang, Y. (2019). Characterizing semen abnormality male infertility using non-targeted blood plasma metabolomics. *PLoS One* 14 (7), e0219179. doi:10.1371/journal.pone.0219179
- Mehdi, W. A., Mehde, A. A., Yusof, F., Raus, R. A., Resen, A. K., and Ghazali, H. (2019). The endothelial nitric oxide synthase gene G894T, glutathione S-transferase (GSTM1 and GSTT1) polymorphisms as a risk factor in the patient with nephrolithiasis. *Int. J. Biol. Macromol.* 140, 719–726. doi:10.1016/j.jbiomac.2019.08.184
- Meng, M., and Xiong, X. D. (2016). Vascular endothelial cell senescence and vascular disease. *Chin. J. Biochem. Mol. Biol.* 32 (03), 253–259. doi:10.13865/j.cnki.cjbmb.2016.03.03
- Mount, P. F., and Power, D. A. (2006). Nitric oxide in the kidney: Functions and regulation of synthesis. *Acta Physiol. (Oxf)* 187 (4), 433–446. doi:10.1111/j.1748-1716.2006.01582.x
- Nam, M., Choi, M. S., Choi, J. Y., Kim, N., Kim, M. S., Jung, S., et al. (2018). Effect of green tea on hepatic lipid metabolism in mice fed a high-fat diet. *J. Nutr. Biochem.* 51, 1–7. doi:10.1016/j.jnutbio.2017.09.002
- Nikolac-Perkovic, M., Pucic-Bakovic, M., Kristic, J., Novokmet, M., Huffman, J. E., Vitart, V., et al. (2014). The association between galactosylation of immunoglobulin g and body mass index. *Prog. Neuropsychopharmacol. Biol. Psychiatry.* 48, 20–25. doi:10.1016/j.pnpbp.2013.08.014
- Petry, K. G., and Reichardt, J. K. (1998). The fundamental importance of human galactose metabolism: Lessons from genetics and biochemistry. *Trends Genet.* 14 (3), 98–102. doi:10.1016/s0168-9525(97)01379-6
- Raber, P., Ochoa, A. C., and Rodríguez, P. C. (2012). Metabolism of L-arginine by myeloid-derived suppressor cells in cancer: mechanisms of T cell suppression and therapeutic perspectives. *Immunol. Invest.* 41 (6–7), 614–634. doi:10.3109/08820139.2012.680634
- Ralston, J. C., Lyons, C. L., Kennedy, E. B., Kirwan, A. M., and Roche, H. M. (2017). Fatty acids and NLRP3 inflammasome-mediated inflammation in metabolic tissues. *Annu. Rev. Nutr.* 37, 77–102. doi:10.1146/annurev-nutr-071816-064836
- Rittchen, S., and Heinemann, A. (2019). Therapeutic potential of hematopoietic prostaglandin D2 synthase in allergic inflammation. *Cells* 8 (6), 619. doi:10.3390/cells8060619
- Sekhar, R. V., Patel, S. G., Guthikonda, A. P., Reid, M., Balasubramanyam, A., Taffet, G. E., et al. (2011). Deficient synthesis of glutathione underlies oxidative stress in aging and can be corrected by dietary cysteine and glycine supplementation. *Am. J. Clin. Nutr.* 94 (3), 847–853. doi:10.3945/ajcn.110.003483
- Sun, E., Wei, Y. J., Zhang, Z. H., Cui, L., Xu, F. J., and Jia, X. B. (2014). Processing Mechanism of Epimedium fried with suet oil based on absorption and metabolism of flavonoids. *Chin. J. Chin. Mater Med.* 39 (03), 383–390. doi:10.4268/cjcm.20140306
- Sun, X. T., Liu, X., and Li, Q. (2017). Research overview of animal model with kidney deficiency syndrome. *Chin. J. Tradit. Chin. Med. Pharm.* 32 (02), 659–662.
- Toledo-Guzmán, M. E., Hernández, M. I., Gómez-Gallegos, Á. A., and Ortiz-Sánchez, E. (2019). ALDH as a stem cell marker in solid tumors. *Curr. Stem Cell Res. Ther.* 14 (5), 375–388. doi:10.2174/1574888X13666180810120012
- Tong, L., Feng, Q., Lu, Q., Zhang, J., and Xiong, Z. (2022). Combined 1H NMR fecal metabolomics and 16S rRNA gene sequencing to reveal the protective effects of Gushudan on kidney-yang-deficiency-syndrome rats via gut-kidney axis. *J. Pharm. Biomed. Anal.* 217, 114843. doi:10.1016/j.jpba.2022.114843
- Wu, Q., Zhang, X. X., Jiao, T. T., Zhang, X. J., Wang, S. Y., Liu, Y. H., et al. (2022). Correlations of characteristics of kidney yang deficiency syndrome with clinical indicators and risk factors of chronic kidney disease. *Chin. J. Exp. Tradit. Med. Form.* 28 (19), 204–213. doi:10.13422/j.cnki.syfx.20221726
- Wu, Z. S., Yu, Y., Liu, C., Xiong, Y. Y., Montani, J. P., Yang, Z. H., et al. (2015). Role of p38 mitogen-activated protein kinase in vascular endothelial aging: Interaction with arginase-II and S6K1 signaling pathway. *Aging (Albany NY)* 7 (1), 70–81. doi:10.18632/aging.100722
- Xia, G., Xu, J., Chen, M., Jin, J., Wang, X., and Ye, Y. (2023). Loss of ALDH2 aggravates mitochondrial biogenesis disorder in cardiac myocytes induced by TAC. *Biochem. Biophys. Res. Commun.* 639, 189–196. doi:10.1016/j.bbrc.2022.12.001
- Xiang, Z., Wang, X. Q., Liu, T., and Lv, D. (2012). Thoughts and exploration on studying pharmacological mechanism of traditional Chinese medicine using network biology approach. *Chin. J. Chin. Mater Med.* 37 (02), 146–151. doi:10.4268/cjcm.20120206
- Xiao, Y., Liu, J., Peng, Y., Xiong, X., Huang, L., Yang, H., et al. (2016). GSTA3 attenuates renal interstitial fibrosis by inhibiting TGF-beta-induced tubular epithelial-mesenchymal transition and fibronectin expression. *PLoS One* 11 (9), e0160855. doi:10.1371/journal.pone.0160855
- Xie, J., Gao, S., Li, L., Xu, Y. L., Gao, S. M., and Yu, C. Q. (2019). Research progress and application strategy on network pharmacology in Chinese Materia medica. *Chin. Tradit. Herb. Drugs* 50 (10), 2257–2265. doi:10.7501/j.issn.0253-2670.2019.10.001
- Xu, S. L., Li, W. H., Jia, B., Cui, J. M., and Shi, N. G. (2014). Study on the differentially expressed genes of aged kidney-yang deficiency syndrome constitution and verify genes with RT-PCR. *Chin. J. Tradit. Chin. Med. Pharm.* 29 (05), 1568–1572.
- You, L., Li, C., Zhao, J., Wang, D. W., and Cui, W. (2018). Associations of common variants at ALDH2 gene and the risk of stroke in patients with coronary artery diseases undergoing percutaneous coronary intervention. *Med. Baltim.* 97 (19), e0711. doi:10.1097/MD.00000000000010711

- Zhang, L. Z., Lang, J. L., Jin, L., Jin, L. H., Cao, B. B., Shao, X., et al. (2020). Effect of hirsutella sinensis fungus on the hypothalamic-pituitary-adrenal Axis in lewis rats with kidney-yang deficiency syndrome. *Evid. Based Complement. Altern. Med.* 2020, 5952612. doi:10.1155/2020/5952612
- Zhang, Z. M., Yang, L., Wan, Y., Jiang, S., Shang, E. X., Qian, D. W., et al. (2021). The synergic renoprotective effect of Rehmanniae Radix Preparata and Corni Fructus on adenine-induced chronic kidney disease rats based on integrated plasma metabolomics and network pharmacology approach. *Life Sci.* 278, 119545. doi:10.1016/j.lfs.2021.119545
- Zhang, Z. Y., Chen, B. J., Zhang, Q., Wang, Y. R., and Su, Y. X. (2014). Establishment method and evaluation index of animal model of kidney yang deficiency syndrome. *Fujian J. Tradit. Chin. Med.* 45 (02), 61–63. doi:10.13260/j.cnki.jfjtc.010691
- Zhao, Y. Y., Wang, H. L., Cheng, X. L., Wei, F., Bai, X., Lin, R. C., et al. (2015). Metabolomics analysis reveals the association between lipid abnormalities and oxidative stress, inflammation, fibrosis, and Nrf2 dysfunction in aristolochic acid-induced nephropathy. *Sci. Rep.* 5, 12936. doi:10.1038/srep12936
- Zhou, S. G., Wang, P., Pi, R. B., Gao, J., Fu, J. J., Fang, J., et al. (2008). Reduced expression of GSTM2 and increased oxidative stress in spontaneously hypertensive rat. *Mol. Cell Biochem.* 309 (1-2), 99–107. doi:10.1007/s11010-007-9647-7
- Zhou, X. H., Zhang, A. H., Wang, L., Tan, Y. L., Guan, Y., Han, Y., et al. (2016). Novel chinmedomics strategy for discovering effective constituents from ShenQiWan acting on ShenYangXu syndrome. *Chin. J. Nat. Med.* 14 (8), 561–581. doi:10.1016/S1875-5364(16)30067-X



OPEN ACCESS

EDITED BY

Rong Wang,
People's Liberation Army Joint Logistics
Support Force 940th Hospital, China

REVIEWED BY

Judit Morello,
New University of Lisbon, Portugal
Xuan Qin,
Baylor College of Medicine, United States

*CORRESPONDENCE

Yongfu Chen,
✉ nmgyfchen@126.com

SPECIALTY SECTION

This article was submitted to Drug
Metabolism and Transport,
a section of the journal
Frontiers in Pharmacology

RECEIVED 19 September 2022

ACCEPTED 17 January 2023

PUBLISHED 26 January 2023

CITATION

Li B, Kwok L-Y, Wang D, Li L, Guo S and
Chen Y (2023), Integrating metabolomics,
bionics, and culturomics to study
probiotics-driven drug metabolism.
Front. Pharmacol. 14:1047863.
doi: 10.3389/fphar.2023.1047863

COPYRIGHT

© 2023 Li, Kwok, Wang, Li, Guo and Chen.
This is an open-access article distributed
under the terms of the [Creative Commons
Attribution License \(CC BY\)](#). The use,
distribution or reproduction in other
forums is permitted, provided the original
author(s) and the copyright owner(s) are
credited and that the original publication in
this journal is cited, in accordance with
accepted academic practice. No use,
distribution or reproduction is permitted
which does not comply with these terms.

Integrating metabolomics, bionics, and culturomics to study probiotics-driven drug metabolism

Bohai Li^{1,2,3}, Lai-Yu Kwok^{1,2,3}, Dandan Wang^{1,2,3}, Lu Li^{1,2,3},
Shuai Guo^{1,2,3} and Yongfu Chen^{1,2,3*}

¹Key Laboratory of Dairy Biotechnology and Engineering, Ministry of Education, Inner Mongolia Agricultural University, Hohhot, Inner Mongolia, China, ²Inner Mongolia Key Laboratory of Dairy Biotechnology and Engineering, Inner Mongolia Agricultural University, Hohhot, Inner Mongolia, China, ³Key Laboratory of Dairy Products Processing, Ministry of Agriculture and Rural Affairs, Inner Mongolia Agricultural University, Hohhot, Inner Mongolia, China

Many drugs have been shown to be metabolized by the human gut microbiome, but probiotic-driven drug-metabolizing capacity is rarely explored. Here, we developed an integrated metabolomics, culturomics, and bionics framework for systematically studying probiotics-driven drug metabolism. We discovered that 75% (27/36 of the assayed drugs) were metabolized by five selected probiotics, and drugs containing nitro or azo groups were more readily metabolized. As proof-of-principle experiments, we showed that *Lactocaseibacillus casei* Zhang (LCZ) could metabolize racecadotril to its active products, S-acetylthiorphan and thiorphan, in monoculture, in a near-real simulated human digestion system, and in an *ex vivo* fecal co-culture system. However, a personalized effect was observed in the racecadotril-metabolizing activity of *L. casei* Zhang, depending on the individual's host gut microbiome composition. Based on data generated by our workflow, we proposed a possible mechanism of interactions among *L. casei* Zhang, racecadotril, and host gut microbiome, providing practical guidance for probiotic-drug co-treatment and novel insights into precision probiotics.

KEYWORDS

drug metabolism, probiotics, metabolomics, culturomics, bionics

1 Introduction

Aging, along with physical inactivity, overnutrition, and obesity, are major risk factors for chronic diseases, which have become a legitimate public health issue that limits healthspan (Franceschi et al., 2018). An increasing number of the global population suffers from cardiometabolic diseases, such as type 2 diabetes, obesity, hyperlipidemia, hypertension, and coronary artery disease, which oblige patients to take multiple drugs every day for months or even years (Ndisang and Rastogi, 2013). However, it has been widely recognized that the efficacy and toxicity of many drugs vary considerably between individuals. The typical response rates for commercially available drugs have been reported to be between 50%–75%, suggesting that on-sale drugs may not be effective in a large population of patients (Spear et al., 2001). Besides, severe drug side effects have killed more than 1,00,000 people and cost \$30–100 billion per year in the United States (Sultana et al., 2013). Thus, inter-individual variability in drug responsiveness is a valid concern that not only delays treatment, posing uncertain impacts on patients' health, but also causes enormous clinical and financial burdens to patients and society. Thus, it would be of significance to understand factors that result in the wide inter-individuality of drug responses.

The gut microbiota is a complex ecosystem that comprises trillions of cells, including bacteria, viruses, and fungi, and it encodes over three million genes, showing a broader metabolic potential than human cells (Kaoutari et al., 2013). The gut microbiota composition presents a high degree of inter-individual variation due to various environmental (e.g., diet, lifestyle, habits), physiological (e.g., age, health status), and genetic (e.g., ethnicity) factors (Falony et al., 2016). Growing evidence suggests that the gut microbiome is actively involved in drug metabolism. For example, Zimmermann et al. (2019a) systematically studied the interactions between drugs and microorganisms, reporting that 176 commonly used drugs could be metabolized by 76 human gut bacteria *via* chemical transformation (Zimmermann et al., 2019a). Various rodent and human studies have also shown that gut microbiota-mediated drug modifications could affect the bioavailability, bioactivity, and toxicity of drugs (Fu et al., 2015; Koppel et al., 2017; Zimmermann et al., 2019b). The large inter-individuality of human gut microbiota can thus contribute to the variation in drug responses, and it can be considered as a potential target for modulating drug efficacy and toxicity.

Probiotics are “live microorganisms which when administered in adequate amounts confer a health benefit on the host” (FAO/WHO, 2001). Driven by an increasing health consciousness of the general public, the trend of consuming probiotics is on the rise. The probiotics market size is predicted to reach around US\$ 133.92 billion by 2030 from US\$ 63.11 billion in 2021 (GlobeNewswire, 2022). Probiotics have gained wide popularity and are commonly added to various food and health products, e.g., yogurts, cheese, juices, nutrition bars, infant formulas, sweeteners, waters, pizza crust, gum, lozenges, dietary supplements, and so on (Sadiq et al., 2022). Moreover, probiotics have been increasingly applied in clinical settings for preventing and treating multiple medical conditions, partly due to their capacity to restore a healthier gut microbiota from disease-associated gut dysbiotic state (Gagliardi et al., 2018). Like other gut microorganisms, probiotics encode a variety of enzymes and have been demonstrated to metabolize various chemicals, such as organophosphorus pesticides, mycotoxins, and nitrosamines in both *vitro* and *vivo* studies (Średnicka et al., 2021). Thus, the wide application of probiotics as active food components can also influence drug efficacy and side effects. However, data on probiotic-drug interactions are very scant.

This work comprises a series of experiments aiming to assay probiotic-drug interactions systematically by: 1) profiling the capacity of five selected probiotic strains [namely, *Bifidobacterium animalis* subsp. *lactis* Probio-M8 (M8), *B. animalis* subsp. *lactis* V9 (V9), *Lactiplantibacillus plantarum* P8 (P8), *Lacticaseibacillus rhamnosus* Probio-M9 (M9), and *Lacticaseibacillus casei* Zhang (LCZ)] in degrading 36 commonly used clinical oral drugs; 2) further characterizing the ability of LCZ in metabolizing racecadotril into its active forms in monoculture, in a near-real simulator human digestion system, and as part of the *ex vivo* human fecal culture. Our work demonstrated the ability of probiotics to degrade commonly used drugs through their own metabolism and/or *via* modulating the gut microbiome in a selective manner. This study has provided a framework for studying probiotic-drug interactions and novel insights into probiotic-drug co-treatment and probiotic-based personalized therapy.

2 Materials and methods

2.1 Chemicals

All 36 investigated drugs and the two standard solutions (thiorphan and S-acetylthiorphan) were commercially purchased from Sigma-Aldrich (St. Louis, MO, United States), and the detailed information about these compounds is listed in Supplementary Table S1. Acetonitrile, methanol, dimethyl sulfoxide, formic acid, and ammonium acetate were HPLC grade, and along with KCl, KH₂PO₄, NaHCO₃, NaCl, MgCl₂(H₂O)₆, (NH₄)₂CO₃, CaCl₂(H₂O)₂, L-cysteine, ethyl acetate, HCl, and NaOH were bought from Merck (Darmstadt, Germany). Bryant and Burkey Medium (BB), de Man Rogosa Sharpe (MRS) broth, glycerol, human salivary α -amylase, porcine pepsin, rabbit gastric extract for gastric lipase, bovine bile, and porcine pancreatin were purchased from Sigma-Aldrich (St. Louis, MO, United States). Modified Gifu anaerobic medium (mGAM) broth was purchased from HyServe GmbH and Co., KG (Germany). Ultrapure water used throughout the study was prepared by a Milli-Q water purification system (Millipore, Molsheim, France).

2.2 Probiotic strains and culture conditions

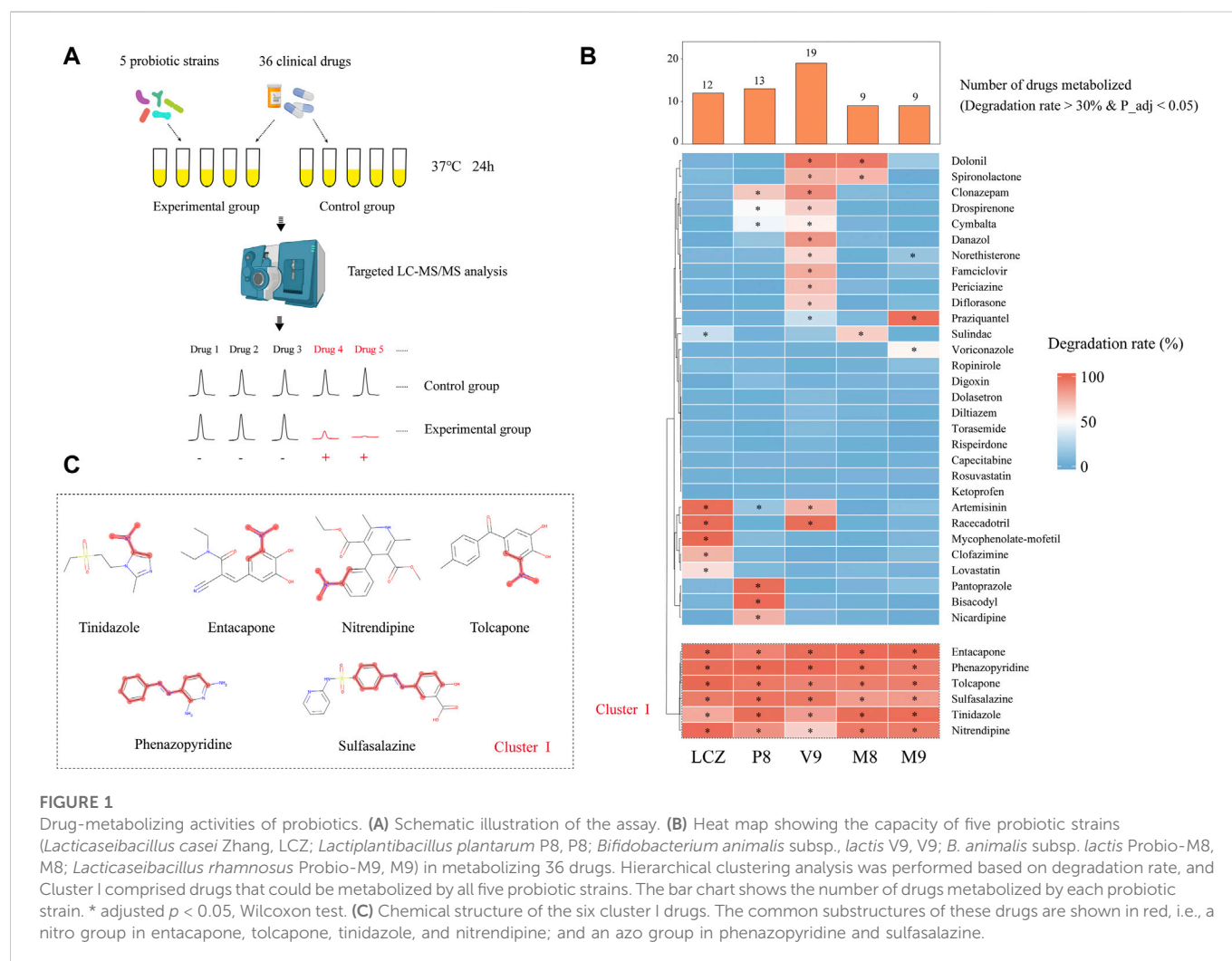
Five probiotic strains were used in this study, including M8, V9, P8, M9, and LCZ. They were obtained from the Lactic Acid Bacteria Culture Collection (LABCC) of the Key Laboratory of Dairy Biotechnology and Engineering, Inner Mongolia Agricultural University. These five strains have been proven to possess favorable probiotic properties and are applied in food, beverage, silage, and other products.

The five bacterial strains were cultured anaerobically for 24 h at 37°C in the MRS medium with 0.5 g/L L-cysteine (ML medium). Each strain was subcultured twice in the ML medium before use.

2.3 Assaying the drug-metabolizing capacity of five different probiotic strains

2.3.1 Sample preparation

In an anaerobic chamber (Don Whitley Scientific, Bingley, United Kingdom), each probiotic strain (adjusted to 5×10^6 CFU/mL) was inoculated into 10 mL of ML medium. Then, 10 μ L of each of the 36 tested drugs (dissolved in dimethyl sulfoxide, 1 mg/mL) was added to the probiotic-inoculated medium. A negative control was processed in parallel by adding 10 μ L of each drug to sterile ML medium without bacterial inoculation. Cultures and controls were incubated under the same conditions (at 37°C) in the anaerobic chamber for 24 h. Afterward, cultures were extracted with 20 mL of ethyl acetate, and the organic phase was collected and concentrated using the Genevac EZ-2.3 ELITE centrifugal evaporator (SP Scientific, Inc., New York, United States). The residue was resuspended in 500 μ L methanol and centrifuged at 13,000 g, 4°C for 10 min, and the supernatants were passed through 0.22 μ m microporous membrane filters and were stored at –80°C for further liquid chromatography-mass spectrometry (LC-MS) analysis. The experiments were performed in triplicate.



2.3.2 Standards and calibration

Stock solutions of 10 mg/mL concentration (dissolved in HPLC grade dimethyl sulfoxide) were prepared for all reference standards. Each stock standard solution was then subjected to serial dilution with sterile ML medium from a concentration range of 5 ng/mL to 1 µg/mL. The diluted stocks were extracted using the method described above and were stored at -80°C before LC-MS analysis.

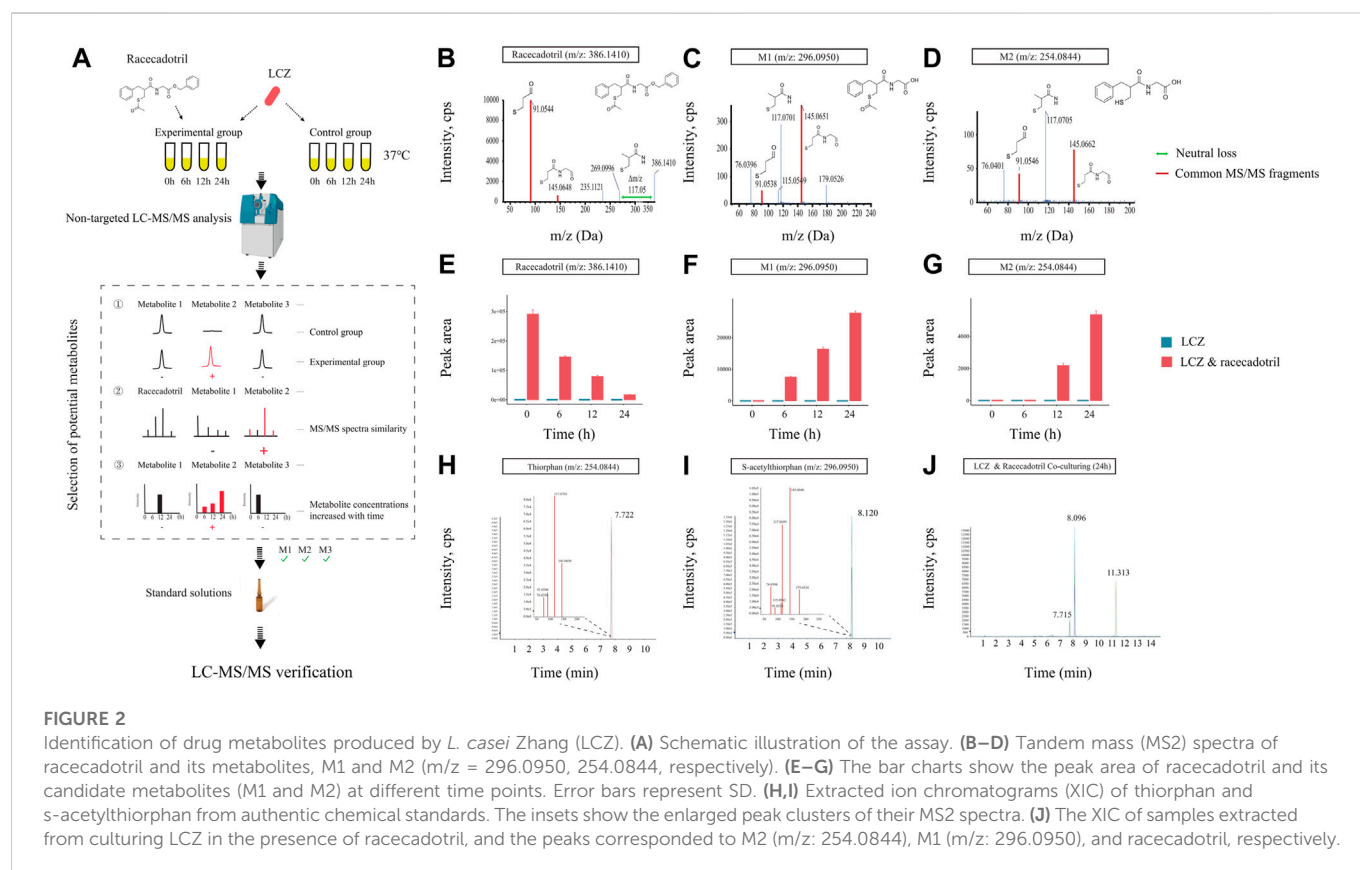
2.3.3 Targeted quantitative metabolomics analysis

Targeted quantitative metabolomics analysis was performed on an ultra high performance liquid chromatography coupled with triple quadrupole mass spectrometry (UPLC-QqQ-MS/MS) system (SCIEX Exion LC coupled to a SCIEX QTRAP 6500+; SCIEX, Foster City, CA, United States) along with a Kinetex EVO C18 column (2.1 mm \times 100 mm, 1.7 µm, Phenomenex, California, Co, United States). The conditions of UPLC were as follows: autosampler compartment temperature, 4°C ; column compartment temperature, 40°C ; mobile phase A, ultrapure water containing 0.1% formic acid; mobile phase B, methanol containing 0.1% formic acid. The gradient elution was programmed as follows: 0.0–1.0 min, 5.0% B; 1.0–6.5 min, 5.0%–100.0% B; 6.5–9.5 min, 100.0%–100.0% B; 9.5–11.0 min, 100.0%–5.0% B; 11.0–12.0 min 5.0% B. The flow rate was 0.4 mL/min, and the injection volume was 1 µL. The parameters of mass spectrometry

were set as follows: curtain gas, 25 psi; ion source gas 1, 50 psi; ion source gas 2, 50 psi; source temperature, 550°C ; ion spray voltage in positive mode, 5,500 V; ion spray voltage in negative mode, $-4,500\text{ V}$; carrier gas, nitrogen. Multiple reaction monitoring was used for drug detection and quantification.

2.3.4 UPLC-QqQ-MS/MS data analysis

Data were acquired by the Analyst 1.7.1 software and analyzed with the SCIEX OS-Q software (both supplied by SCIEX, Foster City, CA, United States), including standard curve construction and sample quantification. All further data processing was performed in R-4.1.2 (<https://www.R-project.org/>) after sample quantification. The drug degradation rate was calculated according to the following formula: degradation rate (%) = $(R_2 - R_1) / R_2 \times 100$, where R_1 and R_2 represented the concentrations of drugs after 24 h incubation with and without inoculation with probiotics, respectively. The LC-MS system has an instrument-dependent random systematic error range of around 20%–30% (Chong et al., 2019). Thus, in this study, the degradation rate threshold was set at 30% to ensure that the detected drop in drug concentration was a specific probiotic metabolic effect. Wilcoxon tests (calculated by `kruskal.test` function in `dplyr` R package) were applied to test whether drug levels were significantly lower in the probiotics-drug conditions compared with the controls.



All p -values were adjusted for multiple hypothesis testing with the Benjamini-Hochberg procedure (p .adjust function in graphics R package).

2.4 Identification of racecadotril metabolites produced by *in vitro* LCZ culture

2.4.1 Growth curve construction

In the anaerobic chamber, 5×10^6 CFU/mL of LCZ was inoculated into 10 mL of ML medium and incubated anaerobically at 37°C for 24 h. The growth curves of LCZ were determined by measuring the optical density of cultures at 600 nm (OD600) using a Bioscreen C system (Oy Growth Curves AB Ltd., Helsinki, Finland). The experiments were performed in triplicate.

2.4.2 Sample preparation

In the anaerobic chamber, LCZ was inoculated at 5×10^6 CFU/mL into 10 mL of ML medium. Then, 10 μL of racecadotril (10 mg/mL) was added to the ML medium with and without LCZ. Three groups were included in this experiment: LCZ-drug (LCZ was cultivated with racecadotril), LCZ-medium (LCZ was cultivated without racecadotril), and drug-medium (contained only racecadotril without bacteria). All groups were incubated under the same conditions for 24 h at 37°C in the anaerobic chamber. Samples were collected at 0, 6, 12, and 24 h, respectively, and collected samples were extracted (using methods described above) and were stored at -80°C until further analysis. The experiments were performed in triplicate.

2.4.3 Non-targeted qualitative metabolomics analysis

Non-targeted qualitative metabolomics analysis was performed on an ultra-performance liquid chromatography to quadrupole time-of-flight (UPLC- Q-TOF) system (SCIEX Exion LC coupled to a SCIEX Triple TOF 6600+) along with an ACQUITY UPLC HSS T3 C18 (2.1 mm \times 100 mm, 1.8 μm , Waters, Co., Milford, United States). The conditions of UPLC, including carrier gas, autosampler compartment temperature, column compartment temperature, mobile phase A, mobile phase B, injection volume, and the flow rate, were the same as described above. The gradient elution was programmed as follows: 0.0–1.5 min, 5.0% B; 1.5–15.0 min, 5.0%–100.0% B; 15.0–18.0 min, 100.0%–100.0% B; 18.0–19.0 min, 100.0%–5.0% B; 19.0–20.0 min, 5.0% B. The parameters of the electrospray ionization (ESI) source were set as follows: curtain gas, 30 psi; ion source gas 1, 55 psi; ion source gas 2, 55 psi; source temperature, 550°C ; ion spray voltage, 5,500 V in positive mode and $-4,500$ V in negative mode; declustering potential, 60 V in positive mode and -60 V in negative mode; collision energy, 20, 35, and 50 eV in positive mode, and -20 , -35 , and -50 eV in negative mode. Information-dependent acquisition together with dynamic background subtraction was applied in the time-of-flight mass spectrometry data acquisition to simultaneously collect the full scan spectrum and the product ion spectra of the most abundant ions, enhancing the robustness of MS/MS data for metabolite identification.

2.4.4 UPLC- Q-TOF data analysis

Raw data were acquired by Analyst 1.7.1 software (SCIEX, Foster City, CA, United States) and checked/viewed with PeakView 2.2 software (SCIEX, Foster City, CA, United States). Metabolites

search and prediction were performed by MetabolitePilot™ 2.0.4 software using default settings (SCIEX, Foster City, CA, United States).

2.4.5 Metabolite verification

Predicted metabolites of interest were selected for further verification by comparing their MS profiles (fragments and retention time) to reference standards solutions of S-acetylthiorphan and thiorphan (purchased from Sigma-Aldrich, St. Louis, MO). Standard solutions of 10 mg/mL (10 μ L) were diluted in 10 mL of sterile ML medium and were subjected to the same procedures of sample extraction and non-targeted qualitative metabolomics analysis described above. The experiments were performed in triplicate.

2.5 Racecadotril-metabolizing capacity of LCZ in an *in vitro* simulated human digestion system

An advanced near-real dynamic *in vitro* human gastrointestinal (GI) digestion system (DHS-IV; Xiao Dong Pro-health Instrumentation Co., Ltd., Suzhou, China) was used to study the racecadotril-metabolizing capacity of LCZ.

The DHS-IV system comprised mainly the esophagus model, human stomach model, and human intestine model, and a lot of rolling-extrusion devices (Supplementary Figures S1A–C). These were silicone models created by 3D-printing technology and had similar dimensions, morphology, and anatomy to an actual human GI tract. The human digestive juices and GI kinetic parameters were prepared and set to simulate the human digestion process.

Three types of simulated digestive juices (simulated saliva fluid, gastric fluid, and intestinal fluid) were used to simulate the chemical environments in the respective models, which were prepared according to a previous study (Huang et al., 2020). Simulated saliva fluid (final pH adjusted to 7) was composed of human salivary α -amylase (75.0 U/mL), $\text{MgCl}_2(\text{H}_2\text{O})_6$ (0.15 mmol/L), KH_2PO_4 (3.7 mmol/L), NaHCO_3 (13.6 mmol/L), KCl (15.1 mmol/L), and $(\text{NH}_4)_2\text{CO}_3$ (0.06 mmol/L). Simulated gastric fluid (final pH adjusted to 1.6 with HCl) was composed of pepsin (250.0 U/mL), KCl (6.9 mmol/L), KH_2PO_4 (0.9 mmol/L), NaHCO_3 (25.0 mmol/L), NaCl (47.2 mmol/L), $\text{MgCl}_2(\text{H}_2\text{O})_6$ (0.1 mmol/L), and $(\text{NH}_4)_2\text{CO}_3$ (0.5 mmol/L). Simulated intestinal fluid (final pH adjusted to 7) was composed of pancreatin (200 U/mL), bile salts (8.17 g/L), KCl (6.8 mmol/L), KH_2PO_4 (0.8 mmol/L), NaHCO_3 (85 mmol/L), and NaCl (38.4 mmol/L). The DHS-IV system was maintained at 37°C, and all components were sterilized before use.

Racecadotril (40 μ L, 1 mg/mL) was added to 40 mL ML medium with or without pre-inoculated with LCZ (2×10^7 CFU/mL). The cultures were mixed with 5 mL of simulated saliva fluid and then shaken in a water bath at 55 rpm, 37°C for 20 s to simulate the chewing action. The “chewed” oral digestive fluid mixtures were then transferred to the stomach system (pre-loaded with 10 mL of simulated gastric fluid to simulate the fasting state) through the esophagus model. During sample loading, simulated gastric fluid was continuously delivered to the stomach model by a syringe pump at a controlled rate of 1.75 mL/min for 60 min. Meanwhile, the pneumatically-controlled driving device was immediately activated, pressing the silicone stomach model at a rate of three

compressions per minute by rolling extrusion plates. The pylorus sieving valve was simultaneously activated to squeeze the pylorus model at a constant speed of 8 mm/s, adjusting the opening size of the pylorus model in the range of 0–4.5 mm. The gastric digestive fluid passing through the pylorus model next entered the intestinal digestion system. In this process, simulated intestinal fluid was continuously injected in the intestinal digestion system at a controlled rate of 1.0 mL/min for 60 min. The intestinal model was compressed with six sets of rolling extrusion plates at a rate of 36 extrusions per minute. All parameters mentioned above were set according to previous studies (Peng et al., 2021; Wang et al., 2022) to mimic the human digestive process. Four milliliters of samples were collected at the end of the intestinal model at 6, 12, and 24 h. The experiment was performed in triplicate.

The total viable counts of LCZ were determined from serially diluted samples by the pour plate technique on ML agar. The inoculated ML agar plates were incubated anaerobically at 37°C for 48 h before counting the number of bacterial colonies. The survival rate of LCZ at different time points was calculated according to a previous study (Peng et al., 2020). The concentration of racecadotril, S-acetylthiorphan, and thiorphan was determined by the targeted quantitative metabolomics analysis described above.

2.6 *Ex vivo* degradation of racecadotril by LCZ as part of the personalized microbiome

2.6.1 Fecal samples collection

The fecal samples were voluntarily provided by 26 healthy subjects recruited from the Key Laboratory of Dairy Biotechnology and Engineering, Inner Mongolia Agricultural University. The included subjects did not have diabetes, obvious GI, oral, or skin infections or diseases, malignancies, or a history of antibiotic use 3 months prior to or during sample collection. This study complied with the Chinese regulations regarding observational clinical studies and was examined and permitted by the Ethics Committee of the Affiliated Hospital of Inner Mongolia Medical University (No. KY2020006).

The fecal sample of each subject represented one personalized human gut microbiome. Fecal sample processing and *ex vivo* culture were performed according to the protocol reported by Javdan et al. (2020). Briefly, fresh human fecal samples were collected and transferred to an anaerobic chamber within 15 min of defecation. To make the frozen fecal glycerol stocks, fecal samples (1 g per sample) were re-suspended in 15 mL of sterile phosphate buffer supplemented with 0.1% L-cysteine, allowed to stand for 5 min, mixed evenly with an equal volume of 40% glycerol, and aliquoted (1 mL) in sterile cryogenic vials for storage at -80°C until use.

2.6.2 16S rRNA gene amplicon sequencing analysis of personalized microbiome

The personalized microbiota of each subject was determined by sequencing the 16S rRNA amplicons generated from metagenomic DNA extracted from subjects' fecal microbiota or the *ex vivo* fecal culture. To prepare for *ex vivo* fecal culture, 200 μ L from each donor glycerol stock was inoculated into 20 mL of BG medium and cultured anaerobically at 37°C. The BG medium comprised the liquid BB medium and liquid mGAM medium in a ratio of 7:3. After 24 h, cultures were centrifuged at 13,000 g, 4°C for 10 min. The pellets and the corresponding fecal samples were used for DNA extraction with

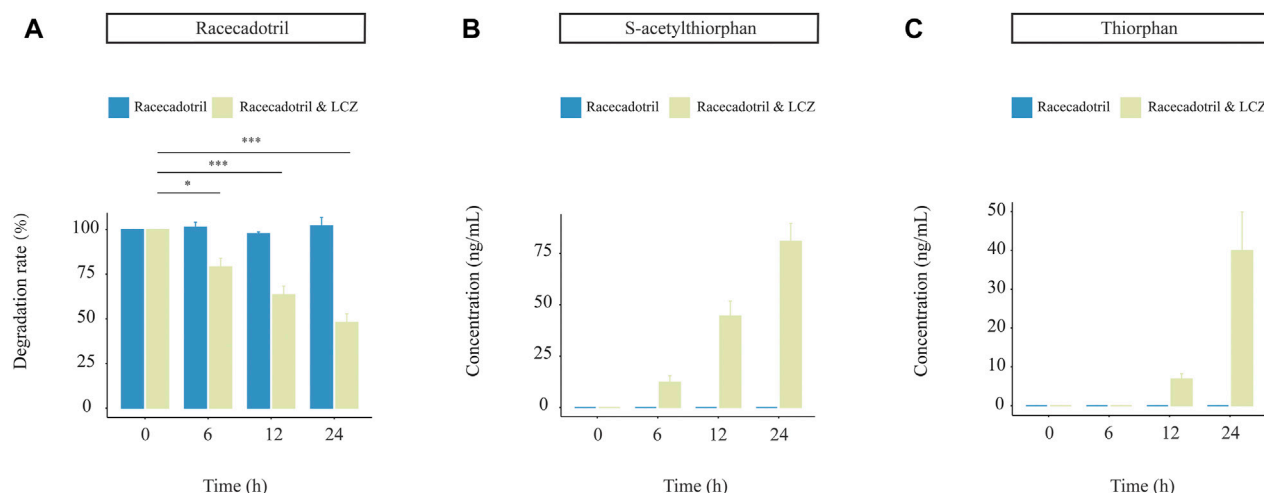


FIGURE 3

Drug-metabolizing activities of *L. casei* Zhang (LCZ) in a near-real human digestion system (DHS-IV). (A) racecadotril and (B,C) changes in concentrations of s-acetylthiorphan and thiorphan at different time points after digestion in the *in vitro* human simulated digestion system in the presence or absence of LCZ. The drug and metabolites were detected by targeted metabolomics. Error bars represent SD. *** $p < 0.001$, * $p < 0.05$, Wilcoxon test.

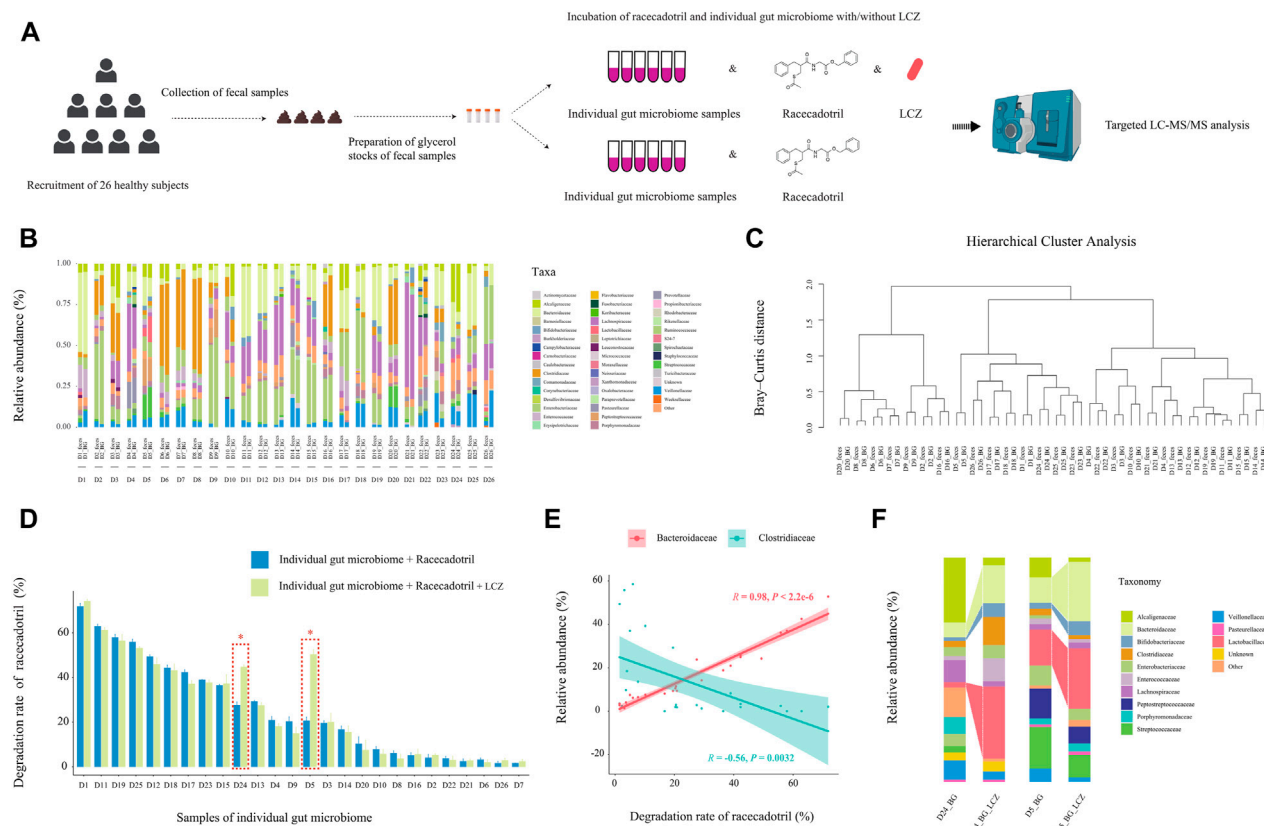


FIGURE 4

Effect of individuality of gut microbiome on *L. casei* Zhang (LCZ)-driven drug degradation. (A) Schematic illustration of the assay. (B) Family-level bacterial microbiota composition of fecal samples in comparison with their *ex vivo* fecal culture counterparts of 26 subjects (D1–26; the prefix sample code represents the subject number, and the suffix code represents type of sample, i.e., feces or *ex vivo* fecal culture in BG medium [BG]; BG medium comprised liquid BB medium and liquid mGAM medium in a ratio of 7:3). “Other” represents taxa that were below 1% of total sequences. (C) Hierarchical cluster analysis of microbiota profile of fecal samples and their *ex vivo* fecal culture counterparts. (D) The bar chart compares differences in racecadotril degradation rate in *ex vivo* fecal culture of each individual in the presence/absence of LCZ. The concentration of racecadotril was detected by targeted metabolomics. Error bars represent SD. * adjusted $p < 0.05$, Wilcoxon test. (E) Correlation (Pearson’s) between racecadotril degradation rate and *Bacteroidaceae*/*Clostridiaceae*. (F) Family-level bacterial composition of *ex vivo* fecal cultures of subjects D5 and D24 before and after incubation with LCZ for 24 h.

the PowerSoil DNA Isolation kit (QIAGEN, United States). The concentration and purity of the extracted DNA were monitored on 1% agarose gels. The V4 region of 16S rRNA was amplified using a specific primer pair, 515F and 806R (Walters et al., 2016). Illumina sequencing libraries were prepared using the TruSeq® DNA PCR-Free Sample Preparation Kit (Illumina, United States). The library quality was assessed with a Qubit® 2.0 Fluorometer (Thermo Scientific) and an Agilent Bioanalyzer 2100 system. The libraries were sequenced on an Illumina NovaSeq platform, and a dataset of 2 bp × 250 bp of an average depth of ~50,000 reads was generated.

Raw sequencing reads were de-multiplexed based on sample barcodes, and the barcode and primer sequences were trimmed. Then, unmerged paired-end sequences were filtered and analyzed using QIIME 2 Core 2022.2 distribution (Bolyen et al., 2019). Taxonomy was assigned to the resulting amplicon sequencing variants with a naive Bayes classifier trained on the Greengenes database. Downstream analyses were performed in R (version 4.1.2) with the ggplot2 package.

2.6.3 Personalized effect of LCZ on racecadotril degradation

The effect of exogenous addition of LCZ on racecadotril degradation by personalized microbiome was investigated. An aliquot of 200 µL of the glycerol stock was inoculated into 20 mL of BG medium for anaerobic cultivation at 37°C. After 24 h, 20 µL of racecadotril (1 mg/mL) was added to the culture together with or without 5×10^6 CFU/mL of LCZ. In the control culture without LCZ inoculation, equal volume of BG medium was added instead. Additionally, there was also a drug-medium control (contained only racecadotril without any bacteria). Both the inoculated cultures and the controls were anaerobically cultured for another 24 h at 37°C. The concentration of the undegraded portion of racecadotril in the culture was determined by the targeted quantitative metabolomics analysis described above. The experiment was performed in triplicate.

3 Results

3.1 Five probiotic strains showed a variable drug-metabolizing capacity

First, the capacity of five probiotic strains in metabolizing 36 commonly used clinical oral drugs was tested *in vitro* by incubating each drug with/without inoculating with each probiotic strain, and the drops in the drug concentrations after 24-h incubation with each probiotic strain compared with culture without bacterial inoculation were measured by targeted UPLC-QqQ-MS/MS (total number of tested probiotic-drug interactions, $n = 36$ drugs × 5 probiotic strains; 3 replicates per test; a total of 1,080 samples were analyzed, including the negative control; Figure 1A). These 36 drugs were chosen to be tested in this study because they are commonly used, and they have been reported to be metabolized by human gut bacteria (Zimmermann et al., 2019a). Supplementary Table S1 shows the optimized multiple reaction monitoring transitions, retention time, standard curve equation, and correlation coefficient (R^2) of each analyte. Good linearity was found in all drugs and standards with R^2 greater than 0.9900, indicating a good quantitative accuracy.

After the 24-h incubation with probiotic, a significant drug concentration drop (>30% degradation, adjusted $p < 0.05$; Figure 1B) was observed in 75% (27/36) of the assayed drugs. The V9 strain was able to metabolize the highest number (19/36) of drugs, followed by P8 (13 drugs), LCZ (12 drugs), M8 (9 drugs), and M9 (9 drugs). Notably, the profile of the drug-metabolizing capacity varied among the five tested probiotic strains. Three (mycophenolate-mofetil, clofazimine, and lovastatin), three (pantoprazole, bisacodyl, and nicardipine), four (danazol, famciclovir, pericizine, diflorasone), and one (voriconazole) drug could only be metabolized by LCZ, P8, V9, and M9, respectively, suggesting strain specificity in the drug-metabolizing capacity.

Notably, clustering based on the probiotic-metabolizing capacity identified six drugs (namely entacapone, phenazopyridine, tolcapone, sulfasalazine, tinidazole, and nitrendipine) that were metabolized by all five probiotic strains. Interestingly, these six drugs were found to share common substructures (a nitro group in entacapone, tolcapone, tinidazole, and nitrendipine; an azo group in phenazopyridine and sulfasalazine; Figure 1C), suggesting that these two functional groups could be the potential targets for the metabolic modifications by probiotics.

3.2 LCZ metabolized racecadotril into S-acetylthiorphan and thiorphan in monoculture

Microbial transformation can activate or inactivate drugs, or produce toxic compounds which can induce serious side effects on the host. Thus, it is important to identify probiotic-produced drug metabolites and characterize the biotransformation in each probiotic-drug interaction. A non-targeted LC-MS/MS-based assay was developed to identify drug metabolites (Figure 2A). A previous study reported that *L. casei* could improve diarrhea in children (Lai et al., 2019), and here we found that LCZ could metabolize racecadotril (Figure 1B) - a drug for treating diarrhea. So, the probiotic-drug interaction between LCZ and racecadotril was used to establish this protocol, which would provide valuable data for future use of probiotic-drug co-treatment.

First, the *in vitro* growth response of LCZ was evaluated. No significant difference was observed in the growth of LCZ regardless of the presence of racecadotril in the culture medium, suggesting that this drug did not influence the growth of LCZ in culture (Supplementary Figure S2). Based on the growth curves, it took approximately 6 and 12 h for LCZ to reach the logarithmic and stationary phases, respectively, and the bacterial cultures remained at the stationary phase until at least 24 h. Therefore, samples were collected at 0, 6, 12, and 24 h to monitor changes in the concentration of racecadotril and metabolite production by metabolomics analyses.

The concentration of racecadotril in the ML medium was monitored by targeted qualitative metabolomics analysis for auto-degradation. No significant change was observed in the concentration of racecadotril after 6-, 12-, and 24-h of incubation at 37°C compared with 0-h (Supplementary Figure S3), suggesting that racecadotril did not auto-degrade.

Meanwhile, changes in the concentration of racecadotril and the formation of its metabolites at these time points were monitored by non-targeted qualitative metabolomics analysis. The retention time of all samples showed good coincidence on the overlay TICs in both

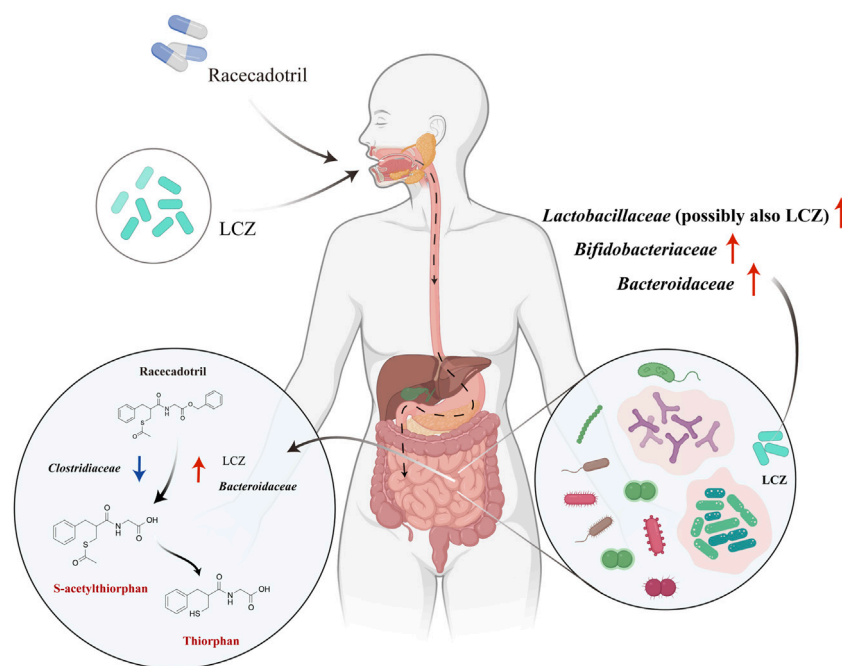


FIGURE 5

Proposed mechanisms of *in vivo* racecadotril degradation via direct metabolic action of *L. casei* Zhang (LCZ) and interactions between LCZ and host gut microbiome. Red arrows in the right circle indicate the effects of LCZ on the gut microbial communities. Arrows in the left circle indicate the effects of *Bacteroidaceae*/*Clostridiaceae*/LCZ on the metabolism of racecadotril (Red arrows indicate promotion, blue arrows indicate inhibition). Chemicals marked in red are metabolites of racecadotril verified by targeted metabolomics.

positive and negative modes (Supplementary Figures S4A, B), indicating good stability of the LC-MS system. Racecadotril was detected only in the positive but not the negative mode by searching its theoretical mass to charge ratio (m/z ; Supplementary Figures S4C, D). Thus, the data acquired in positive mode was used for further metabolite searching through MetabolitePilot™ software. MetabolitePilot™ is a powerful software package that allows comparative analysis between two mass spectra for extracting compounds that appear only in samples but not controls, and it only extracts compounds that have common MS/MS fragments or neutral loss compared with the target compound (Supplementary Figure S5). In our analysis, a compound was deemed as a drug metabolite when it: 1) was only observed in the LCZ-racecadotril culture; 2) had common MS/MS fragments or neutral loss with racecadotril; 3) could be detected in three independent experiments and increased as the incubation prolonged.

At 0 h, only racecadotril but no other metabolites were detected in the LCZ-racecadotril culture (Supplementary Figure S6A). At 6 h, a new compound (referred to as M1; m/z = 296.0940, retention time = 8.09; Supplementary Figure S6B) was detected, and its peak size increased further at 12 h (Supplementary Figure S6C). At 24 h, in addition to M1, another new compound emerged (M2; m/z = 254.0644, retention time = 7.71 min; Supplementary Figure S6D). These two compounds had two MS/MS fragments (i.e., 145.0645 m/z and 91.0546 m/z) common to racecadotril, and racecadotril had one neutral loss [Δ (386.1426–269.0940) m/z], which is the same as the fragment seen in the mass spectra of M1 and M2 (corresponding to 117.0696 m/z). Their possible chemical structures were predicted by the MetabolitePilot™ software (Figures 2B–D; Supplementary Figure S6). The levels of these two compounds increased as the incubation

prolonged, accompanied by corresponding decreases in racecadotril (Figures 2E–G; Supplementary Figures S7A, B). The M2 peak was not picked up by MetabolitePilot™ at 12 h due to its low signal intensity (intensity <1,000; Supplementary Figure S7C) and lack of MS/MS fragments data.

Based on the mass spectra features and chemical structures, M1 and M2 were predicted to be S-acetylthiorphan and thiorphan, respectively. Thus, corresponding standard solutions were purchased from Sigma-Aldrich for UPLC-Q-TOF analysis under the same conditions as the sample runs, confirming that S-acetylthiorphan and thiorphan had identical mass, retention time, and MS/MS fragments as M1 and M2, respectively (Figures 2H–J; Supplementary Figures S8A, B). These results confirmed that S-acetylthiorphan and thiorphan were the drug metabolites produced by LCZ from racecadotril.

3.3 LCZ metabolized racecadotril in a dynamic simulated digestion system

Probiotics are not the native inhabitants of the human GI tract. Thus, it is essential to study the capacity of probiotics in drug metabolism together with their viability during the GI transit. A near-real dynamic *in vitro* human GI digestion system (DHS-IV) was applied to further validate the ability of LCZ in metabolizing racecadotril meanwhile monitoring changes in the bacterial viability. Samples were collected at the end of the intestinal model at 6, 12, and 24 h to determine the bacterial viability by plate counts. Our results showed that the viable counts of LCZ dropped with time in the *in vitro* digestion system (59.68%, 41.07%,

and 25.21% at 6, 12, and 24 h, respectively; [Supplementary Table S2](#)).

Meanwhile, the concentration of racecadotril in the *in vitro* simulated human digestion system dropped significantly in the presence of LCZ ($p < 0.05$; average degradation rate = 77.23%, 61.54%, and 49.56% compared with the baseline; [Figure 3A](#)), and such drop was not observed in the negative control without adding LCZ. Similarly, the decrease in racecadotril was accompanied by the increases in the concentrations of s-acetylthiorphan (detected at 6, 12, and 24 h; [Figure 3B](#)) and thiorphan (only detected at 12 and 24 h; [Figure 3C](#)) in the presence of LCZ. Again, such changes were not observed in the negative control without LCZ.

3.4 LCZ exhibited personalized effects on racecadotril metabolism

Our data so far suggested that LCZ had the capacity of metabolizing racecadotril in monoculture; however, whether its drug biotransformation capacity would be affected by the great complexity and compositional individuality of the human microbiome when present as part of the gut microbial community remained to be answered. Thus, the capacity of LCZ in metabolizing racecadotril was tested in an *ex vivo* fecal co-culture system ([Javdan et al., 2020](#)) of stool samples collected from 26 healthy human donors ([Figure 4A](#)).

First, the 16S rDNA amplicon profiles of the fecal microbiota and *ex vivo* fecal culture microbiota were compared to ensure that the *ex vivo* culture procedure would not cause significant bias in preferentially expanding only few taxa ([Figure 4B](#)). Our results showed that the family-level compositional profiles of the original fecal microbiota and *ex vivo* culture of each subject were largely similar in terms of bacterial relative abundance and diversity, which was also confirmed by unsupervised hierarchical cluster analysis, showing the shortest dissimilarity distance between the fecal microbiota and their *ex vivo* culture counterparts in most subjects, and they are joining together as a pair in the dendrogram ([Figure 4C](#)). These results suggested that the *ex vivo* culturing system supported the growth a wide variety of the intrinsic fecal microbiota and was representative of the original personalized fecal microbiome of each subject.

Next, the ability of the *ex vivo* fecal culture (with/without exogenous addition of LCZ) to metabolize racecadotril was investigated. Notably, around two-thirds (18/26; the range of degradation rate = 7.72%–71.83%, adjusted $p = 0.0002$ to 0.0286 ; [Supplementary Figures S9](#); [Figure 4D](#)) of the samples (without the addition of LCZ) showed varying but significant degree of racecadotril degradation into S-acetylthiorphan and thiorphan, compared with the blank control; and, in most cases (24/26), the addition of LCZ did not exhibit significant differences in racecadotril degradation compared with the natural degradation rate (adjusted $p > 0.05$). Interestingly, the supplementation of LCZ in two *ex vivo* human fecal culture samples, D5 and D24, significantly enhanced racecadotril degradation (adjusted $p < 0.05$; [Figure 4D](#)).

To identify potential taxa that might be responsible for the racecadotril metabolism, correlation analysis was performed. The relative abundance of *Bacteroidaceae* was positively correlated with the degradation rate of racecadotril ($R = 0.95$, $p < 2.2 \times 10^{-6}$; [Figure 4E](#); [Supplementary Figure S10](#)), and the formation of thiorphan ($R = 0.91$, $p = 1.5 \times 10^{-5}$) and S-acetylthiorphan ($R = 0.86$, $p = 0.0013$; [Supplementary Figure S12A](#)). In contrast, the relative abundance of *Clostridiaceae* was negatively correlated with the degradation rate of racecadotril ($R = -0.56$,

$p = 0.0032$; [Figure 4E](#); [Supplementary Figure S10](#)), and the formation of thiorphan ($R = -0.50$, $p = 0.0095$) and S-acetylthiorphan ($R = -0.56$, $p = 0.0029$; [Supplementary Figure S12B](#)).

On the other hand, to find out whether the 24-h exogenous addition of LCZ had any effect on the microbiota composition of the *ex vivo* cultures D5 and D24, metagenomic DNA from these incubated co-cultures was extracted for comparative V4-16S-rRNA-based microbiota analysis against its pre-incubation counterpart. After 24-h incubation with LCZ, the relative abundance of *Bifidobacteriaceae*, *Bacteroidaceae*, and *Lactobacillaceae* increased significantly only in D5 and D24 *ex vivo* cultures ([Figure 4F](#), $p < 0.05$) but not other samples ([Supplementary Figure S11](#), $p > 0.05$).

4 Discussion

Current applications of probiotics are not limited to food and cosmetic products, but are also increasingly used by clinicians to ameliorate symptoms and/or as adjuvant therapeutics in various diseases. Probiotics presented good clinical efficacies in GI dysbiosis, metabolic diseases, and even neurological disorders ([Aponte et al., 2020](#)). The therapeutic effect of probiotics is usually not as direct, fast, and effective as drugs; therefore, they are often used in combination with other drugs as therapeutic adjuvants rather than drug replacement. One of the proposed symptom-alleviating mechanisms of probiotics is their ability to restore a healthier gut microbiota from disease-associated dysbiotic states. Increasing evidence supports that the gut microbiota is involved in drug metabolism; thus, as a part of the regular gut microbiota after being ingested, probiotics are anticipated to take part in drug interaction as well. Few studies have yet addressed the drug metabolizing effects of ingested probiotics.

In this study, we first demonstrated that 75% (27/36) of commonly used oral drugs could be variably metabolized by five probiotic strains. Notably, the drug-metabolizing profile differed greatly between strains, suggesting that the drug-metabolizing activity of probiotics is strain-specific. Such variation, on the one hand, might reflect the different original niches of the tested strains [V9 isolated from a stool sample ([Sun et al., 2010](#)); M8 and M9 isolated from human breast milk ([Zhang et al., 2020](#); [Xu et al., 2021](#)); LCZ and P8 isolated from traditional fermented dairy products ([Ya et al., 2008](#); [Wang et al., 2015](#))] and their environmental/metabolic adaptation. For example, a previous large-scale comparative genomic study of 455 *L. plantarum* genomes identified clear habitat-specific features; isolates obtained from fermented dairy products, animal and human gut/clinical specimens were found to contain multiple environment-specific genes ([Li et al., 2022](#)). In contrast, many early life-associated bifidobacteria isolated from breastfed infant gut, presumably acquired from mother's milk, are functionally specialized in metabolizing human milk ([Lawson et al., 2020](#)). The V9 strain was originally isolated from a human stool sample. Provided the repetitive exposure of the human GI tract to a wide variety of drugs, it is not surprising that V9 could metabolize the most assayed drugs among the tested strains. On the other hand, the chemical structures of the drugs could be an important factor in determining whether they could be easily metabolized. Six of the assayed drugs were found to be metabolized by all five probiotic strains, and common to these drugs is the presence of a nitro or an azo group, rendering them degradable under anaerobic conditions, possibly by azoreductases and nitroreductases that are frequently

present across lactobacilli, bifidobacteria, and other anaerobes (Marteau et al., 1990). Thus, the source of probiotics and the functional groups carried by the drugs are important information to guide the combined use of probiotics and drugs.

The metabolism of drugs by probiotics can alter their structure, changing their bioavailability, bioactivity, and toxicity, which will inevitably lead to concerns about therapeutic efficacy and safety. Therefore, we conducted an untargeted metabolomics analysis to identify probiotic-produced drug metabolites to gain insights into the biotransformation process. Two key differences set our approach apart from previous studies. First, instead of collecting samples at the end of the incubation, samples were collected at multiple time points to reduce false-positive. Second, previous studies always relied on searching across existing tandem mass spectral (MS2) databases, such as KEGG, HMDB, METLIN, mzCloud, and MassBank, for metabolite identification, which are collections of data from different platforms, such as QTOF, Orbitrap, and QqQ, with widely varied instrumental conditions, e.g., collision energy and column types. These variations greatly limit the accuracy of the identification. Thus, this study used MetabolitePilot™ software to identify the metabolites of interest, followed by experimental verification of the retention time, accurate precursor mass (MS1), and MS2 spectra with authentic chemical standards under the same conditions, which is the “gold” standard for metabolite identification (Vinaixa et al., 2016). By untargeted metabolomics analysis, it was confirmed that racecadotril was metabolized into S-acetylthiorphan and thiorphan by LCZ. S-acetylthiorphan and thiorphan are reported active metabolites of racecadotril (Spillantini et al., 1986; Eberlin et al., 2012), implicating that the metabolic transformation of LCZ can contribute to the bioactivity of racecadotril. It was reported that the liver can metabolize thiorphan into inactive metabolites such as sulfoxide of S-methylthiorphan, S-methyl thiorphan, 2-methane-sulfinyl methyl propionic acid, and 2-methyl sulfanyl methyl propionic acid *via* cytochromes P450 enzymes (Eberlin et al., 2012). Those inactive metabolites were not identified in this study. A possible reason for this is that P450 enzymes are generally not present in *Lactobacillaceae* (Padayachee et al., 2020).

Both the probiotics and oral drugs would pass through the harsh conditions in the GI tract, including challenges under low pH, exposure to multiple digestive enzymes and bile salts, and prolonged peristaltic churning and mixing actions in their journey through the mouth, stomach, and intestine. These physical and chemical factors may directly affect probiotic-drug interactions. So, a dynamic GI model which simulated both the biochemical and mechanical processes of human digestion was used to validate the ability of LCZ in metabolizing racecadotril. The bacterial survival rate in the digestate collected at the end of the human intestine model was around 25% after 24-h of simulated digestion, suggesting that LCZ could tolerate human digestive juices and mechanical churning for a sufficiently long time. The survival rate of LCZ observed in this model was lower than that reported in previously static simulated GI juice tolerance tests (including sequential testing of tolerances to GI juices and bile; and evaluation of bile salt hydrolase activity) (Wu et al., 2009), indicating that traditional probiotic screening methods could overestimate the survival of probiotics through the human GI tract. Particularly, the mechanical churning stress is not considered in conventional assaying methods. Consistently, S-acetylthiorphan and thiorphan were mainly detected in the digestate of the intestinal model in the presence of LCZ but not in the negative control without bacterial inoculation. These results together suggested that LCZ could reach the intestine alive and remain active

in racecadotril degradation. Moreover, the observation of the gradual decrease in racecadotril accompanied by progressive increases in S-acetylthiorphan and thiorphan in both the monoculture assay and simulated human digestive system suggested that the biotransformation process is a continuous process occurring only in the presence of LCZ.

We then investigated the racecadotril degradation ability of LCZ in an *ex vivo* fecal co-culture system, which simulated the natural colonic environment where probiotics would indeed become part of the host gut microbiome, at least temporally. Notably, the *ex vivo* fecal cultures showed variable racecadotril degradation ability without exogenous addition of LCZ, suggesting that the gut microbiota can naturally metabolize racecadotril, though such capacity is personalized due to the highly individualized gut microbiota composition. Differences in the host gut microbiome have been shown to lead to inter-individual phenotypic variations in digestive capacity and pharmacokinetic/pharmacodynamic responses (Zhu et al., 2015). We further found that the degradation rate of racecadotril had a strong positive correlation with *Bacteroidaceae* while negatively correlated with *Clostridiaceae*, highly suggestive of an active role of these two bacterial families in racecadotril degradation. Our result is consistent with Zimmermann et al. (2019a), reporting that racecadotril could be fully metabolized by human gut isolates belonging to the phylum *Bacteroidetes*. Interesting, the exogenous addition of LCZ to the *ex vivo* fecal culture with racecadotril did not significantly increase the drug degradation rate in most cases, except for the fecal cultures of donors 5 and 24, suggesting that the biotransformation of racecadotril by an individual strain in a microbiota community is a lot more complicated than in monoculture. It is possible that the growth and gene expression of LCZ were somehow suppressed by the fecal microbes present in the co-culture environment in most cases. However, tracking strain-level microbial dynamics and gene expression changes remain technically difficult, which need to be addressed in future studies. Our results also did not rule out the chance that the drug metabolism could be contributed partly by the endogenous microbiota of the fecal culture. The current study was only able to show that the increase in racecadotril degradation in the LCZ-fecal co-cultures of donors 5 and 24 was accompanied by a significant expansion of the families *Bacteroidaceae*, *Bifidobacteriaceae*, and *Lactobacillaceae*. The taxonomic resolution of our 16S rRNA analysis was limited to the family level, but presumably at least part of the *Lactobacillaceae* enrichment was a direct effect of LCZ inoculation and growth. Our previous work found strong positive correlations between LCZ and specific taxa, including *Bifidobacteriaceae*, *Lactobacillaceae*, and *Bacteroidaceae*, in human gut (Zhang et al., 2014). The positive correlations might suggest symbiotic and even mutually stimulating relationships among these taxa when living under the provided environmental conditions. Thus, a microbiota community with a higher proportion of *Lactobacillaceae* (relative abundance >1%; Supplementary Figure S11) may benefit the growth of LCZ, which will in turn stimulate the growth of *Bifidobacteriaceae* and *Bacteroidaceae*. On the other hand, *Clostridiaceae* showed a strong negative correlation with the racecadotril degradation rate, suggesting its potential role in inhibiting drug degradation reaction. The relative abundance of *Clostridiaceae* in the LCZ-*ex vivo* fecal co-cultures of donors 5 and 25 showed opposite trends after the 24-h incubation with racecadotril (expanded in the co-culture of donor 24, increased from 3.25% to 9.43%; diminished in the co-culture of donor 5, decreased from 2.16% to 1.37%; Figure 4F). The contradictory result could again be due to the limited taxonomic resolution of our 16S rRNA analysis. *Clostridiaceae* is a highly diverse family, including a number of genera that contribute to different nutrient digestibility (Bermingham et al., 2017). It is possible that the observed responses in *Clostridiaceae* only represented some of the

genera within this family. After all, these observations together suggested that the drug-metabolizing action of LCZ is greatly dependent on its interactions with the environmental microbiota.

These results provide important insights: 1) previous *in vitro* studies showing drug metabolism of single bacterial strains should be carefully interpreted and needed to be reproduced in assay conditions taken into account of the complex interactions in the gut microbial community; 2) probiotic applications, particular in clinical scenarios, should not be treated as “one-size-fits-all” supplement but as “precision probiotics” for the best benefits of patients and consumers (Sakandar and Zhang, 2022).

Based on our findings, we propose a possible *in vivo* mechanism of interactions between LCZ, racecadotril, and host gut microbiota (Figure 5). Viable LCZ cells transit through the harsh conditions in the stomach and the small intestine, gaining access to the colon. In the colon environment, the growth and metabolism of LCZ are favored, in the presence of some symbiotic and mutually supportive gut commensals, e.g., *Bifidobacteriaceae*, *Bacteroidaceae*, and particularly *Lactobacillaceae*. The expansion of these taxa, particularly *Bacteroidaceae* and possibly LCZ, enhances racecadotril metabolism into its active products, S-acetylthiorphan and thiorphan.

Although the current study design has already taken into account of multiple factors, such as probiotic specificity, different types of drugs, and the complex physiological environment of the human gastrointestinal tract, some important aspects in clinical drug therapy have still not been considered. For example, whether multiple administration of racecadotril (or other drugs, particularly those that are known to have a gut microbiota modulatory effect, e.g., proton pump inhibitors, metformin, selective serotonin reuptake inhibitors and laxatives) (Weersma et al., 2020) can change the capacity of LCZ and/or microbiota to metabolize the drug; and whether single or multiple probiotics administration could change the microbiota. Generally, combined probiotic formulations are considered more effective than single-strain probiotic products in preventing and managing diseases (Mathipa and Thantsha, 2015). These are relevant but complicated aspects that should be addressed in further studies. Finally, future experiments should target to increase the sample size and track microbial dynamics at a finer taxonomic resolution, ideally to a strain-level precision, which would further confirm the findings of this work and provide insights into microbiota-probiotic-drug interactions.

5 Conclusion

Nowadays, interest in using probiotics for preventing and treating multiple diseases is growing. Many probiotics are now used as adjuvants to drug therapy. This work provided a workflow for the first time to systematically study probiotic-drug interactions. By using the established framework, we demonstrated that probiotics could degrade commonly used drugs through their own metabolism and/or *via* modulating the gut microbiota in a host selective manner. Although the established workflow does not reveal the effect of probiotic intake on the bioavailability, bioactivity, and toxicity of drugs, it provides practical reference information for the combined use of probiotics and drugs, as well as valuable data for designing *in vivo* validation assays. We envisage that incorporating metabolomics, bionics, and especially culturomics would help elucidate inter-individual variabilities in drug responses and promote the transition to a precision probiotic use approach.

Data availability statement

The datasets presented in this study can be found in online repositories. The names of the repository/repositories and accession number(s) can be found in the article/Supplementary Material.

Ethics statement

The studies involving human participants were reviewed and approved by the Ethics Committee of the Affiliated Hospital of Inner Mongolia Medical University (No. KY2020006). The patients/participants provided their written informed consent to participate in this study.

Author contributions

YC and BL designed the research; BL, DW, LL, and SG performed the bench work; BL analyzed the data and wrote the paper; L-YK critically revised the paper and provided advice.

Funding

This research was supported by the National Natural Science Foundation of China (31972053) and Innovation Team Development Plan for Higher Education Institutions in Inner Mongolia (NMGIRT2220).

Acknowledgments

We are grateful to Teng Ma for his helpful suggestions on data visualization.

Conflict of interest

The authors declare that the research was conducted in the absence of any commercial or financial relationships that could be construed as a potential conflict of interest.

Publisher's note

All claims expressed in this article are solely those of the authors and do not necessarily represent those of their affiliated organizations, or those of the publisher, the editors and the reviewers. Any product that may be evaluated in this article, or claim that may be made by its manufacturer, is not guaranteed or endorsed by the publisher.

Supplementary material

The Supplementary Material for this article can be found online at: <https://www.frontiersin.org/articles/10.3389/fphar.2023.1047863/full#supplementary-material>

References

- Aponte, M., Murru, N., and Shoukat, M. (2020). Therapeutic, prophylactic, and functional use of probiotics: A current perspective. *Front. Microbiol.* 11, 562048. doi:10.3389/fmicb.2020.562048
- Bermingham, E. N., Maclean, P., Thomas, D. G., Cave, N. J., and Young, W. (2017). Key bacterial families (Clostridiaceae, Erysipelotrichaceae and Bacteroidaceae) are related to the digestion of protein and energy in dogs. *PeerJ* 5, e3019. doi:10.7717/peerj.3019
- Bolyen, E., Rideout, J. R., Dillon, M. R., Bokulich, N. A., Abnet, C. C., Al-Ghalith, G. A., et al. (2019). Reproducible, interactive, scalable and extensible microbiome data science using QIIME 2. *Nat. Biotechnol.* 37 (8), 852–857. doi:10.1038/s41587-019-0209-9
- Chong, J., Wishart, D. S., and Xia, J. (2019). Using MetaboAnalyst 4.0 for comprehensive and integrative metabolomics data analysis. *Curr. Protoc. Bioinforma.* 68 (1), e86. doi:10.1002/cpbi.86
- Eberlin, M., Mück, T., and Michel, M. C. (2012). A comprehensive review of the pharmacodynamics, pharmacokinetics, and clinical effects of the neutral endopeptidase inhibitor racecadotril. *Front. Pharmacol.* 3, 93. doi:10.3389/fphar.2012.00093
- Falony, G., Joossens, M., Vieira-Silva, S., Wang, J., Darzi, Y., Faust, K., et al. (2016). Population-level analysis of gut microbiome variation. *Science* 352 (6285), 560–564. doi:10.1126/science.aad3503
- FAO/WHO (2001). Health and nutritional properties of probiotics in food including powder milk with live lactic acid bacteria. Available at: <https://www.fao.org/3/a0512e/a0512e.pdf>.
- Franceschi, C., Garagnani, P., Morsiani, C., Conte, M., Santoro, A., Grignolio, A., et al. (2018). The continuum of aging and age-related diseases: Common mechanisms but different rates. *Front. Med.* 5, 61. doi:10.3389/fmed.2018.00061
- Fu, J., Bonder, M. J., Cennit, M. C., Tigchelaar, E. F., Maatman, A., Dekens, J. A., et al. (2015). The gut microbiome contributes to a substantial proportion of the variation in blood lipids. *Circulation Res.* 117 (9), 817–824. doi:10.1161/CIRCRESAHA.115.306807
- Gagliardi, A., Totino, V., Cacciotti, F., Iebba, V., Neroni, B., Bonfiglio, G., et al. (2018). Rebuilding the gut microbiota ecosystem. *Int. J. Environ. Res. public health* 15 (8), 1679. doi:10.3390/ijerph15081679
- GlobeNewswire (2022). Probiotics market size to expanding US\$ 133.92 billion by 2030. Precedence Research <https://www.globenewswire.com/news-release/2022/03/15/2403971/0/en/Probiotics-Market-Size-to-Expanding-US-133-92-Billion-by-2030.html>.
- Huang, J., Liu, Z., Rui, X., L'Hocine, L., Zhang, Q., Li, W., et al. (2020). Assessment of the effect of lactic acid fermentation on the gastroduodenal digestibility and immunoglobulin E binding capacity of soy proteins via an *in vitro* dynamic gastrointestinal digestion model. *Food & Funct.* 11 (12), 10467–10479. doi:10.1039/D0FO02023K
- Javdan, B., Lopez, J. G., Chankhamjon, P., Lee, Y.-C. J., Hull, R., Wu, Q., et al. (2020). Personalized mapping of drug metabolism by the human gut microbiome. *Cell* 181 (7), 1661–1679. doi:10.1016/j.cell.2020.05.001
- Kaoutari, A. E., Armougom, F., Gordon, J. I., Raoult, D., and Henrissat, B. (2013). The abundance and variety of carbohydrate-active enzymes in the human gut microbiota. *Nat. Rev. Microbiol.* 11 (7), 497–504. doi:10.1038/nrmicro3050
- Koppel, N., Maini Rekdal, V., and Balskus, E. P. (2017). Chemical transformation of xenobiotics by the human gut microbiota. *Science* 356 (6344), eaag2770. doi:10.1126/science.aag2770
- Lai, H.-H., Chiu, C.-H., Kong, M.-S., Chang, C.-J., and Chen, C.-C. (2019). Probiotic lactobacillus casei: Effective for managing childhood diarrhea by altering gut microbiota and attenuating fecal inflammatory markers. *Nutrients* 11 (5), 1150. doi:10.3390/nu11051150
- Lawson, M. A., O'Neill, I. J., Kujawska, M., Gowrinadh Javvadi, S., Wijeyesekera, A., Flegg, Z., et al. (2020). Breast milk-derived human milk oligosaccharides promote Bifidobacterium interactions within a single ecosystem. *ISME J.* 14 (2), 635–648. doi:10.1038/s41396-019-0553-2
- Li, K., Wang, S., Liu, W., Kwok, L.-Y., Bilige, M., and Zhang, W. (2022). Comparative genomic analysis of 455 Lactiplantibacillus plantarum isolates: Habitat-specific genomes shaped by frequent recombination. *Food Microbiol.* 104, 103989. doi:10.1016/j.fm.2022.103989
- Marteau, P., Pochart, P., Flourie, B., Pelletier, S., Santos, L., Desjeux, J., et al. (1990). Effect of chronic ingestion of a fermented dairy product containing Lactobacillus acidophilus and Bifidobacterium bifidum on metabolic activities of the colonic flora in humans. *Am. J. Clin. Nutr.* 52 (4), 685–688. doi:10.1093/ajcn/52.4.685
- Mathapa, M. G., and Thantsha, M. S. (2015). Cocktails of probiotics pre-adapted to multiple stress factors are more robust under simulated gastrointestinal conditions than their parental counterparts and exhibit enhanced antagonistic capabilities against *Escherichia coli* and *Staphylococcus aureus*. *Gut Pathog.* 7 (1), 5–14. doi:10.1186/s13099-015-0053-5
- Ndisang, J. F., and Rastogi, S. (2013). *Cardiometabolic diseases and related complications: Current status and future perspective*. Hindawi.
- Padayachee, T., Nzuza, N., Chen, W., Nelson, D. R., and Syed, K. (2020). Impact of lifestyle on cytochrome P450 monooxygenase repertoire is clearly evident in the bacterial phylum Firmicutes. *Sci. Rep.* 10 (1), 13982–14012. doi:10.1038/s41598-020-70686-8
- Peng, W., Juan, W., Jingjing, W., Xiaodong, C., Man-Yau, S. I., and Sufang, D. (2020). Evaluation of probiotics viability in fermented milk based on a biomimetic gastrointestinal model (in Chinese). *Food Ferment. Industries* 47 (12), 147–153.
- Peng, Z., Wu, P., Wang, J., Dupont, D., Menard, O., Jeantet, R., et al. (2021). Achieving realistic gastric emptying curve in an advanced dynamic *in vitro* human digestion system: Experiences with cheese—a difficult to empty material. *Food & Funct.* 12 (9), 3965–3977. doi:10.1039/D0FO03364B
- Sadiq, M. B., Azhar, F.-u.-A., and Ahmad, I. (2022). “Probiotic and prebiotic interactions and their role in maintaining host immunity,” in *Microbiome-gut-brain Axis* (Springer), 425–443.
- Sakandar, H. A., and Zhang, H. (2022). Precision probiotics: Does one-size-fit-all? *Precis. Nutr.* 1 (2), e00015. doi:10.1097/PN9.0000000000000015
- Spear, B. B., Heath-Chiozzi, M., and Huff, J. (2001). Clinical application of pharmacogenetics. *Trends Mol. Med.* 7 (5), 201–204. doi:10.1016/S1471-4914(01)01986-4
- Spillantini, M. G., Geppetti, P., Fanciullacci, M., Michelacci, S., Lecomte, J. M., and Sicuteri, F. (1986). *In vivo* ‘enkephalinase’ inhibition by acetorphan in human plasma and CSF. *Eur. J. Pharmacol.* 125 (1), 147–150. doi:10.1016/0014-2999(86)90094-4
- Średnicka, P., Juszczuk-Kubiak, E., Wójcicki, M., Akimowicz, M., and Roszko, M. (2021). Probiotics as a biological detoxification tool of food chemical contamination: A review. *Food Chem. Toxicol.* 153, 112306. doi:10.1016/j.fct.2021.112306
- Sultana, J., Cutroneo, P., and Trifirò, G. (2013). Clinical and economic burden of adverse drug reactions. *J. Pharmacol. Pharmacother.* 4 (1), S73–S77. doi:10.4103/0976-500X.120957
- Sun, Z., Chen, X., Wang, J., Gao, P., Zhou, Z., Ren, Y., et al. (2010). Complete genome sequence of probiotic Bifidobacterium animalis subsp. lactis strain V9. *J. Bacteriol.* 192 (15), 4080–4081. doi:10.1128/JB.00369-10
- Vinaixa, M., Schymanski, E. L., Neumann, S., Navarro, M., Salek, R. M., and Yanes, O. (2016). Mass spectral databases for LC/MS- and GC/MS-based metabolomics: State of the field and future prospects. *TrAC Trends Anal. Chem.* 78, 23–35. doi:10.1016/j.trac.2015.09.005
- Walters, W., Hyde, E. R., Berg-Lyons, D., Ackermann, G., Humphrey, G., Parada, A., et al. (2016). Improved bacterial 16S rRNA gene (V4 and V4-5) and fungal internal transcribed spacer marker gene primers for microbial community surveys. *mSystems* 1 (1), e00009–e00015. doi:10.1128/mSystems.00009-15
- Wang, J., Wu, P., Wang, J., Wang, J., Gu, B., Ge, F., et al. (2022). *In vitro* gastric digestion and emptying of cooked white and Brown rice using a dynamic human stomach system. *Food Struct.* 31, 100245. doi:10.1016/j.foodstr.2021.100245
- Wang, L., Liu, C., Chen, M., Ya, T., Huang, W., Gao, P., et al. (2015). A novel Lactobacillus plantarum strain P-8 activates beneficial immune response of broiler chickens. *Int. Immunopharmacol.* 29 (2), 901–907. doi:10.1016/j.intimp.2015.07.024
- Weersma, R. K., Zhernakova, A., and Fu, J. (2020). Interaction between drugs and the gut microbiome. *Gut* 69 (8), 1510–1519. doi:10.1136/gutjnl-2019-320204
- Wu, R., Wang, L., Wang, J., Li, H., Menghe, B., Wu, J., et al. (2009). Isolation and preliminary probiotic selection of lactobacilli from koumiss in Inner Mongolia. *J. basic Microbiol.* 49 (3), 318–326. doi:10.1002/jobm.200800047
- Xu, H., Hiraishi, K., Kurahara, L.-H., Nakano-Narusawa, Y., Li, X., Hu, Y., et al. (2021). Inhibitory effects of breast milk-derived lactobacillus rhamnosus probio-M9 on colitis-associated carcinogenesis by restoration of the gut microbiota in a mouse model. *Nutrients* 13 (4), 1143. doi:10.3390/nu13041143
- Ya, T., Zhang, Q., Chu, F., Merritt, J., Bilige, M., Sun, T., et al. (2008). Immunological evaluation of lactobacillus casei Zhang: A newly isolated strain from koumiss in inner Mongolia, China. *BMC Immunol.* 9 (1), 68–69. doi:10.1186/1471-2172-9-68
- Zhang, J., Wang, L., Guo, Z., Sun, Z., Gesudu, Q., Kwok, L., et al. (2014). 454 pyrosequencing reveals changes in the faecal microbiota of adults consuming Lactobacillus casei Zhang. *FEMS Microbiol. Ecol.* 88 (3), 612–622. doi:10.1111/1574-6941.12328
- Zhang, W., Wang, Y., Li, K., Kwok, L.-Y., Liu, W., and Zhang, H. (2020). Short communication: Modulation of fatty acid metabolism improves oxygen tolerance of Bifidobacterium animalis ssp. lactis Probio-M8. *J. dairy Sci.* 103 (10), 8791–8795. doi:10.3168/jds.2019-18049
- Zhu, A., Sunagawa, S., Mende, D. R., and Bork, P. (2015). Inter-individual differences in the gene content of human gut bacterial species. *Genome Biol.* 16 (1), 82–13. doi:10.1186/s13059-015-0646-9
- Zimmermann, M., Zimmermann-Kogadeeva, M., Wegmann, R., and Goodman, A. L. (2019a). Mapping human microbiome drug metabolism by gut bacteria and their genes. *Nature* 570 (7762), 462–467. doi:10.1038/s41586-019-1291-3
- Zimmermann, M., Zimmermann-Kogadeeva, M., Wegmann, R., and Goodman, A. L. (2019b). Separating host and microbiome contributions to drug pharmacokinetics and toxicity. *Science* 363 (6427), eaat9931. doi:10.1126/science.aat9931



OPEN ACCESS

EDITED BY

Rong Wang,
People's Liberation Army Joint Logistics
Support Force 940th Hospital, China

REVIEWED BY

Margarita Aguilera,
University of Granada, Spain
Yukuang Guo,
Takeda Oncology, United States

*CORRESPONDENCE

Slavica Lazarević,
✉ slavica.lazarevic@mf.uns.ac.rs

SPECIALTY SECTION

This article was submitted to Drug
Metabolism and Transport,
a section of the journal
Frontiers in Pharmacology

RECEIVED 29 November 2022

ACCEPTED 30 January 2023

PUBLISHED 09 February 2023

CITATION

Đanić M, Pavlović N, Lazarević S,
Stanimirov B, Vukmirović S, Al-Salami H,
Mooranian A and Mikov M (2023),
Bioaccumulation and biotransformation of
simvastatin in probiotic bacteria: A step
towards better understanding of drug-bile
acids-microbiome interactions.
Front. Pharmacol. 14:1111115.
doi: 10.3389/fphar.2023.1111115

COPYRIGHT

© 2023 Đanić, Pavlović, Lazarević,
Stanimirov, Vukmirović, Al-Salami,
Mooranian and Mikov. This is an open-
access article distributed under the terms
of the [Creative Commons Attribution
License \(CC BY\)](https://creativecommons.org/licenses/by/4.0/). The use, distribution or
reproduction in other forums is permitted,
provided the original author(s) and the
copyright owner(s) are credited and that
the original publication in this journal is
cited, in accordance with accepted
academic practice. No use, distribution or
reproduction is permitted which does not
comply with these terms.

Bioaccumulation and biotransformation of simvastatin in probiotic bacteria: A step towards better understanding of drug-bile acids-microbiome interactions

Maja Đanić¹, Nebojša Pavlović², Slavica Lazarević^{1*},
Bojan Stanimirov³, Saša Vukmirović¹, Hani Al-Salami^{4,5},
Armin Mooranian^{4,5} and Momir Mikov¹

¹Department of Pharmacology, Toxicology and Clinical Pharmacology, Faculty of Medicine, University of Novi Sad, Novi Sad, Serbia, ²Department of Pharmacy, Faculty of Medicine, University of Novi Sad, Novi Sad, Serbia, ³Department of Biochemistry, Faculty of Medicine, University of Novi Sad, Novi Sad, Serbia, ⁴The Biotechnology and Drug Development Research Laboratory, Curtin Medical School and Curtin Health Innovation Research Institute, Curtin University, Bentley, WA, Australia, ⁵Hearing Therapeutics Department, Ear Science Institute Australia, Queen Elizabeth II Medical Centre, Nedlands, WA, Australia

Introduction: Although pharmacogenetics and pharmacogenomics have been at the forefront of research aimed at finding novel personalized therapies, the focus of research has recently extended to the potential of intestinal microbiota to affect drug efficacy. Complex interplay of gut microbiota with bile acids may have significant repercussions on drug pharmacokinetics. However, far too little attention has been paid to the potential implication of gut microbiota and bile acids in simvastatin response which is characterized by large interindividual variations.

The Aim: In order to gain more insight into the underlying mechanism and its contribution in assessing the clinical outcome, the aim of our study was to examine simvastatin bioaccumulation and biotransformation in probiotic bacteria and the effect of bile acids on simvastatin bioaccumulation in *in vitro* conditions.

Materials and methods: Samples with simvastatin, probiotic bacteria and three different bile acids were incubated at anaerobic conditions at 37°C for 24 h. Extracellular and intracellular medium samples were collected and prepared for the LC-MS analysis at predetermined time points (0 min, 15 min, 1 h, 2 h, 4 h, 6 h, 24 h). The concentrations of simvastatin were analyzed by LC-MS/MS. Potential biotransformation pathways were analyzed using a bioinformatics approach in correlation with experimental assay.

Results: During the incubation, simvastatin was transported into bacteria cells leading to a drug bioaccumulation over the time, which was augmented upon addition of bile acids after 24 h. A decrease of total drug level during the incubation indicates that the drug is partly biotransformed by bacterial enzymes. According to the results of bioinformatics analysis, the lactone ring is the most susceptible to metabolic changes and the most likely reactions include ester hydrolysis followed by hydroxylation.

Conclusion: Results of our study reveal that bioaccumulation and biotransformation of simvastatin by intestinal bacteria might be the underlying mechanisms of altered simvastatin bioavailability and therapeutic effect. Since this study is based only on selected bacterial strains *in vitro*, further more in-depth research is needed in order

to elicit completely the contribution of complex drug-microbiota-bile acids interactions to overall clinical response of simvastatin which could ultimately lead to novel approaches for the personalized lipid-lowering therapy.

KEYWORDS

pharmacomicrobiomics, gut microflora, simvastatin, bile acids, drug metabolism, drug transport

1 Introduction

Given that each individual has its own unique and relatively stable bacterial composition (“bacterial fingerprint”), gut microbiota has attracted a great deal of attention among the scientific community in the field of personalized medicine. Most research to date has focused on the relationship between the state of the microbiome and disease risk (Cullen et al., 2020). In addition to the role in the pathogenesis of many diseases, pharmacomicrobiomic studies have demonstrated that gut microbiota may also affect the bioavailability, clinical efficacy and toxicity of a wide range of drugs. Therefore, pharmacomicrobiomics has become the focus of many research works as a valuable tool for predicting therapy outcomes (ElRakaiby et al., 2014; Scher et al., 2020; Lazarević et al., 2022).

Intestinal microbiota-drugs interactions are possible at different levels, through both direct and indirect mechanisms, *via* bacterially derived metabolites, modulation of barrier function and regulating the gene expression of different transporters and enzymes in gastrointestinal tract (Wilson and Nicholson, 2017). Since the capability of the gut microbiome to metabolize drugs has been recognized for over 80 years (Fuller, 1937), the most studied interaction is the biotransformation of drugs by bacterial enzymes (Enright et al., 2016; Wilson and Nicholson, 2017; Zimmermann et al., 2019). Gut microbiota performs a wide range of metabolic reactions on drugs that may affect the pharmacokinetics of numerous drugs and the final clinical outcome (Wilson and Nicholson, 2017; Danić and Mikov, 2020). Metabolic transformation of drugs by gut microbiota and probiotic bacteria may result in the production of active, inactive or even toxic metabolites contributing to therapeutic effects or even adverse reactions. While the liver is primarily responsible for the metabolism *via* oxidation and conjugation producing polar and high molecular weight metabolites, the intestinal bacteria is mainly involved in reductive and hydrolytic reactions but deamination, dehydroxylation, decarboxylation, demethylation, deconjugation and proteolysis are also described, therefore representing an extremely important site of first-pass metabolism (Stojančević et al., 2014; Wilson and Nicholson, 2017; Danić and Mikov, 2020). To date, over one hundred drug molecules have been reported to be metabolized by intestinal bacteria (Zimmermann et al., 2019). However, this number is likely much higher since no large-scale systematic screenings for bacterial metabolism have taken place (Bisanz et al., 2018).

Beyond the increasingly recognized scenario of biotransformation by the bacterial enzymes, in a previously published study, we have demonstrated that drugs may also accumulate in gut bacteria (Đanić et al., 2019). To the best of our knowledge, no previous research had considered drug-bacteria interactions in terms of bioaccumulation so this type of interaction is a completely new aspect that needs special attention in future studies to gain a more in-depth understanding of its influence on drug bioavailability. In a recently published study in the

journal *Nature*, a group of authors has studied the interactions of 15 diverse drugs with 25 common strains of gut bacteria, revealing 70 bacteria-drug interactions that included even 29 entirely novel mechanisms. It was surprising that the majority of the new interactions were the drugs accumulating within the bacteria with or without chemical transformation highlighting the role of the microbiome in drug delivery, effectiveness and safety (Klünemann et al., 2021).

Drugs that are particularly susceptible to the effect of gut microbiota are those characterized by low solubility and/or permeability, or modified-release, thereby contributing to longer residence times of a drug within the gastrointestinal tract wherein biotransformation by intestinal bacteria may occur (Stojančević et al., 2014; Enright et al., 2016). Additionally, functional group analysis suggests that particular chemical structures (such as lactones, nitro, azo and urea groups) predispose drugs for microbial metabolism (Zimmermann et al., 2019). One such candidate is simvastatin, a lipid-lowering drug from a group of statins, which acts as a 3-hydroxy-3-methyl-glutaryl-CoA (HMG-CoA) reductase inhibitor. The simvastatin molecule consists of aromatic backbone attached to dimethylbutanoic acid arm with an ester bond and the ethyl pyranil arm with a covalent C–C-bond forming a lactone structure which represents an inactive form of the drug (Aura et al., 2011). This, simvastatin is administered as a prodrug while the active carboxylate form of the drug is β -hydroxy acid which is produced upon hydrolysis by esterases, paraoxonases and by non-enzymatic hydrolysis in the human body (Geboers et al., 2016). The binding of statins to the catalytic domain of HMG-CoA-reductase is stereoselective and simvastatin *in vivo* rapidly converts to the active (3R, 5R)-3,5-dihydroxypentanoic acids, which in turn inhibit this enzyme (Ye and Devasthale, 2016). It is known that simvastatin undergoes extensive hepatic metabolism *via* various pathways including acid/lactone interconversion. According to the biopharmaceutical classification system (BCS), simvastatin belongs to the second class of drugs characterized by low water solubility and high permeability. For this group of drugs, dissolution rate is a limiting factor for bioavailability (Đanić et al., 2016b). The bioavailability of simvastatin is rather low (less than 5%) due to variable absorption (60%–80%), intensive presystemic elimination and drug efflux pathways (De Angelis, 2004; Korani et al., 2019). Despite the confirmed effectiveness of statins therapy in the prophylaxis and management of cardiovascular disease, a number of studies have drawn attention to large inter-individual variability in response, with roughly a third of treated patients achieving the lipid-lowering goals specified in international guidelines indicating a highly unpredictable therapeutic outcome in patients (Postmus et al., 2014; Trompet et al., 2016). Patient-specific factors like genetic predisposition and the drug characteristics such as low solubility and dissolution rate of simvastatin may only partly explain these differences (Pasanen et al., 2006; Ramsey et al., 2014; Danić et al.,

2016b; Lee and Ho 2017; Karaźniewicz-Łada et al., 2018). There are still difficulties with treatment decisions and personalized approaches to simvastatin therapy remain limited (Reiter-Brennan et al., 2020). Therefore, insights into the additional factors that may affect the efficacy of drug are urgently needed to maximize the clinical response. With an attempt to fill this gap, the research group investigated the link between gut microbiota and simvastatin response and demonstrated that antibiotic treatment not only changed the gut microbiota composition but also attenuated the hypolipidemic effect of simvastatin in hyperlipidemic mice (He et al., 2017). Additionally, the metabolomics analysis showed that higher pre-treatment levels of bacterial derived bile acids correlated with low-density lipoprotein cholesterol (LDL-C) lowering in patients who had a good response to simvastatin (Kaddurah-Daouk et al., 2011). These findings indicate that variability might lie in the interactions with intestinal microbiota, which will be the topic of this research.

A growing body of studies over the last few decades has recognized the role of bile acids in the modulation of drug transport through biological membranes, by affecting their solubility or permeability through biological membranes (Đanić et al., 2018; Đanić et al., 2021; Mooranian et al., 2021; Pavlović et al., 2022). The final outcome of bile acids on drug transport across the biological membrane depends on many factors including type and structure of bile acids, their hydrophobicity and concentration. It should be noted that bile acids increase the solubility and dissolution rate of non-polar drugs primarily at the levels higher than the critical micellar concentration (CMC), while in submicellar concentrations, they mostly influence the drug transport across the biological membranes (Pavlović et al., 2018). Most common drug-bile salt interaction is ion-pairing and the formed complexes may have either higher or lower polarity compared to the drug molecule itself (Đanić et al., 2018). The influence of bile acids on drug transport may be achieved through the effect on active and passive transport (Stojančević et al., 2013; Đanić et al., 2021; Pavlović et al., 2022). Much of the current literature pays particular attention to the effect of bile acids on the transport into eukaryotic cells through biological barriers such as the blood brain barrier, skin, buccal, nasal, pulmonary and intestinal membranes (Moghimipour et al., 2015).

Due to the physiological presence of bile acids in the gastrointestinal tract and the complex crosstalk between bile acids and gut microbiota in terms of bacterial biotransformation of bile acids that affects their composition and signaling pathways (Wahlström et al., 2016; Đanić et al., 2018), it would be of immense importance to study the effect of bile acids on the drug transport into bacterial cells as well.

It is clear that the behavior of prodrugs such as simvastatin in the gastrointestinal tract, which includes interactions with intestinal bacteria and bile acids, may have significant repercussions on intestinal drug absorption, metabolism and overall pharmacokinetics. *In vitro* testing of these interactions is clearly an important step in assessing the final effect on the clinical outcome in patients. To gain more insight into the mechanisms underlying this process, we investigated: 1) simvastatin bioaccumulation in probiotic bacteria in *in vitro* conditions, 2) the influence of different bile acids on the simvastatin bioaccumulation in probiotic bacteria and 3) the biotransformation of simvastatin by probiotic bacteria using a bioinformatics approach in correlation with experimental assay.

2 Materials and methods

2.1 Materials and reagents

Commercial capsules of probiotics (PROBIOTIC[®], Ivančić i sinovi d. o.o, Serbia) containing 5×10^9 lyophilized cells of *Lactobacillus acidophilus* Rosell-52, *Lactobacillus rhamnosus* Rosell-11 and *Bifidobacterium longum* Rosell-175 strains, were used in the study as representatives of intestinal microbiota. The accuracy of label claims was confirmed by pretesting the number of viable bacteria in capsules using traditional methods of cultivation. Bacterial strains have been identified and characterized by Pasteur Institute, France. Simvastatin was obtained from Hemofarm AD, Serbia. Cholic acid (CA) and deoxycholic acid (DCA) were purchased from Sigma Chemicals Co., St Louis, MO, United States while 12-monoketocholic acid (MKC) was synthesized at the Department of Pharmacology, Toxicology and Clinical Pharmacology, Faculty of Medicine, Novi Sad, Serbia according to the previously published method of Miljkovic et al. (Miljkovic et al., 1996). Water, acetonitrile, ethanol and formic acid were of LC-MS grade and obtained from J.T. Baker (Phillipsburg, NJ, United States). Phosphate buffered saline pH 7.4 was purchased from Gibco, Life Technologies, Grand Island, NY, United States.

2.2 Preparation of stock standard and working standard solutions

The stock solution of simvastatin (5 mg/ml) was prepared by dissolving the appropriate amount of simvastatin in ethanol. A series of standard solutions was prepared using the appropriate dilution of stock solution in PBS buffer:AcN (1:4) to reach the final concentrations in the range of 0.625–20 µg/ml. These standard solutions were used for the determination of linearity and the construction of the calibration curve. The dependence of the peak area on the concentration was analyzed. The calibration curve equation was $y = 2621x + 33447$. The correlation coefficient of the calibration curve was $R^2 = 0.9974$.

Stock solutions of DCA, 12-MKC and CA at concentrations of 25 mM were prepared by dissolving the appropriate amount of respective bile acids in DMSO. In this study, submicellar concentrations of bile acids were used (0.25 mM) (Natalini et al., 2007).

2.3 Experimental protocol and sample preparation

5×10^9 probiotic bacteria were mixed and shaken with 10 ml of simvastatin solution in PBS buffer (50 µg/ml) in a test tube with a screw cap making suspension of probiotic bacteria (5×10^8 /mL). Experimental groups with probiotics were labeled with SP, SPD, SPM and SPC (without bile acids, with DCA, 12-MKC and CA, respectively). Control groups were prepared in the same way but without probiotic bacteria (S, SD, SM, SC, respectively) in order to distinguish the spontaneous degradation of simvastatin during the time from the effect of probiotics.

The tubes were incubated at anaerobic conditions at 37°C for 24 h, gently shaking the tubes occasionally. Extracellular and intracellular medium samples were collected and prepared for the LC-MS analysis

at predetermined time points (0 min, 15 min, 1 h, 2 h, 4 h, 6 h, 24 h) according to previously published procedure (Danić et al., 2019). In each time point, after the gentle shaking the tubes to uniformly distribute the content, 100 μ L of samples were withdrawn and centrifuged for 5 min at 15,000 rpm to precipitate bacteria. Precipitated bacteria were used for the analysis of intracellular content and the remaining supernatant were carefully poured off and used for analysis of extracellular content. Precipitation of the proteins in the remaining supernatant was achieved by acetonitrile which was added to supernatant in ratio 1:4. Then, samples were centrifuged for 10 min at +4°C and at 15,000 rpm. The obtained supernatant was used for the analysis of extracellular concentration of simvastatin. An aliquot of 10 μ L was directly injected in LC-MS/MS system. Precipitated bacteria that remained after the first step of centrifugation were used for the analysis of intracellular content. Cells were washed three times gently with PBS and resuspended in 100 μ L of deionized water followed by ultrasonic disruption that was achieved by three 2-min consecutive ultrasound exposure with 3-min rest intervals between in an ice bath. Bacterial cell debris were then pelleted by a centrifugation step and the supernatant was diluted 5-fold with acetonitrile and centrifuged for 10 min at +4°C and at 15,000 rpm before loaded onto a column for the analysis of intracellular fraction of simvastatin. During the analysis, 5-fold dilution with acetonitrile was considered. The concentrations of simvastatin were analyzed by LC-MS/MS. Total concentrations were calculated theoretically as a sum of extracellular and intracellular concentrations. In order to avoid misinterpretation of results due to possible loss of drug by washing the cells, we have prepared control samples of all studied groups in the last time point and measured the concentrations of simvastatin after lysis of total content which contained the total amount of drug. All experiments were performed in triplicates protected from direct sunlight to prevent photodegradation of the drug.

2.4 LC-MS analysis

Sample analysis was performed with The LCQ Fleet ion trap mass spectrometer from Thermo Fisher Scientific, Germany operated in positive electrospray mode. The mass spectrometer was coupled to an HPLC system (Thermo Fisher Scientific, Germany) consisting of a quaternary gradient Surveyor LC pump Plus (Thermo Finnigan) and a Surveyor Autosampler Plus (Thermo Finnigan). The system was controlled by Xcalibur LC/MS software (Thermo Fisher Scientific Corporation, v 2.0.7, 2007). Quantitative analysis was performed using LC-MS according to a previously published method (Gambhira et al., 2011) with minor modifications. In brief, the analysis was performed using a reverse-phase column Zorbax Eclipse Plus-C18 (150 mm \times 2.1 mm, 5 μ m, Agilent Technologies, United States), and a guard column Zorbax extend C18 (12.5 mm \times 2.1 mm, 5 μ m, Agilent Technologies, United States). The mobile phase for isocratic elution consisted of 0.1% formic acid in water and acetonitrile (30:70% v/v), at a constant flow rate of 300 μ L/min. The injection volume was 10 μ L, the column temperature was 20°C and the duration of one analysis was 15 min. The retention time for simvastatin was 9.73 min. The operating conditions of the mass spectrometer were as follows: temperature of the heated capillary 350°C, sheat gas flow (nitrogen) 32.00, auxiliary gas flow (helium) 8.0 (in arbitrary units), source voltage 5.5 kV, source current 100 μ A, 1 micro-scan with a

maximum ion injection time of 100 ms. MS analysis was performed in positive ion mode in the whole mass range of m/z 90-600. The ion of the adduct molecule with sodium $[M + Na]^+$ was selected for quantitative analysis.

Identification of simvastatin metabolites i.e. qualitative analysis was conducted using LC-MS/MS according to method described previously (Hirth, 2011) with slight modifications. Gradient elution was performed with the mobile phase consisting of 0.1% formic acid (A) and acetonitrile containing 0.1% formic acid (B) starting at 42% B followed by a linear gradient to 90% B over 40 min, holding at 90% B from 40 to 50 min, back to starting conditions (42% B) over 1.5 min, and allowing the column to re-equilibrate to the starting conditions (42% B) during the last 8.5 min period (51.5–60 min). The flow rate was set to 200 μ L/min. Samples were stored at 15°C in an Agilent autosampler throughout the analyses.

Mass spectral data were acquired on LCQ Fleet™ Ion Trap Mass Spectrometer (Thermo Fischer Scientific, Germany), equipped with an electrospray ionization (ESI) source operated in positive ionization mode and used Xcalibur software (ThermoFisher Scientific Corporation, version 2.0.7, 2007) for system operation and data manipulation. MS instrument parameters were optimized by infusing the SV (10 μ g/ml) with a syringe pump into the MS source at a flow rate of 5 μ L/min with LC solvent.

Two scan events were prescribed to run in the LCQ mass spectrometry. The first event was a full-scan spectrum to acquire data on the on protonated molecules $[M + H]^+$ or adducts with alkali metal $[M + Na]^+$ within the scan range from m/z 150 to 600. The second scan event was performed using a Data Dependent Scan on $[M + H]^+$ or $[M + Na]^+$. In this mode, three most abundant mass peaks from the first scan are selected for fragmentation. One μ scan was used for data acquisition, and the maximum injection time was 100 ms. Product ion MS/MS scans were performed at normalized collision energy of 30.0 (expressed in relative units, %), the isolation width 2 m/z, the activation q value 0.250, charge state 2 and the activation time 30 ms. For the dependent scans, dynamic exclusion was enabled with the following settings: repeat count 2, repeat duration 15 s, exclusion list size 500, and exclusion duration 60 s.

All data were processed using Qual Browser, which is a part of the ThermoFinnigan Xcalibur software in combination with software used for Deconvolution is Automated Mass Spectrometry Deconvolution and Identification System (AMDIS) developed by NIST (National Institute of Standards and Technology).

2.5 Analysis of simvastatin biotransformation pathways by bacterial enzymes: Databases and bioinformatics approaches

Potential simvastatin biotransformation pathways were analyzed also using a bioinformatics approach and appropriate software packages.

Simvastatin metabolism was anticipated using freely available MetaPrint 2D tool (<http://www.metaprint2d.ch.cam.ac.uk/metaprint2d/>), which predicts metabolism through data-mining and statistical analysis of known metabolic transformations reposted in the literature. The atoms of a xenobiotic at which metabolic transformations are centered are termed its 'sites of metabolism (SOM)'. By uploading the SMILES string of simvastatin molecule, MetaPrint2D predicted metabolic reactions and sites of a molecule that are most likely to undergo the metabolism, based

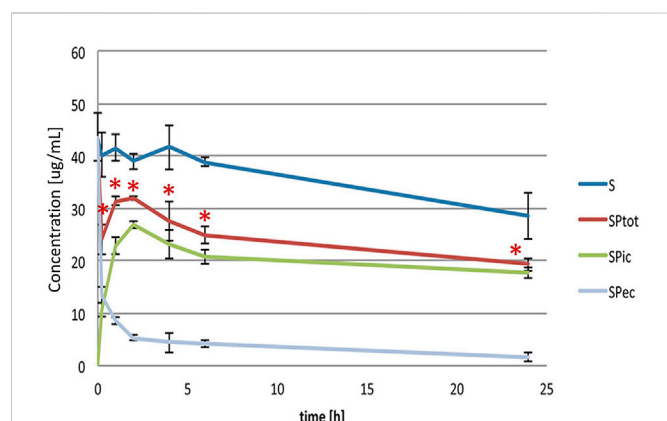


FIGURE 1

Extracellular, intracellular and total simvastatin level over the 24-h incubation with (SP_{ec}, SP_{ic}, SP_{tot}) and without probiotic bacteria (S). Statistically significant difference of total simvastatin level, calculated as a sum of intracellular and extracellular amount, was noted versus control, without probiotic bacteria, during the entire study period (* $p < 0.05$).

on their similarity to known sites of metabolism and sites that are known not to be metabolized. The predicted metabolic sites/atoms are represented by a color code, indicating the probability of biotransformation. For each marked site in the structure, Normalized Occurrence Ratio (NOR) value was generated representing the probability of enzymatic reaction on the particular atom. The most probable SOM is shown in red and the least probable in gray, with probability values ranging from 0 to 1 [red (0.66–1), orange (0.33–0.66), green (0.33–0.15), white (0.15–0.00), and gray (little/no data)] (Carlsson et al., 2010). Additionally, to predict the structures of potential metabolites, the EAWAG-BBD Pathway Prediction System was used (EAWAG-BBD Pathway Prediction System, 2010).

In order to link suggested metabolic pathways with genes and enzymes in tested bacteria, we have searched for different databases which contain a collection of microbial genomes and metabolic pathways. These predictions are based on data on sequenced genomes, computationally inferred data and existing information from the scientific literature (Karp et al., 2019). Databases-driven analysis of bacterial enzymes is an established technique applied in research on drug–microbiota interactions (Liu et al., 2017; Rezazadeh and Babaeipour, 2020; Ankrah and Barker, 2021). The organism search (*Lactobacillus rhamnosus*, *Lactobacillus acidophilus*, *Bifidobacterium longum*) was performed on verified BRENDA, BioCyc and KEGG platforms in order to check their enzymes. Entering a search term resulted in the list of enzymes that was reviewed for the presence of specific enzymes which may act on simvastatin as a substrate.

2.6 Statistics

Obtained data were analyzed using statistical software IBM SPSS Statistics, ver. 21 (Systat Software Inc, San Jose, CA, United States). The analysis concerned triplicate results. All data were expressed as mean \pm standard deviation (SD). The statistical significance of the difference between the average values of the parameters was tested using one-factor analysis of variance (ANOVA) with Tukey's *post-hoc* test for simultaneous comparison of multiple samples, and ANOVA test of repeated measures with the Sidak test for

comparing different time points within the same group. Statistical hypotheses were tested at the level of statistical significance of 5% ($p < 0.05$).

3 Results

3.1 Bioaccumulation of simvastatin into bacterial cells

Figure 1 shows the levels of simvastatin in extracellular (SP_{ec}), intracellular (SP_{ic}) and total (SP_{tot}) content during a 24-h incubation with probiotic bacteria compared to the control (S), without probiotic bacteria. It can be observed that during the incubation of simvastatin with probiotic bacteria there was a statistically significant decrease of the simvastatin level in the extracellular content (SP_{ec}), which was the most pronounced in the first 15 minutes (from 43.60 ± 4.55 µg/ml at 0 min to 13.38 ± 1.51 µg/ml at 15 min, $p < 0.05$). This trend of decreasing the concentration of simvastatin in the extracellular content continued throughout the entire observed period, but to a lesser extent.

Accordingly, already after 15 minutes of incubation, the presence of simvastatin in the intracellular medium was recorded (10.72 ± 1.37 µg/ml). The concentration continued to increase during the first 2 hours of incubation reaching the value 26.82 ± 0.72 µg/ml, after which it remained relatively stable up to the end of the incubation period with a slight drop from the second hour reaching the value 17.69 ± 1.01 µg/ml after 24 h.

The total concentrations of simvastatin, calculated as a sum of extracellular and intracellular concentrations, were statistically significantly lower in the group with probiotics (SP_{tot}) compared to the control group without probiotics (S) during the entire study period. The total concentration of simvastatin in the group with probiotics at 24 h was 19.27 ± 1.16 µg/ml compared to the control where the concentration was 28.53 ± 4.37 µg/ml ($p < 0.05$). The level of simvastatin in the control group was relatively stable during the first 6 h of incubation while it fell significantly at 24 h of incubation, reaching approximately 35% lower values compared to the initial concentration (from 43.60 ± 4.55 µg/ml at 0 min to 28.53 ± 4.37 µg/ml at 24 h, $p < 0.05$).

There were no significant differences in any group between total drug content experimentally and theoretically calculated as a sum of intracellular and extracellular concentration. Therefore, we can conclude that the decrease of a drug is a result of metabolic biotransformation.

3.2 Effect of bile acids on the bioaccumulation of simvastatin by bacterial cells

Extracellular and intracellular concentrations of simvastatin in groups with probiotic bacteria and bile acids (SPC, SPM, SPD) were compared to the group without bile acids (SP) and shown in Figures 2A, B, respectively. LC-MS chromatograms for tested groups are provided as Supplementary Data (Supplementary Figure S1). In order to make a comparison between the certain bile acids and to avoid their membranolytic effect, concentrations of bile acids in the experiment were equimolar 0.25 mM and under their CMC (4.09 mM,

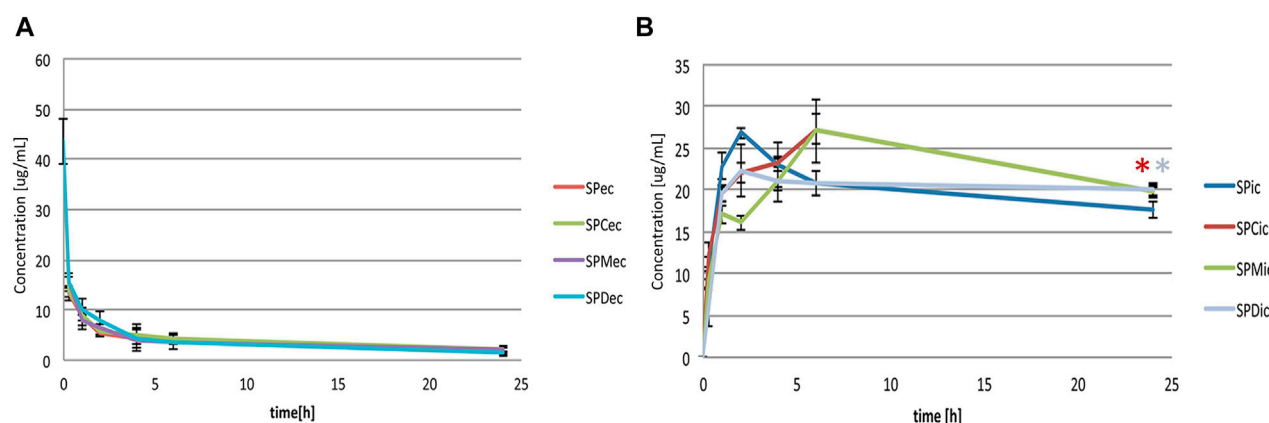


FIGURE 2

(A) Effect of bile acids on extracellular simvastatin concentration over the 24-h incubation (SP_{ec} - simvastatin with probiotics; SPC_{ec}, SPM_{ec}, SPD_{ec} - simvastatin with probiotics and addition of CA, 12-MKC, DCA, respectively) (B) Effect of bile acids on bioaccumulation of simvastatin by probiotic bacteria over the 24-h incubation (SP_{ic} - simvastatin with probiotics; SPC_{ic}, SPM_{ic}, SPD_{ic} - simvastatin with probiotics and addition of CA, 12-MKC, DCA, respectively). Bile acids did not lead to a significant change in the concentrations of simvastatin in extracellular medium during the 24-h incubation. During the first 4 hours of incubation with probiotic bacteria, statistically lower intracellular concentrations were observed in groups with bile acids compared to the control group. At the end of incubation higher levels of simvastatin in groups with bile acids were recorded (in groups with CA and DCA with statistically significant difference compared to the control, **p* < 0.05) with no significant differences between bile acids themselves.

13.35 mM and 1.69 mM for CA, 12-MKC and DCA, respectively) (Yang et al., 2009).

It can be observed that bile acids did not generally lead to a significant change in the concentrations of simvastatin in extracellular medium during the 24-h incubation. However, statistically lower intracellular concentrations were observed in groups with bile acids compared to the control group during the first 4 hours of incubation. On the other hand, higher levels of simvastatin in groups with bile acids compared to the control were recorded at the end of incubation, with statistical significance in groups with CA and DCA ($19.82 \pm 0.44 \mu\text{g/ml}$ vs. $17.69 \pm 1.01 \mu\text{g/ml}$ and $20.02 \pm 0.93 \mu\text{g/ml}$ vs. $17.69 \pm 1.01 \mu\text{g/ml}$, *p* < 0.05, respectively) with no significant differences between bile acids themselves.

3.3 Biotransformation of simvastatin: Databases and bioinformatics approaches

In order to predict potential microbial metabolic pathways of simvastatin, *in silico* bioinformatics analysis using the MetaPrint2D Program was performed. The results of the analysis are shown in Figure 3. The atoms in the simvastatin molecule that are most susceptible to metabolic reactions are marked, as well as reactions that can take place on them. For each atom marked, NOR value is assigned indicating the probability of predicted reactions occurring. It can be observed that the most likely metabolic reaction sites are atoms with the highest NOR value which are colored in red. In simvastatin molecule, such atoms belong to the lactone ring and the most likely reactions are dealkylation and ester hydrolysis at atom O23, which lead to lactone ring opening, as well as dealkylation, dehydration, dehydroxylation, oxidation and oxidative elimination at C18 atom. Structures of simvastatin metabolites predicted by EAWAG-BBD Pathway Prediction System are shown in Supplementary Figure S2. The presence of enzymes that can catalyze these reactions in tested

bacterial strains was confirmed by searching various databases and existing literature.

3.4 Biotransformation of simvastatin: Experimental assay

Two simvastatin metabolites were detected in incubation medium. Representative extracted ion chromatograms for simvastatin and its metabolites M1 and M2 are shown in Figure 4 and their structures are represented in Figure 5. The relevant ms1 and MS/MS spectra were provided as Supplementary Figure S3. First metabolite (labeled as M1) was identified as an hydroxy acid metabolite based on a molecular weight increase of 18 Da compared to simvastatin molecule, and its fragmentation pattern. This metabolite represents the open acid form resulted from hydrolysis of lactone. The fragmentation pattern is similar with that of simvastatin with the noticeable fragment ion located at *m/z* 321 that corresponds to neutral loss of a side chain i.e. 2,2-dimethyl butyric acid molecule (*m/z* = 116) from molecular ion, at *m/z* 437. Detected metabolite (labeled as M2) was postulated as a hydroxylated hydroxy acid metabolite, based on a molecular weight increase of 34 Da compared to simvastatin molecule and its fragmentation pattern. Molecular weight of M2 metabolite was determined from the ms1 spectra in the positive mode, through the assignment of molecule adducts with proton $[M + H]^+$ (*m/z* 453) and ions of alkali metals $[M + Na]^+$ (*m/z* 475) and $[M + K]^+$ (*m/z* 491). As the most intense ions from a full MS scan was molecule adduct with Na, it was selected for fragmentation. MS2 spectra shows ion peaks located at 359 and 341 that correspond to the loss of side chain i.e. 2,2-dimethylbutyric acid molecule (*m/z* 116) and water molecule (*m/z* 18) from $[M + Na]^+$ (*m/z* 475), respectively. It may be concluded that hydroxylation occurs in naphthalene ring but the accurate position of OH group was not possible to determine. Based on results of MetaPrint 2D analysis, carbon atoms 5, 6 and 10 are the potential

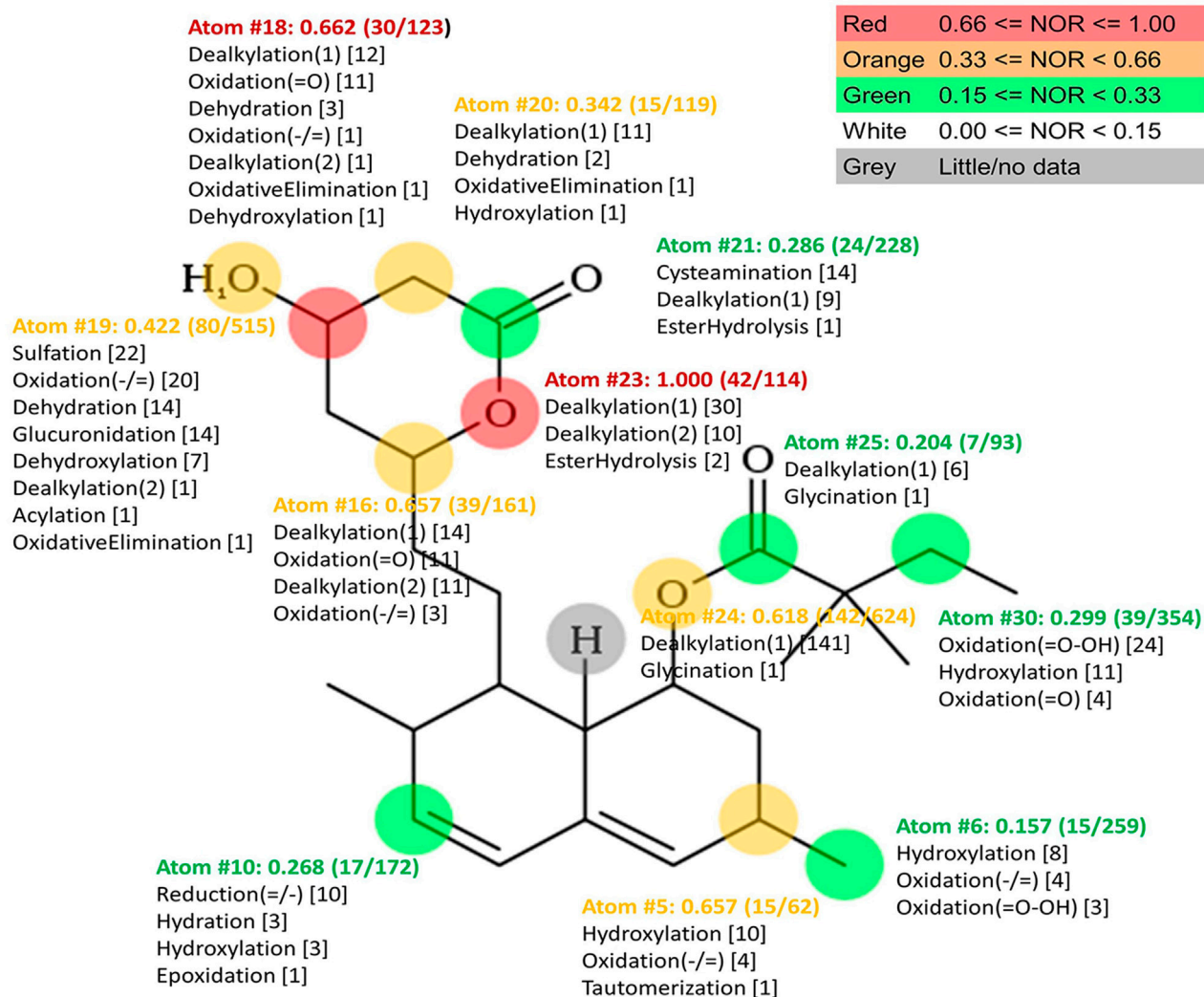


FIGURE 3

Plot of MetaPrint2D predictions. Atoms which are most likely to be biotransformed and reactions predicted by Meta Print2D are marked. NOR value for each marked atom is assigned indicating the probability of predicted reaction occurring. The most likely metabolic reaction sites are atoms with the highest NOR value which are colored in red.

targets for hydroxylation. Structures of simvastatin and identified metabolites are shown in Figure 5.

4 Discussion

Simvastatin is a drug characterized by large interindividual variations in clinical response and the causes of these differences have not yet been fully elucidated. Although pharmacogenetics and pharmacogenomics have been at the forefront of research examining the variations in drug response in general, the focus of research has been recently extended to the potential of intestinal microbiota to affect drug efficacy. However, far too little attention has been paid to the potential implication of gut microbiota in simvastatin response, and therefore, in the focus of our study were simvastatin-gut microbiota interactions. Considering the lack of information on drug metabolism by gut microbiota generally, the aim of our study was to develop a fast and reliable method that might be

useful for pre-evaluation of the gut microbiota impact on drug metabolism and transport using probiotic bacteria from a commercially available product. The first reason is that probiotics are a normal part of gut microbiota and the second one is that they are readily available and do not require special preparation since they contain viable bacteria. Therefore, probiotics are a good option for intestinal microbiota representatives to gain preliminary results on the influence of intestinal bacteria on drug metabolism and pharmacokinetics. Potential interactions were studied in *in vitro* conditions during the incubation of simvastatin with selected probiotic strains and using a bioinformatics approach. The influence of bile acids on these interactions was examined too, considering the complex crosstalk between gut bacteria and bile acids and their effects on drugs transport through biological membranes by affecting both, drug solubility and permeability. Both, bacterial biotransformation of simvastatin, and the novel mechanism, drug bioaccumulation, have been reported and discussed.

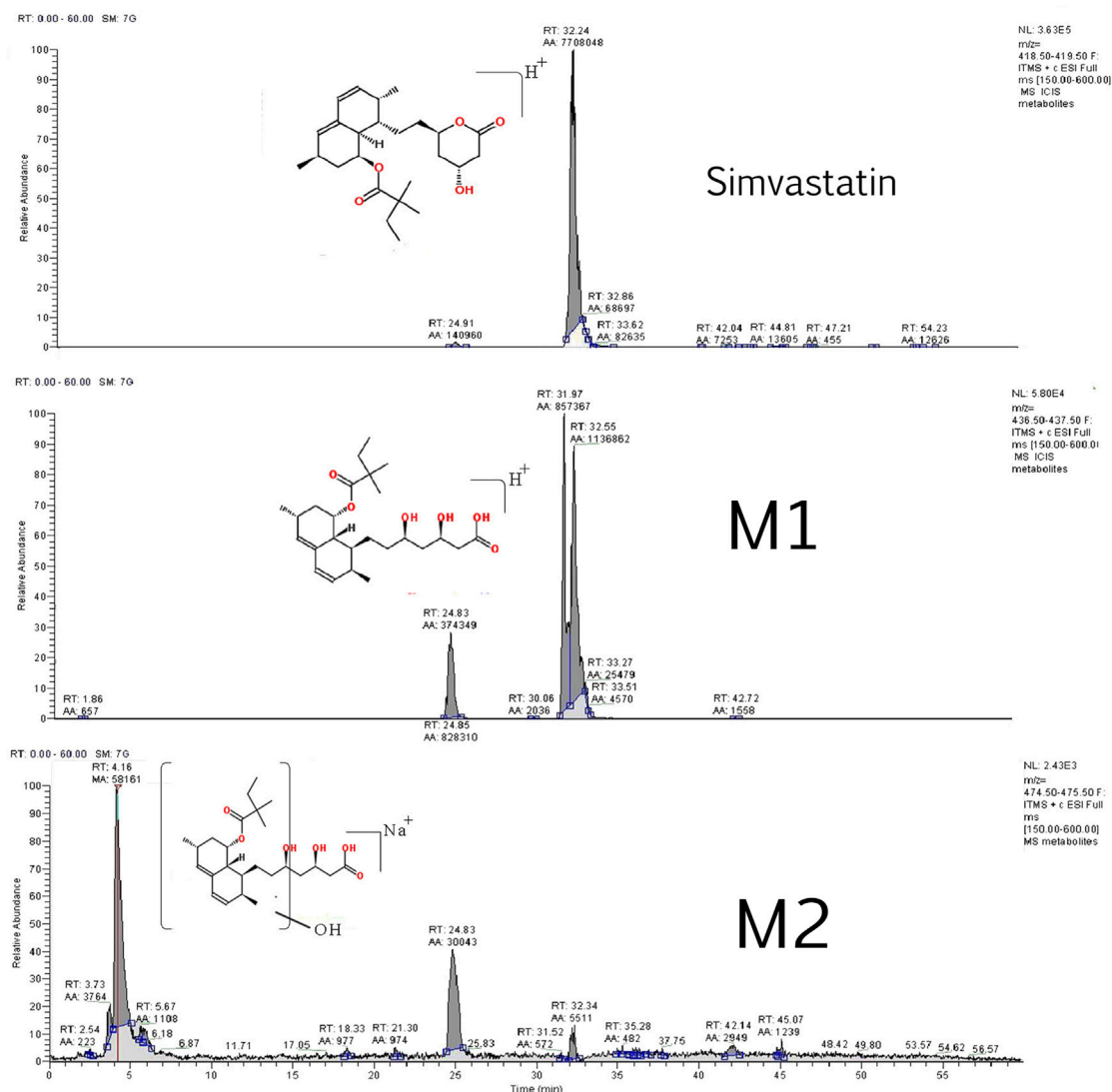


FIGURE 4
Representative extracted ion chromatograms for simvastatin and its metabolites M1 and M2.

4.1 Bioaccumulation of simvastatin by bacterial cells

Although a grown body of evidence indicate that intestinal microbiota can modulate the availability and efficacy of therapeutic drugs, the systematic mapping of the interactions between drugs and bacteria has only started recently. Much of the research up to now has proposed the biotransformation as the main underlying mechanism of interactions between drugs and bacteria. New aspect that gains a great interest of scientific community is a potential of bacteria to accumulate drugs that may largely affect drug bioavailability and effectiveness (Klünemann et al., 2021). Since there are no previous studies on simvastatin bioaccumulation in intestinal bacteria, in this paper we address this mechanism of potential interaction and its implication in simvastatin action.

From the results obtained which pointed to the increase in intracellular level of drug and decrease in extracellular level, it may be concluded that simvastatin has been transported into bacterial cells leading to a drug bioaccumulation over the time. In addition, a decrease in the total

concentration of the drug after 24 h of incubation in the group with probiotic bacteria compared to the control group without bacteria, indicates that the drug has been additionally partly biotransformed by bacterial enzymes (discussed in Section 4.3).

The analysis of the experimental group with probiotic bacteria revealed a significant decrease in the concentration of simvastatin in the extracellular content. At the same time, the drug has been detected in intracellular medium and the concentration rises up to the second hour showing a slight drop after that time. It indicates that the drug has been bioaccumulated by the cells and after some time it has been either metabolized or excreted out from the cells. In addition to the spontaneous release of the drug from the cells, it is assumed that *in vivo* release of the “trapped” drug that remains in the cells will occur only after the cell lysis in the digestive system, which could lead to delayed absorption of simvastatin. Similarly to these results, our previous study demonstrated that antidiabetic drug gliclazide has been transported into probiotic bacteria, being accumulated and partly metabolized through the 24-h incubation (Đanić et al., 2019). Since gliclazide belongs to the same class of drugs as simvastatin according to

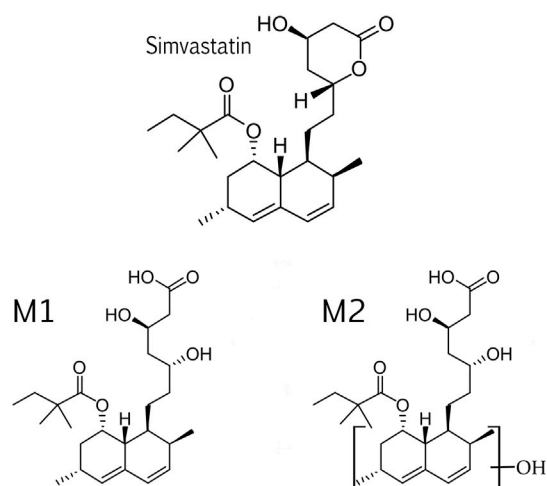


FIGURE 5
Structures of simvastatin and its metabolites, M1 and M2.

the BCS, it may be concluded that similar behavior is to be expected from other drugs with low aqueous solubility and good permeability properties. Furthermore, a recently published study has discovered new examples of drugs that accumulate in bacteria including antidepressant duloxetine, anti-diabetic rosiglitazone, antiasthmatic drug montelukast and roflumilast which is used for chronic obstructive pulmonary disease (Klünemann et al., 2021). Some of these drugs were shown exclusively to be accumulated, while the others were found to be both bioaccumulated and metabolized. The different capacity of drugs bioaccumulation by bacterial species is likely due to specificity in uptake and efflux systems between the cells. Given that drug metabolism by bacterial enzymes has long been considered as the major mechanism of how the bacteria affect the fate of drugs in human body, these results have provided potentially additional mechanisms of drug-bacterial interactions that could largely affect drug bioavailability and therapeutic outcome.

4.2 The influence of bile acids on simvastatin bioaccumulation by bacterial cells

Given that the final outcome of bile acids on drug transport across the biological membrane depends on many factors including type and structure of bile acids, we selected three of them as representatives; one is representative of hydrophilic bile acids (CA), one is representative of lipophilic (DCA) and the third one is semisynthetic bile acid (12-MKC) that has been synthesized in our laboratory. Although there were no significant differences in simvastatin extracellular levels upon addition of bile acids, there was a lower level of a drug in bacterial cells up to the fourth hour, and higher level at the end of the incubation in groups with bile acids compared to the group without bile acids, thus reaching to the conclusion that bile acids may slow down the bioaccumulation process. It indicates that bile acids could to some extent prevent the delayed absorption of simvastatin that may be caused by “trapping” the drug into bacterial cells. The effect of bile acids on simvastatin transport into the cells may be explained from two different aspects, the effect on active and passive transport. In a previously published study, it was demonstrated that all three studied bile acids led to the decrease of the distribution coefficient of

simvastatin in the octanol-buffer system which may be useful in predicting the effect of bile acids on the passive transport of simvastatin across membranes. Decreased distribution coefficient means the reduced affinity for the lipid layer and increased affinity for the aqueous medium, which may explain the reduced drug transport into cells by passive diffusion (Đanić et al., 2016b). Significant insight into the interactions between bile acids and simvastatin has been provided by the computational studies and molecular mechanics calculations where the formation of more hydrophilic aggregates between bile acids and simvastatin has been confirmed, in which bile acids are bonded to simvastatin by hydrophobic interactions, while hydroxyl and keto groups are oriented toward the outer side of the aggregate, thus explaining the higher affinity of the complex for water (Đanić et al., 2016b). Given that the formation of this complex is a reversible process, the free fraction of simvastatin was able to pass through the bacterial membrane, shifting the equilibrium towards the degradation of the complex, thus explaining the slightly higher concentration of simvastatin in bacteria after 24-h incubation. However, the disadvantage of these systems like computational studies and determination of distribution coefficient is the uncertainty of predicting drug behavior in living systems due to additional factors such as the presence of membrane transporters which may be also involved in drug transport across membranes (Kell and Oliver, 2014). Namely, simvastatin may be actively imported into and exported out of the cells *via* bacterial transporters. This assumption is supported by the fact that the same eukaryotic transport proteins (P-gp, MRP2 and OATP1B1) participate in the transport of bile acids and simvastatin (Chen et al., 2005; Klaassen et al., 2010). As there are close homologous proteins of eukaryotic transporters in the bacterial cells with similar substrate specificity (Kourtesi et al., 2013), it is expected that it is possible to achieve competition of simvastatin and bile acids at the level of bacterial transporters as well (Đanić et al., 2016a; Choi et al., 2018). A great affinity of bile acids for a number of so-called multidrug transporters in tested probiotic bacteria has been proved by the molecular docking analyses (Đanić et al., 2016a). Therefore, interactions at the level of transport proteins may be expected. According to our knowledge, this is the very first study examining the uptake of simvastatin into bacterial cells and the effect of bile acids on that process so more in-depth molecular analysis is highly recommended to gain insight into precise transport mechanisms and the affinity of these molecules towards membrane transport proteins in prokaryotic cells.

4.3 Analysis of simvastatin biotransformation pathways by bacterial enzymes

A large number of studies have proved that the intestinal microbiota possesses a variety of metabolic activities that are able to modulate the fate of orally administered drugs and their bioavailability. Drug biotransformation by intestinal bacteria may have either a positive or a negative effect on drug activity and efficacy. Although some drugs such as sulfasalazine are converted by microbial enzymes into their active forms, bacterial metabolism can also inactivate drugs such as digoxin, or cause toxic effects as in the case of irinotecan (Stojančević et al., 2014; Swanson, 2015; Sun et al., 2019).

To expand our understanding of simvastatin-microbiota interactions, we sought to determine whether the depletion of a drug in our screen can be explained partly by the microbial biotransformation and gave preliminary insights into these reactions.

In terms of chemical structure, the simvastatin molecule contains an aromatic backbone attached to dimethylbutanoic acid arm with an ester bond and the ethyl pyranil arm with a covalent C–C-bond forming a lactone structure (Aura et al., 2011). The lactone ring in simvastatin molecule is susceptible to spontaneous hydrolysis, which is pH dependent, being more pronounced in alkaline than in acidic media (Álvarez-Lueje et al., 2005; Malenović et al., 2010; Beltrán et al., 2019). As the experiment was performed at pH 7.4, and the drug level in the control group without probiotic bacteria at the end of the incubation period were 35% lower compared to the initial concentration it is assumed that simvastatin has been partially spontaneously hydrolyzed to the acid. However, during the whole incubation period the total drug level (as a sum of intracellular and extracellular level) in the group with probiotic bacteria was generally significantly lower compared to the control group indicating that in addition to the potential spontaneous degradation, a drug has been also metabolized by the bacterial enzymes. Hydrolysis of the lactone ring and the formation of M1 metabolite i.e. hydroxy acid form of simvastatin may be the also the result of metabolic biotransformation by esterases of probiotic bacteria *Lactobacillus* and *Bifidobacterium* (Arora et al., 1990; Gavini et al., 1991; Brod et al., 2010). Hydroxylated hydroxy acid metabolite, confirmed by experimental assay as M2 metabolite, may be the result of further metabolic biotransformation of M1 metabolite i.e. subsequent hydroxylation that is in agreement with computational predictions. Additionally, these findings are directly in line with results of a previously published *in vivo* study related to gut microbiota-mediated interactions with lovastatin, which differs only in one methyl group in side chain from simvastatin, showing that upon ester hydrolysis and lactone ring opening, subsequent reaction of hydroxylation is likely to occur (Yoo et al., 2014). The enzymes responsible for this reaction, hydroxylases, have been documented in examined bacteria (Brod et al., 2010; Kim and Oh, 2013; Szaleniec et al., 2018).

5 Conclusion

In summary, the results of our study suggest that bioaccumulation and biotransformation of simvastatin by intestinal bacteria might be the underlying mechanisms of altered drug availability and therapeutic effect. It has been shown that bile acids affect the bacterial bioaccumulation of a drug affecting both, the active and passive transport that can consequently reflect on absorption rate of a drug. Obtained results and proposed metabolic pathways may be of the vital importance in further elucidation of microbial implication into simvastatin therapeutic outcome. However, the limitation of this study is that it is based only on selected bacterial strains in *vitro* conditions, and further more in-depth research is thus needed in order to reveal how bioaccumulation and biotransformation of simvastatin by intestinal microbiota manifests inside the human body and to elicit completely the contribution of complex drug-microbiota-bile acids interactions to overall clinical response. Therefore, the results of this study provide a strong rationale for further investigations of the effects of drug-gut microbiota-bile acids interactions outside of the usual box of biotransformation. Mapping these interactions would help us better

predict clinical outcome in patients providing a good basis for the optimized personalized therapy with the long-term goal of integrating this information into clinical practice.

Data availability statement

The original contributions presented in the study are included in the article/Supplementary Material, further inquiries can be directed to the corresponding author.

Author contributions

MĐ performed the literature search and drafted the manuscript. MĐ, NP, SL, and SV contributed to designing the experiments, analyzing and interpreting the data. MĐ, BS, and SV performed the experiments. All authors edited, revised critically and approved the final version of this review.

Funding

This work was supported by the Project of Ministry of Education, Science and Technological Development, Republic of Serbia No 451-03-68/2022-14/200114 and the Project for Scientific and Technological Development of Vojvodina (142-451-3179/2022). The work has been partially supported by Telethon Project grant (2022), by Curtin Faculty ORS-WAHAI Consortium (2021) and the Australian National Health and Medical Research (APP9000597).

Conflict of interest

The authors declare that the research was conducted in the absence of any commercial or financial relationships that could be construed as a potential conflict of interest.

Publisher's note

All claims expressed in this article are solely those of the authors and do not necessarily represent those of their affiliated organizations, or those of the publisher, the editors and the reviewers. Any product that may be evaluated in this article, or claim that may be made by its manufacturer, is not guaranteed or endorsed by the publisher.

Supplementary material

The Supplementary Material for this article can be found online at: <https://www.frontiersin.org/articles/10.3389/fphar.2023.1111115/full#supplementary-material>

References

- Álvarez-Lueje, A., Valenzuela, C., Squella, J. A., and Núñez-Vergara, L. J. (2005). Stability study of simvastatin under hydrolytic conditions assessed by liquid chromatography. *J. AOAC Int.* 88, 1631–1636. doi:10.1093/jaoac/88.6.1631
- Ankrah, N. Y. D., and Barker, B. E. (2021). Predicted Metabolic Function of the Gut Microbiota of *Drosophila melanogaster*. *mSystems* 6 (3), e01369-20. doi:10.1128/mSystems.01369-20

- Arora, G., Lee, B., and Lamoureux, M. (1990). Characterization of enzyme profiles of *Lactobacillus casei* species by a rapid API ZYM system. *J. Dairy Sci.* 73, 264–273. doi:10.3168/jds.S0022-0302(90)78669-9
- Aura, A. M., Mattila, I., Hyötyläinen, T., Gopalacharyulu, P., Bounsaythip, C., Orešič, M., et al. (2011). Drug metabolome of the simvastatin formed by human intestinal microbiota *in vitro*. *Mol. Biosyst.* 7, 437–446. doi:10.1039/c0mb00023j
- Beltrán, D., Frutos-Lisón, M. D., Espín, J. C., and García-Villalba, R. (2019). Re-examining the role of the gut microbiota in the conversion of the lipid-lowering statin monacolin K (lovastatin) into its active β -hydroxy acid metabolite. *Food Funct.* 10 (4), 1787–1791. doi:10.1039/c8fo02594k
- Bisanz, J. E., Spanogiannopoulos, P., Pieper, L. M., Bustion, A. E., and Turnbaugh, P. J. (2018). How to determine the role of the microbiome in drug disposition. *Drug Metab. Dispos.* 46, 1588–1595. doi:10.1124/dmd.118.083402
- Brod, F. C., Vernal, J., Bertoldo, J. B., Terenzi, H., and Arisi, A. C. (2010). Cloning, expression, purification, and characterization of a novel esterase from *Lactobacillus plantarum*. *Mol. Biotechnol.* 44, 242–249. doi:10.1007/s12033-009-9232-2
- Carlsson, L., Spjuth, O., Adams, S., Glen, R. C., and Boyer, S. (2010). Use of historic metabolic biotransformation data as a means of anticipating metabolic sites using MetaPrint2D and Bioclipse. *BMC Bioinforma.* 11, 362. doi:10.1186/1471-2105-11-362
- Chen, C., Mireles, R. J., Campbell, S. D., Lin, J., Mills, J. B., Xu, J. J., et al. (2005). Differential interaction of 3-hydroxy-3-methylglutaryl-coa reductase inhibitors with ABCB1, ABCG2, and OATP1B1. *Drug Metab. Dispos.* 33, 537–546. doi:10.1124/dmd.104.002477
- Choi, M. S., Yu, J. S., Yoo, H. H., and Kim, D. H. (2018). The role of gut microbiota in the pharmacokinetics of antihypertensive drugs. *Pharmacol. Res.* 130, 164–171. doi:10.1016/j.phrs.2018.01.019
- Cullen, C. M., Aneja, K. K., Beyhan, S., Cho, C. E., Woloszynek, S., Convertino, M., et al. (2020). Emerging priorities for microbiome research. *Front. Microbiol.* 11, 136. doi:10.3389/fmicb.2020.00136
- Danić, M., and Mikov, M. (2020). “Biotransformation of xenobiotics in living systems—metabolism of drugs: Partnership of liver and gut microflora,” in *Pharmaceutical biocatalysis* (Jenny Stanford Publishing), 129–166.
- Danić, M., Pavlović, N., Stanimirov, B., Lazarević, S., Vukmirović, S., Al-Salami, H., et al. (2021). PAMPA model of glizalide permeability: The impact of probiotic bacteria and bile acids. *Eur. J. Pharm. Sci.* 158, 105668. doi:10.1016/j.ejps.2020.105668
- Danić, M., Pavlović, N., Stanimirov, B., Stojančević, T., Goločorbin-Kon, S., Bojić, G., et al. (2016a). Docking-based preliminary study on the interactions of bile acids with drugs at the transporter level in intestinal bacteria. *Eur. Rev. Med. Pharmacol. Sci.* 20, 553–560. doi:10.26355/eurrev_202112_27449
- Danić, M., Pavlović, N., Stanimirov, B., Vukmirović, S., Nikolić, K., Agbaba, D., et al. (2016b). The influence of bile salts on the distribution of simvastatin in the octanol/buffer system. *Drug Dev. Ind. Pharm.* 42, 661–667. doi:10.3109/03639045.2015.1067626
- Danić, M., Stanimirov, B., Pavlović, N., Goločorbin-Kon, S., Al-Salami, H., Stankov, K., et al. (2018). Pharmacological applications of bile acids and their derivatives in the treatment of metabolic syndrome. *Front. Pharmacol.* 9, 1382. doi:10.3389/fphar.2018.01382
- Danić, M., Stanimirov, B., Pavlović, N., Vukmirović, S., Lazić, J., Al-Salami, H., et al. (2019). Transport and biotransformation of glizalide and the effect of deoxycholic acid in a probiotic bacteria model. *Front. Pharmacol.* 10, 1083. doi:10.3389/fphar.2019.01083
- De Angelis, G. (2004). The influence of statin characteristics on their safety and tolerability. *Int. J. Clin. Pract.* 58 (10), 945–955. doi:10.1111/j.1368-5031.2004.00355.x
- EAWAG-BBD Pathway Prediction System (2010). *Switzerland: Eawag - Swiss federal Institute of aquatic science and Technology*. Available at: <https://www.eawag.ch/en/> (Accessed Dec 29, 2022).
- ElRakaiby, M., Dutilh, B. E., Rizkallah, M. R., Boleij, A., Cole, J. N., and Aziz, R. K. (2014). Pharmacomicrobiomics: The impact of human microbiome variations on systems pharmacology and personalized therapeutics. *Omicron J. Integr. Biol.* 18, 402–414. doi:10.1089/omi.2014.0018
- Enright, E. F., Gahan, C. G. M., Joyce, S. A., and Griffin, B. T. (2016). The impact of the gut microbiota on drug metabolism and clinical outcome. *Yale J. Biol. Med.* 89, 375–382. doi:10.1021/acs.molpharmaceut.6b01155
- Fuller, A. T. (1937). Is p-Aminobenzenesulphonamide the active agent in prontosil therapy? *Lancet* 229, 194–198. doi:10.1016/S0140-6736(00)97447-6
- Gambhira, M., Bhalekar, M., and Shrivastava, B. (2011). Bioavailability assessment of simvastatin loaded solid lipid nanoparticles after oral administration. *Asian J. Pharm. Sci.* 6, 6.
- Gavini, F., Pourcher, A. M., Neut, C., Monget, D., Romond, C., Oger, C., et al. (1991). Phenotypic differentiation of bifidobacteria of human and animal origins. *Int. J. Syst. Bacteriol.* 41, 548–557. doi:10.1099/00207713-41-4-548
- Geboers, S., Stappaerts, J., Tack, J., Annaert, P., and Augustijns, P. (2016). *In vitro* and *in vivo* investigation of the gastrointestinal behavior of simvastatin. *Int. J. Pharm.* 510, 296–303. doi:10.1016/j.ijpharm.2016.06.048
- He, X., Zheng, N., He, J., Liu, C., Feng, J., Jia, W., et al. (2017). Gut microbiota modulation attenuated the hypolipidemic effect of simvastatin in high-fat/cholesterol-diet fed mice. *J. Proteome Res.* 16 (5), 1900–1910. doi:10.1021/acs.jproteome.6b00984
- Hirth, D. (2011). A new combined LC (ESI+) MS/MS QTOF impurity fingerprinting and chemometrics approach for discriminating active pharmaceutical ingredient origins: example of simvastatin. *Anal. Chem.*, dumas-00960820.
- Kaddurah-Doak, R., Baillie, R. A., Zhu, H., Zeng, Z. B., Wiest, M. M., Nguyen, U. T., et al. (2011). Enteric microbiome metabolites correlate with response to simvastatin treatment. *PLoS One* 6 (10), e25482. doi:10.1371/journal.pone.0025482
- Karąźniewicz-Lada, M., Bąba, K., Dolatowski, F., Dobrowolska, A., and Rakicka, M. (2018). The polymorphism of statins and its effect on their physicochemical properties. *Polim. Med.* 48, 77–82. doi:10.17219/pim/102978
- Karp, P. D., Billington, R., Caspi, R., Fulcher, C. A., Latendresse, M., Kothari, A., et al. (2019). The BioCyc collection of microbial genomes and metabolic pathways. *Brief. Bioinform* 20, 1085–1093. doi:10.1093/bib/bbx085
- Kell, D. B., and Oliver, S. G. (2014). How drugs get into cells: Tested and testable predictions to help discriminate between transporter-mediated uptake and lipid bilayer diffusion. *Front. Pharmacol.* 5, 231. doi:10.3389/fphar.2014.00231
- Kim, K. R., and Oh, D. K. (2013). Production of hydroxy fatty acids by microbial fatty acid-hydroxylation enzymes. *Biotechnol. Adv.* 31, 1473–1485. doi:10.1016/j.biotechadv.2013.07.004
- Klaassen, C. D., and Aleksunes, L. M. (2010). Xenobiotic, bile acid, and cholesterol transporters: Function and regulation. *Pharmacol. Rev.* 62, 1–96. doi:10.1124/pr.109.002014
- Klünemann, M., Andrejev, S., Blasche, S., Mateus, A., Phapale, P., Devendran, S., et al. (2021). Bioaccumulation of therapeutic drugs by human gut bacteria. *Nature* 597, 533–538. doi:10.1038/s41586-021-03891-8
- Korani, S., Bahrami, S., Korani, M., Banach, M., Johnston, T. P., and Sahebkar, A. (2019). Parenteral systems for statin delivery: A review. *Lipids Health Dis.* 18, 193. doi:10.1186/s12944-019-1139-8
- Kourtesi, C., Ball, A. R., Huang, Y.-Y., Jachak, S. M., Vera, D. M. A., Khondkar, P., et al. (2013). Microbial efflux systems and inhibitors: Approaches to drug discovery and the challenge of clinical implementation. *Open Microbiol. J.* 7, 34–52. doi:10.2174/1874285801307010034
- Lazarević, S., Danić, M., Al-Salami, H., Mooranian, A., and Mikov, M. (2022). Gut microbiota metabolism of azathioprine: A new hallmark for personalized drug-targeted therapy of chronic inflammatory bowel disease. *Front. Pharmacol.* 13, 879170. doi:10.3389/fphar.2022.879170
- Lee, H. H., and Ho, R. H. (2017). Interindividual and interethnic variability in drug disposition: Polymorphisms in organic anion transporting polypeptide 1B1 (OATP1B1; SLC01B1). *Br. J. Clin. Pharmacol.* 83, 1176–1184. doi:10.1111/bcp.13207
- Liu, F., Ma, R., Riordan, S. M., Grimm, M. C., Liu, L., Wang, Y., et al. (2017). Azathioprine, mercaptopurine, and 5-aminosalicylic acid affect the growth of IBD-associated campylobacter species and other enteric microbes. *Front. Microbiol.* 8, 527. doi:10.3389/fmicb.2017.00527
- Malenović, A., Jančić-Stojanović, B., Ivanović, D., and Medenica, M. (2010). Forced degradation studies of simvastatin using microemulsion liquid chromatography. *J. Liq. Chromatogr. Relat. Technol.* 33, 536–547. doi:10.1080/10826070903574576
- Miljković, D., Kuhajda, K., and Hranisavljević, J. (1996). Selective C-12 oxidation of cholic acid. *J. Chem. Research-Part S Synop.*, 106–107. doi:10.1002/chin.199631177
- Moghimpour, E., Ameri, A., and Handali, S. (2015). Absorption-enhancing effects of bile salts. *Mol. (Basel, Switz.)* 20, 14451–14473. doi:10.3390/molecules200814451
- Mooranian, A., Ionescu, C. M., Wagle, S. R., Kovacevic, B., Walker, D., Jones, M., et al. (2021). Chenodeoxycholic acid pharmacology in biotechnology and transplantable pharmaceutical applications for tissue delivery: An acute preclinical study. *Cells* 10 (9), 2437. doi:10.3390/cells10092437
- Natalini, B., Sardella, R., Camaioni, E., Gioiello, A., and Pellicciari, R. (2007). Correlation between CMC and chromatographic index: Simple and effective evaluation of the hydrophobic/hydrophilic balance of bile acids. *Anal. Bioanal. Chem.* 388, 1681–1688. doi:10.1007/s00216-007-1360-6
- Pasanen, M. K., Neuvonen, M., Neuvonen, P. J., and Niemi, M. (2006). SLC01B1 polymorphism markedly affects the pharmacokinetics of simvastatin acid. *Pharmacogenet Genomics* 16, 873–879. doi:10.1097/01.fpc.0000230416.82349.90
- Pavlović, N., Bogičević, I. A., Zaklan, D., Danić, M., Goločorbin-Kon, S., Al-Salami, H., et al. (2022). Influence of bile acids in hydrogel pharmaceutical formulations on dissolution rate and permeation of clindamycin hydrochloride. *Gels* 8, 35. doi:10.3390/gels8010035
- Pavlović, N., Goločorbin-Kon, S., Danić, M., Stanimirov, B., Al-Salami, H., Stankov, K., et al. (2018). Bile acids and their derivatives as potential modifiers of drug release and pharmacokinetic profiles. *Front. Pharmacol.* 9, 1283. doi:10.3389/fphar.2018.01283
- Postmus, I., Trompet, S., Deshmukh, H. A., Barnes, M. R., Li, X., Warren, H. R., et al. (2014). Pharmacogenetic meta-analysis of genome-wide association studies of LDL cholesterol response to statins. *Nat. Commun.* 5, 5068. doi:10.1038/ncomms6068
- Ramsey, L. B., Johnson, S. G., Caudle, K. E., Haidar, C. E., Voora, D., Wilke, R. A., et al. (2014). The clinical pharmacogenetics implementation consortium guideline for SLC01B1 and simvastatin-induced myopathy: 2014 update. *Clin. Pharmacol. Ther.* 96, 423–428. doi:10.1038/clpt.2014.125
- Reiter-Brennan, C., Osei, A. D., Iftikhar Uddin, S. M., Orimoloye, O. A., Obisesan, O. H., Mirbolouk, M., et al. (2020). ACC/AHA lipid guidelines: Personalized care to prevent cardiovascular disease. *Cleve Clin. J. Med.* 87 (4), 231–239. doi:10.3949/ccjm.87a.19078

- Rezazadeh, M., and Babaeipour, V. (2020). Reconstruction, verification and in-silico analysis of a genome-scale metabolic model of bacterial cellulose producing *Komagataeibacter xylinus*. *Bioprocess. Biosyst. Eng.* 43 (6), 1017–1026. doi:10.1007/s00449-020-02299-4
- Scher, J. U., Nayak, R. R., Ubeda, C., Turnbaugh, P. J., and Abramson, S. B. (2020). Pharmacomicrobiomics in inflammatory arthritis: Gut microbiome as modulator of therapeutic response. *Nat. Rev. Rheumatol.* 16, 282–292. doi:10.1038/s41584-020-0395-3
- Stojančević, M., Bojić, G., Salami, H. A., and Mikov, M. (2014). The influence of intestinal tract and probiotics on the fate of orally administered drugs. *Curr. Issues Mol. Biol.* 16, 55–68. doi:10.21775/cimb.016.055
- Stojančević, M., Pavlović, N., Goločorbin-Kon, S., and Mikov, M. (2013). Application of bile acids in drug formulation and delivery. *Front. Life Sci.* 7, 112–122. doi:10.1080/21553769.2013.879925
- Sun, C., Chen, L., and Shen, Z. (2019). Mechanisms of gastrointestinal microflora on drug metabolism in clinical practice. *Saudi Pharm. J.* 27 (8), 1146–1156. doi:10.1016/j.jpsp.2019.09.011
- Swanson, H. I. (2015). Drug metabolism by the host and gut microbiota: A partnership or rivalry? *Drug Metab. Dispos.* 43 (10), 1499–1504. doi:10.1124/dmd.115.065714
- Szaleniec, M., Wojtkiewicz, A. M., Bernhardt, R., Borowski, T., and Donova, M. (2018). Bacterial steroid hydroxylases: Enzyme classes, their functions and comparison of their catalytic mechanisms. *Appl. Microbiol. Biotechnol.* 102, 8153–8171. doi:10.1007/s00253-018-9239-3
- Trompet, S., Postmus, I., Slagboom, P. E., Heijmans, B. T., Smit, R. A. J., Maier, A. B., et al. (2016). Non-response to (statin) therapy: The importance of distinguishing non-responders from non-adherers in pharmacogenetic studies. *Eur. J. Clin. Pharmacol.* 72, 431–437. doi:10.1007/s00228-015-1994-9
- Wahlström, A., Sayin, S. I., Marschall, H.-U., and Bäckhed, F. (2016). Intestinal crosstalk between bile acids and microbiota and its impact on host metabolism. *Cell Metab.* 24, 41–50. doi:10.1016/j.cmet.2016.05.005
- Wilson, I. D., and Nicholson, J. K. (2017). Gut microbiome interactions with drug metabolism, efficacy, and toxicity. *Transl. Res. J. laboratory Clin. Med.* 179, 204–222. doi:10.1016/j.trsl.2016.08.002
- Yang, L., Zhang, H., Mikov, M., and Tucker, I. G. (2009). Physicochemical and biological characterization of monoketocholic acid, a novel permeability enhancer. *Mol. Pharm.* 6 (2), 448–456. doi:10.1021/mp800143w
- Ye, X. Y., and Devasthale, P. (2016). “Carboxylic acids and lactones as HMG-CoA reductase inhibitors,” in *Bioactive carboxylic compound classes: Pharmaceuticals and agrochemicals*. Editors C. Lamberth and J. Dinges (John Wiley & Sons).
- Yoo, D. H., Kim, I. S., Van Le, T. K., Jung, I. H., Yoo, H. H., and Kim, D. H. (2014). Gut microbiota-mediated drug interactions between lovastatin and antibiotics. *Drug Metab. Dispos.* 42, 1508–1513. doi:10.1124/dmd.114.058354
- Zimmermann, M., Zimmermann-Kogadeeva, M., Wegmann, R., and Goodman, A. L. (2019). Mapping human microbiome drug metabolism by gut bacteria and their genes. *Nature* 570, 462–467. doi:10.1038/s41586-019-1291-3



OPEN ACCESS

EDITED BY

Junmin Zhang,
Lanzhou University, China

REVIEWED BY

Ying-yuan Lu,
Peking University, China
Ping Wang,
Shanghai University of Traditional Chinese
Medicine, China

*CORRESPONDENCE

Lingyi Huang,
✉ lingyi.huang@fjmu.edu.cn

[†]These authors have contributed equally to
this work

SPECIALTY SECTION

This article was submitted to Drug
Metabolism and Transport,
a section of the journal
Frontiers in Pharmacology

RECEIVED 26 November 2022

ACCEPTED 30 January 2023

PUBLISHED 15 February 2023

CITATION

Lin F, Lin X, Wang X, Mei G, Chen B, Yao H
and Huang L (2023), Inhibitory effect of
Selaginella doederleinii hieron on human
cytochrome P450.
Front. Pharmacol. 14:1108867.
doi: 10.3389/fphar.2023.1108867

COPYRIGHT

© 2023 Lin, Lin, Wang, Mei, Chen, Yao and
Huang. This is an open-access article
distributed under the terms of the [Creative
Commons Attribution License \(CC BY\)](#).
The use, distribution or reproduction in
other forums is permitted, provided the
original author(s) and the copyright
owner(s) are credited and that the original
publication in this journal is cited, in
accordance with accepted academic
practice. No use, distribution or
reproduction is permitted which does not
comply with these terms.

Inhibitory effect of *Selaginella doederleinii* hieron on human cytochrome P450

Fei Lin^{1†}, Xinhua Lin^{1†}, Xuewen Wang², Guanghui Mei¹, Bing Chen¹,
Hong Yao¹ and Lingyi Huang^{1*}

¹Department of Pharmaceutical Analysis, School of Pharmacy, Fujian Medical University, Fuzhou, China,

²Department of Preventive Medicine, School of Public Health, Fujian Medical University, Fuzhou, China

Introduction: *Selaginella doederleinii* Hieron is a traditional Chinese herbal medicine, the ethyl acetate extract from *Selaginella doederleinii* (SDEA) showed favorable anticancer potentials. However, the effect of SDEA on human cytochrome P450 enzymes (CYP450) remains unclear. To predict the herb-drug interaction (HDI) and lay the groundwork for further clinical trials, the inhibitory effect of SDEA and its four constituents (Amentoflavone, Palmatine, Apigenin, Delicaflavone) on seven CYP450 isoforms were investigated by using the established CYP450 cocktail assay based on LC-MS/MS.

Methods: Appropriate substrates for seven tested CYP450 isoforms were selected to establish a reliable cocktail CYP450 assay based on LC-MS/MS. The contents of four constituents (Amentoflavone, Palmatine, Apigenin, Delicaflavone) in SDEA were determined as well. Then, the validated CYP450 cocktail assay was applied to test the inhibitory potential of SDEA and four constituents on CYP450 isoforms.

Results: SDEA showed strong inhibitory effect on CYP2C9 and CYP2C8 ($IC_{50} \approx 1 \mu g/ml$), moderate inhibitory effect against CYP2C19, CYP2E1 and CYP3A ($IC_{50} < 10 \mu g/ml$). Among the four constituents, Amentoflavone had the highest content in the extract (13.65%) and strongest inhibitory effect ($IC_{50} < 5 \mu M$), especially for CYP2C9, CYP2C8 and CYP3A. Amentoflavone also showed time-dependent inhibition on CYP2C19 and CYP2D6. Apigenin and Palmatine both showed concentration-dependent inhibition. Apigenin inhibited CYP1A2, CYP2C8, CYP2C9, CYP2E1 and CYP3A. Palmatine inhibited CYP3A and had a weak inhibitory effect on CYP2E1. As for Delicaflavone, which has the potential to develop as an anti-cancer agent, showed no obvious inhibitory effect on CYP450 enzymes.

Conclusion: Amentoflavone may be one of the main reasons for the inhibition of SDEA on CYP450 enzymes, the potential HDI should be considered when SDEA or Amentoflavone were used with other clinical drugs. On the contrast, Delicaflavone is more suitable to develop as a drug for clinical use, considering the low level of CYP450 metabolic inhibition.

KEYWORDS

herb-drug interaction, the ethyl acetate extract from *S. doederleinii*, CYP inhibition, cocktail CYP450 assay, time-dependent inhibition, delicaflavone, amentoflavone

1 Introduction

Numerous studies have shown that drug-drug interaction (DDI) can cause serious adverse reactions, drug ineffectiveness and even death (Han et al., 2012; Kozakai et al., 2012; Al-Ramahi et al., 2015; Guengerich, 2021). Induction or inhibition of human Cytochromes P450 (CYP450) enzyme by compounds is the main cause for drug-drug metabolic interaction (Qin et al., 2013). About 60%–70% of the clinical drugs are clear by phase I reaction, where 75% of the involved metabolizing enzymes are CYP450 isoforms (Kim et al., 2005; Lee and Kim, 2013). Usually, CYP450 inhibition leads to drug accumulation and even toxicity (Lin and Lu, 1998; Guengerich, 2008; Hakkola et al., 2020). Based on that, DDI test is necessary for a chemical from pre-clinical stage into clinical trials in pharmaceutical industry. The United States Food and Drug Administration (FDA) guidelines for DDI test have recommended several major human CYP450 isoforms, including CYP1A2, CYP2C8, CYP2C9, CYP2C19, CYP2D6 and CYP3A. Those CYP450 isoforms have account for mostly enzymatic metabolism of clinical drugs (Prueksaritanont et al., 2013; Sudsakorn et al., 2020). Although CYP2E1 was not clearly specified in the FDA guidelines, many studies have revealed that CYP2E1 can metabolize Coumarin, Quinoline, Isoniazid, ethanol, Caffeine, acetaminophen and other substances. Therefore, it is reasonable to include CYP2E1 when conducting the DDI study (Valicherla et al., 2019).

Nowadays, many people consume herbal products for self-health or medical use in their daily life. Similar to small molecule medicine, when people take herbal products and drugs at the same time, potential herb-drug interaction (HDI) should be considered as well (van Breemen, 2015). In the past 20 years, more and more studies have shown that there are significant CYP450 enzyme interaction between herbal products and prescription medicines, which will increase patients' risk of unnecessary and unintended adverse effect. For example, *Angelica dahurica* root extract inhibited CYP450 enzymes such as CYP2C, CYP3A and CYP2D1, and caused pharmacokinetic and pharmacodynamic interactions with Tolbutamide and Diazepam (Ishihara et al., 2000). Shenmai injection, one of the most popular herbal medicines in China, has reported to inhibit CYP3A1/2 and CYP2C6 (Xia et al., 2010). Researchers have found that Huanglian [*Rhizoma coptidis* (L.)] has obvious inhibition on CYP2D6 (Han et al., 2011). *Newbouldia laevis* extract inhibited the enzyme activities of CYP1A2, CYP2C9, CYP2C19, and *Newbouldia laevis* showed time-dependent inhibition effect on CYP1A2 (Thomford et al., 2016). Licorice is a common use dietary supplement even is consumed as a condiment, which was found to inhibit several CYP450 enzymes. What's more, three major licorice species (*G. glabra*, *G. uralensis* and *G. inflata*) showed unique pattern of enzyme inhibition (Li et al., 2017). The most reported CYP450 isoforms involved in HDI are CYP1A2, CYP2C, CYP2D6 and CYP3A, which is similar to the list of small molecules DDI test according to FDA guideline (Choi et al., 2016; Awortwe et al., 2018).

Selaginella doederleinii Hieron belongs to *Selaginella* genus of the Selaginellaceae family and is commonly used as a traditional Chinese herbal medicine, which was reported to have anti-hyperglycemia, anti-virus, anti-cancer and other pharmacological activities, and used in the treatment of nasopharyngeal carcinoma, lung cancer and trophoblastic tumor (Zheng et al., 2005; Chen et al., 2018). The previous *in vitro* and *in vivo* studies have revealed that the ethyl acetate extract from *S. doederleinii* (SDEA) had anti-cancer effect (Yao

et al., 2017), especially for lung and colorectal cancer (Sui et al., 2016; Li et al., 2020). Those main ingredients from the extract, such as Amentoflavone, Palmatine, Apigenin and Delicaflavone, may account for the pharmacological activities of SDEA. Among those components, Delicaflavone was proved to induce apoptosis in cervical cancer HeLa cells (Yao et al., 2019), colorectal cancer cells (Yao et al., 2020) and lung cancer cells (Sui et al., 2017). Moreover, Delicaflavone can reverse cisplatin resistance via endoplasmic reticulum stress signaling pathway in non-small cell lung cancer cells, which may serve as a useful adjunct in treatment of cisplatin-resistant lung cancer (Wang et al., 2020). Therefore, SDEA and Delicaflavone are the most promising anti-tumor agents, whether use alone or in combination with other drugs.

Although the pharmacological activities of SDEA and its bioactive compounds have been extensively studied, there is no report on HDI of SDEA on human CYP450 enzymes. As a plant extract, the composition of SDEA is complex, whose metabolic process in human body is not fully understood. Meanwhile, the HDI study for the bioactive components of SDEA have not been conducted either. The pre-clinical study on the ADME properties of candidate compound is of great significance for improving success rate, reducing cost and toxic risk, which is crucial for further drug development. This rule also applies to herbal product drug development (Brantley et al., 2014). Regulatory agencies in most countries, such as FDA, EMA, NMPA, et al., all require that new chemicals should be clarified the possible inhibition or induction effect on human CYP450 enzyme in the investigational new drug (IND) application stage. For newly developed medicines, they are likely to be accepted on the market only if they have clear human metabolic information (Sudsakorn et al., 2020). Based on that, it is necessary for SDEA and its bioactive compounds to screen the potential HDI before moving into clinical trials stage. Thus, a reliable HDI test assay is needed.

Compared to *in vivo* animal test, *in vitro* CYP450 probe substrate approach can provide reliable context and prospective knowledge in terms of less cost and time (Bjornsson et al., 2003; Venkatakrishnan et al., 2003), which are widely used in DDI and HDI study. Moreover, since human and animals (rat, mice et al.) have essential differences in basic tissue, cell structure and metabolic types, *in vitro* HDI assay usually uses commercial human liver microsomes (HLM) or human recombinant CYP450 enzymes (Lu and Di, 2020). Traditional CYP450 substrate method owns low efficiency because it only uses one probe substrate to test the activity of one metabolic enzyme at a time ("one-in-one" assay), which is difficult to meet the requirements of high throughput screening (Lin and Lu, 1998). However, as the development of high performance liquid chromatography-tandem mass spectrometry (HPLC-MS/MS), this problem has been solved finally. The triple quadrupole LC-MS can select specific substrate metabolites for determination by using multiple reaction monitoring (MRM), which has better selectivity and specificity compared with other analytical methods (liquid chromatography-UV, fluorescence and luminescence detections, etc.) (Youdim and Saunders, 2010). Based on the advantages of LC-MS/MS, the cocktail CYP450 assay ("N-in-one" assay) have been developed, which can simultaneously test the inhibitory effects of several CYP450 isoforms in one assay, with the effect of significantly reducing cost and time to evaluate DDI or HDI (Li et al., 2015; Liua et al., 2015; Spaggiari et al., 2016). The cocktail assay is very suitable for high-throughput screening in drug development process, especially for early drug metabolism studies, which is extremely important for dose design of those compounds

with multiple metabolic pathways. It has been applied to monitor the *in vitro* inhibition activity of various CYP450 enzymes and time-dependent inhibition study (Chen et al., 2016). Therefore, in our study, an *in vitro* cocktail CYP450 assay was established with LC-MS/MS to reflect the activities of corresponding CYP450 isoforms. This assay was able to monitor the metabolic changes of specific substrates and validated by known enzymes inhibitors, so that it could achieve more accurate detection, better sensitivity and less interference.

In summary, we established an *in vitro* cocktail CYP450 assay by LC-MS/MS to detect the inhibitory effects of SDEA and its four constituents (Amentoflavone, Palmatine, Apigenin and Delicaflavone) on seven human CYP450 isoforms: CYP1A2, CYP2C8, CYP2C9, CYP2C19, CYP2D6, CYP2E1 and CYP3A. To determine whether SDEA and its components are the potential inhibitors of any of those important human CYP450 isoforms. Our research could reveal the metabolic interactions between CYP450 enzymes and SDEA constituents, which could clarify the clinical safety issues and promote the drug development of SDEA and its constituents.

2 Materials and methods

2.1 Materials and chemicals

Pooled mixed gender human liver microsomes from 50 donors were purchased from XenoTech (Lenexa, United States), β -nicotinamide adenine dinucleotide phosphate (NADPH) were purchased from solarbiobio (Beijing, China), Omeprazole (HPLC purity > 99%), Taxol (HPLC purity > 99%), Tolbutamide (HPLC purity > 99%), Chlorzoxazone (HPLC purity > 99%), Dextromethorphan Hydrobromide (HPLC purity > 98%), Alpha-Naphthoflavone (HPLC purity > 98%), Fluconazole (HPLC purity > 98%), Quercetin (HPLC purity > 98%) and Ketoconazole (HPLC purity > 99%) were purchased from Dalian Meilunbio. Co. Ltd (Dalian, China), Phenaceti (HPLC purity > 99%), Sulfaphenazolum (HPLC purity > 99%), Quinidine (HPLC purity > 99%) were purchased from Shyuanye Biotechnology Co. Ltd (Shanghai, China), Testosterone (HPLC purity > 98%) were purchased from Derick Biotechnology Co. Ltd (Chengdu, China), 4-Methylpyrazole (HPLC purity > 97%) were purchased from J&K Scientific (San Jose, United States).

The SDEA extract was prepared following our previously described procedure (Sui et al., 2016; Yao et al., 2017). Delicaflavone (purity \geq 98%, determined by the peak area normalization method using HPLC-PDA) were isolated from *S. doederleinii* and the structure was fully elucidated by MS, UV, ^1H -NMR and ^{13}C -NMR, which was confirmed by comparison with the literatures (Li et al., 2013; Li et al., 2014; Yao et al., 2017; Chen et al., 2018). Amentoflavone (HPLC purity > 98%) and Apigenin (HPLC purity > 98%) were purchased from Dalian Meilunbio. Co. Ltd (Dalian, China), Palmatine (HPLC purity > 98%) was purchased from Shyuanye Biotechnology Co. Ltd (Shanghai, China).

Methanol and acetonitrile (HPLC grade) were purchased from Merck KGaA (Darmstadt, Germany), formic acid (HPLC grade) was purchased from Aladdin (Shanghai, China), ethanol (analytical grade) was obtained from Sinopharm Chemical Reagents (Shanghai, China), and ultrapure water was prepared by a Millipore Milli-Q system (Bedford, United States).

2.2 Quantitative analysis of four constituents in SDEA

Amentoflavone, Delicaflavone, Apigenin, Palmatine and Rutin (internal standard) were precisely weighed and dissolved in methanol to obtain a stock solution with a concentration of 1 mg/ml, which was stored in refrigerator at 4°C. Before use, the stock solution was diluted with methanol into standard working solution and quality control working solution.

The concentrations of Amentoflavone and Apigenin standard curve working solution were: 3.125, 6.25, 12.5, 25, 50, 100, 200, 400 and 800 ng/ml; the concentrations of Amentoflavone and Apigenin quality control (QC) working solution were as 30, 150 and 650 ng/ml. The concentrations of Palmatine standard curve working solution were: 0.39, 0.78, 1.56, 3.125, 6.25, 12.5, 25, 50, 100 and 200 ng/ml; three level QCs were as 3, 30, and 150 ng/ml. The concentrations of Delicaflavone standard curve working solution were: 3.125, 6.25, 12.5, 25, 50, 100 and 200 ng/ml; and three QCs were as 8, 30 and 150 ng/ml. SDEA solid was accurately weighed and dissolved with methanol, then sonicated until complete dissolution. Diluted it with methanol to 1, 5, 25, 40 $\mu\text{g/ml}$ and mix with the 40 ng/ml internal standard (Rutin) respectively. The mixture was vortexed for 2 min, then centrifuged at 13000 rpm for 10 min at room temperature. The supernatant was acquired for LC-MS/MS quantitative analysis.

2.3 Establishment of cytochrome P450 cocktail inhibition assay

Potassium phosphate buffer (200 μl , 0.1 M, pH 7.4) containing 1 mM NADPH, 0.5 mg/mL human liver microsomes, and a cocktail assay of seven probe substrates (Phenacetin for CYP1A2, Paclitaxel for CYP2C8, Tolbutamide for CYP2C9, Omeprazole for CYP2C19, Dextromethorphan for CYP2D6, Chlorzoxazone for CYP2E1, Dextromethorphan and Testosterone for CYP3A) or a single substrate ($\leq K_m$) were incubated at 37°C for 15 min (Supplementary Table S1). The contents of organic solvent and DMSO in incubation mixture was under 1% (v/v) and 0.1% (v/v) respectively. Reactions were terminated by adding 200 μl of an ice-cold stop solution consisting of methanol containing Rutin (2 $\mu\text{g/ml}$) as internal standard. Samples were subsequently cooled in ice bath to precipitate proteins. Supernatants were collected into clean tubes after centrifugation at 12000 rpm at 4°C for 10 min prior to inject into LC-MS/MS.

2.3.1 Determination of linearity of metabolite formation

To determine the optimal incubation time for each CYP substrate, human liver microsomes (0.5 mg/mL) were incubated at 37°C for 0, 5, 10, 20, 30 and 60 min with each CYP substrates. All substrates concentration were 1 μM . After quantitative analysis using LC-MS/MS, the linearity of metabolite formation was evaluated.

2.3.2 Validation of direct CYP450 inhibition

For the determination of inhibition curves using single substrate and the cocktail, seven selective CYP inhibitors were used at different concentrations as follows: 0.05–1 μM α -Naphthoflavone for

CYP1A2, 1–50 μ M Fluconazole for CYP2C19, 0.1–15 μ M Quercetin for CYP2C8, 0.01–5 μ M Sulfaphenazole for CYP2C9, 0.005–2 μ M Quinidine for CYP2D6, 0.1–5 μ M 4-Methylpyrazole for CYP2E1, and 0.005–1 μ M Ketoconazole for CYP3A (Supplementary Table S2).

2.4 Concentration-dependent inhibitory effect of SDEA on CYP450 isoforms

Inhibitory effect of SDEA on CYP450 isoforms was determined by cocktail assay. SDEA at 10 concentrations from 0 to 200 μ g/ml were used to measure IC_{50} value. The amount of metabolites produced by incubation without SDEA (control group) was taken as 100%, then draw inhibition efficiency curve.

2.5 Concentration-dependent inhibitory effect of four components in SDEA on CYP450 isoforms

Single-point inhibition was assessed by Delicaflavone, Amentoflavone, Apigenin and Palmatine at 10 μ M, using the same protocol as described in Section 2.3. Percentages of control activity were calculated to determine inhibition potency. The inhibition curves were obtained by incubating the cocktail of substrates with 10–11 different compounds' concentrations, where Delicaflavone and Amentoflavone were 0–50 μ M.

2.6 Time-dependent inhibition study of SDEA, Delicaflavone and Amentoflavone

In order to explore whether SDEA, Delicaflavone and Amentoflavone have time-dependent inhibition on CYP450 isoforms, the cocktail inhibition assay (Section 2.3.) was used. First, SDEA (0.5 μ g/ml), Delicaflavone (2 μ M), and Amentoflavone (0.1 μ M) were incubated with HLM (0.5 mg/ml) in the presence and absence of 1 mM NADPH for 35 min. After pre-incubation, a 20 μ l aliquot of the incubation mixture was transferred to 180 μ l potassium phosphate buffer (0.1 M, pH 7.4) containing 1 mM NADPH and mixed probe substrates for secondary culture, then stopped reaction after 15 min. Enzymes that may be involved in time-dependent were pre-incubated for 0, 5, 10, 15 and 35 min respectively, and then re-incubated to determine the type of inhibition. Residual enzyme activity pre-incubated without NADPH was set as the control group, then drawing suppression curves based on the measured data.

2.7 LC-MS/MS conditions

All metabolites and surrogate standards were analyzed by using LC-MS/MS on a Shimadzu (Kyoto, Japan) LCMS-8040 triple quadrupole mass spectrometer. Chromatographic separation was performed using an Ultimate® XB-C18 (100 \times 2.1 mm, 3 μ m) with gradient elution of water (0.2% formic acid) and methanol at 0.3 mL/min (gradient B). Column maintained at 40°C. 5 μ l of supernatant was injected for LC-MS/MS analysis.

The following optimized MS parameters were used: ion spray voltage: 6.0 kV; Nebulizer gas flow: 3 L/min; Drying gas flow: 12 L/min; DL temperature: 250°C; Heatblock temperature: 400°C.

2.7.1 Quantitative analysis of SDEA constituents

The gradient elution procedure is: 0–1 min, 30%–45% B; 1–3 min, 40%–75% B; 3–5 min, 75%–85% B; 5–8 min, 85%–95% B; 8–12 min, 95% B; 12–13 min, 95%–30% B; 30% B for equilibration.

Detection was carried out using electrospray with polarity switching, collision-induced dissociation, and multiple reaction monitoring (MRM). The MRM mode transition: m/z 536.90 \rightarrow 375.00 (–) for Amentoflavone; m/z 538.9 \rightarrow 256.95 (+) for Delicaflavone; m/z 352.00 \rightarrow 336.10 (+) for Palmatine; m/z 271.15 \rightarrow 153.05 (+) for Apigenin; m/z 611.00 \rightarrow 302.85 (+) for Rutin (IS). The collision energies (CE) of the four components were 33 V, –45 V, –35 V, –35 V and –35 V respectively.

2.7.2 Determination of the inhibitory effects of SDEA and four constituents on CYP450 enzymes by cocktail assay

A gradient condition was applied with the following program: 0–1 min, 10%–20% B; 1–1.01 min, 20%–75% B; 1.01–3 min, 75%–77% B; 3–5 min, 77%–80% B; 5–8 min, 80%–85% B; 8–9 min, 85%–95% B; 9–12 min, 95% B; and then 10% B for equilibration. For specific MRM parameters, please refer to Supplementary Table S3.

2.8 Data analysis

Quantitative LC-MS/MS data were analyzed using Shimadzu LabSolutions software (Kyoto, Japan). The K_m and IC_{50} values were determined by using the GraphPad Prism 5.0 software (San Diego, United States).

3 Results

3.1 The content of four constituents in SDEA

The structures of Amentoflavone, Delicaflavone, Palmatine, and Apigenin were shown in Figure 1. Amentoflavone and Apigenin were linearly related in a range of 3.125–800 ng/mL by using $1/X^2$ weighting. Palmatine showed a linear relationship in the range of 0.391–200 ng/ml, and Delicaflavone showed a linear relationship in the range of 3.125–200 ng/ml. The four SDEA constituents showed a good linear relationship over their concentration range with coefficient of determination $r^2 \geq 0.99$ (Supplementary Table S4).

QC samples in three levels (Low QC, Medium QC and High QC) were prepared separately and used to evaluate those quantitative methods, all samples were analyzed by three replicates. The related standard deviation (RSD) of the tested compounds ranged from –8.88% to 12.60% (Supplementary Table S4). MRM mass spectrum of blank sample and Limit of Quantity (LOQ) were displayed in Supplementary Figure S1. As well, all of them demonstrated the feasibility of this analytical methods.

1 μ g/ml, 5 μ g/ml, 25 μ g/ml and 40 μ g/ml SDEA samples were prepared and injected into LC-MS/MS respectively. Using the established quantitative method, the content of four constituents in

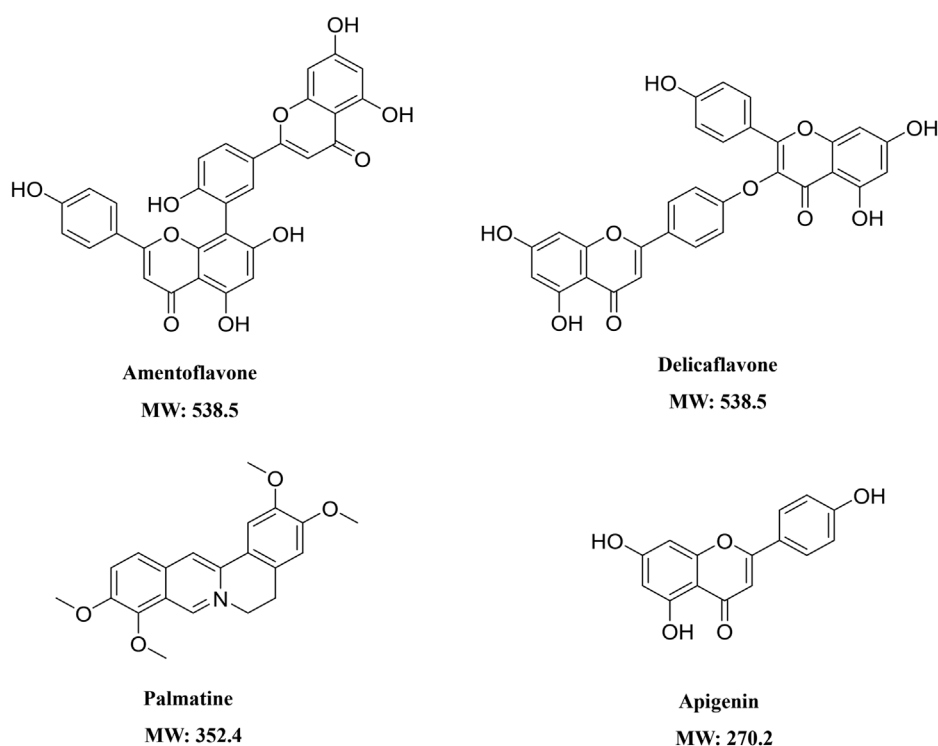


FIGURE 1
Structural formula and molecular weight of the components in SDEA.

TABLE 1 Contents (% w/w) of the four constituents in SDEA. (Higher SDEA concentrations were used because Apigenin and Palmatine are less in SDEA).

Compound	SDEA conc. (μg/ml)	Content (%)	Average content (%)
		% weight compound/weight extract	
Amentoflavone	1	13.78	13.65
	5	13.53	
Delicaflavone	1	2.29	2.21
	5	2.13	
Palmatine	5	0.019	0.019
	25	0.019	
Apigenin	25	0.026	0.024
	40	0.023	

SDEA was determined. The average w/w % (Weight compound/weight extract) showed that Delicaflavone, Palmatine, Apigenin were 2.21%, 0.019% and 0.024% respectively, and Amentoflavone reached 13.65%, which was the most abundant one in those four constituents (Table 1).

3.2 Development of CYP450 cocktail assay

The probe substrates in this cocktail assay were recommended based on FDA guidance. CYP3A sub-family can bind multiple

structurally different substrates (Wrighton et al., 2000; Ekroos and Sjögren, 2006; Watanabe et al., 2007), it is necessary to use more than two CYP3A *in vitro* marker reactions to evaluate the activity of CYP3A (Wrighton et al., 2000), so that can show more accurate results (Galetin et al., 2005). We selected Testosterone and Dextromethorphan as two different substrates of CYP3A subfamily, their specific products metabolized by CYP3A were Testosterone: 6β-hydroxytestosterone; Dextromethorphan: 3-methoxymorphine. The MRM parameters of substrates corresponding to seven human CYP450 isoforms were summarized in Supplementary Table S3. LC-MS/MS

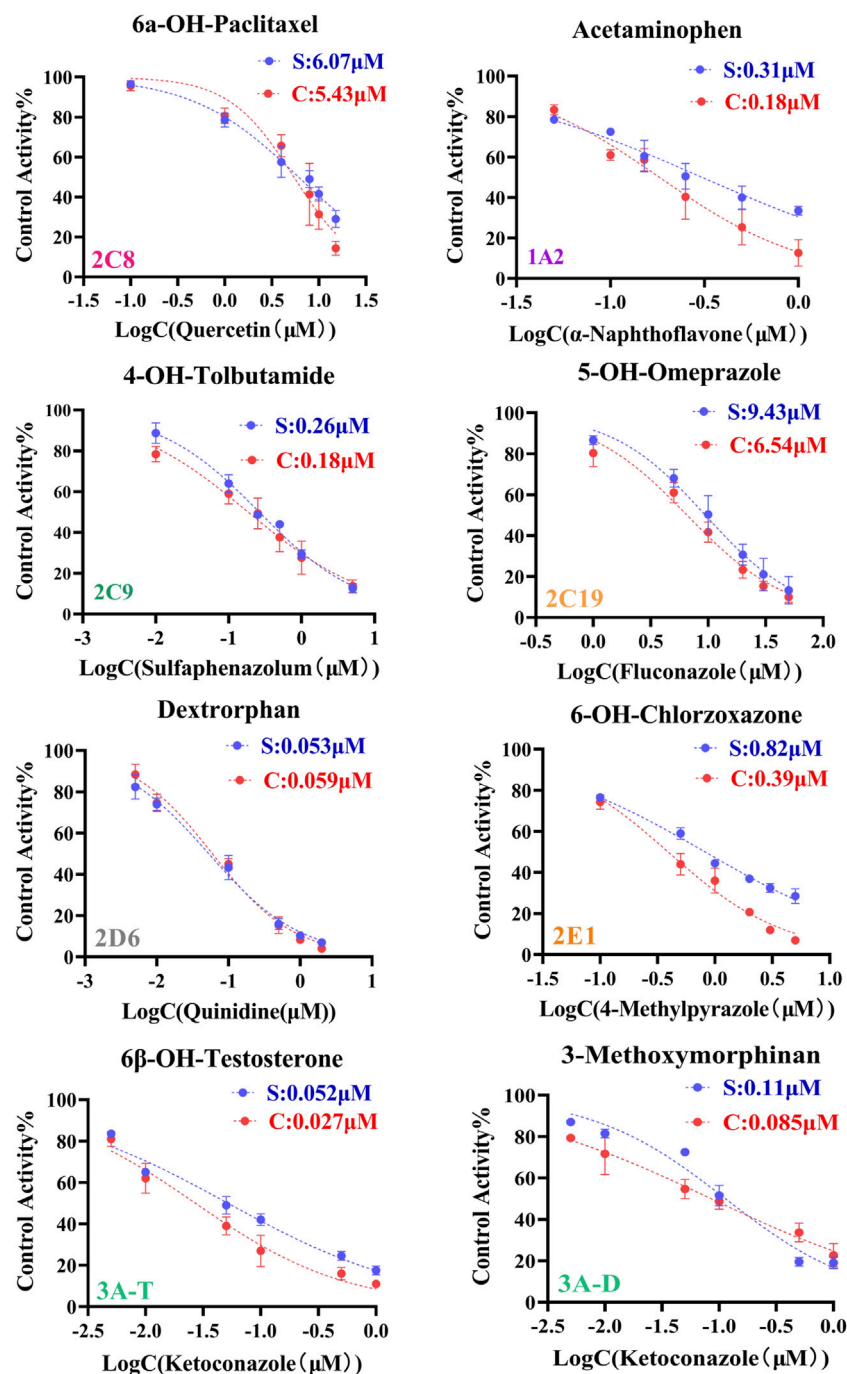


FIGURE 2

Inhibition curves each substrate incubated with cocktail assay and single substrate method. Note: 3A-T, CYP3A (Testosterone); 3A-D, CYP3A (Dextromethorphan).

chromatography of substrates and their metabolites were included in [Supplementary Figure S2](#).

To determine the optimum incubation time for all substrates, we measured time-dependent trends in amount of metabolites produced by seven CYP450 enzyme substrates. Although Dextromethorphan (CYP2D6), Chlorzoxazone (CYP2E1), Paclitaxel (CYP2C8) remained linear for first 20 min and metabolic rates of Tolbutamide (CYP2C9), Omeprazole (CYP2C19), Phenacetine (CYP1A2) were linear for up to 15 min, Testosterone (CYP3A4) remained linear only for first 10 min

and then flattened out. Trend diagram of the generation of metabolites for seven enzyme substrates with time was included in [Supplementary Figure S3](#). Compromising sensitivity to detect metabolites formed at low substrate concentrations and high inhibitor concentrations, an incubation time of 15 min was finally determined.

Considering the linear curve of metabolic reaction, the final concentration of substrate is usually lower than its K_m value in order to ensure linear relationship of metabolic rate range and high affinity. What's moreover, enzyme-substrate affinity data illustrated

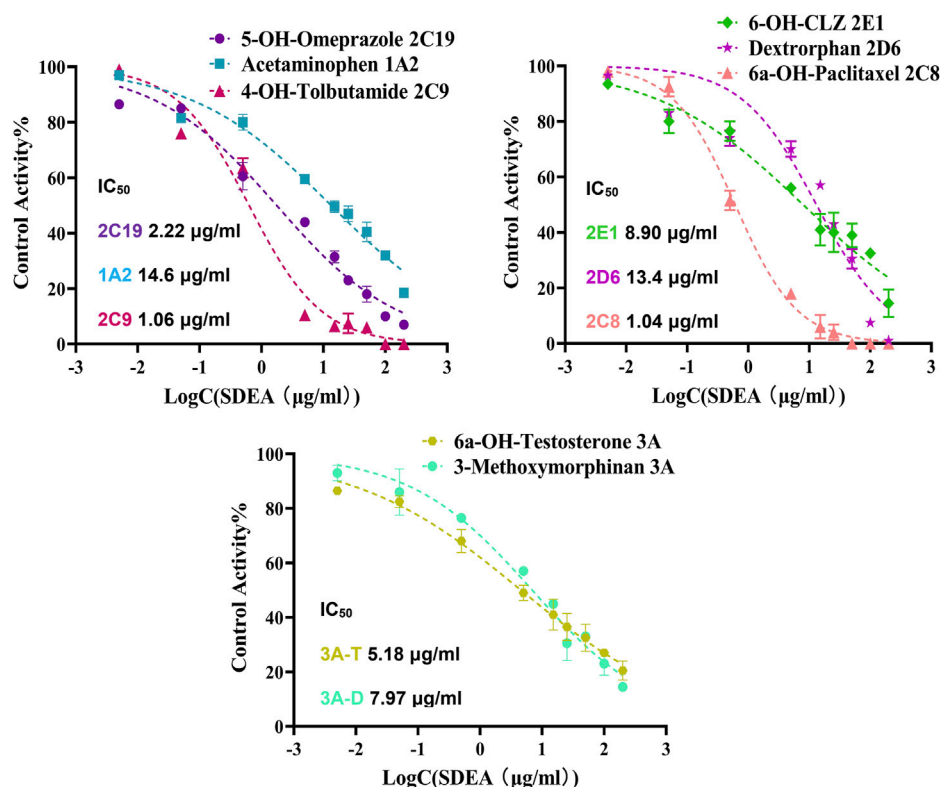


FIGURE 3

Inhibitory potency curves and IC₅₀ values of SDEA on seven CYP450 enzyme isoforms. Note: 3A-T, CYP3A (Testosterone); 3A-D, CYP3A (Dextromethorphan).

that the K_m value should be similar for a specific enzyme and substrate, regardless of enzyme source (Donnell et al., 2007). Since the incubated substrates could interact with each other (Spaggiari et al., 2014), reducing substrate concentration is the most direct and effective way to reduce the interference (Pillai et al., 2013). Therefore, the final incubation concentration of each substrate was ideal when it was below K_m . According to the recommended data in literature (Spaggiari et al., 2014) and sensitivity of MS, final substrate concentration in assay were determined: Phenacetin (1A2), Paclitaxel (2C8) and Tolbutamide (2C9) were 10 μ M, Dextromethorphan (2D6) and Testosterone (3A) were 5 μ M, Omeprazole (2C19) was 2 μ M, and Chlorzoxazone (2E1) was 15 μ M. All data were summarized in Supplementary Table S1.

The IC₅₀ values obtained by cocktail assay was compared with a single substrate using known inhibitors of each enzyme reaction alone, so as to verify the feasibility of this assay. a-Naphthoflavone was inhibitor of CYP1A2, our cocktail assay showed that IC₅₀ value of a-Naphthoflavone on CYP1A2 was 0.18 μ M, and the value was 0.31 μ M from single substrate assay, which indicated similar results. The IC₅₀ value of Quercetin on CYP2C8 was 5.43 μ M in cocktail assay, while the number was 6.07 μ M in single substrate experiment, all of them were located in desirable range by literature (Kozakai et al., 2012; Chen et al., 2016; Valicherla et al., 2019). IC₅₀ values of other CYP450 isoforms inhibitors (Sulfaphenazole for CYP2C9, Fluconazole for CYP2C19, Quinidine for CYP2D6, 4-Methylpyrazole for CYP2E1, Ketoconazole for CYP3A) on cocktail assay and single substrate method were also

performed and compared. Inhibition curves were shown in Figure 2 and IC₅₀ values were summarized in Supplementary Table S2, all of them showed good agreement between cocktail assay and single-substrate approach, which indicated the accuracy of this cocktail inhibition assay.

3.3 Concentration-dependent inhibition effect of SDEA and four constituents on CYP450 isoforms

The established cocktail assay was used to determine potential HDI of SDEA. Results showed that SDEA has strong inhibitory effect on CYP2C8 and CYP2C9, where IC₅₀ values were 1.04 μ g/ml and 1.06 μ g/ml. SDEA also showed moderate inhibitory ability on CYP2C19 (IC₅₀ was 2.22 μ g/ml), CYP2E1 (IC₅₀ was 8.90 μ g/ml) and CYP3A (IC₅₀ was 5.18 μ g/ml for Testosterone and 7.97 μ g/ml for Dextromethorphan). The inhibition activities for CYP1A2, CYP2D6 were mildly, both IC₅₀ values were above 10 μ g/ml (Figure 3).

We also determined the inhibitory effects of SDEA constituents on seven cytochrome P450 isoforms. At the concentration of 10 μ M, Amentoflavone showed more than 50% inhibitory effect on seven enzyme types, the inhibitory effect of Apigenin on CYP1A2, CYP2C8, CYP2C9, CYP2E1 and CYP3A (Testosterone) was more than 50%. Palmatine inhibits CYP3A (Testosterone) by more than 50% and has a weak inhibitory effect on CYP2E1. Delicaflavone has a weak inhibitory

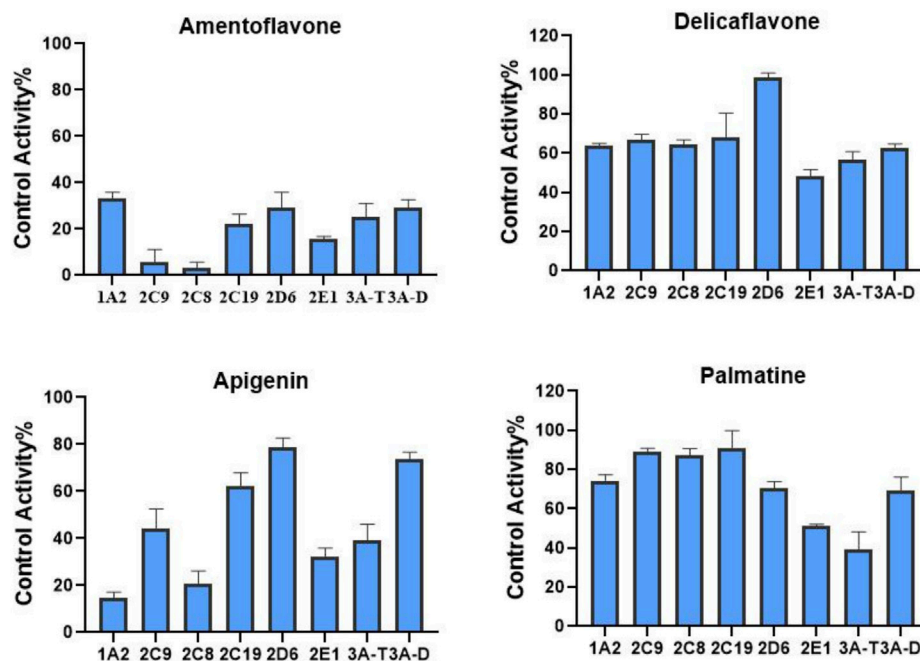


FIGURE 4

Inhibition of CYP enzymes by Amentoflavone, Delicaflavone, Apigenin, and Palmatine at 10 µM. Inhibition Activity was expressed as a percentage of remaining activity compared to a control test without enzyme inhibitor. Note: 3A-T, CYP3A (Testosterone); 3A-D, CYP3A (Dextromethorphan).

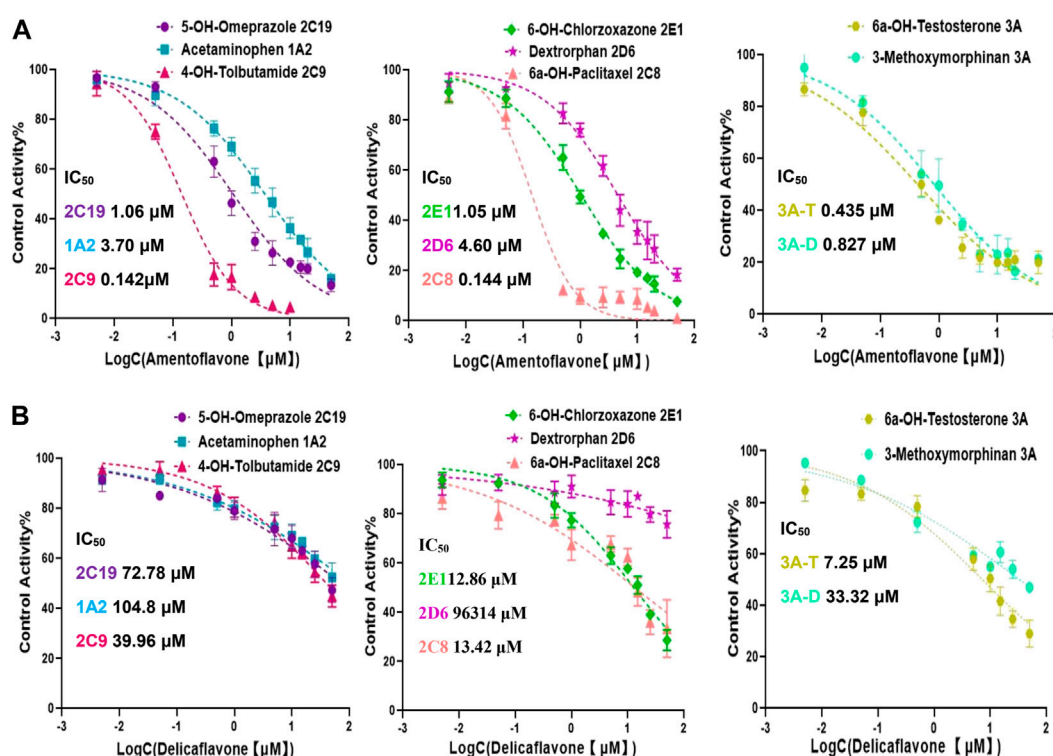


FIGURE 5

Inhibition curves and IC₅₀ values of Amentoflavone (A) and Delicaflavone (B) against seven CYP450 isoforms. Note: 3A-T, CYP3A (Testosterone); 3A-D, CYP3A (Dextromethorphan).

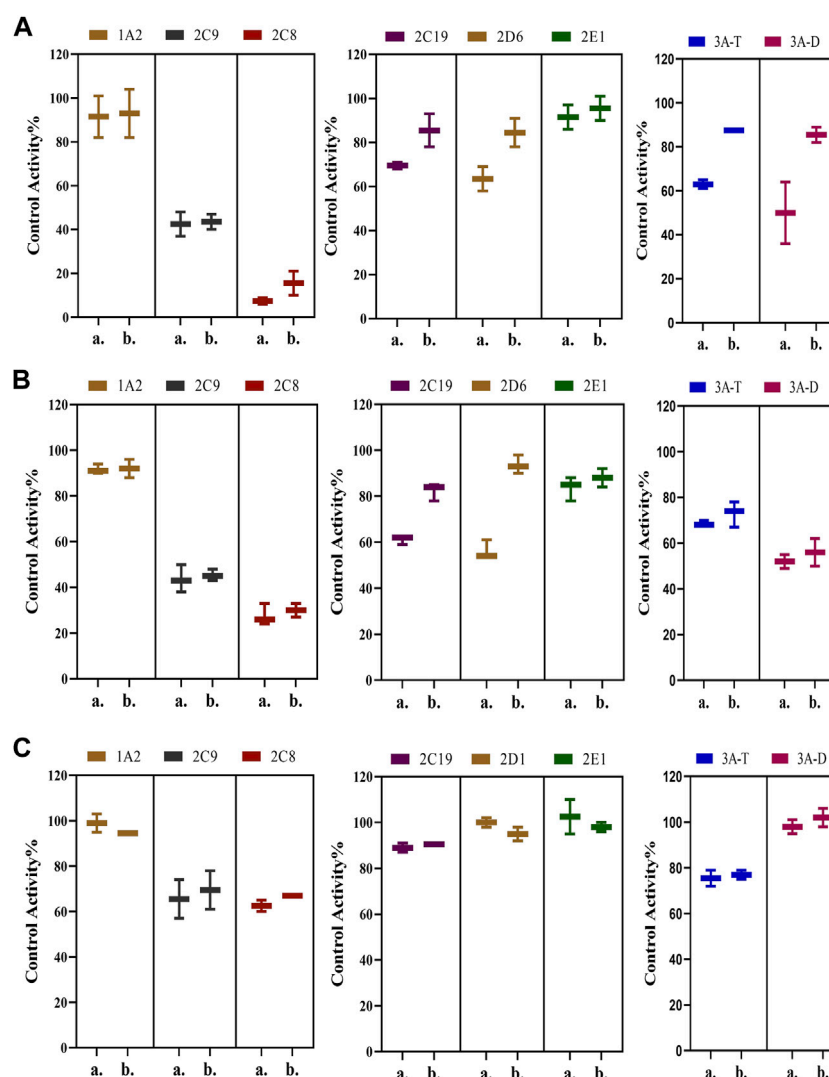


FIGURE 6

Percentage reduction in activity of seven enzymes after incubation with SDEA (A), Amentoflavone (B) and Delicaflavone (C) using a single point time-dependent inhibition screening assay. The experiment was carried out three times. Note: (1) a. presence of NADPH; b. without NADPH. (2) 3A-T, CYP3A (Testosterone); 3A-D, CYP3A (Dextromethorphan).

effect on CYP2E1 and CYP3A, but it had no obvious inhibitory effect on the other CYP450 isomers at this concentration (Figure 4).

Amentoflavone were most abundant in four SDEA constituents (13.65% w/w, Table 1), which showed a broad-spectrum potent CYP enzymes inhibitory effect. The IC_{50} values were less than 5 μ M for the seven cytochrome P450 isoforms, especially for CYP2C9, CYP2C8 and CYP3A, the IC_{50} values were even less than 0.5 μ M (Figure 5A). In contrast, Delicaflavone only had a moderate inhibitory effect on CYP3A (Testosterone), weak inhibitory effect on CYP2C8, CYP2E1 and had almost no inhibitory effect on the other CYP isoforms (Figure 5B).

3.4 Time-dependent inhibition study

Possible time-dependent inhibition of SDEA, Amentoflavone and Delicaflavone was tested using cocktail assay. Single point screening assay showed that SDEA (0.5 μ g/ml) demonstrated a time-dependent

inhibition on CYP2C19, CYP2D6, CYP3A (Testosterone) (Figure 6A), and Amentoflavone (0.1 μ M) showed the time-dependent inhibition on CYP2C19, CYP2D6 (Figure 6B). While Delicaflavone (2 μ M) did not produce time-dependent inhibition effect on those enzymes (Figure 6C).

Based on these results, we have determined the inhibition effect of incubation time with SDEA or Amentoflavone on CYP2C19, CYP2D6, CYP3A (Testosterone) activity. When HLM was co-incubated with SDEA (0.5 μ g/ml) in presence of NADPH for 0–35 min, the metabolic activity of CYP2C19 decreased from 95.5% to 69.5%; the activity of CYP2D6 decreased from 84.5% to 63.5% and CYP3A (Testosterone) decreased from 98.5% to 63% (Figure 7A). As for Amentoflavone (0.1 μ M), the CYP2C19 activity decreased from 92% to 61% and CYP2D6 activity decreased from 91% to 56%, during the 0–35 min of incubation with HLM and NADPH (Figure 7B). The control group was without NADPH, after 0–35 min co-incubation of HLM with SDEA or Amentoflavone, no significant change in enzymes activity was observed. Those data indicated that SDEA and Amentoflavone may follow a time-dependent inhibition on CYP450 enzymes.

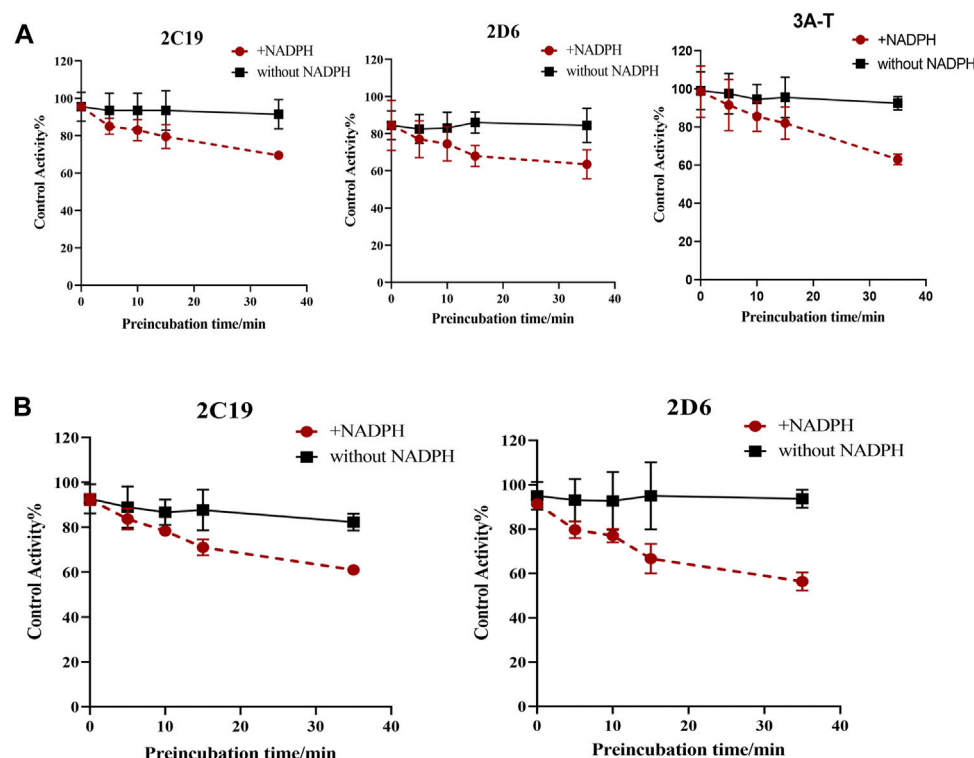


FIGURE 7
Effect of incubation time on the inhibition of CYP3A, CYP2D6 and CYP2C19, with SDEA (A) and Amentoflavone (B). Note: 3A-T, CYP3A (Testosterone).

4 Discussion

In vitro model of human CYP450 enzymes inhibition cocktail assay used in this study can discover the potential of interaction between herb and drugs, reduce the risk of using clinical drug, lay a foundation for clinical medication. Incubation time (15 min) and substrate concentration were determined by combining literature data with experimental conditions (Supplementary Table S1). The established cocktail assay was then validated with known CYP450 enzymes inhibitors, and was applied to evaluate whether SDEA and its bioactive constituents produce concentration-dependent or time-dependent inhibition on the selected CYP450 enzymes. Amentoflavone and Delicaflavone are the main active pharmacological components of SDEA and have high content in SDEA. Palmatine and Apigenin are also SDEA constituents and have been reported to show inhibitory effects on CYP450 enzymes (von Moltke et al., 2004; Kim et al., 2000). Moreover, Palmatine and Apigenin are more common in everyday life than other ingredients, the results will be more practical. Thus, those four compounds were selected for HDI test.

The experiment results showed that SDEA had a strong concentration-dependent inhibition effect on CYP2C9 and CYP2C8 (Figure 3), time-dependent inhibition effect on CYP2D6, CYP2C19 and CYP3A (Figure 7A), which may lead to some serious adverse effects in clinical use. CYP3A subfamily is a particularly important CYP metabolizing, mediating over 50% *in vivo* biotransformation of clinical drugs (Liu et al., 2006; Xia et al., 2015). In addition, CYP3A subfamily also plays an important role in maintaining metabolic balance of important endogenous substances such as bile acids, steroid

hormones and cholesterol (Liang et al., 2015; Xia et al., 2015; Liang et al., 2016), and it is also the main metabolic enzyme of many narrow-window drugs, such as Paclitaxel, Bortezomib, and Gefitinib. SDEA not only inhibits CYP3A ($IC_{50} < 10 \mu\text{g/ml}$), more importantly, after 35 min co-incubation of SDEA with NADPH, CYP3A activity was reduced from 98.5% to 63%, which significantly increases the risk of herb-drug interaction with serious consequences. Some oral hypoglycemic agents, such as Glyburide, Rosiglitazone, and Repaglinide, are mainly metabolized by CYP2C8 or CYP2C9, it may increase hypoglycemia risk when those medicines are used together with SDEA. For epilepsy patients, SDEA should be used with caution when taking Phenytoin and Valproic acid (metabolized by CYP2C19) at the same time, in order to avoid serious adverse reactions.

The contents of Amentoflavone and Delicaflavone in SDEA were 13.65% w/w and 2.21% w/w respectively, which were similar to results of previous studies (Li et al., 2013) (Table 1). Amentoflavone not only shows pharmacological activities, such as anti-tumor (Ndongo et al., 2015), antiviral (Coulerie et al., 2013), antioxidant (Arwa et al., 2015), anti-inflammatory (Abdallah et al., 2015), but also has therapeutic effects on central nervous (Zhang et al., 2015) and cardiovascular system (Yu et al., 2017). The data indicated that Amentoflavone may be the main contributor for SDEA to inhibit CYP enzymes activity. Amentoflavone showed high content in SDEA and strong or moderate inhibitory effect on CYP1A2, CYP2C8, CYP2C9, CYP2C19, CYP2D6, CYP2E1, CYP3A (Figure 5A). The inhibitory effect was even stronger than some specific inhibitors of CYP2C9, CYP2C8 and CYP3A. In previous reports, Amentoflavone had a strong inhibitory effect on various CYP450 isoforms such as CYP2C9, CYP2C19, CYP2D6 and CYP3A4 (von Moltke et al., 2004; Kimura et al., 2010), which were consistent with

the experiment results. It should be noted that this paper found a strong inhibitory effect on CYP2C8 and a moderate inhibitory effect on CYP1A2 and CYP2E1 by Amentoflavone, which were not reported in previous article (von Moltke et al., 2004). The researchers did not find the inhibitory effect of Amentoflavone on CYP1A2, which may be related to the differences in enzyme sources, substrate types and concentrations.

Similar to SDEA, Amentoflavone also has time-dependent inhibitory effects on CYP2D6 and CYP2C19 (Figure 7B). Although CYP2D6 accounts for a small fraction of CYP450 expression in liver, it participates in metabolism of various drugs. As a therapeutic drug for breast cancer, Tamoxifen (TAM) has better pharmacological activity only after the formation of 4-hydroxy-N-demethylamoxifen (Endoxifen), which is a metabolite catalyzed by CYP2D6 (Kleina et al., 2013). What's more, CYP2D6 is the most polymorphic metabolic enzyme, which is of great significance in genetics, especially in pharmacogenetics. CYP2D6 and CYP2C19 are jointly involved in the metabolism of psychotropic drugs, such as Selective Serotonin Receptor Inhibitors (SSRIs), Clozapine (CZ) (Caetano and Piatkov, 2016; Menkes et al., 2018) and Risperidone. For those patients who have weak CYP2D6 and CYP2C19 activities, the inhibition is more dangerous and may lead to serious consequences (Lymperopoulos et al., 2015). A recent study has found that Amentoflavone was a strong and broad-spectrum UDP-glucuronosyltransferase (UGT) inhibitor (Lv et al., 2018). Since UGT enzymes involve in the most phase II elimination in body, the inhibition of UGT would bring potential risks for those medicines mainly clearing by this pathway. Considering the relationship of SDEA and Amentoflavone, we speculate that SDEA may also have the potential to produce significant inhibition on UGT, which needs further experiments to confirm.

Because the content determination and single concentration inhibition showed that Palmatine and Apigenin contents were low (Table 1), and the inhibitory effect on enzyme type was not as strong as Amentoflavone (Figure 4), so no further time-dependent study was conducted for Palmatine and Apigenin. Unlike SDEA, Amentoflavone, Apigenin or Palmatine, Delicaflavone shown no significant inhibition effect on the selected CYP450 isomers at 10 μ M, only a weak inhibitory effect on CYP2E1 and CYP3A. Although Delicaflavone is the isomer of Amentoflavone, the difference on CYP450 enzymes inhibition effect may account in the steric hindrance. There are active site (responsible for substrate binding and NADPH-CYP450 oxidase reaction) and allosteric site (responsible for outside molecules to modulate enzyme activity) in CYP450 enzymes (Deodhar et al., 2020). It is possible that Amentoflavone binds to the allosteric site on CYP450 enzymes and lead to a strong inhibition effect. Delicaflavone did not bind to or weakly work on the allosteric site on CYP450 enzymes, resulting in the different CYP450 inhibition activities for those two isomers. Delicaflavone also has excellent anti-cancer and tumor-suppressing ability, the less influence on the CYP450 enzymes activity will make it a better candidate for next step drug development than SDEA or Amentoflavone.

5 Conclusion

Through the established reliable cocktail assay, SDEA was found to have concentration-dependent inhibition on several CYP450 enzymes, and inhibited CYP2D6, CYP2C19, CYP3A in a time-dependent manner. The inhibition activity may be mainly due to the higher content of component: Amentoflavone (13.65%). Amentoflavone has inhibitory effects on all tested CYP450 enzymes, the inhibitory effects on

CYP2C9, CYP2C8 and CYP3A were even greater than the corresponding specific inhibitors. Amentoflavone also has time-dependent inhibition on CYP2D6 and CYP2C19. The other two constituents from SDEA, Apigenin and Palmatine, both showed concentration-dependent inhibition. For Delicaflavone, no significant inhibitory effect on CYP450 enzymes was observed. Since Delicaflavone owns excellent anti-cancer ability and low HDI potential, it was more suitable to develop as a new anti-cancer drug.

Data availability statement

The original contributions presented in the study are included in the article/Supplementary Material, further inquiries can be directed to the corresponding author.

Author contributions

FL: methodology, data analysis and writing (original draft). XL: conceptualization and supervision. GM: writing (review and editing). XW, BC, and HY: methodology. LH: methodology, data analysis, conceptualization, supervision and writing (review and editing). All authors have read and agreed to the published version of the manuscript.

Funding

This research work was supported by those funds: (1) The High Level Talent Foundation of Fujian Medical University (grant number XRCZX2021005); (2) The Young Teachers Education Foundation of Fujian Province, China (grant number JAT220080); (3) National Nature Science Foundation of China (grant number 22074017); (4) Key Project Supported by the Natural Science Foundation of Fujian Province, China (grant number 2021J02034).

Conflict of interest

The authors declare that the research was conducted in the absence of any commercial or financial relationships that could be construed as a potential conflict of interest.

Publisher's note

All claims expressed in this article are solely those of the authors and do not necessarily represent those of their affiliated organizations, or those of the publisher, the editors and the reviewers. Any product that may be evaluated in this article, or claim that may be made by its manufacturer, is not guaranteed or endorsed by the publisher.

Supplementary material

The Supplementary Material for this article can be found online at: <https://www.frontiersin.org/articles/10.3389/fphar.2023.1108867/full#supplementary-material>

References

- Abdallah, H. M., Almowallad, F. M., Esmat, A., Shehata, I. A., and Essam, A. (2015). Anti-inflammatory activity of flavonoids from *Chrozophora tinctoria*. *Phytochem. Lett.* 13, 74–80. DOI: doi:10.1016/j.phytol.2015.05.008
- Al-Ramahi, R., Jaradat, N., Shalalfeh, R., Nasir, S., Manasra, Y., Shalalfeh, I., et al. (2015). Evaluation of potential drug-herb interactions among a group of palestinian patients with chronic diseases. *BMC Complement. Altern. Med.* 15, 221–225. DOI: doi:10.1186/s12906-015-0764-7
- Arwa, P. S., Zeraik, M. L., Ximenes, V. F., da Fonseca, L. M., da Silva Bolzani, V., and Silva, D. H. S. (2015). Redox-active biflavonoids from *Garcinia brasiliensis* as inhibitors of neutrophil oxidative burst and human erythrocyte membrane damage. *J. Ethnopharmacol.* 174, 410–418. DOI: doi:10.1016/j.jep.2015.08.041
- Awortwe, C., Makiwane, M., Reuter, H., Muller, C., Louw, J., and Rosenkranz, B. (2018). Critical evaluation of causality assessment of herb-drug interactions in patients. *Br. J. Clin. Pharmacol.* 84 (4), 679–693. doi:10.1111/bcp.13490
- Bjornsson, T. D., Callaghan, J. T., Einolf, H. J., Fischer, V., Gan, L., Grimm, S., et al. (2003). The conduct of *in vitro* and *in vivo* drug-drug interaction studies: A PhRMA perspective. *J. Clin. Pharmacol.* 43, 443–469. DOI: doi:10.1177/0091270003252519
- Brantley, S. J., Argikar, A. A., Lin, Y. S., Nagar, S., and Paine, M. F. (2014). Herb-drug interactions: Challenges and opportunities for improved predictions. *Drug Metab. Dispos.* 42 (3), 301–317. doi:10.1124/dmd.113.055236
- Caetano, D., and Piatkov, I. (2016). Ultrarapid clozapine metabolism and CYP2D6 gene duplication in a patient with schizophrenia. *Per. Med.* 13 (2), 113–117. doi:10.2217/pme.15.56
- Chen, B., Wang, X. W., Zou, Y. L., Chen, W. Y., Wang, G., Yao, W. S., et al. (2018). Simultaneous quantification of five biflavonoids in rat plasma by LC-ESI-MS/MS and its application to a comparatively pharmacokinetic study of *Selaginella doederleinii* Hieron extract in rats. *J. Pharm. Biomed. Anal.* 149, 80–88. doi:10.1016/j.jpba.2017.10.028
- Chen, Z. H., Zhang, S. X., Long, N., Lin, L. S., Chen, T., Zhang, F. P., et al. (2016). An improved substrate cocktail for assessing direct inhibition and time-dependent inhibition of multiple cytochrome P450s. *Acta Pharmacol. Sin.* 37 (5), 708–718. doi:10.1038/aps.2016.10
- Choi, J. G., Eom, S. M., Kim, J., Kim, S. H., Huh, E., Kim, H., et al. (2016). A comprehensive review of recent studies on herb-drug interaction: A focus on pharmacodynamic interaction. *J. Altern. Complement. Med.* 22 (4), 262–279. doi:10.1089/acm.2015.0235
- Coulerie, P., Nour, M., Maciuk, A., Eydoux, C., Guillemot, J. C., Lebouvier, N., et al. (2013). Structure-activity relationship study of biflavonoids on the Dengue virus polymerase DENV-NS5 RdRp. *Planta Med.* 79, 1313–1318. doi:10.1055/s-0033-1350672
- Deodhar, M., Rihani, S. B. A., Arwood, M. J., Darakjian, L., Dow, P., Turgeon, J., et al. (2020). Mechanisms of CYP450 inhibition: Understanding drug-drug interactions due to mechanism-based inhibition in clinical practice. *Pharmaceutics* 12 (9), 846. doi:10.3390/pharmaceutics12090846
- Donnell, C. J., Grime, K., Courtney, P., Slee, D., and Riley, R. J. (2007). The development of a cocktail CYP2B6, CYP2C8, and CYP3A5 inhibition assay and a preliminary assessment of utility in a drug discovery setting. *Drug Metab. Dispos.* 35, 381–385. doi:10.1124/dmd.106.012344
- E Kroos, M., and SjOgren, T. (2006). Structural basis for ligand promiscuity in cytochrome P450 3A4. *Proc. Natl. Acad. Sci. U.S.A.* 103, 13682–13687. doi:10.1073/pnas.0603236103
- Galetin, A., Ito, K., Hallifax, D., and Houston, J. B. (2005). CYP3A4 substrate selection and substitution in the prediction of potential drug-drug interactions. *J. Pharmacol. Exp. Ther.* 314, 180–190. doi:10.1124/jpet.104.082826
- Guengerich, P. F. (2021). A history of the roles of cytochrome P450 enzymes in the toxicity of drugs. *Toxicol. Res.* 37 (1), 1–23. doi:10.1007/s43188-020-00056-z
- Guengerich, P. F. (2008). Cytochrome p450 and chemical toxicology. *Chem. Res. Toxicol.* 21 (1), 70–83. doi:10.1021/tx700079z
- Hakkola, J., Hukkanen, J., Turpeinen, M., and Pelkonen, O. (2020). Inhibition and induction of CYP enzymes in humans: An update. *Arch. Toxicol.* 94 (11), 3671–3722. doi:10.1007/s00204-020-02936-7
- Han, Y. L., Li, D., Renb, B., Jing, G. P., Menga, X. L., Zhoua, Z. Y., et al. (2012). Evaluation of impact of herba erigerontis injection, a Chinese herbal prescription, on rat hepatic cytochrome P450 enzymes by cocktail probe drugs. *J. Ethnopharmacol.* 139 (1), 104–109. doi:10.1016/j.jep.2011.10.019
- Han, Y. L., Yu, H. L., Li, D., Meng, X. L., Zhou, Z. Y., Yu, Q., et al. (2011). *In vitro* inhibition of huanglian[*Rhizoma coptidis* (L.)] and its six active alkaloids on six cytochrome P450 isoforms in human liver microsomes. *Phytother. Res.* 25, 1660–1665. doi:10.1002/ptr.3475
- Ishihara, K., Kushida, H., Yuzurihara, M., WakuiYanagisawa, Y. T., Kamei, H., et al. (2000). Interaction of drugs and Chinese herbs: Pharmacokinetic changes of tolbutamide and diazepam caused by extract of *Angelica dahurica*. *J. Pharm. Pharmacol.* 52, 1023–1029. doi:10.1211/0022357001774750
- Kim, H. J., Chun, H. S., and Yang, R. (2000). Inhibition of benzo[a]pyrene-induced cytotoxicity and cytochrome P450 1A activity by dietary flavonoids in human liver cell model: Structure-activity relationship. *Biotechnol. Lett.* 22, 1941–1946. doi:10.1023/A:1026749606363
- Kim, M. J., Kim, H., Cha, I. J., Park, J. S., Shon, J. H., Liu, K. H., et al. (2005). High throughput screening of inhibitory potential of nine cytochrome P450 enzymes *in vitro* using liquid chromatography/tandem mass spectrometry. *Rapid Commun. Mass Spectrom.* 19 (18), 2651–2658. doi:10.1002/rcm.2110
- Kimura, Y., Ito, H. K., Ohnishi, R., and Hatano, T. (2010). Inhibitory effects of polyphenols on human cytochrome P450 3A4 and 2C9 activity. *Food Chem. Toxicol.* 48, 429–435. doi:10.1016/j.fct.2009.10.041
- Kleina, D. J., Thorna, C. F., Destac, Z., Flockhart, D. A., Altmana, R. B., and Kleina, T. E. (2013). PharmGKB summary: Tamoxifen pathway, pharmacokinetics. *Pharmacogenet. Genomics* 23, 643–647. doi:10.1097/fpc.0b013e3283656bc1
- Kozakai, K., Yamada, Y., Oshikata, M., Kawase, T., Suzuki, E., Haramaki, Y., et al. (2012). Reliable high-throughput method for inhibition assay of 8 cytochrome p450 isoforms using cocktail of probe substrates and stable isotope-labeled internal standards. *Drug Metab. Pharmacokinet.* 27 (5), 520–529. doi:10.2133/dmpk.dmpk-12-rg-014
- Lee, K. S., and Kim, S. K. (2013). Direct and metabolism-dependent cytochrome P450 inhibition assays for evaluating drug-drug interactions. *J. Appl. Toxicol.* 33 (2), 100–108. doi:10.1002/jat.1720
- Li, G., Huang, K., Nikolic, D., and van Breemen, R. B. (2015). High-throughput cytochrome P450 cocktail inhibition assay for assessing drug-drug and drug-botanical interactions. *Drug Metab. Dispos.* 43 (11), 1670–1678. doi:10.1124/dmd.115.065987
- Li, G., Simmler, C., ChenNikolic, L. D., Chen, S. N., Pauli, G. F., et al. (2017). Cytochrome P450 inhibition by three licorice species and fourteen licorice constituents. *Eur. J. Pharm. Sci.* 15 (109), 182–190. doi:10.1016/j.ejps.2017.07.034
- Li, S. G., Wang, X. W., Wang, G., Shi, P. Y., Lin, S. L., Xu, D. F., et al. (2020). Ethyl acetate extract of *Selaginella doederleinii* hieron induces cell autophagic death and apoptosis in colorectal cancer via PI3K-Akt-mTOR and AMPKa-signaling pathways. *Front. Pharmacol.* 11, 565090. doi:10.3389/fphar.2020.565090
- Li, S. G., Yao, H., Zhao, M. F., Li, Y. X., Huang, L. Y., and Lin, X. H. (2013). Determination of seven biflavones of *Selaginella doederleinii* by high performance liquid chromatography. *Anal. Lett.* 46, 2835–2845. doi:10.1080/00032719.2013.831426
- Li, S., Zhao, M. F., Li, Y. X., Sui, Y. X., Yao, H., Huang, L. Y., et al. (2014). Preparative isolation of six anti-tumour biflavonoids from *Selaginella doederleinii* Hieron by high-speed counter-current chromatography. *Phytochem. Anal.* 25, 127–133. doi:10.1002/pca.2478
- Liang, S. C., Ge, G. B., Xia, Y. L., Wei, J. Z., Qi, X. Y., Tu, C. X., et al. (2015). *In vitro* evaluation of the effect of 7-methyl substitution on glucuronidation of daphnetin: Metabolic stability, isomeric selectivity, and bioactivity analysis. *J. Pharm. Sci.* 104 (10), 3557–3564. doi:10.1002/jps.24538
- Liang, S. C., Xia, Y. L., Hou, J., Ge, G. B., Zhang, J. W., He, Y. Q., et al. (2016). Methylation, glucuronidation, and sulfonation of daphnetin in human hepatic preparations *in vitro*: Metabolic profiling, pathway comparison, and bioactivity analysis. *J. Pharm. Sci.* 105 (2), 808–816. doi:10.1016/j.xphs.2015.10.010
- Lin, J. H., and Lu, A. Y. (1998). Inhibition and induction of cytochrome P450 and the clinical implications. *Clin. Pharmacokinet* 35 (5), 361–390. doi:10.2165/00003088-199835050-00003
- Liu, Y., Zhang, J. w., Li, W., Ma, H., Sun, J., Denge, M. C., et al. (2006). Ginsenoside metabolites, rather than naturally occurring ginsenosides, lead to inhibition of human cytochrome P450 enzymes. *Toxicol. Sci.* 91 (2), 356–364. doi:10.1093/toxsci/kfj164
- Liu, L. Y., Hana, Y. L., Zhua, J. H., Yua, Q., Yang, Q. J., Lua, J., et al. (2015). A sensitive and high-throughput LC-MS/MS method for inhibition assay of seven major cytochrome P450s in human liver microsomes using an *in vitro* cocktail of probe substrates. *Biomed. Chromatogr.* 29 (3), 437–444. doi:10.1002/bmc.3294
- Lu, C., and Di, L. (2020). *In vitro* and *in vivo* methods to assess pharmacokinetic drug-drug interactions in drug discovery and development. *Biopharm. Drug Dispos.* 41 (1–2), 3–31. doi:10.1002/bdd.2212
- Lv, X., Zhang, J. B., Wang, X. X., Hu, W. Z., Shi, Y. S., Liue, S. W., et al. (2018). Amentoflavone is a potent broad-spectrum inhibitor of human UDP-glucuronosyltransferases. *Chem.-Biol. Interact.* 284, 48–55. doi:10.1016/j.cbi.2018.02.009
- Lymperopoulos, A., McCrink, K. A., and Brill, A. (2015). Impact of CYP2D6 genetic variation on the response of the cardiovascular patient to carvedilol and metoprolol. *Curr. Drug Metab.* 17 (1), 30–36. doi:10.2174/1389200217666151105125425
- Menkes, D. B., Glue, P., Gale, C., Lam, F., Hung, C. T., and Hung, N. (2018). Steady-state clozapine and norclozapine pharmacokinetics in Maori and European patients. *EBioMedicine* 27, 134–137. doi:10.1016/j.ebiom.2017.11.030
- Ndongoa, J. T., Issab, M. E., Messic, A. N., Mbingc, J. N., Cuendetb, M., Pegnyemb, D. E., et al. (2015). Cytotoxic flavonoids and other constituents from the stem bark of *Ochna schweinfurthiana*. *Nat. Prod. Res.* 29 (17), 1684–1687. doi:10.1080/14786419.2014.991321
- Pillai, V. C., Stromb, S. C., Caritis, S. N., and Venkataramanana, R. (2013). A sensitive and specific CYP cocktail assay for the simultaneous assessment of human cytochrome P450 activities in primary cultures of human hepatocytes using LC-MS/MS. *J. Pharm. Biomed. Anal.* 74, 126–132. doi:10.1016/j.jpba.2012.10.016

- Prueksaritanont, T., Chu, X., Gibson, C., Cui, D., Yee, K. L., Ballard, J., et al. (2013). Drug–drug interaction studies: Regulatory guidance and an industry perspective. *AAPS J.* 15 (3), 629–645. doi:10.1208/s12248-013-9470-x
- Qin, C. Z., Renb, X., Tana, Z. R., Chena, Y., Yina, J. Y., Yua, J., et al. (2013). A high-throughput inhibition screening of major human cytochrome P450 enzymes using an *in vitro* cocktail and liquid chromatography–tandem mass spectrometry. *Biomed. Chromatogr.* 28 (2), 197–203. doi:10.1002/bmc.300
- Spaggiari, D., Daali, Y., and Rudaz, S. (2016). An extensive cocktail approach for rapid risk assessment of *in vitro* CYP450 direct reversible inhibition by xenobiotic exposure. *Toxicol. Appl. Pharmacol.* 302, 41–51. doi:10.1016/j.taap.2016.04.013
- Spaggiari, D., Geiser, L., Daali, Y., and Rudaz, S. (2014). A cocktail approach for assessing the *in vitro* activity of human cytochrome P450s: An overview of current methodologies. *J. Pharm. Biomed. Anal.* 101, 221–237. doi:10.1016/j.jpba.2014.03.018
- Sudsakorn, S., Bahadduri, P., Fretland, J., and Lu, C. (2020). 2020 FDA drug–drug interaction guidance: A comparison analysis and action plan by pharmaceutical industrial scientists. *Curr. Drug Metab.* 21 (6), 403–426. doi:10.2174/1389200221666200620210522
- Sui, Y. X., Li, S. G., Shi, P. Y., Wu, Y. J., Li, Y. X., Chen, W. Y., et al. (2016). Ethyl acetate extract from *Selaginella doederleinii* Hieron inhibits the growth of human lung cancer cells A549 via caspase-dependent apoptosis pathway. *J. Ethnopharmacol.* 190, 261–271. doi:10.1016/j.jep.2016.06.029
- Sui, Y. X., Yao, H., Li, S. G., Jin, L., Shi, P. Y., Li, Z. J., et al. (2017). Delicaflavone induces autophagic cell death in lung cancer via Akt/mTOR/p70S6K signaling pathway. *J. Mol. Med.* 95 (3), 311–322. doi:10.1007/s00109-016-1487-z
- Thomford, N., Dzobo, K., Chopera, D., Wonkam, A., Maroyi, A., Blackhurst, D., et al. (2016). *In vitro* reversible and time-dependent CYP450 inhibition profiles of medicinal herbal plant extracts *newbouldia laevis* and *Cassia abbreviata*: Implications for herb–drug interactions. *Molecules* 21 (7), 891. doi:10.3390/molecules2107089
- Valicherla, G. R., Mishra, A., Lenkalapelly, S., Jillela, B., Francis, F. M., Rajagopalan, L., et al. (2019). Investigation of the inhibition of eight major human cytochrome P450 isozymes by a probe substrate cocktail *in vitro* with emphasis on CYP2E1. *Xenobiotica* 49 (12), 1396–1402. doi:10.1080/00498254.2019.1581301
- van Breemen, R. B. (2015). Development of safe and effective botanical dietary supplements. *J. Med. Chem.* 58 (21), 8360–8372. doi:10.1021/acs.jmedchem.5b00417
- Venkatakrishnan, K., von Moltke, L. L., Obach, R. S., and Greenblatt, D. J. (2003). Drug metabolism and drug interactions: Application and clinical value of *in vitro* models. *Curr. Drug Metab.* 4, 423–459. doi:10.2174/1389200033489361
- von Moltke, L. L., Weemhoff, J. L., Bedir, E., Khan, I. A., Harmatz, J. S., Goldman, P., et al. (2004). Inhibition of human cytochromes P450 by components of *Ginkgo biloba*. *J. Pharm. Pharmacol.* 56 (8), 1039–1044. doi:10.1211/0022357044021
- Wang, X. W., Chen, B., Xu, D. F., Li, Z. J., Sui, Y. X., and Lin, X. H. (2020). Delicaflavone reverses cisplatin resistance via endoplasmic reticulum stress signaling pathway in non-small cell lung cancer cells. *Onco Targets Ther.* 13, 10315–10322. doi:10.2147/ott.s255586
- Watanabe, A., Nakamura, K., Okudaira, N., Okazaki, O., and Sudo, K. I. (2007). Risk assessment for drug–drug interaction caused by metabolism-based inhibition of CYP3A using automated *in vitro* assay systems and its application in the early drug discovery process. *Drug Metab. Dispos.* 35, 1232–1238. doi:10.1124/dmd.107.015016
- Wrighton, S. A., Schuetz, E. G., Thummel, K. E., Shen, D. D., Korzekwa, K. R., Watkinspaul, B., et al. (2000). The human CYP3A subfamily: Practical considerations. *Drug Metab. Rev.* 32, 339–361. doi:10.1081/dmr-100102338
- Xia, C. H., Sun, J. G., Wang, G. J., Shang, L. L., ZhangZhang, X. X. R., et al. (2010). Herb–drug interactions: *In vivo* and *in vitro* effect of shenmai injection, a herbal preparation, on the metabolic activities of hepatic cytochrome P450 3A1/2, 2C6, 1A2, and 2E1 in rats. *Planta Med.* 76, 245–250. doi:10.1055/s-0029-1186082
- Xia, Y. L., Ge, G. B., Wang, P., Liang, S. C., He, Y. Q., Ning, J., et al. (2015). Structural modifications at the C-4 position strongly affect the glucuronidation of 6,7-dihydroxycoumarins. *Drug Metab. Dispos.* 43 (4), 553–560. doi:10.1124/dmd.114.060681
- Xia, Y. L., Liang, S. C., Zhu, L. L., Ge, G. B., He, G. Y., Ning, J., et al. (2014). Identification and characterization of human UDP-glucuronosyltransferases responsible for the glucuronidation of fraxetin. *Drug Metab. Pharmacokinet.* 29 (2), 135–140. doi:10.2133/dmpk.dmpk-13-rg-059
- Yao, H., Chen, B., Zhang, Y. Y., Ou, H. G., Li, Y. X., Li, S. G., et al. (2017). Analysis of the total biflavonoids extract from *Selaginella doederleinii* by HPLC-QTOF-MS and its *in vitro* and *in vivo* anticancer effects. *Molecules* 22, 325–342. doi:10.3390/molecules22020325
- Yao, W. S., Lin, Z., Shi, P. Y., Chen, B., Wang, G., Huang, J. Y., et al. (2020). Delicaflavone induces ROS-mediated apoptosis and inhibits PI3K/AKT/mTOR and Ras/MEK/Erk signaling pathways in colorectal cancer cells. *Biochem. Pharmacol.* 171, 113680–680. doi:10.1016/j.bcp.2019.113680
- Yao, W. S., Lin, Z., Wang, G., Li, S. G., Chen, B., Sui, Y. X., et al. (2019). Delicaflavone induces apoptosis via mitochondrial pathway accompanying G2/M cycle arrest and inhibition of MAPK signaling cascades in cervical cancer HeLa cells. *Phytomedicine* 62, 152973–973. doi:10.1016/j.phymed.2019.152973
- Youdim, K. A., and Saunders, K. C. (2010). A review of LC–MS techniques and high-throughput approaches used to investigate drug metabolism by cytochrome P450s. *J. Chromatogr. B* 878, 1326–1336. doi:10.1016/j.jchromb.2010.02.013
- Yu, S., Yan, H., Zhang, L., Shan, M., Chen, P., Ding, A., et al. (2017). A review on the phytochemistry, pharmacology, and pharmacokinetics of amentoflavone, a naturally-occurring biflavonoid. *Molecules* 22 (2), 299. doi:10.3390/molecules22020299
- Zhang, Z., Sun, T., Niu, J. g., He, Z. q., Liu, Y., and Wang, F. (2015). Amentoflavone protects hippocampal neurons: Anti-inflammatory, antioxidative, and antiapoptotic effects. *Neural Regen. Res.* 10, 1125–1133. doi:10.4103/1673-5374.160109
- Zheng, X. K., Li, Y. J., Zhang, L., Feng, W. S., and Zhang, X. (2011). Antihyperglycemic activity of *Selaginella tamariscina* (beauv.) spring. *J. Ethnopharmacol.* 133, 531–537. doi:10.1016/j.jep.2010.10.028



OPEN ACCESS

EDITED BY

Junmin Zhang,
Lanzhou University, China

REVIEWED BY

Guoping Yang,
Central South University, China
Jordan Baye,
Sanford Health Imagenetics,
United States

*CORRESPONDENCE

Fuchun Zheng,
✉ zhengfuchunsh@163.com
Yanqiang Peng,
✉ pengyqgzsums@163.com

[†]These authors have contributed equally
to this work and share first authorship

SPECIALTY SECTION

This article was submitted to Drug
Metabolism and Transport,
a section of the journal
Frontiers in Pharmacology

RECEIVED 19 November 2022

ACCEPTED 15 February 2023

PUBLISHED 27 February 2023

CITATION

Jiang Z, Wu Z, Liu R, Du Q, Fu X, Li M,
Kuang Y, Lin S, Wu J, Xie W, Shi G, Peng Y
and Zheng F (2023), Effect of
polymorphisms in drug metabolism and
transportation on plasma concentration
of atorvastatin and its metabolites in
patients with chronic kidney disease.
Front. Pharmacol. 14:1102810.
doi: 10.3389/fphar.2023.1102810

COPYRIGHT

© 2023 Jiang, Wu, Liu, Du, Fu, Li, Kuang,
Lin, Wu, Xie, Shi, Peng and Zheng. This is
an open-access article distributed under
the terms of the [Creative Commons
Attribution License \(CC BY\)](#). The use,
distribution or reproduction in other
forums is permitted, provided the original
author(s) and the copyright owner(s) are
credited and that the original publication
in this journal is cited, in accordance with
accepted academic practice. No use,
distribution or reproduction is permitted
which does not comply with these terms.

Effect of polymorphisms in drug metabolism and transportation on plasma concentration of atorvastatin and its metabolites in patients with chronic kidney disease

Zebin Jiang^{1†}, Zemin Wu^{2†}, Ruixue Liu², Qin Du², Xian Fu¹, Min Li²,
Yongjun Kuang², Shen Lin², Jiaxuan Wu³, Weiwei Xie⁴,
Ganggang Shi², Yanqiang Peng^{5*} and Fuchun Zheng^{1,2*}

¹Clinical Pharmacology Laboratory, First Affiliated Hospital of Shantou University Medical College, Shantou, China, ²Department of Pharmacology, Shantou University Medical College, Shantou, China, ³Department of Anesthesiology, Second Affiliated Hospital of Shantou University Medical College, Shantou, China, ⁴Department of Nephrology, Second Affiliated Hospital of Shantou University Medical College, Shantou, China, ⁵Department of Nephrology, First Affiliated Hospital of Shantou University Medical College, Shantou, China

Dyslipidemia due to renal insufficiency is a common complication in patients with chronic kidney diseases (CKD), and a major risk factor for the development of cardiovascular events. Atorvastatin (AT) is mainly used in the treatment of dyslipidemia in patients with CKD. However, response to the atorvastatin varies inter-individually in clinical applications. We examined the association between polymorphisms in genes involved in drug metabolism and transport, and plasma concentrations of atorvastatin and its metabolites (2-hydroxy atorvastatin (2-AT), 2-hydroxy atorvastatin lactone (2-ATL), 4-hydroxy atorvastatin (4-AT), 4-hydroxy atorvastatin lactone (4-ATL), atorvastatin lactone (ATL)) in kidney diseases patients. Genotypes were determined using TaqMan real time PCR in 212 CKD patients, treated with 20 mg of atorvastatin daily for 6 weeks. The steady state plasma concentrations of atorvastatin and its metabolites were quantified using ultraperformance liquid chromatography in combination with triple quadrupole mass spectrometry (UPLC–MS/MS). Univariate and multivariate analyses showed the variant in ABCC4 (rs3742106) was associated with decreased concentrations of AT and its metabolites (2-AT+2-ATL: $\beta = -0.162$, $p = 0.028$ in the dominant model; AT+2-AT+4-AT: $\beta = -0.212$, $p = 0.028$ in the genotype model), while patients carrying the variant allele ABCC4-rs868853 ($\beta = 0.177$, $p = 0.011$) or NR1I2-rs6785049 ($\beta = 0.123$, $p = 0.044$) had higher concentrations of 2-AT+2-ATL in plasma compared with homozygous wildtype carriers. Luciferase activity was enhanced in HepG2 cells harboring a construct expressing the rs3742106-T allele or the rs868853-G allele ($p < 0.05$ for each) compared with a construct expressing the rs3742106G or the rs868853-A allele. These findings suggest that two functional polymorphisms in the ABCC4 gene may affect transcriptional activity, thereby directly or indirectly affecting release of AT and its metabolites from hepatocytes into the circulation.

KEYWORDS

atorvastatin, genetic polymorphism, drug-metabolizing enzymes, transporters, plasma concentration, ABCC4

1 Introduction

China has one of the largest populations of patients with chronic kidney diseases (CKD) in Asia (up to 159.8 million in 2020) (Liyanage et al., 2022). Dyslipidemia due to renal insufficiency is a common complication in patients with CKD, leads to further development of kidney damage and deterioration of kidney function (Jungers et al., 1997). Both CKD and dyslipidemia are considered to be major risk factors for cardiovascular events (Sarnak et al., 2003; Kopin and Lowenstein, 2017). Therefore, for CKD patients, treatment of dyslipidemia is particularly important.

Atorvastatin (AT) is currently the first-line drug for lipid lowering and prevention of cardiovascular disease (Arca and Gaspardone, 2007). As an HMG-CoA reductase inhibitor, atorvastatin reduces cholesterol synthesis and increases the number of LDL receptors on the surface of hepatocytes, thereby reducing plasma LDL cholesterol levels, and has a stronger lipid-lowering effect in women or in patients with non-familial hyperlipidemia (Adams et al., 2015). In addition to its lipid-lowering effects, atorvastatin also protects the cardiovascular system and reduces damage to the kidney through its multiple anti-inflammatory, antioxidative, endothelial protective and anti-cell proliferative effects (Aviram et al., 1998; Mason, 2006). CKD patients who are not on dialysis or renal transplantation were are now recommended to adopt lipid-regulating therapy with statins, according to the Kidney Disease Improving Global Outcomes (KDIGO) Clinical Practice Guideline (Tonelli and Wanner, 2014).

However, there are significant individual differences in clinical responses (efficacy or toxicity) to atorvastatin among different patients. Previous studies have reported that nearly one-third of patients fail to achieve lipid-lowering goals despite dose adjustments to statins based on patient response to treatment (Mangravite et al., 2006). Observational studies have found that 10%–15% of statin users experience varying degrees of statin-related muscle side effects, including mild muscle pain, muscle cramps, muscle weakness and even the rare and serious symptom of rhabdomyolysis (Abd and Jacobson, 2011). This individual variation in pharmacodynamics is related to the level of drug in the plasma (Link et al., 2008). However, the plasma AT levels are not only influenced by clinical factors such as gender, age, BMI, co-morbidities and co-administration (Turner et al., 2020a; Hirota et al., 2020), but also are strongly associated with polymorphisms in genes related to drug absorption, distribution, metabolism and excretion (ADME) (DeGorter et al., 2013; Cruz-Correa et al., 2017; Turner et al., 2020b) which have been reported to have high inter-individual variability (45-fold) (DeGorter et al., 2013). It is also noteworthy that genetic variability may contribute to >90% of the variance in plasma AT concentrations, and mainly occurs in genes for drug metabolizing enzymes and transporters (DeGorter et al., 2013; Cruz-Correa et al., 2017; Turner et al., 2020b).

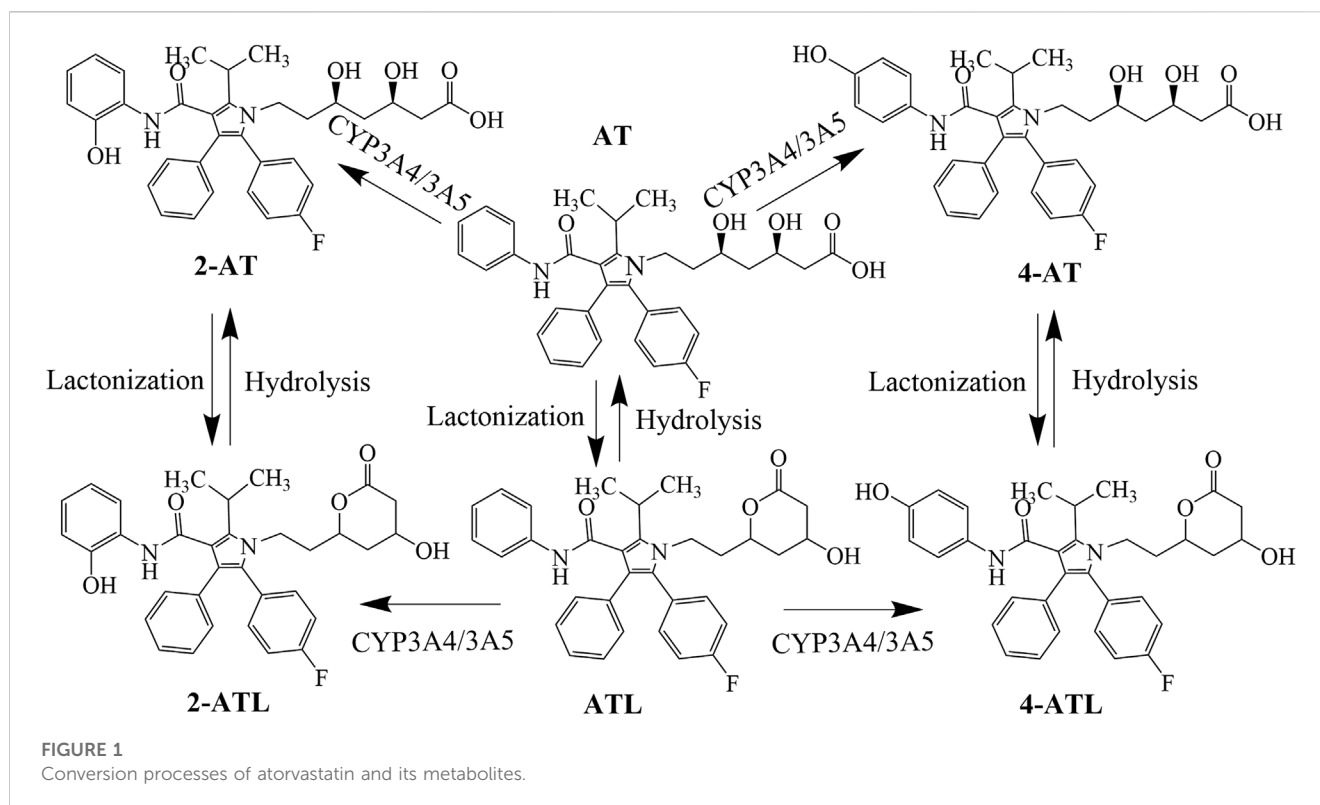
AT is administered orally as a calcium salt that is absorbed into the blood *via* the small intestine and taken up by the OATP transporter into hepatocytes, where it is metabolized by CYP3A4 and CYP3A5 to the partially bioactive hydroxylated derivatives (2-

hydroxy atorvastatin (2-AT) and 4-AT) (Lennernäs, 2003). AT and its active metabolites undergo lactonization *via* an unstable acyl glucuronide intermediate to produce AT lactone (ATL), 2-ATL and 4-ATL (Prueksaritanont et al., 2002). These lactone metabolites can be hydrolyzed to the corresponding hydroxy acids by plasma paraoxonases or by pH changes (Riedmaier et al., 2011) (Figure 1). AT and its metabolites are mainly eliminated by bile, with only about 1% excreted by the kidneys (Lennernäs, 2003). Its hydroxylated metabolite was found to inhibit HMG-CoA reductase as much as AT *in vitro*, about 70% of the total plasma HMG-CoA reductase inhibitory activity is accounted for by active metabolites (Lea and McTavish, 1997; Drake-Davis, 2004). In addition, the active metabolites of AT also protect the cardiovascular system with pleiotropic effects such as anti-oxidation and improvement of endothelial function.^[20, 21] Therefore, the plasma concentration of AT metabolites should also be of concern.

CYP3A4 and CYP3A5 enzymes are the main metabolizing enzymes for AT, playing an important role in disposition of AT. It has been reported that rs2242480, located on intron 10 of CYP3A4, is associated with the lipid-lowering efficacy of atorvastatin (Gao et al., 2008; Peng et al., 2018), and the presence of rs4646437 in CYP3A4 intron 7 affects CYP3A4 protein expression and enzymatic activity in a gender-dependent manner (Schirmer et al., 2007), but there has been no study on the effects of these polymorphisms on plasma AT concentration. CYP3A5*3 (rs776746C) in intron 3 of CYP3A5 leads to aberrant splicing of mRNA and truncation of protein, resulting in deletion of CYP3A5 protein in individuals homozygous for this allele (Kuehl et al., 2001), and has been shown to be associated with increased systemic atorvastatin in a prior bioequivalence study in healthy volunteers (Zubiaur et al., 2021).

The OATP1B1 transporter, encoded by *SLC O 1B1* (König et al., 2000), mediates the absorption of drugs into hepatocytes, and is the rate-limiting step in the hepatic clearance of atorvastatin (Maeda et al., 2011). Previous studies have revealed that single coding single-nucleotide polymorphisms (SNPs, rs4149056 and rs2306283) of *SLC O 1B1* are associated with the plasma AT concentration (DeGorter et al., 2013). Moreover, *SLC O 1B1* rs4149056 contributes to statin-induced myopathy, and the Clinical Pharmacogenetics Implementation Consortium (CPIC) has published guidelines for the use of atorvastatin in carriers of this SNP (Cooper-DeHoff et al., 2022), but it is not specifically indicated for CKD complications.

Atorvastatin is a substrate for the efflux transporters P-glycoprotein, encoded by *ABCB1*, and BCRP, encoded by *ABCG2*, which may limit intestinal absorption and biliary clearance of AT. The common SNPs of *ABCB1* (rs1045642, rs1128503 and rs2032582) have been reported to be associated with the lipid-lowering efficacy of atorvastatin (Thompson et al., 2005; Hoenig et al., 2011; Prado et al., 2018), but their association with plasma AT concentration is unknown. The *ABCG2* (421C>A) variant (rs2231142) contains a replacement of glutamine with lysine at position 141 in the intracellular region of the protein, and demonstrates lower protein expression and transport capacity in cells transfected with the variant than with the wild type (Imai et al.,



2002; Kondo et al., 2004). Although many studies have shown a correlation between rs2231142 and plasma concentrations of atorvastatin, the phenotypic results of the effects differ in different populations (Birmingham et al., 2015; Lee et al., 2019).

In addition to the above transporters, MRP3, MRP4 and MRP5, which are localized in the basolateral membrane of hepatocytes, have also been found to be involved in the transport of atorvastatin *in vitro* (Knauer et al., 2010; Deng et al., 2021), and their polymorphisms may play an important role in the plasma concentration of AT and its metabolites. Previous studies have indicated that rs4793665 located in the *ABCC3* promoter region, affects the plasma concentration of morphine and its metabolites, and it is now clear that polymorphisms in *ABCC4* rs2274407, rs3742106, rs868853 and rs9561778 have a significant effect on plasma levels, drug efficacy and disease susceptibility (Anderson et al., 2006; Low et al., 2009; Venkatasubramanian et al., 2014; Tanaka et al., 2015; Sánchez-Martín et al., 2016; Chidambaran et al., 2017; Che et al., 2018). Similarly, *ABCC5* variants (rs562 and rs3749438) also have been reported to be associated with severe irinotecan-induced toxicity and its plasma concentration (Chen et al., 2015; Teft et al., 2015).

The pregnane X receptor (PXR, *NR1I2*), a prototypical member of the nuclear receptor superfamily, can be activated by a range of steroids or exogenous drugs to regulate the transcription of target genes, and plays an important role in the regulation of the environmental homeostasis and pathophysiological processes (Rogers et al., 2021). Atorvastatin acts as a ligand for PXR and activates transcription of target genes, including *CYP3A4*, *CYP3A5*, *SLC O 1B1* and *ABCB1* (Marino et al., 2011; Hoffart et al., 2012), thereby affecting the metabolic process of the drug. Many studies

have reported that polymorphisms in *NR1I2* (rs6785049 and rs1523127) impact the pharmacokinetics of a variety of drugs, including immunosuppressive agents (Fanta et al., 2010; Mbatchi et al., 2017), antifungal agents (Zeng et al., 2020), antineoplastic agents (Liu et al., 2017) and anti-AIDS agents (Swart et al., 2012).

Accordingly, we examined the effects of reported polymorphisms in metabolic enzymes (*CYP3A4* and *CYP3A5*) and transporters (*SLC O 1B1*, *ABCB1* and *ABCG2*) associated with atorvastatin efficacy, as well as other drug transport-related gene (*ABCC3*, *ABCC4*, *ABCC5* and *NR1I2*) variants on plasma concentrations of atorvastatin and its metabolites in patients with CKD. The study of individual variation in plasma concentrations of atorvastatin and its metabolites at the genetic level is helpful to predict the efficacy and toxicity of atorvastatin in CKD patients accurately, and has practical guiding significance for clinical individualized drug application.

2 Materials and methods

2.1 Clinical pharmacogenetic study

2.1.1 Study population

A prospective study was performed with Chinese Han chronic kidney disease patients recruited from both out-patients and in-patients of the Nephrology Departments of the First and Second Affiliated Hospitals of Shantou University Medical College, from May 2014 to September 2019 (Chinese Clinical Trial Registry No. ChiCTR2000041391). According to the inclusion and exclusion criteria (Supplementary Table S1),

there were 354 eligible CKD patients, 142 patients were excluded due to missing data, a total of 212 CKD patients participated in our study. All patients were prescribed atorvastatin (Pfizer, NY, America) 20 mg/day for 6 weeks. Overnight fasting blood samples were collected from patients to measure biochemical parameters and drug levels. Baseline parameters were measured the morning of the day of treatment initiation, and final parameters were measured the day the 6-week treatment was completed. Demographic and clinical information, including age, sex, body, and medical histories were recorded. Estimated glomerular filtration rate (eGFR) was calculated according to the Chronic Kidney Disease Epidemiology Collaboration (CKD-EPI) equation (Levey et al., 2009). Experimental subjects were not randomized into groups and the experimenters were not blinded because these were deemed inappropriate for the design of this study. This study was approved by the ethics committees of the First and Second Affiliated Hospitals of Shantou University Medical College. All enrolled patients were informed of the purpose and other matters of the study, understood and signed the informed consent form.

2.1.2 Genotyping

DNA was isolated from EDTA-coated whole blood tubes, following patient blood collection, using a TIANamp blood DNA kit (TIANGEN, Beijing, China). The concentration and purity of extracted DNA following the manufacturer's protocols were determined with a Nanodrop 2000.

Genotyping was performed using TaqMan® Real Time Polymerase Chain Reaction (PCR) allelic discrimination assays, with a Drug Metabolism Enzyme or predesigned probe and primer (Applied Biosystems, CA, United States), according to the manufacturer's instructions. TaqMan drug metabolism enzyme genotyping assays (for *ABCB1* rs1128503, rs2032582, rs1045642, *ABCG2* rs2231142, *SLC O 1B1* rs2306283, rs4149056, *CYP3A5* rs776746, *CYP3A4* rs2242480, *ABCC4* rs3742106, rs2274407 and *NR1I2* rs1523127) used different PCR conditions from the predesigned TaqMan SNP genotyping assays (for *CYP3A4* rs4646437, *ABCC4* rs9561778, rs868853, *ABCC3* rs4793665, *ABCC5* rs562, rs3749438 and *NR1I2* rs6785049). Conditions for the former were as follows: 95°C for 10 min, followed by 50 cycles of 95°C for 15 s and 60°C for 90 s. For the latter, 40 cycles of a 1 min annealing/1 min extension were used. Hardy-Weinberg equilibrium tests were performed using chi square tests, where the allele frequencies of the study population were consistent with the law of genetic equilibrium, as indicated by a *p*-value >0.05.

2.1.3 Determination of atorvastatin and its metabolite concentrations

The concentrations of atorvastatin and its metabolites (2-AT, 4-AT, ATL, 2-ATL and 4-ATL) were quantified in EDTA plasma samples from the 6 week, when the concentration of atorvastatin and its metabolites were considered to remain at a steady-state level, by using an UPLC-MS/MS assay with a lower limit of quantification of 5 ng/mL. Blood samples from patients were mixed with 300ul internal standard solution (100 ug/ml methaqualone) in 2 ml polypropylene tubes, and the mixtures were vortex-mixed for 30 s then centrifuged at 14,000 rpm for

10 min at 4°C. A 3 µL aliquot was injected into a 2.7 µm Poroshell 120 EC-C18 column (4.6 × 100 mm, Agilent Technologies, Santa Clara, CA United States of America), and analytes were separated using gradient elution with 0.1% formic acid in water and methanol at a flow rate of 0.3 mL/min. Analyte detection was via multiple reaction monitoring (Sciex triple quadrupole 6,500 QTRAP mass spectrometer with a Turbo V electrospray source, AB Sciex, United States) using transitions of (*M* + *H*⁺) *m/z*: AT 559.3→440.2, 2-AT 575.2→440.2 4-AT 575.2→440.2, ATL 541.3→448.3, 2-ATL 557.2→448.2, 4-ATL 557.2→448.2, and methaqualone 251.2→132.2.

2.2 Plasmid construction and luciferase assay

Human embryonic kidney 293T cells (HEK293T) and human hepatocellular carcinoma cells (HepG2) were cultured at 37°C with 5% CO₂ and 95% humidity in Dulbecco's modified Eagle's medium (Gibco, United States) supplemented with 10% fetal bovine serum, 100 U/mL penicillin G sodium, and 100 µg/mL streptomycin sulfate (Gibco).

The 1740 bp 3'UTR of *ABCC4* (NM_005845), with incorporated terminal XbaI restriction sites, was amplified human genomic DNA with PCR primers. The fragment was then cloned into the luciferase reporter plasmid pGL3-promoter, and creation of the rs3742106 (T/G) polymorphism was achieved by site-directed mutagenesis. Similarly, the promoter of *ABCC4* gene was amplified with the primers 5'-TTTCTCTATCGATAGGTACCTAGGATTATAGGCGTGAGCC-3' (forward) and 5'-CTTAGATCGCAGATCTCGAGGCTGGGGCTCCGGCCGCCACGCC-3' (reverse). The products were digested with restriction endonucleases KpnI and XhoI, and then were cloned into pGL3-Basic vector, and the rs868853 (G/A) polymorphism was generated by using PCR-based site-directed mutagenesis. The recombinant plasmids were validated by PCR, endonuclease digestion, and DNA sequencing.

Plasmid DNA was isolated with a PureLink HiPure Plasmid Midiprep kit (Invitrogen, CA, United States), and supercoiled plasmid DNA was transfected into HEK293T and HepG2 cells using Lipofectamine 2,000 transfection reagent (Invitrogen) according to the manufacturer's protocol. The cells were plated in 12-well plates 1 day before transfection at a density of 1 × 10⁵ cells per well, and then were transfected with 2 µg of the reporter construct, 200 ng Renilla plasmid DNA and 2 µL Lipofectamine 2,000 after reaching 70%–80% confluence. After transfection for 24 h, cells were lysed for sequential measurement with the dual luciferase assay system (Promega, United States) in the ultra-sensitive GloMax Navigator Detection System instrument (Promega). Luciferase results are expressed as the ratio of firefly luciferase activity to Renilla luciferase activity from triplicate transfections.

2.3 Statistical analysis

Categorical data are presented as percentages, and continuous variables complied with normal distribution were

TABLE 1 Clinical and demographic characteristics of the study population for atorvastatin treatment (20 mg/day/6 weeks).

Characteristics		Total study population (n = 212)		
Age (years)		56.4 ± 10.9		
Males, N (%)		116 (54.7)		
Body mass index (kg/m ²)		23.2 ± 4.64		
Systolic blood pressure (mmHg)		142.0 ± 30.0		
Diastolic blood pressure (mmHg)		85.5 ± 12.0		
Hypertension, N (%)		167 (79.5)		
Diabetes, N (%)		87 (42.6)		
Cardiovascular disease, N (%)		53 (29.1)		
Smoking, N (%)		61 (28.9)		
Alcohol Consumption, N (%)		14 (6.6)		
Lipid level	Baseline	Post-Treatment	Change	p-value
TC (mmol/L)	5.89 ± 1.86	4.06 ± 1.09	−1.77 ± 1.56	<0.001
TG (mmol/L)	2.08 ± 1.72	1.54 ± 1.01	−0.32 ± 0.81	<0.001
HDL-C (mmol/L)	1.26 ± 0.41	1.23 ± 0.38	−0.04 ± 0.29	0.026
LDL-C (mmol/L)	3.86 ± 1.29	2.51 ± 0.96	−1.32 ± 1.06	<0.001
ApoAI (g/L)	1.40 ± 0.33	1.48 ± 0.37	0.04 ± 0.26	0.033
ApoB100 (g/L)	1.09 ± 0.34	0.74 ± 0.30	−0.33 ± 0.3	<0.001
LP(a) (mg/L)	292.75 ± 255.75	295.46 ± 279.41	−2.7 ± 89.45	0.831

Abbreviations: TC, total cholesterol; TG, HDL-C, High Density Lipoprotein-Cholesterol; LDL-C, Low Density Lipoprotein-Cholesterol; ApoAI, Apolipoprotein AI; ApoB100, Apolipoprotein B100; LP(a), Lipoprotein (a).

expressed as mean ± standard deviation (M ± SD). The Shapiro-Wilk test was used for normality testing and non-normal distributed variables are presented as the median ± interquartile range (M ± Q). The correlation between plasma concentrations of atorvastatin and its metabolites were analyzed by Spearman correlation analysis as these variables were skewed even with a log transformation.

Considering that the lactonization and hydrolysis of atorvastatin and its metabolites are reversible processes, the lactone metabolisms and their corresponding hydroxyl acids were analyzed as a whole (AT + ATL, 2-AT+2-ATL, 4-AT+4-ATL). The sum of the active components of atorvastatin (AT+2-AT+4-AT) was also analyzed. Plasma concentrations of atorvastatin and its metabolites below the lower limit of detection were excluded. Outlier values (mean ± 3*SD) suggestive of errors in sampling procedure, technical measurements or data manipulation were excluded from the analysis.

Ancestral alleles from the Ensembl Genome database were defined as wild-type alleles, and the association between the

genetic polymorphisms and the plasma concentration of atorvastatin and its metabolites were assessed in different genetic models (general, dominant, recessive models) by Mann–Whitney *U* or Kruskal–Wallis *H* tests. The addition concentration of atorvastatin lactone metabolites and their corresponding hydroxyl acids was log-transformed and then analyzed with clinical variables in univariate analyses. Any independent variables with a *p*-value of <0.1 in the univariate analysis were entered into a model of multivariable regression analysis to assess the influences of clinical variables on drug concentrations using the stepwise method. Finally, adjusting for gender, age, smoking and alcohol consumption, multivariable linear regression methods were used to evaluate the effects of genetic variation and baseline biochemical indices on plasma concentrations of atorvastatin and its metabolites. Statistical significance was defined having a two-sided *p*-value <0.05. Statistical analyses were performed using SPSS software (version 23, IBM, United States), and box and whisker plotting was performed using GraphPad Prism software (version 8.0.2.263, GraphPad, United States).

3 Results

3.1 Clinical characteristics of the study population

A total of 212 CKD patients were included in this study. The baseline clinical information of the patients is shown in Table 1. The average age of the patients was about 56 years old, and the male to female ratio was 1.2:1, 79.5% of patients had hypertensive disease, 42.6% had diabetes mellitus and 29.1% had cardiovascular disease. After 6 weeks of atorvastatin treatment, lipid levels of patients with CKD significantly improved.

Genotyped variants and their distribution in the population studied are shown in Table 2. All genotypes tested were in Hardy–Weinberg equilibrium with the exception of *CYP3A5* rs776746 (*p* = 0.003) and *ABCB1* rs2032582 (*p* = 0.027), and the minor allele frequency (MAF) was close to the MAF of the Southern Chinese Han Chinese in the 1,000 Genomes database (<https://www.ncbi.nlm.nih.gov/snp/>) except for rs776746 and rs2032582, and are given in Supplementary Table S2.

3.2 Atorvastatin and its metabolite concentrations

The plasma concentrations of atorvastatin and its metabolites varied widely among individuals, with patient plasma concentrations of atorvastatin ranging from 0.097 to 16.520 ng/mL, 2-hydroxy atorvastatin from 0.062 to 19.900 ng/mL, 4-hydroxy atorvastatin from 0.179 to 9.785 ng/mL, atorvastatin lactone from 0.064 to 66.390 ng/mL, 2-hydroxy atorvastatin lactone concentrations ranged from 0.196 to 11.510 ng/mL and 4-hydroxy atorvastatin lactone concentrations ranged from 0.398 to 81.700 ng/mL. Spearman's analysis of the correlation between atorvastatin and its metabolites showed that the concentrations of atorvastatin metabolites significantly correlated with the parent drug (*r* > 0.5, *p* < 0.0001) (Figure 2).

TABLE 2 Genotyped variants and their distribution in the studied population (n = 210).

Gene	SNPs	CHR	Location	Genotype	N (%)	MAF
<i>CYP3A4</i>	rs2242480 (intron)	7	99763843	TT	21 (10.0)	T = 0.312
				CT	89 (42.4)	
				CC	100 (47.6)	
<i>CYP3A4</i>	rs4646437 (intron)	7	99767460	AA	12 (5.7)	A = 0.193
				AG	57 (27.1)	
				GG	141 (67.1)	
<i>CYP3A5</i>	rs776746 (intron)	7	99672916	CC	69 (32.9)	T = 0.474
				CT	83 (39.5)	
				TT	58 (27.6)	
<i>SLC O 1B1</i>	rs4149056 (missense variant)	12	21178615	CC	4 (1.9)	C = 0.114
				CT	40 (19.0)	
				TT	166 (79.0)	
<i>SLC O 1B1</i>	rs2306283 (missense variant)	12	21176804	AA	10 (4.8)	A = 0.202
				AG	65 (31.0)	
				GG	135 (64.3)	
<i>ABCB1</i>	rs1128503 (synonymous variant)	7	87550285	AA	98 (46.7)	G = 0.31
				AG	94 (44.8)	
				GG	18 (8.6)	
<i>ABCB1</i>	rs1045642 (missense variant)	7	87509329	AA	31 (14.8)	A = 0.412
				AG	111 (52.9)	
				GG	68 (32.4)	
<i>ABCB1</i>	rs2032582 (missense variant)	7	87531302	CC	49 (23.3)	T = 0.1
				CA/CT	106 (50.5)	
				AA/TT/AT	55 (26.2)	
<i>ABCG2</i>	rs2231142 (missense variant)	4	88131171	GG	78 (37.1)	T = 0.369
				GT	109 (51.9)	
				TT	23 (11.0)	
<i>ABCC3</i>	rs4793665 (2 kb upstream)	17	50634726	CC	5 (2.4)	C = 0.131
				CT	45 (21.4)	
				TT	160 (76.2)	
<i>ABCC4</i>	rs3742106 (3'UTR)	13	95021537	AA	43 (20.5)	A = 0.486
				AC	118 (56.2)	
				CC	49 (23.3)	
<i>ABCC4</i>	rs9561778 (intron)	13	95061461	GG	92 (43.8)	T = 0.331
				GT	97 (46.2)	
				TT	21 (10.0)	
<i>ABCC4</i>	rs2274407 (missense variant)	13	95206781	AA	5 (2.4)	A = 0.152
				AC	54 (25.7)	

(Continued on following page)

TABLE 2 (Continued) Genotyped variants and their distribution in the studied population (n = 210).

Gene	SNPs	CHR	Location	Genotype	N (%)	MAF
ABCC4	rs868853 (2 kb upstream)	13	95302822	CC	151 (71.9)	C = 0.129
				CT	5 (2.4)	
				TT	44 (21.0)	
ABCC5	rs562 (3'UTR)	3	183920057	CC	161 (76.7)	C = 0.493
				CT	46 (21.9)	
				TT	115 (54.8)	
ABCC5	rs3749438 (intron)	3	183987396	CC	49 (23.3)	A = 0.436
				AG	103 (49.0)	
				GG	40 (19.0)	
NR1I2	rs6785049 (intron)	3	119814886	AA	78 (37.1)	A = 0.412
				AG	91 (43.3)	
				GG	41 (19.5)	
NR1I2	rs1523127 (5'UTR)	3	119782192	AA	121 (57.6)	C = 0.229
				AC	82 (39.0)	
				CC	7 (3.3)	

Notes: 2 blood samples were missing.
Abbreviations: SNP, single nucleotide polymorphism; CHR, chromosome; MAF, minor allele frequency.

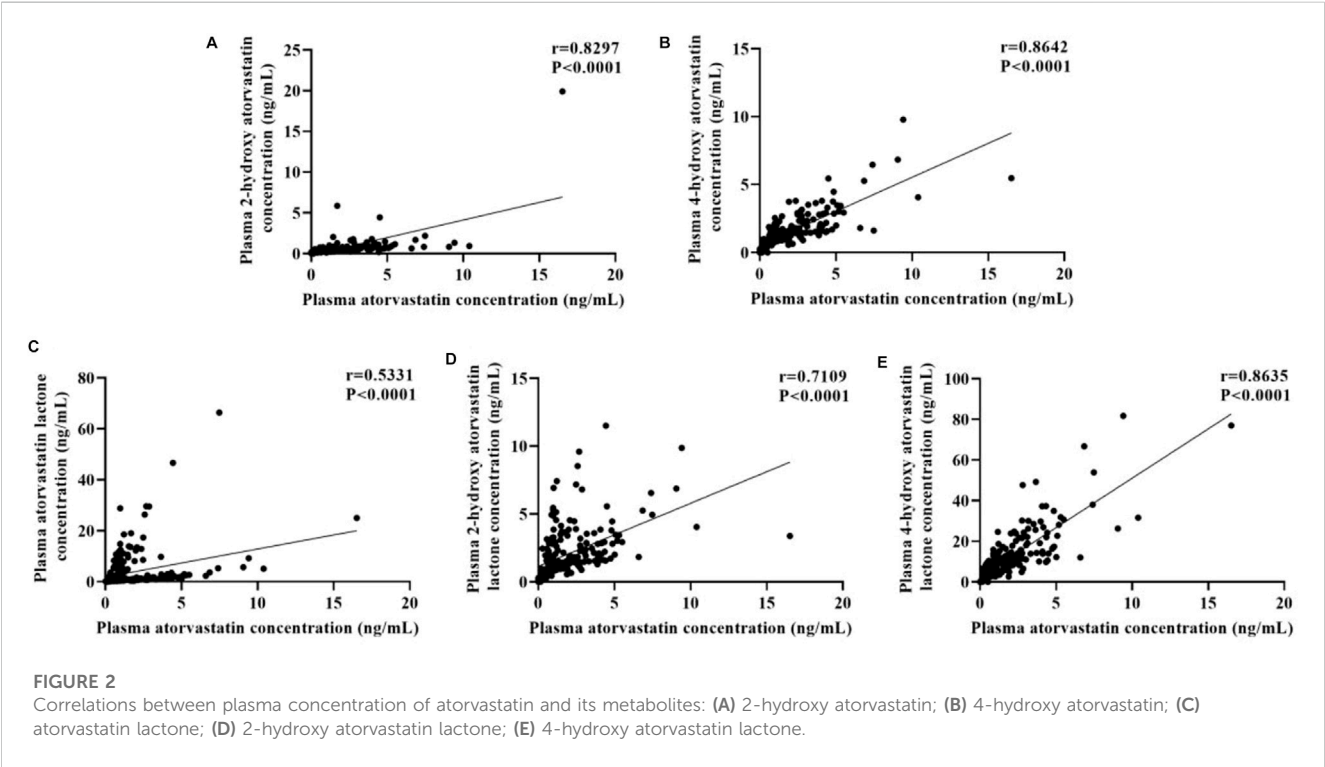


TABLE 3 Association between SNPs and plasma concentrations of AT + ATL.

Gene	SNP	Model	Genotypes	Cases	AT + ATL, $\mu\text{mol/L}$	<i>p</i> -value
					M \pm Q	
<i>ABCC4</i>	rs9561778	General	GG	88	0.0075 \pm 0.0105	Ref
			GT	94	0.0051 \pm 0.0095	0.05
			TT	20	0.0080 \pm 0.0150	0.458
<i>ABCC4</i>	rs9561778	Dominant	GG	88	0.0075 \pm 0.0105	0.039
			GT + TT	114	0.0053 \pm 0.0098	
<i>ABCC4</i>	rs3742106	Dominant	AA	42	0.0078 \pm 0.0174	0.034
			AC + CC	160	0.0059 \pm 0.0094	
<i>ABCB1</i>	rs1128503	Recessive	AA	95	0.0084 \pm 0.0111	0.047
			AG + GG	107	0.0050 \pm 0.0090	

Notes: bold fonts indicates $p < 0.05$.

TABLE 4 Association analysis between SNP and plasma concentration of 2-AT+2-ATL.

Gene	SNP	Model	Genotypes	Cases	2-AT+2-ATL, $\mu\text{mol/L}$	<i>p</i> -value
					M \pm Q	
<i>ABCC4</i>	rs3742106	General	AA	40	0.0050 \pm 0.0049	Ref
			AC	111	0.0039 \pm 0.0042	0.158
			CC	48	0.0029 \pm 0.0040	0.017
<i>ABCC4</i>	rs3742106	Dominant	AA	40	0.0050 \pm 0.0049	0.015
			AC + CC	159	0.0036 \pm 0.0044	
<i>ABCC4</i>	rs3742106	Recessive	CC	48	0.0029 \pm 0.0040	0.046
			AC + AA	151	0.0041 \pm 0.0041	
<i>ABCC4</i>	rs868853	General	TT	155	0.0036 \pm 0.0042	Ref
			CT	39	0.0056 \pm 0.0056	0.015
			CC	5	0.0026 \pm 0.0055	0.219
<i>ABCC4</i>	rs868853	Dominant	TT	155	0.0036 \pm 0.0042	0.017
			CT + CC	44	0.0050 \pm 0.0057	
<i>NR1I2</i>	rs6785049	Dominant	GG	75	0.0035 \pm 0.0045	0.048
			AG + AA	124	0.0039 \pm 0.0043	
<i>CYP3A5</i>	rs776746	Recessive	CC	66	0.0044 \pm 0.0054	0.049
			CT + TT	133	0.0036 \pm 0.0042	

Notes: bold fonts indicates $p < 0.05$.

3.3 Association between gene polymorphisms with plasma concentrations of atorvastatin and its metabolites

First, the effect of baseline clinical characteristics of plasma concentrations of atorvastatin and its metabolites was evaluated by univariate and multivariate analyses. A high Apolipoprotein AI (apoAI) level was correlated with higher plasma levels of AT +

ATL ($\beta = 0.421$, $p = 0.003$), and baseline Lipoprotein a (LPa) ($\beta = 2.44\text{E-}04$, $p = 0.037$) and glucose ($\beta = -0.019$, $p = 0.027$) had an independent influence on the concentration of 2-AT+2-ATL. In terms of the plasma level of AT+2-AT+4-AT, it depended in part on levels of apoAI ($\beta = 0.374$, $p < 0.001$), ALB ($\beta = -0.013$, $p = 0.012$), glucose ($\beta = -0.023$, $p = 0.012$), eGFR ($\beta = -0.004$, $p = 0.031$) and alcohol consumption ($\beta = -0.303$, $p = 0.015$), indicating exposure levels of atorvastatin and its metabolites

TABLE 5 Association analysis between genetic variants and plasma concentration of AT+2-AT+4-AT.

Gene	SNP	Model	Genotypes	Cases	AT+2-AT+4-AT,μmol/L	p-value
					M ± Q	
ABCC4	rs3742106	General	AA	42	0.0065 ± 0.0069	Ref
			AC	114	0.0053 ± 0.0074	0.377
			CC	49	0.0038 ± 0.0057	0.027
ABCC4	rs3742106	Recessive	CC	49	0.0038 ± 0.0057	0.008
			AC + AA	156	0.0056 ± 0.0074	

Notes: bold fonts indicates $p < 0.05$.

TABLE 6 Plasma atorvastatin and its metabolite concentrations-linear regression model coefficients.

Variable	Effect (β)	p-value	R ²
2-AT+2-ATL			
Glucose	−0.019	0.025	0.14
LP(a)	2.00E-04	0.083	
ABCC4 rs3742106	−0.162	0.028	
ABCC4 rs868853	0.177	0.011	
NR1I2 rs6785049	0.123	0.044	
AT+2-AT+4-AT			
ApoAI	0.352	0.001	0.19
ALB	−0.013	0.006	
Glucose	−0.021	0.026	
eGFR	−0.004	0.016	
ABCC4 rs3742106CC	−0.212	0.028	
ABCC4 rs3742106AC	−0.029	0.723	

Notes: bold fonts indicates $p < 0.05$.

Adjusted for gender, age, smoking and alcohol consumption.

LP(a), lipoprotein (a); ApoAI, Apolipoprotein AI; ALB, albumin; eGFR, estimated glomerular filtration rate.

may be affected by hepatic and renal function (Supplementary Table S3).

The effect of genetic polymorphisms on plasma concentration of atorvastatin and its metabolites was analyzed in different genetic models (Supplementary Tables S4A–C). In the general model, three SNPs of *ABCC4* were significantly associated with the concentration of atorvastatin and its metabolites, showing that plasma 2-AT+2-ATL and AT+2-AT+4-AT levels were lower in individuals with the rs3742106 homozygous variant allele (CC) than the wild-type allele carriers (approximately reduced by 42% in both, $p < 0.05$, Table 4, Table 5), but the plasma concentration of 2-AT+2-ATL significantly increased in patients with the rs868853 heterozygous genotype (CT) when compared with the TT genotype ($p = 0.015$, CT vs TT) (Table 4). After correcting p -values with the Bonferroni-Dunn test, no association between rs9561778 polymorphism and plasma AT + ATL levels was observed (Table 3).

In the dominant model, patients carrying the variant rs3742106 allele had lower levels of 2-AT+2-ATL than homozygous wild-type allele carriers ($p = 0.015$, AA vs AC + CC) (Table 4), and the homozygous wild-type rs9561778 allele carriers showed higher plasma concentrations of AT + ATL ($p = 0.029$, GG vs GT + TT). Interestingly, subjects with one or two

copies of the variant *ABCC4* rs868853 or *NR1I2* rs6785049 allele had increased plasma concentrations of 2-AT+2-ATL ($p = 0.017$, TT vs CT + TT; $p = 0.048$, GG vs AG + AA) (Table 4). For the *CYP3A4* rs464637 polymorphism, although the plasma concentration of 4-AT+4-ATL was distributed differently in carriers of different genotypes, there were only 10 cases of the AA genotype in CKD patients, which may reduce the statistical power.

In the recessive model, the wild-type rs1128503 allele carriers had lower AT + ATL levels ($p = 0.047$, AA vs AG + GG) (Table 3), but plasma levels of 2-AT+2-ATL and AT+2-AT+4-AT decreased in individuals with the homozygous rs3742106 variant than wild-type allele carriers ($p = 0.046$; $p = 0.008$; CC vs AC + AA) (Table 4, Table 5). There were no significant associations between these polymorphisms and the plasma concentrations of 4-AT+4-ATL (Supplementary Table S4).

Furthermore, multivariate linear regression analysis showed that the rs3742106 and rs868853 variants of *ABCC4* and the *NR1I2* rs6785049 polymorphism were predictors of plasma 2-AT+2-ATL levels after adjustment for gender, age, smoking and alcohol consumption. In addition, baseline levels of lipoprotein (a) and glucose were correlated to the plasma 2-AT+2-ATL concentration, which together explained 14% of the variance in the plasma 2-AT+2-ATL concentration (Table 6; Figure 3). The *ABCC4* rs3742106CC

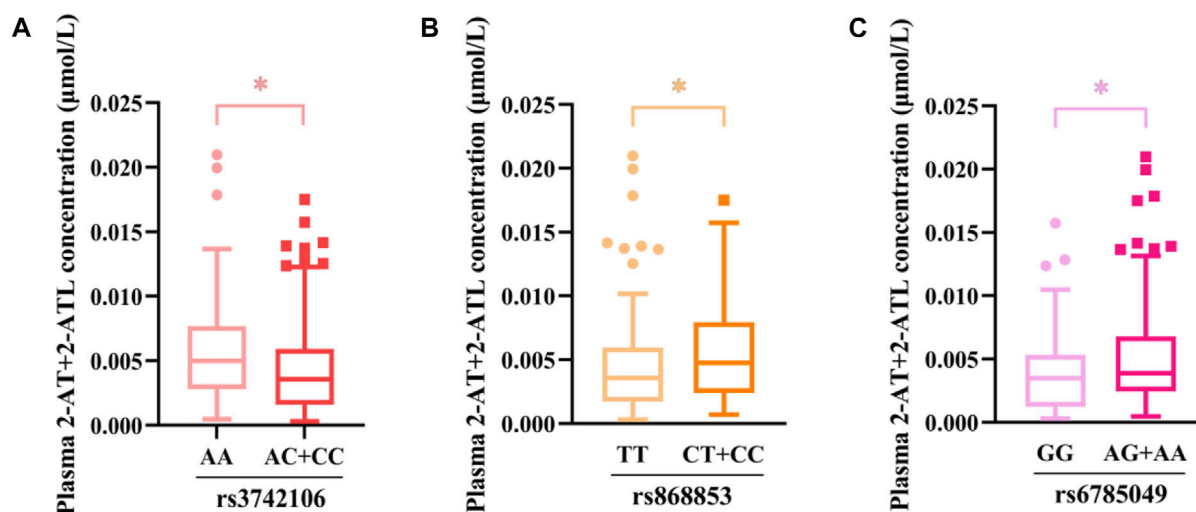


FIGURE 3
Association between genetic variants and the plasma concentration of 2-AT+2-ATL as determined using the Mann–Whitney *U* test. **p* < 0.05. (A) rs3742106; (B) rs868853; (C) rs6785049.

genotype was a predictor of lower AT+2-AT+4-AT levels ($\beta = -0.212$, $p = 0.028$), and explained 19% of the variance in the plasma levels of this component with other significantly non-genetic clinical factors (Table 6).

3.4 Functional effects of genetic variants *in vitro*

The clinical trial showed significant associations between *ABCC4* and *NR1I2* polymorphisms (rs868853, rs3742106 and rs6785049) with plasma levels of atorvastatin and its metabolites, so we further investigated the functional effects of these genetic variants *in vitro*. Since rs6785049 is located in intron of *NR1I2*, we only studied *ABCC4* polymorphisms, in the promoter and 3' untranslated (3'UTR) regions, using a luciferase assay *in vitro*. The luciferase constructs and information of the polymorphism sites are shown in Figures 4A,D. The constructs, which were comprised of the *ABCC4* sequence (promoter or 3'UTR region) and a luciferase reporter gene, were transfected into HEK293T and HepG2 cells. Functional studies showed variant alleles of rs868853-A had significantly lower luciferase activities than rs868853-G in both cell lines (HEK293T $p = 0.0026$, HepG2 $p = 0.022$), rs3742106-G had significantly lower luciferase activities than rs3742106-T in HepG2 cells lines ($p = 0.0031$), but not significantly in HEK293T ($p = 0.31$). (Figure 4).

4 Discussion

Individual differences in response to atorvastatin exist between patients. In this study, we investigated the association between genetic variants in drug metabolism- and transportation-related genes, and plasma concentrations of atorvastatin and its metabolites in patients with chronic kidney disease. Eighteen

polymorphisms in 9 genes (*CYP3A4*, *CYP3A5*, *SLC O 1B1*, *ABCB1*, *ABCG2*, *ABCC3*, *ABCC4*, *ABCC5* and *NR1I2*) were identified and displayed non-significant deviation from Hardy-Weinberg equilibrium, except for rs776746 and rs2032582, indicating that the study population is representative. However, the reason why two SNPs were not in equilibrium in our population is unclear.

DeGorter et al. demonstrated a high, 45-fold inter-individual variability in circulating atorvastatin levels following treatment with the same dose (DeGorter et al., 2013). Similarly, we found large individual differences in plasma concentrations of atorvastatin and its metabolites, especially for its lactone metabolites (over 80-fold). Considering that lactonization and hydrolysis of atorvastatin is reversible with a change in pH (Jemal and Xia, 2000), the lactone metabolites and their corresponding hydroxyl acids were analyzed as a whole, avoiding conversion that might be affected by environmental factors in the disposal of blood samples, and correlated with genetic polymorphisms. The results from univariate and multivariate analyses showed that the *ABCC4* rs3742106 polymorphism was associated with plasma concentrations of AT and its metabolite, indicating patients carrying the wild-type allele (C) have higher 2-AT+2-ATL and AT+2-AT+4-AT levels than variant allele (A) carriers. We further show rs3742106, located in the region of *ABCC4* encoding the 3'UTR, is an independent factor affecting plasma concentrations of AT and its metabolites.

ABCC4 is located on chromosome 13q32.1, contains 31 exons and encodes the multidrug resistance-associated protein MRP4, which is localized in the basolateral membrane of cells in the liver, but is more highly expressed in the parietal membrane of renal tubular cells in the kidney (Russel et al., 2008). *ABCC4* polymorphisms have mostly been reported to correlate with tumor prognosis and the efficacy of anti-HIV drugs. Anderson et al. reported that plasma lamivudine triphosphate concentrations were 20% higher in patients carrying the

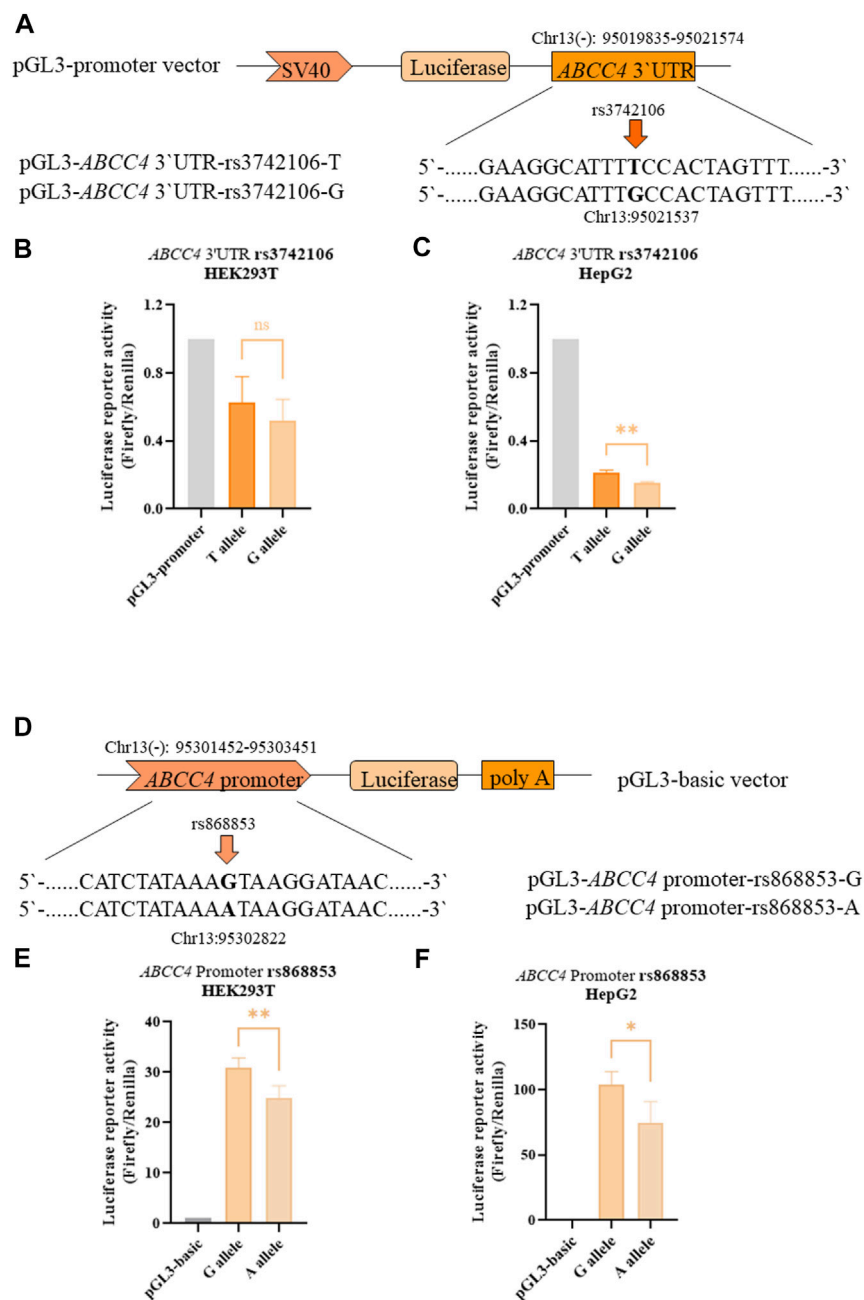


FIGURE 4

ABCC4 rs3742106 and rs868853 affect luciferase reporter activity. (A) Schematic representation of the *ABCC4* 3'UTR expression plasmid and the position of corresponding mutant sites. Firefly luciferase constructs contained the SV40 promoter, luciferase coding region and a fragment of the *ABCC4* 3'UTR. The rs3742106 SNP polymorphism site is indicated by the arrow. Plasmid constructs were transfected into HEK293T (B) and HepG2 cells (C). (D) Schematic representation of the *ABCC4* promoter expression plasmid and the position of the corresponding mutant sites. Firefly luciferase constructs contained 2 kb fragment of the *ABCC4* promoter, luciferase coding region and SV40 poly (A). The rs868853SNP polymorphism site is indicated by the arrow. Plasmid constructs were transfected into HEK293T (E) and HepG2 cells (F). Data represent the mean values of four independent experiments \pm SD. Each experiment was conducted in triplicate. Ns indicates statistically non-significant; * $p < 0.05$, ** $p < 0.01$ were considered as significant.

rs3742106 variant allele C than in carriers with the homozygous AA genotype (Anderson et al., 2006). Similarly, Rungtivasuwan et al. also found the plasma concentrations of tenofovir were 30% higher in patients carrying variant allele than in the AA genotype carriers infected with HIV (Rungtivasuwan et al., 2015), which is opposite to our findings. However, these seemingly paradoxical results can be

explained on the basis of the metabolic characteristics of the drug and the localization of MRP4. Anti-HIV drugs are mainly excreted by the kidneys, thus the level of MRP4 efflux transport in the parietal membrane of renal tubular cells can directly influence the plasma level of anti-HIV drugs. Thus, rs3742106C may reduce MRP4 protein expression, resulting in reduced efflux of drugs in

renal tubular cells (Anderson et al., 2006), allowing an increase in drug plasma concentrations. In contrast, atorvastatin is metabolized in the liver and mostly eliminated by the bile, with only about 1% excreted by the kidneys (Lennernäs, 2003). Combining the correlation between rs3742106 and plasma concentrations of AT and its metabolites with the reporter gene results, it is hypothesized that rs3742106C also decreases hepatic MPR4 protein expression, leading to a decrease in drug excretion from hepatocytes into the hepatic sinusoids and into the circulation, resulting in a decrease in plasma levels of AT and its metabolites. These results further validate Anderson's first hypothetical description of rs3742106 affecting the expression of *ABCC4*.

Variant allele carriers of rs868853(C), which is located in the *ABCC4* promoter, exhibited higher 2-AT+2-ATL levels than homozygous wild-type carriers (TT), and rs868853 was found to be an independent influence on plasma concentrations of 2-AT+2-ATL after adjusting for non-genetic factors by multiple linear regression. Palikhe et al. showed asthma patients with the rs868853G allele had higher concentrations of asthma severity markers in blood and urine, and that the rs868853G SNP increased *ABCC4* promoter transcriptional activity, suggesting that rs868853C may be associated with the transport of metabolites from immune cells (Palikhe et al., 2017). Additionally, carriers of the rs868853T allele were found to have a lower susceptibility to Kawasaki disease in a southern Chinese population (Che et al., 2018). However, there has been no reported on the association between this SNP and the pharmacokinetics or pharmacodynamics of drugs. To the best of our knowledge, this is the first report on the influence of rs868853 on plasma concentrations of AT and its metabolites. Interestingly, luciferase assays demonstrated the *ABCC4* rs868853G allele enhanced transcription compared with the rs868853A allele, which is consistent with Palikhe's results. Taken together, the rs868853(C/G) variant allele may enhance the transcriptional activity of *ABCC4*, resulting in enhanced expression of MRP4, leading to increased efflux of AT and its metabolites from the basal membrane of the hepatocyte into the circulation.

It was reported that rs9561778, located in an intron of *ABCC4*, was associated with cyclophosphamide-induced adverse effects (gastrointestinal toxicity and leukopenia or neutropenia) in patients with breast cancer, and FASTSNP suggested that rs9561778 may be located within transcription factor binding sites or intron enhancer sequences, and is a pathogenic variant affecting gene expression (Low et al., 2009). In our study, we found patients carrying the rs9561778 (T) variant allele had decreased concentrations of AT + ATL compared to homozygous wild-type (GG) carriers, but there was no statistical difference in our multiple linear regression analysis, suggesting that rs9561778 is not an independent factor affecting plasma concentrations of AT and its metabolites. Therefore, the association between the rs9561778 and plasma concentration of AT and its metabolites still needs to be further explored. Our results explain the clinical and cellular evidence that the polymorphisms of *ABCC4* are associated with the circulating levels of AT and its metabolites, which changed the expression of the transporter encoded by *ABCC4*.

The pregnane X receptor (PXR), is encoded by *NR1I2* on chromosome 3q12/13.3, and contains nine exons, but only

exons two to nine are involved in encoding protein (Zhang et al., 2001). PXR is widely expressed in a variety of tissues, mainly in the liver and intestine (Lamba et al., 2005). Genetic polymorphisms in PXR may explain the variation in the expression of the target genes (Lamba et al., 2005), which may affect the pharmacokinetics or pharmacodynamics of atorvastatin. Several studies have demonstrated a relationship between rs6785049 and the plasma concentrations of various drugs (Miura et al., 2008; Mbachi et al., 2017; Zeng et al., 2020). When we considered polymorphisms in *NR1I2*, we found rs6785049A was associated with increased concentration of 2-AT+2-ATL. Additionally, active metabolites (2-AT and 4-AT) of atorvastatin also are ligands of PXR, and 4-AT reduced induction of genes regulated by PXR compared to 2-AT and AT *in vitro*, which may be due to the weaker ability of the 4-AT to induce expression of target genes as the result of the retention of co-repressors during ligand activation (Hoffart et al., 2012). We show a genetic variant in PXR is associated with the plasma concentration of 2-AT+2-ATL, which may partly be explained in part by the metabolism of atorvastatin, i.e. since active metabolites are produced by CYP3A, acting as ligand to activate PXR regulates CYP3A4/CYP3A5, thereby producing more hydroxylated metabolites especially of 2-AT. Moreover, it has been reported that individuals with the GG genotype have twice the expression levels of CYP3A in enterocytes, than rs6785049A carriers, after the activation of PXR (Zhang et al., 2001). Taken together, these results imply that multiple pathways act together to cause differences in plasma 2-AT+2-ATL concentrations in patients carrying different genotypes.

CYP3A5 is another atorvastatin metabolizing enzyme, and its genetic polymorphisms have an important impact on the distribution of drugs (Zubiaur et al., 2021), although it has been found that CYP3A5 contributes less than 15% to atorvastatin metabolism *in vitro* (Park et al., 2008). CYP3A5*3 (rs776746C) is the major CYP3A5 allele that found in all ethnic groups (Zhou et al., 2017) and is functionally deficient (Kuehl et al., 2001). In our study, we found patients with the homozygous CC variant genotype have higher levels of 2-AT+2-ATL compared to the wild-type allele carriers. A previous study by Kim et al. found that after a single dose of simvastatin, the AUC₀₋₁₂ was 3.3-fold higher in healthy individuals with the CC genotype than in those with the TT genotype (Kim et al., 2007). On the contrary, Zubiaur et al. indicated individuals carrying the C allele had lower plasma concentration of atorvastatin than the TT genotype carriers (Zubiaur et al., 2021). Significantly, the CYP3A5 rs776746 polymorphism was not in equilibrium in our population. Thus, further association analysis between rs776746 and plasma concentrations of AT and its metabolites, in large representative groups, is needed to clarify the reason for the different conclusions.

The P-glycoprotein protein encoded by *ABCB1* plays an important role in the absorption of oral drugs in the intestine, and polymorphisms of this gene have been reported to be related to the lipid-lowering effect of atorvastatin (Thompson et al., 2005; Rebecchi et al., 2009; Hoenig et al., 2011; Kadam et al., 2016). Although rs1045642, located in exon 26 of *ABCB1*, does not change the expression of mRNA and protein, it may change of P-glycoprotein folding (Kimchi-Sarfaty et al., 2007). Non-

etheless, there is a lack of studies into the effect of *ABCB1*-rs1045642 on the metabolism of patients to atorvastatin. *ABCB1* rs1045642AA was associated with higher plasma concentrations of AT + ATL in this study. Therefore, this association still needs to be further verified.

Although a number of polymorphisms have been suggested as candidates for the pharmacokinetic variability of atorvastatin, the present study is the first to indicate the involvement of *ABCC4*-rs3742106 and rs868853, as well as *NR1I2*-rs6785049. While the current study demonstrates the contribution of genetic polymorphisms to the plasma concentrations of atorvastatin and its metabolites, there are a number of limitations. First, the sample size of this study is limited, and of a single ethnic population. Secondly, although drugs that may interact with atorvastatin have been excluded from the inclusion criteria, patients may have taken other medications during the 6 weeks of statin use, which may have had an impact on atorvastatin, and some drugs may have undetected effects on the statin, so factors of drug combination should be carefully analyzed in future research. In addition, it has been reported that chronic kidney disease affects the pharmacokinetics of drugs cleared by non-renal mechanisms (Yeung et al., 2014), thus the results of this study are only applicable to the CKD population.

5 Conclusion

In conclusion, the genetic variants in drug metabolism- and transportation-related genes and their effects on plasma concentrations of atorvastatin and its metabolites were identified and characterized in CKD patients. The present findings suggest the CC genotype of *ABCC4*-rs3742106 is associated with decreased concentrations of AT and its metabolites, whereas patients carrying the *ABCC4*-rs868853 or *NR1I2*-rs6785049 variant had higher concentrations of 2-AT+2-ATL in plasma compared with homozygous wild-type carriers with CKD. In addition, we also found that two *ABCC4* SNPs may affect transcriptional activity, thereby affecting release of AT and its metabolites from hepatocytes into the circulation. These novel findings increase the panel of potential genetic biomarkers related to atorvastatin metabolism, and the results also help to improve the efficacy and toxicity prediction of atorvastatin in patients with CKD.

Data availability statement

The original contributions presented in the study are included in the article/Supplementary Materials, further inquiries can be directed to the corresponding authors.

References

- Abd, T. T., and Jacobson, T. A. (2011). Statin-induced myopathy: A review and update. *Expert Opin. Drug Saf.* 10 (3), 373–387. doi:10.1517/14740338.2011.540568
- Adams, S. P., Tsang, M., and Wright, J. M. (2015). Lipid-lowering efficacy of atorvastatin. *Cochrane Database Syst. Rev.* 2015 (3), Cd008226. doi:10.1002/14651858.CD008226.pub3
- Anderson, P. L., Lamba, J., Aquilante, C. L., Schuetz, E., and Fletcher, C. V. (2006). Pharmacogenetic characteristics of indinavir, zidovudine, and lamivudine therapy in HIV-infected adults: A pilot study. *J. Acquir Immune Defic. Syndr.* 42 (4), 441–449. doi:10.1097/01.qai.0000225013.53568.69
- Arca, M., and Gaspardone, A. (2007). Atorvastatin efficacy in the primary and secondary prevention of cardiovascular events. *Drugs* 67, 29–42. doi:10.2165/00003495-200767001-00004
- Aviram, M., Rosenblat, M., Bisgaier, C. L., and Newton, R. S. (1998). Atorvastatin and gemfibrozil metabolites, but not the parent drugs, are potent antioxidants against lipoprotein oxidation. *Atherosclerosis* 138 (2), 271–280. doi:10.1016/s0021-9150(98)00032-x

Ethics statement

The studies involving human participants were reviewed and approved by the ethics committees of the First and Second Affiliated Hospitals of Shantou University Medical College. All enrolled patients were informed of the purpose and other matters of the study, understood and signed the informed consent form. The patients/participants provided their written informed consent to participate in this study.

Author contributions

FZ, GS, and YP designed the study, ZJ and ZW performed the experiments, wrote the manuscript and analyzed the data. RL, QD, XF, ML, YK, SL, JW, and WX helped collect the sample and recorded the information.

Funding

This study was supported by First Affiliated Hospital of Shantou University Medical College (NO: 2016067223-21).

Conflict of interest

The authors declare that the research was conducted in the absence of any commercial or financial relationships that could be construed as a potential conflict of interest.

Publisher's note

All claims expressed in this article are solely those of the authors and do not necessarily represent those of their affiliated organizations, or those of the publisher, the editors and the reviewers. Any product that may be evaluated in this article, or claim that may be made by its manufacturer, is not guaranteed or endorsed by the publisher.

Supplementary material

The Supplementary Material for this article can be found online at: <https://www.frontiersin.org/articles/10.3389/fphar.2023.1102810/full#supplementary-material>

- Birmingham, B. K., Bujac, S. R., Elsby, R., Azumaya, C. T., Wei, C., Chen, Y., et al. (2015). Impact of ABCG2 and SLCO1B1 polymorphisms on pharmacokinetics of rosuvastatin, atorvastatin and simvastatin acid in caucasian and asian subjects: A class effect? *Eur. J. Clin. Pharmacol.* 71 (3), 341–355. doi:10.1007/s00228-014-1801-z
- Che, D., Pi, L., Fang, Z., Xu, Y., Cai, M., Fu, L., et al. (2018). ABCG4 variants modify susceptibility to Kawasaki disease in a southern Chinese population. *Dis. Markers* 2018, 8638096. doi:10.1155/2018/8638096
- Chen, S., Villeneuve, L., Jonker, D., Couture, F., Laverdière, I., Cecchin, E., et al. (2015). ABCG5 and ABCG1 polymorphisms predict irinotecan-induced severe toxicity in metastatic colorectal cancer patients. *Pharmacogenet. Genomics* 25 (12), 573–583. doi:10.1097/fpg.0000000000000168
- Chidambaram, V., Venkatasubramanian, R., Zhang, X., Martin, L. J., Niu, J., Mizuno, T., et al. (2017). ABCG3 genetic variants are associated with postoperative morphine-induced respiratory depression and morphine pharmacokinetics in children. *Pharmacogenomics J.* 17 (2), 162–169. doi:10.1038/tpj.2015.98
- Cooper-DeHoff, R. M., Niemi, M., Ramsey, L. B., Luzum, J. A., Tarkainen, E. K., Straka, R. J., et al. (2022). The clinical pharmacogenetics implementation Consortium guideline for SLCO1B1, ABCG2, and CYP2C9 genotypes and statin-associated musculoskeletal symptoms. *Clin. Pharmacol. Ther.* 111, 1007–1021. doi:10.1002/cpt.2557
- Cruz-Correa, O. F., León-Cachón, R. B., Barrera-Saldaña, H. A., and Soberón, X. (2017). Prediction of atorvastatin plasma concentrations in healthy volunteers using integrated pharmacogenetics sequencing. *Pharmacogenomics* 18 (2), 121–131. doi:10.2217/pgs-2016-0072
- DeGorter, M. K., Tirona, R. G., Schwarz, U. I., Choi, Y. H., Dresser, G. K., Suskin, N., et al. (2013). Clinical and pharmacogenetic predictors of circulating atorvastatin and rosuvastatin concentrations in routine clinical care. *Circ. Cardiovasc. Genet.* 6 (4), 400–408. doi:10.1161/circgenetics.113.000099
- Deng, F., Tuomi, S. K., Neuvonen, M., Hirvensalo, P., Kulju, S., Wenzel, C., et al. (2021). Comparative hepatic and intestinal efflux transport of statins. *Drug Metab. Dispos.* 49 (9), 750–759. doi:10.1124/dmd.121.000430
- Fanta, S., Jönsson, S., Karlsson, M. O., Niemi, M., Holmberg, C., Hopppu, K., et al. (2010). Long-term changes in cyclosporine pharmacokinetics after renal transplantation in children: Evidence for saturable presystemic metabolism and effect of NR1I2 polymorphism. *J. Clin. Pharmacol.* 50 (5), 581–597. doi:10.1177/0091270009348223
- Gao, Y., Zhang, L., and Fu, Q. (2008). CYP3A4*1G polymorphism is associated with lipid-lowering efficacy of atorvastatin but not of simvastatin. *Eur. J. Clin. Pharmacol.* 64 (9), 877–882. doi:10.1007/s00228-008-0502-x
- Hirota, T., Fujita, Y., and Ieiri, I. (2020). An updated review of pharmacokinetic drug interactions and pharmacogenetics of statins. *Expert Opin. Drug Metab. Toxicol.* 16 (9), 809–822. doi:10.1080/17425255.2020.1801634
- Hoenig, M. R., Walker, P. J., Gurnsey, C., Beadle, K., and Johnson, L. (2011). The C3435T polymorphism in ABCB1 influences atorvastatin efficacy and muscle symptoms in a high-risk vascular cohort. *J. Clin. Lipidol.* 5 (2), 91–96. doi:10.1016/j.jacl.2011.01.001
- Hoffart, E., Ghebregiorghis, L., Nussler, A. K., Thasler, W. E., Weiss, T. S., Schwab, M., et al. (2012). Effects of atorvastatin metabolites on induction of drug-metabolizing enzymes and membrane transporters through human pregnane X receptor. *Br. J. Pharmacol.* 165, (5), 1595–1608. doi:10.1111/j.1476-5381.2011.01665.x
- Imai, Y., Nakane, M., Kage, K., Tsukahara, S., Ishikawa, E., Tsuruo, T., et al. (2002). C21A1 polymorphism in the human breast cancer resistance protein gene is associated with low expression of Q141K protein and low-level drug resistance. *Mol. Cancer Ther.* 1 (8), 611–616.
- Jemal, M., and Xia, Y. Q. (2000). Bioanalytical method validation design for the simultaneous quantitation of analytes that may undergo interconversion during analysis. *J. Pharm. Biomed. Anal.* 22 (5), 813–827. doi:10.1016/s0731-7085(00)00245-4
- Junger, P., Massy, Z. A., Nguyen Khoa, T., Fumeron, C., Labrunie, M., Lacour, B., et al. (1997). Incidence and risk factors of atherosclerotic cardiovascular accidents in predialysis chronic renal failure patients: A prospective study. *Nephrol. Dial. Transpl.* 12 (12), 2597–2602. doi:10.1093/ndt/12.12.2597
- Kadam, P., Ashavaid, T. F., Ponde, C. K., and Rajani, R. M. (2016). Genetic determinants of lipid-lowering response to atorvastatin therapy in an Indian population. *J. Clin. Pharm. Ther.* 41 (3), 329–333. doi:10.1111/jcpt.12369
- Kim, K. A., Park, P. W., Lee, O. J., Kang, D. K., and Park, J. Y. (2007). Effect of polymorphic CYP3A5 genotype on the single-dose simvastatin pharmacokinetics in healthy subjects. *J. Clin. Pharmacol.* 47 (1), 87–93. doi:10.1177/0091270006295063
- Kimchi-Sarfaty, C., Oh, J. M., Kim, I. W., Sauna, Z. E., Calcagno, A. M., Ambudkar, S. V., et al. (2007). A “silent” polymorphism in the MDR1 gene changes substrate specificity. *Science* 315 (5811), 525–528. doi:10.1126/science.1135308
- Knauper, M. J., Urquhart, B. L., Meyer zu Schwabedissen, H. E., Schwarz, U. I., Lemke, C. J., Leake, B. F., et al. (2010). Human skeletal muscle drug transporters determine local exposure and toxicity of statins. *Circ. Res.* 106 (2), 297–306. doi:10.1161/circresaha.109.203596
- Kondo, C., Suzuki, H., Itoda, M., Ozawa, S., Sawada, J., Kobayashi, D., et al. (2004). Functional analysis of SNPs variants of BCRP/ABCG2. *Pharm. Res.* 21 (10), 1895–1903. doi:10.1023/b:pham.0000045245.21637.d4
- König, J., Cui, Y., Nies, A. T., and Keppler, D. (2000). A novel human organic anion transporting polypeptide localized to the basolateral hepatocyte membrane. *Am. J. Physiology-Gastrointestinal Liver Physiology* 278 (1), G156–G164. doi:10.1152/ajpgi.2000.278.1.G156
- Kopin, L., and Lowenstein, C. (2017). Dyslipidemia. *Ann. Intern. Med.* 167 (11), Itc81–itc96. doi:10.7326/aitc201712050
- Kuehl, P., Zhang, J., Lin, Y., Lamba, J., Assem, M., Schuetz, J., et al. (2001). Sequence diversity in CYP3A promoters and characterization of the genetic basis of polymorphic CYP3A5 expression. *Nat. Genet.* 27 (4), 383–391. doi:10.1038/86882
- Lamba, J., Lamba, V., and Schuetz, E. (2005). Genetic variants of PXR (NR1I2) and CAR (NR1I3) and their implications in drug metabolism and pharmacogenetics. *Curr. Drug Metab.* 6 (4), 369–383. doi:10.2174/1389200054633880
- Lea, A. P., and McTavish, D. (1997). Atorvastatin. A review of its pharmacology and therapeutic potential in the management of hyperlipidaemias. *Drugs* 53 (5), 828–847. doi:10.2165/00003495-199753050-00011
- Lee, N., Maeda, K., Fukizawa, S., Ieiri, I., Tomaru, A., Akao, H., et al. (2019). Microdosing clinical study to clarify pharmacokinetic and pharmacogenetic characteristics of atorvastatin in Japanese hypercholesterolemic patients. *Drug Metab. Pharmacokinet.* 34 (6), 387–395. doi:10.1016/j.dmpk.2019.08.004
- Lennernas, H. (2003). Clinical pharmacokinetics of atorvastatin. *Clin. Pharmacokinet.* 42 (13), 1141–1160. doi:10.2165/00003088-200342130-00005
- Levey, A. S., Stevens, L. A., Schmid, C. H., Zhang, Y. L., Castro, A. F., 3rd, Feldman, H. I., et al. (2009). A new equation to estimate glomerular filtration rate. *Ann. Intern. Med.* 150 (9), 604–612. doi:10.7326/0003-4819-150-9-200905050-00006
- Link, E., Parish, S., Armitage, J., Bowman, L., Heath, S., Matsuda, F., et al. (2008). SLCO1B1 variants and statin-induced myopathy—a genome-wide study. *N. Engl. J. Med.* 359 (8), 789–799. doi:10.1056/NEJMoa0801936
- Liu, J., Chen, Z., Chen, H., Hou, Y., Lu, W., He, J., et al. (2017). Genetic polymorphisms contribute to the individual variations of imatinib mesylate plasma levels and adverse reactions in Chinese GIST patients. *Int. J. Mol. Sci.* 18 (3), 603. doi:10.3390/ijms18030603
- Liyanage, T., Toyama, T., Hockham, C., Ninomiya, T., Perkovic, V., Woodward, M., et al. (2022). Prevalence of chronic kidney disease in Asia: A systematic review and analysis. *BMJ Glob. Health* 7 (1), e007525. doi:10.1136/bmjgh-2021-007525
- Low, S. K., Kiyotani, K., Mushihiro, T., Daigo, Y., Nakamura, Y., and Zembutsu, H. (2009). Association study of genetic polymorphism in ABCG4 with cyclophosphamide-induced adverse drug reactions in breast cancer patients. *J. Hum. Genet.* 54 (10), 564–571. doi:10.1038/jhg.2009.79
- Maeda, K., Ikeda, Y., Fujita, T., Yoshida, K., Azuma, Y., Haruyama, Y., et al. (2011). Identification of the rate-determining process in the hepatic clearance of atorvastatin in a clinical cassette microdosing study. *Clin. Pharmacol. Ther.* 90 (4), 575–581. doi:10.1038/clpt.2011.142
- Mangravite, L. M., Thorn, C. F., and Krauss, R. M. (2006). Clinical implications of pharmacogenomics of statin treatment. *Pharmacogenomics J.* 6 (6), 360–374. doi:10.1038/sj.tpj.6500384
- Marino, M., di Masi, A., Trezza, V., Pallottini, V., Polticelli, F., and Ascenzi, P. (2011). Xenosensors CAR and PXR at work: Impact on statin metabolism. *Curr. Drug Metab.* 12 (3), 300–311. doi:10.2174/138920011795101859
- Mason, R. P. (2006). Molecular basis of differences among statins and a comparison with antioxidant vitamins. *Am. J. Cardiol.* 98, 34p–41p. doi:10.1016/j.amjcard.2006.09.018
- Mbatchi, L. C., Gassiot, M., Pourquier, P., Goberna, A., Mahammedi, H., Mourey, L., et al. (2017). Association of NR1I2, CYP3A5 and ABCB1 genetic polymorphisms with variability of temsirolimus pharmacokinetics and toxicity in patients with metastatic bladder cancer. *Cancer Chemother. Pharmacol.* 80 (3), 653–659. doi:10.1007/s00280-017-3379-5
- Miura, M., Satoh, S., Inoue, K., Kagaya, H., Saito, M., Inoue, T., et al. (2008). Influence of CYP3A5, ABCB1 and NR1I2 polymorphisms on prednisolone pharmacokinetics in renal transplant recipients. *Steroids* 73 (11), 1052–1059. doi:10.1016/j.steroids.2008.04.002
- Palikhe, S., Uganbayar, U., Trinh, H. K. T., Ban, G. Y., Yang, E. M., Park, H. S., et al. (2017). A role of the ABCG4 gene polymorphism in airway inflammation of asthmatics. *Mediat. Inflamm.* 2017, 3549375. doi:10.1155/2017/3549375
- Park, J. E., Kim, K. B., Bae, S. K., Moon, B. S., Liu, K. H., and Shin, J. G. (2008). Contribution of cytochrome P450 3A4 and 3A5 to the metabolism of atorvastatin. *Xenobiotica* 38 (9), 1240–1251. doi:10.1080/00498250802334391
- Peng, C., Ding, Y., Yi, X., Shen, Y., Dong, Z., Cao, L., et al. (2018). Polymorphisms in CYP450 genes and the therapeutic effect of atorvastatin on ischemic stroke: A

- retrospective cohort study in Chinese population. *Clin. Ther.* 40 (3), 469–477.e2. doi:10.1016/j.clinthera.2018.02.002
- Prado, Y., Zambrano, T., and Salazar, L. A. (2018). Transporter genes ABCG2 rs2231142 and ABCB1 rs1128503 polymorphisms and atorvastatin response in Chilean subjects. *J. Clin. Pharm. Ther.* 43 (1), 87–91. doi:10.1111/jcpt.12607
- Prake-Davis (2004). Prake-davis, *Product information: Lipitor (atorvastatin calcium)*. Ann Arbor, MI: Prake-Davis(Divisiioin of Pfizer Inc.
- Prueksaritanont, T., Subramanian, R., Fang, X., Ma, B., Qiu, Y., Lin, J. H., et al. (2012). Glucuronidation of statins in animals and humans: A novel mechanism of statin lactonization. *Drug Metab. Dispos.* 30 (5), 505–512. doi:10.1124/dmd.30.5.505
- Rebecchi, I. M., Rodrigues, A. C., Arazi, S. S., Genvigir, F. D., Willrich, M. A., Hirata, M. H., et al. (2009). ABCB1 and ABCB1 expression in peripheral mononuclear cells is influenced by gene polymorphisms and atorvastatin treatment. *Biochem. Pharmacol.* 77 (1), 66–75. doi:10.1016/j.bcp.2008.09.019
- Riedmaier, S., Klein, K., Winter, S., Hofmann, U., Schwab, M., and Zanger, U. M. (2011). Paraoxonase (PON1 and PON3) polymorphisms: Impact on liver expression and atorvastatin-lactone hydrolysis. *Front. Pharmacol.* 2, 41. doi:10.3389/fphar.2011.00041
- Rogers, R. S., Parker, A., Vainer, P. D., Elliott, E., Sudbeck, D., Parimi, K., et al. (2021). The interface between cell signaling pathways and pregnane X receptor. *Cells* 10 (11), 3262. doi:10.3390/cells10113262
- Rungtivasuwan, K., Avihingsanon, A., Thammajaruk, N., Mitruk, S., Burger, D. M., Ruxrungtham, K., et al. (2015). Influence of ABCC2 and ABCC4 polymorphisms on tenofovir plasma concentrations in Thai HIV-infected patients. *Antimicrob. Agents Chemother.* 59 (6), 3240–3245. doi:10.1128/aac.04930-14
- Russel, F. G., Koenderink, J. B., and Masereeuw, R. (2008). Multidrug resistance protein 4 (MRP4/ABCC4): A versatile efflux transporter for drugs and signalling molecules. *Trends Pharmacol. Sci.* 29 (4), 200–207. doi:10.1016/j.tips.2008.01.006
- Sánchez-Martín, A., Cabrera Figueroa, S., Cruz, R., Porras-Hurtado, L., Calvo-Boyer, F., Rasool, M., et al. (2016). Gene-gene interactions between DRD3, MRP4 and CYP2B6 polymorphisms and its influence on the pharmacokinetic parameters of efavirenz in HIV infected patients. *Drug Metab. Pharmacokinet.* 31 (5), 349–355. doi:10.1016/j.dmpk.2016.06.001
- Sarnak, M. J., Levey, A. S., Schoolwerth, A. C., Coresh, J., Culleton, B., Hamm, L. L., et al. (2003). Kidney disease as a risk factor for development of cardiovascular disease: A statement from the American heart association councils on kidney in cardiovascular disease, high blood pressure research, clinical cardiology, and Epidemiology and prevention. *Circulation* 108 (17), 2154–2169. doi:10.1161/01.Cir.0000095676.90936.80
- Schirmer, M., Rosenberger, A., Klein, K., Kulle, B., Toliat, M. R., Nürnberg, P., et al. (2007). Sex-dependent genetic markers of CYP3A4 expression and activity in human liver microsomes. *Pharmacogenomics* 8 (5), 443–453. doi:10.2217/14622416.8.5.443
- Swart, M., Whitehorn, H., Ren, Y., Smith, P., Ramesar, R. S., and Dandara, C. (2012). PXR and CAR single nucleotide polymorphisms influence plasma efavirenz levels in South African HIV/AIDS patients. *BMC Med. Genet.* 13, 112. doi:10.1186/1471-2350-13-112
- Tanaka, Y., Manabe, A., Fukushima, H., Suzuki, R., Nakadate, H., Kondoh, K., et al. (2015). Multidrug resistance protein 4 (MRP4) polymorphisms impact the 6-mercaptopurine dose tolerance during maintenance therapy in Japanese childhood acute lymphoblastic leukemia. *Pharmacogenomics J.* 15 (4), 380–384. doi:10.1038/tpj.2014.74
- Teft, W. A., Welch, S., Lenehan, J., Parfitt, J., Choi, Y. H., Winquist, E., et al. (2015). OATP1B1 and tumour OATP1B3 modulate exposure, toxicity, and survival after irinotecan-based chemotherapy. *Br. J. Cancer* 112 (5), 857–865. doi:10.1038/bjc.2015.5
- Thompson, J. F., Man, M., Johnson, K. J., Wood, L. S., Lira, M. E., Lloyd, D. B., et al. (2005). An association study of 43 SNPs in 16 candidate genes with atorvastatin response. *Pharmacogenomics J.* 5 (6), 352–358. doi:10.1038/sj.tpj.6500328
- Tonelli, M., and Wanner, C. Kidney Disease: Improving Global Outcomes Lipid Guideline Development Work Group Members (2014). Lipid management in chronic kidney disease: Synopsis of the kidney disease: Improving global Outcomes 2013 clinical practice guideline. *Ann. Intern. Med.* 160 (3), 182. doi:10.7326/m13-2453
- Turner, R. M., Fontana, V., FitzGerald, R., Morris, A. P., and Pirmohamed, M. (2020a). Investigating the clinical factors and comedications associated with circulating levels of atorvastatin and its major metabolites in secondary prevention. *Br. J. Clin. Pharmacol.* 86 (1), 62–74. doi:10.1111/bcp.14133
- Turner, R. M., Fontana, V., Zhang, J. E., Carr, D., Yin, P., FitzGerald, R., et al. (2020b). A genome-wide association study of circulating levels of atorvastatin and its major metabolites. *Clin. Pharmacol. Ther.* 108 (2), 287–297. doi:10.1002/cpt.1820
- Venkatasubramanian, R., Fukuda, T., Niu, J., Mizuno, T., Chidambaram, V., Vinks, A. A., et al. (2014). ABCC3 and OCT1 genotypes influence pharmacokinetics of morphine in children. *Pharmacogenomics* 15 (10), 1297–1309. doi:10.2217/pgs.14.99
- Yeung, C. K., Shen, D. D., Thummel, K. E., and Himmelfarb, J. (2014). Effects of chronic kidney disease and uremia on hepatic drug metabolism and transport. *Kidney Int.* 85 (3), 522–528. doi:10.1038/ki.2013.399
- Zeng, G., Wang, L., Shi, L., Li, H., Zhu, M., Luo, J., et al. (2020). Variability of voriconazole concentrations in patients with hematopoietic stem cell transplantation and hematological malignancies: Influence of loading dose, procainolone, and pregnane X receptor polymorphisms. *Eur. J. Clin. Pharmacol.* 76 (4), 515–523. doi:10.1007/s00228-020-02831-1
- Zhang, J., Kuehl, P., Green, E. D., Touchman, J. W., Watkins, P. B., Daly, A., et al. (2001). The human pregnane X receptor: Genomic structure and identification and functional characterization of natural allelic variants. *Pharmacogenetics* 11 (7), 555–572. doi:10.1097/00008571-200110000-00003
- Zhou, Y., Ingelman-Sundberg, M., and Lauschke, V. M. (2017). Worldwide distribution of cytochrome P450 alleles: A meta-analysis of population-scale sequencing projects. *Clin. Pharmacol. Ther.* 102 (4), 688–700. doi:10.1002/cpt.690
- Zubiaur, P., Benedicto, M. D., Villapalos-García, G., Navares-Gómez, M., Mejía-Abril, G., Román, M., et al. (2021). SLCO1B1 phenotype and CYP3A5 polymorphism significantly affect atorvastatin bioavailability. *J. Personalized Med.* 11 (3), 204. doi:10.3390/jpm11030204



OPEN ACCESS

EDITED BY

Junmin Zhang,
Lanzhou University, China

REVIEWED BY

An Kang,
Nanjing University of Chinese Medicine,
China
Yuan Wei,
Jiangsu University, China

*CORRESPONDENCE

Jing Lu,
✉ lujing28@mail.sysu.edu.cn
Jianwen Chen,
✉ 573016880@qq.com
Peiqing Liu,
✉ liupq_sysu@163.com

[†]These authors have contributed equally
to this work and share first authorship

SPECIALTY SECTION

This article was submitted to Drug
Metabolism and Transport,
a section of the journal
Frontiers in Pharmacology

RECEIVED 19 December 2022

ACCEPTED 27 February 2023

PUBLISHED 09 March 2023

CITATION

He X, Zhong Z, Wang Q, Jia Z, Lu J,
Chen J and Liu P (2023),
Pharmacokinetics and tissue distribution
of bleomycin-induced idiopathic
pulmonary fibrosis rats treated
with cryptotanshinone.
Front. Pharmacol. 14:1127219.
doi: 10.3389/fphar.2023.1127219

COPYRIGHT

© 2023 He, Zhong, Wang, Jia, Lu, Chen
and Liu. This is an open-access article
distributed under the terms of the
Creative Commons Attribution License
(CC BY). The use, distribution or
reproduction in other forums is
permitted, provided the original author(s)
and the copyright owner(s) are credited
and that the original publication in this
journal is cited, in accordance with
accepted academic practice. No use,
distribution or reproduction is permitted
which does not comply with these terms.

Pharmacokinetics and tissue distribution of bleomycin-induced idiopathic pulmonary fibrosis rats treated with cryptotanshinone

Xiangjun He^{1†}, Zhi Zhong^{1†}, Quan Wang¹, Zhenmao Jia¹, Jing Lu^{2*},
Jianwen Chen^{2*} and Peiqing Liu^{2*}

¹National and Local United Engineering Lab of Druggability and New Drugs Evaluation, School of Pharmaceutical Sciences, Sun Yat-Sen University, Guangzhou, China, ²Guangdong Provincial Key Laboratory of New Drug Design and Evaluation, School of Pharmaceutical Sciences, Sun Yat-Sen University, Guangzhou, China

Introduction: Cryptotanshinone(CTS), a compound derived from the root of *Salvia miltiorrhiza*, has been linked to various of diseases, particularly pulmonary fibrosis. In the current study, we investigated the benefit of CTS on Sprague-Dawley (SD) rats induced by bleomycin (BLM) and established high performance liquid chromatography-tandem mass spectrometry (HPLC-MS/MS) methods to compare pharmacokinetics and tissue distribution in subsequent normal and modulated SD rats.

Methods: The therapeutic effect of CTS on BLM-induced SD rats was evaluated using histopathology, lung function and hydroxyproline content measurement, revealing that CTS significantly improved SD rats induced by BLM. Additionally, a simple, rapid, sensitive and specific HPLC-MS/MS method was developed to determine the pharmacokinetics of various components in rat plasma.

Results: Pharmacokinetic studies indicated that CTS was slowly absorbed by oral administration and had low bioavailability and a slow clearance rate. The elimination of pulmonary fibrosis in 28-day rats was slowed down, and the area under the curve was increased compared to the control group. Long-term oral administration of CTS did not accumulate *in vivo*, but the clearance was slowed down, and the steady-state blood concentration was increased. The tissue distribution study revealed that CTS exposure in the lungs and liver.

Discussion: The lung CTS exposure was significantly higher in the model group than in the control group, suggesting that the pathological changes of pulmonary fibrosis were conducive to the lung exposure of CTS and served as the target organ of CTS.

KEYWORDS

cryptotanshinone, pulmonary fibrosis, comparative pharmacokinetic, tissue distribution, HPLC-MS/MS

1 Introduction

Pulmonary Fibrosis (PF) is a chronic, progressive and irreversible lung disease common in clinical practice. In the early stage, it is characterized by alveolar epithelial cell injury, interstitial lung inflammation and interstitial lung edema. In the end stage, a large amount of Extracellular Matrix (ECM) deposition, abnormal proliferation, activation of fibroblasts and destruction of tissue structure destruction occur (Urban et al., 2015; Barratt et al., 2018; Sgalla et al., 2018). The lung tissue thickens, scar tissue forms and lung function decrease significantly, eventually developing organ dysfunction and respiratory failure (King et al., 2011). Pulmonary fibrosis is prevalent in the elderly, and its incidence increases yearly. The average life expectancy after diagnosis is approximately 2.8 years, and the salvage rate is lower than for most tumors (Chanda et al., 2019). The etiology of pulmonary fibrosis is complex. Many factors are known to cause pulmonary fibrosis, such as smoking, environmental pollution, lung injury, virus and drugs (Rangarajan et al., 2016). Idiopathic pulmonary fibrosis (IPF), the most severe form of pulmonary fibrosis, has a high mortality rate and a poor prognosis (Richeldi et al., 2017). Pulmonary fibrosis is treated primarily with glucocorticoids, anti-inflammatory drugs, immunosuppressants, and antifibrotic drugs. Although drug therapy can alleviate disease symptoms and improve respiratory function, long-term use is prone to adverse reactions (du Bois, 2010) and cannot significantly improve the survival rate of patients (Spagnolo et al., 2015). It is important to obtain more effective drugs due to adverse reactions and the limited effectiveness of existing drugs in preventing and treating fibrosis. Additionally, recent studies (Li et al., 2022) reveal that various natural small-molecule compounds have certain therapeutic effects on pulmonary fibrosis, so developing natural small-molecule compounds is important.

Cryptotanshinone (CTS) is a diterpenoid quinone lipid-soluble compound extracted from the root of *S. miltiorrhiza*. It benefits from abundant sources, low toxicity and low relative molecular weight. It has high biological activity and high content among the extracts of *S. miltiorrhiza*. Recently, CTS has been proven to have anti-inflammatory, antioxidant, anti-angiogenic and anti-proliferative activities, and play a role in various malignant tumors (Wang et al., 2017; Qi et al., 2019; Chen et al., 2020; Luo et al., 2020), cardiovascular diseases (Zhang et al., 2021), neuroprotection (Kwon et al., 2020) and other diseases. Our laboratory has conducted multiple studies on CTS, and discovered that CTS could significantly improve pulmonary fibrosis in rats induced by bleomycin (BLM), and reverse the fibrosis level of human fetal lung fibroblasts (HLF) induced by factor-beta 1 (TGF- β 1) by inhibiting the STAT3 and Smad2/3 phosphorylation (Zhang et al., 2019). Furthermore, our laboratory revealed that treatment with CTS attenuates adult rat cardiac fibroblasts and cardiac fibrosis rats induced by angiotensin II (Ma et al., 2014). However, the comparative pharmacokinetics and tissue distribution of CTS under normal and model conditions remain unclear.

Pharmacokinetic (PK) based studies are considered a reliable approach for identifying and screening potential bioactive components that contribute to the pharmacological effects of natural compounds and to better elucidate their mechanisms of

action (Sun et al., 2012). Numerous factors, including species, age, sex, mode of administration, dose of administration, and disease (Labrecque and Bélanger, 1991; Lin, 1995; Meibohm et al., 2002; Shi and Klotz, 2011), affect drug absorption (A), distribution (D), metabolism (M), and excretion (E). Diabetes (Pass et al., 2002; Wang et al., 2003; Lam et al., 2010), liver injury (Adawi et al., 2007; Li et al., 2010), chronic heart failure (Huang et al., 2021), inflammatory diseases (Gong et al., 2009; Cressman et al., 2012) and fever (Gao et al., 2014) may cause significant changes in the body's drug metabolic enzymes, transporters, cell permeability and intestinal microbiota, affecting the ADME process of drugs. Therefore, studying animal or human pharmacokinetic parameters under pathophysiological and normal conditions may help us better understand the mechanism of pharmacodynamic action. According to pharmacokinetic studies, CTS is widely distributed in fat and mucosal tissues, accumulating most in rat lungs after oral or intravenous injection (Pan et al., 2008).

This study examines the pharmacokinetics of A in rats using the LC-MS/MS method established by Song et al. (2005). This method has the advantages of sensitivity and high efficiency. It plays an important role in a pharmacokinetic study. This study may promote the CTS for the first time based on a study of the pharmacodynamics of rats with pulmonary fibrosis and normal rats lavage for drug pharmacokinetics and reveal the CTS in the dynamic change law of pulmonary fibrosis in rats *in vivo*. Tissue distribution study may discuss the distribution of the CTS in the body, and lung targeting intends to elucidate the relationship between distribution and pharmacodynamics *in vivo*.

2 Materials and methods

2.1 Reagents and chemicals

Cryptotanshinone standard (HPLC) was purchased from Aladdin, and a Loratadine (LTD) standard (HPLC) from China Institute for Pharmaceutical and Biological Products. Methanol (HPLC) was acquired from Amethyst. Ethyl acetate (HPLC), purchased from Kermel and formic acid (HPLC) from Aladdin. Ultrapure water was attained from made by laboratory, Bleomycin from Macklin, Hydroxyproline test box from Nanjing Jiancheng Bioengineering Institute and sodium carboxymethylcellulose cellulose from Tianjin Zhiyuan Chemical Reagent Co., LTD., Normal saline was attained from Jiangxi Kelun Pharmaceutical Co., LTD., Sodium pentobarbital, purchased from Beijing Huayue Huanyu Chemical Co., LTD. and 4% paraformaldehyde from Sevier Bio.

- (1) Bleomycin sulfate solution: The molding dose was 5 mg/kg, and the volume of trachea infusion was 0.1 mL/100 g. The concentration of bleomycin solution prepared with normal saline was 5 mg/mL.
- (2) Sodium carboxymethyl cellulose slurry: Weigh 5.0 g sodium carboxymethyl cellulose powder, sprinkle it in a beaker containing 1,000 mL distilled water, stir well, and place it overnight, make it fully expanded, get 0.5% sodium carboxymethyl cellulose slurry.

- (3) Cryptotanshinone suspension: The administration dose was 60 mg/kg, and the administration volume was 1 mL/100 g by gavage, that is, the concentration of prepared cryptotanshinone suspension was 6 mg/mL. The powder was fully ultrasonic to form a stable suspension for use.
- (4) 1% sodium pentobarbital: The anesthetic dose of rats was 45 mg/kg and intraperitoneally injected. Check whether any crystals precipitate before use. Heat it in a 37°C water bath to dissolve it completely.

2.2 Animals and treatments

This study followed the Guide for the Care and Use of Laboratory Animals (NIH Publication No. 85-23, revised 1996). Specific Pathogen Free (SPF) male Sprague-Dawley (SD) rats weighing 220–260 g were provided and raised in an SPF environment in by the Animal Experiment Center of Sun Yat-sen University East Campus (license number: SCXK 2011-0029). Animal quarantine observation was 3–5 days. The animals' appearance and physical signs, behavioral activities, body weight, diet and other indicators were observed during this period. Animals in good condition with no abnormal behavior and activity can be tested.

2.2.1 Model establishment and evaluation

Thirty male SD rats were randomly divided into six groups ($n = 5$ rats per group), A to F: (A) 14-day control group; (B) 14-day model group; (C) 28-day control group; (D) 28-day model group; (E) 28-day control group; and (F) 28-day model group. Pulmonary fibrosis was induced through the tracheal infusion of 5 mg/kg bleomycin in the model group, but not in the control group. E and F were administrated 60 mg/kg CTS from the second day after modeling for 28 days, and other groups were not administrated CTS. Lung function and pathology tests were performed in groups A and B on the 15th day after modeling, and in group C-F on the 29th day after modeling.

2.2.2 Single-dose pharmacokinetic study

Twenty male SD rats were randomly divided according to body weight into four groups ($n = 5$ rats per group), 1 to 4: (1) 14-day control group; (2) 14-day model group; (3) 28-day control group; (4) 28-day model group. The rat model of pulmonary fibrosis induced by tracheal infusion of bleomycin was established in the model group, while the control group was not interfered. The 14-day group rats underwent blood were collected at 0.25, 0.5, 1, 1.5, 2, 3, 4, 6, 8, 12, and 24 h after administration CTS on the 14th day after modeling. The 28-day group rats underwent blood were collected at 0.25, 0.5, 1, 1.5, 2, 3, 4, 6, 8, 12, and 24 h after administration CTS on the 28th day after modeling.

2.2.3 Multi-dose pharmacokinetic study

Ten male SD rats were randomly divided into two groups according to body weight ($n = 5$ rats per group): (5) multi-dose control group and (6) multi-dose model group. The model group was induced pulmonary fibrosis by tracheal drip bleomycin, while the control group did not interfere. The rats in the two groups were administrated 60 mg/kg CTS by gavage on the second day after modeling for 28 days. Blood were collected at the 26th and 27th day

and 0, 0.25, 0.5, 1, 1.5, 2, 3, 4, 6, 8, 12, and 24 h on the 28th day after modeling after administration.

2.2.4 Tissue distribution study

Forty male SD rats were randomly divided into two groups according to body weight ($n = 20$ rats per group): (7) control group and (8) model group. The model group was induced pulmonary fibrosis *via* tracheal drip bleomycin, while the control group did not interfere. After 28 days of modeling, they were randomly divided into four subgroups according to body weight: 0.5 h group, 3 h group, 10 h group and 24 h group. At 0.5, 3, 10, and 24 h after administration on the 28th day after modeling, the corresponding subgroups of heart, liver, spleen, lung, kidney, and brain tissues were collected separately.

2.3 Pulmonary function assay

Lung function indicators of each rat were collected using a small animal pulmonary function instrument (EMKA, France) on the 14th day after modeling for groups A and B and on the 28th day after modeling for groups C–F. The rats were placed into the whole body plethysmography system, and the environment was kept quiet and the ambient air flow rate was stable. After the rats had reached a state of calm, data were collected continuously for more than 5 min. The indexes of lung function can be obtained: inspiratory time, expiratory time, relaxation time, maximum inspiratory volume, maximum expiratory volume, ventilatory volume per min, respiratory rate, end-inspiratory apnea, end-expiratory apnea, and mid-expiratory flow rate.

2.4 Histology and morphological analysis

SD rats in groups A and B were sacrificed on the 14th day after modeling, and rats in groups C–F were sacrificed on the 28th day after modeling; their whole lungs of rats were quickly removed. Immediately fixed with 4% paraformaldehyde for 24 h, left lung tissue embedded paraffin and cut into slices of 5 μ m. Sections were stained with hematoxylin and eosin (HE), and Masson's trichrome and lung histopathological changes were evaluated. Sections were photographed using a light microscope (EVOS FL Auto Cell Imaging System, United States).

2.5 Measurement of hydroxyproline (HYP) assay

HYP, a unique distribution in connective tissue collagen, is a post-translational product of proline hydroxylation. The hydroxyproline content reflects collagen metabolism and regulation. In this study, HYP content in lung tissue was determined using alkaline hydrolysis (da Silva et al., 2015). Fresh right lung tissue (weight of 80–100 mg) was chopped *in vitro*, add 1 mL of hydrolyzed was added to a test tube. After cooling the tube to room temperature with tap water, the pH of the lysate was adjusted to 6.0–6.8 and 10 mL of double distilled water was added. Then, centrifuged at 3,500 rpm for 10 min, and suck on 1 mL to new

TABLE 1 Ionic reaction pairs and collision energies of cryptotanshinone and loratadine.

Compounds	Precursor ion (m/z)	Product ion (m/z)	Mode	CE (V)
Cryptotanshinone	297	251	Positive	21
Loratadine	383	266	Positive	31

test tubes. The following steps of HYP test Kit instructions (Nanjing Jianchen Bioengineering Institute, China, #A030-2) were followed. Each sample was measured at 550 nm using the following formula to calculate HYP content:

$$\begin{aligned} & \text{Hydroxproline content } (\mu\text{g}/\text{mg}) \\ &= \frac{\text{Measured OD value} - \text{Blank OD value}}{\text{Standard OD value} - \text{Blank OD value}} \times \text{Standard content} \\ & \times \frac{\text{Lysate total volume (mL)}}{\text{Organization wet weight (mg)}} \end{aligned}$$

2.6 Sample processing

The whole blood was extracted quickly from SD rats through main abdominal vein, and the blood was placed in the heparinized collection vessel, centrifuged at 3,000 rpm for 10 min, and the upper plasma was obtained. Precise measurement of 100 μL plasma sample, add 10 μL of loratadine working solution (plasma, heart, spleen, kidney, brain samples use 200 ng/mL LTD working solution; liver and lung samples use 500 ng/mL LTD working solution) and 500 μL ethyl acetate for liquid-liquid extraction. The mixture was vortexed for 1 min and centrifuged at 12,000 $\times g$ for 4 min. The organic phase of the upper layer was 400 μL and dried in a vacuum for 2 h at room temperature. The mobile phase [100 μL ; methanol-1% formic acid water (90:10, V/V)] was added to redissolve, vortex for 1 min, and centrifuged at 12,000 $\times g$ for 3 min at low temperature. Add 100 μL mobile phase [methanol-1% formic acid water (90:10, V/V)] to redissolve, vortex for 1 min, and centrifuge at 12,000 $\times g$ for 3 min at low temperature. An aliquot (80 μL) of the supernatant was transferred into a sample vial for HPLC-MS/MS analysis.

2.7 HPLC-MS/MS conditions

The injection volume was 5 μL and the flow rate was kept at 0.2 mL/min. The separation was performed using a HyPURITY C18 (I.D. 2.1 mm \times 50 mm, 3 μm , Thermo Scientific, US) column. The mobile phase consisted of methanol and water with 1% formic acid (90:10, V/V). The column temperature was 30°C.

Liquid chromatography-mass spectrometry (Thermo Finnigan, TSQ Quantum) was used to detect CTS in biological samples. The sub-source was electrospray ionization (ESI) with positive ion scanning mode, and the scanning mode was Selected Reaction Monitor (SRM). Spray voltage: 4,000 V; Sheath gas: 35 psi; Auxiliary gas: 10 psi; Capillary temperature: 350°C; Peak width of

color filter: 20.0 s; Collision gas pressure: 1.9 mtorr; Scanning width: 0.7 m/z; Scanning time: 0.1 s. Our optimized SRM parameters for the analyte and internal standards (ISs) detection are shown in Table 1.

2.8 Preparation of stock solutions, working solutions, and quality control samples

CTS and LTD standard substances were precisely weighed and dissolved in 50% methanol to prepare 1 mg/mL CTS and LTD reserve solutions. The working solution was marked into blank rat plasma to generate calibration curves, and the following concentrations were obtained:

(1) The first set (for plasma, heart, spleen, kidney and brain samples): the CTS reserve solution was diluted step by step with 50% methanol to obtain the CTS standard curve working solution with the concentration of 10–2,000 ng/mL. CTS Quality control (QC) samples were prepared at low, middle and high concentrations of 20, 200, and 2,000 ng/mL, respectively.

The LTD reserve liquid was diluted step by step with 50% methanol to obtain 200 ng/mL LTD internal standard working liquid.

(2) The second set (for liver and lung samples): the CTS reserve solution was diluted with 50% methanol step by step to obtain the CTS standard curve working solution with a the concentration of 20–5,000 ng/mL. CTS QC samples were prepared at low, middle and high concentrations of 50, 500, and 3,000 ng/mL, respectively.

The LTD reserve liquid was diluted step by step with 50% methanol to obtain 500 ng/mL LTD internal standard working liquid.

All samples were stored at 4°C before UPLC-MS/MS analysis.

2.9 Method validation

The developed HPLC-MS/MS method was validated in terms of specificity, linearity, lower limit of quantification, precision, and accuracy.

Specificity was assessed by comparing chromatograms of drug-free blank samples, low-concentration CTS quality control samples, and biological samples treated with 60 mg/kg CTS. The weighted least square regression method was used for linear regression analysis. The horizontal coordinate was the concentration of CTS drug (ng/mL), and the vertical coordinate was the ratio of chromatographic peak area between CTS and LTD. Intraday accuracy and precision were assessed progressively using five replicates of the high, medium, and low QC samples over a single day, whereas intraday accuracy and precision were assessed using five replicates over three consecutive days. The lower limit of

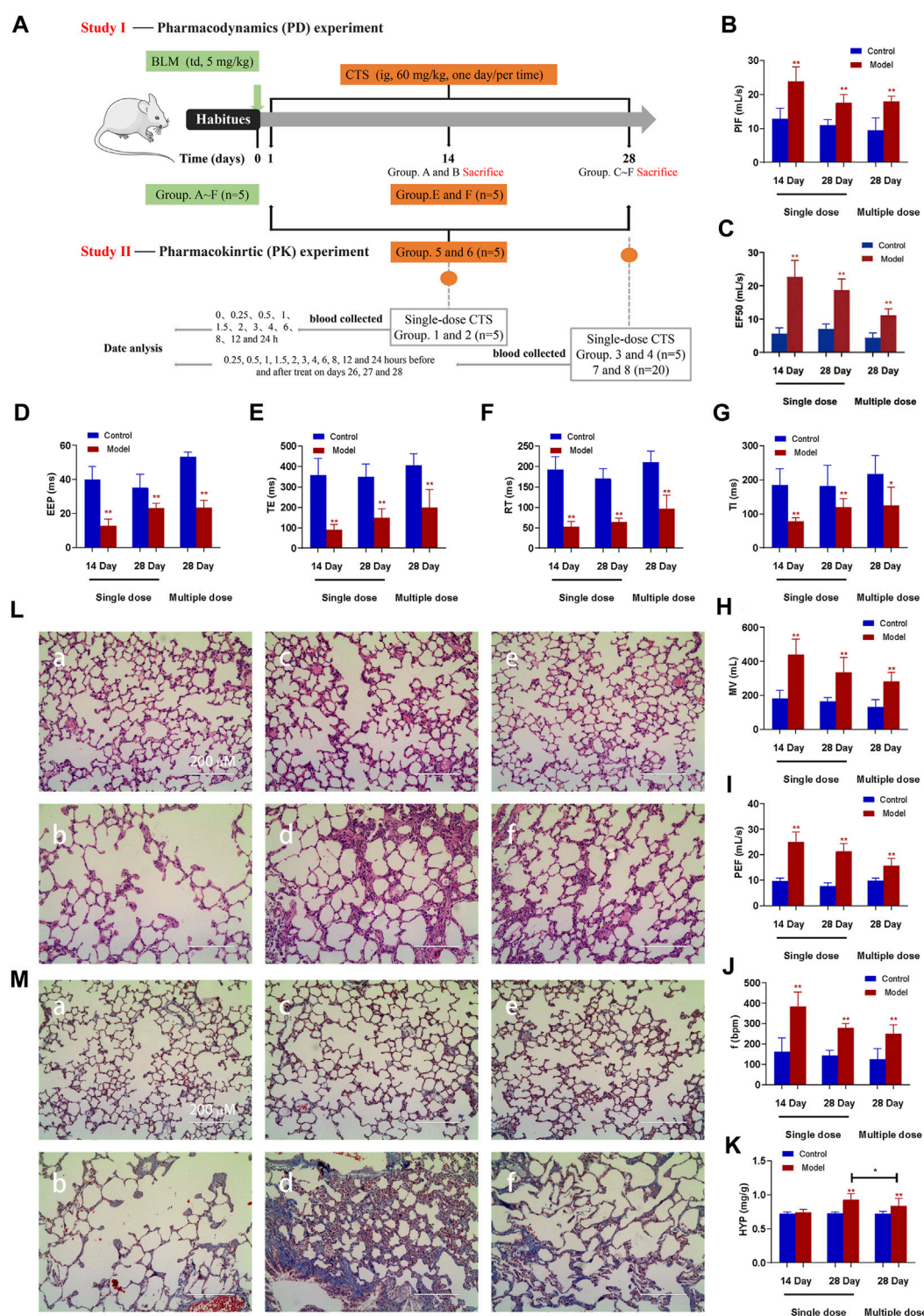


FIGURE 1

Effect of CTS treatment on BLM-induced SD rats. (A) Animal Experiment Diagram for Pharmacodynamic Study (Study I) and Animal experiment diagram for pharmacokinetic Study (Study II). (B–J) Measurement of pulmonary function parameters. (K) Determination of hydroxyproline in lung tissue. (L,M) H&E and Masson staining of heart tissue in each group; a: 14-day control group; b: 14-day model group; c: 28-day control group; d: 28-day model group; e: control group after 28 days of CTS administration; f: Model group after 28 days of CTS administration; Scale bar = 200 μ m. One-way analysis of variance combined with Dunnett's multiple comparison method was used for analysis, and all data were expressed as mean \pm SD. * $p < 0.05$; ** $p < 0.01$.

quantitation was assessed by substituting the peak area ratio of CTS and LTD into the standard curve and comparing it with the standard concentration.

2.10 Pharmacokinetic data and statistical analysis

The experimental data were statistically processed using GraphPad Prism 9.0 biostatistics software (GraphPad Prism 9.0, San Diego, CA, United States). The data was analyzed using one-way Analysis of Variance (ANOVA) combined with Dunnett's multiple comparison method. The pharmacokinetic software DAS 2.0 was used to calculate the main pharmacokinetic parameters according to the non-av model: the calculated parameters were the maximum plasma concentration (C_{max}), elimination half-life ($t_{1/2}$), time to reach maximum plasma concentration (T_{max}), area under the plasma concentration curve (AUC) versus time (AUC_{0-t}) from time zero to the time of last measured concentration, AUC from time zero to infinity ($AUC_{0-\infty}$), and total body clearance (CL), mean residence time (MRT), Apparent clearance rate (CL/F), Apparent distribution volume (V_d/F), Mean drug concentration at steady state (C_{av}), Steady-state plasma concentration (AUC_{ss}) and degree of fluctuation (DF).

3 Results

3.1 Therapeutic effects of CTS on BLM-induced SD rats

Pharmacokinetic studies in model animals are based on the assumption that the animal models are stable and that the pathological changes are consistent with clinical disease characteristics. Endotracheal administration of a single dose of BLM (5 mg/kg) resulted in decreased lung function, implying successful induction of pulmonary fibrosis in SD rats. The maximum inspiratory capacity (PIF, Figure 1B), mid-expiratory flow rate (EF50, Figure 1C), ventilation volume per minute (MV, Figure 1H), maximum expiratory volume (PEF, Figure 1I) and respiratory rate (f , Figure 1J) of rats in each model group were significantly increased. End expiratory apnea (EEP, Figure 1D), expiratory time (TE, Figure 1E), relaxation time (RT, Figure 1F) and inspiratory time (TI, Figure 1G) were significantly reduced compared to the corresponding control group. Nevertheless, the variation trend of all model groups is consistent (Figures 1A–J). The 14-day model group displayed a significant change, followed by the 28-day model group, while the 28-day model group revealed the least change.

At 14 days after BLM treatment, the pulmonary morphology and structure were obviously disordered, with numerous pulmonary bullae and increased infiltration of inflammatory cells, but the pulmonary tissue fibrosis was mild (Figures 1K, L). After 28 days of BLM treatment, numerous collagen fibers appeared in lung tissue, and the thickness of the fibrous scar increased, and the degree of fibrosis aggravated (Figures 1K, L). All indicators were remission in the rat model group treated with CTS for 28 days (Figures 1K, L). Additionally, consistent with MASSON staining results, HYP did

not significantly increase after 14 days of BLM treatment, but significantly increased after 28 days. The HYP level was significantly downregulated after CTS treatment (Figure 1M). These results indicated that severe inflammatory reactions destroyed the alveolar structure and seriously affected the respiratory function of rats in the early stage of the model. The alveolar structure was repaired and respiratory function improved with the self-repair of lung tissue. However, the abnormal repair resulted in the production of many collagen fibers and irreversible structural changes in lung tissue. In conclusion, we have successfully constructed pulmonary fibrosis SD rats induced by BLM, and continuous treatment with CTS has a good therapeutic effect on the pathological changes of pulmonary fibrosis SD rats induced by BLM.

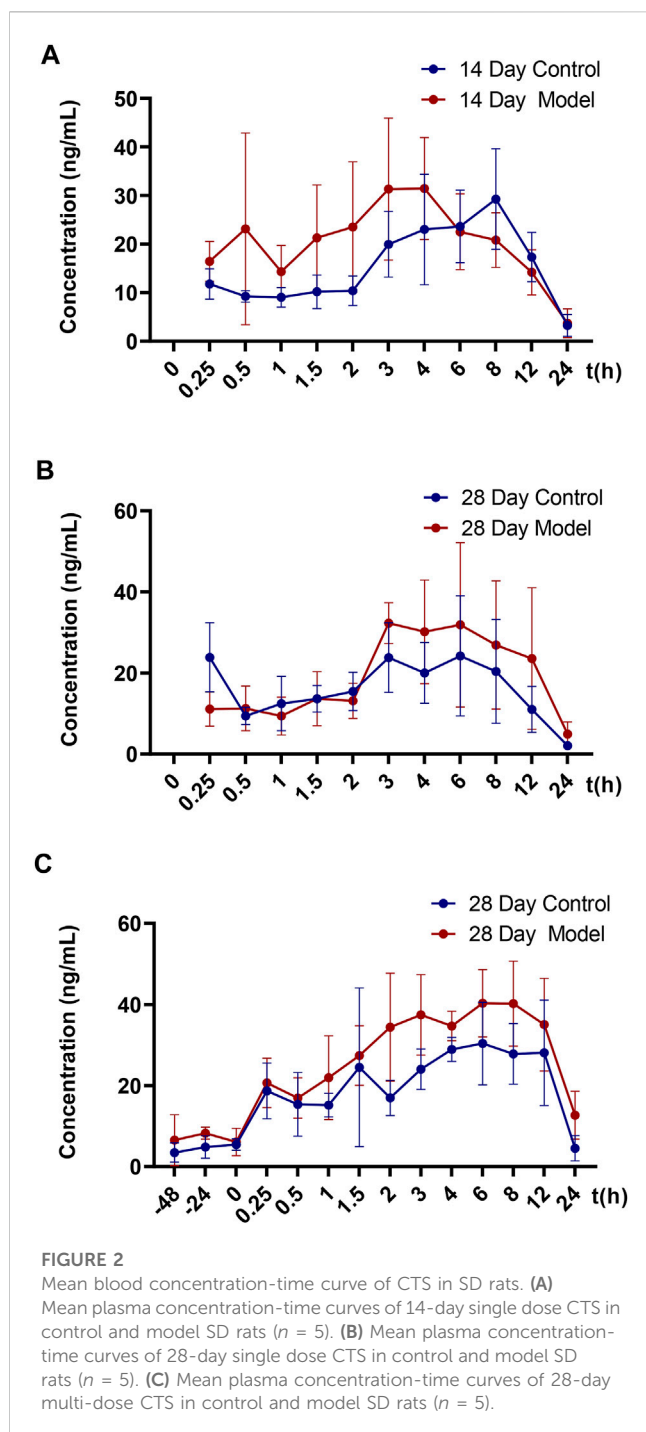
3.2 HPLC-MS/MS method optimization

Different chromatographic columns were tested to develop an efficient HPLC-MS/MS method for quantitative analysis of CTS. The HyPURITY C18 (I.D. 2.1 mm × 50 mm, 3 μm, Thermo Scientific, US) was compared to Hypersil BDS C18 (I.D. 2.1 mm × 150 mm, 5 μm, Elite HPLC, Dalian, China). The chromatographic column has the advantages of small particle size, short length, high separation potency and high efficiency. After gradient modification of the mobile phase, CTS and LTD exhibited a relatively long retention time, a good peak shape and a high degree of separation when the methanol-1% formic acid water ratio was 90:10 (V/V). The CTS and LTD response and separation were better when the injection volume was 5 μL. Furthermore, spray voltage, capillary temperature, sheath gas and auxiliary gas were optimized for CTS and LTD standard solutions to improve the charged rate of the compounds. The CTS and LTD were completely decomposed into stable daughter ions by optimizing collision energy and collision gas pressure. Appropriate collision conditions and daughter ions were selected respectively to conduct quantitative analysis on ion pairs.

3.3 Validation of the HPLC-MS/MS method for simultaneous quantitative analysis of CTS

The CTS and INTERNAL standard LTD specific chromatograms obtained from blank plasma samples, low-concentration CTS quality control samples, and 60 mg/kg CTS after oral administration were detected. The peak times of CTS and internal standard LTD were about 1.54 and 1.38 min, respectively. There was no interference with each other and no interference from endogenous substances. It demonstrated that the analytical method is specific.

The linear range of CTS concentration in plasma, heart, spleen, kidney, and brain samples was 1–200 ng/mL, whereas the linear range of CTS concentration in liver and lung samples was 2–500 ng/mL. Analysis of plasma quality control samples from the same batch demonstrated RE of −9.2% to −3.0% and RSD of 2.7%–8.6%. Plasma quality control samples were analyzed for three consecutive days with RE of −5.8% to −1.5% and RSD of 4.0%–7.2%. Additionally, the RE of the same batch and the



quality control samples of each organization for three consecutive days were all in the range of -20% to 20% , with RSD of less than 20% , all in line with the guidelines. According to the HPLC-MS/MS analysis established in this study, the lower limit of quantification of CTS in plasma samples was 1 ng/mL . The lower limit of quantification was 1 ng/mL in heart, spleen, kidney, and brain samples, while 2 ng/mL in liver and lung samples. The RE and RSD of six LLOQ samples in plasma were 0.0% and 7.1% respectively. The RE of LLOQ samples in

each tissue was in the range of -20% to 20% , with RSD less than 20% .

The results demonstrated that the experiments were consistent and reproducible, that the method provided sufficient exclusivity, and that the HPLC-MS/MS method was sensitive and efficient enough to be used for routine analysis and pharmacokinetic studies of analyses.

3.4 Pharmacokinetic study

Normal rats and pulmonary fibrosis models were given a single dose of 60 mg/kg CTS on days 14 and 28, and normal rats and pulmonary fibrosis models were given a continuous dose of 60 mg/kg CTS for 28 days. The validated assay was successfully applied to both groups. Simultaneously, the concentration data of plasma CTS at different time points were measured for pharmacokinetic study. The mean plasma concentration-time curves based on the data and the major pharmacokinetic parameters calculated based on the non-AV model are provided in the Figure/Table.

Figure 2 and Table 2 illustrate the 14-day and 28-day data of CTS single dose, whereas Figure 2 and Table 3 depict the 28-day data of multiple doses.

The results of the t -test demonstrated no significant differences in major pharmacokinetic parameters between the control and the model groups at 14 days of a single dose ($p < 0.05$). Based on the average blood concentration-time curve, the model group exhibited faster absorption and an earlier peak time. The control group and model groups indicated a bimodal phenomenon with low oral bioavailability. After a single dose of 28 days, the elimination half-life and mean dwell time were significantly different between the control and the model groups ($p < 0.05$), but there was no significant difference in other parameters ($p < 0.05$). The elimination half-life and average dwell time of the model group were significantly longer than those of the control group. The area under the curve was larger than that in the control group, but there was no statistical difference between individuals. The control group rats and the model group rats also exhibited a bimodal phenomenon.

After 28 days of continuous administration, there were significant differences in the curve area and clearance rate between the control and the model groups ($p < 0.05$), and there was no significant difference in other parameters ($p > 0.05$). The elimination half-life, average dwell time, average steady-state concentration and steady-state drug administration curve area of the model group were also significantly increased compared to the control rats, but there was no statistical difference due to the large individual differences. The blood concentration values demonstrated that the three steady-state blood concentrations were all low.

The model group had a higher blood concentration than the control group at each time point. At the last blood collection point, the plasma concentration of CTS in the model group was still higher. The average blood concentration-time curve observation revealed that the bimodal phenomenon also exists in multi-dose administration. Additionally, the

TABLE 2 Major pharmacokinetic parameters of rats in the single-dose control group and model group on days 14 and 28 (mean \pm SD, $n = 5$, * $p < 0.05$ versus Day 28 Control group).

PK parameters	Day 14		Day 28	
	Control	Model	Control	Model
T_{max} (h)	6.40 \pm 2.19	4.00 \pm 1.22	5.00 \pm 1.41	4.60 \pm 2.30
C_{max} (ng/mL)	32.23 \pm 6.65	41.52 \pm 10.79	32.79 \pm 10.57	40.80 \pm 15.48
AUC_{0-t} (ng/mL·h)	325.9 \pm 140.8	366.8 \pm 58.8	297.8 \pm 137.9	467.2 \pm 258.1
$AUC_{0-\infty}$ (ng/mL·h)	426.9 \pm 99.9	385.8 \pm 70.7	310.4 \pm 145.7	518.1 \pm 276.8
CL/F (L/h)	147.5 \pm 37.2	160.1 \pm 31.6	220.0 \pm 74.4	146.1 \pm 74.2
V_d/F (L)	1408.3 \pm 634.5	1139.3 \pm 152.7	1441.7 \pm 417.5	1570.7 \pm 1067.2
$t_{1/2}$ (h)	6.88 \pm 3.22	5.02 \pm 0.81	4.63 \pm 0.59	7.03 \pm 1.20*
MRT (h)	12.83 \pm 4.43	9.42 \pm 1.37	8.85 \pm 0.63	11.13 \pm 0.99*

TABLE 3 Major pharmacokinetic parameters of 28-day multi-dose control group and model group (Mean \pm SD, $n = 5$, * $p < 0.05$ versus Control group).

Parameter	Day 28	
	Control	Model
T_{max} (h)	7.40 \pm 4.34	8.00 \pm 2.45
C_{max} (ng/mL)	39.30 \pm 14.31	45.10 \pm 7.42
AUC_{0-t} (ng/mL·h)	507.0 \pm 152.2	709.6 \pm 143.8
$AUC_{0-\infty}$ (ng/mL·h)	567.0 \pm 178.2	988.4 \pm 318.8*
CL/F (L/h)	113.6 \pm 31.5	65.8 \pm 21.0*
V_d/F (L)	1128.5 \pm 285.7	1081.1 \pm 394.8
$t_{1/2}$ (h)	7.11 \pm 1.86	12.71 \pm 8.01
MRT (h)	10.95 \pm 2.77	19.40 \pm 10.48
$C_{av(ss)}$ (ng/mL)	4.14 \pm 1.74	7.41 \pm 3.08
DF	9.18 \pm 2.52	6.03 \pm 2.69
AUC_{ss} (ng/mL·h)	99.3 \pm 41.74	177.9 \pm 73.9

individual differences of model group rats were significantly greater than those of control group rats.

3.5 Tissue distribution study

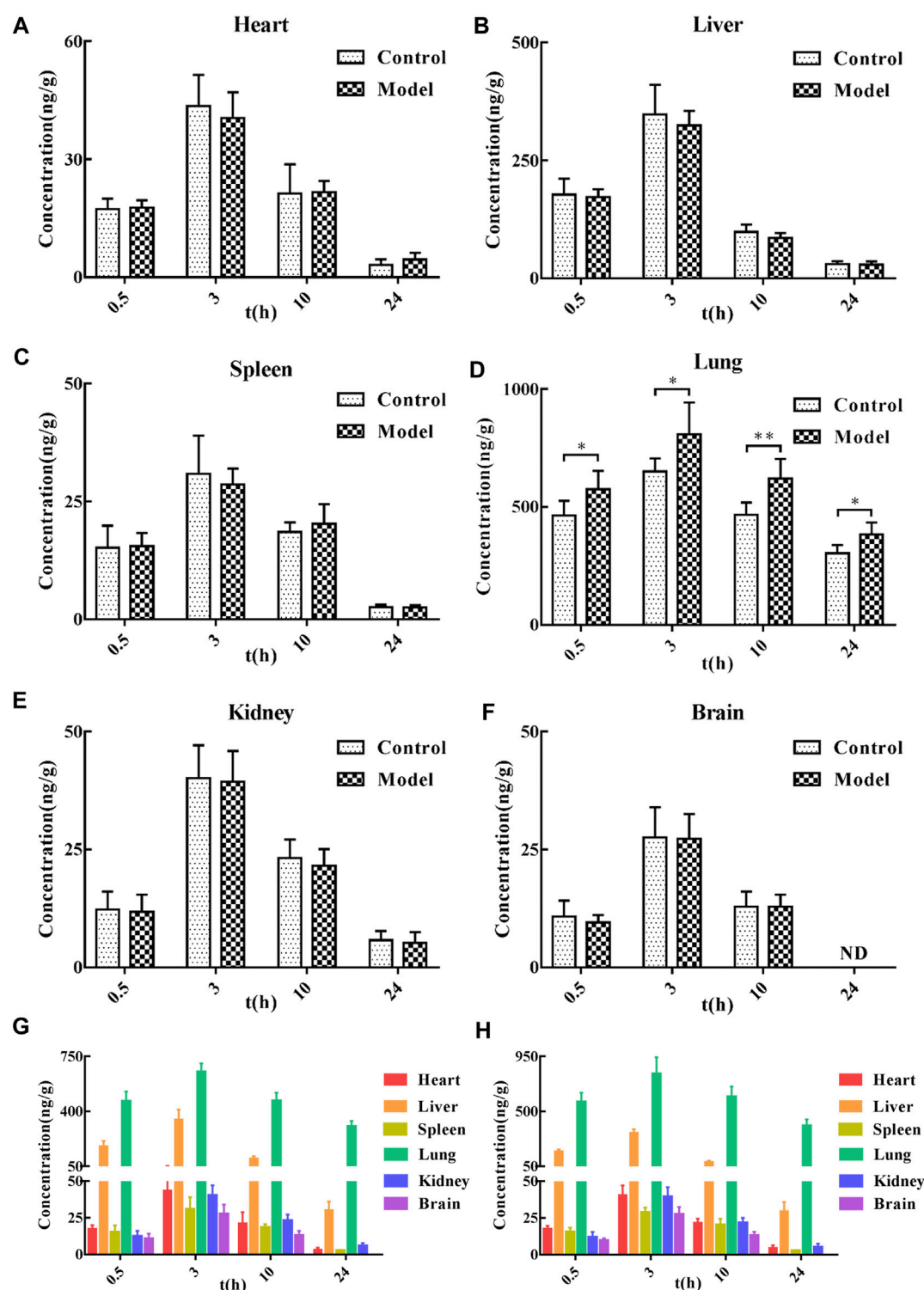
After a single oral administration of 60 mg/kg CTS, the concentrations of CTS in various tissues (heart, liver, spleen, lung, kidney, and brain) at different time points were measured (Figure 3). CTS was widely distributed in various organs, including the lung and liver. In the control and the model groups, the distribution trend of CTS was consistent: lung > liver > heart > spleen > kidney > brain at 0.5 h, lung > liver > heart > kidney > spleen > brain at 3 h, lung > liver > heart \approx kidney > spleen > brain at 10 h, lung > liver > kidney > heart >

spleen > brain at 24 h. The amount of CTS exposure in the heart, liver, spleen, kidney, and brain of the two groups of rats did not differ significantly. However, the exposure amount in the lungs of the model group was significantly higher than that in the control group.

4 Discussion

Pharmacokinetic research is an important part of the process of new drug development, because it guides the entire process and serves as a foundation for pharmacodynamics, toxicology and drug preparation research. Pharmacokinetic studies in animal models of disease can better reflect the dynamic changes of drugs and explain the pharmacokinetic basis of the pharmacological effects of drugs. BLM is a basic glycopeptide anticancer antibiotic. It is frequently used as an intratracheal infusion in experimental animals to cause severe inflammation and pulmonary fibrosis (Della Latta et al., 2015) due to its strong pulmonary toxicity (Moeller et al., 2008). In the previous pharmacodynamic study of CTS in pulmonary fibrosis rats treatment, the high-dose group of 60 mg/kg exhibited a good pharmacodynamic effect and no side effects (Zhang et al., 2019). Additionally, the amount of oral CTS inhaled into the systemic circulation was small (Song et al., 2007; Wang et al., 2020), so choosing a higher dose may be beneficial to compare the pharmacokinetic characteristics of CTS in normal and pulmonary fibrosis rats.

After intragastric administration of CTS to rats, the absorption was slow, the amount absorbed into the systemic circulation was low, the CTS was widely distributed in the body, and the elimination rate was relatively slow. At 14 days, the pharmacokinetic characteristics of the control and the model groups were the same. The faster absorption of the rats in the model group may be due to the increased permeability of vascular endothelial cells caused by the inflammatory reaction (Wautier and Wautier, 2022). The 28-day model group had slower elimination and longer dwell time, and the area under the curve was significantly higher than in the control group. This may be due to the decline of lung function or even the overall

**FIGURE 3**

Tissue distribution of CTS in SD rats. (A–F) The concentration of SD rats in the control group and model group at different time points after oral administration of 60 mg/kg CTS. (G) The concentration of SD rats in the control group at different time points after oral administration of 60 mg/kg CTS. (H) The concentrations of 60 mg/kg CTS in each tissue at different time points in the model group. One-way analysis of variance combined with Dunnett's multiple comparison method was used for analysis, and all data were expressed as mean \pm SD. * $p < 0.05$; ** $p < 0.01$.

physiological function of rats; the speed of CTS clearance metabolism is reduced. It is also possible that the drug accumulation in the substantively diseased lungs increased,

and CTS released slowly from the lungs into the blood. Changes in intestinal microbiota under pathological conditions may lead to slower metabolic rates (Morgan et al.,

2018; Parvez et al., 2021). However, the steady-state blood concentration and the area under the curve of the model group were slightly higher than those of the control group, and the area under the curve and clearance rate of the model group were significantly higher than those of the control group, which was further amplified by long-term administration. These results suggest that in rats with advanced pulmonary fibrosis, the substantial lung lesions may greatly influence the pharmacokinetic behavior of CTS, resulting in the slow elimination of CTS. Moreover, a bimodal phenomenon occurred in all experimental groups, a common phenomenon in non-intravenous drug injection, possibly because CTS is widely distributed *in vivo* and tissue redistribution occurs. Gastrointestinal imbalance (Hatton et al., 2019) and liver-intestinal circulation also caused the bimodal phenomenon.

The tissue distribution study revealed that CTS could be detected in all tissues 0.5 h after administration of 60 mg/kg CTS administration by gavage, indicating that CTS could be rapidly and widely distributed in various tissues and organs after oral administration. The peak concentration of all tissues reached 3 h after administration, and high concentrations of CTS could still be detected at 10 h after administration. CTS could be detected at 24 h after administration except in brain tissue, indicating that CTS was retained in all tissue and organs for a long time. After gavage of CTS to rats, the concentration of CTS in lungs and liver was higher than in other tissues and organs, indicating that they are likely to be the effector organs or toxic organs of CTS. This result is consistent with literature reports: CTS has therapeutic effects in liver cancer, ethanol-induced liver injury (Nagappan et al., 2019), liver failure (Jin et al., 2014), liver fibrosis (Han et al., 2019), lung cancer (Vundavilli et al., 2020) and pulmonary fibrosis (Zhang et al., 2020), among other diseases (Liu et al., 2021), and is metabolized through in the liver (Zeng et al., 2018). Compared to the control group, there was no significant difference in the amount of CTS exposure in the heart, liver, spleen, kidney, and brain of rats in the model group after the gavage of CTS. However, the amount of CTS exposure in the lung tissue was significantly increased, indicating that the pathological changes of pulmonary fibrosis are conducive to the targeted distribution of CTS in the lung. This phenomenon may be caused by pulmonary vascular hyperplasia accompanied by increased permeability of vascular endothelial cells. It is also possible that components of lung dysplasia (collagen, collagen fibers, aminoglycans, or cytokines) have a better binding effect on CTS.

5 Conclusion

This was the first study to investigate the pharmacokinetic characteristics and tissue distribution of CTS in normal and pulmonary fibrosis rats, and to compare the pharmacokinetic and tissue distribution differences between the two rat groups. The results demonstrated that the distribution and metabolism of CTS and the targeted distribution of CTS in the lungs were affected by the pathological conditions of pulmonary fibrosis, as evidenced by the increase of the area under the curve, clearance half-life, average dwell time and high exposure of CTS in the lungs of pulmonary fibrosis rats.

Data availability statement

The original contributions presented in the study are included in the article/Supplementary Material, further inquiries can be directed to the corresponding authors.

Ethics statement

The animal study was reviewed and approved by Animal Ethics Committee of Sun Yat-Sen University.

Author contributions

PL, JL, and JC were corresponding authors and reviewed the manuscript; XH and ZJ wrote the manuscript; ZZ and QW conducted animal experiments.

Funding

Fund Project Support: 1) National Engineering and Technology Research Center for New drug Druggability Evaluation (Seed Program of Guangdong Province, 2017B090903004). 2) Local Innovative and Research Teams Project of Guangdong Pearl River Talents Program (2017BT01Y093). 3) National Natural Science Foundation of China (U21A20419). 4) Guangdong Provincial Key Laboratory of Construction Foundation (2017B030314030). 5) Natural Science Foundation of Guangdong Province (2021B1515020100). 6) The Discipline Construction Project of Guangdong Medical University (4SG21233G).

Conflict of interest

The authors declare that the research was conducted in the absence of any commercial or financial relationships that could be construed as a potential conflict of interest.

Publisher's note

All claims expressed in this article are solely those of the authors and do not necessarily represent those of their affiliated organizations, or those of the publisher, the editors and the reviewers. Any product that may be evaluated in this article, or claim that may be made by its manufacturer, is not guaranteed or endorsed by the publisher.

Supplementary material

The Supplementary Material for this article can be found online at: <https://www.frontiersin.org/articles/10.3389/fphar.2023.1127219/full#supplementary-material>

References

- Adawi, D., Kasravi, F. B., and Molin, G. (2007). Manipulation of nitric oxide in an animal model of acute liver injury. The impact on liver and intestinal function. *Libyan J. Med.* 2, 73–81. doi:10.4176/070212
- Barratt, S. L., Creamer, A., Hayton, C., and Chaudhuri, N. (2018). Idiopathic pulmonary fibrosis (IPF): An overview. *J. Clin. Med.* 7, 201. doi:10.3390/jcm7080201
- Chanda, D., Otopalova, E., Smith, S. R., Volckaert, T., De Langhe, S. P., and Thannickal, V. J. (2019). Developmental pathways in the pathogenesis of lung fibrosis. *Mol. Asp. Med.* 65, 56–69. doi:10.1016/j.mam.2018.08.004
- Chen, L., Yang, Q., Zhang, H., Wan, L., Xin, B., Cao, Y., et al. (2020). Cryptotanshinone prevents muscle wasting in CT26-induced cancer cachexia through inhibiting STAT3 signaling pathway. *J. Ethnopharmacol.* 260, 113066. doi:10.1016/j.jep.2020.113066
- Cressman, A. M., Petrovic, V., and Piquette-Miller, M. (2012). Inflammation-mediated changes in drug transporter expression/activity: Implications for therapeutic drug response. *Expert Rev. Clin. Pharmacol.* 5, 69–89. doi:10.1586/ecp.11.66
- da Silva, C. M., Spinelli, E., and Rodrigues, S. V. (2015). Fast and sensitive collagen quantification by alkaline hydrolysis/hydroxyproline assay. *Food Chem.* 173, 619–623. doi:10.1016/j.foodchem.2014.10.073
- Della Latta, V., Cecchetti, A., Del Ry, S., and Morales, M. A. (2015). Bleomycin in the setting of lung fibrosis induction: From biological mechanisms to counteractions. *Pharmacol. Res.* 97, 122–130. doi:10.1016/j.phrs.2015.04.012
- du Bois, R. M. (2010). Strategies for treating idiopathic pulmonary fibrosis. *Nat. Rev. Drug Discov.* 9, 129–140. doi:10.1038/nrd2958
- Gao, R., Lin, Y., Liang, G., Yu, B., and Gao, Y. (2014). Comparative pharmacokinetic study of chlorogenic acid after oral administration of *Lonicera japonica* Flos and *Shuang-Huang-Lian* in normal and febrile rats. *Phytother. Res.* 28, 144–147. doi:10.1002/ptr.4958
- Gong, H. L., Tang, W. F., Yu, Q., Xiang, J., Xia, Q., Chen, G. Y., et al. (2009). Effect of severe acute pancreatitis on pharmacokinetics of Da-Cheng-Qi Decoction components. *World J. Gastroenterol.* 15, 5992–5999. doi:10.3748/wjg.15.5992
- Han, Z., Liu, S., Lin, H., Trivett, A. L., Hannifin, S., Yang, D., et al. (2019). Inhibition of murine hepatoma tumor growth by cryptotanshinone involves TLR7-dependent activation of macrophages and induction of adaptive antitumor immune defenses. *Cancer Immunol. Immunother.* 68, 1073–1085. doi:10.1007/s00262-019-02338-4
- Hatton, G. B., Madla, C. M., Rabbie, S. C., and Basit, A. W. (2019). Gut reaction: Impact of systemic diseases on gastrointestinal physiology and drug absorption. *Drug Discov. Today* 24, 417–427. doi:10.1016/j.drudis.2018.11.009
- Huang, C., Qiu, S., Fan, X., Jiao, G., Zhou, X., Sun, M., et al. (2021). Evaluation of the effect of Shengxian Decoction on doxorubicin-induced chronic heart failure model rats and a multicomponent comparative pharmacokinetic study after oral administration in normal and model rats. *Biomed. Pharmacother.* 144, 112354. doi:10.1016/j.biopha.2021.112354
- Jin, Q., Jiang, S., Wu, Y. L., Bai, T., Yang, Y., Jin, X., et al. (2014). Hepatoprotective effect of cryptotanshinone from *Salvia miltiorrhiza* in D-galactosamine/lipopolysaccharide-induced fulminant hepatic failure. *Phytomedicine* 21, 141–147. doi:10.1016/j.phymed.2013.07.016
- King, T. E., Jr., Pardo, A., and Selman, M. (2011). Idiopathic pulmonary fibrosis. *Lancet* 378, 1949–1961. doi:10.1016/s0140-6736(11)60052-4
- Kwon, H., Cho, E., Jeon, J., Kim, K. S., Jin, Y. L., Lee, Y. C., et al. (2020). Cryptotanshinone enhances neurite outgrowth and memory via extracellular signal-regulated kinase 1/2 signaling. *Food Chem. Toxicol.* 136, 111011. doi:10.1016/j.fct.2019.111011
- Labrecque, G., and Bélanger, P. M. (1991). Biological rhythms in the absorption, distribution, metabolism and excretion of drugs. *Pharmacol. Ther.* 52, 95–107. doi:10.1016/0163-7258(91)90088-4
- Lam, J. L., Jiang, Y., Zhang, T., Zhang, E. Y., and Smith, B. J. (2010). Expression and functional analysis of hepatic cytochromes P450, nuclear receptors, and membrane transporters in 10- and 25-week-old db/db mice. *Drug Metab. Dispos.* 38, 2252–2258. doi:10.1124/dmd.110.034223
- Li, L. Y., Zhang, C. T., Zhu, F. Y., Zheng, G., Liu, Y. F., Liu, K., et al. (2022). Potential natural small molecular compounds for the treatment of chronic obstructive pulmonary disease: An overview. *Front. Pharmacol.* 13, 821941. doi:10.3389/fphar.2022.821941
- Li, Y. T., Wang, L., Chen, Y., Chen, Y. B., Wang, H. Y., Wu, Z. W., et al. (2010). Effects of gut microflora on hepatic damage after acute liver injury in rats. *J. Trauma* 68, 76–83. doi:10.1097/TA.0b013e31818ba467
- Lin, J. H. (1995). Species similarities and differences in pharmacokinetics. *Drug Metab. Dispos.* 23, 1008–1021.
- Liu, H., Zhan, X., Xu, G., Wang, Z., Li, R., Wang, Y., et al. (2021). Cryptotanshinone specifically suppresses NLRP3 inflammasome activation and protects against inflammasome-mediated diseases. *Pharmacol. Res.* 164, 105384. doi:10.1016/j.phrs.2020.105384
- Luo, Y., Song, L., Wang, X., Huang, Y., Liu, Y., Wang, Q., et al. (2020). Uncovering the mechanisms of cryptotanshinone as a therapeutic agent against hepatocellular carcinoma. *Front. Pharmacol.* 11, 1264. doi:10.3389/fphar.2020.01264
- Ma, Y., Li, H., Yue, Z., Guo, J., Xu, S., Xu, J., et al. (2014). Cryptotanshinone attenuates cardiac fibrosis via downregulation of COX-2, NOX-2, and NOX-4. *J. Cardiovasc Pharmacol.* 64, 28–37. doi:10.1097/fjc.0000000000000086
- Meibohm, B., Beierle, I., and Derendorf, H. (2002). How important are gender differences in pharmacokinetics? *Clin. Pharmacokinet.* 41, 329–342. doi:10.2165/00003088-200241050-00002
- Moeller, A., Ask, K., Warburton, D., Gaudie, J., and Kolb, M. (2008). The bleomycin animal model: A useful tool to investigate treatment options for idiopathic pulmonary fibrosis? *Int. J. Biochem. Cell Biol.* 40, 362–382. doi:10.1016/j.biocel.2007.08.011
- Morgan, E. T., Dempsey, J. L., Mimche, S. M., Lamb, T. J., Kulkarni, S., Cui, J. Y., et al. (2018). Physiological regulation of drug metabolism and Transport: Pregnancy, microbiome, inflammation, infection, and fasting. *Drug Metab. Dispos.* 46, 503–513. doi:10.1124/dmd.117.079905
- Nagappan, A., Kim, J. H., Jung, D. Y., and Jung, M. H. (2019). Cryptotanshinone from the *Salvia miltiorrhiza* bunge attenuates ethanol-induced liver injury by activation of AMPK/SIRT1 and Nrf2 signaling pathways. *Int. J. Mol. Sci.* 21, 265. doi:10.3390/ijms21010265
- Pan, Y., Bi, H. C., Zhong, G. P., Chen, X., Zuo, Z., Zhao, L. Z., et al. (2008). Pharmacokinetic characterization of hydroxypropyl-beta-cyclodextrin-included complex of cryptotanshinone, an investigational cardiovascular drug purified from *Danshen* (*Salvia miltiorrhiza*). *Xenobiotica* 38, 382–398. doi:10.1080/00498250701827685
- Parvez, M. M., Basit, A., Jariwala, P. B., Gáborik, Z., Kis, E., Heyward, S., et al. (2021). Quantitative investigation of irinotecan metabolism, Transport, and gut microbiome activation. *Drug Metab. Dispos.* 49, 683–693. doi:10.1124/dmd.121.000476
- Pass, G. J., Becker, W., Kluge, R., Linnartz, K., Plum, L., Giesen, K., et al. (2002). Effect of hyperinsulinemia and type 2 diabetes-like hyperglycemia on expression of hepatic cytochrome p450 and glutathione s-transferase isoforms in a New Zealand obese-derived mouse backcross population. *J. Pharmacol. Exp. Ther.* 302, 442–450. doi:10.1124/jpet.102.033553
- Qi, P., Li, Y., Liu, X., Jafari, F. A., Zhang, X., Sun, Q., et al. (2019). Cryptotanshinone suppresses non-small cell lung cancer via microRNA-146a-5p/EGFR Axis. *Int. J. Biol. Sci.* 15, 1072–1079. doi:10.7150/ijbs.31277
- Rangarajan, S., Locy, M. L., Luckhardt, T. R., and Thannickal, V. J. (2016). Targeted therapy for idiopathic pulmonary fibrosis: Where to now? *Drugs* 76, 291–300. doi:10.1007/s40265-015-0523-6
- Richeldi, L., Collard, H. R., and Jones, M. G. (2017). Idiopathic pulmonary fibrosis. *Lancet* 389, 1941–1952. doi:10.1016/s0140-6736(17)30866-8
- Sgalla, G., Iovene, B., Calvello, M., Ori, M., Varone, F., and Richeldi, L. (2018). Idiopathic pulmonary fibrosis: Pathogenesis and management. *Respir. Res.* 19, 32. doi:10.1186/s12931-018-0730-2
- Shi, S., and Klotz, U. (2011). Age-related changes in pharmacokinetics. *Curr. Drug Metab.* 12, 601–610. doi:10.2174/138920011796504527
- Song, M., Hang, T. J., Zhang, Z., and Chen, H. Y. (2007). Effects of the coexisting diterpenoid tanshinones on the pharmacokinetics of cryptotanshinone and tanshinone IIA in rat. *Eur. J. Pharm. Sci.* 32, 247–253. doi:10.1016/j.ejps.2007.07.007
- Song, M., Hang, T. J., Zhang, Z., Du, R., and Chen, J. (2005). Determination of cryptotanshinone and its metabolite in rat plasma by liquid chromatography-tandem mass spectrometry. *J. Chromatogr. B Anal. Technol. Biomed. Life Sci.* 827, 205–209. doi:10.1016/j.jchromb.2005.09.014
- Spagnolo, P., Wells, A. U., and Collard, H. R. (2015). Pharmacological treatment of idiopathic pulmonary fibrosis: An update. *Drug Discov. Today* 20, 514–524. doi:10.1016/j.drudis.2015.01.001
- Sun, H., Dong, W., Zhang, A., Wang, W., and Wang, X. (2012). Pharmacokinetics study of multiple components absorbed in rat plasma after oral administration of *Stemona radix* using ultra-performance liquid-chromatography/mass spectrometry with automated MetaboLynx software analysis. *J. Sep. Sci.* 35, 3477–3485. doi:10.1002/jssc.201200791
- Urban, M. L., Manenti, L., and Vaglio, A. (2015). Fibrosis--A common pathway to organ injury and failure. *N. Engl. J. Med.* 373, 96. doi:10.1056/NEJMc1504848
- Vundavilli, H., Datta, A., Sima, C., Hua, J., Lopes, R., and Bittner, M. (2020). Cryptotanshinone induces cell death in lung cancer by targeting aberrant feedback loops. *IEEE J. Biomed. Health Inf.* 24, 2430–2438. doi:10.1109/jbhi.2019.2958042
- Wang, D., Yu, W., Cao, L., Xu, C., Tan, G., Zhao, Z., et al. (2020). Comparative pharmacokinetics and tissue distribution of cryptotanshinone, tanshinone IIA, dihydrotanshinone I, and tanshinone I after oral administration of pure tanshinones and liposoluble extract of *Salvia miltiorrhiza* to rats. *Biopharm. Drug Dispos.* 41, 54–63. doi:10.1002/bdd.2213
- Wang, Y., Lu, H. L., Liu, Y. D., Yang, L. Y., Jiang, Q. K., Zhu, X. J., et al. (2017). Cryptotanshinone sensitizes antitumor effect of paclitaxel on tongue squamous cell carcinoma growth by inhibiting the JAK/STAT3 signaling pathway. *Biomed. Pharmacother.* 95, 1388–1396. doi:10.1016/j.biopha.2017.09.062

- Wang, Z., Hall, S. D., Maya, J. F., Li, L., Asghar, A., and Gorski, J. C. (2003). Diabetes mellitus increases the *in vivo* activity of cytochrome P450 2E1 in humans. *Br. J. Clin. Pharmacol.* 55, 77–85. doi:10.1046/j.1365-2125.2003.01731.x
- Wautier, J. L., and Wautier, M. P. (2022). Vascular permeability in diseases. *Int. J. Mol. Sci.* 23, 3645. doi:10.3390/ijms23073645
- Zeng, J., Fan, Y. J., Tan, B., Su, H. Z., Li, Y., Zhang, L. L., et al. (2018). Characterizing the metabolism of cryptotanshinone by human P450 enzymes and uridine diphosphate glucuronosyltransferases *in vitro*. *Acta Pharmacol. Sin.* 39, 1393–1404. doi:10.1038/aps.2017.144
- Zhang, Q., Gan, C., Liu, H., Wang, L., Li, Y., Tan, Z., et al. (2020). Cryptotanshinone reverses the epithelial-mesenchymal transformation process and attenuates bleomycin-induced pulmonary fibrosis. *Phytother. Res.* 34, 2685–2696. doi:10.1002/ptr.6699
- Zhang, Y., Lu, W., Zhang, X., Lu, J., Xu, S., Chen, S., et al. (2019). Cryptotanshinone protects against pulmonary fibrosis through inhibiting Smad and STAT3 signaling pathways. *Pharmacol. Res.* 147, 104307. doi:10.1016/j.phrs.2019.104307
- Zhang, Y., Luo, F., Zhang, H., He, W., Liu, T., Wu, Y., et al. (2021). Cryptotanshinone ameliorates cardiac injury and cardiomyocyte apoptosis in rats with coronary microembolization. *Drug Dev. Res.* 82, 581–588. doi:10.1002/ddr.21777



OPEN ACCESS

EDITED BY

Junmin Zhang,
Lanzhou University, China

REVIEWED BY

Guozheng Huang,
Anhui University of Technology, China
Alina Kurylowicz,
Mossakowski Medical Research Institute
(PAN), Poland

*CORRESPONDENCE

Hana Malinska,
✉ hana.malinska@ikem.cz

SPECIALTY SECTION

This article was submitted to Drug
Metabolism and Transport,
a section of the journal
Frontiers in Pharmacology

RECEIVED 06 December 2022

ACCEPTED 24 March 2023

PUBLISHED 03 April 2023

CITATION

Hüttl M, Markova I, Mikláňková D,
Zapletalova I, Kujal P, Šilhavý J,
Pravenec M and Malinska H (2023),
Hypolipidemic and insulin sensitizing
effects of salsalate beyond suppressing
inflammation in a prediabetic rat model.
Front. Pharmacol. 14:1117683.
doi: 10.3389/fphar.2023.1117683

COPYRIGHT

© 2023 Hüttl, Markova, Mikláňková,
Zapletalova, Kujal, Šilhavý, Pravenec and
Malinska. This is an open-access article
distributed under the terms of the
[Creative Commons Attribution License
\(CC BY\)](https://creativecommons.org/licenses/by/4.0/). The use, distribution or
reproduction in other forums is
permitted, provided the original author(s)
and the copyright owner(s) are credited
and that the original publication in this
journal is cited, in accordance with
accepted academic practice. No use,
distribution or reproduction is permitted
which does not comply with these terms.

Hypolipidemic and insulin sensitizing effects of salsalate beyond suppressing inflammation in a prediabetic rat model

Martina Hüttl¹, Irena Markova¹, Denisa Mikláňková¹,
Iveta Zapletalova², Petr Kujal³, Jan Šilhavý⁴, Michal Pravenec⁴ and
Hana Malinska^{1*}

¹Center for Experimental Medicine, Institute for Clinical and Experimental Medicine, Prague, Czech,

²Department of Pharmacology, Faculty of Medicine and Dentistry, Palacky University, Olomouc, Czech,

³Department of Pathology, Third Faculty of Medicine, Charles University, Prague, Czech, ⁴Institute of
Physiology, Czech Academy of Sciences, Prague, Czech

Background and aims: Low-grade chronic inflammation plays an important role in the pathogenesis of metabolic syndrome, type 2 diabetes and their complications. In this study, we investigated the effects of salsalate, a non-steroidal anti-inflammatory drug, on metabolic disturbances in an animal model of prediabetes—a strain of non-obese hereditary hypertriglyceridemic (HHTg) rats.

Materials and Methods: Adult male HHTg and Wistar control rats were fed a standard diet without or with salsalate delivering a daily dose of 200 mg/kg of body weight for 6 weeks. Tissue sensitivity to insulin action was measured *ex vivo* according to basal and insulin-stimulated ¹⁴C-U-glucose incorporation into muscle glycogen or adipose tissue lipids. The concentration of methylglyoxal and glutathione was determined using the HPLC-method. Gene expression was measured by quantitative RT-PCR.

Results: Salsalate treatment of HHTg rats when compared to their untreated controls was associated with significant amelioration of inflammation, dyslipidemia and insulin resistance. Specifically, salsalate treatment was associated with reduced inflammation, oxidative and dicarbonyl stress when inflammatory markers, lipoperoxidation products and methylglyoxal levels were significantly decreased in serum and tissues. In addition, salsalate ameliorated glycaemia and reduced serum lipid concentrations. Insulin sensitivity in visceral adipose tissue and skeletal muscle was significantly increased after salsalate administration. Further, salsalate markedly reduced hepatic lipid accumulation (triglycerides –29% and cholesterol –14%). Hypolipidemic effects of salsalate were associated with differential expression of genes coding for enzymes and

Abbreviations: COX, cyclooxygenase; Fas, fatty acid synthase; Glo-1, glyoxalase-1; GPx, glutathione peroxidase; GSH, reduced form of glutathione; GSSG, oxidized form of glutathione; GR, glutathione reductase; HHTg, hereditary hypertriglyceridemic; Hmgcr, 3-hydroxy-3-methylglutaryl-coenzyme A reductase; IL-6, interleukin 6; Ldlr, LDL receptors; MCP-1, monocyte chemoattractant protein-1; NAFLD, non-alcoholic fatty liver disease; NFκB, nuclear factor κB; Ppara, peroxisome proliferator-activated receptor α; RAGE, receptor for advanced glycation end-products; SOD, superoxide dismutase; Srebp1f, sterol regulatory element-binding protein; TAG, triacylglycerols; TNFα, tumor necrosis factor α.

transcription factors involved in lipid synthesis (*Fas*, *Hmgcr*), oxidation (*Ppara*) and transport (*Ldlr*, *Apo* transporters), as well as changes in gene expression of cytochrome P450 proteins, in particular decreased *Cyp7a* and increased *Cyp4a* isoforms.

Conclusion: These results demonstrate important anti-inflammatory and anti-oxidative effects of salsalate that were associated with reduced dyslipidemia and insulin resistance in HHTg rats. Hypolipidemic effects of salsalate were associated with differential expression of genes regulating lipid metabolism in the liver. These results suggest potential beneficial use of salsalate in prediabetic patients with NAFLD symptoms.

KEYWORDS

salsalate, low-grade inflammation, prediabetes, lipid metabolism, cytochrome P450, oxidative stress

1 Introduction

Prediabetic states characterized by insulin resistance, impaired glucose tolerance and disturbances in lipid metabolism, are accompanied by low-chronic inflammation that can contribute to the onset of T2DM and its complications. Thus, the amelioration of inflammation can have preventive and beneficial effects and represents a potential target for treatment of patients with metabolic syndrome, prediabetes or T2DM (Wu and Ballantyne, 2020).

Salicylate is one of the oldest drugs in clinical practice for treating inflammation. Salicylates exist in 2 forms: acetylated form - aspirin and non-acetylated form—salsalate. Unlike aspirin, which can lead to impaired coagulation and gastric irritation, especially at increased doses, salsalate is insoluble in the acidic gastric environment, is absorbed only in the small intestine and thus omits the gastric mucosa (Scheiman and Elta, 1990; Vane, 2002). Therefore, it is relatively safe for long-term clinical use.

In general, salicylates provide anti-inflammatory effect through the inhibition of cyclooxygenase (COX) enzymes. However, salsalate only mildly inhibits the COX pathway, but strongly inhibits NF- κ B cascade and thus decreases the production of pro-inflammatory cytokines (Higgs, et al., 1987). It has been previously reported that anti-inflammatory action of salsalate can participate in improving glucose homeostasis (Liang, et al., 2015) suggesting that salsalate might have antidiabetic efficacy with minimal side effects.

In addition to its anti-inflammatory and anti-diabetic effects, salsalate can have other beneficial effects, in particular the effects on insulin sensitivity and lipid metabolism, some of which may be related to the anti-inflammatory effects of salsalate, others may be independent of these effects. Several recent studies confirmed the hypolipidemic effects of salsalate in diabetic mice (Nie, et al., 2017) and rats with inflammation induced by transgenic expression of human CRP (Trnovska, et al., 2017), as well as in individuals with abnormal glucose tolerance (Goldfine, et al., 2013) and patients with T2DM (Barzilay, et al., 2014). On the other hand, mechanisms responsible for metabolic effects of salsalate have not been fully elucidated. Accordingly, in this study, we investigated the effects of salsalate treatment on glucose and lipid metabolism, liver steatosis, glutathione system, inflammatory parameters and dicarbonyl stress in a rat prediabetic model with insulin resistance - a strain of

hereditary hypertriglyceridemic (HHTg) rats, which exhibits most of symptoms of metabolic syndrome but without fasting hyperglycemia and obesity (Zicha et al., 2006). In contrast to the high-fat or high-sucrose diet induced obesity and subsequent symptoms, the strain of HHTg rats represents a model of insulin resistance with genetically determined presence of aggravated lipid spectrum in circulation as well as increased ectopic lipid storage and all in absence excessive obesity. Thus, this animal model could refer to non-obese patients suffer from metabolic syndrome symptoms as insulin resistance and severe dyslipidemia, especially. Given the low cost of salicylates, administration of salsalate to people with prediabetes and metabolic syndrome could be an additional and alternative therapy.

2 Methods

2.1 Animals and experimental procedure

All experiments were performed in accordance with the Animal Protection Law of the Czech Republic (311/1997), which is in compliance with the European Community Council recommendations for the use of laboratory animals (86/609/ECC) and were approved by the Ethical Committee of the Ministry of Education of the Czech Republic as well as by the Ethical Committee of the Institute for Clinical and Experimental Medicine. The study was carried out on 6-month-old male hereditary hypertriglyceridemic rats (HHTg) from the Institute for the Clinical and Experimental Medicine, Prague, Czech Republic as the non-obese prediabetic model and on Wistar rats (obtained from Charles River, Germany) as the control group. Rats were maintained in a 12-h light/12-h dark cycle room with the temperature at 22°C–25°C, allowed free access to food and water. Animals were randomized into groups (each group $n = 8$) and were fed standard laboratory diet (maintenance diet for rats and mice; Altromin, Lage, Germany) with or without salsalate (Cayman chemical, United States, Item 11911) supplementation at daily dose 200 mg/kg of body weight for 6 weeks. At the end of the experiments, rats were sacrificed after light anesthesia (zoletil 5 mg/kg b. wt.) in a postprandial state, blood and tissues were collected and stored at -80°C .

2.2 Analytical methods and biochemical analysis

Serum glucose, triglycerides and total cholesterol were determined using kits from Erba Lachema, (Czech Republic). HDL-cholesterol, non-esterified fatty acid (NEFA) with kits from Roche Diagnostic, (Germany). Serum insulin, glucagon, high molecular weight (HMW) adiponectin, hs CRP, leptin, MCP-1, IL-6 and TNF α concentrations were determined using rat ELISA kit (Mercodia, Sweden; MyBioSource, United States; eBioscience, United States; BioVendor, Czech Republic). Alanine aminotransferase (ALT) and aspartate aminotransferase (AST) enzyme activity was determined spectrophotometrically using diagnostic kit (Roche Diagnostics, Mannheim, Germany).

For the oral glucose tolerance test (oGTT), blood glucose was determined after a glucose load (3 g of glucose/kg b. wt.) administrated intragastrically after overnight fasting. Preceding the glucose load, blood was drawn from the tail at 0 min and then 30, 60 and 120 min thereafter.

To determine triglycerides and cholesterol content in the liver and skeletal muscle, samples were extracted using a chloroform/methanol mixture. The resulting pellet was dissolved in isopropyl alcohol, with triglycerides content determined by enzymatic assay (Erba-Lachema, Brno, Czech Republic).

2.3 Basal and insulin-stimulated glucose utilization in adipose tissue and skeletal muscle

For measurement of insulin-stimulated incorporation of glucose into lipids or glycogen, epididymal adipose tissue or skeletal muscle was incubated for 2 h in 95% O₂ + 5% CO₂ in Krebs-Ringer bicarbonate buffer, pH 7.4, containing 0.1 μ Ci/mL of ¹⁴C-U glucose, 5 mmol/L of unlabeled glucose, and 2.5 mg/mL of bovine serum albumin (Fraction V, Sigma, Czech Republic), with or without 250 μ U/mL insulin. Extraction of lipids or glycogen was followed by a determination of insulin-stimulated incorporation of glucose into lipids or glycogen (Malinska, et al., 2015). In epididymal adipose tissue, basal and adrenaline-stimulated lipolysis were measured *ex vivo* based on the release of NEFA into the incubating medium.

2.4 Parameters of oxidative and dicarbonyl stress

Concentrations of reduced (GSH) and oxidized (GSSG) form of glutathione were determined using HPLC diagnostic kit with fluorescence detection (ChromSystems, Germany). Methylglyoxal concentrations were measured using the same HPLC method with fluorescence detection after derivatization with 1,2-diaminobenzene (Thornalley, et al., 1999). Activities of superoxide dismutase (SOD), glutathione peroxidase (GPx), glutathione reductase (GR), and glutathione transferase were analyzed using Cayman Chemicals assay kits (MI, United States). Concentration of conjugated dienes was determined by extraction in media (heptan: isopropanol = 2:

1) and measured spectrophotometrically in heptan layer. Lipoperoxidation products were assessed based on levels of thiobarbituric acid-reactive substances (TBARS) by assaying the reaction with thiobarbituric acid.

2.5 Relative mRNA expression

Total RNA was isolated from the liver or adipose tissue using RNA Blue (Top-bio, Czech Republic). Reverse transcription and quantitative real-time PCR analyses were performed using the TaqMan RNA-to CT 1-Step Kit and TaqMan Gene Expression Assay (Applied Biosystems, United States) and carried out using a ViiATM 7 Real Time PCR System (Applied Biosystems, United States). Relative expressions were determined after normalization against β -actin and *Hprt1* as an internal reference and calculated using the 2^{- $\Delta\Delta$ Ct} method. The results were run in triplicates.

2.6 Histological evaluation

Liver tissue slices in middle sagittal plane and stomach specimens dissected along the greater curvature were fixed in 4% formaldehyde for 24 h, dehydrated and embedded in paraffin. The sections stained with hematoxylin eosin and picosirius red were assessed in blind-test fashion. The non-alcoholic fatty liver disease (NAFLD) activity scores (NASS) as defined by Kleiner et al. (Kleiner, et al., 2005) were used to evaluate the liver parenchyma damage. Stomach samples were examined for any regressive or inflammatory changes.

2.7 Statistical analyses

Our hypothesis was to determine whether the effects of salsalate treatment would be different in prediabetic HHTg rats than in control Wistars. In this case, we used two-way ANOVA to test for strain effects, treatment effects and treatment vs. strain interaction, that determine whether the salsalate administration have different effect in prediabetic strain than in control Wistar strain. We used Fisher's *post hoc* LSD test for multiple comparison to determine whether the effects of salsalate treatment are significant in prediabetic HHTg and in control Wistar strain. All data are expressed as mean \pm SEM and were evaluated on StatSoft[®] Statistica software (version 14, Statsoft CZ, Czech Republic). Normality distribution was tested by the Shapiro-Wilk test. Statistical significance was defined as $p < 0.05$.

3 Results

3.1 The effects of salsalate on body composition

After salsalate treatment, HHTg rats had lower body weight, while body weight of Wistar rats were not significantly affected

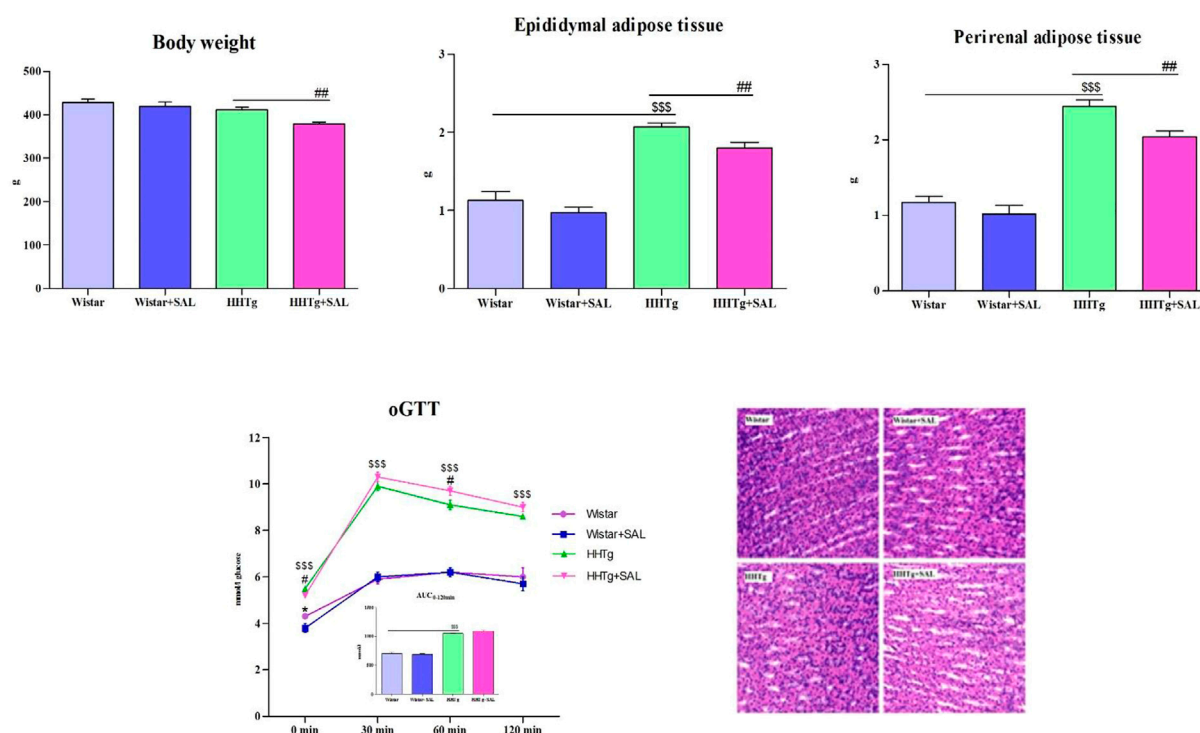


FIGURE 1

Effect of salsalate treatment on body weight and relative weight of visceral adipose tissues—epididymal and perirenal, and oral glucose tolerance test in Wistar control and hereditary hypertriglyceridemic (HHTg) rats. Values are expressed as mean \pm SEM; $n = 8$; Effect of salsalate on histological evaluation of the stomach wall. Representative histological images of intact gastric mucosa of each group showing neither inflammatory changes nor bleeding (hematoxylin and eosin (H&E) staining, 400 \times). * denotes significance reflecting the effect of Wistar vs. Wistar + SAL, # denotes significance reflecting the effect of HHTg vs. HHTg + SAL, ^{SSS} denotes significance reflecting the effect of Wistar vs. HHTg; * $p < 0.05$; # $p < 0.05$; ^{SSS} $p < 0.001$.

(Figure 1). Decreased body weight in HHTg rats was associated with decreased relative weight of visceral adipose tissue when epididymal and perirenal adipose tissue weight was significantly reduced ($p < 0.01$) (Figure 1). Salsalate treatment did not affect food and water intake in both animal groups.

3.2 The effects of salsalate on inflammatory parameters

Salsalate-treated Wistar animals exhibited decreased serum inflammatory markers MCP-1 and leptin while salsalate-treated HHTg animals exhibited decreased serum MCP-1 and TNF α (Table 1). On the other hand, serum levels of IL6 and hs CRP in Wistar and HHTg groups were not affected by salsalate administration. No inflammatory changes were observed in histological evaluation in the liver in salsalate-treated animals when compared to controls (Figure 1).

3.3 The effects of salsalate on oxidative and dicarbonyl stress

Salsalate administration in HHTg rats *versus* untreated controls was associated with reduced oxidative stress in the liver as suggested by increased activity of antioxidant enzymes

SOD and GPx as well as decreased levels of oxidized form of glutathione and parameters of lipoperoxidation (Table 2). In addition, salsalate-treated HHTg rats showed reduced dicarbonyl stress when hepatic levels of methylglyoxal were reduced (Figure 4).

3.4 The effects of salsalate on glucose tolerance and insulin sensitivity

Fasting as well as non-fasting glucose was decreased in HHTg-treated group and only fasting glucose was decreased in Wistar-treated group when compared to their respective controls (Table 1). On the other hand, salsalate administration did not significantly change AUC for glucose tolerance in both experimental groups (Figure 1). In salsalate-treated Wistar group, the levels of insulin and glucagon were markedly reduced ($p < 0.001$) while no significant effects of salsalate was observed in HHTg rats (Table 1). Epididymal adipose tissue of salsalate-treated HHTg rats was more sensitive to insulin action when insulin-stimulated lipogenesis was significantly increased ($p < 0.001$) *versus* untreated controls (Figure 3). Salsalate treatment was associated with increased lipolytic activity of epididymal adipose tissue in both Wistar and HHTg rats when compared to their respective controls (Figure 3). Skeletal muscles of HHTg rats treated with

TABLE 1 Effect of salsalate treatment on serum parameters in Wistar control and prediabetic HHTg rats.

	Wistar	Wistar + SAL	HHTg	HHTg + SAL	P _S	P _T	P _I
Fasting glucose (mmol/L)	4.3 ± 0.1	3.8 ± 0.2*	5.5 ± 0.1 ^{sss}	5.2 ± 0.1 [#]	0.001	0.01	n.s.
Non-fasting glucose (mmol/L)	7.0 ± 0.2	6.7 ± 0.1	8.3 ± 0.2 ^{sss}	7.8 ± 0.2 [#]	0.001	0.05	n.s.
Insulin (nmol/L)	0.46 ± 0.06	0.16 ± 0.01***	0.24 ± 0.02 ^{sss}	0.21 ± 0.02	0.05	0.001	0.001
Glucagon (pg/mL)	371 ± 44	184 ± 10***	165 ± 9 ^{sss}	150 ± 5	0.001	0.001	0.001
HMW adiponectin (μg/mL)	2.87 ± 0.11	2.51 ± 0.15	2.54 ± 0.16	2.29 ± 0.16	n.s.	n.s.	n.s.
TAG (mmol/L)	1.19 ± 0.05	0.88 ± 0.08	5.71 ± 0.18 ^{sss}	2.24 ± 0.12 ^{***}	0.001	0.001	0.001
Total cholesterol (mmol/L)	1.32 ± 0.07	1.17 ± 0.06	1.52 ± 0.03 [§]	1.25 ± 0.04 ^{***}	0.05	0.001	n.s.
HDL-cholesterol (mmol/L)	1.06 ± 0.06	0.94 ± 0.07	0.75 ± 0.02 ^{sss}	0.81 ± 0.04	0.001	n.s.	n.s.
NEFA (mmol/L)	0.30 ± 0.08	0.28 ± 0.05	0.50 ± 0.02 [§]	0.47 ± 0.04	0.001	n.s.	n.s.
Leptin (ng/mL)	7.29 ± 0.42	5.50 ± 0.61*	11.37 ± 0.24 ^{sss}	11.28 ± 0.49	0.001	n.s.	n.s.
MCP-1 (ng/mL)	283 ± 17	219 ± 25*	244 ± 21	174 ± 10 [#]	0.05	0.01	n.s.
TNFα (pg/mL)	2.02 ± 0.13	1.77 ± 0.07	3.75 ± 0.16 ^{sss}	2.82 ± 0.06 ^{***}	0.001	0.001	0.01
IL-6 (pg/mL)	9.35 ± 1.83	8.41 ± 1.51	12.67 ± 1.05	9.72 ± 0.62	n.s.	n.s.	n.s.
hs CRP (μg/mL)	247 ± 27	282 ± 17	230 ± 17	254 ± 18	n.s.	n.s.	n.s.
ALT (μkat/L)	1.05 ± 0.20	1.11 ± 0.04	1.16 ± 0.13	1.22 ± 0.07	n.s.	n.s.	n.s.
AST (μkat/L)	2.43 ± 0.16	2.72 ± 0.51	2.38 ± 0.21	2.84 ± 0.04	n.s.	n.s.	n.s.

Two-way ANOVA results: P_S denotes the significance of Wistar vs. HHTg (strain effects), P_T denotes the significance of salsalate (treatment effects); P_I denotes the significance of salsalate in both strains (treatment vs. strain interaction). For multiple comparisons Fisher's LSD *post hoc* test was used; * denotes significance reflecting the effect of Wistar vs. Wistar + SAL, [#] denotes significance reflecting the effect of HHTg vs. HHTg + SAL, [§] denotes significance reflecting the effect of Wistar vs. HHTg, n.s. denotes not significant; **p* < 0.05, ****p* < 0.001; [§]*p* < 0.05, ^{sss}*p* < 0.001. Data are mean ± SEM; *n* = 8 for each group. HHTg, hereditary hypertriglyceridemic rats; TAG, triacylglycerols; MCP-1, monocyte chemoattractant protein; TNFα–tumor necrosis factor α; IL-6, interleukin-6; hs CRP, high-sensitivity C-reactive protein.

TABLE 2 Effect of salsalate treatment on hepatic oxidative stress parameters in Wistar control and prediabetic HHTg rats.

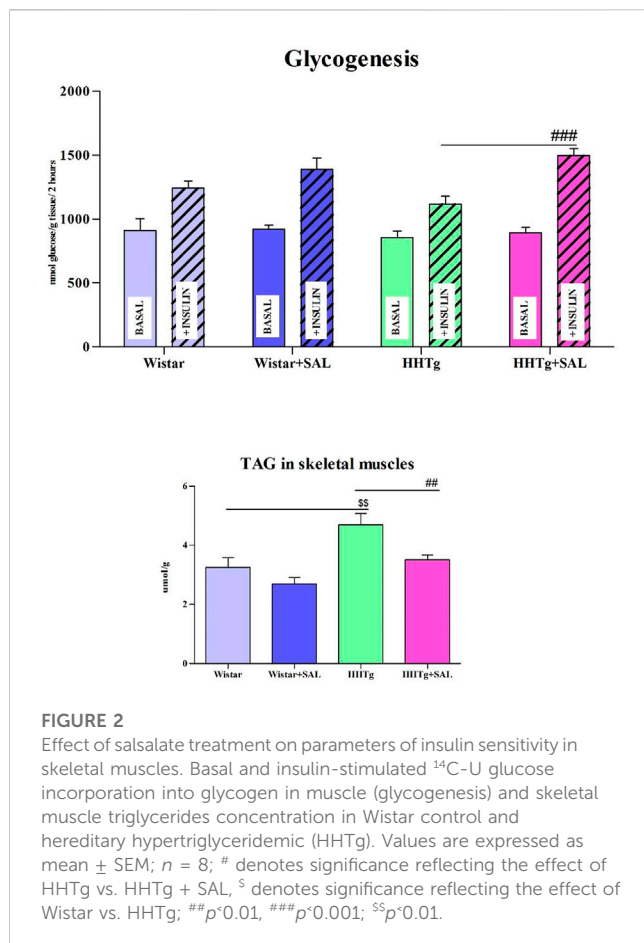
	Wistar	Wistar + SAL	HHTg	HHTg + SAL	P _S	P _T	P _I
TBARS, nmol/mg _{prot}	1.32 ± 0.13	1.22 ± 0.12	1.64 ± 0.10 [§]	1.20 ± 0.06 ^{**}	n.s.	0.05	n.s.
Conjugated dienes, nmol/mg _{prot}	32.0 ± 2.4	28.6 ± 2.2	41.6 ± 2.4 ^{§§}	28.8 ± 1.2 ^{***}	0.05	0.001	0.05
GSH, μmol/mg _{prot}	68.61 ± 4.33	71.31 ± 4.94	62.89 ± 2.56	73.06 ± 2.96 [#]	n.s.	0.05	n.s.
GSSG, μmol/mg _{prot}	1.11 ± 0.10	1.27 ± 0.10	1.74 ± 0.16 ^{§§}	1.22 ± 0.10 ^{**}	0.05	n.s.	0.01
GSH/GSSG	62.86 ± 3.11	56.97 ± 2.65	37.49 ± 3.10 ^{sss}	63.20 ± 6.12 ^{***}	0.05	0.05	0.01
SOD, U/mg _{prot}	0.16 ± 0.01	0.17 ± 0.01	0.11 ± 0.01 ^{§§}	0.14 ± 0.01 [#]	0.01	0.05	n.s.
GPx, μmol NADPH/min/mg _{prot}	276 ± 28	259 ± 20	222 ± 10	301 ± 27 [#]	n.s.	n.s.	0.05
GR, nmol NADPH/min/mg _{prot}	166 ± 13	210 ± 29	133 ± 12	136 ± 13	0.01	n.s.	n.s.

Two-way ANOVA, results; P_S denotes the significance of Wistar vs. HHTg (strain effects), P_T denotes the significance of salsalate (treatment effects); P_I denotes the significance of salsalate in both strains (treatment vs. strain interaction). For multiple comparisons Fisher's LSD, *post hoc* test was used; * denotes significance reflecting the effect of Wistar vs. Wistar + SAL, [#] denotes significance reflecting the effect of HHTg vs. HHTg + SAL, [§] denotes significance reflecting the effect of Wistar vs. HHTg, n.s. denotes not significant; **p* < 0.05, ***p* < 0.01, ****p* < 0.001; [§]*p* < 0.05, ^{§§}*p* < 0.01, ^{sss}*p* < 0.001. Data are mean ± SEM; *n* = 8 for each group. HHTg, hereditary hypertriglyceridemic rats; GSH, glutathione; GSSG, oxidized form of glutathione; SOD, superoxide dismutase; GPx, glutathioneperoxidase; GR, glutathione reductase; TBARS, thiobarbituric acid-reactive substance.

salsalate contained less triglycerides and showed increased sensitivity to insulin action when insulin-stimulated glycogenesis was significantly higher (*p* < 0.001) compared to untreated controls (Figure 2). There were no significant differences in insulin sensitivity parameters in the Wistar group after salsalate administration.

3.5 The effect of salsalate on serum and hepatic lipids

After salsalate administration, serum levels of triacylglycerols and total cholesterol were significantly decreased (*p* < 0.001) in HHTg rats *versus* their untreated controls, but HDL cholesterol and



NEFA were not affected (Table 1). Salsalate administration significantly reduced hepatic triglyceride ($p < 0.001$) and cholesterol ($p < 0.01$) concentrations in HHTg rats versus untreated controls (Figure 4).

3.6 The effects of salsalate on gene expression

To search for responsible molecular mechanisms of salsalate protective effects against inflammation and metabolic disturbances we determined mRNA abundance of selected genes in tissues. Anti-inflammatory effects of salsalate in HHTg rats compared to untreated controls were associated with reduced expression of *Ccl2* gene (coding for the MCP-1 cytokine) in adipose tissue ($p < 0.01$) and in the liver ($p < 0.01$) (Figures 3, 5). Reduced carbonyl stress in the liver after treatment of HHTg rats with salsalate was associated with increased hepatic expression of *Glo1* gene ($p < 0.01$) that codes for an enzyme involved in methylglyoxal degradation.

Amelioration of dyslipidemia in salsalate-treated HHTg rats was associated with reduced hepatic expression of *Fasn* ($p < 0.001$) and *Srebp1* ($p < 0.001$) genes coding for lipogenic enzyme and lipogenic transcription factor, respectively (Figure 4). Reduced hepatic cholesterol content in HHTg rats after salsalate treatment was associated with decreased relative expression of *Hmgcr* gene ($p < 0.05$), coding for an enzyme involved in cholesterol synthesis, and

Ldlr gene ($p < 0.001$), involved in cholesterol transport into the cells (Figure 4). Salsalate treatment also affected expression of genes coding for hepatic membrane cholesterol transporters—relative mRNA expression of *Abcg5* was significantly elevated ($p < 0.001$ for Wistar group; $p < 0.05$ for HHTg group) while expression of *Abcb1b* gene ($p < 0.05$ for Wistar group; $p < 0.001$ for HHTg group) was markedly decreased in both treated groups compared to untreated controls (Figure 5). In Wistar salsalate-treated rats, mRNA expression of *Abcb1a* and *Abca1* genes was significantly decreased ($p < 0.01$; $p < 0.05$, respectively.). Salsalate treatment increased mRNA expression of *Abcg8* in Wistar group while decreased in HHTg group of rats (Figure 5). Increased gene expression of *Ppara* gene coding for transcription factor in salsalate-treated animals can contribute to increased hepatic lipid oxidation (Figure 4). On the other hand, no differences in mRNA expression of *Ppar γ* , *Srebf2* and *Lpl* (Figure 4). Compared to untreated group, salsalate-treated HHTg rats also exhibited decreased mRNA expression of *Nfe212* (Figure 4).

In the liver, salsalate treatment affected expression of some genes coding for cytochrome P450 proteins involved in lipid metabolism. As shown in Figure 5, relative gene expression of *Cyp7a1* and *Cyp5a1* genes was significantly decreased in both salsalate-treated Wistar ($p < 0.01$; $p < 0.001$, respectively.) and HHTg ($p < 0.01$; $p < 0.05$, respectively.) groups of rats whereas markedly elevated relative gene expression of *Cyp4a1*, *Cyp4a2*, *Cyp4a3* was observed in salsalate-treated animals ($p < 0.001$; $p < 0.01$, respectively.) (Figure 5). On the other hand, no differences in relative gene expression of *Cyp11a1* and *Cyp2e1* were observed in both Wistar and HHTg rats (Figure 5). According to histological evaluations of liver parenchyma we observed no apparent abnormality in any experimental group (Figure 5).

4 Discussion

In the present study, we investigated metabolic effects of salsalate and examined responsible mechanisms of these effects in HHTg rats, a prediabetic model with hypertriglyceridemia and insulin resistance. Insulin resistance—a typical sign of prediabetic state was accompanied by changes in lipid metabolism, increased oxidative stress and the presence of low-grade inflammation. HHTg rats exhibit all disorders associated with prediabetes but without the complications of high-fat-diet-induced obesity. Our results demonstrate that salsalate treatment improved glycaemia, insulin sensitivity and exhibited hypolipidemic properties.

The anti-inflammatory effects of salsalate are believed to be attributable to inhibition of pro-inflammatory mediators such as prostaglandins (Morris, et al., 1985). Salsalate treatment is associated with inhibition of the COX activity, a key enzyme in biosynthesis of pro-inflammatory prostanooids, but also inhibition of neutrophil activation and strongly inhibits NF κ B inflammatory pathway (Rumore and Kim, 2010). Transcription factor NF κ B is the master switch of the inflammatory pathway and stimulating its activity in adipose tissue and the liver results in insulin resistance (Goldfine, et al., 2008). In the present study, salsalate treatment exhibited anti-inflammatory effect in circulation, as well as in visceral adipose tissue and liver. Decreased MCP-1 expression in adipose tissue and liver can reduce macrophage infiltration and can

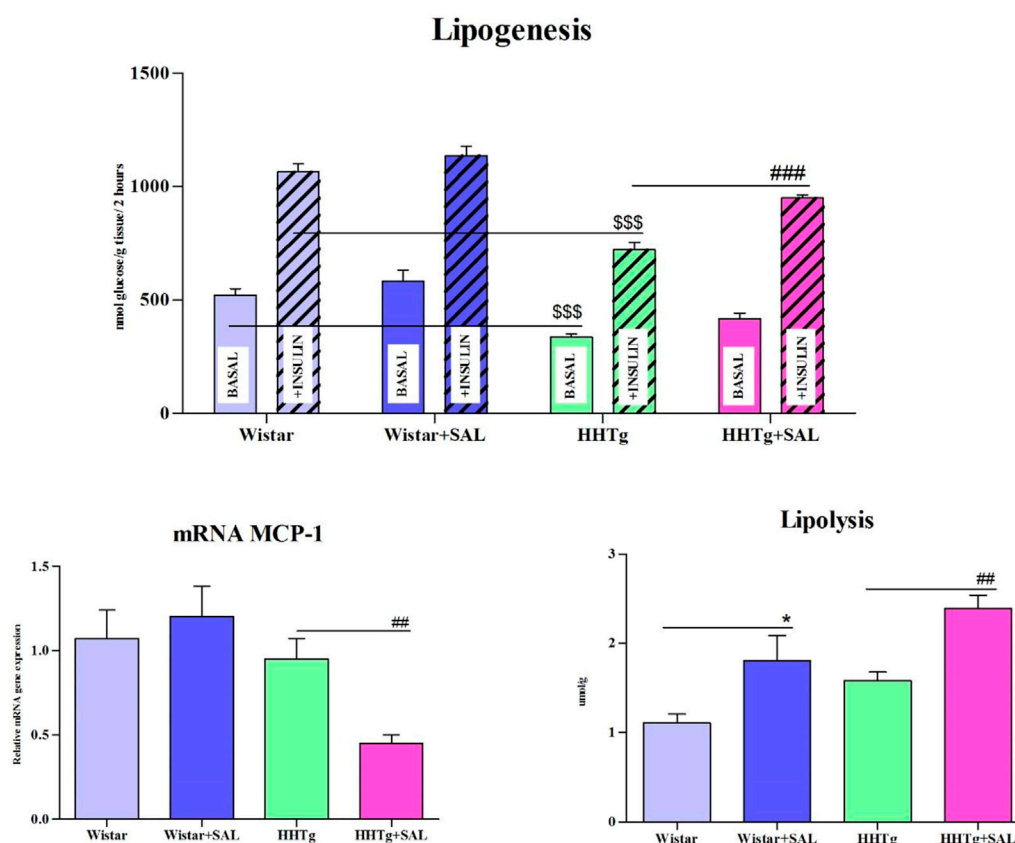


FIGURE 3

Effect of salsalate treatment on metabolic activity of epididymal adipose tissue. Basal and insulin-stimulated ^{14}C -U glucose incorporation into lipids in epididymal adipose tissue (lipogenesis), lipolysis and relative mRNA expression of MCP1 in Wistar control and hereditary hypertriglyceridemic (HHTg) rats. Values are expressed as mean \pm SEM; $n = 8$; * denotes significance reflecting the effect of Wistar vs. Wistar + SAL, # denotes significance reflecting the effect of HHTg vs. HHTg + SAL, \$\$\$ denotes significance reflecting the effect of Wistar vs. HHTg; * $p < 0.05$; # $p < 0.01$; ### $p < 0.001$; \$\$\$ $p < 0.001$.

affect other pro-inflammatory gene expression. These effects can ameliorate insulin sensitivity and NAFLD progression.

Beneficial effects of salsalate on lipid metabolism in the liver may be related to reduce oxidative and dicarbonyl stress in HHTg rats. Salsalate treatment ameliorated oxidative stress by stimulating antioxidant enzyme activity that can inactivate free radicals in the liver directly. In addition, increased activity of SOD and GPx may play a role in decreasing hepatic lipid peroxidation by participating in the removal of lipoperoxidation products. Increased GPx activity after salsalate treatment was also linked to increased levels of glutathione, a sensitive marker of hepatic oxidative damage. Markedly increased GSH/GSSG ratio following salsalate administration can mitigate oxidative as well dicarbonyl stress. Reduced methylglyoxal accumulation can occur due to increased gene expression of glutathione-dependent *Glo-1*, enzyme involved in methylglyoxal degradation. Dicarbonyl stress may be involved in the pathogenesis of hepatic steatosis and methylglyoxal can contribute *via* several mechanisms to the development of hepatic steatosis. Methylglyoxal decreases glutathione levels, induces lipoperoxidation, may impair insulin signaling and activates RAGE receptors (Hüttel, et al., 2020). In addition, some inflammatory pathways, in particular those related to NF κ B, are activated by methylglyoxal (Neves, et al., 2019).

According to our previous results (Malinska, et al., 2021), hepatic methylglyoxal concentrations well correlated with hepatic triglycerides concentrations. Thus, mitigation of dicarbonyl stress through decreased methylglyoxal and increased *Glo1* expression, can protect against NAFLD development and/or progression.

Our results showed that salsalate administration improved glucose tolerance and insulin sensitivity in peripheral tissues. Glucose-lowering effect of salsalate was previously observed in diabetic (Goldfine, et al., 2010) as well in prediabetic individuals (Faghihimani, et al., 2012), however the exact mechanism was not clarified yet. It was suggested that salsalate suppresses hepatic glucose production, positively affects insulin and glucagon and protects β -cells (Penesova, et al., 2015; Han, et al., 2019). Smith et al. suggested that the mechanism by which salsalate improves glucose homeostasis and NAFLD is *via* salicylate-driven mitochondrial uncoupling (Smith, et al., 2016). Antidiabetic effect of salsalate may be also related to reducing intestinal inflammation and improved gut dysbiosis that was observed in ZDF rats (Zhang, et al., 2020). Although several studies have found increased adiponectin levels after salsalate administration (Wang, et al., 2014; Salastekar, et al., 2017), which could contribute to improvement of insulin sensitivity, in the present study salsalate did not affect adiponectin levels. It has been also suggested that the

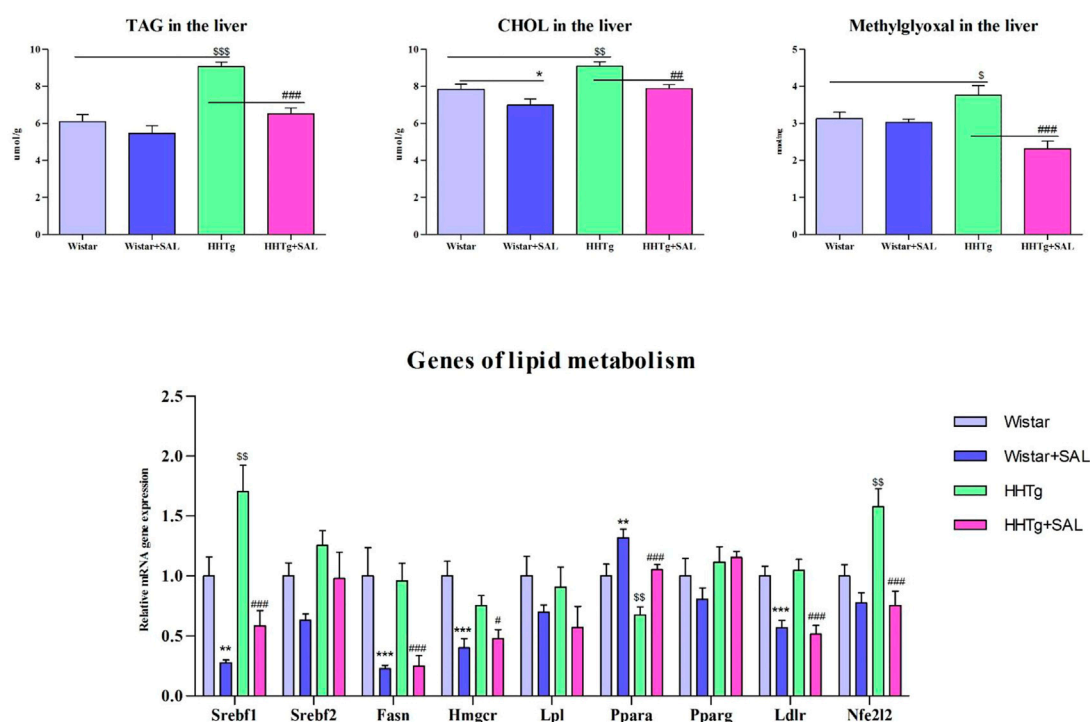


FIGURE 4

Effect of salsalate treatment on hepatic lipids and methylglyoxal accumulation and relative mRNA expression of enzymes and transcription factors involved of lipid metabolism in Wistar control and hereditary hypertriglyceridemic (HHTg) rats. Values are expressed as mean \pm SEM; $n = 8$; * denotes significance reflecting the effect of Wistar vs. Wistar + SAL, # denotes significance reflecting the effect of HHTg vs. HHTg + SAL, s denotes significance reflecting the effect of Wistar vs. HHTg; * $p < 0.05$, ** $p < 0.01$, *** $p < 0.001$; # $p < 0.05$, ## $p < 0.01$, ### $p < 0.001$; $^s p < 0.05$, $^{ss} p < 0.01$, $^{sss} p < 0.001$.

IKK β pathway is a target for insulin sensitizing effects of salsalate (Yuan, et al., 2001).

Severe hepatic lipid accumulation in HHTg rats was ameliorated following salsalate treatment when both hepatic triglyceride and cholesterol concentrations were markedly reduced. Lower ectopic fat accumulation could contribute to increased insulin sensitivity and reduced lipid peroxidation. Compared to the anti-inflammatory and antidiabetic effects, the hypolipidemic effects are more pronounced in the prediabetic HHTg model. Higher efficacy of salsalate in the presence of serious dyslipidemia and hepatic lipid accumulation is promising for a potential use of salsalate in prediabetic patients with NAFLD.

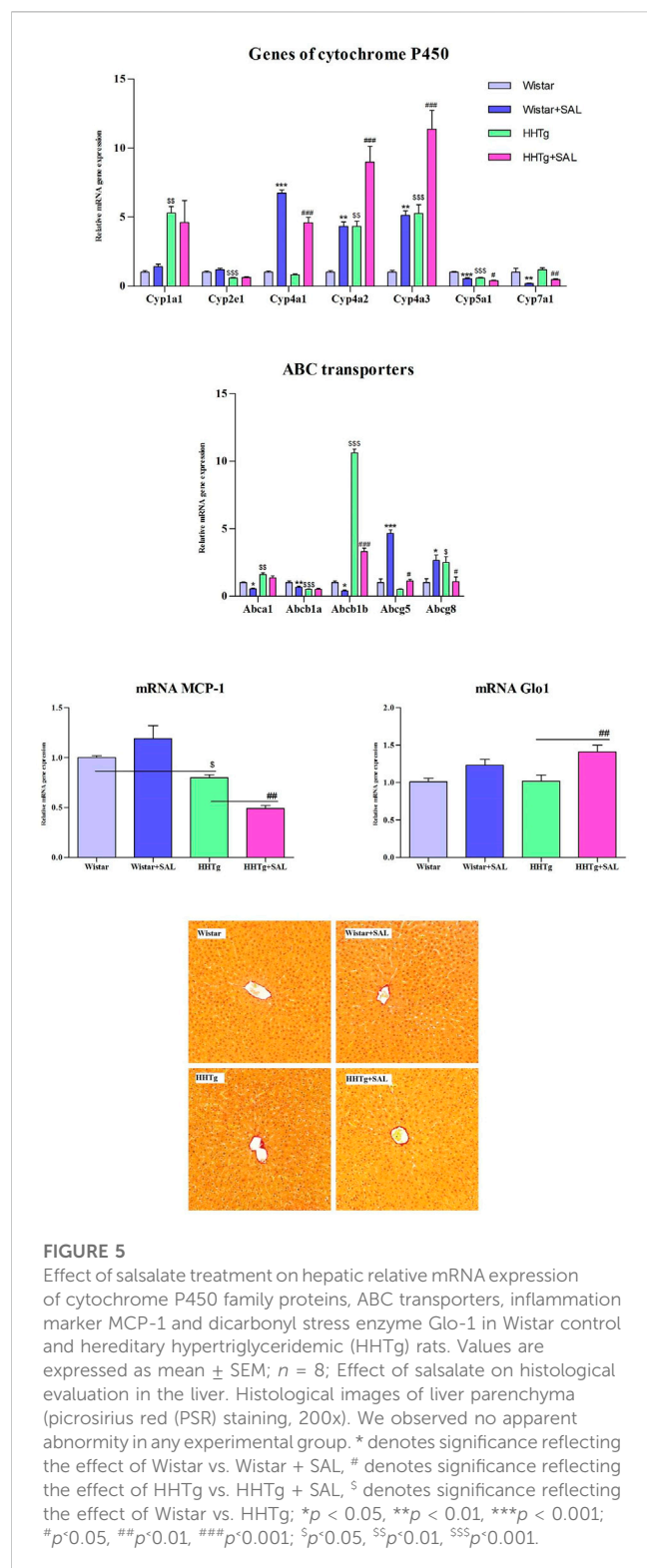
Our analysis revealed differential hepatic expression of selected genes that may be responsible for hypolipidemic effects of salsalate. These are genes coding for enzymes or transcription factors which are involved in lipid synthesis (*Fas*, *Hmgcr*, *Srebp1*), oxidation (*Ppara*) as well as transport into the cells (*Ldl* receptors, *Abc* transporters). Accordingly, reduction of hepatic lipid accumulation can be a product of decreasing *de novo* synthesis as well as increasing lipid oxidation. Decreased gene expression of transcription factor *Srebp1* can reduce hepatic lipid accumulation *via* suppression of lipogenesis, in turn contributing to improved insulin sensitivity.

Salsalate may modulate fatty acid oxidation, lipid synthesis, and lipoprotein metabolism. Recently, salsalate has been reported to directly activate AMP-activated protein kinase, which plays an important role in the regulation of inflammation and hepatic lipid metabolism (Hawley, et al., 2012). Salsalate was found to potently suppress hepatic *de novo*

lipogenesis *in vitro* and *in vivo* (Smith et al., 2016). A recent report indicates that salicylates reduced hepatic NF κ B activity and hepatic VLDL triglycerides production in high-fat fed mice (Baker, et al., 2011). Other study with diet-induced NASH in mice (Liang et al., 2015) revealed an important role for PPARG-mediated pathways with regards to the beneficial effects of salsalate on lipid metabolism. In our previous study in SHR-CRP rats, a model of inflammation and metabolic disturbances, we also observed increased hepatic expression of *Ppara* gene after salsalate treatment that was associated with reduced ectopic fat accumulation in the liver (Trnovská et al., 2017).

Abcg5/8 transporters not only play an important role in sterol absorption and excretion but also provide an important pathway for cholesterol elimination (Poruba, et al., 2019). Increased gene expression of *Abcg8* transporter indicated higher cholesterol secretion from hepatocytes into bile. Beyond a role in cellular cholesterol homeostasis, ABC transporters can be involved in the secretion and bioavailability of key molecules controlling glucose and lipid metabolism, such as lipoprotein lipase or insulin (Hardy, et al., 2017). Thus, modulation of ABC transporters can associate with metabolic disorders including T2DM and insulin resistance. In the present study, in a prediabetic HHTg model with severe hypertriglyceridemia we observed markedly increased expression of *Abcb1b*, *Abca1*, and *Abcg8* genes and decreased expression of *Abcb1a* and *Abcg5* genes.

In the present study, salsalate treatment was associated with alterations in hepatic expression of genes coding for cytochrome P450 family proteins, especially those that can be associated with



lipid metabolism and fatty liver development. Hepatic lipid accumulation in HHTg rats was associated with markedly increased hepatic gene expression of *Cyp1a1*, *Cyp4a2* and *Cyp4a3* and decreased *Cyp2e1* and *Cyp7a1* that can be involved in hepatic lipid dysmetabolism and fatty liver development as was reviewed by Jamwal and Barlock 2020.

According to recent reports, CYP4A isoforms are markedly elevated in the liver tissues of NAFLD patients (Ryu, et al., 2019), as well as in diabetic and obese mice with hepatic steatosis (Zhang, et al., 2017). CYP4A cytochromes metabolize EETs (epoxyeicosatrienoic acids) to HEETs (hydroxy-epoxyeico-satrienoic acids) and act as PPAR- α agonists. Increased CYP4A after salsalate treatment can contribute to increased fatty acid oxidation in the liver through increased transcription factor PPAR α (Zhang and Klaassen, 2013). The effect of salsalate on CYP4a proteins in our study is in agreement with results in model with essential hypertension and chronic inflammation, the SHR-CRP rats. In this study, SHR rats with transgenic expression of human CRP exerted increased gene expression of *Cyp4a1* in the liver following salsalate administration that was also associated with increased *Ppara* gene expression (Trnovska, et al., 2017).

In our study, salsalate treatment was associated with reduced gene expression of *Cyp5a1*–CYP450 isoform that metabolizes the cyclooxygenase product prostaglandin H2 into thromboxane A2, a potent inducer of vasoconstriction and platelet aggregation. (Ershov, et al., 2021). Thus, it is possible that salsalate can improve vascular complications also through decreased CYP5a1.

The hepatic CYP7a1 protein is a rate-limiting enzyme responsible for cholesterol conversion to 7 α -hydroxycholesterol, which is secreted into bile acids and eliminated (Chiang and Ferrell, 2020). Since hepatic expression of *Cyp7a1* gene was reduced in HHTg rats after salsalate treatment, we assume that decreased hepatic cholesterol concentrations after salsalate administration are not due to increased elimination, rather to decreased hepatic synthesis. Taken together, changes in hepatic gene expressions of CYP family proteins following salsalate treatment may be involved in reducing lipid accumulation in the liver. Possible study limitation as well as the strength may be related to the used strain of rats because the found results can be applied to specific group of patients in human medicine. However, this is consistent with the requirements of personalized medicine.

5 Conclusion

Salsalate treatment in HHTg rats markedly reduced inflammation, oxidative and dicarbonyl stress, ameliorated hepatic lipid metabolism and ectopic lipid deposition. These effects were associated with increased insulin sensitivity in peripheral tissues and protect against the progression and/or development of NAFLD and its symptoms. The mechanism of beneficial effect of salsalate on metabolic disorders associated with prediabetic conditions may consist of the changes in cytochrome P450 proteins and the alleviation in oxidative and dicarbonyl stress in the liver. In contrast to the anti-inflammatory effect, hypolipidemic and insulin sensitizing effects of salsalate were more pronounced in the prediabetic HHTg model which suggests that salsalate can have potential beneficial use in prediabetic patients with NAFLD symptoms.

Data availability statement

The datasets presented in this study can be found in online repositories. The names of the repository/repositories and accession number(s) can be found in the article/supplementary material.

Ethics statement

The animal study was reviewed and approved by Ethical Committee of the Institute for Clinical and Experimental Medicine.

Author contributions

MH and HM—study conception and design, manuscript draft and composition; IM—biochemical/molecular analysis and data interpretation; DM—statistical and biochemical analysis; IZ and JŠ—molecular analysis; PK—histological evaluation and interpretation; MP—study conception. All authors have critically revised the manuscript for intellectual content and have approved the final version for publication. All authors have read and agreed to the published version of the manuscript.

Funding

This work was supported by the project National Institute for Research of Metabolic and Cardiovascular Diseases—Program EXCELES, Project No. LX22NPO5104—funded by the European

Union—Next-Generation EU and by a grant from Ministry of Health of the Czech Republic no. IGA_LF_2023_004.

Acknowledgments

We thank Olena Oliarynyk for technical assistance.

Conflict of interest

The authors declare that the research was conducted in the absence of any commercial or financial relationships that could be construed as a potential conflict of interest.

Publisher's note

All claims expressed in this article are solely those of the authors and do not necessarily represent those of their affiliated organizations, or those of the publisher, the editors and the reviewers. Any product that may be evaluated in this article, or claim that may be made by its manufacturer, is not guaranteed or endorsed by the publisher.

References

- Baker, R. G., Hayden, M. S., and Ghosh, S. (2011). NF- κ B, inflammation, and metabolic disease. *Cell Metab.* 13, 11–22. doi:10.1016/j.cmet.2010.12.008
- Barzilay, J. I., Jablonski, K. A., Fonseca, V., Shoelson, S. E., Goldfine, A. B., Strauch, C., et al. (2014). The impact of salsalate treatment on serum levels of advanced glycation end products in type 2 diabetes. *Diabetes Care* 37, 1083–1091. doi:10.2337/dc13-1527
- Chiang, J. Y. L., and Ferrell, J. M. (2020). Up to date on cholesterol 7 α -hydroxylase (CYP7A1) in bile acid synthesis. *Liver Res.* 4, 47–63. doi:10.1016/j.livres.2020.05.001
- Ershov, P. V., Yablokov, E., Zgoda, V., Mezentsev, Y., Gnedenko, O., Kaluzhskiy, L., et al. (2021). A new insight into subinteractomes of functional antagonists: Thromboxane (CYP5A1) and prostacyclin (CYP8A1) synthases. *Cell Biol. Int.* 45, 1175–1182. doi:10.1002/cbin.11564
- Faghihi, E., Aminorroaya, A., Rezvanian, H., Adibi, P., Ismail-Beigi, F., and Amini, M. (2012). Reduction of insulin resistance and plasma glucose level by salsalate treatment in persons with prediabetes. *Endocr. Pract.* 18, 826–833. doi:10.4158/EP12064.0R
- Goldfine, A. B., Conlin, P. R., Halperin, F., Koska, J., Permana, P., Schwenke, D., et al. (2013). A randomised trial of salsalate for insulin resistance and cardiovascular risk factors in persons with abnormal glucose tolerance. *Diabetologia* 56, 714–723. doi:10.1007/s00125-012-2819-3
- Goldfine, A. B., Fonseca, V., Jablonski, K. A., Pyle, L., Staten, M. A., Shoelson, S. E., et al. (2010). The effects of salsalate on glycemic control in patients with type 2 diabetes: A randomized trial. *Ann. Intern. Med.* 152, 346–357. doi:10.7326/0003-4819-152-6-201003160-00004
- Goldfine, A. B., Silver, R., Aldhahi, W., Cai, D., Tatso, E., Lee, J., et al. (2008). Use of salsalate to target inflammation in the treatment of insulin resistance and type 2 diabetes. *Clin. Transl. Sci.* 1, 36–43. doi:10.1111/j.1752-8062.2008.00026.x
- Han, F., Li, X., Yang, J., Liu, H., Zhang, Y., Yang, X., et al. (2019). Salsalate prevents beta-cell dedifferentiation in OLETF rats with type 2 diabetes through Notch1 pathway. *Aging Dis.* 10, 719–730. doi:10.14336/AD.2018.1221
- Hardy, L. M., Frisdal, E., and Le Goff, W. (2017). Critical role of the human ATP-binding cassette G1 transporter in cardiometabolic diseases. *Int. J. Mol. Sci.* 18, 1892. doi:10.3390/ijms18091892
- Hawley, S. A., Fullerton, M. D., Ross, F. A., Schertzer, J. D., Chevtzoff, C., Walker, K. J., et al. (2012). The ancient drug salicylate directly activates AMP-activated protein kinase. *Science* 336, 918–922. doi:10.1126/science.1215327
- Higgs, G. A., Salmon, J. A., Henderson, B., and Vane, J. R. (1987). Pharmacokinetics of aspirin and salicylate in relation to inhibition of arachidonate cyclooxygenase and antiinflammatory activity. *Proc. Natl. Acad. Sci. U. S. A.* 84, 1417–1420. doi:10.1073/pnas.84.5.1417
- Hüttel, M., Markova, I., Miklankova, D., Makovicky, P., Pelikanova, T., Seda, O., et al. (2020). Adverse effects of methylglyoxal on transcriptome and metabolic changes in visceral adipose tissue in a prediabetic rat model. *Antioxidants (Basel)* 9, 803. doi:10.3390/antiox9090803
- Jamwal, R., and Barlock, B. J. (2020). Nonalcoholic fatty liver disease (NAFLD) and hepatic cytochrome P450 (CYP) enzymes. *Pharm. (Basel)* 13, 222. doi:10.3390/ph13090222
- Kleiner, D. E., Brunt, E. M., Van Natta, M., Behling, C., Contos, M. J., Cummings, O. W., et al. (2005). Design and validation of a histological scoring system for nonalcoholic fatty liver disease. *Hepatology* 41, 1313–1321. doi:10.1002/hep.20701
- Liang, W., Verschuren, L., Mulder, P., van der Hoorn, J. W., Verheij, J., van Dam, A. D., et al. (2015). Salsalate attenuates diet induced non-alcoholic steatohepatitis in mice by decreasing lipogenic and inflammatory processes. *Br. J. Pharmacol.* 172, 5293–5305. doi:10.1111/bph.13315
- Malinska, H., Hüttel, M., Miklankova, D., Trnovska, J., Zapletalova, I., Poruba, M., et al. (2021). Ovariectomy-induced hepatic lipid and cytochrome P450 dysmetabolism precedes serum dyslipidemia. *Int. J. Mol. Sci.* 22, 4527. doi:10.3390/ijms22094527
- Malinska, H., Hüttel, M., Oliarynyk, O., Bratova, M., and Kazdova, L. (2015). Conjugated linoleic acid reduces visceral and ectopic lipid accumulation and insulin resistance in chronic severe hypertriglyceridemia. *Nutrition* 31, 1045–1051. doi:10.1016/j.nut.2015.03.011
- Morris, H. G., Sherman, N. A., McQuain, C., Golglust, M. B., Chang, S. F., and Harrison, L. I. (1985). Effects of salsalate (nonacetylated salicylate) and aspirin on serum prostaglandins in humans. *Ther. Drug Monit.* 7, 435–438. doi:10.1097/00007691-198512000-00012
- Neves, C., Rodrigues, T., Sereno, J., Simoes, C., Castelhana, J., Goncalves, J., et al. (2019). Dietary glycotoxins impair hepatic lipidemic profile in diet-induced obese rats causing hepatic oxidative stress and insulin resistance. *Oxid. Med. Cell Longev.* 2019, 6362910. doi:10.1155/2019/6362910
- Nie, L., Yuan, X. L., Jiang, K. T., Jiang, Y. H., Yuan, J., Luo, L., et al. (2017). Salsalate activates skeletal muscle thermogenesis and protects mice from high-fat diet induced metabolic dysfunction. *EBioMedicine* 23, 136–145. doi:10.1016/j.ebiom.2017.08.004
- Penesova, A., Koska, J., Ortega, E., Bunt, J. C., Bogardus, C., and de Courten, B. (2015). Salsalate has no effect on insulin secretion but decreases insulin clearance: A randomized, placebo-controlled trial in subjects without diabetes. *Diabetes Obes. Metab.* 17, 608–612. doi:10.1111/dom.12450
- Poruba, M., Matuskova, Z., Hüttel, M., Malinska, H., Oliarynyk, O., Markova, I., et al. (2019). Fenofibrate decreases hepatic P-glycoprotein in a rat model of hereditary hypertriglyceridemia. *Front. Pharmacol.* 10, 56. doi:10.3389/fphar.2019.00056
- Rumore, M. M., and Kim, K. S. (2010). Potential role of salicylates in type 2 diabetes. *Ann. Pharmacother.* 44, 1207–1221. doi:10.1345/aph.1M483

- Ryu, J. S., Lee, M., Mun, S. J., Hong, S. H., Lee, H. J., Ahn, H. S., et al. (2019). Targeting CYP4A attenuates hepatic steatosis in a novel multicellular organotypic liver model. *J. Biol. Eng.* 13, 69. doi:10.1186/s13036-019-0198-8
- Salastekar, N., Desai, T., Hauser, T., Schaefer, E. J., Fowler, K., Joseph, S., et al. (2017). Salsalate improves glycaemia in overweight persons with diabetes risk factors of stable statin-treated cardiovascular disease: A 30-month randomized placebo-controlled trial. *Diabetes Obes. Metab.* 19, 1458–1462. doi:10.1111/dom.12940
- Scheiman, J. M., and Elta, G. H. (1990). Gastroduodenal mucosal damage with salsalate versus aspirin: Results of experimental models and endoscopic studies in humans. *Semin. Arthritis Rheum.* 20, 121–127. doi:10.1016/0049-0172(90)90025-b
- Smith, B. K., Ford, R. J., Desjardins, E. M., Green, A. E., Hughes, M. C., Houde, V. P., et al. (2016). Salsalate (salicylate) uncouples mitochondria, improves glucose homeostasis, and reduces liver lipids independent of AMPK- β 1. *Diabetes* 65, 3352–3361. doi:10.2337/db16-0564
- Thornalley, P. J., Langborg, A., and Minhas, H. S. (1999). Formation of glyoxal, methylglyoxal and 3-deoxyglucosone in the glycation of proteins by glucose. *Biochem. J.* 344, 109–116. doi:10.1042/bj3440109
- Trnovska, J., Silhavy, J., Kuda, O., Landa, V., Zidek, V., Mlejnek, P., et al. (2017). Salsalate ameliorates metabolic disturbances by reducing inflammation in spontaneously hypertensive rats expressing human C-reactive protein and by activating Brown adipose tissue in nontransgenic controls. *PLoS One* 12, e0179063. doi:10.1371/journal.pone.0179063
- Vane, J. R. (2002). Biomedicine. Back to an aspirin a day? *Science* 296, 474–475. doi:10.1126/science.1071702
- Wang, X., DuBois, D. C., Cao, Y., Jusko, W. J., and Almon, R. R. (2014). Diabetes disease progression in goto-kakizaki rats: Effects of salsalate treatment. *Diabetes Metab. Syndr. Obes.* 7, 381–389. doi:10.2147/DMSO.S65818
- Wu, H., and Ballantyn, e. C. M. (2020). Metabolic inflammation and insulin resistance in obesity. *Circ. Res.* 126, 1549–1564. doi:10.1161/CIRCRESAHA.119.315896
- Yuan, M., Konstantopoulos, N., Lee, J., Hansen, L., Li, Z. W., Karin, M., et al. (2001). Reversal of obesity- and diet-induced insulin resistance with salicylates or targeted disruption of Ikk β . *Science* 293, 1673–1677. doi:10.1126/science.1061620
- Zhang, X., Cui, X., Jin, X., Han, F., Wang, J., Yang, X., et al. (2020). Preventive role of salsalate in diabetes is associated with reducing intestinal inflammation through improvement of gut dysbiosis in ZDF rats. *Front. Pharmacol.* 11, 300. doi:10.3389/fphar.2020.00300
- Zhang, X., Li, S., Zhou, Y., Su, W., Ruan, X., Wang, B., et al. (2017). Ablation of cytochrome P450 omega-hydroxylase 4A14 gene attenuates hepatic steatosis and fibrosis. *Proc. Natl. Acad. Sci. U. S. A.* 114, 3181–3185. doi:10.1073/pnas.1700172114
- Zhang, Y., and Klaassen, C. D. (2013). Hormonal regulation of Cyp4a isoforms in mouse liver and kidney. *Xenobiotica* 43, 1055–1063. doi:10.3109/00498254.2013.797622
- Zicha, J., Pechánová, O., Cacanyiová, S., Cebová, M., Kristek, F., Török, J., et al. (2006). Hereditary hypertriglyceridemic rat: a suitable model of cardiovascular disease and metabolic syndrome? *Physiol Res.* 55, S49–S63. doi:10.33549/physiolres.930000.55.S1.49



OPEN ACCESS

EDITED BY

Rong Wang,
People's Liberation Army Joint Logistics
Support Force 940th Hospital, China

REVIEWED BY

Haibo Song,
National Center for ADR Monitoring,
China
Thomas Hsueh,
Taipei City Hospital, Taiwan

*CORRESPONDENCE

Yuhong Huang,
✉ hyh101@126.com
Chunxiao Lv,
✉ lvchunxiao1989@163.com

[†]These authors have contributed equally
to this work and share first authorship

RECEIVED 23 November 2022

ACCEPTED 24 April 2023

PUBLISHED 04 May 2023

CITATION

Chen X, Zuo X, Zhao Y, Huang Y and Lv C
(2023), Evaluation and clinical
implications of interactions between
compound Danshen dripping pill and
warfarin associated with the epoxide
hydrolase gene.
Front. Pharmacol. 14:1105702.
doi: 10.3389/fphar.2023.1105702

COPYRIGHT

© 2023 Chen, Zuo, Zhao, Huang and Lv.
This is an open-access article distributed
under the terms of the [Creative
Commons Attribution License \(CC BY\)](#).
The use, distribution or reproduction in
other forums is permitted, provided the
original author(s) and the copyright
owner(s) are credited and that the original
publication in this journal is cited, in
accordance with accepted academic
practice. No use, distribution or
reproduction is permitted which does not
comply with these terms.

Evaluation and clinical implications of interactions between compound Danshen dripping pill and warfarin associated with the epoxide hydrolase gene

Xixi Chen^{1,2†}, Xurui Zuo^{1†}, Yingqiang Zhao³, Yuhong Huang^{1*} and Chunxiao Lv^{1*}

¹Department of Clinical Pharmacology, Second Affiliated Hospital of Tianjin University of Traditional Chinese Medicine, Tianjin, China, ²Department of Cardiology, Qingdao Hise Hospital Affiliated of Qingdao University (Qingdao Traditional Chinese Medicine Hospital), Qingdao, China, ³Department of Cardiology, Second Affiliated Hospital of Tianjin University of Traditional Chinese Medicine, Tianjin, China

Introduction: In clinical practice, warfarin is often combined with Compound Danshen dripping pill (CDDP) for the treatment of cardiovascular diseases. However, warfarin has a narrow therapeutic index, wide interindividual variability (genetic and non-genetic factors), and is susceptible to drug-drug interactions. Our previous study indicated that CDDP might interact with warfarin in individuals with the epoxide hydrolase gene (EPHX1; single-nucleotide polymorphism: rs2292566) A/A subtype. We sought to clarify the interaction between CDDP and warfarin associated with EPHX1 in a comprehensive and accurate manner.

Methods: Here, EPHX1 A and EPHX1 G cell lines were established. Expression of microsomal epoxide hydrolase (mEH), vitamin K epoxide reductase (VKOR), and vitamin K-dependent clotting factors (FII, FVII, FIX, FX) was measured by western blotting upon incubation with CDDP and warfarin. mEH activity was evaluated by measuring the transformation of epoxyeicosatrienoic acids into dihydroxyeicosatrienoic acids. Then, healthy volunteers (HVs) with the EPHX1 A/A genotype were recruited and administered warfarin and CDDP to investigate the pharmacokinetics and pharmacodynamics of warfarin.

Results: CDDP combined with warfarin could decrease expression of mEH and VKOR, and increase protein expression of FII, FVII, FIX, and FX, in EPHX1 A cells. CDDP could slightly influence the pharmacokinetics/pharmacodynamics of warfarin in HVs with the EPHX1 A/A genotype.

Discussion: Rational combination of CDDP and warfarin was safe with no risk of bleeding, but the therapeutic management is also needed. The clinical study is posted in the China Clinical Trial Registry (ChiCTR190002434).

KEYWORDS

warfarin, compound Danshen dripping pill, epoxide hydrolase gene (EPHX1), microsomal epoxide hydrolase (mEH), pharmacokinetic, pharmacodynamics

1 Introduction

Use of herbs and herbal products is widespread and increasing steadily worldwide (Reddy et al., 2021). Sales of herbal supplements in the USA were more than \$8 billion in 2017 and \$9.6 billion in 2019 (Suroowan et al., 2021). In 2020, the world trade in medicinal plants was \$138.35 billion and is expected to reach \$218.94 billion by 2026 (Cnudde et al., 2022; Hossain et al., 2022). Furthermore, an estimated one-third of adults in developed countries and approximately 75%–80% of the population in developing countries consume herbal medicines for primary healthcare (Claire-Del Granado and Espinosa-Cuevas, 2021).

However, the increasing use of medicinal plants has attracted growing concern with regard to their efficacy and safety if combined with conventional medicines. Herbal plants contain multiple phytochemicals that act upon different targets and pathways. Hence, there is a risk of interactions if another drug is administered simultaneously or successively (Gomes et al., 2021). Therefore, comprehensive evaluation of interactions between herbal drugs and conventional drugs is essential.

Warfarin has a narrow therapeutic index, wide variability in efficacy between individuals, and can interact with other drugs (Mar et al., 2022). It acts by inhibiting vitamin K epoxide reductase (VKOR) and disruption of the synthesis of biologically active forms of vitamin K-dependent (VKD) clotting factors (FII, FVII, FIX, FX), as well as regulatory factors (protein C, protein S) (Wang et al., 2021; Abdelnabi et al., 2022). Thus, warfarin is employed commonly for the prevention and treatment of the coagulopathic and thromboembolic disorders associated with cardiac valve-replacement, atrial fibrillation, and other cardiovascular conditions (Zhang et al., 2021).

In China, the most prevalent herbal medicine used against cardiovascular diseases is Compound Danshen dripping pill (CDDP). It was first launched by the China Food and Drug Administration in 1995, and has been approved by the Australian Therapeutic Goods Administration. It is undergoing a phase-III clinical trial overseen by the US Food and Drug Administration (Yan et al., 2021; Hu et al., 2022).

In clinical practice, warfarin often combines with CDDP, and many scholars have reported on this interaction (Chu et al., 2011; Zhang et al., 2020; Zhuang et al., 2021; Muyambo et al., 2022). However, most reports have focused on animals, healthy volunteers (HVs), or pharmacometrics models to predict this interaction. Moreover, whether CDDP interacts with warfarin has been reported inconsistently.

Recently, we recruited patients with coronary heart diseases and atrial fibrillation to investigate the interaction between CDDP and warfarin (Lv et al., 2017; Lv et al., 2019). CDDP did not influence the stable dose, stable concentration, or International Normalized Ratio (INR) of warfarin in most patients. However, the INR seemed to be higher in patients with the epoxide hydrolase gene (EPHX1; single nucleotide polymorphism (SNP): rs2292566) A/A subtype than in those with other EPHX1 subtypes. There were 33 SNPs identified in the EPHX1 gene and mainly two variant EPHX1 alleles (A, G) (Saito et al., 2001). The people carrying the A allele was 30% for Caucasian and nearly 50% for Chinese. Interestingly, previous reports indicated EPHX1 polymorphisms were not related with warfarin dosage in Caucasian (Ciccacci et al., 2011; Özer et al., 2013). However,

EPHX1 A>G could explain about 43% of the interindividual variability in warfarin dosage requirements for Chinese (Gu et al., 2010). EPHX1 is the encoding gene of microsomal epoxide hydrolase (mEH), a crucial enzyme that catalyzes epoxides reactions (Lin et al., 2020). The potential associations between mEH genotypes and the susceptibility to certain diseases have been investigated in various laboratories (Saito et al., 2001). Moreover, mEH is an important component of VKOR, and EPHX1 variants may alter mEH activity, thereby influencing the efficacy of warfarin therapy (Cain et al., 1998). On the other hand, CDDP contained multiple phytochemicals, which mostly included phenolic acids, saponins and tanshinones (Liu et al., 2014). These multiple ingredients would undergo complex metabolic processes in the body, which might effect the mEH activity and furtherly influence the coagulation function of warfarin *in vivo*.

Thus, we wished to clarify the interaction between CDDP and warfarin associated with EPHX1 in a comprehensive and accurate manner. Hence, transfected EPHX1 A cells and transfected EPHX1 G cells were adopted to explore the interaction between CDDP and warfarin, and the result was verified using HVs with the EPHX1 A/A genotype.

2 Materials and methods

2.1 Evaluation of the interaction between CDDP and warfarin associated with EPHX1 A cells and EPHX1 G cells

2.1.1 Preparation of EPHX1 A cells and EPHX1 G cells

Human hepatocarcinoma (HepG2) cells were purchased from the Chinese Academy of Medical Sciences & Peking Union Medical College (Beijing, China). They were cultured in Dulbecco's modified Eagle's medium supplemented with 10% fetal bovine serum and 1% penicillin/streptomycin in an atmosphere of 5% CO₂ at 37°C. EPHX1 A cells or EPHX1 G cells were prepared as shown in Figure 1A. Briefly, HepG2 cells were transduced with overexpressed EPHX1 A lentiviral particles or EPHX1 G lentiviral particles, which were incorporated within an antibiotic puromycin gene and a green fluorescent protein plasmid that could co-express with the target protein, at a multiplicity of infection of 10. For comparison, we set a negative control group (BL) of transfected cells that lacked an overexpressed EPHX1 gene.

Transfected cells were cultured in medium containing puromycin (2 µg/mL) to select stably transfected cells. Subsequently, a microscope (IX71; Olympus, Tokyo, Japan) equipped with a bandpass filter of 488 nm was used to capture images of intracellular green fluorescence. Then, we used a flow cytometer (Accuri C6; Becton Dickinson Biosciences, San Jose, CA, United States) to measure the proportion of intracellular green fluorescence from the green fluorescent protein that integrated with transfected cells. Finally, western blotting was applied to measure mEH expression in transfected cells.

2.1.2 Determination of the incubation time and concentration of CDDP and warfarin in cell lines

CDDP was manufactured by Tianjin Tasly Group (Tianjin, China). Warfarin was obtained from Orion Corporation (Espoo,

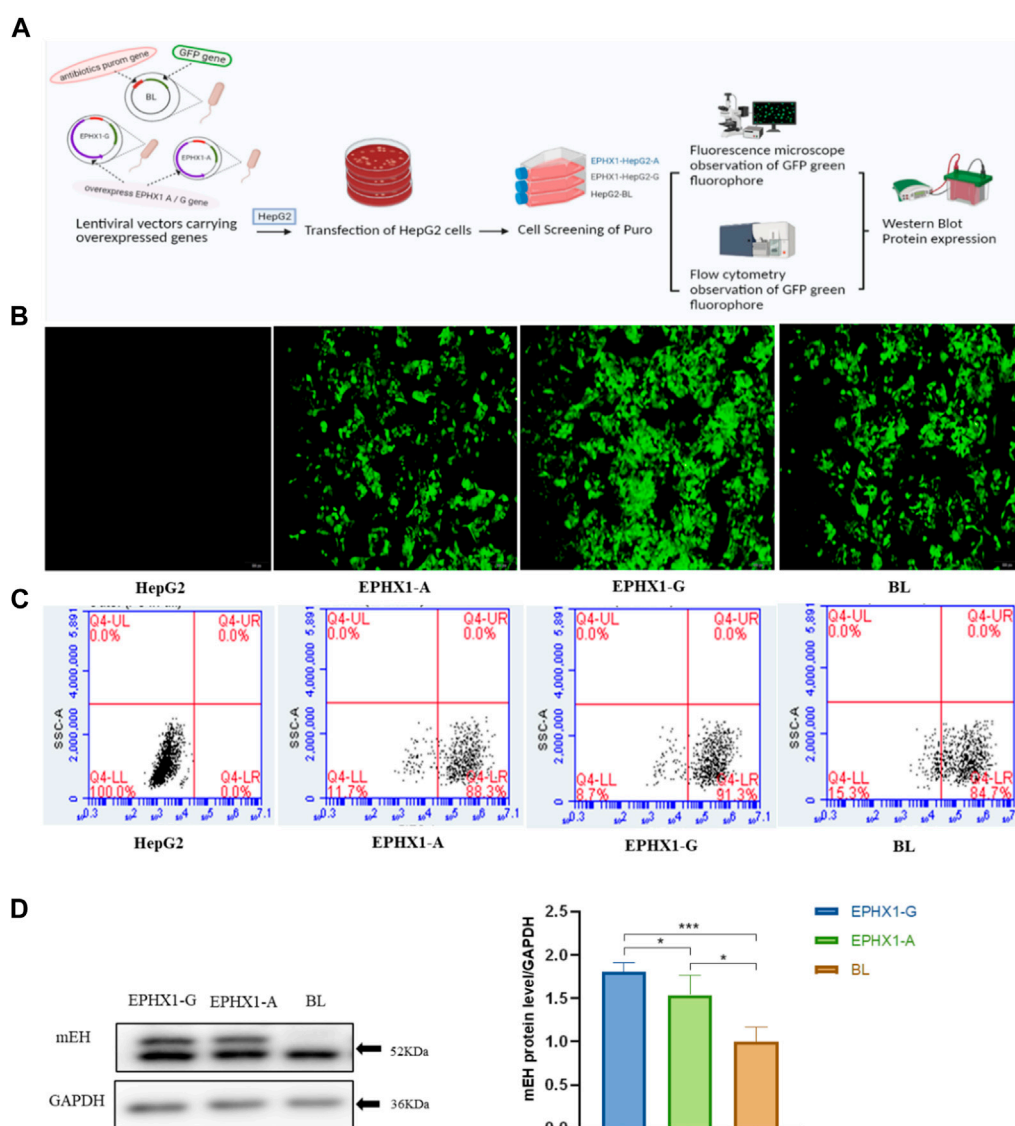


FIGURE 1

Establishment and verification of transfected EPHX1 A cells and transfected EPHX1 G cells. (A) Flowchart for establishment and verification of transfected EPHX1 A cells and transfected EPHX1 G cells. (B) We used a fluorescence microscope (x10 objective lens) to evaluate transfected EPHX1 A cells, transfected EPHX1 G cells, and transfected BL cells. Transfected EPHX1 A cells, transfected EPHX1 G cells, and transfected BL cells had abundant light-green spots, and HepG2 cells had no fluorescence. (C) Fluorescence ratio for transfected EPHX1 A cells, transfected EPHX1 G cells, and transfected BL cells according to flow cytometry. (D) Protein expression of mEH in transfected EPHX1 A cells, transfected EPHX1 G cells, and transfected BL cells detected by western blotting.

Finland). Transfected cells were plated evenly on a 96-well cell-culture plate with ~8,000 cells/well. They were cultured for 24 h at 37°C. Then, they were treated with CDDP or warfarin at 0.0625–8.00 mg/mL for 24 h or 72 h. Subsequently, to each well was added 10 µL of 3-(4,5-Dimethylthiazol-2-yl)-2,5-diphenyltetrazolium bromide solution (5 mg/mL), and cells were allowed to incubate for an additional 4 h in an atmosphere of 5% CO₂ at 37°C. Then, the cells were centrifuged and the supernatant was retained. Finally, the blue-purple crystals were dissolved using dimethyl sulfoxide (150 µL) with agitation for 10 min. The absorbance of each well was determined at 490 nm. Cell viability (Supplementary Figure S1) was calculated according to the formula:

$$\text{Cell viability} = \frac{\text{absorbance}_{\text{experiment}}}{\text{absorbance}_{\text{control}}} \times 100\%$$

2.1.3 Determination of expression of VKD coagulation factors

We wished to measure expression of mEH, VKOR, FII, FVII, FIX, and FX. Whole-cell extracts were prepared using radio immunoprecipitation assay buffer (Solarbio, Beijing, China) incubated on ice for 30 min. Cell lysates were centrifuged (13,000 rpm, 25 min, 4°C). The protein concentration of the supernatant was determined by a bicinchoninic acid protein assay kit (CWBIO, Beijing, China). Lysates (10 µg) were subjected to sodium dodecyl sulfate-polyacrylamide gel electrophoresis

using 10% gels. Proteins were transferred to polyvinylidene fluoride (PVDF) membranes (Thermo Fisher Scientific, Waltham, MA, United States). PVDF membranes were blocked with 10% non-fat dried milk at room temperature (Solarbio) for 1.5 h and incubated overnight at 4°C with antibody directed against mEH (1:1000 dilution; Santa Cruz Biotechnology, Houston, TX, United States), VKOR, FII, and FIX (1:1000; Abcam, Cambridge, United Kingdom), FVII (1:8,000; Abcam), FX (1:10,000; Abcam), and glyceraldehyde 3-phosphate dehydrogenase (GAPDH; 1:10,000; Solarbio) in TBS-T buffer (Tris (20 mM), pH 7.6, NaCl (100 mM), 0.1% Tween-20) for immunoblotting. After incubation for 2 h at room temperature with secondary anti-rabbit immunoglobulin-G antibody conjugated with horseradish peroxidase (1:5000; Solarbio), proteins were visualized by an electrochemiluminescence detection system. Western-blotting signals were quantified using ImageJ 1.6.0.20 (US National Institutes of Health, Bethesda, MD, United States) and were normalized to GAPDH expression.

2.1.4 Enzyme activity of mEH

mEH catalyzes the hydrolysis of lipophilic epoxides to their corresponding dihydrodiols (Oesch et al., 1971; Gautheron and Jeru, 2021). Free epoxyeicosatrienoic acids (EETs) are epoxides that can be degraded further by mEH into dihydroxyeicosatrienoic acids (DHETs) (McReynolds et al., 2020) (Figure 3E). Thus, the metabolic efficiency of the substrate (DHETs/EETs) (Arand et al., 1999) was determined to characterize the catalytic activity of mEH on the endogenous substrates of 14,15-EET. Valpromide was selected as an inhibitor of mEH.

The concentration of 14,15-EET and 14,15-DHET was measured by liquid chromatography tandem-mass spectrometry (LC-MS/MS). The separation and detection of 14,15-EET (319.2→219.2) and 14,15-DHET (337.2→207.0) was undertaken in an Acquity ultra-performance liquid chromatography (UPLC) system (Waters, Milford, MA, United States) with a Triple Quad 5500 MS/MS detector (AB Sciex, Foster City, CA, United States). Detailed information and method validation are shown in [Supplementary Materials](#).

Transfected EPHX1 A cells, transfected EPHX1 G cells, and transfected BL cells were seeded 1 day before treatment with a substrate or inhibitor. Then, the cell-culture medium was replaced with complete medium containing CDDP (0.5 mg/mL) and warfarin (0.125 mg/mL) (CDDP + War group), or warfarin (0.125 mg/mL) (War group), or valpromide (100 mg/mL) (valpromide group, VPD). After incubation with 14,15-EET, 60 µL of the cell culture medium was harvested at 0, 0.25, 0.5, 1, 1.5, 2, and 3 h after addition of 14,15-EET. Subsequently, to the harvested cell-culture medium was added 3 µL of chloramphenicol (internal standard) and extracted with ethyl acetate (180 µL) with vortex-mixing for 3 min and centrifugation (14,000 rpm, 10 min, room temperature). The supernatant was evaporated under a stream of nitrogen and re-dissolved by 50% methanol/water (60.0 µL), then 2.00 µL was injected into the LC-MS/MS system.

2.2 Evaluation of the interaction between CDDP and warfarin associated with the EPHX1 A/A genotype in HVs

2.2.1 Design of the clinical trial

This was an open-label, three-period, controlled before-and-after trial (China Clinical Trial Registry: ChiCTR1900024344). It

was conducted at the Second Affiliated Hospital within Tianjin University of Traditional Chinese Medicine (Tianjin, China). The protocol was approved by the ethics committees of the Second Affiliated Hospital within Tianjin University of Traditional Chinese Medicine. Written informed consent was provided by all participants. This trial was in accordance with the Declaration of Helsinki 1964 and its later amendments.

Men and women aged 18–45 years participated in this trial if they were healthy and the EPHX1 A/A genotype was confirmed. The key exclusion criteria were coagulation disorders or allergies to drugs.

2.2.2 Treatment in the clinical trial

Our trial comprised three periods. In the first period, warfarin (3 mg, p. o.) was taken once a day. After 3 days, individuals entered the second period, in which CDDP (10 pills, p. o., t.d.s.) was administered for 5 days. Finally, participants were treated with a combination of warfarin (3 mg, p. o.) and CDDP (10 pills, p. o.) in the third period.

During the first and third period, 15 blood samples (2-mL each time) were collected for the concentration analysis of warfarin at 0.5, 1, 1.5, 2, 3, 4, 6, 8, 12, 24, 36, 48, and 72 h after administration. Eight blood samples were collected for the detection of coagulation indices before as well as 12, 24, 30, 36, 48, 54, and 72 h after administration. Moreover, blood samples were taken from participants once a day before CDDP administration for assays of coagulation indices to ensure safety.

2.2.3 Markers of the pharmacokinetics and pharmacodynamics of warfarin

The plasma concentration of S-warfarin and R-warfarin was measured by LC-MS/MS, as described previously (Lv et al., 2017; Lv et al., 2019). The pharmacokinetic parameters of warfarin were calculated using the “non-compartmental analysis” tool of Phoenix WinNonlin 6.4 (Certara, Princeton, NJ, United States). The parameters were the peak plasma concentration (C_{max}), time to reach C_{max} (t_{max}), the area under the curve from time 0 h–144 h (AUC_{0-144}), the area under the curve from time 0 to infinity ($AUC_{0-\infty}$), half-life ($t_{1/2}$), volume of distribution (V_d), and clearance (CL).

In addition, the coagulation indices of prothrombin time (PT), INR, thrombin time (TT), activated prothrombin time (APTT), and fibrinogen level were detected according to the manufacturer instructions of assay kits in the clinical laboratory of the Second Affiliated Hospital within Tianjin University of Traditional Chinese Medicine.

2.2.4 Enzyme-linked immunosorbent assays (ELISAs) to determine the content of VKD coagulation factors in HVs with the EPHX1 A/A genotype

Blood samples of the trough concentration and peak concentration of warfarin were used to measure the content of mEH, VKOR, FII, FVII, FIX, FX, and FIIa using the respective human ELISA kits. mEH and VKOR kits were from Lanso (Shanghai, China). FII and FX kits were from Cusabio (Wuhan, China). FVII and FIX kits were from Ruifan (Shanghai, China). The FIIa kit was from Abcam. FIIa is also called thrombin and not exist *in vitro*.

2.3 Statistical analyses

Statistical analyses were carried out using SPSS 22.0 (IBM, Armonk, NY, United States). Graphs were plotted using Prism 8.0 (GraphPad, La Jolla, CA, United States). ANOVA was used to compare the results of transfected EPHX1 A cells or transfected EPHX1 G cells by western blotting. For HVs with the EPHX1 A/A genotype, *p*-values (two-sided) were calculated and paired *t*-tests were used for statistical analyses if the data passed the normality (Shapiro–Wilk) test, or the Wilcoxon matched-pairs test if the distribution was not normal. Results are the mean \pm SD for continuous variables with a normal distribution. *p* < 0.05 was considered significant.

3 Results

3.1 Evaluation of the interaction between CDDP and warfarin associated with EPHX1 A cells and EPHX1 G cells

3.1.1 Establishment and validation of transfected EPHX1 A cells and transfected EPHX1 G cells

Transfected EPHX1 A cells and transfected EPHX1 G cells were established to explore differences between EPHX1 A and EPHX1 G subtypes *in vitro* (Figure 1A). Subsequently, the green fluorescence located in transfected EPHX1 A cells, transfected EPHX1 G cells, and transfected BL cells was observed by fluorescence microscopy, and non-transfected HepG2 cells showed no fluorescence (Figure 1B). The efficiency of transfection was examined by flow cytometry: it was 88.3% in transfected EPHX1 A cells, 91.3% in transfected EPHX1 G cells, and 84.7% in BL cells (Figure 1C). Western blotting demonstrated that mEH expression in transfected EPHX1 A cells and transfected EPHX1 G cells was increased compared with that in transfected BL cells (*p* < 0.05) (Figure 1D). These results suggested that transfected EPHX1 A cells and transfected EPHX1 G cells had been constructed successfully.

3.1.2 CDDP combined with warfarin influenced expression of mEH, VKOR, and VKD clotting factors (FII, FVII, FIX, FX) in transfected EPHX1 A cells

For the control group, mEH expression (Figures 2A, B) in transfected EPHX1 A cells was reduced significantly, protein expression of FII, FVII, FIX, and FX (Figures 2A, D–G) was increased, and VKOR expression was not significantly different, compared with transfected EPHX1 G cells. These data suggested that expression of mEH, FII, FVII, FIX, and FX in transfected EPHX1 A cells and transfected EPHX1 G cells was significantly different.

Protein expression of mEH and VKOR (Figures 2A–C) was decreased in the CDDP + War group (*p* < 0.05) compared with that in the War group in transfected EPHX1 A cells. Protein expression of FII, FVII, FIX, and FX (Figures 2A, D–G) in the CDDP + War group was increased significantly compared with that in the War group (*p* < 0.05) in transfected EPHX1 A cells, and there was no significant difference between the two groups for transfected EPHX1 G cells and transfected BL cells (*p* > 0.05). Thus, various concentrations of CDDP (0.125, 0.5, 1 mg/mL) combined with

warfarin (0.125 mg/mL) were incubated in transfected EPHX1 A cells to assess the interaction with CDDP. Expression of mEH and FIX was significantly different (*p* < 0.05), whereas the other indicators did not show a significant difference between the three concentrations of CDDP (Figures 2H, I). Expression of all the indicators did not change continually as the CDDP dose increased.

3.1.3 CDDP combined with warfarin influenced the hydrolytic activity of mEH

CDDP combined with warfarin might affect mEH expression in transfected EPHX1 A cells, but not in transfected EPHX1 G cells or transfected BL cells. We wished to ascertain if a combination of CDDP and warfarin affected the enzyme activity of mEH. Thus, the substrate of mEH (14,15-EET) was chosen and metabolic efficiency was calculated. The curves for the metabolic efficiency of 14,15-EET in transfected EPHX1 A cells and transfected EPHX1 G cells were higher than that for transfected BL cells (*p* < 0.05) (Figure 3A).

The metabolic efficiency of 14,15-EET at all time points in the CDDP + War group was lower than that represented in the War group for transfected EPHX1 A cells or transfected EPHX1 G cells, and the difference was significant at 1 h (*p* < 0.05) (Figures 3B, C, D). When comparing with VPD group at 1 h, CDDP + War group in transfected EPHX1 A cells and G cells were both significantly decreased (*p* < 0.05) (Figures 3C, D). These findings suggested that mEH was the primary enzyme involved in the metabolism of 14,15-EET in transfected EPHX1 A cells and transfected EPHX1 G cells, and that CDDP combined with warfarin might inhibit the enzyme activity of mEH to decrease the hydrolysis of the substrate (14,15-EET), but there was no significant difference between transfected EPHX1 A cells and transfected EPHX1 G cells.

3.2 Evaluation of the interaction between CDDP and warfarin associated with the EPHX1 A/A genotype in HVs

3.2.1 Study population

From March 2019 to September 2019, 15 HVs with the EPHX1 A/A genotype were selected from the Second Affiliated Hospital within Tianjin University of Traditional Chinese Medicine. Eight HVs were enrolled and seven [four males; mean age = 29.25 (range, 22–34) years] completed our clinical trial (Figure 4).

3.2.2 CDDP combined with warfarin influenced the pharmacokinetic profile of warfarin in HVs with the EPHX1 A/A genotype

A concentration–time curve was plotted (Figure 5A). The plasma concentration (ng/mL) of warfarin 72 h after administration in the first period and third period was determined, and was 100.6 ± 28.50 and 124.1 ± 29.64 for warfarin, 71.94 ± 19.92 and 88.73 ± 21.10 for R-warfarin, and 28.65 ± 9.578 and 35.32 ± 10.50 for S-warfarin, respectively. The plasma concentration (ng/mL) 144 h after administration in the first period and third period was 47.93 ± 14.07 and 60.97 ± 22.67 for warfarin, 35.61 ± 11.23 and 45.84 ± 17.89 for R-warfarin, and 12.33 ± 3.713 and 15.12 ± 6.294 for S-warfarin, respectively. Hence, the warfarin concentration 72 h and 144 h after administration was higher in the third period than that in the first period (Supplementary Table S3, Figure 5A).

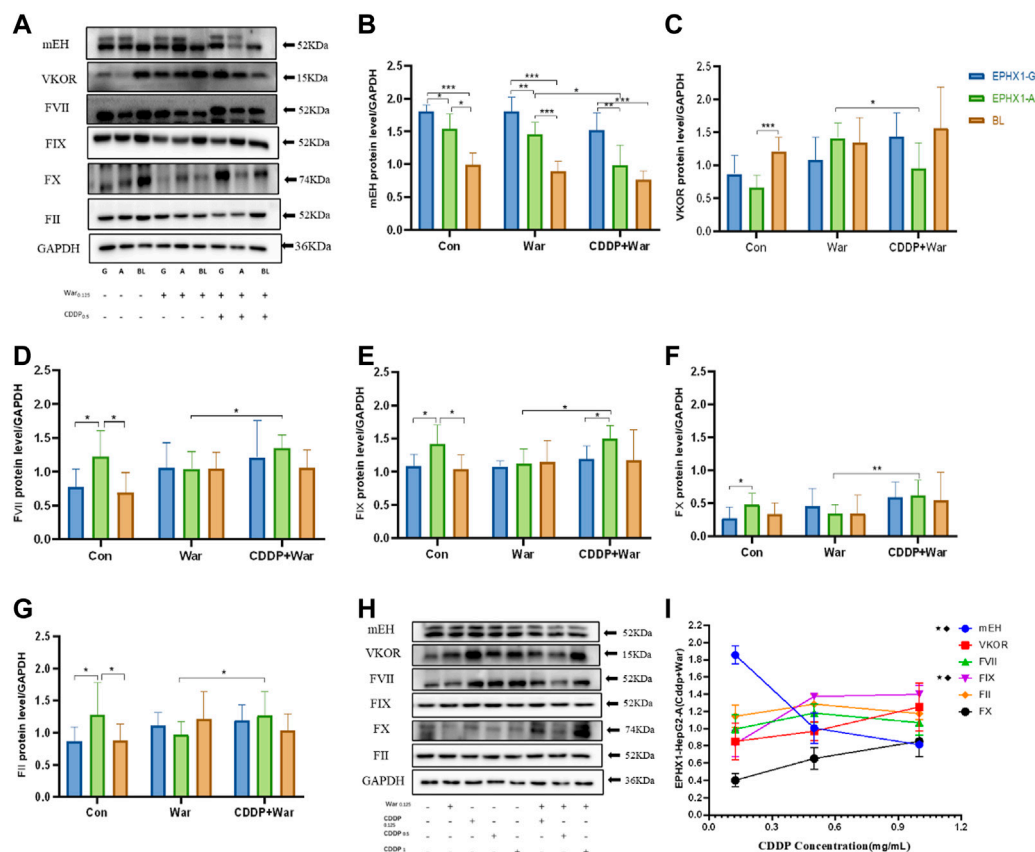


FIGURE 2

Protein expression of mEH, VKOR, FVII, FIX, FX, and FII. (A) Protein expression of mEH, VKOR, FVII, FIX, FX, and FII was measured using western blotting. (B–G) Protein expression of mEH, VKOR, FVII, FIX, FX, and FII normalized to that of GAPDH. (H) Protein expression of mEH, VKOR, FII, FIX, FX, and FII at various concentrations of CDDP combined with warfarin. (I) Line chart of protein expression of mEH, VKOR, FVII, FIX, FX, and FII normalized to that of GAPDH at various concentrations of CDDP combined with warfarin. ★Significant difference when comparing the CDDP (0.125 mg/mL) group with the CDDP (0.5 mg/mL) group ($p < 0.05$); ♦Significant difference when comparing the CDDP (0.5 mg/mL) group with the CDDP (1 mg/mL) group ($p < 0.05$). Data are the mean \pm SD ($n \geq 3$). * $p < 0.05$, ** $p < 0.01$ and *** $p < 0.001$. EPHX1-A: transfected EPHX1 A cells; EPHX1 (G) transfected EPHX1 G cells; BL: transfected BL cells; Con: incubated with cell culture; War: incubated with warfarin; CDDP + War: incubated with CDDP and warfarin.

The pharmacokinetic parameters of warfarin were calculated using Phoenix WinNonlin. There was a significant difference ($p < 0.05$) in the AUC, C_{max} , CL, and V_d between the first period and third period, whereas $t_{1/2}$ and T_{max} did not show a significant difference (Table 1). However, drug elution in HVs was incomplete in the second period. The residual drug concentration was converted into a dose, and pharmacokinetic parameters were re-calculated (Supplementary Table S4): there was no significant difference in V_d or CL between the two periods. Thus, CDDP might influence the AUC and C_{max} of warfarin in HVs with the EPHX1 A/A genotype, but would not influence warfarin elimination.

3.2.3 CDDP combined with warfarin influenced coagulation indices in HVs with the EPHX1 A/A genotype

PT, INR, and TT were clearly increased at 36 and 72 h in the third period when compared with those in the first period, and the differences were significant (Figure 5B). There were significant differences in PT and the INR at 48 h, TT at 48 h, and the

fibrinogen level 72 h after administration between the two periods. A significant difference was not observed in APTT at the various time points, or PT, the INR, TT, or fibrinogen level at 0, 12, 30, and 54 h between the two periods.

3.2.4 CDDP combined with warfarin influenced the content of VKDs coagulation factors in HVs with the EPHX1 A/A genotype

The content of mEH, VKOR, FVII, FIX, FX, and FIIa in HVs with the EPHX1 A/A genotype was measured. Samples were chosen from the trough concentration (C_{min}) and peak concentration (C_{max}) time points of warfarin as measured by ELISAs.

The content of all indices did not show a significant difference between C_{min} and C_{max} in the War group or CDDP + War group (Figure 6). Thus, C_{min} and C_{max} were combined to obtain a “Sum” group. In the latter, the content of mEH, VKOR, and FIIa was decreased significantly, and the content of FVII, FIX, FX, and FII was increased significantly, in the third period compared with those in the first period ($p < 0.05$). These results suggested that CDDP combined with warfarin might affect the content of mEH,

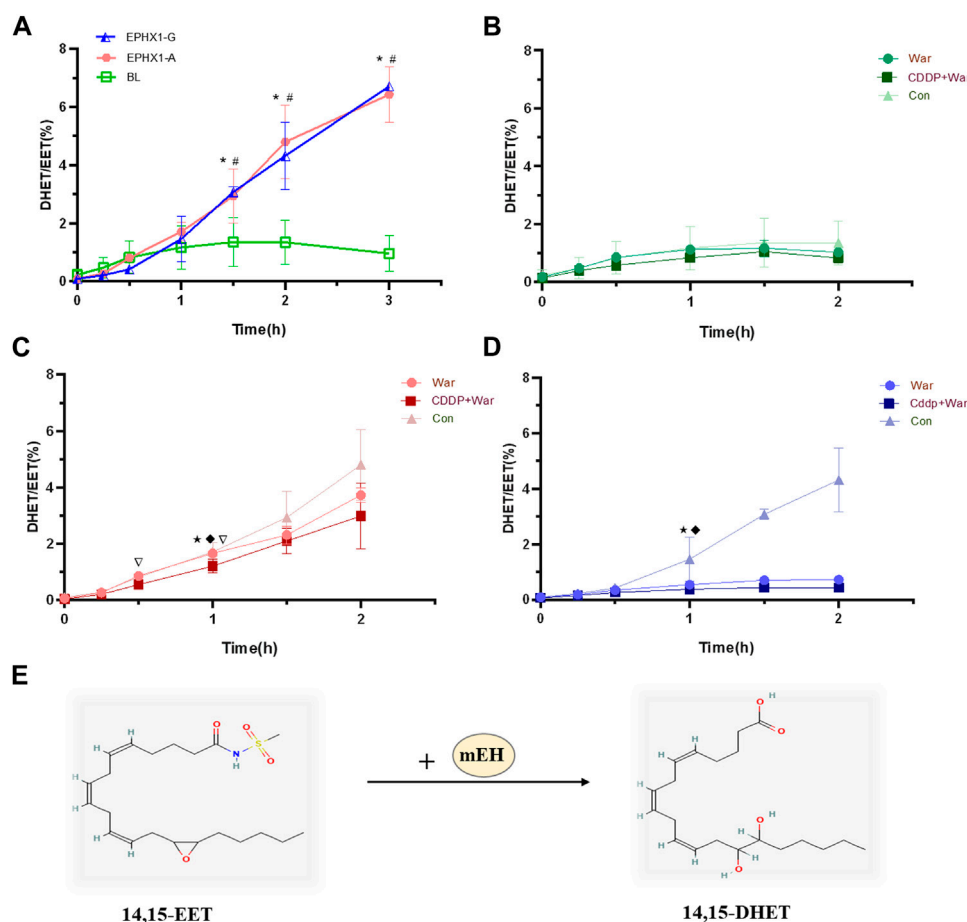


FIGURE 3

Metabolic efficiency curve of 14,15-EET in transfected EPHX1 A cells, transfected EPHX1 G cells, and transfected BL cells. (A) Comparison of the metabolic efficiency of 14,15-EET in transfected EPHX1 A cells, transfected EPHX1 G cells, and transfected BL cells without drug administration. Effect of warfarin, valproic acid, and CDDP in combination with warfarin on the metabolic efficiency of 14,15-EET in transfected BL cells (B), transfected EPHX1 A cells (C) and transfected EPHX1 G cells (D). (E) mEH metabolizes EET to DHET. Data are the mean \pm SD ($n \geq 3$). *Significant difference when comparing transfected EPHX1 A cells to transfected BL cells ($p < 0.05$). #Significant difference when comparing transfected EPHX1 G cells to transfected BL cells ($p < 0.05$). *Significant difference when comparing the CDDP + War group with the VPD group ($p < 0.05$); ♦Significant difference when comparing the War group with the VPD group ($p < 0.05$). ▽Significant difference when comparing the CDDP + War group with the War group ($p < 0.05$).

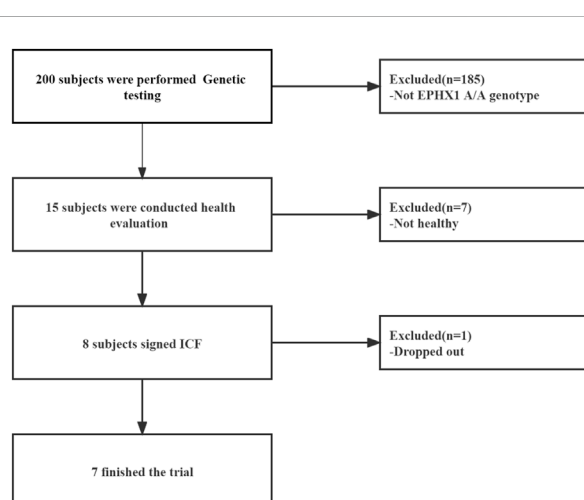


FIGURE 4

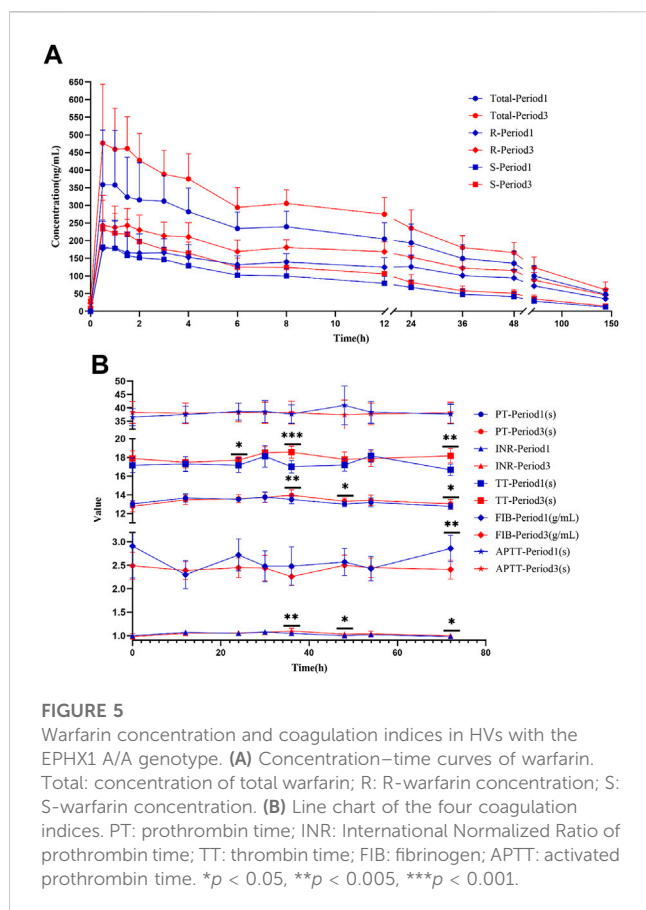
Flowchart of our clinical study.

VKOR, FVII, FIX, FX, FII, and FIIa in HVs with the EPHX1 A/A genotype compared with those taking only warfarin.

4 Discussion

In recent years, formulations based on traditional Chinese medicine (TCM) have been used widely in clinical therapy and are, in general, considered safe (Shi et al., 2022). However, an increased risk of interactions between TCM formulations and western medicines has been documented.

Warfarin and CDDP are often used in combination for treatment of cardiovascular diseases (Chu et al., 2011). Previously, we focused on the EPHX1 A/A subtype (Lv et al., 2017; Lv et al., 2019). In the present study, overexpressing EPHX1 cells were established and applied to evaluate the interaction between CDDP and warfarin. Then, *in vitro* results were verified in HVs with the EPHX1 A/A genotype.



mEH was first purified from rabbit liver (Watabe and Kanehira, 1970) and then characterized in human liver (Oesch, 1974). mEH plays a prominent part in human hepatic physiology because of its enzyme activity (Gautheron and Jeru, 2021). In hepatocytes, the primary function of mEH is detoxifying many xenobiotic compounds (El-Sherbeni and El-Kadi, 2014). It catalyzes the hydrolysis of various endogenous fatty-acid epoxides to their respective diols (Edin and Zeldin, 2021), including the metabolism of endocannabinoid EETs to DHETs. Moreover, mEH is an essential component in VKOR, which suggests that modulation of mEH activity might contribute to blood coagulation and further influence VKD coagulation factors (Guenther et al., 1998). On the other hand, the multiple ingredients from CDDP would finally eliminate from the body. The mEH acted as a detoxification role and could convert compounds with epoxides into a more water-soluble metabolites which would eliminate easier. During these metabolic pathways, some ingredients or metabolites from CDDP would influence the expression or activity of mEH, and finally leading to a content fluctuation of coagulation factors.

In humans, the EPHX1 (SNP: rs2292566) gene includes A/A, A/G, and A/A subtypes. A genetic polymorphism is a potential determinant of mEH activity, and contributes to differences among individuals (Nguyen et al., 2013). The different genes of EPHX1 (A/G) led to a significant difference in expression of mEH, FII, FVII, FIX, and FX (Figure 2), which might influence biological functions. Moreover, the warfarin dose is assumed to be associated with SNP rs2292566 in the EPHX1 gene, so the warfarin dose must be

managed carefully before the initiation of warfarin therapy (Pautas et al., 2010).

CDDP combined with warfarin in EPHX1 A cells could reduce expression of mEH and VKOR, inhibit the enzyme activity of mEH (Figure 3), increase protein expression of FII, FVII, FIX, and FX (Figure 2), reduce activation of FII (FIIa), and lead to lower activity of coagulation factors in HVs with the EPHX1 A/A genotype (Figure 6). However, a significant difference was not observed in EPHX1 G cells. Therefore, CDDP worked in tandem with warfarin in HVs with the EPHX1 A/A genotype to restrain the catalytic activity of mEH and VKOR (Hassett et al., 1994; Shen et al., 2017) that is required to sustain blood coagulation. Thus, we speculated that a combination of CDDP and warfarin might prolong PT and elevate the INR in HVs with the EPHX1 A/A genotype.

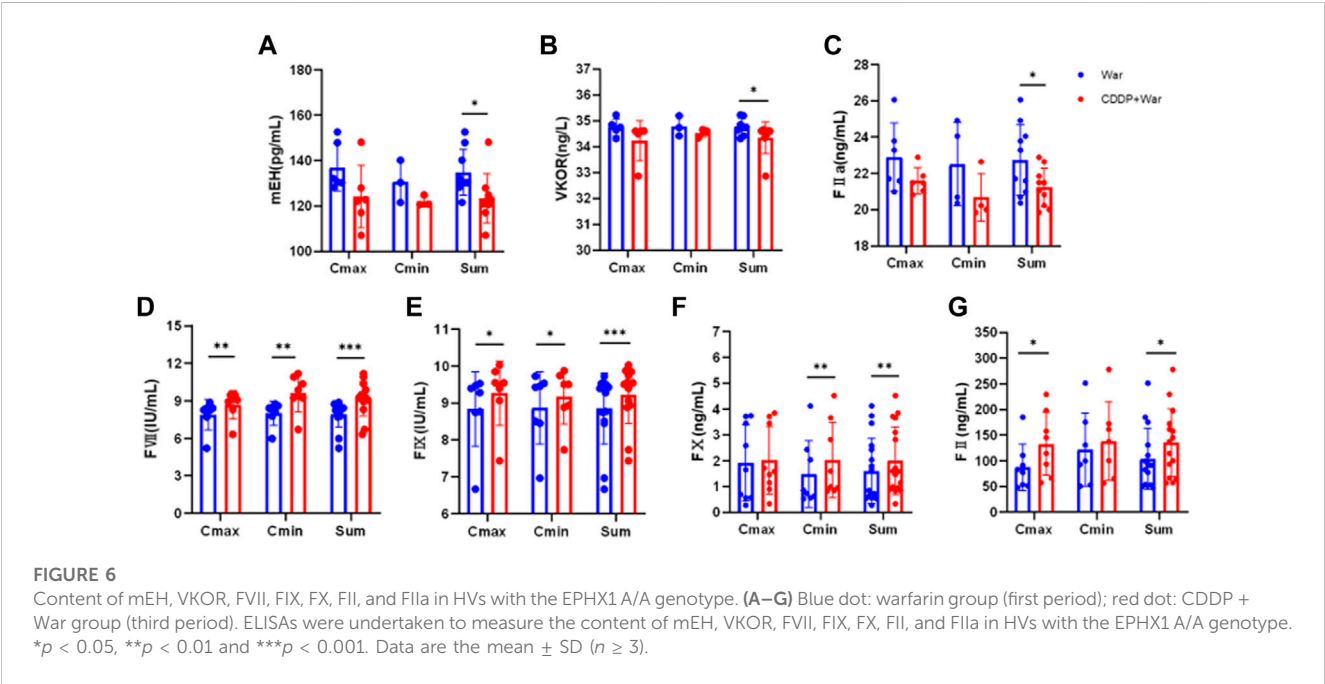
Warfarin combined with CDDP impacted the blood concentrations and pharmacokinetic parameters of warfarin in HVs with the EPHX1 A/A genotype, which were increased by ~30%. The trough concentration of warfarin in the third period (Supplementary Table S3) suggested that drug elution was incomplete from the first period. Then, residual drugs were converted to a dose of drug administered, and pharmacokinetic parameters were recalculated. Ultimately, there was no significant difference in V_d and CL between the two periods after this adjustment (Supplementary Table S4).

The INR is used routinely to monitor the level of anticoagulation elicited by warfarin (Al Ammari et al., 2020). According to certain clinical trials as well as criteria set by the Division of Microbiology and Infectious Diseases within the American National Institute of Allergy and Infectious Diseases, a 1.01–1.25-fold increase in the upper limit of normal in coagulation indices is considered to denote a “mild” difference (Kovacevic et al., 2019; Akdag et al., 2020). In our study, the increase in PT, the INR, and fibrinogen level was <10% after a combination of CDDP and warfarin, and all INR values were within 0.91–1.18 (a normal value for a healthy person is 0.8–1.2). Thus, CDDP combined with warfarin had a very low impact on the INR and did not show a bleeding risk in HVs with the EPHX1 A/A genotype. Conversely, expression of mEH, VKOR, FII, FVII, FIX, and FX plateaued gradually with increasing concentrations of CDDP (Figure 2I), indicating that VKD clotting factors (FII, FVII, FIX, FX) would not be inhibited infinitely with increasing concentrations of CDDP. Thus, the dose safety of CDDP was shown to be in a combination of CDDP and warfarin. Collectively, these observations suggest that the interactions might occur if warfarin is co-administered with CDDP in HVs with the EPHX1 A/A genotype, but the effect on the pharmacokinetics/pharmacodynamics of warfarin is slight with no risk of bleeding.

There are some limitations in this study. The dose and ratio of warfarin and CDDP in cell experiment were not inconsistent with the clinical dose. For the cell experiment, the concentration of warfarin and CDDP were determined by the MTT assay (Supplementary Figure S1) and the survival rate of cells was the major concern. However, the clinical efficacy and safety were the essential issue for the patients in clinical. In this study, the results of cell experiment were further verified by the clinical trial, which indicated that the cell experiment with different dose from the clinical could also provide some guidance for the clinical research. On the other hand, the medication time of the subjects administrated of warfarin and CPPD was relatively short, and the subjects were all healthy person. Thus, although there was no risk of

TABLE 1 Pharmacokinetic parameters of Warfarin in EPHX1 A/A healthy subjects.

Ingredient	PK parameter	The first period	The third period	<i>p</i> -Value
		Mean ± SD (ng/mL)	Mean ± SD (ng/mL)	
Warfarin	<i>t</i> _{1/2} (h)	64.77 ± 7.072	66.42 ± 16.11	0.795
	AUC ₀₋₁₄₄ (ng/h/mL)	17443 ± 4477	21818 ± 4570	0.000***
	AUC _{0-∞} (ng/h/mL)	21984 ± 5883	28081 ± 8220	0.003**
	<i>V</i> _d (mL)	13393 ± 3036	10437 ± 1239	0.016*
	CL (mL/h)	144.9 ± 36.87	114.3 ± 30.01	0.004**
	<i>C</i> _{max} (ng/mL)	403.4 ± 148.2	535.8 ± 112.4	0.001***
	<i>T</i> _{max} (h)	1.857 ± 1.435	0.7143 ± 0.3934	0.094
R-Warfarin	<i>t</i> _{1/2} (h)	68.87 ± 9.371	73.76 ± 23.80	0.583
	AUC ₀₋₁₄₄ (ng/h/mL)	11630 ± 2938	14594 ± 3088	0.000***
	AUC _{0-∞} (ng/h/mL)	15255 ± 4280	19962 ± 6805	0.008*
	<i>V</i> _d (mL)	20505 ± 4506	16283 ± 2164	0.022*
	CL (mL/h)	210.3 ± 57.13	164.8 ± 51.16	0.003**
	<i>C</i> _{max} (ng/mL)	204.6 ± 71.38	273.9 ± 58.10	0.001***
	<i>T</i> _{max} (h)	1.857 ± 1.435	0.7143 ± 0.3934	0.094
S-Warfarin	<i>t</i> _{1/2} (h)	55.84 ± 5.110	54.57 ± 8.595	0.777
	AUC ₀₋₁₄₄ (ng/h/mL)	5812 ± 1632	7223 ± 1727	0.001***
	AUC _{0-∞} (ng/h/mL)	6808 ± 1890	8476 ± 2455	0.004**
	<i>V</i> _d (mL)	37594 ± 9569	28630 ± 3437	0.017*
	CL (mL/h)	466.0 ± 109.7	374.1 ± 82.69	0.009*
	<i>C</i> _{max} (ng/mL)	199.0 ± 76.90	261.9 ± 54.50	0.002**
	<i>T</i> _{max} (h)	1.500 ± 1.414	0.714 ± 0.393	0.199



bleeding for the healthy person, the therapeutic management is also needed if warfarin is combined with CDDP in patients, especially those exposed to risks of over-anticoagulation and bleeding.

5 Conclusion

CDDP combined with warfarin might reduce expression of mEH and VKOR, and increase protein expression of FII, FVII, FIX, and FX, in EPHX1 A cells. In HVs with the EPHX1 A/A genotype, CDDP could influence the pharmacokinetics/pharmacodynamics of warfarin slightly, but the combination is safe with no risk of bleeding, but this is still a warning signal for patients with EPHX1 A/A.

Data availability statement

The original contributions presented in the study are included in the article/[Supplementary Material](#), further inquiries can be directed to the corresponding authors.

Ethics statement

The studies involving human participants were reviewed and approved by the Ethics committees of the Second Affiliated Hospital of Tianjin University of Traditional Chinese medicine. The patients/participants provided their written informed consent to participate in this study.

Author contributions

XC, XZ, and CL wrote manuscript; YZ, YH, and CL designed research; XC and XZ performed research; XC, XZ, YH, and CL analyzed data; YZ and YH contributed new reagents/analytical tools.

References

- Abdelnabi, M., Benjanuwattra, J., Okasha, O., Almaghraby, A., Saleh, Y., and Gerges, F. (2022). Switching from warfarin to direct-acting oral anticoagulants: It is time to move forward. *Egypt Heart J.* 74, 18. doi:10.1186/s43044-022-00259-9
- Akdag, D., Isikgoz-Tasbakan, Y., Pullukcu, H., Sipahi, H., and Sipahi, O. R. (2020). Tigecycline versus INR increase; more than expected? *Expert Opin. Drug Saf.* 19, 335–337. doi:10.1080/14740338.2020.1723546
- Al Ammari, M., AlBalwi, M., Sultana, K., Alabdulkareem, I. B., Almuzzaini, B., Almakhlafi, N. S., et al. (2020). The effect of the VKORC1 promoter variant on warfarin responsiveness in the Saudi Warfarin Pharmacogenetic (SWAP) cohort. *Sci. Rep.* 10, 11613. doi:10.1038/s41598-020-68519-9
- Arand, M., Muller, F., Mecky, A., Hinz, W., Urban, P., Pompon, D., et al. (1999). Catalytic triad of microsomal epoxide hydrolase: Replacement of glu(404) with asp leads to a strongly increased turnover rate. *Biochem. J.* 337, 37–43. doi:10.1042/bj3370037
- Cain, D., Hutson, S. M., and Wallin, R. (1998). Warfarin resistance is associated with a protein component of the vitamin K 2,3-epoxide reductase enzyme complex in rat liver. *Thromb. Haemost.* 80, 128–133. doi:10.1055/s-0037-1615151
- Chu, Y., Zhang, L., Wang, X. Y., Guo, J. H., Guo, Z. X., and Ma, X. H. (2011). The effect of Compound Danshen Dripping Pills, a Chinese herb medicine, on the pharmacokinetics and pharmacodynamics of warfarin in rats. *J. Ethnopharmacol.* 137, 1457–1461. doi:10.1016/j.jep.2011.08.035
- Ciccacci, C., Paolillo, N., Fusco, D. D., Novelli, G., and Borgiani, P. (2011). EPHX1 polymorphisms are not associated with warfarin response in an Italian population. *Clin. Pharmacol. Ther.* 89 (6), 791. doi:10.1038/clpt.2011.31
- Claire-Del Granado, R., and Espinosa-Cuevas, M. (2021). Herbal nephropathy. *Contributions Nephrol.* 199, 143–154. doi:10.1159/000517693
- Cnudde, A., Watrin, P., and Souard, F. (2022). HDI highlighter, the first intelligent tool to screen the literature on herb-drug interactions. *Clin. Pharmacokinet.* 61, 761–788. doi:10.1007/s40262-022-01131-4
- Edin, M. L., and Zeldin, D. C. (2021). Regulation of cardiovascular biology by microsomal epoxide hydrolase. *Tox Res.* 37, 285–292. doi:10.1007/s43188-021-00088-z
- El-Sherbeni, A. A., and El-Kadi, A. O. S. (2014). The role of epoxide hydrolases in health and disease. *Arch. Toxicol.* 88, 2013–2032. doi:10.1007/s00204-014-1371-y
- Gautheron, J., and Jeru, I. (2021). The multifaceted role of epoxide hydrolases in human health and disease. *Int. J. Mol. Sci.* 22, 13. doi:10.3390/ijms22010013
- Gomes, J. V. D., Herz, C., Helmig, S., Forster, N., Mewis, I., and Lamy, E. (2021). Drug-drug interaction potential, cytotoxicity, and reactive oxygen species production of salix cortex extracts using human hepatocyte-like HepaRG cells. *Front. Pharmacol.* 12, 779801. doi:10.3389/fphar.2021.779801
- Gu, Q., Kong, Y., Schneede, J., Xiao, Y. B., Chen, L., Zhong, Q. J., et al. (2010). VKORC1-1639G>A, CYP2C9, EPHX1691A>G genotype, body weight, and age are important predictors for warfarin maintenance doses in patients with mechanical heart valve prostheses in southwest China. *Eur. J. Clin. Pharmacol.* 66, 1217–1227. doi:10.1007/s00228-010-0863-9
- Guenther, T. M., Cai, D. L., and Wallin, R. (1998). Co-purification of microsomal epoxide hydrolase with the warfarin-sensitive vitamin K-1 oxide reductase of the vitamin K cycle. *Biochem. Pharmacol.* 55, 169–175. doi:10.1016/s0006-2952(97)00431-0

Funding

This work was supported by the National Natural Science Foundation of China (81803930 and 81273936) and Youth Qihuang Scholars Support Project from National Administration of Traditional Chinese Medicine of China.

Acknowledgments

The authors thank all volunteers who participated in our clinical trial.

Conflict of interest

The authors declare that the research was conducted in the absence of any commercial or financial relationships that could be construed as a potential conflict of interest.

Publisher's note

All claims expressed in this article are solely those of the authors and do not necessarily represent those of their affiliated organizations, or those of the publisher, the editors and the reviewers. Any product that may be evaluated in this article, or claim that may be made by its manufacturer, is not guaranteed or endorsed by the publisher.

Supplementary material

The Supplementary Material for this article can be found online at: <https://www.frontiersin.org/articles/10.3389/fphar.2023.1105702/full#supplementary-material>

- Hasset, C., Aicher, L., Sidhu, J. S., and Omiecinski, C. J. (1994). Human microsomal epoxide hydrolase: Genetic polymorphism and functional expression *in vitro* of amino acid variants. *Hum. Mol. Genet.* 3, 421–428. doi:10.1093/hmg/3.3.421
- Hossain, S., Yousaf, M., Liu, Y., Chang, D. N., and Zhou, X. (2022). An overview of the evidence and mechanism of drug-herb interactions between propolis and pharmaceutical drugs. *Front. Pharmacol.* 13, 876183. doi:10.3389/fphar.2022.876183
- Hu, Y. X., You, H. M., Ren, C. Z., Hu, B. W., Zhang, L. J., Zhang, Y. D., et al. (2022). Proangiogenesis effects of compound danshen dripping pills in zebrafish. *BMC Complement. Med. Ther.* 22 (112), 112. doi:10.1186/s12906-022-03589-y
- Kovacevic, M. P., Lupi, K. E., Wong, A., Gilmore, J. F., and Malloy, R. (2019). Evaluation of the effect of apixaban on INR in the inpatient population. *J. Cardiovasc Pharmacol. Ther.* 24, 355–358. doi:10.1177/1074248419838502
- Lin, X. L., Chen, H., Ni, L., Yu, Y. Q., Luo, Z. R., and Liao, L. H. (2020). Effects of EPHX1 rs2260863 polymorphisms on warfarin maintenance dose in very elderly, frail Han-Chinese population. *Pharmacogenomics* 21, 863–870. doi:10.2217/pgs-2020-0054
- Liu, P., Yang, H., Long, F., Hao, H. P., Xu, X. J., Liu, Y., et al. (2014). Bioactive equivalence of combinatorial components identified in screening of an herbal medicine. *Pharm. Res.* 31, 1788–1800. doi:10.1007/s11095-013-1283-1
- Lv, C. X., Liu, C. X., Liu, J., Li, Z. Q., Du, X., Li, Y. F., et al. (2019). The effect of compound danshen dripping pills on the dose and concentration of warfarin in patients with various genetic polymorphisms. *Clin. Ther.* 41, 1097–1109. doi:10.1016/j.clinthera.2019.04.006
- Lv, C. X., Liu, C. X., Yao, Z. H., Gao, X. M., Sun, L. J., Liu, J., et al. (2017). The clinical pharmacokinetics and pharmacodynamics of warfarin when combined with compound danshen: A case study for combined treatment of coronary heart diseases with atrial fibrillation. *Front. Pharmacol.* 8, 826. doi:10.3389/fphar.2017.00826
- Mar, P. L., Gopinathannair, R., Gengler, B. E., Chung, M. K., Perez, A., Dukes, J., et al. (2022). Drug interactions affecting oral anticoagulant use. *Circ-Arrhythmia Electrophysiol.* 15, e007956. doi:10.1161/CIRCEP.121.007956
- McReynolds, C., Morisseau, C., Wagner, K., and Hammock, B. (2020). “Epoxy fatty acids are promising targets for treatment of pain, cardiovascular disease and other indications characterized by mitochondrial dysfunction, endoplasmic stress and inflammation,” in *Druggable lipid signaling pathways*. Editor Y Kihara (Cham: Springer International Publishing Ag), 71–99.
- Muyambo, S., Ndadza, A., Soko, N. D., Kruger, B., Kadzirange, G., Chimusa, E., et al. (2022). Warfarin pharmacogenomics for precision medicine in real-life clinical practice in southern africa: Harnessing 73 variants in 29 pharmacogenes. *Omiics* 16, 35–50. doi:10.1089/omi.2021.0199
- Nguyen, H. L., Yang, X., and Omiecinski, C. J. (2013). Expression of a novel mRNA transcript for human microsomal epoxide hydrolase (EPHX1) is regulated by short open reading frames within its 5'-untranslated region. *Rna* 19, 752–766. doi:10.1261/rna.037036.112
- Oesch, F., Jerina, D. M., and Daly, J. W. (1971). Substrate specificity of hepatic epoxide hydrazinase in microsomes and in a purified preparation: Evidence for homologous enzymes. *Archives Biochem. biophysics* 144, 253–261. doi:10.1016/0003-9861(71)90476-0
- Oesch, F. (1974). Purification and specificity of a human microsomal epoxide hydratase. *Biochem. J.* 139, 77–88. doi:10.1042/bj1390077
- Özer, M., Demirci, Y., Hizel, C., Sarikaya, S., Karalti, I., Kaspar, C., et al. (2013). Impact of genetic factors (CYP2C9, VKORC1 and CYP4F2) on warfarin dose requirement in the Turkish population. *Basic Clin. Pharmacol. Toxicol.* 112 (3), 209–214. doi:10.1111/bcpt.12024
- Pautas, E., Moreau, C., Gouin-Thibault, I., Golmard, J. L., Mahe, I., Legendre, C., et al. (2010). Genetic factors (VKORC1, CYP2C9, EPHX1, and CYP4F2) are predictor variables for warfarin response in very elderly, frail inpatients. *Clin. Pharmacol. Ther.* 87, 57–64. doi:10.1038/clpt.2009.178
- Reddy, V. P., Jo, H., and Neuhoof, S. (2021). Food constituent- and herb-drug interactions in oncology: Influence of quantitative modelling on Drug labelling. *Br. J. Clin. Pharmacol.* 87, 3988–4000. doi:10.1111/bcp.14822
- Saito, S., Iida, A., Sekine, A., Eguchi, C., Miura, Y., and Nakamura, Y. (2001). Seventy genetic variations in human microsomal and soluble epoxide hydrolase genes (EPHX1 and EPHX2) in the Japanese population. *J. Hum. Genet.* 46, 325–329. doi:10.1007/s100380170067
- Shen, G. M., Cui, W. D., Zhang, H., Zhou, F. B., Huang, W., Liu, Q., et al. (2017). Warfarin traps human vitamin K epoxide reductase in an intermediate state during electron transfer. *Nat. Struct. Mol. Biol.* 24, 69–76. doi:10.1038/nsmb.3333
- Shi, Y., Tang, L., Luo, F. M., Li, H., Pan, Z. X., Xu, G. G., et al. (2022). The diagnosis and management of allergic reactions caused by Chinese materia medica. *Clin. Rev. Allergy Immunol.* 62, 103–122. doi:10.1007/s12016-020-08812-7
- Suroowan, S., Abdallah, H. H., and Mahomoodally, M. F. (2021). Herb-drug interactions and toxicity: Underscoring potential mechanisms and forecasting clinically relevant interactions induced by common phytoconstituents via data mining and computational approaches. *Food Chem. Toxicol.* 156, 112432. doi:10.1016/j.fct.2021.112432
- Wang, Z. T., Xiang, X. Q., Liu, S. B., Tang, Z. J., Sun, H., Parvez, M., et al. (2021). A physiologically based pharmacokinetic/pharmacodynamic modeling approach for drug-drug interaction evaluation of warfarin enantiomers with sorafenib. *Drug Metab. Pharmacokinet.* 39, 100362. doi:10.1016/j.dmpk.2020.10.001
- Watabe, T., and Kanehira, S. (1970). Solubilization of epoxide hydrolase from liver microsomes. *Chem. Pharm. Bull.* 18, 1295–1296. doi:10.1248/cpb.18.1295
- Yan, J. Y., Ruan, P. P., Ge, Y. X., Gao, J., Tan, H. L., Xiao, C. R., et al. (2021). Mechanisms and molecular targets of compound danshen dropping pill for heart disease caused by high altitude based on network Pharmacology and molecular docking. *ACS Omega* 6, 26942–26951. doi:10.1021/acsomega.1c03282
- Zhang, L., Chen, W., and Gan, D. N. (2021). Analysis of the physiological and pathological factors of hospitalized patients taking warfarin and the correlation between drug interactions and warfarin efficacy. *Ann. Palliat Med.* 10, 5400–5406. doi:10.21037/apm-21-830
- Zhang, Y. F., Yang, M. B., Ho, N. J., Mok, R. Y., Zhang, Z., Ge, B. K., et al. (2020). Is it safe to take radix salvia miltiorrhiza - radix pueraria lobate product with warfarin and aspirin? A pilot study in healthy human subjects. *J. Ethnopharmacol.* 262, 113151. doi:10.1016/j.jep.2020.113151
- Zhuang, W., Liu, S. L., Zhao, X. S., Sun, N., He, T., Wang, Y. L., et al. (2021). Interaction between Chinese medicine and warfarin: Clinical and research update. *Front. Pharmacol.* 12, 751107. doi:10.3389/fphar.2021.751107

Frontiers in Pharmacology

Explores the interactions between chemicals and living beings

The most cited journal in its field, which advances access to pharmacological discoveries to prevent and treat human disease.

Discover the latest Research Topics

[See more →](#)

Frontiers

Avenue du Tribunal-Fédéral 34
1005 Lausanne, Switzerland
frontiersin.org

Contact us

+41 (0)21 510 17 00
frontiersin.org/about/contact



Frontiers in Pharmacology

